UNIVERSIDAD DE LA LAGUNA

DEPARTAMENTO DE QUÍMICA

APROXIMACIÓN MICROELECTROQUÍMICA A LOS FENÓMENOS DE CORROSIÓN: LA PASIVACIÓN DE METALES Y LA INHIBICIÓN DE LA CORROSIÓN METÁLICA POR MEDIO DE SUSTANCIAS ORGÁNICAS

Memoria para optar al grado de
DOCTOR EN QUÍMICA

JAVIER IZQUIERDO PÉREZ

La Laguna, 2014

UNIVERSIDAD DE LA LAGUNA
DEPARTAMENTO DE QUÍMICA

Memoria para optar al grado de
DOCTOR EN QUÍMICA

APROXIMACIÓN MICROELECTROQUÍMICA A LOS FENÓMENOS DE CORROSIÓN: LA PASIVACIÓN DE METALES Y LA INHIBICIÓN DE LA CORROSIÓN METÁLICA POR MEDIO DE SUSTANCIAS ORGÁNICAS

Realizada por

Javier Izquierdo Pérez

en

Departamento de Química, Universidad de La Laguna, España

Institut für Analytische und Bioanalytische Chemie, Universität Ulm, Ulm, Alemania

bajo la supervisión de

Profesor Sergio González González

Profesor Ricardo M. Souto Suárez

Profesor Juan J. Santana Rodríguez

La Laguna 2014

UNIVERSITY OF LA LAGUNA
DEPARTMENT OF CHEMISTRY

MICROELECTROCHEMICAL INVESTIGATION OF CORROSION PROCESSES: METAL PASSIVATION AND CORROSION INHIBITION BY ORGANIC SUBSTANCES

by

Javier Izquierdo Pérez

carried out at the

Department of Chemistry, University of La Laguna, Spain

Institute of Analytical and Bioanalytical Chemistry, University of Ulm, Ulm, Germany

Under the supervision of

Professor Sergio González González

Professor Ricardo M. Souto Suárez

Professor Juan J. Santana Rodríguez

in order to fulfill the legal requirements to obtain the academic title
Doctor in Chemistry

La Laguna 2014

AGRADECIMIENTOS / ACKNOWLEDGMENTS

A mis directores, por la gran apuesta que han hecho conmigo desde un principio, confiando en que hayan visto cumplidas sus expectativas sobre mí.

Al Departamento de Química Física, por el apoyo recibido de directivos, profesores, personal y compañeros, en pasillos, despachos o cafetería. También a miembros de áreas afines que han regalado su colaboración, tiempo y conocimiento.

A mi pareja (ella ha insistido en que pusiera "a mi churry"), por su apoyo incondicional, pese a las intermitentes y prolongadas ausencias.

A mis padres, en especial a mi madre, quien me recibía a diario, con frecuencia "exhausto de ciencia".

Por nombrar sólo a unos pocos de los muchos más que podría citar aquí, a mi hermana, madrina, familiares cercanos y amigos, incluyendo a aquellos que aunque físicamente estén lejos se les siente cerca.

Let me move into English to express my gratitude to those who have been my *family* during my stays abroad, with especial mention for colleagues at Pécs (Hungary) and Ulm (Germany).

Also to collaborators who have spent some time "playing" with our equipments in Tenerife, exchanging knowledge and experiences.

Danke

Grazie

Köszönöm

Mulţumiri

Obrigado

Thanks

سپاسگزارم

Gracias

LIST OF ABREVIATIONS AND SYMBOLS

a	Diameter of the tip microdisk
a_{Mg}	Activity of Mg^{2+} in solution
a_{Zn}	Activity of Zn^{2+} in solution
A/D	Analog / digital (referred to a signal converter)
AC	Alternating current
AE	Auxiliary electrode
AES	Auger electron spectroscopy
AFM	Atomic force microscopy
$BMIM^+$	1-butyl-3-methylimidazolium
BTA	Deprotonated benzotriazole
BTAH	Benzotriazole
CCLM	Cold crucible levitation melting
CP Ti	Commercially pure titanium
CPE	Constant phase element
CPP	Cyclic potentiodynamic polarization
CV	Cyclic voltammogram
CVD	Chemical vapour deposition
d	Tip-substrate distance
DC	Direct current (in opposition to alternating current)
E	Potential
E_{bp}	Pitting potential
EC	Equivalent circuit
EC-AFM	Electrochemically-controlled atomic force microscopy
EC-STM	Electrochemically-controlled scanning tunnelling microscopy
E_{corr}	Corrosion potential (open circuit potential)
EDOT	3,4-ethylenedioxythiophene
EDX	Energy-dispersive X-ray spectroscopy
$E_{lc\text{-}ISME}$	Potential of the liquid-contact ion-selective microelectrode
EMF	Electromotive force
E_{pass}	Passivation potential
EQMC	Electrochemical quartz crystal microbalance
E_{rp}	Repassivation potential
$E_{sc\text{-}ISME}$	Potential of the solid-contact ion-selective microelectrode
E_{tip}	Tip potential
f	Frequency of the AC signal
FIB	Focus ion beam
HER	Hydrogen evolution reaction
i	Current
i_{lim}	Limiting time-independent current measured in bulk solution with an UME
i_{max}	Maximum current measured at the tip during a given experiment

LIST OF ABREVIATIONS AND SYMBOLS (2)

ICP	Inductively coupled plasma
ISE	Ion-selective electrode
ISME	Ion-selective microelectrode
j	Current density
j_{corr}	Corrosion current density
j_{pass}	Passive current density
KEX	Potassium ethyl xanthate
KTFPB	Tetrakis(4-chlorophenyl)borate
LAMMA	Laser micro mass analysis
LEIS	Localized electrochemical impedance spectroscopy
LIA	Lock-in amplifier
MBI	2-mercaptobenzimidazole
MBTAH	5-methyl-benzotriazole
mV_{pp}	Amplitude of AC-voltage perturbation expressed in milivolts peak-to-peak
n_{dL}	Coefficient of the constant phase element related to the double layer
n_{ox}	Coefficient of the constant phase element related to the oxide layer
NDE	Negative difference effect
NHE	Normal hydrogen electrode
2-NPOE	2-nitrophenyl octyl ether
OA	Operational amplifier
OCP	Open circuit potential
OES	Optical emission spectroscopy
PE-	Plasma enhanced-
pMg	-log ($\gamma_{Mg}[Mg^{2+}]$)
PP	Potentiodynamic polarization
PPM	Potentiodynamic polarization methods
PTFE	Polytetrafluoroethylene
PVC	Poly(vinyl-chloride)
pZn	-log ($\gamma_{Zn}[Zn^{2+}]$)
Q_{dL}	Constant phase element related to the double layer
Q_{ox}	Constant phase element related to the passive layer
RE	Reference electrode
R_{ct}	Resistance of the charge transference process at an electrified interface
R_{ISME}	Internal resistance of the ion-selective microelectrode
R_k	Resistor employed in the determination of R_{ISME}
R_{ox}	Resistance of the oxide layer (passive layer)
R_{sol}	Ohmic resistance of the solution

LIST OF ABREVIATIONS AND SYMBOLS (3)

SCE	Saturated calomel electrode
SECM	Scanning electrochemical microscopy
SEM	Scanning electron microscopy
SG-TC	Substrate generation – tip collection
SIET	Scanning ion-electrode technique
SIMS	Secondary ion mass spectrometry
SKP	Scanning Kelvin probe
SS	Stainless steel
SPM	Scanning probe microscopy
SRET	Scanning reference electrode technique
STM	Scanning tunneling microscopy
SVET	Scanning vibrating electrode technique
TEM	Transmission electron microscopy
THF	Tetrahydrofurane
TRIS	Tris(hydroxymethyl)aminomethane
U_k	Steady state potential value attained in the measurement of R_{ISME}
UME	Ultramicroelectrode
XPS	X-ray photoelectron spectroscopy
XRD	X-ray diffraction
[Z]	Impedance modulus
γ	Activity coefficient
ΔU	Voltage drop produced in the measurement of R_{ISME}
Φ	Phase angle of impedance
ω	Angular frequency (= 2 π f) of the AC signal

INDEX

CAPÍTULO 1

Introducción

Index

1.1

Motivation of this thesis

1.1.1. Abstract

The corrosion resistance of metallic materials is primarily derived from the development of passive films on their surface formed by oxides and oxy-hydroxides of the metal. Their adhesion and chemical stability in the environments they are exposed to will determine their ability to counteract the driving force to corrosion. Furthermore, these surface films maybe modified through the interaction of organic molecules which may operate as corrosion inhibitors when they contribute to the formation of more resistant surface films [1], or they effectively originate a barrier film on the surface of the material, physically separating it from the aggressive environment [2,3]. The organic compounds may either be dissolved in the electrolyte or adsorbed on the metal surface. In this Thesis the interaction of model inhibitors with metal surfaces was further investigated in order to establish the stability of the passive oxy-hydroxide surface layers and their modification by organic molecules. Special attention was devoted to the analysis of local effects and surface distribution by the combination of scanning microelectrochemical techniques such as the the scanning electrochemical microscope (SECM) and the scanning vibrating electrode technique (SVET). New operation modes including the use of potentiometric monitoring using ion-selective electrodes (ISE), application of AC potential signals to the scanning probe (AC-SECM), or the association with atomic force microscopy (AFM), have been implemented so as to detect local differences in electrochemical activity in the metal surface.

1.1.2. Resumen

La resistencia a la corrosión de los materiales metálicos se deriva principalmente del desarrollo de películas pasivas en su superficie, formadas por óxidos y oxi-hidróxidos del metal. Su adhesión y estabilidad química a los ambientes a los que se exponen determinará su habilidad para contrarrestar la tendencia a la corrosión. Más aún, esas películas superficiales pueden ser modificadas a través de su interacción con moléculas orgánicas que pueden actuar como inhibidores de corrosión al contribuir a la formación de películas superficiales más resistentes [1], u originar barreras físicas efectivas mediante una película depositada en la superficie del metal, separándolo de forma efectiva del ambiente agresivo [2,3]. Los compuestos orgánicos pueden bien estar disueltos en el electrolito o bien adsorberse en la superficie del metal. En esta Tesis se ha continuado investigando la interacción de inhibidores modelo con superficies metálicas, con el fin de establecer la estabilidad de la capa pasiva superficial de oxi-hidróxidos y su modificación por moléculas orgánicas. Se ha prestado especial atención al análisis de los efectos locales y su distribución espacial a través de la combinación de técnicas de barrido microelectroquímicas tales como la microscopía electroquímica de barrido (SECM) y la técnica de barrido del electrodo vibrante (SVET). Para ello se han desarrollado nuevos modos de operación, incluyendo el uso de la potenciometría usando electrodos de ión-selectivo (ISE), la aplicación de señales de potencial AC en el sensor de barrido (AC-SECM), o su asociación con la microscopía de fuerzas atómicas (AFM), favoreciendo la detección de diferencias locales en la actividad electroquímica de la superficie metálica.

1.1.3. Introducción

La Electroquímica suministra procedimientos muy poderosos para el estudio de las reacciones que tienen lugar en interfases, particularmente aquellas relacionadas con las transformaciones en procesos corrosivos. De hecho, una gran parte del conocimiento adquirido sobre los distintos procesos corrosivos tiene su origen en el uso de métodos electroquímicos en el laboratorio. Sin embargo, las reacciones de corrosión se inician a escalas nano y micrométrica, por lo que es necesario generar datos experimentales a esos niveles para lograr una comprensión adecuada de los aspectos mecanísticos de estas reacciones. Desafortunadamente las técnicas electroquímicas convencionales no poseen discriminación espacial, por lo que aportan muy poca información sobre el comportamiento de los sistemas en los lugares en los que se inicia la corrosión o en defectos. Por ello se ha hecho necesario el desarrollo de otras técnicas de elevada resolución lateral que puedan adquirir datos experimentales en tiempo real, y puedan así generar evidencias que apoyen los hechos conocidos o aporten nueva información sobre los mecanismos de las reacciones que se producen.

En esta Tesis se ha intentado desarrollar nuevos procedimientos y metodologías experimentales dirigidos a la investigación de las etapas iniciales de los mecanismos de corrosión en base al empleo de microscopías de proximidad en operación electroquímica. Como sistemas experimentales se han seleccionado el régimen de pasividad y los procesos de inicio de formas localizadas de corrosión en metales en régimen de pasividad, con el objetivo de esclarecer la acción específica de las diversas variables químicas operativas en el sistema. La resistencia frente a la corrosión de los materiales metálicos se deriva primariamente del desarrollo de películas pasivas sobre su superficie las cuales están formadas por óxidos y oxi-hidróxidos del metal. Su adhesión y su estabilidad química frente a los ambientes a los que están expuestas determinan su habilidad para contrarrestar la tendencia a la corrosión.

También se ha considerado el acoplamiento galvánico de metales, utilizado frecuentemente para aumentar la resistencia anticorrosiva de sistemas metálicos como en el caso de la galvanización de los aceros, o inevitable en el caso de las soldaduras; o bien como constituyente del material por contener éste inclusiones o mezclas de fases en su microestructura, que por otro lado son necesarias para garantizar unas propiedades mecánicas óptimas.

Además, las características fisicoquímicas de las películas superficiales pasivas pueden modificarse a través de la interacción de moléculas orgánicas que pueden actuar como inhibidores de la corrosión cuando éstas contribuyen a la formación de películas superficiales más resistentes, o bien originan una película de barrera sobre la superficie del material que separa de forma efectiva al metal del medio agresivo. Los compuestos orgánicos pueden encontrarse bien disueltos en la fase electrolítica (inhibidores convencionales) o adsorberse sobre la superficie del metal. Por ello, en esta Tesis también se ha investigado la interacción de

inhibidores con la superficie de un metal, el cobre, tomado como sistema modelo para obtener información más detallada relativa a la estabilidad de las moléculas orgánicas, así como de la composición química y estructura de las películas superficiales formadas sobre los electrodos metálicos.

Para abordar estos objetivos, se han empleado el microscopio electroquímico de barrido (SECM) y la técnica de barrido del electrodo vibrante (SVET), y se ha explorado la aplicación de nuevos desarrollos consistentes en el empleo de microelectrodos selectivos como sondas para la operación potenciométrica, la superposición de señales de corriente alterna con la operación en modo AC (AC-SECM), o la combinación con la microscopía de fuerzas atómicas (AFM) para aprovechar la elevada resolución topográfica de esta técnica dotándole de sensibilidad química (AFM-SECM).

1.1.4. Justificación del trabajo.

El ataque corrosivo de los materiales expuestos a la atmósfera supone un coste económico en el orden de miles de millones de euros al año [4], y su impacto se extiende más allá de las valoraciones económicas a consideraciones de índole ambiental (la pérdida de los materiales conlleva la necesidad de consumo de materias primas para su reposición, en tanto que durante el proceso corrosivo se liberan en el ambiente sustancias químicas altamente contaminantes), o de bienestar social (infraestructuras y sistemas pueden alcanzar estados en los que dejan de ser utilizables, además de los riesgos que puede generar el colapso o fallo durante su vida operativa).

Aunque un trozo de metal permanece estable durante un periodo de tiempo casi indefinido si se conserva en el vacío, éste se altera y pierde sus buenas propiedades mecánicas cuando, sin protección alguna, permanece en contacto con el aire. La superficie se oxida y desprende las películas de óxido o se disuelve. La corrosión de los materiales metálicos es un proceso interfacial, de naturaleza electroquímica, pues las reacciones de corrosión se producen en la interfase que se establece entre el metal y el medio al que se expone [5,6]. De esta manera tienen lugar procesos superficiales de transferencia de carga eléctrica, en su fundamento semejante al que tiene lugar en una pila. Por tanto, en la mayoría de los casos se trata de un fenómeno de naturaleza electroquímica, y como tal puede ser medida, estudiada y caracterizada por empleo de técnicas y métodos electroquímicos. Debido a la aplicación de las técnicas electroquímicas convencionales se han logrado importantes avances en el ámbito de la Ciencia de la Corrosión, especialmente en base a la aplicación de técnicas de corriente alterna, y posteriormente con la introducción de técnicas de análisis de superficies, las cuales aportan información complementaria sobre la estructura y composición de las superficies en las que se produce el ataque corrosivo [7]. De esta manera, se ha

avanzado en la construcción del conocimiento fundamental que corresponde a la comprensión de los mecanismos y los fenómenos participantes, que pudiera permitir el control efectivo de los procesos corrosivos.

Sin embargo, las técnicas electroquímicas convencionales, incluyendo la espectroscopía de impedancias electroquímica (EIS), y las técnicas analíticas de caracterización superficial, realizan un promediado del comportamiento de la superficie expuesta, como si ésta fuera homogénea. Sin embargo, los sistemas metálicos suelen presentar numerosas inhomogeneidades a nivel superficial debidas a la existencia de granos, sistemas multifase, o incluso defectos derivados de los propios procesos de formación o de posterior tratamiento de las muestras. Además, la existencia de procesos en las reacciones de corrosión que ocurren a escala microscópica es lo que ha justificado que se considerara tradicionalmente que los procesos de corrosión se inician realmente en el rango de los nanómetros y los micrómetros, aún cuando no se dispusiera de las herramientas adecuadas para realizar estudios en estas dimensiones.

La reciente introducción de las microscopías de proximidad bajo operación electroquímica en el laboratorio de corrosión está posibilitando la superación de estas limitaciones en el estudio de problemas de corrosión. En este proceso es necesario el desarrollo de nuevas metodologías y procedimientos que permitan su aplicación a la solución de estos problemas. Por su amplia incidencia así como elevado interés fundamental, tres son los problemas de corrosión en los que su empleo está especialmente indicado [7].

1. *Pasividad y corrosión localizada*. La mayoría de los materiales metálicos se emplean en un estado de pasividad, esto es, una situación en la que la velocidad de corrosión es muy baja debido a la interposición de una película de óxido creada por la reacción del metal con el medio [5,6]. Esta película actúa como una barrera muy eficaz frente a la migración iónica, de manera que retarda la velocidad con la que los iones metálicos pasan a la fase disolución, a pesar de la existencia de una muy grande fuerza energética que favorece el avance de la corrosión. Desafortunadamente, se puede producir la despasivación local del material si el régimen de pasividad se pierde para dar lugar a procesos de corrosión localizada, lo que es un fenómeno muy frecuente para una amplia variedad de materiales metálicos [8]. Ello ocurre cuando tales materiales se encuentran en contacto con disoluciones acuosas que contienen especies promotoras de estas formas de corrosión, particularmente la influencia de ciertos iones agresivos que pueden encontrarse presentes en el medio, entre las que destacan especialmente los iones cloruro. Durante la corrosión localizada la mayoría del metal permanece pasivo, determinándose una velocidad de corrosión muy baja, pero en zonas aisladas se desarrollan picaduras, de dimensiones microscópicas en sus inicios, pero que eventualmente progresan hasta alcanzarse la destrucción del material por perforación [5,9].

Aunque las causas responsables del inicio de la despasivación de los metales pueden ser muy diversas, se ha podido establecer una serie de características

comunes, entre las que cabe destacar que los procesos de corrosión localizada solo tienen lugar sobre superficies que continuarían estando pasivas de no haberse iniciado éstos, y además, que la velocidad de la corrosión localizada, una vez iniciada, es muy rápida. Los procesos de corrosión localizada están conformados por etapas de nucleación y de propagación separadas, consistiendo fundamentalmente en la ruptura del régimen de pasividad o despasivación las primeras, mientras que las segundas corresponden al proceso de corrosión subsiguiente propiamente dicho [10]. Aunque en la literatura científica se puede encontrar un número muy elevado de estudios dirigidos al análisis de las causas responsables de la corrosión localizada por picado, e incluso de los mecanismos de propagación de las picaduras de corrosión una vez se han iniciado [10-15], hasta el momento no se ha podido establecer un modelo único que permita describir el conjunto de observaciones realizadas, lo cual se deriva fundamentalmente del escaso conocimiento que se tiene todavía de las etapas iniciales del proceso relacionadas con la despasivación o nucleación de las picaduras de corrosión, las cuales ocurren en dimensiones de escala microscópica. Es decir, la cuestión acerca de qué sea concretamente lo que origina la nucleación de una picadura sigue sin conocerse.

2. *Corrosión bimetálica*. La corrosión galvánica o bimetálica es una forma de corrosión que ocurre cuando dos metales diferentes se acoplan o entran en contacto eléctrico entre sí [6,16]. Bajo estas condiciones se produce simultáneamente el deterioro acelerado del metal del par que sea menos noble (con un potencial de corrosión menos positivo) y la protección catódica total o parcial del metal con potencial más noble. Este principio se emplea para la protección de metales por medio de capas de conversión y capas metálicas, entre las que la combinación de uso tecnológico más frecuente es el procedimiento de galvanizado de aceros.

El potencial de corrosión de los dos metales, M_A y M_B, en el medio a estudiar proporciona información de la dirección del flujo de electrones transferidos [6]. Si el potencial de corrosión de M_A es más positivo que el de M_B, la transferencia de electrones será de M_B a M_A, lo que conlleva que la velocidad de corrosión de M_B aumente y la de M_A decrezca, de manera más acentuada que si se comparara con la velocidad de corrosión de los metales si no estuvieran conectados. Pero el potencial de corrosión, en ningún caso, proporciona información alguna de la cinética del proceso corrosivo que tiene lugar.

Aunque estos sistemas se suelen describir en términos de mecanismos homogéneos de corrosión, la posible existencia de inhomogeneidades a nivel micrométrico y sub-micrométrico no se ha podido descartar hasta el presente.

3. *Empleo de inhibidores de la corrosión*. Otro tema de gran interés en la investigación en Ciencia y Tecnología de la Corrosión lo constituyen los métodos de inhibición de la corrosión metálica. En este proyecto se persigue obtener información básica acerca de los mecanismos por los que se produce la inhibición de la corrosión metálica. Para ello se considerarán los efectos que las especies

inhibidoras generan sobre la cinética y el mecanismo de formación de las capas pasivas sobre el metal, responsables de modificaciones químicas y eléctricas del sustrato metálico.

Puesto que el origen de los procesos corrosivos, a pesar de su evidente diversidad, tiene lugar en escalas micrométricas y submicrométricas, se requiere del uso de métodos e instrumentación apropiadas para lograrse una resolución espacial elevada. La investigación de la corrosión en la **nanoescala** se puede realizar con las microscopías de efecto túnel y de fuerzas atómicas en operación en celda electroquímica, EC-STM y EC-AFM respectivamente. Estos estudios se orientan fundamentalmente a los procesos de reorganización superficial que tienen lugar durante la electrodisolución de metales (pudiéndose situar el inicio de esta metodología científica en los trabajos de los grupos del profesor Philippe Marcus en París sobre la estructura de superficies pasivadas en aleaciones Fe-Cr o monocristales de Ni [17-19], y del profesor Roger Behm en Ulm para el cobre [20-22]); y la investigación de las interacciones entre átomos y moléculas con la superficie de metales, particularmente orientados a la caracterización de sistemas inhibidores de la corrosión [23,24].

Las técnicas nanoscópicas también encuentran utilidad en el laboratorio de corrosión como métodos de nanoindentación, por medio de los cuales se pueden producir defectos locales de geometría localizada tanto en películas poliméricas protectoras aplicadas sobre metales como recubrimientos anticorrosivos con propiedades de barrera, así como para producir pérdidas locales del régimen de pasividad en metales pasivos. De esta forma, se intenta progresar en el estudio de los procesos de delaminación de metales pintados [25,26], y en los procesos de repasivación de metales [27,28].

Por otra parte, las técnicas de proximidad electroquímicas son un conjunto de técnicas que permiten el análisis *in situ* de la reactividad y funcionalidad de superficies a partir de medidas electroquímicas, físicas o químicas sobre el metal o en la interfase metal-electrolito. De esta manera se definen tres grupos de técnicas [29]:

1. Sondeo *in situ*: la sonda se introduce en el electrolito realizándose una medida local electroquímica sobre la que se aplican las leyes cinéticas convencionales de la electroquímica. Se incluyen en este grupo la técnica del electrodo de referencia de barrido (SRET), la técnica de barrido del electrodo vibrante (SVET), y la espectroscopía de impedancia electroquímica localizada (LEIS) [30]. En términos de cinética de la corrosión, la técnica de mayor interés al presente es la técnica SVET pues permite la medida de densidades de corriente locales en la fase electrolítica. La sonda que vibra es un electrodo de pseudo-referencia que oscila a una frecuencia característica respecto a la superficie objeto de estudio. La vibración de la punta sensible bajo un campo de potencial convierte el campo DC en una señal AC cuya frecuencia específica puede seleccionarse con un amplificador detector de fase. De esta manera se pueden medir gradientes de potencial del rango de nV, lo que está especialmente indicado para detectar

distribuciones de potencial locales, como las que se presentan cuando hay defectos, o medir las corrientes que fluyen en una muestra metálica como consecuencia de la separación de las regiones anódicas y catódicas durante un proceso de corrosión. Esta técnica, introducida por Hugh Isaacs y colaboradores en Brookhaven [31], ha encontrado una gran utilidad en la caracterización de los procesos de corrosión bajo pinturas anticorrosivas a partir de cortes laterales [32-34], en la caracterización de procesos de corrosión bimetálica [35,36], y en los procesos de corrosión localizada de metales pasivos a partir de inclusiones [37].

2. Medidas electroanalíticas *in situ* con ultramicroelectrodos. Es el caso de la microscopía electroquímica de barrido (SECM) que permite analizar los cambios que se producen en el electrolito en torno a lugares localizados de corrosión [38,39]. Los cambios en el electrolito pueden producirse en relación a procesos redox (SECM convencional) [40] o en su conductividad (AC-SECM) [41]. Hasta ahora su uso mayoritario en el laboratorio de corrosión se ha dirigido a la inducción de procesos localizados de corrosión al modificarse localmente la composición del electrolito [38].

3. Microceldas electroquímicas: en ellas se emplea un volumen muy reducido de electrolito [43]. De esta manera, la exposición selectiva de una muy pequeña porción de la muestra, aunque permite seleccionar dominios microestructurales, conlleva la limitación de ignorar los acoplamientos entre los distintos dominios presentes, los cuales están operativos en un sistema corrosivo.

Aunque actualmente las técnicas microelectroquímicas de proximidad operan en la escala de los micrómetros, ya se ha logrado alcanzar resoluciones submicrométricas gracias a la fabricación de sondas cada vez más finas. Por otra parte, se ha introducido recientemente una técnica combinada AFM-SECM muy poderosa, pues a nivel nanoscópico permite tanto la monitorización de los procesos corrosivos como su inducción, bien a través de la nanoindentación con el AFM, o de la modificación de las condiciones locales del electrolito con el SECM. En este caso se logra una muy poderosa sinergia de las potencialidades de las dos técnicas [44-46].

1.1.5. Objetivos.

Aparte de los costes que se generan al forzar la detención de la maquinaria industrial, la corrosión consume ingentes cantidades de materiales y la energía requerida para producirlos. De hecho, el funcionamiento de la mayoría de los componentes materiales de uso en nuestra sociedad tecnológica está limitado finalmente por la corrosión. Por ello la investigación en el ámbito de la Ciencia de la Corrosión se orienta, entre otros, al conocimiento de los mecanismos de corrosión y pasivación, la ruptura localizada de las películas pasivas y la nucleación de formas localizadas de corrosión, las interacciones superficiales responsables de la

adsorción de especies orgánicas que actúan como inhibidores de la corrosión y la formación de películas superficiales protectoras, y al desarrollo de métodos de vida remanente de los materiales, para lo que también se desarrollan y ponen a punto nuevos métodos instrumentales que permitan detectar y monitorizar los múltiples procesos microscópicos que tienen lugar en las superficies electródicas.

Los objetivos generales de una investigación microelectroquímica de los fenómenos de corrosión son los siguientes:

- Entender, a escala micrométrica y sub-micrométrica, los mecanismos de las reacciones superficiales que gobiernan la corrosión de los materiales metálicos así como su inhibición.

- Desarrollar nuevas metodologías experimentales que permitan avanzar en una resolución mayor nivel espacial, temporal y químico, de los procesos corrosivos.

- Establecer la relación entre la comprensión a nivel microscópico de las reacciones superficiales y las manifestaciones macroscópicas de la corrosión.

Entre los procesos corrosivos que se han considerado en este estudio se incluyen la disolución anódica (el paso de átomos del metal desde la superficie al medio electrolítico, lo que constituye la reacción fundamental de la corrosión), la pasivación (la formación sobre la superficie metálica de una capa delgada, de espesor de unos pocos nanometros, de óxido u oxi-hidróxido que protege a la superficie del metal frente a más disolución/corrosión), la ruptura de la pasividad (ruptura localizada de la película pasiva) que conlleva al establecimiento de procesos de corrosión localizada, el acoplamiento galvánico (formación de microceldas por diferencias locales de potencial en una estructura o microestructura), y la inhibición de la corrosión (interacción de moléculas orgánicas con superficies metálicas desnudas u oxidadas, y formación de películas superficiales modificadas).

1.1.6. Referencias:

1. V. Fox Martínez. Estudio Electroquímico, XPS y SEM de la Inhibición de la Corrosión del Cobre por Benzotriazol, 5-Metil-1H-benzotriazol, Mercaptobencimidazol y Etilxantato de Potasio. Tesis doctoral, Universidad de La Laguna, 1996.
2. Y. González García. Degradación de Recubrimientos Anticorrosivos Poliméricos Aplicados sobre Materiales Metálicos: Estudio Electroquímico y Nanoscópico. Tesis doctoral. Universidad de La Laguna, 2007.
3. J.A. Gongález Guzmán. Protección Frente a la Corrosión Metálica con Recubrimientos Poliméricos: Estudio Electroquímico y Microelectroquímico. Tesis doctoral. Universidad de La Laguna, 2010.
4. M.V. Biezma, J.R. San Cristóbal. Corrosion Engineering Science and Technology 40 (2005) 344.

5. L.L. Shreir, R.A. Jarman, G.T. Burstein (Editores). Corrosion. Buttherworth-Heinemann, Oxford, 1994.
6. D.A. Jones. Principles and Prevention of Corrosion, 2ª edición. Prentice Hall, Nueva York, 1996.
7. P. Marcus, F. Mansfeld (Editores). Analytical Methods in Corrosion Science and Engineering. CRC Press, Boca Raton, 2006.
8. Z. Szklarska-Smialowska. Pitting Corrosion of Metals. NACE, Houston, 1986.
9. P. Marcus, J. Oudar (Editores). Corrosion Mechanisms in Theory and Practice. Marcel Dekker, Nueva York, 1995.
10. P.C. Pistorius, G.T. Burstein. Philosophical Transactions of the Royal Society London A341 (1992) 531.
11. P. Forchhammer, H.J. Engell. Werkstoffe und Korrosion 20 (1969) 1.
12. D.E. Williams, C. Westcott, M. Fleischmann. Journal of the Electrochemical Society 132 (1985) 1796.
13. U. Bertocci, M. Koike, S. Leigh, F. Qiu, G. Yang. Journal of the Electrochemical Society 133 (1986) 1782.
14. L. Stockert, H. Böhni. Materials Science Forum 44-45 (1989) 313.
15. D.E. Williams, J. Stewart, P.H. Balkwill. Corrosion Science 36 (1994) 1213.
16. D.L. Piron. The Electrochemistry of Corrosion. NACE, Houston, 1991.
17. P. Marcus. Electrochimica Acta 43 (1998) 109.
18. M. Legrand, B. Diawara, J.-J. Legendre, P. Marcus. Corrosion Science 44 (2002) 773.
19. I. Frateur, L. Lartundo-Rojas, C. Méthivier, A. Galtayres, P. Marcus. Electrochimica Acta 51 (2006) 1550.
20. R.M. Vogt, A. Lachenwitzer, O.M. Magnussen, R.J. Behm. Surface Science 399 (1998) 49.
21. J. Scherer, O.M. Magnussen, T. Ebel, R.J. Behm. Corrosion Science 41 (1999) 35.
22. O.M. Magnussen, L. Zitzler, B. Gleich, R.M. Vogt, R.J. Behm. Electrochimica Acta 46 (2001) 3725.
23. E. Szöcs, Gy. Vastag, A. Shaban, G. Konczos, E. Kálmán. Journal of Applied Electrochemistry 29 (1999) 1339.
24. E. Szöcs, I. Bakó, T. Kosztolányi, I. Bertóti, E. Kálmán. Electrochimica Acta 49 (2004) 1371.
25. M.R. VanLandingham, S.H. McKnight, G.R. Palmese, X. Huang, T.A. Bogetti, R.F. Eduljee, J.W. Gillespie, Jr. Journal of Adhesion 64 (1997) 31.
26. M.S. Bischel, M.R. VanLandingham, R.F. Eduljee, J.W. Gillespie, Jr., J.M. Schultz. Journal of Materials Science 35 (2000) 221.
27. J. Li, D.J. Meier. Journal of Electroanalytical Chemistry 454 (1998) 53.
28. T. Yamamoto, K. Fushimi, M. Seo, S. Tsuri, T. Adachi, H. Habazaki. Electrochemistry Communications 9 (2007) 1672.
29. R. Oltra. En: Local Probe Techniques for Corrosion Research (Editado por R. Oltra, V. Maurice, R. Akid, P. Marcus). Woodhead Publishing, Cambridge, 2007, p. 1.
30. R.S. Lillard. En: Analytical Methods in Corrosion Science and Engineering (Editado por P. Marcus, F. Mansfeld). CRC Press, Boca Raton, 2006, p. 571.
31. H.S. Isaacs, Y. Ishikawa, Journal of the Electrochemical Society 132 (1985) 1288.

32. I. Sekine. Progress in Organic Coatings 31 (1997) 73.
33. V.J. Gelling, D.E. Tallman, G.P. Bierwagen. Journal of the Electrochemical Society 147 (2000) 3667.
34. M. Khobaib, A. Rensi, T. Matakis, M.S. Donley. Progress in Organic Coatings 41 (2001) 266.
35. H.S. Isaacs. Corrosion Science 28 (1988) 547.
36. C.R. Crowe, R.G. Kasper. Journal of the Electrochemical Society 133 (1986) 879.
37. V. Vignal, H. Krawiec, O. Heintz, R. Oltra. Electrochimica Acta 52 (2007) 4494.
38. J.W. Still, D.O. Wipf. Journal of the Electrochemical Society 144 (1997) 2657.
39. R.M. Souto, Y. González-García, S. González. Corrosion Science 47 (2005) 3312.
40. A.J. Bard, M.V. Mirkin (Editores). Scanning Electrochemical Microscopy, 2ª edición. CRC Press, Boca Raton, 2012.
41. K. Echard, H. Shin, B. Mizaikoff, W. Schuhmann, C. Kranz. Electrochemistry Communications 9 (2007) 1793.
42. C. Gabrielli, S. Joiret, M. Keddam, H. Perrot, N. Portail, P. Rousseau, V. Vivier. Electrochimica Acta 52 (2007) 7706.
43. T. Sutter, H. Böhni. En: Analytical Methods in Corrosion Science and Engineering (Editado por P. Marcus, F. Mansfeld). CRC Press, Boca Raton, 2006, p. 649.
44. M. Janotta, D. Rudolph, A. Kueng, C. Kranz, H.-S. Voraberger, W. Waldhauser, B. Mizaikoff. Langmuir 20 (2004) 8634.
45. A. Davoodi, J. Pan, C. Leygraf, S. Norgren. Applied Surface Science 252 (2006) 5499.
46. K. Eckhard, C. Kranz, H. Shin, B. Mizaikoff, W. Schuhmann. Analytical Chemistry 79 (2007) 5435.

Chapter 2

Scanning microelectrochemical techniques: a highly sensitive route to evaluate degradation reactions and protection methods with chemical selectivity

Index

2.1

Introduction

2.1.1. Motivation

Electrochemistry provides a powerful means of studying interfacial reactions, in particular corrosion transformations. Indeed, a major part of the current knowledge of corrosion processes has been gained from the use of electrochemical methods in the corrosion laboratory. But corrosion reactions are initiated within the range of nanometers and micrometers, and a comprehensive understanding of the mechanistic aspects of corrosion requires the synthesis of data obtained in those scales. Unfortunately, conventional electrochemical techniques lack spatial resolution and provide little information on behaviour at sites of corrosion initiation or at defects. Thus, there is need for ancillary techniques with enhanced spatial resolution which can acquire data in real time, and can provide corroborative or other novel evidence of the underlying reaction schemes.

The recent advent of a number of local probe techniques is greatly contributing to overcome those limitations when applied to the investigation of corrosion processes *in situ*. Investigators have explored a wide variety of methods to characterize local electrochemical processes, which range from the design of microelectrochemical cells and setups to the use of scanning probe techniques [1].

2.1.2. Methodology

This chapter provides a brief presentation of scanning microelectrochemical techniques available for the *in situ* investigation of corrosion processes, with special attention to their measuring principles and operation modes. In all cases, the spatial resolution is attained by rastering the appropriate probe in close vicinity of the investigated surface, allowing to compare local responses in different regions. Either topographical, chemical, or combinations of both kinds of information, may be gathered by adequate selection of the technique employed for a given system.

2.1.3. References

1. Analytical Methods in Corrosion Science and Engineering (Edited by P. Marcus, F. Mansfeld). CRC Press, Boca Raton, 2006.

2.2

Scanning microelectrochemical techniques: principles and operation modes

2.2.1 Abstract

Knowledge about the morphology and chemical activity of heterogeneous materials in micrometer and submicrometer scales is crucial for the comprehensive understanding of the mechanistic aspects of degradation and the development of new material properties for highly specified protection. They require the synthesis of data obtained from a number of experimental techniques. Similarly, the stability of surface layers and their resistance against degradation from electrochemical experiments can be complemented by procedures that reveal the chemical activity and morphology associated with the dynamics and changes occurring during the course of these experiments. Several methods, employing different probes and measuring principles, are currently available for application to processes in corrosion science.

2.2.2 Resumen

El conocimiento de la morfología y la actividad química a escalas micrométrica y submicrométrica de los materiales heterogéneos resulta crucial para una mejor comprensión de los mecanismos responsables de su degradación, y para el desarrollo de materiales con nuevas propiedades que posean una protección específica elevada. Para ello es necesaria la síntesis de datos adquiridos usando combinaciones de técnicas experimentales con distintos niveles de resolución. Asimismo, la estabilidad de las capas superficiales y su resistencia frente a la degradación estudiada mediante técnicas electroquímicas puede complementarse con otros procedimientos instrumentales, que revelen la actividad química y la morfología asociadas a la dinámica y los cambios que ocurren durante el curso de los experimentos. Actualmente están disponibles varios métodos, que emplean diferentes sensores y principios de medida para su aplicación al estudio de procesos de interés de la Ciencia de la Corrosión.

2.2.3. Introduction

In conventional electrochemical experiments such as cyclic voltammetry or electrochemical impedance spectroscopy, both heterogeneous rate constant of electron transfer for adsorbed or dissolved species and kinetics of homogeneous coupled chemical reactions can be determined from the analysis of current and potential variations of the electrode [1,2]. Whatever the measurable quantity, it reflects the reactivity of the whole electrode surface. In other words, the analysis implicitly assumes that the electrochemical behaviour of the interface is uniform. However, electrodes rarely exhibit such an ideal behaviour and the electrode response to a perturbation signal corresponds to an average measurement over the whole electrode surface. In addition, the geometry of the electrode should also be taken into account. For instance, in the case of a disk electrode embedded in an insulator, which is the most popular electrode geometry used by electrochemists, the potential distribution over the disk electrode is not uniform under the conditions where the current density is uniform and, similarly, the current distribution is not uniform under the primary condition where the solution potential is uniform [3,4].

These observations remain valid when the electrode is made of a corroding material. Generalized corrosion is usually described as uniform reactivity of a metal or an alloy, and from the determination of the kinetics of dissolution, it is intended to predict the lifetime corrosion resistance of a metal material. For example, iron and zinc corrode uniformly in a diluted sulphuric acid solution by forming the oxidized species Fe^{2+} and Zn^{2+}, respectively. From a practical point of view, the risk of generalized corrosion remains usually foreseeable from the analysis of the Pourbaix' diagrams showing the electric potential of metal in the presence of thermodynamically-stable corrosion products as a function of the pH of the aqueous solution. Conversely, localized corrosion processes such as pits and crevices, corrosion by cracks, or biocorrosion correspond to attacks on a small surface area of the metal surface. In these cases, the local dissolution of the metal is associated with the initiation and the evolution of either one or several active sites that are scattered over the whole surface, and thus forming an electrode having an overall heterogeneous reactivity. Moreover, these types of corrosion remain very difficult to predict and can quickly propagate in-depth in the bulk of the material depending on the chemical nature of the corrosive media. For example, the passive layer formed on an iron electrode is very sensitive to the presence of halide ions, particularly the chloride species [5-7].

With the development of scanning microelectrochemical techniques it has become possible to gain information about the physical dimensions and morphology of materials, simultaneously providing additional information on their surface chemical activity with a resolution in the micrometer range or below. Such dimensions can be reached by the use of microelectrodes and due to the major improvement of electronics, devices allowing small current measurements are

fabricated. Images with high spatial resolution are thus obtained that provide information on the specific effect of pollutants and the effectiveness of surface layer modifications for materials preservation at microscale.

2.2.4. The scanning vibrating electrode technique (SVET)

The scanning vibrating electrode technique is based upon the measurement of potential field distributions in the electrolyte surrounding an electrochemically-active surface. The sensing probe employed to scan the surface of the material under investigation is a vibrating pseudo-reference electrode.

2.2.4.1. The technique

The scanning vibrating electrode technique (SVET) is known since 1950, a method originally devised by biologists for the measurement of extracellular currents around living cells [8-11]. But it was only in the seventies that it was applied to the investigation of corrosion processes for the first time [12,13].

The SVET is a technique that allows the detection of ionic currents in a solution caused by a concentration gradient. It is based in the detection of electric fields generated in the proximity of a reacting surface with respect to the value obtained in the bulk electrically-neutral solution. The electric field is zero when the solution is at rest, but if there is a gradient of concentration caused by either a source or a sink of ions, potential distributions occur in the solution. Since this potential is solely affected by the electric charge produced by ions arising or being consumed, it can be employed as a direct measurement of the ionic current and ionic gradients appearing over a reacting surface by application of the Ohm's law. In the case of corrosion, production of metal cations and degradation of the material take place at the anodic sites via equation:

$$M \rightarrow M^{z+} + n\, e^{-} \qquad (2.2.1)$$

The release of the metal cations generate positive current density values around the anodes, while the electrons produced in this half-cell reaction flow to adjacent cathodic areas (see Figure 2.2.1).

This flow of electrons through the metal is supported by a flow of ionic current in the electrolyte, which in turn causes potential gradients to exist in the solution close to sites of localized corrosion. The electrons produce the reduction of the oxidant, usually oxygen in aerated aqueous environments at neutral and alkaline pH via equation (2.2.2), or by protons at low pH following the reaction scheme (2.2.3). The half-cell reactions at the cathodic sites lead to the occurrence of negative current densities in the electrolyte due to either the generation of hydroxyl ions (2.2.2) or the consumption of protons (2.2.3):

$$O_2 + H_2O + 4\,e^- \rightarrow 4\,OH^- \qquad (2.2.2)$$

$$2\,H^+ + 2\,e^- \rightarrow \uparrow H_2 \qquad (2.2.3)$$

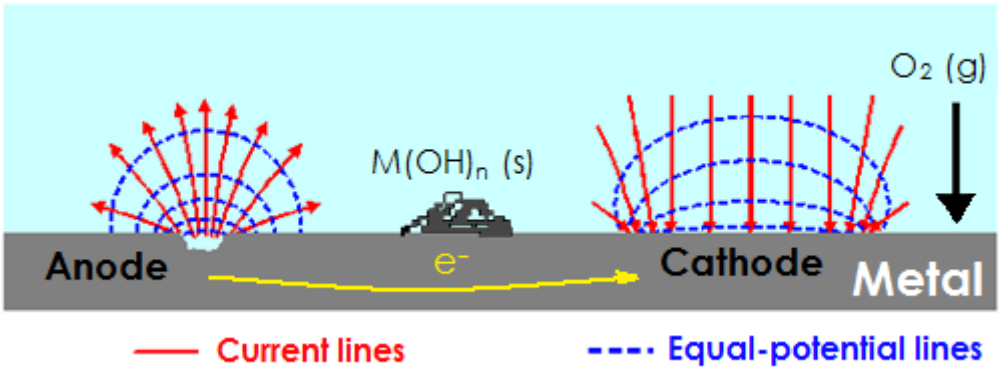

Figure 2.2.1. Scheme of current lines and equal-potential lines, which arise from a corroding metal exposed to a neutral aqueous solution.

However, these gradients in the solution are so small that they cannot be detected using conventional techniques. The scanning vibrating electrode technique uses a microelectrode fixed in the solution and another vibrating microelectrode that scans the surface to measure these gradients *in situ*. Measurement is made by vibrating a fine tip microelectrode at an optimized frequency, usually in a plane perpendicular to the surface, thus letting it go in and out of the equal-potential lines generated over the substrate (cf. Figure 2.2.2).

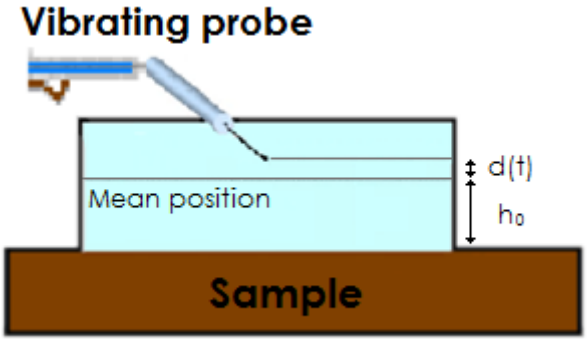

Figure 2.2.2. Sketch of the scanning vibrating electrode technique. The Pt microelectrode is vibrated perpendicular to the surface of the investigated substrate while immersed in a solution of low conductivity.

The electrochemical potential of the microelectrode is recorded at the extremes of the vibration amplitude, resulting in the generation of an oscillating potential AC sinusoidal signal with the same frequency than the vibration, which is given by:

$$h(t) = h_0 + d\,\mathrm{sen}(\Omega t) \qquad (2.2.4)$$

where *d* is the amplitude of the microelectrode vibration, Ω is the angular frequency of the vibration, and h_0 is the average distance between the electrode and the sample. Then this signal is measured using a *lock-in* amplifier, which is tuned to the frequency of probe vibration. The measured potential variation, ΔV, can be related with the ionic currents by use of the equation:

$$I = \frac{E}{\rho} = \frac{1}{\rho}\frac{\Delta V}{\Delta r} \qquad (2.2.5)$$

where *E* is the electric field measured between two points of the solution, ρ is the resistivity of the solution, and Δr the distance between the two extremes or vibration amplitude of the microelectrode.

2.2.4.2. The setup

A scheme of the main components of the technique is shown in Figure 2.2.3. The scanning vibrating electrode instrument is basically constituted by: (1) the electrochemical cell; (2) the piezo-oscillator system which produces the vibration of the microelectrode; (3) two *lock-in* amplifiers that measure and filter the signal produced in the probe; (4) tri-axial motors to control with precision the movement and the position of the vibrating probe; and (5) the computer, interface and display system.

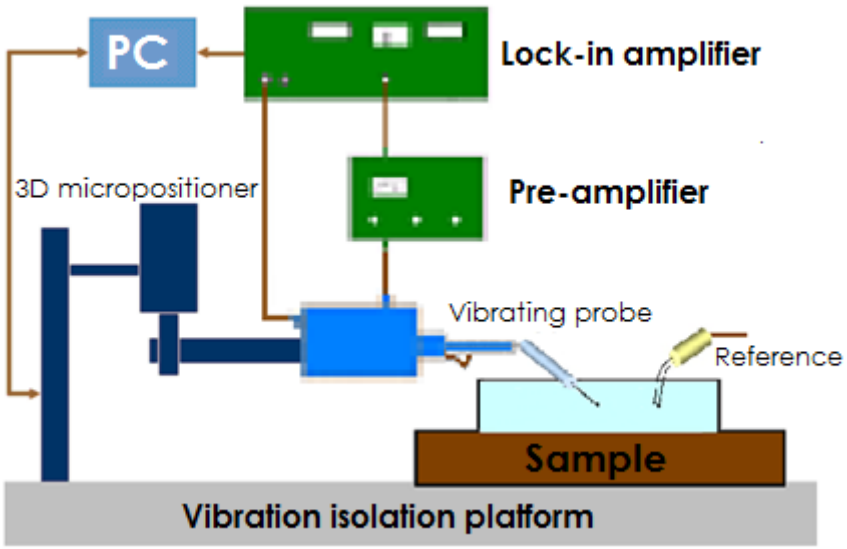

Figure 2.2.3. Scheme of the basic components of an SVET equipment, including those of the electrochemical cell and their general function.

The electrochemical cell consists of the vibrating and fixed microelectrodes, the reference electrode, and the sample. Figure 2.2.3 also shows the distribution of the elements in the cell. Despite the achieved great sensitivity, the used vibration can obviously interfere in the measurement by stirring the solution, and a limitation in

the spatial resolution becomes critical. Measurements at the very close vicinity from the surface might seem interesting since we are more likely to locally resolve phenomena taking place on each of the microcells, which may occur very close one to another. But if the surrounding media is agitated at such small probe-substrate distances, homogenization of the electrolyte through convection takes place. Thus, it is mandatory to minimize the vibration in order to resolve the separated half-cell processes [14].

2.2.5. The scanning ion-selective electrode technique (SIET)

Scanning ion-selective electrode technique (SIET) works as a micro-potentiometric tool allowing measurements of specific ions at a quasi-constant micro-distance over an active surface in solution. Potentiometric measurements are performed in a two-electrode galvanic cell configuration under zero current conditions. A potentiometric cell is composed of a reference electrode and an ion-selective microelectrode.

2.2.5.1. The technique

The glass-capillary microelectrode with liquid membrane was introduced by life scientists [15]. Since then, microbiologists have continued developing instrumentation and experimental approaches for micro-potentiometric research. Today, glass-capillary microelectrodes are well-established analytical tools. The principles of experimental work with microelectrodes are summarized in [28,29]. Glass-capillary microelectrodes are filled with a selective ionophore-based oil-like membrane to a length comprised between 10 to 100 μm. The diameter of the orifice of an ion-selective glass-capillary microelectrode varies from 0.1 to 5 μm. The microelectrode also comprises an inner reference electrolyte and an Ag/AgCl wire inserted into the electrolyte to provide a reference electrode. Calibration of the ion-selective microelectrode must be performed before and after measuring a sample to correlate the results to the Nernst equation:

$$E_i = E_i^0 + \frac{RT}{z_i F} \ln a_i \qquad (2.2.6)$$

where F is the Faraday constant, R is the universal gas constant and T is the absolute temperature. The calibration of the electrodes is recorded as potential, E_i, vs. time dependence with sequential increase of ion activity, a_i. The selectivity of a microelectrode can be determined using a modified separate solution method which involves calibration of the electrode in solutions of the main ion and then of the interfering ion [13,17].

2.2.5.2. The setup

A SIET device contains an ion-selective microelectrode mounted on a 3D computerized stepper-motors system, used to position and move the microelectrode over the sample. The sample in turn is placed on a movable holder where a reference electrode (e.g. Ag/AgCl mini-electrode) is also mounted. A video camera equipped with a long-distance lens providing magnification up to 400 times is located over the sample. The potential difference measured in the potentiometric cell is amplified and digitalized.

In a recent publication [18], Lamaka *et al.* disclosed the experimental setup for combined SVET-SIET measurements. A dual head stage micromanipulator allowed for precise positioning (±1 μm) of two microprobes, and ASET software (ScienceWares) enabled sequential reading of SVET and SIET data channels.

2.2.6. The scanning electrochemical microscope (SECM)

The scanning electrochemical microscope (SECM) was designed in 1989 by Bard and co-workers [19] by coupling scanning probe techniques with electrochemistry. Since then, the SECM has become a very powerful technique for probing a great variety of electrochemical reactions, due to the combination of its high spatial resolution and its electrochemical sensitivity. The SECM is based in the reaction that occurs on the surface of a mobile ultramicroelectrode (UME) immersed in an electrolyte solution. The UME is rastered in close proximity to a solid surface to characterize the topography and redox activity of the solid/liquid interface. This latter feature is very important, because it allows SECM to gain information concerning reactions that take place in the solution space between the tip and the sample, as well as on those occurring on the surface of the scanned sample [20]. Thus, the scanning electrochemical microscope can be employed for chemical microscopic imaging, which is especially relevant towards the investigation of corrosion and degradation processes, as well as to measure the efficiency of protection procedures for materials [21,22].

2.2.6.1. The technique

The SECM is a technique in which a current flows through a microelectrode immersed in an electrolytic solution and situated close to a substrate. The substrate can either be a conductive, semiconductive or insulating material. The microelectrode and the substrate form part of an electrochemical cell which also contains a reference (RE) and an auxiliary electrode (AE), with the microelectrode as the working electrode, and sometimes the substrate as a second working electrode (Figure 2.2.4A).

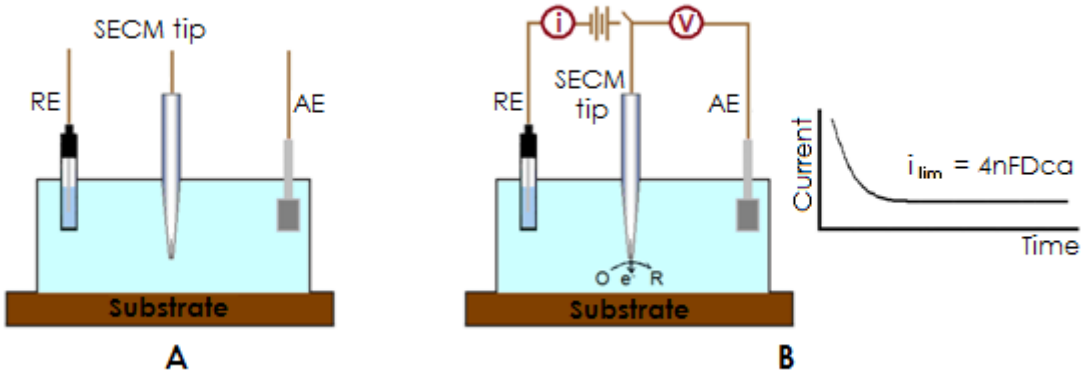

Figure 2.2.4. Sketch of an electrochemical scanning microscope. (A) The UME is immersed in a solution containing a redox species *O*. (B) The potential at the UME is set to a value at which the species *O* can be reduced to *R* under diffusion limiting conditions. The current trace recorded at the UME in the later condition is also given.

Prior to explaining the operation and the response of the SECM, it is necessary to understand the behaviour of the microelectrode inside an electrochemical cell. Let us consider that the microelectrode is immersed in a solution containing an electrolyte and a reducible species, *O*. When a potential sufficiently negative to the standard potential of the reduction reaction (2.2.7) is applied to the microelectrode, the reduction of the species *O* occurs at the UME surface, and a cathodic current flows according to:

$$O + ne^- \leftrightarrow R \qquad (2.2.7)$$

If this reaction is kinetically controlled by the diffusion of *O* from the bulk of the solution to the electrode surface, the current decays due to the formation of a diffusion layer of *O* around the electrode, and attains rapidly a steady-state value. A steady-state current (see Figure 2.2.4B) results from the constant flux of *O* to the electrode surface due to an expanding hemispherical diffusion layer around the microelectrode. In a conventional electrode disk (i.e., for a big ratio between the electrode surface and the electrolyte volume) semi-infinite planar diffusion is attained [23,24], as it is shown in the scheme of Figure 2.2.5A. But, when the electrode surface is smaller than the solution volume, the diffusion process becomes dependent on the size and geometry of the electrode [25,26] (see Figure 2.2.5B). The diffusive regime is the characteristic feature of microelectrodes in this case.

In the later condition, the diffusion problem is determined by the spherical character of the electrode, and the mass transport process is dominated by radial spherical diffusion. The current attains a time-independent steady state value (i_{lim}) given by the following expression [25]:

$$i_{lim} = \frac{nFADc}{r_0} \qquad (2.2.8)$$

where F is the Faraday constant, r_0 the microelectrode radius, D the diffusion coefficient of the reducible species, c its concentration, n the number of transferred electrons and A is the geometrical electrode area. In this case, the steady state response is typical of radial diffusion and arises because the electrolysis rate is equal to the rate at which molecules diffuse to the electrode surface.

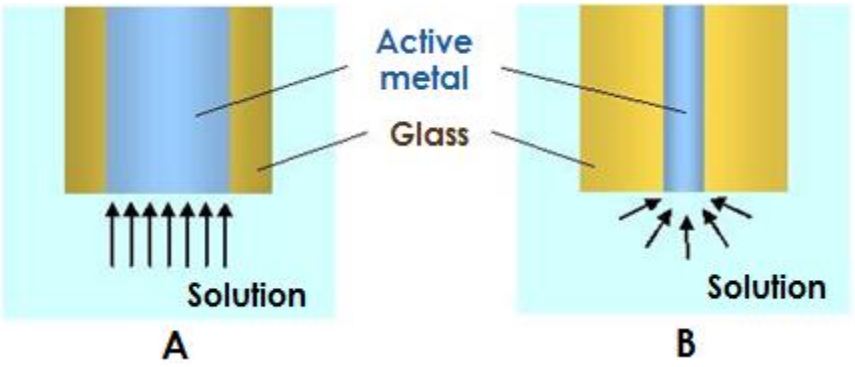

Figure 2.2.5. Scheme of the geometry and diffusion field for (A) conventional electrode, and (B) microelectrode.

Typically, a microelectrode probe is a disk embedded in an infinite insulating plane. The steady-state solution for the microdisk electrode of radius r_0 has been obtained [27], and the limiting steady-state current is given by:

$$i_{lim} = 4nFDcr_0 \qquad (2.2.9)$$

The measurements at an UME, and therefore the measurements at an SECM tip, are no affected by stirring or other convective effects. In SECM, the proximity of the tip to the substrate is the perturbation in the measurement that constitutes the SECM response [19]. If the UME is brought to the vicinity of an insulating substrate, the steady-state current that flows through the tip, i, tends to be smaller than i_{lim} (Figure 2.2.6A).

This is a result of the insulating substrate partially blocking the diffusion of O towards the tip [28]. The current at the tip becomes smaller when the tip is closer to the substrate, and tends to zero when the distance between tip and substrate, d, approaches zero. This effect is known as negative feedback.

In contrast, if the tip is close to a conductive substrate at which the oxidation reaction (2.2.10) can occur, a flux of O from the substrate to the tip occurs, in addition to some flux from the bulk solution towards the tip.

$$R \leftrightarrow O + ne^- \qquad (2.2.10)$$

This effect leads to an enhancement of the current at the tip, i, which is higher than i_{lim} (Figure 2.2.6B). Then the flux of O from the substrate to the tip causes an increase of i_T as d decreases. In this case, when the tip-substrate distance approaches zero, the i_T current tends to infinite, and the oxidation of R on the substrate is diffusion-controlled. This effect is named positive feedback. The tip can be seen as both the

generator of the signal sensing the substrate (the flux of the reduced species, *R*), and the detector (of the flux of *O* from the substrate).

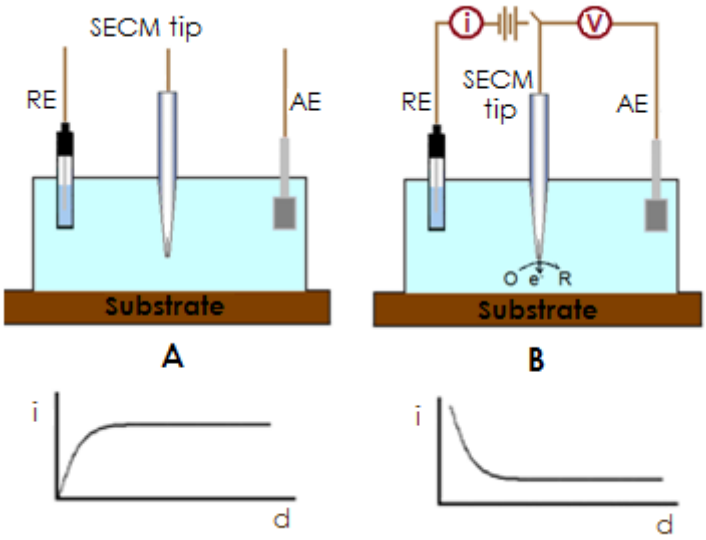

Figure 2.2.6. Basic principle of SECM: (a) Negative feedback: the tip is near an insulating substrate that hinders the diffusion of species *O*. (b) Positive feedback: the tip is located near a conductive substrate where the oxidation of species *R* occurs.

2.2.6.2. Operation modes

The SECM can be employed to image the surfaces of different types of substrates, both insulators and conductors, immersed in solutions. In this case, the SECM operates in the feedback mode. Then, it is necessary an oxidizable/reducible species in the solution which is known as redox mediator (cf. Figure 2.2.7). Generally, redox couples involving a fast, usually one-electron, heterogeneous reaction at the tip are chosen as electrochemical mediators. In this mode, the SECM tip is rastered in the *X-Y* plane of the surface of the sample inside an electrochemical cell. The faradaic current measured at the tip is controlled by diffusion of the mediator, and depends strongly on the tip-sample separation. The variations in the measured current originate from changes in the tip-sample distance and therefore, they are related to the topography of the sample. In the case of an insulator surface such as a non-conductive polymer coating, the diffusion of the redox mediator from the bulk solution to the tip surface becomes progressively hindered as the tip approaches the surface (i.e., negative feedback effect). The diffusion-hindered current is thus directly related to the tip-substrate distance *d*.

Topography imaging is often determined with the SECM operating in the *constant height* mode. In this way, the tip is lowered to a fixed distance from the substrate and then the surface is scanned. In this case, the currents measured at the tip can be directly converted to a height or distance scale. The resolution of the SECM in topographic measurements on a surface strongly depends on the tip radius, *a*, and the dimensions of the shielding insulator around the active surface (*RG* factor).

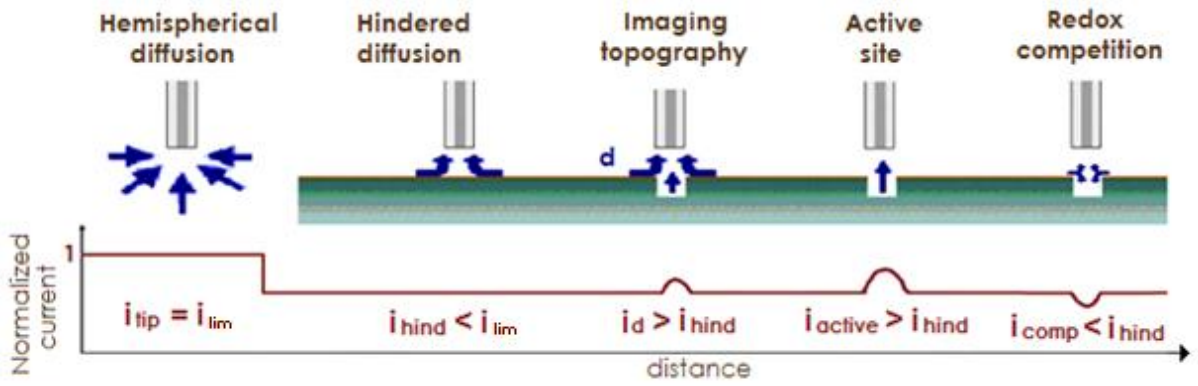

Figure 2.2.7. Operation modes of a SECM and corresponding current responses, expressed as a normalized quantity. Arrows represent the flow of the electroactive species to the SECM tip.

The SECM can be employed as an electrochemical tool to study electrode processes and coupled homogeneous reactions by using the generation-collection operating modes. In the substrate generation – tip collection mode, the tip current is used to monitor the flux of electroactive species from the substrate. This configuration is applied in some cases to determine concentration profiles above a substrate electrode. On the other hand, the SECM can be used in the tip generation – substrate collection mode, in which the substrate monitors the flux generated from the tip. This mode is useful in studies of homogeneous reactions that occur in the tip-substrate gap. Figure 2.2.7 depicts the basic principle of the SECM used in either the substrate generator – tip collector mode for an active site on the otherwise insulating surface.

A variation of the substrate generator – tip collector mode consists in the use of ion-selective microelectrodes (ISME) as the tip. Potentiometric operation results as the potential signal determined at the ISME is directly proportional to the activity (concentration) of a certain chemical ionic species. This method offers greater detection selectivity, and does not modify the local chemistry because no redox conversion is required for monitoring.

A new situation occurs when the same redox species can react at both the tip and the substrate, thus originating a competition for the species between them. In the redox competition mode, the substrate monitors smaller currents than in the corresponding feedback mode due to the partial consumption of the redox mediator at the substrate, this effect becoming increasingly noticeable at smaller tip-substrate distances (see Figure 2.2.7).

2.2.6.3. The setup

The SECM instrument basically consists of a combination of electrochemical components, positioners and computer control. Figure 2.2.8A shows a schematic diagram of the basic SECM instrument employing an amperometric microprobe. The

SECM is a technique in which a faradaic current flows through a microelectrode immersed in an electrolytic solution and situated close to a substrate. The microelectrode and the substrate form part of an electrochemical cell which is also constituted by reference and auxiliary electrodes, and sometimes by a second working electrode. The electrochemical setup is composed by this electrochemical cell together with the bipotentiostat, which is the actual electrochemical interface. It allows the potential of the microelectrode and/or the substrate versus the reference electrode to be controlled, as well as to measure the current flowing between any of the working electrodes and the counter electrode. The microelectrode is a microdisk, in which the active material is surrounded by an insulating shield. The most common procedure for its fabrication is the encapsulation of the electrode material (carbon fibers or noble metal wires) in glass capillaries and the subsequent polishing of the tips to expose the microdisk surface. The microelectrode displacement and its position relative to the substrate are controlled with a three-dimensional microstage that provides independent and accurate control in the *X-Y-Z* axis. The remaining component is the data acquisition and display system, usually conformed by a computer, an interface and a display system. Details on the geometric characterization of the microelectrode tip, and on the operation procedures in amperometric SECM are given in reference [20].

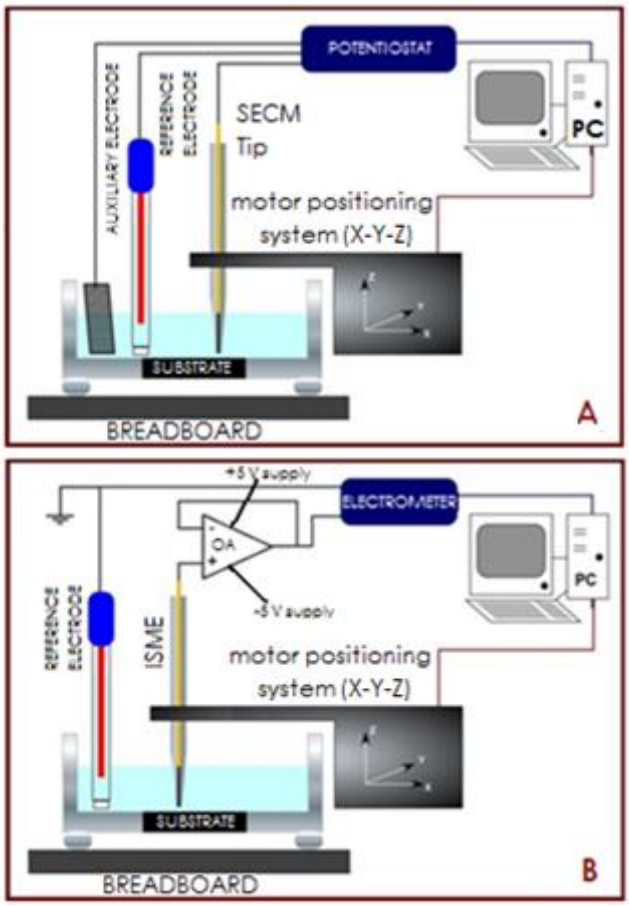

Figure 2.2.8. Sketches showing the main components of the instruments employed for (A) amperometric, and (B) potentiometric SECM measurements, including the high input impedance operational amplifier (OA), and the ion-selective electrode (ISME).

The same SECM instrument can be employed for the potentiometric measurements, though in this case a 10^{12} Ω input impedance operational amplifier must be introduced in the measuring circuit as shown in Figure 2.2.8B. The voltage data developed at the ISME are now collected through the electrometer included in the electrochemical interface (potentiostat/galvanostat).

2.2.7. The alternating-current scanning electrochemical microscope (AC-SECM)

SECM measurements are typically carried out in a DC amperometric mode. Faradaic detection schemes rely on the electrochemical conversion of a redox species in solution to produce a current at the mobile ultramicroelectrode. This current changes in proximity to the studied interface, providing rich information about the topography and reactivity of that interface. Alternatively, SECM measurements can also be carried out under AC amperometric conditions. The theoretical basis of such measurements was given by Horrocks *et al.* [29] but since then only a few papers in this area appeared in the literature until 2004, which may be regarded the origin of AC-SECM. Meanwhile, Alpuche-Aviles and Wipf [30] used AC impedance to generate a feedback signal for scanning electrochemical microscopy, but they monitored changes in the impedance caused by a faradaic process of a redox couple added to the studied solution, so, in fact, their feedback control was very similar to one used in classical SECM measurements. Schuhmann and coworkers [31-33] showed for the first time that under AC conditions SECM imaging can be performed without any redox mediator present in solution. Bringing the electrode tip nearer to the surface of a non-conductive substrate causes an increase in the electrode impedance (due to a change in the solution resistance), and in the case of conductive substrates the trend, in general, is the opposite (although complicated by the interfacial properties of the conductive surface under the tip). Etienne *et al.* [33] described an elegant method that allows the imaging of mixed substrates (containing conductive and nonconductive areas) to a very high resolution under alternating current conditions.

2.2.7.1. The technique

The main experimental difference between AC-SECM and conventional amperometric SECM operations is the fact that an alternating rather than a constant potential is applied to the working electrode. Generally, this is achieved either by a function generator or the internal oscillator of a lock-in amplifier (LIA) sending a sinusoidal wave function to the potential input of the potentiostat. The resulting current –naturally alternating at the same frequency– is detected and the current output of the potentiostat is fed into the signal input of the LIA. AC detection schemes generally display a low noise level due to the frequency-selective amplification of the lock-in technique. The LIA output signal representing the

alternating current signal consists of one value for the current magnitude $|i|$ as well as one value for the phase angle θ by which the sinusoidal current wave is shifted with respect to the perturbation voltage. Thus, the current can also be regarded as a vector in the complex plane with real I' and imaginary part I''. Alternating current is directly proportional to the admittance Y (conductance) and inversely proportional to the impedance Z.

The solution resistance varies with the tip-sample distance as follows:

$$\frac{R(\infty)}{R(d)} = \frac{i(d)}{i(\infty)} \qquad (2.2.11)$$

where $R(\infty)$ is the resistance with the tip positioned in bulk solution, $R(d)$ the resistance at a tip-sample separation of d, $i(d)$ the current at a separation of d, and $i(\infty)$ the current measured in bulk solution. Hence, the normalised conductance approach curve, $R(\infty)/R(d)$, towards an insulating sample follows the amperometric SECM feedback theory [34]. The absolute tip-sample distance can thus be obtained by fitting the conductance, $R(\infty)/R(d)$, to the theoretic curves of $i(d)/i(\infty)$ for the negative amperometric feedback [29].

Figure 2.2.9A illustrates that both the conductance measured in the AC-SECM experiment and the diffusion-limited current from the amperometric feedback theory show a negative feedback response. For a conducting sample a positive feedback-type response is obtained (see Figure 2.2.9B) no matter whether the sample was connected as counter electrode or simply left at open circuit. Although the latter approach curves do not readily fit the theory of the amperometric positive feedback, still the tip-sample distance could be calibrated using the conductance measurement. Thus, any sensor electrode that does not display sufficient distance sensitivity itself could be positioned precisely at known distances from the surface [29].

Although the AC-signal does carry information on the local electroactivity of the sample surface, and the approach curve resembles the one of an amperometric positive feedback, it does so for entirely different reasons; and despite the similar terminology the two concepts should not be confused. As in AC-SECM a positive feedback-type response is observed during the approach to an electrically conducting sample and approaching an insulating sample results in a negative feedback-type response, it is capable to distinguish conducting and non-conducting sites from one another [29]. Thus, if the tip electrode is placed within the near-field distance to the sample, a thin electrolyte film is formed between the surface and the electrode. As the sample blocks the current lines, the resistance increases. However, if the tip electrode is placed above a large conductive sample, the detected solution resistance may decrease. The current always chooses the least resistive pathway; the presence of an electrically conducting surface allows the re-direction of the current through the sample. Since it is an alternating current, no actual electron transfer across the solid/liquid interface has to occur. The lower resistance of the pathway through the sample compared to the surrounding solution causes the current to increase in a positive feedback-type behaviour.

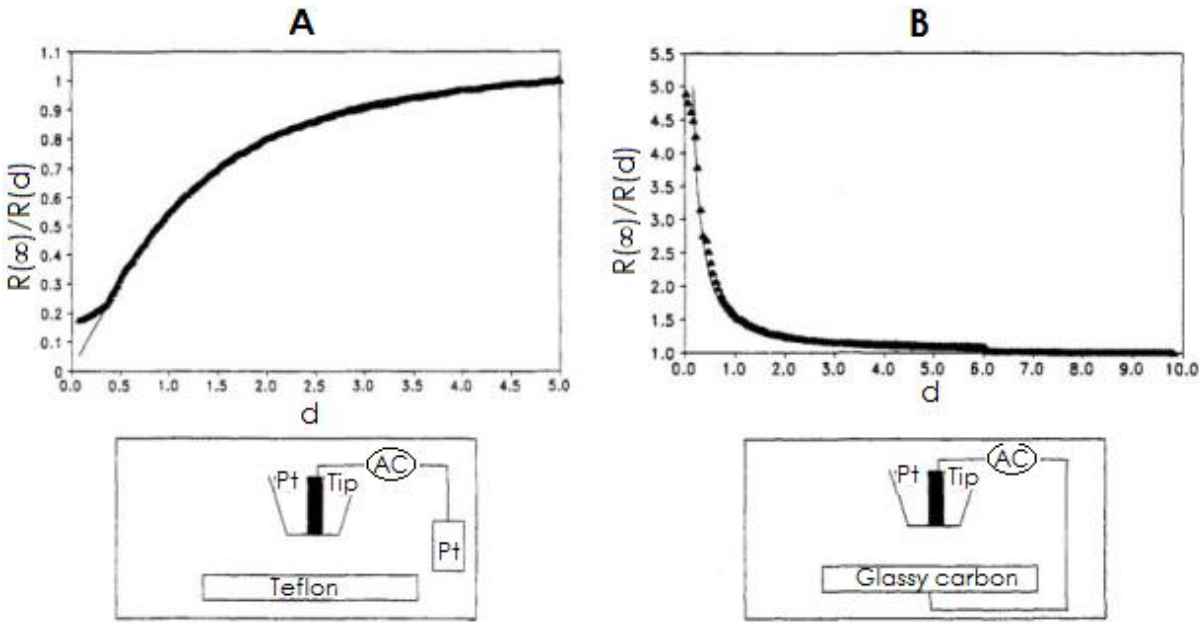

Figure 2.2.9. (A) Conductance-distance curve for a 25 μm diameter platinum UME over a Teflon surface in 1 mM KCl; (B) conductance-distance curve for a 10 μm diameter platinum UME over a glassy carbon surface in 1 mM KCl. Filled triangles are experiment and solid lines are theory [29].

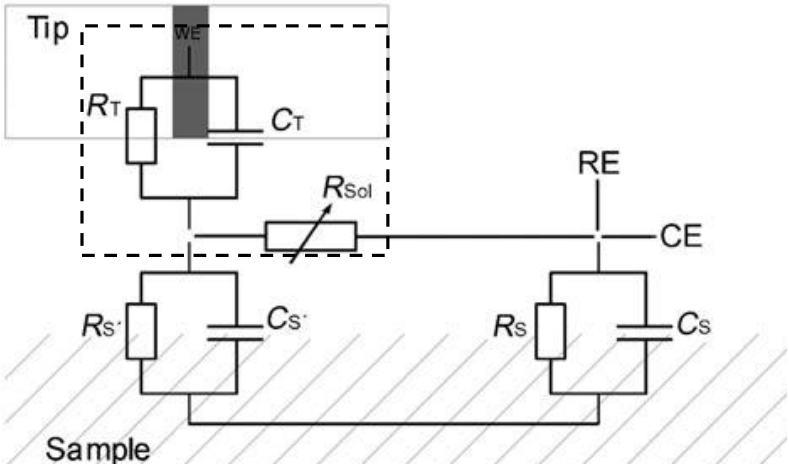

Figure 2.2.10. Equivalent circuit representing the impedance behaviour of the system [35]. R_T and C_T are resistance and capacitance of the tip, respectively; R_{sol} is the solution resistance; R_S and C_S are the resistance and capacitance of the sample, respectively; $R_{S'}$ and $C_{S'}$ are the local resistance and capacitance of the sample at the specific area covered by the AC-SECM tip.

These observations can be explained in terms of the equivalent circuit shown in Figure 2.2.10 [35]. The dotted box in the figure gives the equivalent circuit that applies for a conductive surface exposed to a low conductivity environment. The equivalent circuit consists of the resistance and the capacitance of the tip, R_T and C_T respectively; and the solution resistance R_{sol}. Since R_{sol} changes with the absolute Z

distance between the tip and the sample surface, this is the origin of the near-field response observed in the system. Thus, depending on the applied frequency and the electrochemical characteristics of the surface, the current will preferentially flow through one of the pathways depicted in the figure depending on their corresponding impedances. In this case, the capacitive impedance dominates over the solution impedance while it varies inversely with the frequency of the AC excitation. The negative feedback type effect is observed when the frequency of the signal is smaller than the reversal of the time constant for the interfacial impedance, whereas a positive feedback effect will be observed for frequencies equal or greater than that time constant.

2.2.7.2. The setup

A schematic representation of the instrumentation required for AC-SECM operation is given in Figure 2.2.11. It is built by modifying a conventional SECM instrument to introduce a lock-in amplifier (LIA) that is used both to send a sinusoidal wave function to the potential input of the potentiostat, and to detect the current output of the potentiostat.

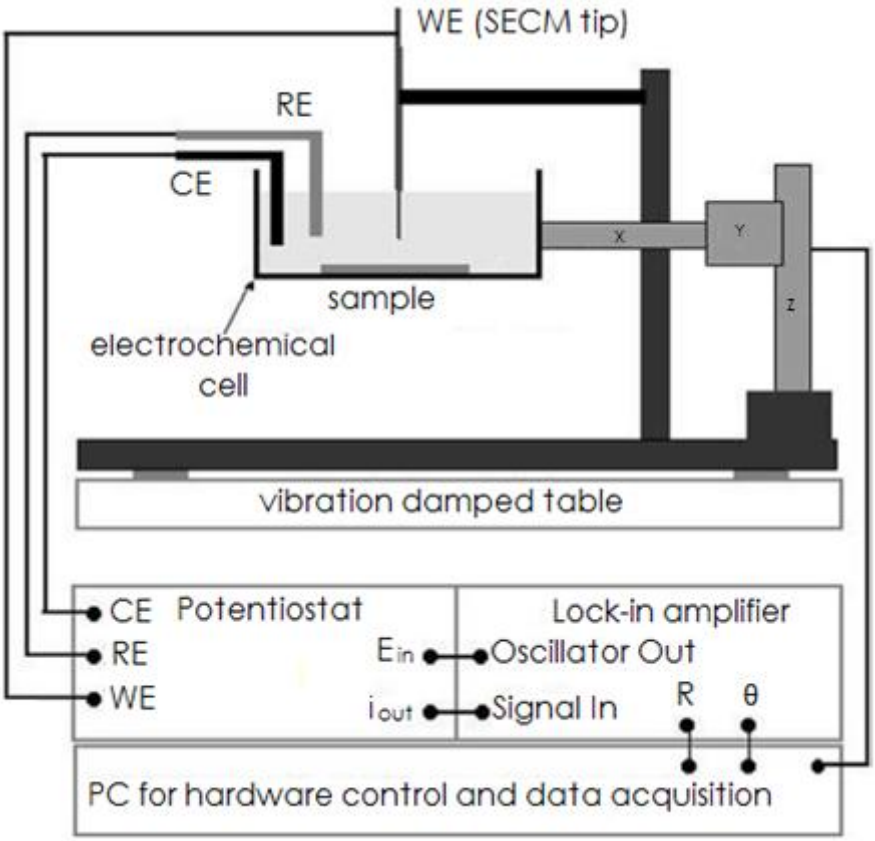

Figure 2.2.11. Schematic representation of the instrumentation used for AC-SECM [31].

2.2.8. Combined atomic force and scanning electrochemical microscopy (AFM-SECM)

Scanning probe microscopes (SPM) are a family of instruments that are used to measure properties of surfaces. SPM includes atomic force microscopy (AFM) and scanning tunneling microscopy (STM). In their first applications, SPM's were used only for measuring 3D surface topography, although they can now be used to measure many other surface properties. SPM's are the most powerful tools for surface metrology, measuring surface features whose dimensions are in the range from interatomic spacing to a tenth of a millimetre.

These techniques are based on a common working feature: a mechanical probe sensor is scanned across an interface. During the scan, the probe sensor samples a specific signal which is interpreted in terms of structure, electronic or force interaction information from the interface.

Until the 1990s, researchers had relied upon other instruments for imaging and measuring the morphology of surfaces. Then, SPM's were the newest entry into the surface metrology field. As opposed to optical microscopes and electron microscopes (SEM, TEM), SPM's measure surfaces in all three dimensions: *X*, *Y*, and *Z*. Like SEM's, SPM's image and measure the surface of the sample. *X* and *Y* topographic resolution for most SPM techniques, including AFM, is typically 2 to 10 nanometres (STM resolution can be as good as 0.1 nm). *Z* resolution is about 0.1 nm.

The first scanning probe microscope was invented in 1982 by Binnig and Rohrer with the scanning tunnelling microscope (STM) [36] for which they received the Nobel Prize in 1986 sharing it with E. Ruska for his achievements in electron optics and the invention of the electron microscope [37]. The STM spread fast into scientific laboratories over the world, because of its simple design, easiness to handle and the possibility to provide atomically resolved images of the surface of every electronically conducting sample. The application of the STM is naturally restricted to conducting or semi-conducting samples.

In 1986, Binnig *et al.* extended the field of application to non-conducting, e.g. biological, samples by introducing the atomic force microscope (AFM) [38]. The STM and AFM may be applied to samples in very different environments. These microscopes work under vacuum conditions as well as in air and, partly with specific modifications, in liquids.

2.2.8.1. The AFM technique

The scanning probe in AFM is a flexible **cantilever, which** is equipped with a sharp tip at one of its ends, and it is scanned over the sample. Due to the topography of the probed sample and/or due to attractive or repulsive forces between the sample surface and the tip [39], the cantilever is bent up and down during scanning. Thus, the atomic force microscope is constituted by the microscope

unit, which contains the piezoelectric scanning system, the probe and the probe motion sensor; the control unit and the computer and display system (see sketch given in Figure 2.2.12). The probe (i.e. the tip/cantilever assembly) is typically microfabricated from Si or Si_3N_4. The probe motion sensor senses the force between the probe and the sample and provides a correction signal to the piezoelectric scanner to keep the force constant. The most common design for this function uses a laser shining onto and reflecting off the back of the cantilever and onto a segmented photodiode to measure the probe motion. Finally, the control unit provides interfacing between the computer, the scanning system, and the probe motion sensor, and contains the feedback control system.

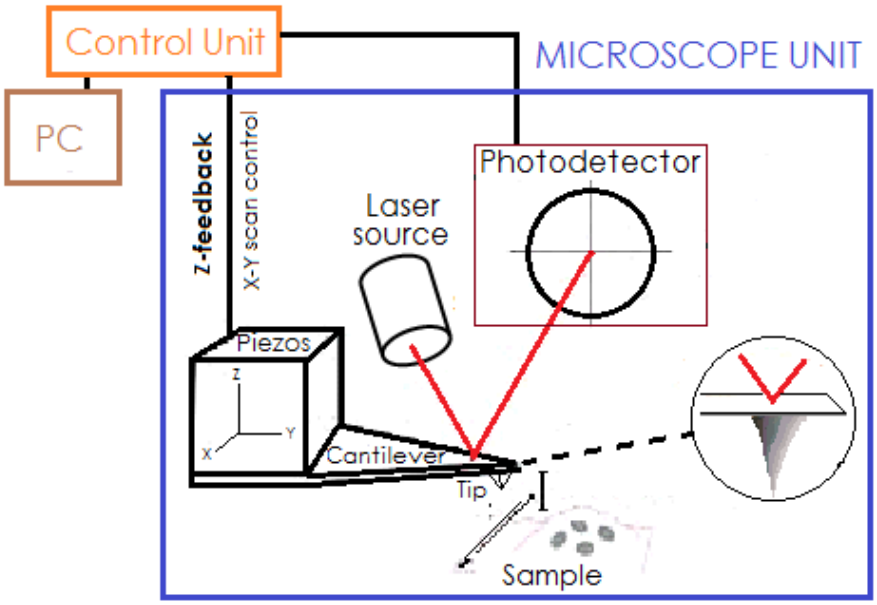

Figure 2.2.12. A schematic illustration of the main components and the method of operation of an AFM. The position of the cantilever is controlled by three piezo-ceramic controllers. A laser beam is directed at the reflective, upper surface of the cantilever, and the deflected light detected. Both the size and position of the current created in the detector are linked by means of a computer.

2.2.8.2. Operation modes in AFM

1. Contact mode. Using the feedback control in the AFM, it is possible to scan a sample with a fixed cantilever deflection. In this mode, the deflection of the cantilever is sensed and compared in a DC feedback amplifier to some desired value of deflection. If the measured deflection is different from the desired value, the feedback amplifier applies a voltage to the piezo to raise or lower the sample relative to the cantilever to restore the desired value of deflection. The voltage that the feedback amplifier applies to the piezo is a measure of the height of features on the sample surface. It is displayed as a function of the lateral position of the sample. This scanning mode is often called "contact" mode. However, because the forces of the probe on the surface are often less than a nanonewton, the probe is minimally touching the surface (see Figure 2.2.13A).

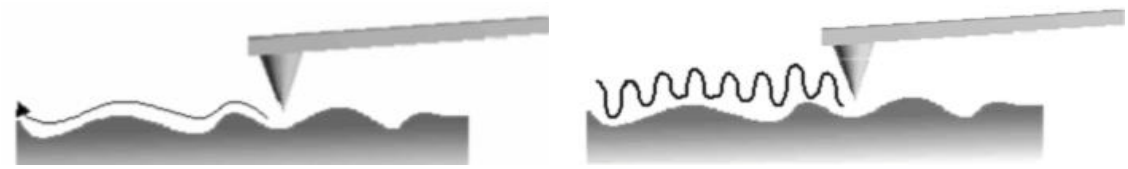

A B

Figure 2.2.13. (A) In contact mode AFM, the probe directly follows the topography of the surface as it is scanned. The force of the probe is kept constant while an image is measured. (B) In non-contact mode, changes in probe's vibrations are monitored to establish the force of the probe onto the surface. The feedback unit is used to keep the vibrating amplitude or phase constant.

2. Non-contact mode. The cantilever in an AFM can be vibrated using a piezoelectric ceramic. When the vibrating cantilever comes close to a surface, the amplitude and phase of the vibrating cantilever may change. These changes are used to identify and measure surface features because they can be related to the force on the surface. During vibrating mode operation, the cantilever oscillation amplitude is maintained constant by a feedback loop. Selection of the optimal oscillation frequency is software-assisted and the force on the sample is automatically set and maintained at the lowest possible level. When the tip passes over a bump in the surface, the cantilever has less room to oscillate and the amplitude of oscillation decreases. Conversely, when the tip passes over a depression, the cantilever has more room to oscillate and the amplitude increases (approaching the maximum free air amplitude). The oscillation amplitude of the tip is measured by the detector and input to controller electronics (Figure 2.2.13B).

3. Tapping mode. In the "tapping"-mode [40], the cantilever oscillates near its resonant frequency using a piezoelectric crystal. As the oscillating cantilever begins to intermittently contact the surface, the cantilever oscillation is necessarily reduced due to energy loss caused by the tip-surface interactions. The reduction in oscillation amplitude is used to identify and measure surface features.

The AFM can also be operated with the sample submerged in a liquid. In this case, the sample is mounted in a cell container, able to contain the desired electrolyte. Once laser signal is realigned, tip approach can be performed and the sample scanned. This assembly may also be adapted to permit the electrochemical control of the sample (EC-AFM). This requires the inclusion of an auxiliary electrode (AE) and a reference or pseudo-reference electrode (RE) connected to a potentiostat, with the sample behaving as working electrode.

2.2.8.3. Integrated AFM-SECM

Among the various highly resolved techniques available, AFM and SECM have shown to be powerful for the *in-situ* resolution of localized corrosion problems. However, despite the many advantages presented by them separately, some

limitations limit the applications for both. On one side, spatial resolution of SECM is typically much lower than that of SPM-based techniques [41]. On the other hand, the conventional AFM lacks chemical specificity, only providing topographical information. A different approach involves the production of a bi-functional probe acting simultaneously as AFM cantilever tip and SECM electrode in the micrometer size. The integration of the AFM-SECM probe has been achieved by combining several methods such as photolithography, metal masking technology, focus ion beam (FIB), ionic and chemical etching, and low pressure chemical vapour (CVD) or plasma-enhanced CVD (PE-CVD) deposition [41-53]. Generally in all these approaches, the main task was to produce a conductive and noble endpoint of micro- or submicrometre size which acts as the SECM sensitive part, embedded in an insulating substrate for simultaneously obtaining topographical information. The differences between the various strategies focus on the starting component for modification. Below, we briefly mention a selection of the most efficient procedures, which are described in detail in the corresponding literature.

The first attempts to combine AFM and SECM were conducted by Unwin and Macpherson, who produced hand-fabricated AFM-SECM probes. For that purpose, Pt or Au microwires were first etched, bent and flattened before being partially coated by a thin isolating film [43]. They later described a procedure for batch microfabrication of an AFM-SECM probe, sized in the typical dimensions of an UME. Direct electron beam lithography (EBL) was employed to define both the shape of the AFM probe and the geometry at the very end of the integrated SECM microelectrode [44]. Similarly shaped AFM-SECM probes were developed by Wain *et al.* based on commercially available metallic needle probes, which were insulated with Parylene C. The nanoscopic electrode was exposed by FIB milling [45].

Modified micrometre sized electrodes were employed to produce integrated AFM-SECM for the investigation of corrosion processes by Davoodi [46]. Two types of probes were used in his work. The first one was made by pulling and embedding a Pt wire into a hard epoxy as insulating material. The insulated endpoint was cut by FIB to produce the desired Pt disk microelectrode and a sharp epoxy tip as AFM probe next to this microdisk. The second type was made by pulling and embedding a Pt wire into a quartz microcapillary, followed by an abrading step in order to expose the Pt wire and produce an inclination angle of 15-25 degrees. With this angle, the glass endpoint was employed for AFM sensing, and the Pt wire in the middle was the SECM microelectrode. A small angle produced a greater blocking effect, whereas sharper endpoints facilitated AFM operation.

Alternative procedures involved integrated probes fabricated from Si wafers or commercial AFM cantilevers. The task is to adequately produce depositions of insulating and conducting layers over them using nanofabrication facilities, including several ionic and chemical etching steps or CVD deposition. With the combination of these processes, the resulting Pt coat can be embedded between two insulating thin films. In this way, only a small fraction of the conductive material remains in contact with the electrolyte [47,48]. To this end, Prinz *et al.* added metal mask technology FIB technique for the precise opening the Pt layer [49]. The incorporation

of carbon nanotubes in the AFM/SECM probe assembly has also been successfully implemented by Macpherson and coworkers [50].

Among the various strategies, we regarded more interesting the procedure described by Christine Kranz and coworkers [51-53], and it was adopted for the fabrication of the AFM-SECM sensors used in this work. They were produced at her laboratories in the University of Ulm (Germany), where the international activities included in this Thesis were performed. The method involves the production of an Au ring nanoelectrode as frame-shape around an AFM tip for integration of the tip for AFM-SECM measurement [51]. A commercial pyramid-shaped AFM tip was cut by using FIB milling. Then a gold layer, and subsequently silicon nitride, were sputtered using PE-CVD on the tip. In the next step, the Au endpoint was exposed by cutting off the top part, leading to the production of a ring nanoelectrode as sketched in Figure 2.2.14A. Finally, the AFM tip was re-shaped as it can be seen in the SEM image of an AFM-SECM probe given in Figure 2.2.14B. The electrochemical response of the SECM tip was finally characterized by cyclic voltammetry in ferrocyanide-containing solution, and its current response was in good agreement with the calculated limiting current.

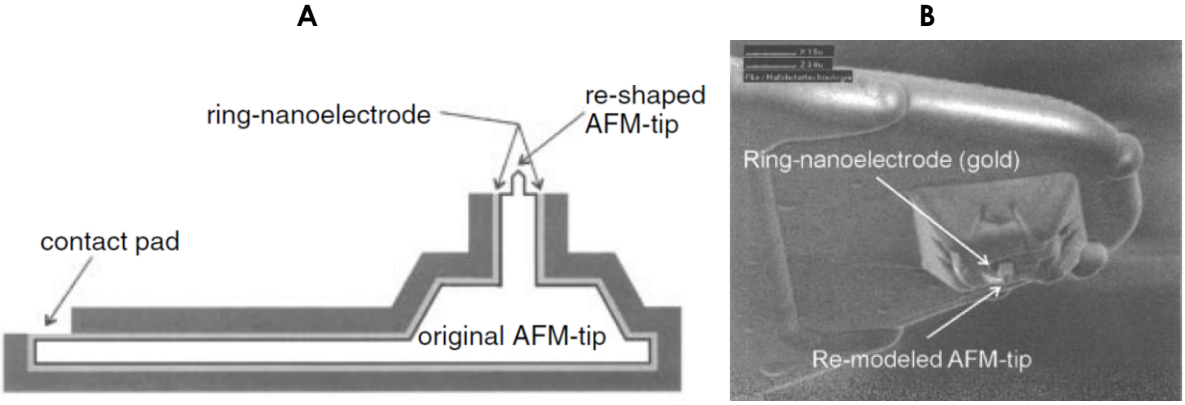

Figure 2.2.14. (A) Schematic description of an integrated SECM ring nanoelectrode in an AFM tip; and (B) FIB image of a ring nanoelectrode integrated in an AFM tip for AFM/SECM measurement [52], reprinted with permission.

2.2.9. References

1. A.J. Bard, L.R. Faulkner. Electrochemical Methods: Fundamentals and Applications, 2nd edn. Wiley-VCH, New York, 2001.
2. C. Gabrielli. In: Physical electrochemistry. Principles, Methods, and Applications (Edited by I. Rubinstein). Marcel Dekker, New York, 1995, Ch. 6.
3. W.H. Smyrl, J. Newman. Journal of the Electrochemical Society 119 (1972) 208.
4. J. Newman. Journal of the Electrochemical Society 113 (1966) 1235.
5. J.A. Bardwell, J.W. Fraser, B. MacDougall, M.J. Graham. Journal of the Electrochemical Society 139 (1992) 366.

6. J.A. Bardwell, B. MacDougall. Electrochimica Acta 34 (1989) 229.
7. M.J. Graham, J.A. Bardwell, G.I. Sproule, D.F. Mitchell, B. R. MacDougall. Corrosion Science 35 (1993) 13.
8. O. Bluh, B. Scott. Review of Scientific Instruments 10 (1950) 867.
9. L.F. Jaffe, R. Nucitelli. Journal of Cell Biology 63 (1974) 269.
10. D. Mackenzie. New Scientist 28 (1982) 217.
11. A.M. Shipley, J.A. Feijó. In: Fertilization in Higher Plants. Molecular and Cytological Aspects. Springer-Verlag, Berlin, 1999, Ch. 17.
12. H.S. Isaacs. Corrosion 43 (1987) 594.
13. H.S. Isaacs. Corrosion Science 28 (1988) 547.
14. H.S. Isaacs. Journal of the Electrochemical Society 138 (1991) 722.
15. J.G. Kunkel, S. Cordeiro, Y. Xu, A.M. Shipley, J.A. Feijó. In: Plant Electrophysiology: Theory and Methods (Edited by A.G. Volkov). Springer-Verlag, Berlin, 2006, p. 109.
16. R.P. Buck, E. Lindner. Pure and Applied Chemistry 66 (1994) 2527.
17. E. Bakker, E. Pretsch, P. Bühlmann. Analytical Chemistry 72 (2000) 1127.
18. S.V. Lamaka, M.G. Taryba, M.F. Montemor, H.S. Isaacs, M.G.S. Ferreira. Electrochemistry Communications 13 (2011) 20.
19. A.J. Bard, F-R.F. Fan, J. Kwak, O. Lev. Analytical Chemistry 61 (1989) 132.
20. A.L. Barker, M. Gonsalves, J.V. Macpherson, C.J. Slevin, P.R.Unwin. Analytical Chimica Acta 385 (1999) 223.
21. J.V. Macpherson, P.R. Unwin. In: Scanning Electrochemical Microscopy (Edited by A.J. Bard, M.V. Mirkin). Marcel-Dekker, New York, 2001, p. 521.
22. L. Niu, Y. Yin, W. Guo, M. Lu, R. Qin, S. Chen. Journal of Materials Science 44 (2009) 4511.
23. J. Heinze. Angewandte Chemie 96 (1984) 823.
24. J. Heinze. Angewandte Chemie International Edition 168 (1984) 831.
25. R.M. Wightman, D.O. Wipf. In: Electroanalytical Chemistry, vol. 15 (Edited by A.J. Bard). Marcel Dekker, New York, 1989, p. 267.
26. A.M. Bond, K.B. Oldham, C.G. Zoski. Analytica Chimica Acta 216 (1989) 177.
27. Y. Saito. Review of Polarography (Japan) 15 (1968) 177.
28. A.J. Bard, G. Denuault, C. Lee, D. Mandler, D.O. Wipf. Accounts of Chemical Research 23 (1990) 357.
29. B.H. Horrocks, D. Schmidtke, A. Heller, A.J. Bard. Analytical Chemistry 65 (1993) 3605.
30. M.A. Alpuche-Aviles, D.O. Wipf. Analytical Chemistry 73 (2001) 4873.
31. B. Ballesteros Katemann, A. Schulte, E.J. Calvo, M. Koudelka-Hep, W. Schuhmann. Electrochemistry Communications 4 (2002) 134.
32. B. Ballesteros Katemann, C.G. Inchauspe, P.A. Castro, A. Schulte, E.J. Calvo, W. Schuhmann. Electrochimica Acta 48 (2004) 1115.
33. M. Etienne, A. Schulte, W. Schuhmann. Electrochemistry Communications 6 (2004) 288.
34. J. Kwak, A.J. Bard. Analytical Chemistry 61 (1989) 1221.
35. K. Eckhard, T. Erichsen, M. Stratmann, W. Schuhmann. Chemistry A European Journal 14 (2008) 3968.
36. G. Binnig, H. Rohrer, C. Gerber. Applied Physics Letters 40 (1982) 178.

37. M. Knoll, E. Ruska. Zeitschrift für Physik 78 (1932) 318.
38. G. Binnig, C.F. Quate, C. Gerber. Physical Review Letters 56 (1986) 930.
39. T.R. Albrecht, P. Grütter, D. Horne, D. Rugar. Journal of Applied Physics 69 (1991) 668.
40. Q. Zhong, D. Inniss, K. Kjoller, V.B. Elings. Surface Science 290 (1993) L688.
41. C.E. Gardner, J.V. Macpherson. Analytical Chemistry 74 (2002) 576A.
42. C. Kranz. Analyst 139 (2014) 336.
43. J.V. Macpherson, P.R. Unwin. Analytical Chemistry 72 (2000) 276.
44. P.S. Dobson, J.M.R. Weaver, M.N. Holder, P.R. Unwin, J.V. Macpherson. Analytical Chemistry 77 (2005) 424.
45. A.J. Wain, D. Cox, S. Zhou, A. Turnbull. Electrochemistry Communications 13 (2011) 78.
46. A. Davoodi, Mechanistic Studies of Localized Corrosion of Al Alloys by High Resolution *in-situ* and *ex-situ* Probing Techniques. Dissertation, Royal Institute of Technology, Stockholm, 2008.
47. Y. Hirata, S. Yabuki, F. Mizutani. Bioelectrochemistry 63 (2004) 217.
48. M.R. Gullo, P.L.T.M. Frederix, T. Akiyama, A. Engel, N.F. deRooji, U. Staufer. Analytical Chemistry 78 (2006) 5436.
49. R.J. Fasching, Y. Tao, F.B. Prinz. Sensors and Actuators B 108 (2005) 964.
50. D.P. Burt, N.R. Wilson, J.M.R. Weaver, P.S. Dobson, J.V. Macpherson. Nanoletters 5 (2005) 639.
51. C. Kranz, G. Friedbacher, B. Mizaikoff, A. Lugstein, J. Smoliner, E. Bertagnolli. Analytical Chemistry 73 (2001) 2491.
52. A. Lugstein, E. Bertagnolli, C. Kranz, B. Mizaikoff. Surface and Interface Analysis 33 (2002) 146.
53. C. Kranz, A. Kueng, A. Lugstein, E. Bertagnolli, B. Mizaikoff. Ultramicroscopy 100 (2004) 127.

CHAPTER 3

In situ characterization of localized corrosion of steel with high lateral and chemical resolutions

Index

3.1

Prologue to the experiments

3.1.1. Introduction

Apart from the cost, (it is generally accepted that the cost of corrosion is around the 3% of the GNP of industrialized countries) [1], affecting almost all areas of technological application (building, industries, bridges and transport, implant materials for the human body, etc.), corrosion consumes huge amounts of materials and the energy required to produce them. The function of most components is ultimately limited by corrosion. Research into corrosion covers mechanisms of corrosion and passivation, and methods of lifetime prediction. New methods of probing the microscopic processes occurring on electrode surfaces are currently under development.

The corrosion resistance of metallic materials is primarily derived from the state of passivity. The formation of protecting oxide and oxy-hydroxide layers on the metal surface renders the metal inert to some extent. Unfortunately, pitting corrosion is a major source of corrosion failure in passivating metals. This form of corrosion is very hazardous, because corrosion processes occur in a highly localized manner, whereas most of the surface of the material remains passive. The causes of pitting corrosion appear to be varied. Pitting corrosion nucleates at the sub-micrometer range, and occurs as a series of microscopically violent steps, which cannot be usually detected by conventional electrochemical techniques until their propagation stage. However, studies of the early growth of individual pits have revealed that there are several stages of growth [2]. The nucleation stage is tiny and very fast. This is followed by a metastable stage in which propagation of the pit is not yet fully stabilised but growth is sustained by the surrounding and covering geometry of the passive surface from which the pit began. This early stage of pit growth may be succeeded by the stable state, or growth may terminate whilst still in the metastable state. The metastable state is interesting because it is a precursor state to stable pitting and appears to be controlled by the same mechanism as that of stable pitting. On stainless steels at least, the pit interior is filled with an anolyte basically saturated with the metal salt. The rate of growth is controlled by outward diffusion of metal cations from this saturated salt solution, the diffusion rate being sustained by the perforated remnants of the passive film that originally protected the site. It is a combination of the residual passive film and the surface geometry of the site that allows the diffusion-controlled state to exist despite the fact that the pit itself has not yet attained the depth required to do so. Stable pit growth occurs when the

pit depth alone provides the boundary depth for diffusion control; the remnants of the passivating cover and the original site geometry become irrelevant once the stable growth state has been achieved [3].

Due to the electrochemical nature of corrosion reactions, they are usually investigated using conventional electrochemical experiments such as cyclic voltammetry (CV), electrochemical impedance spectroscopy (EIS), and chronoamperometry. In this way, both the heterogeneous rate constant of electron transfer for adsorbed or dissolved species, and the kinetics of homogeneous coupled chemical reactions, can be determined from the analysis of current and potential changes at the electrode [4,5]. Yet, whatever the measurable quantity, it reflects the reactivity of the whole electrode surface; in other words its analysis is based on the assumption that the electrochemical behaviour of the interface is uniform. However, electrodes rarely exhibit such an ideal behaviour and the electrode response to a perturbation signal corresponds to an average measurement over the whole electrode surface. In addition, the geometry of the electrode should also be taken into account. For instance, in the case of a disk electrode embedded in an insulator, which is the most popular electrode geometry used by electrochemists, the potential distribution over the disk electrode is not uniform under the conditions where the current density is uniform and, similarly, the current distribution is not uniform under the primary condition where the solution potential is uniform [6,7].

These observations remain valid when the electrode is made of a corroding material. Generalized corrosion is generally described as a uniform reactivity of a metal or an alloy, and from the determination of the kinetics of dissolution, it is intended to predict the lifetime corrosion resistance of a metal material. For example, iron and zinc corrode uniformly in a diluted sulphuric acid solution by forming the oxidized species Fe^{2+} and Zn^{2+}, respectively. Conversely, localized corrosion processes such as pits and crevices, corrosion by cracks, or biocorrosion correspond to attacks on a small surface area of the metal surface. In these cases, the local dissolution of the metal is associated with the initiation and the evolution of either one or several active sites that are scattered over the whole surface, and thus forming an electrode having an overall heterogeneous reactivity. Moreover, these types of corrosion remain very difficult to predict and can quickly propagate in-depth in the bulk of the material depending on the chemical nature of the corrosive media. For example, the passive layer formed on an iron electrode is very sensitive to the presence of halide ions, particularly the chloride species [8-10].

The major development of scanning probe techniques has allowed surface characterization with a resolution in the micrometer range or below. Such dimensions can be reached due to both the use of microelectrodes [11-14] and the significant improvement of electronic devices allowing tiny currents to be measured. In the early 1980's, the work by Binnig and co-workers led to the development of the scanning tunnelling microscope (STM) [15,16] and the atomic force microscope (AFM) [17,18], both allowing atomic resolution to be attained for the first time at conducting and non-conducting substrates, respectively. Due to the development of microelectrodes [11-14], this kind of scanning probe microscopy was adapted to

monitor the electrochemical reactivity of a metal/electrolyte interface [19,20] leading to the development of scanning electrochemical microscopy (SECM) [21-25]. SECM is based on the reaction that occurs at a mobile ultramicroelectrode tip (UME) immersed in an electrolyte solution, and scanned in close vicinity of a surface in order to characterize the topography and/or the redox activity of the solid/liquid interface. A faradaic current is measured at the tip which serves as a local probe. Under steady-state operation, the current is controlled by diffusion of oxidizable/reducible species used as mediator in the solution, and it depends strongly on the tip-sample separation. By scanning the UME over a given surface, an image of the surface can be generated, as well as information concerning reactions that take place either in the solution space between the tip and the sample or on the surface of the scanned sample can be gained.

In SECM, image interpretation requires a fairly complete understanding of the electrochemical behaviour of the system. In order to illustrate this point, the following features can be considered. An electrochemical reaction is made up of a series of chemical and physical steps occurring at very small length scales [26]. For the sake of illustration, let us consider the typical features related to the cathodic half-cell reaction in a naturally-corroding system, which involves a redox species from the bulk of the aqueous phase in contact to the corroding metal to be available to accept the electrons left by the oxidizing substrate. The transfer of an electron between the electrode surface and a redox molecule takes place over a distance no greater that 2 nm and occurs in an interfacial region defined by the radius of the adsorbed ions and solvent molecules (ca. 1 nm, characterized by the Debye length). Prior to electron-transfer step, the molecule must also be transported from the bulk solution to the electrode surface through the depletion layer, a 0.01-100 μm thick interfacial zone in which the composition of the solution has been altered by the electrochemical reaction. With these scales in mind, it is natural to consider what new phenomena might occur if the microelectrodes formed in corrosion processes have micrometric or sub-micrometric dimensions, as it is typical of the early stages of localized corrosion processes (i.e. pitting or crevice corrosion), or the dimensions of inclusions in alloys. Furthermore, restricted geometries involved in localized corrosion features, and the heterogeneous nature of typical corroding systems, require new theoretical models to quantify the kinetics and transport contributions of the species involved in the corrosion reactions, so far only existing for flat, homogeneous and well-defined geometries. The complexity of these systems may account for this technique only effectively being applied in Corrosion Science since the last decade [27], though it currently finds wide range of applications, namely the detection of anodic and cathodic areas [28,29], the dissolution of metals [30], the investigation of the chemical stability of surface coatings [31,32], the degradation of organic films [33-35], the characterization of the metastable regime of pit nucleation [36], the detection of precursor sites for pitting inclusion dissolution [37,38], single pit generation [39-41], the monitoring of inclusion dissolution [42,43], and the imaging of surface changes during hydrogen permeation [44].

Comparison of SECM with the other scanning probe microscopies (SPM) is not straightforward because each SPM has its own advantages and drawbacks. Firstly, a distinctive characteristic of both STM and AFM is that they allow atomic or molecular resolution to be achieved. The former technique is based on the measurement of the tunnelling current that can be established between the probe and a conducting substrate when they are in close proximity, and it was originally developed for operation under high vacuum conditions. However, STM has been modified for operation in an electrochemical system, though significant difficulties are experienced for adequate tip preparation, for the control of the electrochemical conditions and application of electrochemical techniques, and from the high spatial resolution. Alternately, AFM can be used for the characterization of both insulators and conductors with high spatial resolution by measuring local forces between the probe and the substrate. The possibility to perform electrochemistry on the substrate during imaging has been demonstrated especially in the case of corrosion applications [45].

Despite many successful applications, the spatial resolution of SECM is less than that of AFM. However, the conventional AFM lacks chemical specificity. A different approach has been made available by producing a bifunctional probe acting simultaneously as AFM tip and SECM ultramicroelectrode (UME). The integration of the AFM-SECM probe has been achieved by several methods [46-48]. Though the main field of application of this combination has been found in the imaging of living cells, applications in materials science have also been described [49-52].

In summary, the advent of scanning microelectrochemical techniques, which combine electrochemical and spatial resolutions, provide a new route to investigate the origin of passivity breakdown, with a view to develop new strategies to improve the corrosion resistance of stainless steel surfaces. The research will generate new methods of analysis, more sensitive than has hitherto been possible. It will also develop a better understanding of the mechanisms involved, as well as to develop new processes for passive metals which should affect only to the surfaces. Modification of the surface properties of metals without affecting their bulk properties is of technological interest in demanding applications where surface stability and hardness are important. The main objectives were namely, (1) determination of the variables operating in passivity breakdown and pit nucleation in stainless steels; and (2) high resolution imaging of the nucleation of an individual pit growing into the stable regime.

3.1.2. Research aims

In this study the combined use of the scanning electrochemical microscopy (SECM) and the scanning vibrating electrode technique (SVET) for the *in situ*

characterization of pitting corrosion susceptibility of stainless steel in aqueous saline environments is proposed. The effects of solution composition and electric state of the material could thus be investigated *in situ* with high spatial resolution. In addition, a new method for the controlled formation of single pits on iron with greater spatial resolution has been developed using the combined AFM-SECM technique.

3.1.3. References

1. M.V. Biezma, J.R. San Cristóbal. Corrosion Engineering Science and Technology 40 (2005) 344.
2. G.T. Burstein, C.Liu, R.M. Souto, S.P. Vines. Corrosion Engineering Science and Technology 39 (2004) 25.
3. P.C. Pistorius, G.T. Burstein. Philosophical Transactions of the Royal Society London A341 (1992) 531.
4. A.J. Bard, L.R. Faulkner. Electrochemical Methods: Fundamentals and Applications, 2nd edn., Wiley-VCH, New-York, 2001.
5. C. Gabrielli. In: Physical Electrochemistry. Principles, Methods, and Applications (Edited by I. Rubinstein). Marcel Dekker: New York, 1995, Ch. 6.
6. W.H. Smyrl, J. Newman. Journal of the Electrochemical Society 119 (1972) 208.
7. J. Newman. Journal of the Electrochemical Society 113 (1966) 1235.
8. J.A. Bardwell, J.W. Fraser, B. MacDougall, M.J. Graham. Journal of the Electrochemical Society 139 (1992) 366.
9. J. A. Bardwell, B. MacDougall. Electrochimica Acta 34 (1989) 229.
10. M.J. Graham, J.A. Bardwell, G.I. Sproule, D.F. Mitchell, B.R. MacDougall. Corrosion Science 35 (1993) 13.
11. R.M. Wightman. Analytical Chemistry 53 (1981) 1125A.
12. M.A. Dayton, J.C. Brown, K.J. Stutts, R.M. Wightman. Analytical Chemistry 52 (1980) 946.
13. M. Fleischmann, S. Pons, D.R. Rolinson, P.P. Schmidt. Ultramicroelectrodes. Datatech Systems, Morganton, 1987.
14. C. Amatore. In: Physical Electrochemistry. Principles, Methods, and Applications (Edited by I. Rubinstein). Marcel Dekker: New York, 1995, Ch. 4.
15. G. Binnig, H. Rohrer. Helvetica Physica Acta 55 (1982) 726.
16. G. Binnig, H. Rohrer. Surface Science 126 (1983) 236.
17. G. Binnig, C. Gerber, E. Stoll, T.R. Albrecht, C.F. Quate. Europhysics Letters 3 (1987) 1281.
18. D.P.E. Smith, G. Binnig, C.F. Quate. Applied Physics Letters 49 (1986) 1166.
19. R.C. Engstrom, T. Meaney, R. Tople, R.M. Wightman. Analytical Chemistry 59 (1987) 2005.
20. R.C. Engstrom, M. Weber, D.J. Wunder, R. Burgess, S. Winquist. Analytical Chemistry 58 (1986) 844.
21. J. Kwak, A.J. Bard. Analytical Chemistry 61 (1989) 1221.
22. D. Mandler, A.J. Bard. Journal of the Electrochemical Society 136 (1989) 3143.

23. A.J. Bard, F.-R.F. Fan, J. Kwak, O. Lev. Analytical Chemistry 61 (1989) 132.
24. O.E. Husser, D.H. Craston, A.J. Bard. Journal of the Electrochemical Society 136 (1989) 3222.
25. A.J. Bard, G. Denuault, C. Lee, D. Mandler, D.O. Wipf. Accounts of Chemical Research 23 (1990) 357.
26. L.R. Faulkner. Journal of Chemical Education 60 (1983) 262.
27. L. Niu, Y. Yin, W. Guo, M. Lu, R. Qin, S. Chen. Journal of Materials Science 44 (2009) 4511.
28. A.C. Bastos, A.M. Simões, S. González, Y. González-García, R.M. Souto. Electrochemistry Communications 6 (2004) 1212.
29. A.M. Simões, A.C. Bastos, M.G. Ferreira, Y. González-García, S. González, R.M. Souto. Corrosion Science 49 (2007) 726.
30. K. Fushimi, M. Seo. Electrochimica Acta 47 (2001) 121.
31. S. Hocevar, S. Daniele, C. Bragato, B. Ogorevic. Electrochimica Acta 53 (2007) 555.
32. D. Battistel, S. Daniele, R. Gerbasi, M.A. Baldo. Thin Solid Films 518 (2010) 2195.
33. R.M. Souto, Y. González-García, S. González, G.T. Burstein. Corrosion Science 46 (2004) 2621.
34. A.M. Simões, D. Battocchi, D.E. Tallman, G.P. Bierwagen. Corrosion Science 49 (2007) 3838.
35. R.M. Souto, Y. González-García, S. González, G.T. Burstein, Electroanalysis 21 (2009) 2569.
36. Y. González-García, G.T. Burstein, S. González, R.M. Souto. Electrochemistry Communications 6 (2004) 637.
37. S.B. Basame, H.S. White. Journal of Physical Chemistry 99 (1995) 16430.
38. Y.Y. Zhu, D.E. Williams. Journal of the Electrochemical Society 144 (1997) L43.
39. K. Fushimi, K. Azumi, M. Seo. Journal of the Electrochemical Society 147 (2000) 552.
40. C. Gabrielli, S. Joiret, M. Keddam, H. Perrot, P. Rousseau, V. Vivier. Journal of the Electrochemical Society 153 (2006) B68.
41. C. Gabrielli, S. Joiret, M. Keddam, N. Portail, P. Rousseau, V. Vivier. Electrochimica Acta 53 (2008) 7539.
42. C.H. Paik, H.S. White, R.C. Alkire. Journal of the Electrochemical Society 147 (2000) 4120.
43. C.H. Paik, R.C. Alkire. Journal of the Electrochemical Society 148 (2001) B276.
44. S. Modiano, J.A.V. Carreno, C.S. Fugivara, R.M. Torresi, V. Vivier, A.V. Benedetti, O. R. Mattos. Electrochimica Acta 53 (2008) 3670.
45. V. Maurice, P. Marcus. In: Analytical Methods for Corrosion Science and Engineering (Edited by P. Marcus, F. Mansfeld). CRC, Boca Raton, 2005, Ch. 5.
46. J.V. Macpherson, P.R. Unwin. Analytical Chemistry 72 (2000) 276.
47. C. Kranz, A. Kueng, A. Lugstein, E. Bertagnolli, B. Mizaikoff. Ultramicroscopy 100 (2004) 127.
48. P.S. Dobson, J.M.R. Weaver, M.N. Holder, P.R. Unwin. J.V. Macpherson, Analytical Chemistry 77 (2005) 424.

49. M. Janotta, D. Rudolph, A. Kueng, C. Kranz, H.S. Voraberger, W. Waldhauser, B. Mizaikoff. Langmuir 20 (2004) 8634.
50. D. Rudolph, S. Neuhuber, C. Kranz, M. Taillefert, B. Mizaikoff. Analyst 129 (2004) 443.
51. A. Davoodi, J. Pan, C. Leygraf, S. Norgren. Electrochimica Acta 52 (2007) 7697.
52. A. Davoodi, J. Pan, C. Leygraf, S. Norgren. Journal of the Electrochemical Society 155 (2008) C211.

3.2

The localized corrosion of 304 stainless steel in electrolyte containing chloride ions studied by SECM and SVET

3.2.1. Abstract

Corrosion processes occurring on stainless steel 304 surfaces under anodic polarization were characterized using scanning electrochemical microscopy (SECM) and the scanning vibrating electrode technique (SVET), complemented with conventional potentiodynamic polarization curves. Stable pit formation was detected by SVET on the samples as result of surface modification under electrochemical control. In the event that the media is not aggressive enough to induce pitting at small overpotentials, previous electrochemical reduction of passive oxide layer was produced. Additionally, the sample generation – tip collection operation mode of the SECM enabled the detection of local release of iron (II) ions, as well as their conversion to iron (III) species. Both processes are strongly affected by the magnitude of potential applied to the substrate.

3.2.2. Resumen

Se han caracterizado los procesos corrosivos que tienen lugar sobre superficies de acero inoxidable 304 bajo polarización anódica, usando la microscopía electroquímica de barrido (SECM) y la técnica de barrido del electrodo vibrante (SVET), complementadas con curvas de polarización potenciodinámicas convencionales. Por medio del SVET, se ha detectado la formación de picaduras estables en las muestras como resultado de la modificación de la superficie bajo control electroquímico, lo que incluye la reducción electroquímica previa de la capa de óxidos si el medio no es suficientemente agresivo para inducir el picado a sobrepotenciales bajos. Además, operando el SECM bajo el modo generación en muestra – recolección en punta ha permitido la detección de producción de iones hierro (II), así como su conversión a hierro (III), estando ambos procesos ampliamente afectados por el valor de potencial aplicado al substrato.

3.2.3. Introduction

Corrosion problems affecting metals have been recognized for centuries, especially in relation to iron and iron-based materials, the most widely employed metallic materials in human societies. Yet, due to their mechanical and electrical properties, iron and steel structures have shown to be valuable enough to still being extensively applied for many industrial purposes and applications. Their degradation accounts for a major portion of the total cost of corrosion in most industrialized countries, which supposes annual economic losses up to 5 % of the Gross Domestic Product [1]. In order to increase the profitability of these materials, different stainless steels are produced by alloying iron with nobler metals, resulting in enhanced anticorrosion protection [2-7]. Nevertheless, some environments are still able to induce local damage to the protective passive layer, especially when halide ions are present. This kind of attack leads to pitting corrosion, highly localized in character though apparently distributed in random manner. This localized attack is known to have its origins in the formation of microcells, microanodes and microcathodes, distributed along the metal surface despite its apparent homogeneity, arising from small chemical asymmetries in the system. The impact of the early stages of this localized attack are evidenced with the help of topographic imaging techniques like scanning electron microscopy (SEM), which provides support for the intrinsically stochastic distribution of the attack, and assists characterization of the subsequent morphology [7-15]. *Post-mortem* microscopical observations are then frequently used to establish that the degradation starts within the range of micrometers or below, so that any global measurement performed on the specimen can be interpreted in terms of highly localized processes. However, this interpretation is an assumption based on extrapolations, and both local effects and their mechanisms are not completely understood due to the lack of spatial resolution of conventional techniques.

Due to the electrochemical nature of the corrosion reactions, electrochemical techniques including DC potentiometric polarization curves [16], potentiostatic noise measurements [17], and AC electrochemical techniques [18], have constituted the main sources of information for the analysis of the general behaviour of a corroding system, though unable to supply relevant data to support conclusions at the local scale. In order to understand the mechanisms involving the generation and eventual deactivation of microanodes and microchathodes, real time electrochemical information in the micrometer scale must be collected. Spatially-resolved chemical information is achieved when electrochemical measurements are performed using capillary microcells [19-21], by selecting small portions of the surface that can be distinguished by some microstructural difference. Yet limitations occur during the characterization of the interactions among distributed heterogeneities present in the surfaces, because the complete surface of the sample is not in contact with the test solution when these local techniques are applied. Conversely, high spatial characterization is achieved using *in situ* AFM. This technique allows monitoring topographical changes occurring on representative

areas of the metal when immersed in a liquid phase, though it lacks chemical selectivity [22-24].

These limitations have been the motivation for the development of various microelectrochemical techniques, capable to locally evaluate the corrosion behaviour of the substrate under study by recording electrical and chemical information. Among them, scanning electrochemical microscopy (SECM) provides adequate sensitivity to investigate the interactions of surface features with the electrolytic environment in contact with the surface [25,26]. By adequate selection of the operation mode of SECM, the chemical species participating in corrosion processes can be monitored with high spatial resolution, including chloride anions [27], and changes in proton activity [27-30], as well as other ions and neutral species either produced or consumed in the anodic [31-39] and the cathodic half-cell reactions [30,31,33,35,37,38,40-42]. In addition, the scanning vibrating electrode technique (SVET) has also been widely employed in corrosion studies of iron-based materials, because it images the ionic fluxes of species involved in the electrochemical processes occurring on the corroding surfaces [30,43-54].

The analysis of the chemical nature of the electrochemically active species involved in the corrosion processes can be performed in micrometer dimensions using the SECM. A typical microdisk electrode, with dimensions between 10 to 25 μm diameter, can be placed in close proximity to the sample, and be used to scan the surface and collect species either produced or consumed by the substrate undergoing corrosion. Iron (II) can be detected in this way, because it is easily oxidized to iron (III) at the microelectrodes. This reaction has been selected to image metastable pitting, localized corrosion, and protection breakdown on iron-based materials under different environmental conditions [31-39]. On the other hand, the Fe^{2+}/Fe^{3+} couple undergoes a reversible redox reaction in acidic conditions, thus allowing iron (III) species to be imaged over reacting samples as well, from their reduction into ferrous species. Interestingly, this option has not been exploited in corrosion studies with the SECM until now, probably because iron (II) is regarded to be the main dissolution species and it is produced in significant amount to be effectively detected in most investigations concerning iron-based materials, and because of the high tendency of ferric ions to precipitate as iron (III) hydroxide.

Information provided by SECM can be complemented with that supplied by SVET, which informs about of the location of the electrochemical reactions that occur over an area provided ion fluxes can be produced in the adjacent electrolytic phase. Thus, ionic fluxes related to anodic and cathodic activity on the surface can be distinguished. Despite the rather extended use of this technique among corrosion researchers, polarization of the investigated surface has scarcely been attempted [43,50,51], and it has been mainly constrained to the coupling of dissimilar metals (i.e., formation of galvanic pairs). This situation may arise from the loss of sensitivity experienced when non-perfectly symmetrical ionic fluxes from current sources are produced under polarization conditions from the sample due to the geometry of the counter electrode. This problem remains even if perfectly symmetrical counter electrodes were employed while scanning heterogeneous specimens such as those

undergoing corrosion. However, valuable semi-quantitative information on the corrosion processes can still be obtained, as it is shown in this chapter. In this way, passivity breakdown of the passive layer, and stable pitting corrosion growth were investigated at the same time by considering the average current transients as well as the local ionic currents related to these processes.

The aim of this Section is to report a combined electrochemical and microelectrochemical characterization of the passivity breakdown of 304 stainless steel in acidic chloride-containing solution on polarized samples. Average electrochemical behaviour has been explored using conventional techniques, whereas spatially resolved distributions of the local ionic fluxes related to anodic and cathodic activities, as well as detection of soluble iron species evolving from the corroding metal substrate, were monitored using SECM and SVET.

3.2.4. Experimental

Experiments were performed on 304 grade austenitic stainless steel supplied as sheet of thickness 1 mm by Goodfellow Materials Ltd (Cambridge, UK). The metal was not analysed, but had the specified nominal composition of 17–20% Cr, 8–11% Ni, <2% Mn, <0.08% C, Fe in balance. The steel sheet was cut into strips of 2 cm length and 2 mm width, and next mounted vertically in Epofix (Struers, Ballerup, Denmark) resin sleeves of 3 cm approximate diameter. In this way, only a 2 mm x 1 mm surface of the material was exposed to the test electrolytes. The mounts were abraded using SiC paper of 1200 and 4000 grit, and subsequently polished using alumina suspension of 0.3 μm particle size. The samples were degreased with ethyl alcohol, cleaned in high purity deionized water, and finally dried under air stream.

The tests were conducted in three chloride containing electrolytes of different compositions, namely 0.1 M NaCl, 0.1 M HCl, and 0.025 M HCl + 0.075 M $HClO_4$. All the reagents were of analytical grade, and solutions were prepared by using ultra pure water purified with a Milli-Q system from Millipore. Measurements were conducted at room temperature (nominally 20 °C) in the naturally aerated solutions.

Electrochemical tests were performed using an Autolab (Metrohm, Herisau, Switzerland) potentiostat controlled by personal computer. A 3-electrode configuration was used, where the steel sample was the working electrode, completed with an Ag/AgCl/KCl (3M) reference electrode, and a platinum counter electrode. Potentiodynamic polarization measurements were conducted at 1 mV s^{-1} scan rate. The freshly polished surface was left unbiased for 1 hour in the corresponding test solution to allow a stable reading of the open circuit potential (OCP) to be attained. Then, the cathodic Tafel branch was first separately acquired by polarizing the specimen from the spontaneous corrosion potential down to -0.25 V from the OCP. The sample was then retrieved from the solution and subject to surface grinding and polishing steps as before. After stabilization for 1 hour in the

solution, the sample was now polarized in the anodic direction up to +1.20 V vs. Ag/AgCl/KCl (3M), and subsequently potential scan was reversed to monitor the corresponding repassivation behaviour. Measurements were repeated by quadruplicate, and average data were obtained for the characteristic electrochemical parameters.

Scanning electrochemical microscopy (SECM) measurements were carried out with an instrument developed by Sensolytics GmbH (Bochum, Germany). The instrument was built around the same Autolab instrument used for conventional electrochemical measurements, though this time operating also as bipotentiostat in selected experiments. The electrochemical activity of the metallic substrate was monitored by SECM employing a 10 μm diameter platinum microdisk as the sensing tip. The tip-sample distance was determined from the measurement of z-approach curves above the surrounding resin using the reduction of the molecular oxygen dissolved in the electrolyte. In this case, the SECM was operated in the negative feedback mode, with the tip potential set at -0.65 V vs. Ag/AgCl/KCl (3M). Once the surface was located, the tip was withdrawn to a distance of 10 μm from the sample surface, and scanned parallel to the surface at a scan rate of to 25 μm s^{-1} to record SECM images. The SECM was operated in the substrate generation – tip collection (SG-TC) mode for the detection of either iron (II) or iron (III) ions evolving from the corroding 304 stainless steel surfaces. These species could be selectively monitored by adequately setting the potential of the Pt microelectrode. The potential of the tip was alternately set at +0.50 and at +0.10 V vs. Ag/AgCl/KCl (3M) to detect the generation of Fe(II) and Fe(III) soluble species, respectively. The Fe(II) species were identified through their oxidation to Fe(III), whereas the reverse reaction was employed for the detection of Fe(III).

SVET experiments were performed using an instrument manufactured by Applicable Electronics Inc. (Forestdale, MA, USA). The sensing probe was a 10 μm PtIr tip with a black platinum deposit electrochemically grown to attain an adequate interfacial capacitance. Probe vibrations of 20 μm amplitude in both the normal and the parallel directions to the surface were applied, with 75 and 170 Hz respective vibration frequencies, maintaining a probe-substrate distance of 60 μm. Sample polarization was imposed using a potentiostat model 283 from EG&G Instruments (Princeton Applied Research, Oak Ridge, TN, USA). The analogic outputs for the current and the potential signals from the potentiostat were connected to the analogic inputs of the SVET instrument, in order to follow these signals during the experiments. An Ag/AgCl/KCl (3M) electrode was used as the reference. In order to minimize the occurrence of asymmetric current distributions in the solution adjacent to the steel surface that would produce eventual artefacts at the sensing probe, the counter electrode was a platinum ring covered with an electrodeposit of platinum black.

In selected experiments, a cathodic potential pulse was applied to the samples before recording the SVET measurements in order to modify the surface films formed on the samples. In those cases, the 283 potentiostat was controlled manually in order to apply to the sample the desired cathodic pulse during 6 seconds,

followed by setting the desired anodic polarization during acquisition of the SVET scan. During all this procedure, the average currents flowing through the polarized sample was recorded by connecting the analogic output of the potentiostat to an A/D converter input available in the computer controlling the SVET instrument. Simultaneously, ionic current densities in the cell were measured as SVET signal with the probe located in a central location of the metal substrate.

3.2.5. Results and discussion

The effect of chloride concentration and pH on the susceptibility of 304 stainless steel was investigated using a combination of conventional and localized electrochemical methods with the aim to gain new insights concerning the distribution of electrochemical activity on the surface of the material, and its susceptibility to the onset of pitting corrosion. Spatially-resolved distributions of ionic currents and concentration gradients related to the formation of corrosion products were determined in the electrolyte phase containing chloride ions by using the scanning vibrating electrode technique (SVET) and scanning electrochemical microscopy (SECM). The metal samples were immersed in chloride-containing electrolytes of various compositions, namely 0.1 M NaCl, 0.1 M HCl, and 0.025 M HCl + 0.075 M $HClO_4$. The latter was chosen to contain a smaller concentration of chloride ions while maintaining the same pH than 0.1 M HCl solution, whereas 0.1 M NaCl and 0.1 M HCl solutions contained the same concentration of chloride ions.

3.2.5.1. Potentiodynamic polarization

The average susceptibility towards corrosion of 304 stainless steel was characterized by recording potentiodynamic polarization curves of the material in the three solutions under consideration. Typical anodic polarization curves are depicted in Figure 3.2.1, whereas Table 3.2.1 shows the main parameters related to the corrosion processes that were extracted from analysis of the curves. According to the E_{corr} data, corrosion is favoured in the solutions containing the highest chloride concentration as expected, whereas a nobler surface was attained in the mixture of acids. A low pH does not seem to be as much an influential factor for this thermodynamic tendency as the chloride concentration, as indicated by the close E_{corr} values determined in the hydrochloric acid and the sodium chloride solutions. Onset of passivity is observed in all the media, though the active – passive transition could not be discerned in either solution below the corresponding pitting potential. The lowest value for this E_{bp} was found in 0.1 M HCl. The related anodic current increase cannot occur in 0.1 M NaCl below +0.556 V vs. Ag/AgCl/KCl (3M), though current transients due to metastable pit formation are clearly distinguished. Conversely, in the 0.025 M HCl + 0.075 M $HClO_4$ medium, an abrupt increase in the

current related to pitting corrosion was only observed when the sample was polarized at more anodic overpotentials, ca. +0.90 V vs. Ag/AgCl/KCl (3M).

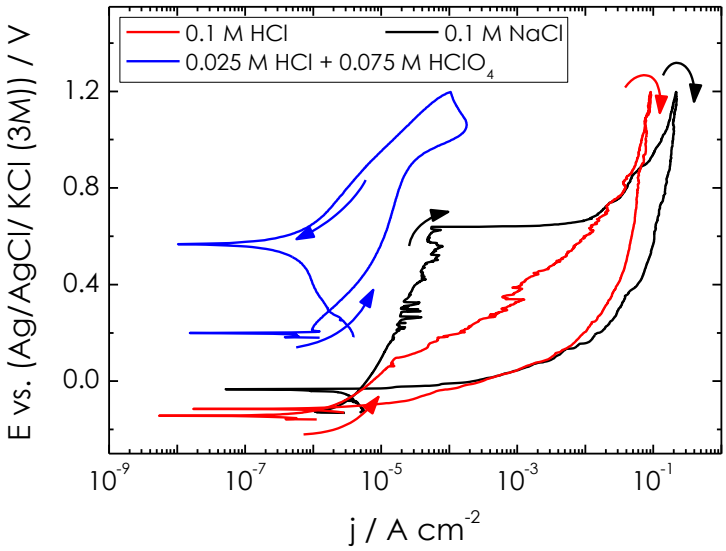

Figure 3.2.1. Typical potentiodynamic polarization curves of 304 stainless steel samples immersed in the solutions indicated in the plot. Scan rate: 1 mV s^{-1}.

Table 3.2.1. Average parameters obtained from the potentiodynamic polarization curves of 304 stainless steel. All potential values are referred to the Ag/AgCl/KCl (3M) reference electrode.

	0.1 M NaCl	0.025 M HCl + 0.075 M $HClO_4$	0.1 M HCl
E_{corr} / V	-0.203	0.159	-0.176
E_{pass} / V	-	0.239	-
E_{bp} / V	0.556	0.907	0.148
E_{rp} / V	-0.129	0.547	-0.093
j_{corr} / µA cm^{-2}	1.36	1.05	0.753
j_{pass} / µAcm^{-2}	-	10.4	-

After the onset of pitting corrosion, 304 stainless steel could only repassivate in the less aggressive media consisting of the mixture of acids, as evidenced by the active passive transition found at +1.06 V vs. Ag/AgCl/KCl (3M), and the negative hysteresis observed when the potential sweep was reversed. In contrast, no repassivation was observed in the two solutions with higher chloride concentration, both exhibiting a positive hysteresis loop instead. This is also evidenced by the repassivation potential values, more positive in the HCl + $HClO_4$ containing environment, where repassivation occurs more easily. In all cases, E_{rp} values are more positive than the corresponding OCP, an indication of the high tendency of the 304 surface to spontaneously form a protective oxide layer, though the 0.1 M HCl medium requires smaller anodic polarizations for this to occur.

3.2.5.2. Scanning vibrating electrode technique

Local effects related to polarization of the sample were evidenced by scanning the samples with the SVET. Current density distributions were first monitored over 304 stainless steel surfaces exposed to 0.1 M HCl media whereas the samples were biased using a sequence of increasingly positive potential values. Only background noise was observed when the sample was either left unbiased or polarized at 0 V vs. Ag/AgCl/KCl (3M). But substrate polarization at +0.10 V vs. Ag/AgCl/KCl (3M) showed the evolution of localized current density from a specific spot of the surface, as it can be seen in Figure 3.2.2A, though it is not visible in the micrograph of Figure 3.2.2B. Despite this low potential value, that is located within the passive region according to average data given in Table 3.2.1, the nucleated pit demonstrated to be stable because it remained at the same position in the following scans. They were recorded while applying progressively more positive polarizations to the substrate using 50 mV steps between subsequent scans. The SVET image recorded when the substrate was polarized at +0.30 V vs. Ag/AgCl/KCl (3M) is shown in Figure 3.2.2C, and the pit is already visible in the optical micrograph in Figure 3.2.2D that was recorded immediately before the scan was completed. It can be noticed that the anodic ionic currents originating from the pit grow with increasing positive polarization, as indicated by the scale bars included in the figures. The SVET image also shows the initiation of a second stable pit that is located at the left of that previously described. Slightly negative current densities are seen during data acquisition in spite of the anodic bias applied to the substrate, which should prevent any cathodic half-cell reaction taking place over the steel substrate. This may arise from the technical limitations originating from asymmetries in the ionic currents flowing between the counter electrode and the substrate of different shapes. This lack of symmetry affects also the current distribution perpendicular to the substrate. These losses are interpreted by the equipment as cathodic currents after comparing the acquired data with the reference measurement taken just before each scan by placing the sensing probe above the center of the substrate though separated ca. 3.5 mm above its surface.

A different behaviour was found by SVET when the steel sample was exposed to the sodium chloride solution. In agreement with the behaviour described by the polarization curve, no stable pitting corrosion could be detected with the SVET for the potentiostatically polarized specimen for potential values up to +0.40 V vs. Ag/AgCl/KCl (3M) (cf. Figure 3.2.3A). That is, the passive oxide film formed on the metal effectively protected it from the aggressive attack of the chloride ions in this natural pH solution. However, after the oxide film was effectively reduced by applying a polarization of -1.50 V vs. Ag/AgCl/KCl (3M) to the sample for approximately 3 seconds, in addition to hydrogen evolution as readily observed with the video camera, this treatment had a clear effect on the susceptibility of the sample towards corrosion. Indeed, new polarization of the sample at +0.40 V vs. Ag/AgCl/KCl (3M) revealed pit formation with the SVET, as shown in Figure 3.2.3B. In addition, there was a significant increase in the average current values measured with the potentiostat while scanning the surface. The same result was also obtained

when recording a series of SVET images with increasing positive potential polarization applied to the sample, starting from -0.75 instead of 0 V vs. Ag/AgCl/KCl (3M), which led to the observation of pitting corrosion at lower positive potential values between +0.30 and +0.40 V vs. Ag/AgCl/KCl (3M) (not shown).

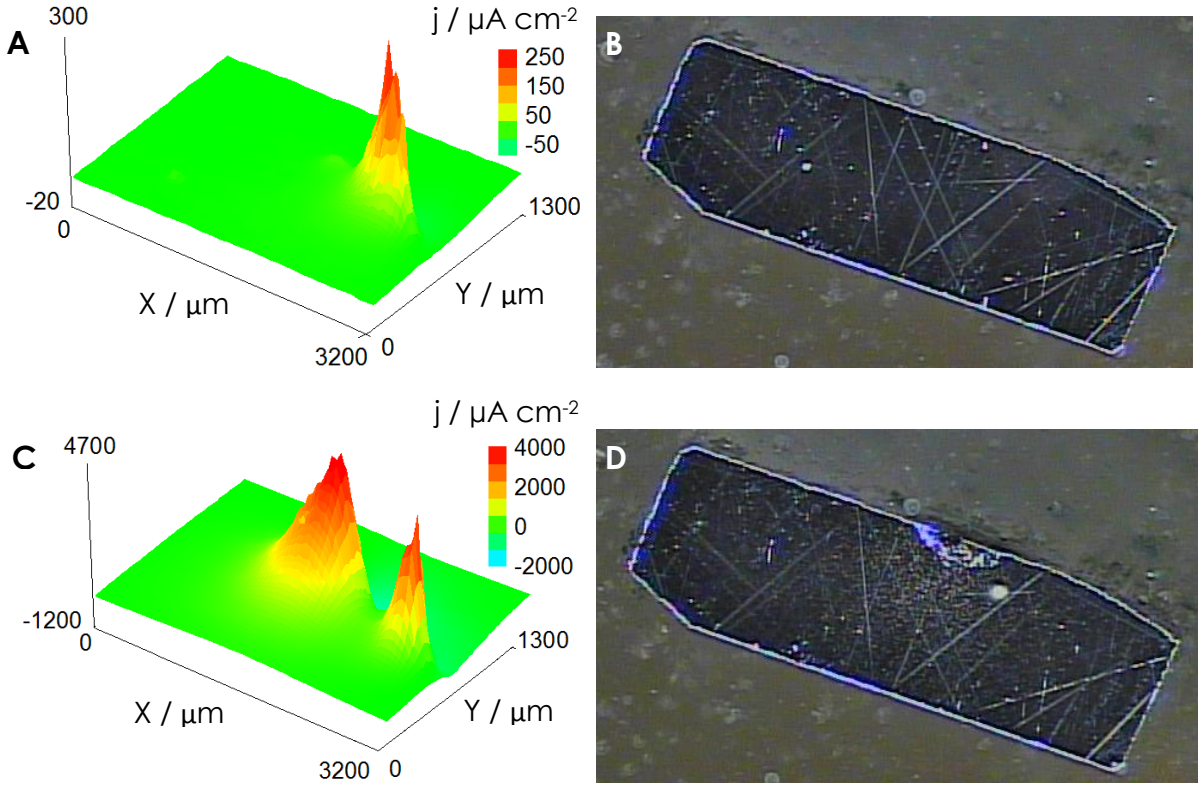

Figure 3.2.2. SVET images (A,C) and optical micrographs (B,D) of 304 stainless steel surface immersed in 0.1 M HCl. The Z scale is the current density in µA cm^{-2}. Polarization values applied to the substrate: (A,B) +0.10, and (C,D) +0.30 V vs. Ag/AgCl/KCl (3M).

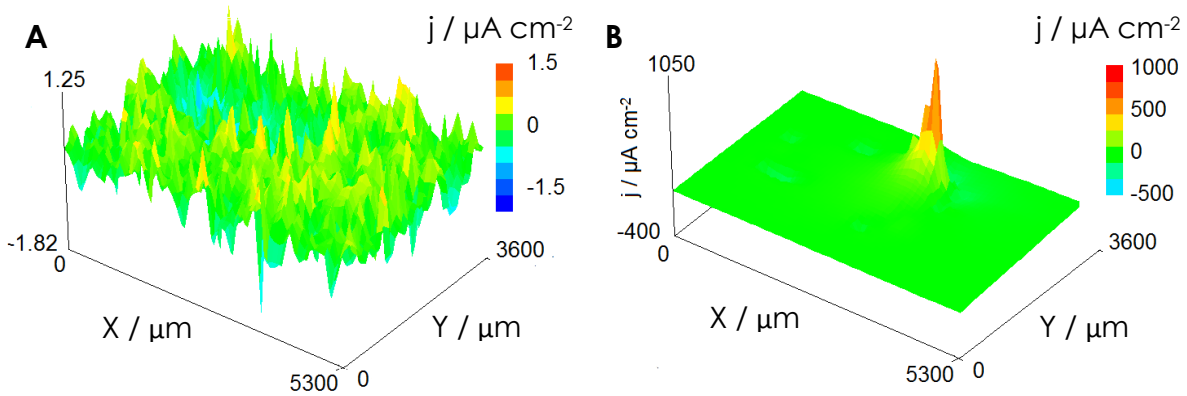

Figure 3.2.3. SVET images of a 304 stainless steel sample polarized at +0.40 V vs. Ag/AgCl/KCl (3M) during immersion in 0.1 M NaCl. They were recorded before (A) and after (B) the application to the sample of a cathodic potential pulse at -1.50 V vs. Ag/AgCl/KCl (3M) during 3 s. The Z scale is the current density in µA cm^{-2}.

The observation of enhanced susceptibility towards corrosion after applying a negative potential to the specimen was further explored using conventional potentiodynamic polarization measurements. A freshly polished sample was immersed in 0.1 M NaCl solution, and subjected to potentiodynamic polarization starting at 0 V (which was the starting potential used for the substrate polarization in SVET measurements given in Figure 3.2.3), up to +0.50 V vs. Ag/AgCl/KCl (3M) (slightly below the E_{bp} value given in Table 3.2.1). At this potential, the direction of the potential sweep was reverted and the sample was polarized in the negative direction down to -1.50 V vs. Ag/AgCl/KCl (3M). Potential reversal was next applied and the potential was raised again up to +0.50 V vs. Ag/AgCl/KCl (3M), and finally swept in the negative direction down to +0.10 V vs. Ag/AgCl/KCl (3M). The corresponding current response during the application of this potential programme is shown in Figure 3.2.4.

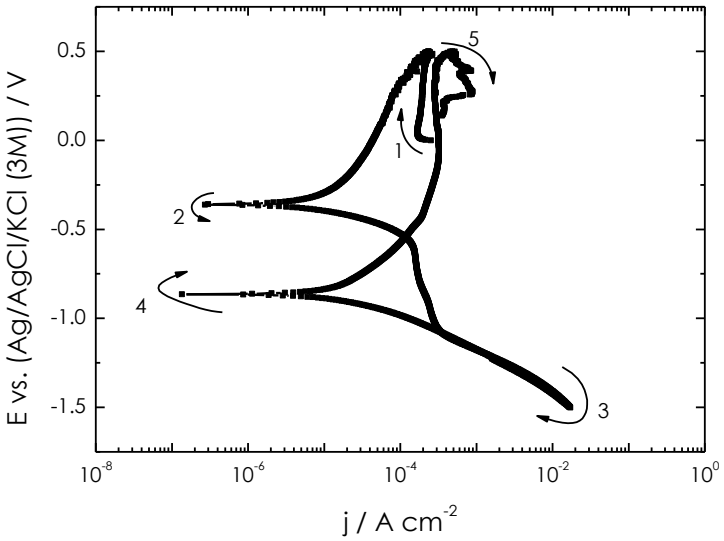

Figure 3.2.4. Potentiodynamic polarization of a 304 stainless steel sample in 0.1 M NaCl. Numbers and arrows in the graph indicate the sequence and the direction of the polarization sweeps applied to the sample. Scan rate: 1 mV s^{-1}.

The initial anodic branch exhibits an anodic current plateau related to passive film formation without any sign of passivity breakdown. Upon potential reversal, the anodic current progressively decreases with smaller anodic overpotentials until the specimen attains cathodic polarization beyond the corresponding corrosion potential. During cathodic polarization, the current trace firstly depicts a plateau related to the diffusion-limited reduction of dissolved oxygen in the electrolyte, followed by the onset of the hydrogen evolution reaction (HER) at potentials more negative than -1.00 V vs. Ag/AgCl/KCl (3M). After potential reversal, the subsequent scan in the positive direction shows three main features. First, the open circuit potential was shifted to more negative potentials compared to that recorded for the passivated sample in the previous scan (namely -0.87 and -0.36 V vs. Ag/AgCl/KCl (3M), respectively). Secondly, the corrosion current extrapolated by graphical

methods as the intersection of both Tafel slopes is in the order of 10^{-5} A cm^{-2} after the potential excursion down to -1.50 V vs. Ag/AgCl/KCl (3M), while that determined from the previous potential sweep in the same graph was one order of magnitude smaller. Finally, the anodic currents measured in the passive range around +0.45 V vs. Ag/AgCl/KCl (3M), denoted as (5) in the graph, are also one order of magnitude bigger than those recorded at the beginning of the experiment (marked as (1)), revealing the higher susceptibility of the material towards anodic dissolution after cathodic polarization. Furthermore, a hysteresis loop was also observed following the last potential reversal produced at +0.50 V vs. Ag/AgCl/KCl (3M), indicating some breakdown of the passive layer formed in these conditions. It is thought that these observations support the previous findings from SVET measurements.

The effect of electrochemical reduction of the oxide layer was further investigated using SVET while subjecting the sample to a two-step polarization programme. It consisted in the application of a cathodic potential relative to the OCP for 5 seconds, followed by anodic polarization of the sample at +0.45 V vs. Ag/AgCl/KCl (3M) during one minute. Both the average current flowing through the sample, monitored at the output of the potentiostat, and the current density registered with the SVET probe placed above the center of the metal strip were recorded. Figure 3.2.5 gives the temporal evolution of these current signals during anodic polarization of the sample, immediately following previous application of a cathodic polarization at various potential values. Short cathodic potential pulses at -1.00 V vs. Ag/AgCl/KCl (3M), effectively increased the susceptibility of the steel sample towards metal dissolution during anodic polarization for the given time and potential. This is evidenced in Figure 3.2.5A through the increasing average currents that are measured from the sample. When a more negative potential value was applied during the cathodic pulse, namely -1.10 V vs. Ag/AgCl/KCl (3M), the subsequent anodic current transient exhibited a continuous increase in the current related to the propagation of a localized corrosion process at the metal surface. Variations in the ionic current flows measured at the SVET probe with time occurred almost at the same times that those reported in the average current (cf. Figure 3.2.5B). In this case, negative ionic current densities were recorded during the prior application of the cathodic step, with greater absolute values the more negative potential applied. This cathodic potential was maintained during 6 seconds in all cases, therefore the SVET signals are related to the flux of anions generated through the cathodic processes taking place on the surface. Next, the application of less negative values to the substrate prior to the anodic pulse led to the measurement of positive ionic current flows almost two orders of magnitude greater during the subsequent application of the anodic polarization. The anodic current flows are due to diffusion of the iron cations generated at the surface, thus supporting that enhanced metal dissolution occurred in the system, as it is expected in the case of a localized corrosion process. Finally, the signals determined with the SVET probe dropped to those typically corresponding to background noise levels upon ceasing substrate polarization (for times longer than 66 s), an indication of substrate repassivation.

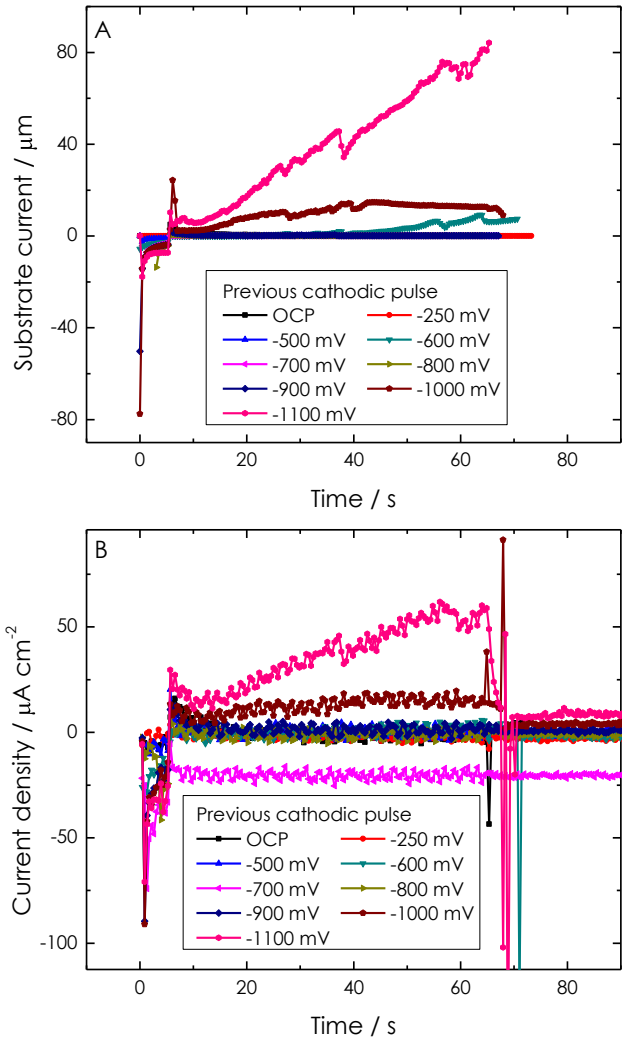

Figure 3.2.5. Time evolution of the average and local currents flowing during the immersion of a 304 stainless steel sample immersed in 0.1 M NaCl. The sample was polarized at +0.45 V vs. Ag/AgCl/KCl (3M) following the application of a cathodic pulse during 5 seconds. The values of the cathodic polarizations are indicated in the plots referred to the Ag/AgCl/KCl (3M) reference electrode. (A) Total current flowing through the specimen; and (B) local ionic current densities detected at the SVET probe placed over the center of the metal strip.

A different behaviour was observed in the 25 mM HCl + 75 mM $HClO_4$. No localized electrochemical activity was observed with the SVET + potentiostat combination for anodic polarization of the substrate up to +0.45 V vs. Ag/AgCl/KCl (3M) following cathodic pulses in the -0.80 to -2.00 V vs. Ag/AgCl/KCl (3M) range. This indicates that passive layer breakdown is promoted by the action of chloride ions rather than pH, as deduced from Table 3.2.1. However, electrolyte exchange between 0.1 M NaCl and 25 mM HCl + 75 mM $HClO_4$ solutions led to pitting corrosion on the steel surface. This was done as follows: initially, the substrate was immersed in the hydrochoric – perchloric acid solution and polarized anodically (without prior application of a cathodic potential to the cell). Subsequently, electrolyte exchange using conductivity water followed by addition of 0.1 M NaCl solution was performed, whereas the substrate was left at its spontaneous open circuit potential during this

stage of the procedure, and SVET images were collected as before. Next, the electrolyte was exchanged to the mixed acid solution in order to repeat the anodic polarization step though with the substrate polarized at a more positive potential value than in the preceding step. New exchange of electrolyte solution to 0.1 M NaCl will be subsequently performed to record the corresponding SVET image. Active pitting corrosion in 0.1 M NaCl solution of the unbiased sample occurred following the anodic polarization at +0.35 V vs. Ag/AgCl/KCl (3M) in the acid solution (see Figure 3.2.6). This local activation of the surface was better observed following polarization at +0.40 V vs. Ag/AgCl/KCl (3M).

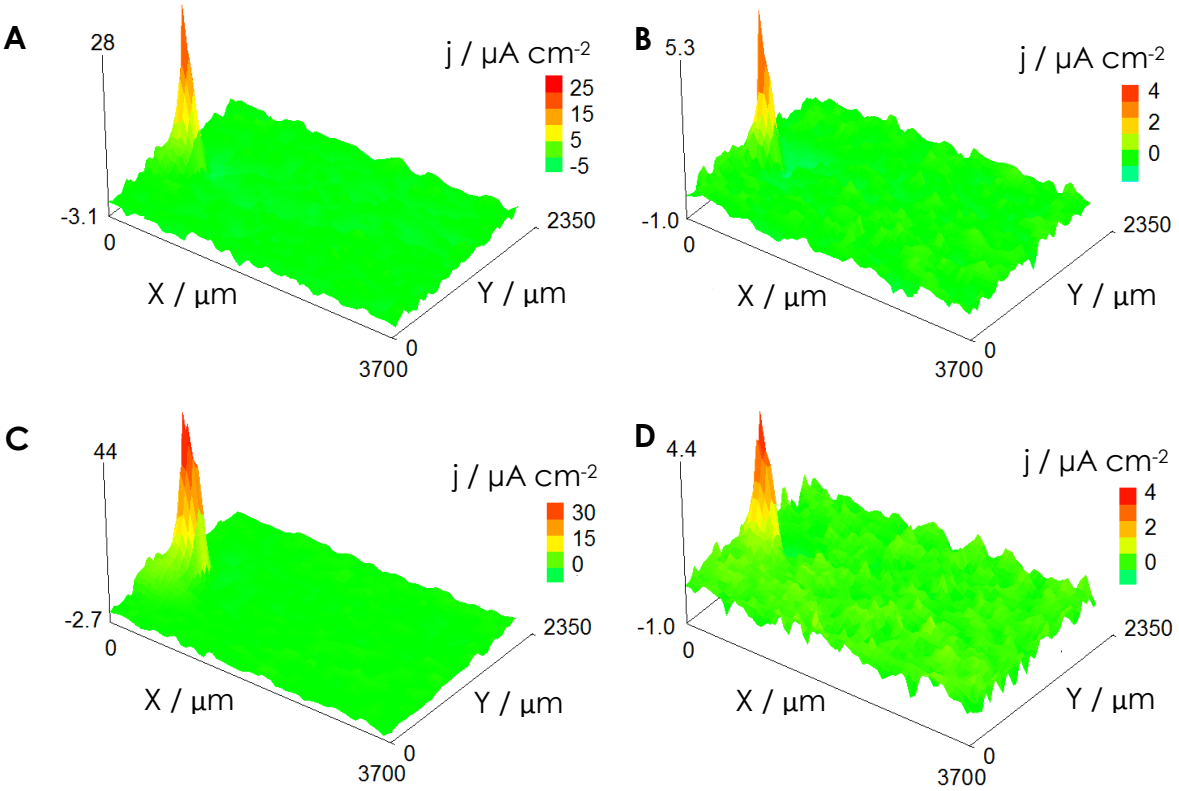

Figure 3.2.6. SVET images of a 304 stainless steel sample recorded during immersion in (A,C) 25 mM HCl + 75 mM $HClO_4$, or in (B,D) 0.1 M NaCl following solution exchange. The *Z* scale is the current density in µA cm^{-2}. Polarization conditioning of the sample: (A) polarized at +0.35 V vs. Ag/AgCl (3M), (B,D) open circuit potential, and (C) polarized at +0.40 V.

3.2.5.3. Scanning electrochemical microscopy

SECM measurements carried out with substrate immersed in 0.1 M HCl were done by recording scan lines along the *X* axis at different fixed *Y* positions. Increasing polarizations were applied to the steel substrate, starting from the OCP and finishing with +0.40 V vs. Ag/AgCl/KCl (3M) anodic polarization. Figure 3.2.7 displays various selections of scan lines chosen to describe the trends observed during the measurements under different polarization conditions. The experiment was initiated

by recording scan lines over the unbiased sample. The tip potential was set at +0.50 V vs. Ag/AgCl/KCl (3M) to follow the oxidation of the iron (II) species evolving from the surface due to metal dissolution. Then, metal dissolution would be detected by measuring faradaic currents at the SECM tip when it passes above the active corroding site. This was indeed the case especially along the first scan lines recorded in the series, those exhibiting the smallest coordinates in Figure 3.2.7A. A tip current peak reaching ca. 100 pA is present in the first scan line, and it progressively became less notorious towards the end of the experimental series, that is, in those lines recorded with the tip scanning with the biggest *Y* coordinates.

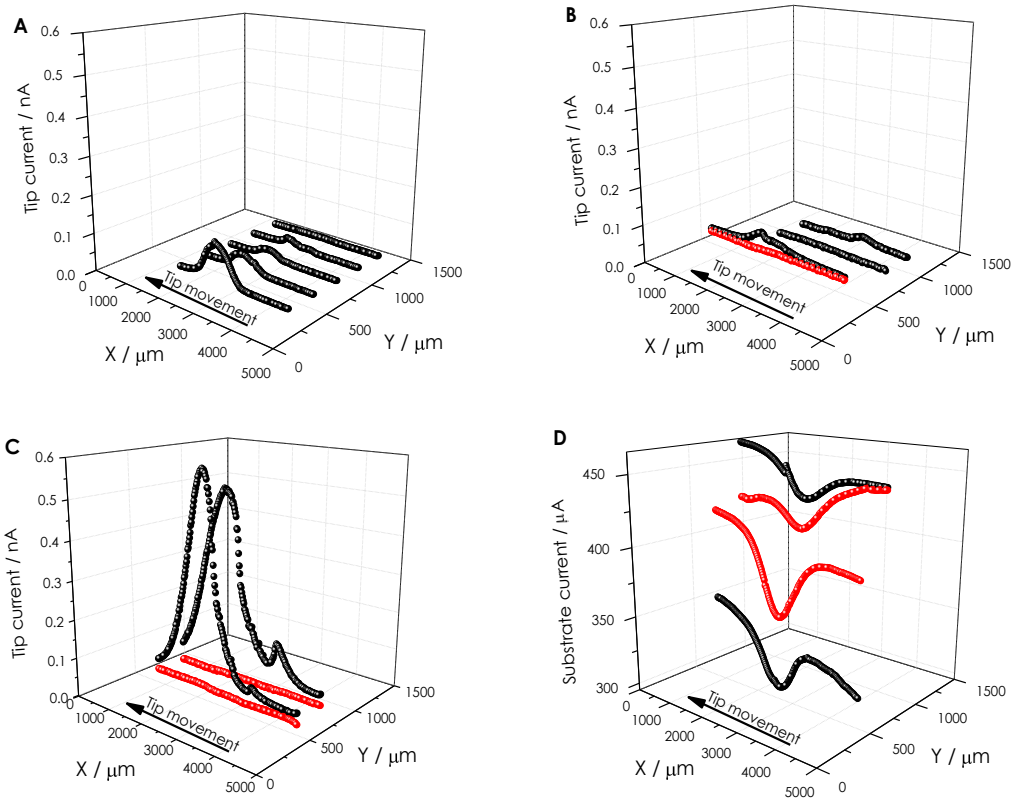

Figure 3.2.7. Current recorded either at the ultramicroelectrode (A,B,C) or at the 304 stainless steel substrate (D) during immersion in 0.1 M HCl solution. Potential condition at the substrate: (A) OCP, (B) +0.30, and (C, D) +0.40 V vs. Ag/AgCl/KCl (3M). Current recordings were performed while the tip was scanned across the steel strip using: tip-sample distance: 10 µm; scan rate: 25 µm s^{-1}. Tip potential: (black) +0.50 V vs. Ag/AgCl/KCl (3M) for the oxidation of Fe(II) species; (red) +0.10 V vs. Ag/AgCl/KCl (3M) for the reduction of Fe(III) species.

Subsequently, the experimental sequence was repeated for various polarizations of the substrate extending from 0 V to more positive values using 100 mV steps. No metal dissolution was detected for the scan lines recorded at 0, +0.10 and +0.20 V vs. Ag/AgCl/KCl (3M) (not shown in the figure). The values of the tip currents recorded in the scan lines could not be separated from the background noise level. Unambiguous current values were recorded when the substrate was polarized at +0.30 V vs. Ag/AgCl/KCl (3M), though they amounted only a few pA (see Figure 3.2.7B). Since the potential applied to the substrate was positive enough

from a thermodynamic standpoint to oxidize the iron (II) species formed as result of the anodic dissolution of the substrate, the surface was scanned over the same scan line exhibiting that signal while setting the tip to +0.10 V vs. Ag/AgCl/KCl (3M). In this way, eventual formation of iron (III) species at that active site on the surface would be detected on the subsequent current trace drawn in red in Figure 3.2.7B. It is readily observable that currents related to iron reduction were not observed from the system. This fact may support that the corroding 304 stainless steel substrate does not produce iron (III) species, neither it provides a surface for electron transfer that would produce the oxidation of the dissolving ferrous ions in this acid environment.

Polarization of the substrate at +0.40 V vs. Ag/AgCl/KCl (3M) was accompanied by the recording of greater currents at the tip associated with iron (II) collection, as observed in Figure 3.2.7C. This observation is consistent with the greater anodic currents observed at this potential in the potentiodynamic polarization curve of 304 steel in 0.1 M HCl shown in Figure 3.2.1. Oxidation of iron (II) ions occurred exclusively at the tip despite the high positive polarization applied to the substrate. This feature is supported by the measurement of zero tip currents related to iron (III) reduction in the scan lines recorded when the tip potential was set at +0.10 V vs. Ag/AgCl/KCl (3M). No evidence for the anodic dissolution of the steel with the formation of iron (III) species could thus be found. Besides, with such corrosion rate, substrate current in this experiment surprisingly seemed to be influenced by the tip location. As observed in Figure 3.2.7D, which shows current of the substrate recorded while measuring lines given in Figure 3.2.7C, when tip was passing across the metal target, located in the centerd position, current detected at the sample significantly decreased when probe was biased at either +0.10 or +0.50 V vs. Ag/AgCl/KCl (3M). In order to provide an explanation to this phenomenon, it must be first considered that the microelectrode is effectively altering the electrochemical properties of the local media in the close proximity of the sample. Then, tip polarization at +0.50 V vs. Ag/AgCl/KCl (3M) and subsequent oxidation of iron to the ferric form could lead to a temporary passive layer formation, since iron (III) is more likely to form hydroxides. However, at this low pH, the hydroxide formation is not so spontaneous, though cannot be discarded at this highly localized range and further exploration of the surrounding media must be given to clarify this. On the other hand, when tip is biased at +0.10 V vs. Ag/AgCl/KCl (3M), apparently there is no electrochemical process taking place at the tip since no current is detected, so the mentioned alteration of the electrochemical properties of the local media does not seem to be enough to explain that effect. Then, the reason might simply arise from the convection produced by the tip movement, which refreshes the solution, probably more acidified during the anodic substrate polarization (and consequently more aggressive) due to the partial hydrolysis of iron cations.

A similar procedure was not performed in the low-containing chloride solution 25 mM HCl + 75 mM $HClO_4$ since it did not show any significant activity related to passivity breakdown by SVET.

On the contrary, SECM characterization of 304 stainless steel in 0.1 M NaCl solution was conducted for the sample subjected to stable pitting conditions. Upon

immersion of the freshly polished samples in the test solution, cathodic pulses were applied in order to promote pitting corrosion during subsequent polarization at +0.45 V vs. Ag/AgCl/KCl (3M). Then, SECM measurements were carried with the tip sequentially polarized at +0.10 and +0.50 V vs. Ag/AgCl/KCl (3M), while the substrate was held at +0.45 V vs. Ag/AgCl/KCl (3M). Figure 3.2.8 shows the SECM maps recorded with the tip polarized at both potentials. 2D scans were recorded instead of scan lines because the media was less aggressive, and it was harder to locate the precise location at which surface activation would occur. Data collected for E_{tip} = +0.50 V vs. Ag/AgCl/KCl (3M) are mostly small current values which are even smaller at the center of the scanned area, where the steel substrate was placed. This behaviour is accompanied by the observation that this surface was showing dissolution currents in the order of hundreds of microamperes. Thus, there is less iron (II) available for oxidation into iron (III) at the tip in the proximity of the sample, providing a response similar to that observed for competitive behaviour. This can be explained considering that in this media the surface is now able to oxidize the iron (II) species from metal dissolution, and iron (III) is the main species formed under these conditions. Furthermore, ferrous ions are produced in a smaller amount, and they can be oxidized on the active metallic sample before diffusing into the electrolyte. This oxidation reaction on the corroding surface of steel is more easily attained in near neutral conditions due to the higher tendency of iron (III) to form hydroxides, a reaction that shifts the equilibrium of iron oxidation to the ferric ion formation. This feature is also evidenced by the negative currents detected from specific locations in a central position of the map recorded for E_{tip} = +0.10 V vs. Ag/AgCl/KCl (3M) that is given in Figure 3.2.8B. These rather high cathodic current values arise from active sites where ferric ions are being produced. However, it is also observed a significant increase of the anodic current at the end of the lines of the scans, precisely where those cathodic intensities were detected.

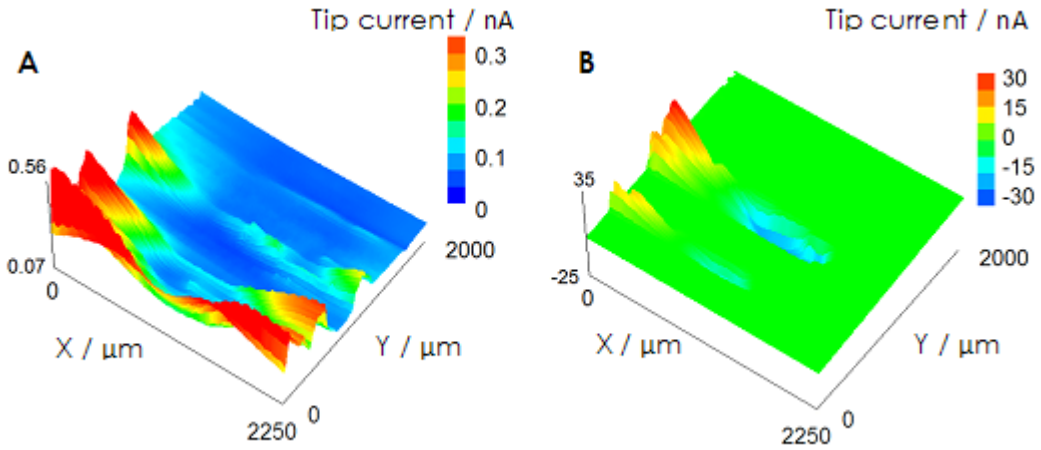

Figure 3.2.8. SECM maps recorded over the 304 stainless steel substrate biased at +0.45 V vs. Ag/AgCl/KCl (3M) during immersion in 0.1 M NaCl. Substrate polarization is located inside the pitting regime of the material. The Z scale is the tip current in nA. Tip potential: (A) +0.50, and (B) +0.10 V vs. Ag/AgCl/KCl (3M); tip-sample distance: 10 µm; scan rate: 25 µm s^{-1}.

The substrate current was then also monitored during scan acquisition. Major variations could be observed during the 3 hours required to record the two SECM images in Figure 3.2.8. A selection of the current response measured at the substrate is given in Figure 3.2.9. Most of them, especially those corresponding to linear scans taken while the tip acquired the lines corresponding to *Y* positions close the half of duration, showed current depletion effects with the proximity of the tip, as it was previously observed in HCl solution. Then, pH background is not (at least not the only one) key factor responsible for this phenomenon, but local pH changes, tip convection and local modification of the electrochemical media should also be considered. Thus, the justification given above will also account for this observation.

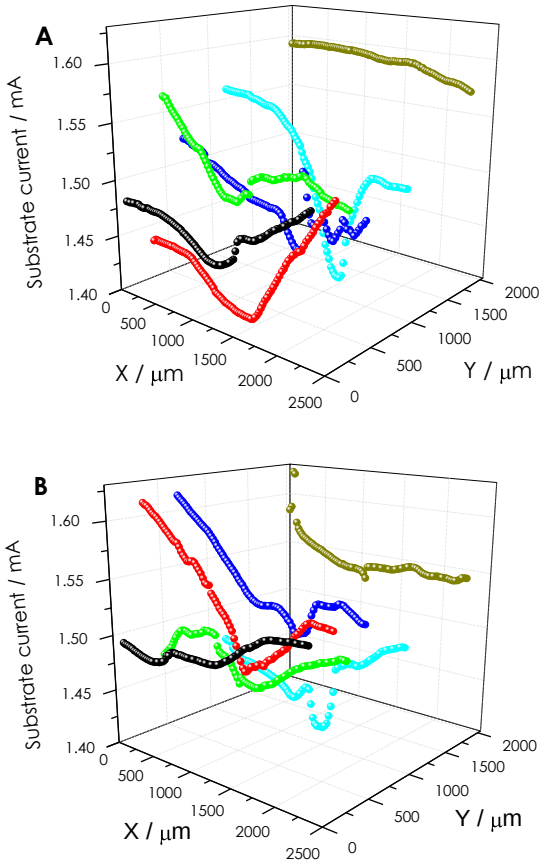

Figure 3.2.9. Current recorded at the 304 stainless steel surface immersed in 0.1 M NaCl while recording the SECM maps shown in Figure 3.2.8. E_{tip}: (A) +0.50, and (B) +0.10 V vs. Ag/AgCl/KCl (3M).

3.2.6. Conclusions

The effect that substrate polarization in 304 stainless steel surfaces produces on the anodic dissolution of the metallic material has been explored. SVET and SECM results indicate vigorous anodic local dissolution in 0.1 M HCl solution, while prior

removal or weakening of the passive layer is mandatory to obtain comparable results in 0.1 M NaCl solution. The controlled modification of acidity and chloride ion concentration in the aqueous solution facilitated to observed the onset of anodic local dissolution by SVET.

SECM experiments have led to identification of the ionic iron species formed during metal dissolution and their distribution above the exposed sample. Release of iron (II) ions was mostly found in 0.1 M HCl solution, but major production of iron (III) was detected in 0.1 M NaCl when the pitting range was reached.

3.2.7. References

1. M.V. Biezma, J.R. San Cristóbal. Corrosion Engineering Science and Technology 40 (2005) 344.
2. C.-O.A. Olsson, D. Landolt. Journal of the Electrochemical Society 148 (2001) B438.
3. D. Hamm, C.-O.A. Olsson, D. Landolt. Corrosion Science 44 (2002) 1009.
4. K.-T. Oh, K.-N. Kim, M. Lee, Y.-S. Park. Journal of the Electrochemical Society 149 (2002) B146.
5. E.-S.M. Sherif, J.H. Potgieter, J.D. Comins, L. Cornish, P.A. Olubambi, C.N. Machio. Corrosion Science 51 (2009) 1364.
6. E.-S.M. Sherif, J.H. Potgieter, J.D. Comins, L. Cornish, P.A. Olubambi, C.N. Machio. Journal of Applied Electrochemistry 39 (2009) 1385.
7. Y. Jiang, H. Tan, Z. Wang, J. Hong, L. Jiang, J. Li. Corrosion Science 70 (2013) 252.
8. A. Legat, V. Doleček. Journal of the Electrochemical Society 142 (1995) 1851.
9. F.J. Pérez, M.P. Hierro, C. Gómez, L. Martínez, P.G. Viguri. Surface and Coatings Technology 155 (2002) 250.
10. C.X. Li, T. Bell. Corrosion Science 46 (2004) 1527.
11. C.X. Li, T. Bell. Corrosion Science 48 (2006) 2036.
12. G.H. Aydoğdu, M.K. Aydinol. Corrosion Science 48 (2006) 3565.
13. K. Prabakaran, S. Rajeswari. Journal of Applied Electrochemistry 39 (2009) 887.
14. M. Azzi, M. Benkahoul, J.E. Klemberg-Sapieha, L. Martinu. Surface and Coatings Technology 205 (2010) 1557.
15. E.A. Ferreira, R.D. Noce, C.S. Fugivara, A.V. Benedetti. Journal of the Electrochemical Society 158 (2011) C95.
16. E. Heitz. In: Analytical Methods in Corrosion Science and Engineering (Edited by P. Marcus, F. Mansfeld). CRC Press, Boca Raton, 2006, p. 435.
17. F. Huet. In: Analytical Methods in Corrosion Science and Engineering (Edited by P. Marcus, F. Mansfeld). CRC Press, Boca Raton, 2006, p. 507.
18. F. Mansfeld. In: Analytical Methods in Corrosion Science and Engineering (Edited by P. Marcus, F. Mansfeld). CRC Press, Boca Raton, 2006, p. 463.
19. H. Böhni, T. Suter, F. Assi. Surface and Coatings Technology 130 (2000) 80.

20. T. Suter, H. Böhni. In: Analytical Methods in Corrosion Science and Engineering (Edited by P. Marcus, F. Mansfeld). CRC Press, Boca Raton, 2006, p. 649.
21. F. Arjmand, A. Adriaens. Electrochimica Acta 59 (2012) 222.
22. J. Li, D.J. Meier. Journal of Electroanalytical Chemistry 454 (1998) 53.
23. V. Maurice, P. Marcus. In: Analytical Methods in Corrosion Science and Engineering (Edited by P. Marcus, F. Mansfeld). CRC Press, Boca Raton, 2006, p. 133.
24. L. Liu, Y. Li, F. Wang. Electrochimica Acta 54 (2008) 768.
25. L. Niu, Y. Yin, W. Guo, M. Lu, R. Qin, S. Chen. Journal of Materials Science 44 (2009) 4511.
26. M.B. Jensen, D.E. Tallman. In: Electroanalytical Chemistry: A Series of Advances, vol. 24 (Edited by A.J. Bard, C.G. Zoski). CRC Press, Boca Raton, 2012, p. 171.
27. T. Misawa, H. Tanabe. ISIJ International 36 (1996) 787.
28. J. Izquierdo, L. Nagy, J.J. Santana, G. Nagy, R.M. Souto. Electrochimica Acta 58 (2011) 707.
29. J. Izquierdo, L. Nagy, Á. Varga, J.J. Santana, G. Nagy, R.M. Souto. Electrochimica Acta 56 (2011) 8846.
30. J. Izquierdo, L. Nagy, S. González, J.J. Santana, G. Nagy, R.M. Souto. Electrochemistry Communications 27 (2013) 50.
31. R.M. Souto, Y. González-García, S. González. Corrosion Science 47 (2005) 3312.
32. E. Völker, C. González-Inchauspe, E.J. Calvo. Electrochemistry Communications 8 (2006) 179.
33. A.M. Simões, A.C. Bastos, M.G. Ferreira, Y. González-García, S. González, R.M. Souto. Corrosion Science 49 (2007) 726.
34. Y. Yin, L. Niu, M. Lu, W. Guo, S. Chen. Applied Surface Science 255 (2009) 9193.
35. M. Terada, A. F. Padilha, A. M. P. Simões, H. G. de Melo, I. Costa. Materials and Corrosion 60 (2009) 889.
36. Y. Yuan, L. Li, C. Wang, Y. Zhu. Electrochemistry Communications 12 (2010) 1804.
37. R.M. Souto, J.J. Santana, L. Fernández-Mérida, S. González. Electrochimica Acta 56 (2011) 9596.
38. M. Terada, R.A. Marques, A.M. Simões, A.F. Padilha, I. Costa. Corrosion Engineering Science and Technology 46 (2011) 599.
39. A. Pilbáth, T. Szabó, J. Telegdi, L. Nyikos. Progress in Organic Coatings 75 (2012) 480.
40. K. Fushimi, K.A. Lill, H. Habazaki. Electrochimica Acta 52 (2007) 4246-4253.
41. J.J. Santana, J. González-Guzmán, L. Fernández-Mérida, S. González, R.M. Souto. Electrochimica Acta 55 (2010) 4488.
42. R. Leiva-García, R. Akid, D. Greenfield, J. Gittens, M.J. Muñoz-Portero, J. García-Antón. Electrochimica Acta 70 (2012) 105.
43. J.A. Wharton, B.G. Mellor, R.J.K. Wood, C.J.E. Smith. Journal of the Electrochemical Society 147 (2000) 3294.
44. H. Uchida, M. Yamashita, S. Inoue, K. Koterazawa. Materials Science and Engineering A 319-321 (2001) 496.
45. B. Vuillemin, X. Philippe, R. Oltra, V. Vignal, L. Coudreuse, L.C. Dufour, E. Finot. Corrosion Science 45 (2003) 1143.

46. H. Krawiec, V. Vignal, R. Oltra. Electrochemistry Communications 6 (2004) 655.
47. H.E. Jamil, A. Shriri, R. Boulif, C. Bastos, M.F. Montemor, M.G.S. Ferreira. Electrochimica Acta 49 (2004) 2753.
48. A.C. Bastos, M.G. Ferreira, A.M. Simões. Corrosion Science 48 (2006) 1500.
49. H. Iken, R. Basseguy, A. Guenbour, A. Ben Bachir. Electrochimica Acta 52 (2007) 2580.
50. V. Vignal, H. Krawiec, O. Heintz, R. Oltra. Electrochimica Acta 52 (2007) 4994.
51. M. Reffass, R. Sabot, M. Jeannin, C. Berziou, Ph. Refait. Electrochimica Acta 52 (2007) 7599.
52. M. Reffass, R. Sabot, M. Jeannin, C. Berziou, Ph. Refait. Electrochimica Acta 54 (2009) 4389.
53. A. Alvarez-Pampliega, M.G. Taryba, K. Van den Bergh, J. De Strycker, S.V. Lamaka, H. Terryn. Electrochimica Acta 102 (2013) 319.
54. G.A. Zhang, Y.F. Cheng. Corrosion Science 51 (2009) 1589.

3.3

Imaging local surface reactivity on stainless steels 304 and 316 in acid chloride solution using scanning electrochemical microscopy and the scanning vibrating electrode technique

3.3.1. Abstract

The release of soluble iron species from 304 and 316 stainless steel substrates under anodic polarization during immersion in acid chloride solution was investigated using scanning electrochemical microscopy (SECM). Speciation of the iron ions formed by anodic dissolution was possible by adequately setting the potential of the microelectrode probe so that iron (II) and iron (III) could be imaged selectively. There is a strong dependence between their generation and the applied substrate potential, in addition to the effect of chemical nature of the substrate. The scanning vibrating electrode technique (SVET) was employed to visualize the ionic currents flowing in the electrolyte adjacent to the corrosion microcells formed on the steels when they were under potentiostatic polarization. The higher resistance against breakdown of the passive layer formed on 316 stainless steel was thus evidenced and directly compared to that formed on 304 stainless steel, and required more positive polarizations for the onset of pitting corrosion.

3.3.2. Resumen

Se ha investigado la producción de especies de hierro desde substratos de acero inoxidable 304 y 316 durante su inmersión en disoluciones de ácido clorhídrico, utilizando la microscopía electroquímica de barrido (SECM). Ha sido posible la especiación de los iones de hierro formados por disolución anódica mediante el ajuste adecuado del potencial de la sonda microelectrodo, permitiéndose la visualización selectiva de hierro (II) y hierro (III). Se ha encontrado una fuerte dependencia entre la generación de estas especies y el potencial de substrato aplicado, además del efecto de la naturaleza química del substrato. La técnica de barrido del electrodo vibrante (SVET) se empleó para visualizar los flujos de corriente iónica en el electrolito adyacente a las microceldas de corrosión que se desarrollan en los aceros cuando se encuentran bajo polarización potenciostática. Se evidencia la mayor resistencia frente a la ruptura de la capa pasiva formada en el acero inoxidable 316 comparándola directamente con la formada en acero inoxidable 304, siendo necesarias polarizaciones más positivas para iniciar la corrosión por picado en el primer caso.

3.3.3. Introduction

Local differences in chemical reactivity related to the development of microcells occur in the corrosion reactions, and they can be visualized *in situ* using scanning microelectrochemical techniques [1,2], thus contributing to a better understanding of the behaviour of the system. Among them, scanning electrochemical microscopy (SECM) is a powerful technique for the characterization of the electrochemical processes occurring at the metal/electrolyte interface of corroding systems [3,4]. The scanning probe is usually an amperometric ultramicrodisk (tip) of a noble metal with diameter comprised between 10 and 25 μm, and it is moved in close proximity to the surface of the investigated material to characterize the electrochemically-active species participating in the process. This technique can be operated when the sample is either unbiased in the electrolyte, or under controlled polarization. In particular, the release of iron (II) ions from corroding iron-based materials can be detected at the tip through their oxidation to iron (III). This procedure has been successfully employed to image the metastable pitting of stainless steel [5], and the breakdown of passive oxide layers and subsequent localized corrosion on iron-based materials [6-11]. On the other hand, the Fe^{2+}/Fe^{3+} couple undergoes a reversible redox reaction in acidic environments, so in principle the release of iron (III) species could also be imaged over reacting samples from their reduction to ferrous species. Yet this possibility has not been exploited for corrosion research using the SECM, possibly because mainly iron (II) ions are produced in significant amount to be adequately detected in most of corrosion problems concerning iron-based materials, in addition to the limitation arising from the high tendency of ferric ion to precipitate as iron (III) hydroxide. Another electrochemically-active species often monitored in SECM studies of corroding systems is the dissolved oxygen in the solution [6,7]. In this case, a redox competition effect between the measuring tip and the sample under investigation occurs when this molecule is consumed in the cathodic sites [12].

Another scanning microelectrochemical method successfully employed to characterize corrosion processes and systems is the scanning vibrating electrode technique (SVET) [13]. It produces complementary information by imaging the ionic fluxes of species involved in the electrochemical processes occurring on surfaces to be imaged, including those related to the corrosion reactions [14-22]. This technique informs about the location of all the electrochemical reactions that occur over an area as long as they produce measurable ionic fluxes. Despite the quite extended employment of the technique in the corrosion laboratory, it is customary to investigate systems without control of its electric state by the operator, that is, in the absence of external polarization [14,18,19]. This is probably due to the loss of sensitivity encountered when the sample is polarized, because the reference signal employed to measure the ionic current fluxes cannot be taken in a position with the adequate symmetry with relation to the auxiliary electrode, needed for the electrochemical control and polarization of the surface under study. Furthermore,

systems experiencing corrosion produce heterogeneous distributions of the corroding microcells that are not symmetrically located in relation to an otherwise perfectly symmetrical auxiliary electrode, thus leading to inhomogeneous current fluxes in the solution. Despite these difficulties, still some valuable semi-quantitative information were collected on polarized substrates, as it will be demonstrated in this Section. With this information, passivity breakdown of the passive layer and stable pitting corrosion could be simultaneously studied through the global transient currents and the local ionic current produced as result.

The aim of this Section is to visualize local reactivity distributions related to passivity breakdown of 304 and 316 stainless steels promoted by sample polarization while the materials were immersed in aqueous chloride solutions of different composition. Stable pit growth has been followed by detecting the release of soluble iron ions from the corroding metal, and its dependence with both the applied potential and the composition of the test environment.

3.3.4. Experimental section

Experiments were performed on 304 and 316 grade austenitic stainless steel supplied as sheet of thickness 1 mm by Goodfellow Materials Ltd, Cambridge, UK. The metals were not analysed, but the nominal compositions provided by the manufacturer were:

- 304 SS: 17 – 20 % Cr, 8 – 11 % Ni, < 2 % Mn, < 0.08 % C, bal. Fe.
- 316 SS: 16.5 – 20 % Cr, < 2 % Mn, 8 – 14 % Ni, < 0.12 % C, 2.0 – 3.5 % Mo, bal. Fe.

Samples were fabricated from 1 mm thick sheets of the steels. They were cut into ca. 2 mm width and 2 cm length strips, and mounted in an Epofix (Struers, Ballerup, Denmark) resin sleeve of approximate diameter 3 cm, so that only 1 mm x 2 mm metallic areas were exposed to the electrolyte. The resulting mounts contained one strip of each material. These samples were abraded using SiC paper of 1200 and 4000 grit, and subsequently polished using alumina suspension 0.3 μm particle size. The strips of the two steels protruded at the rear of the mount to facilitate electrical connection. In this way, they could be either connected between them to form a galvanic pair, or polarized by an external potentiostat. When only one surface was considered, the other metallic strip was covered by Sellotape in order to prevent any eventual interference resulting from its exposure to the electrolyte.

SECM experiments were carried out in 0.25 M and 0.1 M HCl, whereas SVET measurements were done in 0.025 M HCl + 0.075 M $HClO_4$. The choice of the latter was such to obtain a less aggressive attack whereas maintaining the same pH in solution as in 0.1 M HCl. All the reagents were of analytical grade and solutions were prepared by using twice distilled water. Experiments were conducted at ambient temperature in the naturally aerated solutions.

SECM measurements were performed with equipment purchased to Sensolytics GmbH (Bochum, Germany). The instrument was built around an Autolab (Metrohm, Herisau, Switzerland) bipotentiostat, controlled by personal computer. Platinum microdisks of 10 µm diameter were employed as microelectrode tips. The small electrochemical cell (ca. 3.5 mL volume) contained an Ag/AgCl/KCl (3M) reference electrode, and a platinum counter electrode. The system was operated in either three-electrode or four-electrode configuration depending on whether the potential of the substrate was left unbiased or under potentiostatic control.

Scanning electrochemical microscopy was operated in the substrate generation – tip collection (SG-TC) mode to detect either iron (II) or iron (III) cations evolving from stainless steel surfaces under different substrate polarization. Tip-sample distance was established by recording approach curves in the negative feedback mode towards the surrounding insulating sleeve. The tip potential was set at -0.65 V vs. Ag/AgCl/KCl (3M) in order to register the faradaic current related to the reduction of dissolved oxygen. After the surface was located, the tip was withdrawn 10 µm for scanning parallel to the sample. Both linear scans and 2D maps were recorded at maximum scan rate of 25 µm s^{-1}. Tip potential was alternately set at +0.50 and +0.10 V vs. Ag/AgCl/KCl (3M) to detect iron species of different oxidation states. The first value was employed to detect iron (II) species through their oxidation at the microdisk. Tip potential was set at +0.10 V for the eventual reduction of iron (III) species evolving from the substrate while polarized more positive than +0.30 V vs. Ag/AgCl/KCl (3M)

SVET experiments were conducted with an Applicable Electronics Inc. instrument (Forestdale, MA, USA). The sensing probes were 10 µm PtIr wires. They were electrochemically deposited black platinum until they provided adequate capacitance values. Probe vibration in normal direction to the surface was applied, with 75 Hz vibration frequency, with 20 µm amplitude vibration. The tip-sample distance was fixed at 60 µm. Sample polarization was performed in this case using a Potentiostat/Galvanostat Model 283 (Princeton Applied Research, Oak Ridge, TN, USA). The current and potential analogic outputs of the potentiostat were connected to analogic inputs of the SVET instrumentation, so these two parameters were also monitored in the experiments. A platinum ring covered with black platinum electrodeposit was employed as the counter electrode to minimize asymmetries in current distribution due to the geometry of the system, and an Ag/AgCl/KCl (3M) was used as reference electrode.

3.3.5. Results and discussion

Changes in chemical activity related to corrosion of stainless steel 304 and 316 samples left at their spontaneous open circuit potential during immersion in 0.25 HCl solution were monitored using SECM operated in the SG-TC mode. The tip potential

was set at +0.50 V vs. Ag/AgCl/KCl (3M) in order to monitor the oxidation of dissolved iron (II) into iron (III) species.

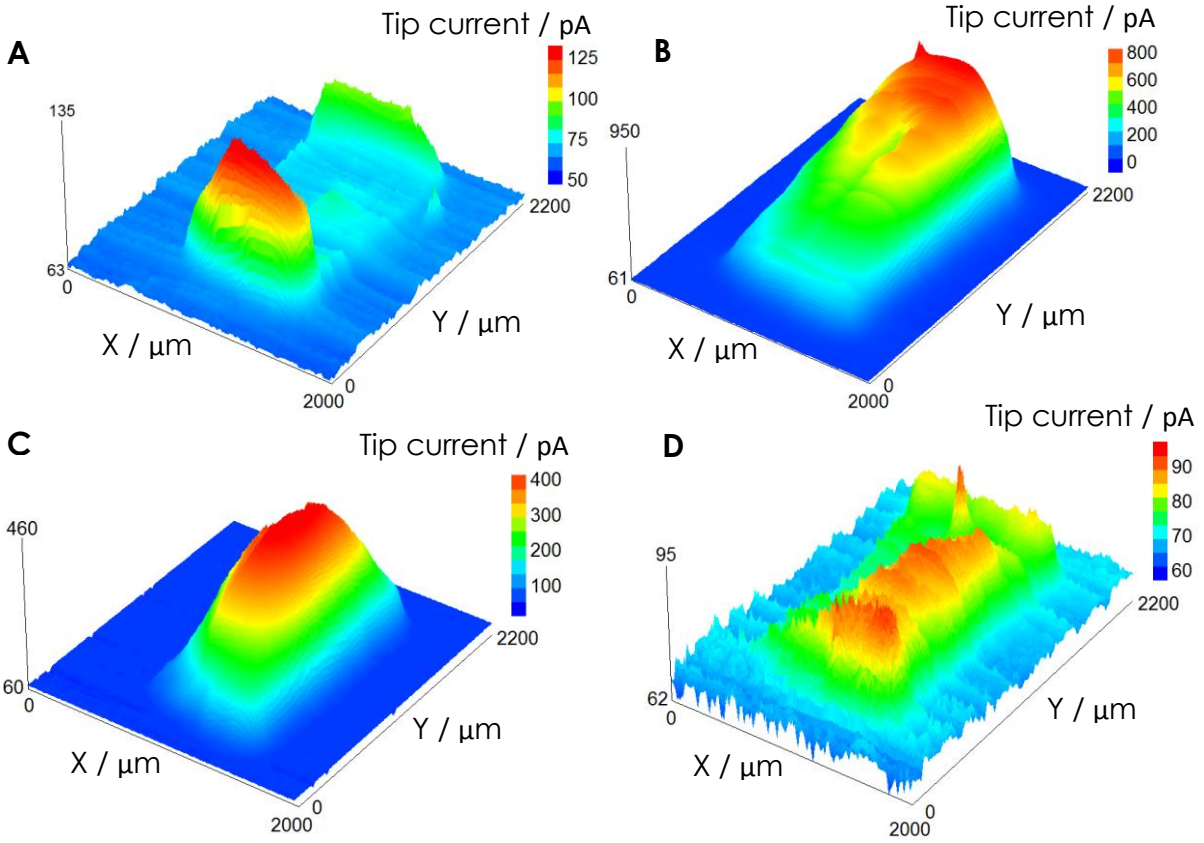

Figure 3.3.1. The distribution of iron (II) ions over a 304 steel surface exposed to 0.25 M HCl at the times: (A) 0.5, (B) 4, (C) 7.5, and (D) 24 h. These times correspond to the initiation of scan recording. The *Z* scale is the tip current in pA. Time for scan acquisition: 3.5 hours. E_{tip} = +0.50 V vs. Ag/AgCl/KCl (3M); tip-substrate distance: 10 µm; scan rate: 25 µm s^{-1}. The sample was left unbiased at its spontaneous open circuit potential in the solution.

Figure 3.3.1 displays the time evolution of iron (II) generation from a 304 stainless steel sample in 0.25 HCl. During the first recorded scan, given in Figure 3.3.1A, high current values in the order of 100 pA were initially registered, evidencing rather high iron dissolution rates leading to the release of bivalent cations. However, current decreased quite abruptly after recording a few scan lines over the metal, and it only increased again towards the end of the scan. This behaviour is characteristic of a system that evolves faster than the time required for the tip to acquire the data, though the occurrence of heterogeneous electrochemical behaviour over the steel strip cannot be discarded yet. The following scan, recorded just after previous one was finished, is given in Figure 3.3.1B and it evidenced a more homogeneous distribution of metal ions. Initial current values recorded when the tip started to scan over the steel surface were close to the last values monitored in the previous map, and they increased with time up to 0.9 nA. Changes in the chemical activity of the exposed surface occurred now at a slower rate, although the tip was still unable to

record data from the complete exposed surface before relevant change took place in the entire metal strip. The following scan in Figure 3.3.1C, taken after 7.5 hours immersion, shows that metal dissolution happened over the complete exposed steel strip. A less active surface was then imaged, as evidenced by the smaller current values recorded in this map. Finally, after 24 hours immersion, metal dissolution from the surface had greatly diminished due to metal passivation, and the smaller tip currents were related to the passivation current. Then, no complete passivation was observed for this steel in this aggressive environment.

Imaging of 316 stainless steel was performed in the same conditions, and it evidenced a significantly less active surface. The images given in Figure 3.3.2 show tip current values smaller than 100 pA, significantly smaller than those previously recorded for 304 steel (cf. Figure 3.3.1). Moreover, only the two first scans, initiated after 25 and 158 minutes immersion in the acid solution, detected iron (II) generation from the substrate, whereas the signals measured in subsequent scans could not be resolved from background noise. First scan acquired with the SECM, displayed in Figure 3.3.2A, suggests a rather homogeneous distribution of electrochemical activity for 316 steel in this aggressive media that allows the contour of the steel strip to be clearly distinguished from the surrounding epoxy sleeve. Yet, electrochemical activity is exclusively related to the onset of passivation, and only a small release of metal ions due to localized corrosion occurred near the center of the strip during the second scan.

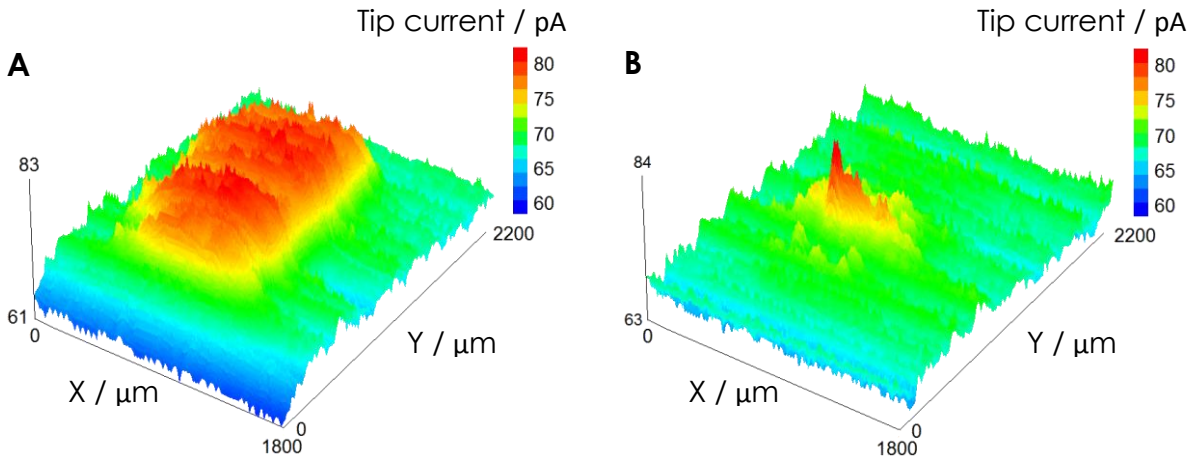

Figure 3.3.2. The distribution of iron (II) ions over a 316 steel surface exposed to 0.25 M HCl at the times: (A) 0.5, and (B) 3 h. These times correspond to the initiation of scan recording. The *Z* scale is the tip current in pA. Time for scan acquisition: 2 hours. E_{tip} = +0.50 V vs. Ag/AgCl/KCl (3M); tip-substrate distance: 10 µm; scan rate: 25 µm s^{-1}. The sample was left unbiased at its spontaneous open circuit potential in the solution.

Effect of polarization on the chemical activity of the two steels during immersion in 0.25 HCl solution was next investigated by SECM. In this case, the samples were polarized anodically with respect to their corresponding OCP values using the bipotentiostat built in the SECM instrument. For that purpose, one scan was firstly taken after immersion of each sample in 0.25 M HCl at its corresponding OCP.

Then, OCP was measured before applying positive polarization to the metal substrate and scanning again. The resulting images for both surfaces are shown in Figure 3.3.3A-B, respectively. The OCP values measured after completing those scans were -0.26 and -0.16 V vs. Ag/AgCl/KCl (3M), for 304 and 316 steels, respectively. These values correspond well with the electrochemical characteristics of both steels. Again rather homogeneous distributions of iron (II) species released from the freshly exposed samples were observed, and the contours of the samples were clearly distinguished. When the substrate was biased at -0.10 V vs. Ag/AgCl/KCl (3M) (see Figures 3.3.3C-D), which is indeed an anodic polarization with respect to their corresponding OCP values, metal dissolution occurred in a more heterogeneous way, leading to enhanced release of iron (II) from sites close to the metal edges. Crevice corrosion is likely to be happening, probably arising from imperfect joint between the insulating resin and the active metal. Still, current values are four times smaller for the nobler 316 surface. The crevice corrosion effect was likely to happen in the system when sample polarization was shifted even more anodically to +0.05 V vs. Ag/AgCl/KCl (3M), as it is shown in Figures 3.3.3E-F for 304 and 316 surfaces, respectively. Tip currents were in the nA range with this polarization for both substrates, though 3 - 4 times bigger for the more active 304 surface. Besides, the substrate currents were measured using the current amplifier function of the bipotentiostat during the duration of the experiment. They ranged between 0.1 and 1.25 mA cm^{-2} for the 316 strip, and between 0.25 and 15.9 mA cm^{-2} for 304 steel. These are rather high current densities related to localized corrosion of the stainless steels.

Experiments were next performed in 0.1 M HCl in order to reduce the impact of localized corrosion using a more diluted solution. Furthermore, the two steels were exposed simultaneously, and the effect of galvanic coupling could also be considered in the same experiment. In this way, a more direct comparison of the electrochemical behaviours of the two steels and their evolution with time could be performed *in situ*. Due to the very large area required to image both steels in one single scan (in excess of 6,000 µm x 2,000 µm), thus requiring very large times for recording one single SECM image, scan lines passing through both steel strips were recorded instead. For the sake of reproducibility, several lines were taken at different locations over the two steels strips to more accurately characterize the behaviour of the two steels.

SECM was firstly employed to image ferrous ions evolving from both steel surfaces (i.e., setting E_{tip} = +0.50 V vs. Ag/AgCl/KCl (3M)). Figure 3.3.4 shows selected scan lines recorded over the sample containing 304 and 316 steel strips at four different electrical conditions of the substrate. Metal release was only observable over the 304 steel when the samples were either left unbiased, or galvanically-coupled by producing an electric contact between both steels at the rear of the mount. It should be noticed that greater tip currents related to detection of released iron (II) from the 304 strip occurred when the sample was left unbiased (cf. Figures 3.3.4A-B). Since 316 is less active material than 304 steel, it could be expected galvanic coupling to promote anodic dissolution of 304 steel, resulting in the

measurement of greater currents at the tip in this case. But it must be noticed that galvanic coupling was produced after recording the scan lines in Figure 3.3.4A, and the surfaces would be somewhat passivated in the medium at the time of coupling. This passive layer was effectively protecting both materials from undergoing further iron oxidation when both metals were simultaneously polarized at potentials between 0 and +0.20 V vs. Ag/AgCl/KCl (3M), since only noise could be detected as tip current.

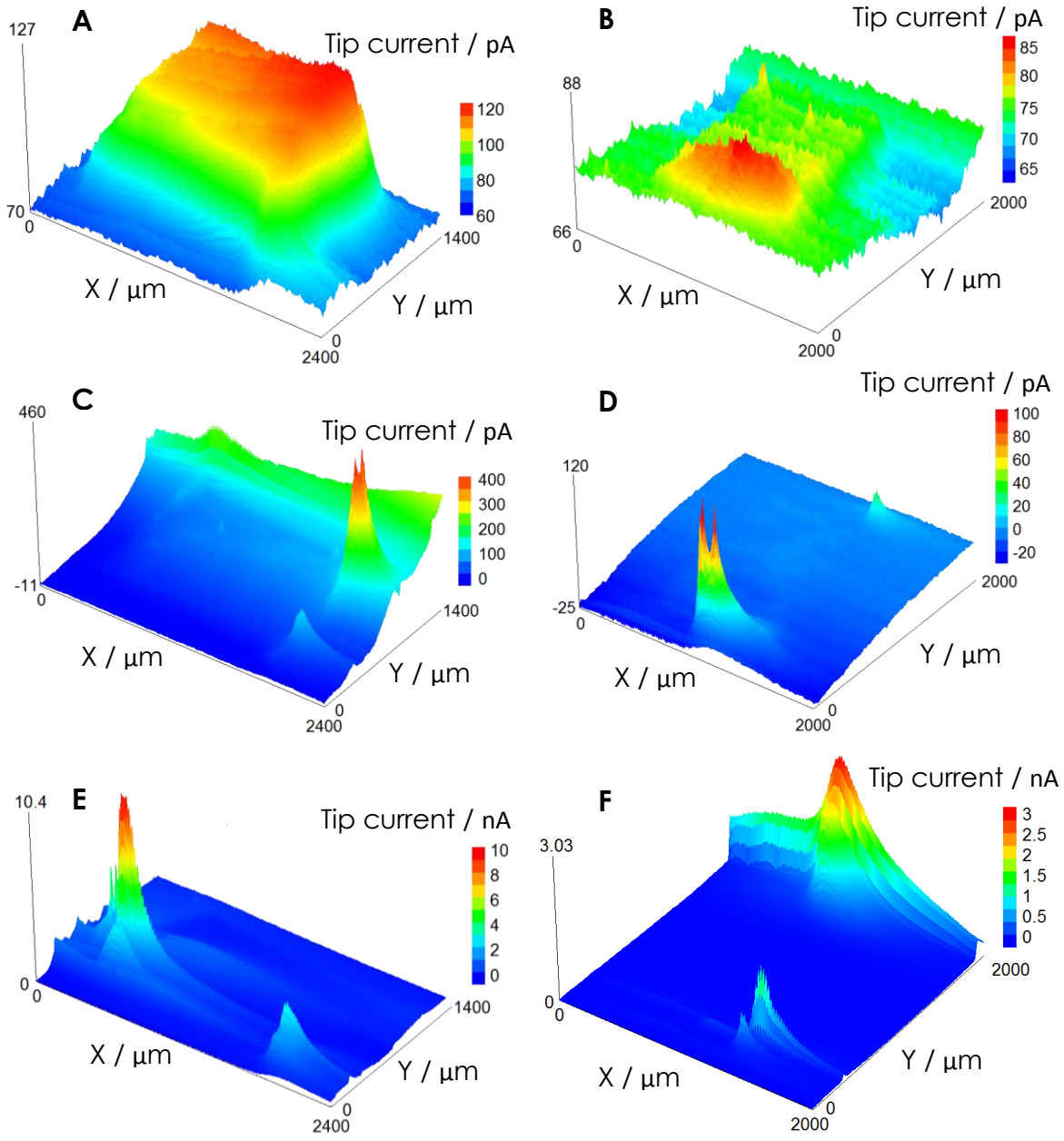

Figure 3.3.3. Effect of sample polarization on the distribution of iron (II) ions over (A,C,E) 304, and (B,D,F) 316 steel surfaces exposed to 0.25 M HCl. The *Z* scale is the tip current in (A-D) pA or (E,F) nA. Potential conditioning of the steel samples: (A,B) unbiased, (C,D) polarized at -0.10 V vs. Ag/AgCl/KCl (3M); and (E,F) polarized at +0.05 V vs. Ag/AgCl/KCl (3M). E_{tip} = +0.50 V vs. Ag/AgCl/KCl (3M); tip-substrate distance: 10 µm; scan rate: 25 µm s^{-1}.

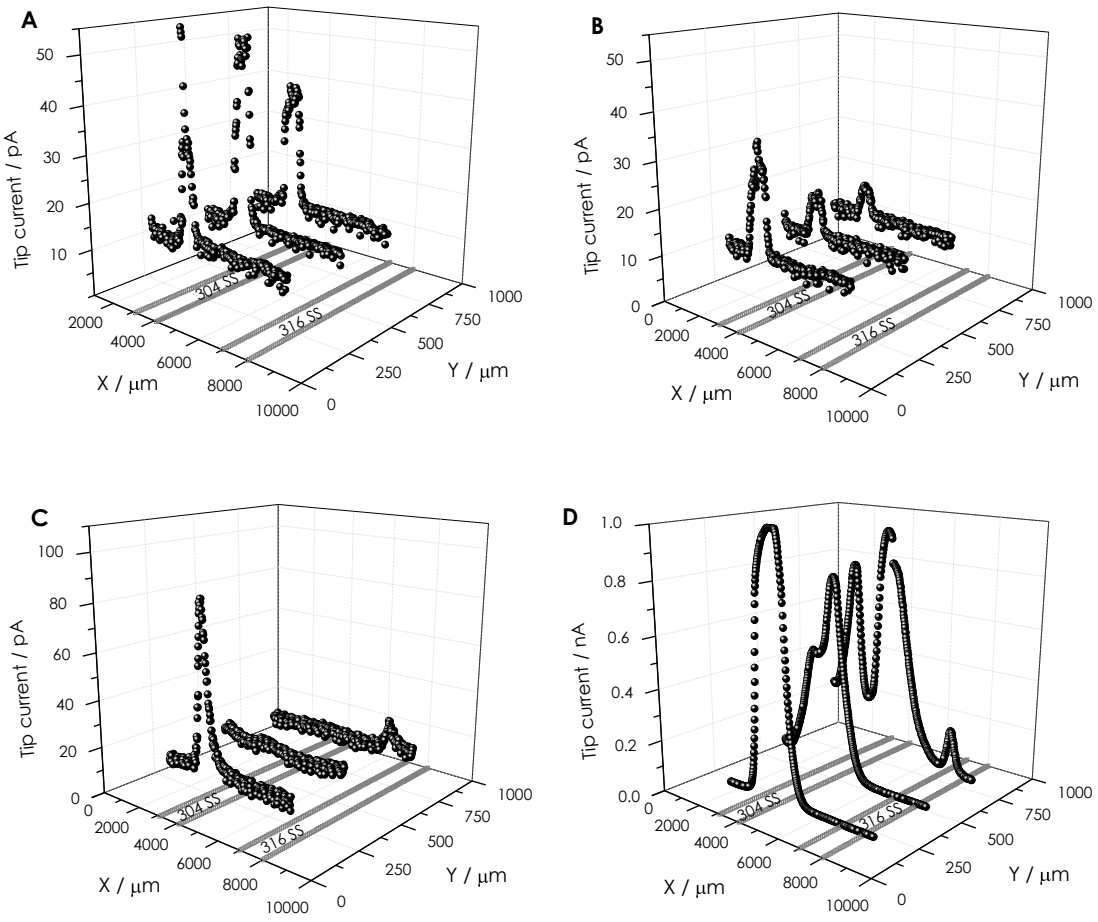

Figure 3.3.4. Effect of sample polarization on the distribution of iron (II) ions over 304 and 316 steel strips exposed to 0.1 M HCl. Potential conditioning of the steel samples: (A) unbiased; (B) galvanic coupling of the two steels; or potentiostatically polarized at (C) +0.25 and (D) +0.30 V vs. Ag/AgCl/KCl (3M). E_{tip} = +0.50 V vs. Ag/AgCl/KCl (3M); tip-sample distance: 10 µm; scan rate: 25 µm s^{-1}.

The situation changed for more positive polarizations of the samples, starting when +0.25 V vs. Ag/AgCl/KCl (3M) was applied, that is plotted in Figure 3.3.4C. In this case, one scan line shows a current peak amounting ca. 90 pA at *Y* position 200 µm, again only over the more active metal 304, showing the onset of localized corrosion. In order to check whether enhanced metal dissolution at this position should be attributed to nucleation of a metastable pit the direction of the tip scan was reverted without shifting the *Y* position, as to detect eventual repassivation of the pit. That was not the case, because even greater tip currents related to the release of Fe(II) ions were measured when the tip passed over the same position approximately 8 min later. Scan lines taken at other positions did not exhibit current signals distinguishable from the background noise levels. A more anodic polarization, namely +0.30 V vs. Ag/AgCl/KCl (3M), led to vigorous release of iron (II) ions above all the extension of the 304 steel strip, as well as a smaller metal release from the 316 strip as well, as observed for *Y* = 800 µm in Figure 3.3.4D. The same scan line also exhibited two peaks over the 304 surface, revealing either edge effects for steel

dissolution, or eventually iron (II) oxidation to iron (III) ions on the surface and subsequent depletion in ferrous concentration and tip current. In order to test the validity of the latter, scan lines were recorded after switching E_{tip} to +0.10 V vs. Ag/AgCl/KCl (3M), that iron (III) species could be detected by reduction at the tip. But only the noise level signal was detected in this way, thus discarding the formation of Fe(III) species at this polarization. Higher anodic polarization of both steel surfaces did not allow determination of species over the 316 stainless steel, since the major dissolution of the metal from the 304 strip was diffusing into the solution even further from the strip and could be detected increasingly closer to the noblest specimen. Therefore, detailed investigation of the effect of polarization on the corrosion behaviour of 316 steel by SECM had to be performed when only this strip was exposed to the corroding environment.

Then, the same sample mount, freshly polished and cleaned, and with the 304 surface covered by adhesive tape to avoid exposure to the electrolyte, was immersed in 0.1 M HCl solution, and scan lines were recorded over the 316 surface in the same way as before. The scan lines recorded for the unbiased steel, as well as those with sample polarization below +0.30 V vs. Ag/AgCl/KCl (3M) only showed noise level signals at the tip. That is, polarization equal or more positive than +0.30 V vs. Ag/AgCl/KCl (3M) was required to promote detectable local dissolution of iron over the steel surface, as it is shown in Figure 3.3.5. When the substrate was biased at +0.30 V vs. Ag/AgCl/KCl (3M), some of the scan lines taken over the steel surface showed local anodic dissolution of iron with the formation of iron (II) species (cf. lines recorded at *Y* position 1100 μm in Figures 3.3.5A-B). Upon detection of iron (II) species in these scan lines, the tip potential was shifted to +0.10 V vs. Ag/AgCl/KCl (3M) to reduce any eventual iron (III) species evolving from surface (red data in graph). In this case, a weak increase in cathodic current over the reactive material was found, probably due to formation of ferric ions on the surface and their reduction at the probe. This fact was more noticeable when the substrate was polarized at +0.40 V vs. Ag/AgCl/KCl (3M) as shown in Figures 3.3.5C-D. In that case, the whole area seemed to be activated for the formation of iron (III) species, though apparently in different ways. Specifically, the current measured at the tip biased at +0.50 V vs. Ag/AgCl/KCl (3M) was smaller while the tip was moved over the steel strip, showing local depletion in iron (II) concentration, whereas an evident cathodic current was measured in the same region when the tip potential was set at +0.10 V vs. Ag/AgCl/KCl (3M). That is, the cathodic currents related to the reduction of iron (III) ions were recorded precisely in the same positions where depleted iron (II) was observed.

Two additional features can be found from observation of the graphs in Figure 3.3.5 that would require further discussion. Firstly, bigger anodic currents were measured over the surrounding epoxy sleeve as the substrate was polarized at more positive potential with the tip biased at +0.5 V vs. Ag/AgCl/KCl (3M), indicating greater diffusion of ferrous metal ions into the surrounding volume of the electrolyte. Secondly, SECM scan lines recorded with the tip potential set at +0.10 V vs. Ag/AgCl/KCl (3M) also showed an anodic current branch following the

measurement of the cathodic currents assigned to the reduction of iron (III). Increased concentration of iron (III) ions in the volume adjacent to the steel surface in the case of the more anodic polarization of the substrate can also originate from oxidation at the metal of the iron (II) ions released from the corroding substrate, since the steel surface is polarized at a potential value high enough to sustain their oxidation if the passive film was broken. The origin of the anodic currents observed at the end of the scan lines measured with E_{tip} = +0.10 V vs. Ag/AgCl/KCl (3M) remains still unknown, though it may be related to the formation of hydrogen peroxide on the substrate in this case, and this species can be oxidized at the tip. Indeed, a similar feature has been previously reported accompanying the degradation reactions occurring from defects in painted steel samples under polarization [23].

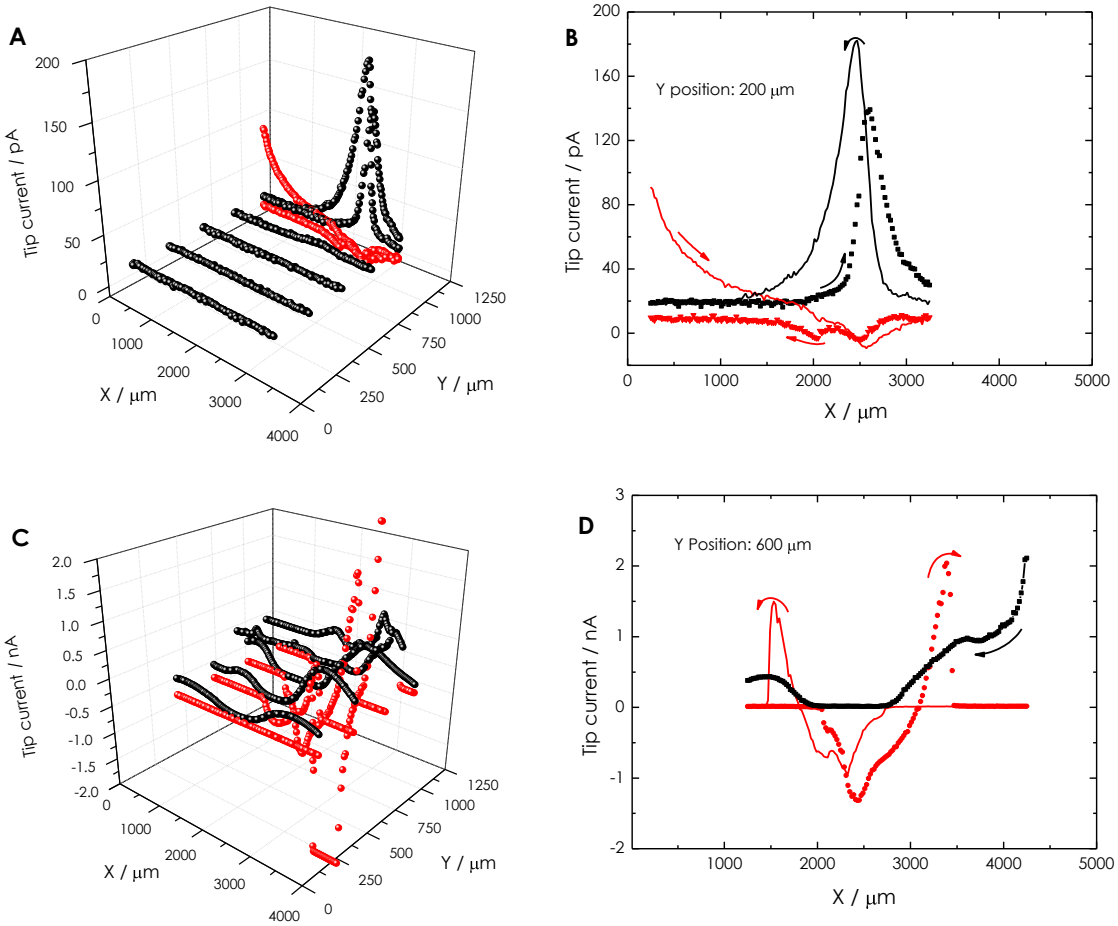

Figure 3.3.5. Effect of sample polarization on the distribution of (black) iron (II) and (red) iron (III) ions over a 316 steel strip exposed to 0.1 M HCl. The steel sample was potentiostatically polarized at (A,B) +0.30, and (C,D) +0.40 V vs. Ag/AgCl/KCl (3M). E_{tip} = +0.50 V vs. Ag/AgCl/KCl (3M) for the detection of Fe(II) ions (lines and symbols in black), and E_{tip} = +0.10 V vs. Ag/AgCl/KCl (3M) for the detection of Fe(III) species (lines and symbols in red). Tip-sample distance: 10 µm; scan rate: 25 µm s^{-1}. Arrows indicate scan direction.

Another effect was discovered by monitoring the total current flowing through the substrate during SECM experiments. It occurred when the substrate was polarized at the highest anodic polarizations under consideration, that is, when localized corrosion was detected by SECM. In principle, it should be expected that the current measured at the substrate must be an average measurement of the electrochemical processes occurring on the total steel surface exposed to the electrolyte, and they should be exclusively related to the electrical state of the sample and the composition of the electrolyte. Thus, no significant influence should be produced by the local shielding of the small tip when it scanned parallel to the surface. Nevertheless, Figure 3.3.6A shows changes in the plots of the substrate current when the tip passed above the steel strip. That is, major decrease of the faradaic current flowing from the sample happened when the tip was passing over the 304 steel strip but not over the 316 steel strip, though they were both potentiostatically polarized at the same potential (namely, +0.35 V vs. Ag/AgCl/KCl (3M)). That the effect is related to the presence of the tip in close proximity to the substrate is further evidenced by observing that the current traces at either side of the 304 steel strip could be connected in a continuous line if the values over the metal were ignored. Next, the magnitude of the effect caused by the moving tip on the substrate decreased with the elapse of time, and it was mostly independent of the potential value applied to the tip. That is, it may be regarded independent of whether iron (II) or iron (III) species are locally consumed at the tip.

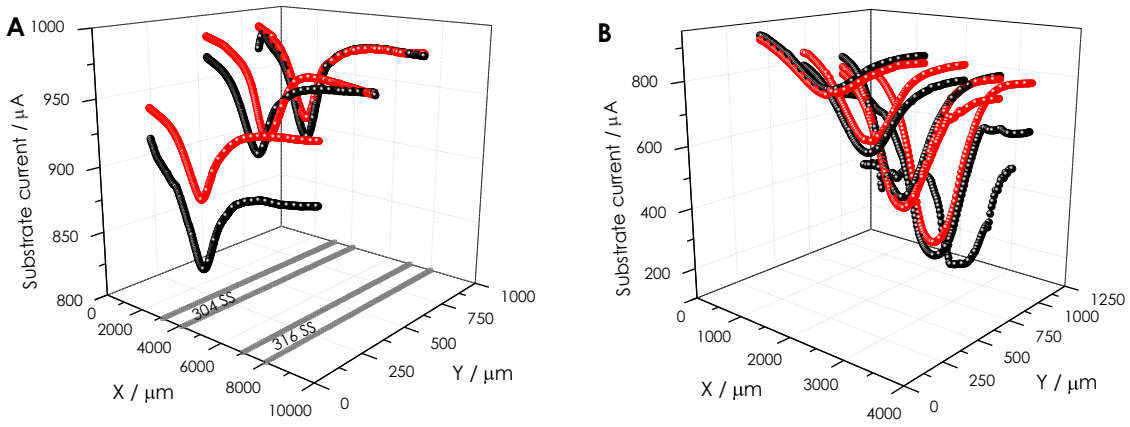

Figure 3.3.6. Current measured at the substrate immersed in 0.1 M HCl while recording SECM data as shown in Figures 3.3.4 and 3.3.5. (A) 304 and 316 steel strips were connected electrically and externally polarized using a potentiostat to +0.35 V vs. Ag/AgCl/KCl (3M). (B) Only 316 steel was exposed to the electrolyte, and polarization was +0.40 V vs. Ag/AgCl/KCl (3M). *X* and *Y* axis refer to the position of the tip while recording the scan lines. E_{tip} = +0.50 V vs. Ag/AgCl/KCl (3M) for the detection of Fe(II) ions (lines and symbols in black), and E_{tip} = +0.10 V vs. Ag/AgCl/KCl (3M) for the detection of Fe(III) species (lines and symbols in red). Tip-substrate distance: 10 µm; scan rate: 25 µm s^{-1}.

Modification of the current response of the substrate by the passage of the tip parallel to the substrate was also found when only the 316 surface was exposed to the surface. In this case, a more anodic polarization was required to detect some changes (i.e., +0.40 V vs. Ag/AgCl/KCl (3M)). The progressive deactivation of the steel surface related to passive layer generation is also viewed in Figure 3.3.6B in the form of greater changes in the substrate current when the tip passed above the metal sample. Again the effect is observed to be independent of the potential applied to the tip. The justification of this feature remains uncertain at present, though it is clearly related to changes in the composition of the electrolyte, which may reduce the susceptibility to passive film breakdown. Since this effect is apparently independent of tip potential, this change might be related to electrolyte convection promoted by movement of the tip, rather than to any eventual electrochemical process taking place at the tip. Actually, hydrolysis of iron cations may produce local acidification and subsequent increase of the aggressiveness of the surrounding electrolyte, so renewal of the solution operated by the tip movement may decrease this aggressiveness, allowing steel surfaces to repassivate in part.

With the objective to gain additional insights on the local reactivity of steels related to passive layer breakdown in acid chloride solution, the scanning vibrating electrode technique was also employed. This technique allows ionic current flows to be measured in the electrolyte with high spatial resolution provided low conductivity electrolytes are employed. In fact, concentrated electrolytes lead to loss of sensitivity. If ionic strength is high in the bulk solution, ions produced or consumed in active regions correspond to charges easily compensated by counter ions from the bulk solution, with the outcome that concentration and charge gradients become less defined. Next, when vigorous formation or consumption of ionic species happens at an active site on the surface, the resistivity of the electrolyte volume next to the site is greatly modified. Considering that SVET measurement involves conversion of a sinusoidal potential signal into an ionic density current signal through the simple application of Ohm's law, which contains the value of the solution resistivity, highly aggressive electrolytes may promote a vigorous metal dissolution process and the SVET response would not be accurate. Therefore, the corrosion behaviour of coupled 304 and 316 steel strips was further investigated in a less concentrated chloride solution. However, protons activity was maintained the same in order to prevent repassivation of nucleated corrosion pits. Mounts containing strips of the two steels surfaces, were investigated by SVET in 0.025 M HCl + 0.075 M $HClO_4$. Both steel strips were electrically connected at the rear of the mount, in order to impose the same polarization to them by the application of an external polarization with a potentiostat. The potential of the substrate was set at several values between -0.75 and +1.20 V vs. Ag/AgCl/KCl (3M) in steps, somewhat resembling the procedure employed in recording potentiostatic polarization curves. A SVET image was recorded at each potential value. Selected scans are displayed in Figure 3.3.7. Polarization at -0.75 V vs. Ag/AgCl/KCl (3M) only shows ionic currents related to reduction of protons on both metal strips (Figure 3.3.7A). No major differences were found between the two steels concerning this cathodic reaction, though the

distribution of the maximum ionic currents depicted as deep blue (corresponding to ca. -250 to -300 µA cm^{-2}), seems to be more extended over the 304 strip leading to a rather homogeneous appearance. Similar ionic current distributions were obtained at potentials more negative than their OCP.

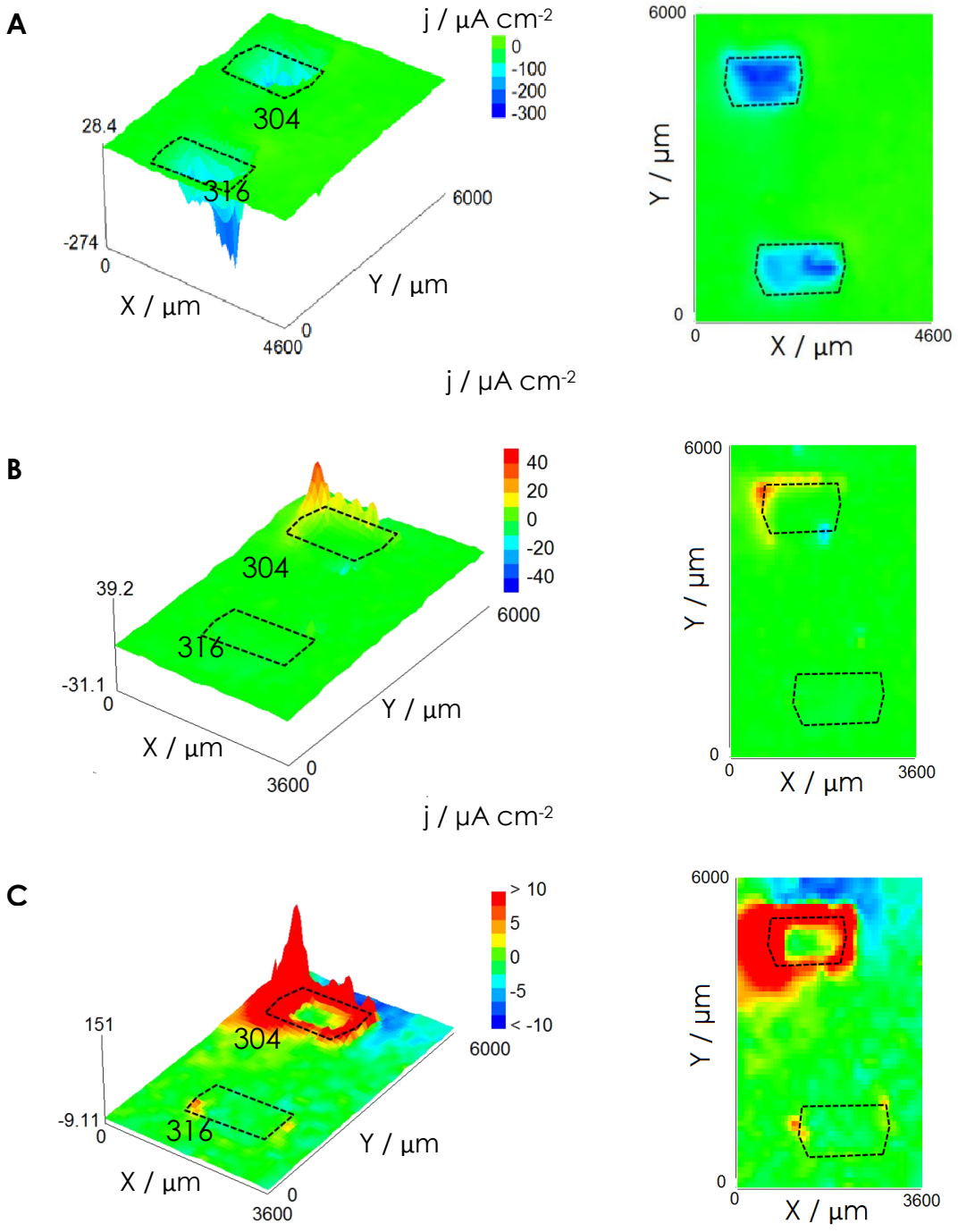

Figure 3.3.7. SVET images of 304 and 316 steel strips immersed in 0.025 M HCl + 0.075 M $HClO_4$. 304 and 316 steel strips were connected electrically and externally polarized using a potentiostat to: (A) -0.75, (B) +0.45, and (C) +1.20 V vs. Ag/AgCl/KCl (3M). The *Z* scale is the current density in µA cm^{-2}. Tip-sample distance: 60 µm.

Anodic polarization was initiated at 0 V vs. Ag/AgCl/KCl (3M), but only background noise was obtained. This behaviour remained for increasingly positive polarizations, and it was necessary to apply +0.45 V vs. Ag/AgCl/KCl (3M) in order to clearly distinguish anodic dissolution from the 304 steel (Figure 3.3.7B), whereas the 316 steel remained inactive. Some crevice corrosion was imaged as well, since dissolution mainly occurred at the edges of the metal surface. This potential is lower than the reported pitting potential for 304 steel in this solution [24], though two facts possibly influencing the pitting potential shift should be noticed: (1) the previous application of the cathodic potential held during the first scan, which may have conducted to partial electrochemical reduction of the oxide layer, and (2) the potentiostatic conditions applied in this Section, different from the potentiodynamic polarization techniques commonly employed to establish pitting corrosion values. Local breakdown of the oxide layer resulting in pitting corrosion occurred at this positive potential for the 304 surface but not for the 316. The latter required a rather high positive bias, namely +1.20 V vs. Ag/AgCl/KCl (3M), in order to distinguish some anodic process taking place on distributed sites on the surface (see Figure 3.3.7C). As expected, vigorous corrosion operated on the 304 strip at this potential.

3.3.6. Conclusions

Scanning microelectrochemical techniques can be employed to visualize the localized breakdown of passive layers on stainless steels and to identify the metal species released at the anodic sites with spatial resolution. Nucleation of corroding pits usually occurs with the formation of iron (II) species, whereas detection of iron (III) requires high positive overpotentials. The corrosion resistance of two different steels, namely 304 and 316 can be compared quite easily using scanning microelectrochemical methods by including the various materials in a common mount whereas they are electrically connected at the rear. This procedure can be extended to the investigation of surface treatments applied to the materials, including the action of corrosion inhibitors. The effect of either galvanic coupling or potentiostatic polarization can be investigated whereas spatially resolved data provide information on the nature and distribution of the corrosive attack.

3.3.7. References

1. P. Marcus, P. Mansfeld (Editors). Analytical Methods in Corrosion Science and Engineering. CRC Press, Boca Raton, 2006.
2. R. Oltra, V. Maurice, R. Akid, P. Marcus (Editors). Local probe techniques for corrosion research. Woodhead Publishing Ltd., Cambridge, 2007.

3. L. Niu, Y. Yin, W. Guo, M. Lu, R. Qin, S. Chen. Journal of Materials Science 44 (2009) 4511.
4. M.B. Jensen, D.E. Tallman. In: Electroanalytical chemistry: A series of advances, vol. 24 (Edited by A.J. Bard, C.G. Zoski). CRC Press, Boca Raton, 2012, p. 171.
5. Y. González-García, G.T. Burstein, S. González, R.M. Souto. Electrochemistry Communications 6 (2004) 637.
6. A.C. Bastos, A.M. Simões, S. González, Y. González-García, R.M. Souto. Electrochemistry Communications 6 (2004) 1212.
7. A.M. Simões, A.C. Bastos, M.G. Ferreira, Y. González-García, S. González, R.M. Souto. Corrosion Science 49 (2007) 726.
8. Y. Yin, L. Niu, M. Lu, W. Guo, S. Chen. Applied Surface Science 255 (2009) 9193.
9. M. Terada, A. F. Padilha, A. M. P. Simões, H. G. de Melo, I. Costa. Materials and Corrosion 60 (2009) 889.
10. M. Terada, R. Albuquerque Marques, A. M. Simões, A. Fernando Padilha, I. Costa. Corrosion Engineering, Science and Technology 46 (2011) 599.
11. R. Leiva-García, R. Akid, D. Greenfield, J. Gittens, M.J. Muñoz-Portero, J. García-Antón. Electrochimica Acta 70 (2012) 105.
12. J.J. Santana, J. González-Guzmán, L. Fernández-Mérida, S. González, R.M. Souto. Electrochimica Acta 55 (2010) 4488.
13. R.S. Lillard. In: Analytical Methods in Corrosion Science and Engineering (Edited by P. Marcus, F. Mansfeld). CRC Press, Boca Raton, 2006, p. 571.
14. J.A. Wharton, B.G. Mellor, R.J.K. Wood, C.J.E. Smith. Journal of the Electrochemical Society 147 (2000) 3294.
15. H. Uchida, M. Yamashita, S. Inoue, K. Koterazawa. Materials Science and Engineering A 319–321 (2001) 496.
16. J.G. Yu, J.L. Luo, P. R. Norton. Langmuir18 (2002) 6637.
17. H.E. Jamil, A. Shriri, R. Boulif, C. Bastos, M.F. Montemor, M.G.S. Ferreira. Electrochimica Acta 49 (2004) 2753.
18. A.C. Bastos, M.G. Ferreira, A.M. Simões. Corrosion Science 48 (2006) 1500.
19. V. Vignal, H. Krawiec, O. Heintz, R. Oltra. Electrochimica Acta 52 (2007) 4994.
20. M. Reffass, R. Sabot, M. Jeannin, C. Berziou, Ph. Refait. Electrochimica Acta 52 (2007) 7599.
21. M. Reffass, R. Sabot, M. Jeannin, C. Berziou, Ph. Refait. Electrochimica Acta 54 (2009) 4389.
22. J. Izquierdo, L. Nagy, S. González, J.J. Santana, G. Nagy, R.M. Souto. Electrochemistry Communications 27 (2013) 50.
23. R.M. Souto, J.J. Santana, L. Fernández-Mérida, S. González. Electrochimica Acta 56 (2011) 9596.
24. J. Izquierdo, L. Martín-Ruíz, B.M. Fernández-Pérez, R. Rodríguez-Raposo, J.J. Santana, R.M. Souto. Applied Surface Science (2014) submitted.

3.4

Local modification and pit corrosion induction on iron surfaces by AFM-SECM

3.4.1. Abstract

Pitting corrosion has been induced in highly localized spots of pure iron surfaces in 0.5 M NaCl solution using combined atomic force – scanning electrochemical microscopy (AFM-SECM). Pits as small as 1.5 µm in diameter could be achieved at deliberately chosen locations by the localized generation of highly concentrated nitric acid. Adding nitrite ions to solution, which act as corrosion inhibitors for iron, ensures its passivation and hinders metal corrosion despite the environment. But nitrite oxidation at the probe-integrated nanoelectrode generates locally aggressive nitric acid, and this acidification combined with the high chloride content leads to a local rapid attack at the surface, and pit generation below the sensing probe. Besides improved spatial resolution and exact control of the pitting corrosion, combined AFM-SECM allows the simultaneous imaging of the generated pits by the conductive AFM tip, overcoming the limitations encountered with the SECM for the same purpose.

3.4.2. Resumen

Se ha inducido corrosión por picado en zonas localizados sobre superficies de hierro puro expuestas en disolución de NaCl 0.5 M, usando la combinación microscopía de fuerzas atómicas – microscopía electroquímica de barrido (AFM-SECM). Se han generado picaduras de diámetros tan pequeños como 1.5 μm micrómetros en localizaciones elegidas empleando de ácido nítrico concentrado generado *in situ*. La adición de iones nitrito en disolución, los cuales actúan como inhibidores de la corrosión para el hierro, asegura su pasivación y protege el metal a pesar del entorno agresivo. Pero la oxidación del nitrito en el nanoelectrodo como sonda integrada genera ácido nítrico localmente, y esta acidificación combinada con el alto contenido en cloruro conlleva a un ataque local rápido en la superficie, resultando en la generación de picaduras bajo la punta del sensor. Además de mejorar la resolución espacial y el control preciso de la corrosión por picado, la combinación AFM-SECM ha permitido la visualización simultánea de las picaduras generadas por la punta AFM conductora, superando las limitaciones encontradas con el SECM para los mismos propósitos.

3.4.3. Introduction

Iron-based materials play an important role in industrial manufacturing, especially for building industries, due to the high strength, easy obtainment and forming. Unfortunately, iron and steel are prone to undergo corrosion when exposed to sufficiently aggressive environment. Even stainless steel materials may undergo highly localized failure through the formation of pits, whose size may be in the order of micrometers or below at the very initial stages. In addition, these pits are frequently nucleated on homogeneous metallic surfaces, in apparent random distribution, as long as aggressive ions such as chlorides are dissolved in the surrounding environment. The analysis of these initial stages of pit formation and evolution requires methods, which provide information with high spatial resolution, in real time about the generation and evolution of the pit formation in the micrometer range. For that purpose, *in situ* measurements during the corrosion process performed in the actual corroding media under study are mandatory, especially for the analysis of the initial stages. But this is not straightforward in the case of homogeneous substrates due to the fast and mainly random characteristics of pitting distribution, which requires pits to be already nucleated in order to be detected. In this way, only pits in the propagation step have been imaged with *in situ* AFM [1-7] or SECM [8-12]. However, it appears effectively impossible to monitor the initiation of pit nucleation.

Aiming to overcome this limitation, one possible strategy is to modify locally the environment in close proximity to single desired spot of the passive surface. This may be achieved by creating locally a high concentration of aggressive species, thus leading to passive breakdown in the site of interest. One of the most direct methods consists in the microinjection of small quantities of dissolved aggressive species, and subsequent surface characterization [13-15]. The application of a strong electric field between deliberately positioned microelectrode and surface area in close proximity has also been proposed and proved to be an interesting approach to create highly active spots [16,17]. Alternately, electrochemical strategies for local modification of the solution composition seem to be more controllable and appropriate. Several procedures have been developed in combination with SECM. Local chloride release for pit generation has been achieved by either the reduction of organic [18] and inorganic [19,20] chloride precursors, or the oxidation of silver / silver chloride microelectrodes [21-24]. Electrolysis of water has also been used to locally alter the pH-value and induce alkaline or acid attacks in the vicinity of susceptible surfaces [25]. Finally, a very interesting approach is the oxidation of nitrite salts, which are converted into highly aggressive nitric acid that promotes the local attack by following reaction 3.4.1 [26,27]:

$$NO_2^- + H_2O \rightarrow NO_3^- + 2\,H^+ \qquad (3.4.1)$$

A significant advantage of this approach is based on the fact that nitrite behaves as corrosion inhibitor for iron, thus protecting the iron substrate outside the local spot of eventual nitric acid formation from corrosion, keeping the remaining surface passive.

Corrosion inhibition by nitrite ions has been considered to follow two main proposed mechanisms, which are listed below in equations (3.4.2) and (3.4.3). One of the mechanisms follows the nitrite oxidation through half-reaction (3.4.2), leading to generation of oxide anions. The solubility product K_S for iron oxides is immediately exceeded with the iron cations produced in the corrosion process and their precipitation occurs. An alternative explanation involves the redox reaction shown in equation (3.4.3), between the dissolved iron (II) and nitrite, which again serves as oxidant agent, generating the poorly soluble ferric oxide, which precipitates on the substrate, [28-31].

$$2\ NO_2^- + 4e^- \rightarrow 2\ N_2O + 3\ O^{2-} \qquad (3.4.2)$$

$$Fe^{2+} + 2\ OH^- + 2\ NO_2^- \rightarrow 2\ NO + Fe_2O_3 + H_2O \qquad (3.4.3)$$

The above shown approaches for pit local induction were applied for a variety of coated and uncoated metallic substrates. Hence, the ability to induce the local initiation of the corrosive attack could be demonstrated, providing new opportunities for the investigation of pitting corrosion at its very early stages. Nevertheless, the achievable spot size is limited by the size of the UMEs typically employed in SECM, which rarely is smaller than 10 µm in diameter. Furthermore, this subsequent analysis is not only influenced by the electrochemical nature (composition and activity) of the electrolyte in the close vicinity of the formed pit, but also by the topography and roughness increase as a consequence of the attack, which makes the distinction between both effects challenging. This difficulty may be overcome with the combination of SECM with a complementary topographically sensitive technique. In this sense, the development of the combined AFM-SECM technique has permitted to take advantage of both, the simultaneous electrochemical abilities of the SECM in addition to the excellent topographic information provided by the AFM. Combining AFM with SECM was demonstrated fabricating a modified AFM cantilevers, with a conductive frame or ring electrode around the AFM tip [32-36]. Alternatively, a disc microelectrode next to an AFM tip consisting of Parylene C was demonstrated by Davoodi *et al*. [37]. The latter probe design has been used in corrosion studies for the characterization of heterogeneous alloys [37-41].

Within this Thesis, in collaboration with the Institute of Analytical and Bioanalytical Chemistry, a new methodology for locally inducing pitting corrosion at well-defined spots on an iron surface using AFM-SECM has been developed. Applying sufficient oxidation potential at the AFM tip integrated electrode, locally a high concentration of nitric acid from nitrite anions was generated. As additionally a fairly high concentration of chloride anions was present in solution, a highly localized fast corrosion process was induced in the vicinity of the combined AFM-SECM tip. Whereas the bulk substrate is protected by the inhibiting effect of the sodium nitrite, which behaves as corrosion inhibitor for iron surfaces in nitrite / chloride medium with a ratio of 1:5 for 0.5 M chloride concentration [31,42-44].

3.4.4. Experimental section

Pure 99.99 % iron sheets of 1 mm thickness supplied by Goodfellow (Cambridge, UK) were employed as substrate material. They were cut into 2.5 cm x 2.5 cm square specimens, manually grounded with silicon carbide papers of increasing grit size from 220 to 4000, and subsequently mechanically polished with alumina micropolish suspension (0.05 µm particle size) in milipore water (18.0 MΩ cm^{-1}) until a mirror-like surface was obtained. The polished sample was thoroughly rinsed with double distilled water, immersed in ethanol and sonicated for 20 minutes in ultrasonic bath for cleaning, and finally dried under argon flow.

An atomic force microscope from Agilent Technologies (Chandler, AZ, USA) equipped, with a 90 um scanner was used for combined measurements. The beta-version of a SECM module of the same company in combination with a picostat potentiostat (Agilent) and the electrochemical AFM liquid cell were used for measurements. The SECM module included a specialized nose-cone with built-in operation amplifier and all the necessary connections for SECM operation. The iron substrate was carefully mounted in the AFM-SECM cell but left disconnected. Hence, the substrate was always kept at its spontaneous OCP. The exposed surface area was circular shaped and approximately 1.75 cm in diameter. The total volume of electrolyte was approx. 1 mL. A ring-shaped counter electrode made of platinum, and a pseudo-reference electrode made of silver chlorinated wire completed the three electrodes cell with the modified AFM cantilever as working electrode. Potential of the Ag/AgCl wire pseudo-reference electrode resulted in +48 mV vs. Ag/AgCl (sat.) reference electrode in the test solution, consisting of 0.5 M NaCl + 0.1 M $NaNO_2$, in good agreement with the theoretical value predicted by the Nernst equation considering the 0.5 M chloride concentration used during experiments.

The fabrication of the AFM-SECM probes has been described elsewhere [32-34]. A sketch and a micrograph of the resulting electrode are given in Figure 3.4.1. In brief, a portion of the chip, the silicon nitride AFM cantilever and the tip are coated with gold as electrode layer by sputtering. Consecutively, the metalized AFM probe was electrically insulated by depositing a silicon nitride layer via chemical vapour deposition (CVD). Afterwards, focus ion beam (FIB) is employed for precisely exposing a frame-shaped electrode and re-shaping the very end of the tip to form the thorn for high-resolution topography measurement. The individual milling steps were observed with scanning electron microscopy (SEM), which enables to determine the actual electrode surface. Quanta 3D Dual Beam system from FEI (Hillsboro, Oregon, USA) was used for FIB milling and SEM imaging. Finally, part of the insulating silicon nitride coating was manually removed at the AFM chip to make electric contact with silver epoxy glue to a metallic wire. The obtained cantilever can be mounted on the nose-cone fitting into the Agilent scanner. The resulting tip employed in experiments detailed here, given in Figure 3.4.1, presented a square ring area of 1.07 µm in length, and a thorn of 0.46 µm in height. AFM-SECM probes were characterized in deoxygenated 10 mM potassium hexaaminruthenium (III)

solutions with 0.1 M KCl as supporting electrolyte. All solutions referred in this Section were prepared using analytical grade chemicals dissolved in Millipore water (18.0 MΩ cm^{-1}). All the experiments were carried out at approximately 20ºC (room temperature).

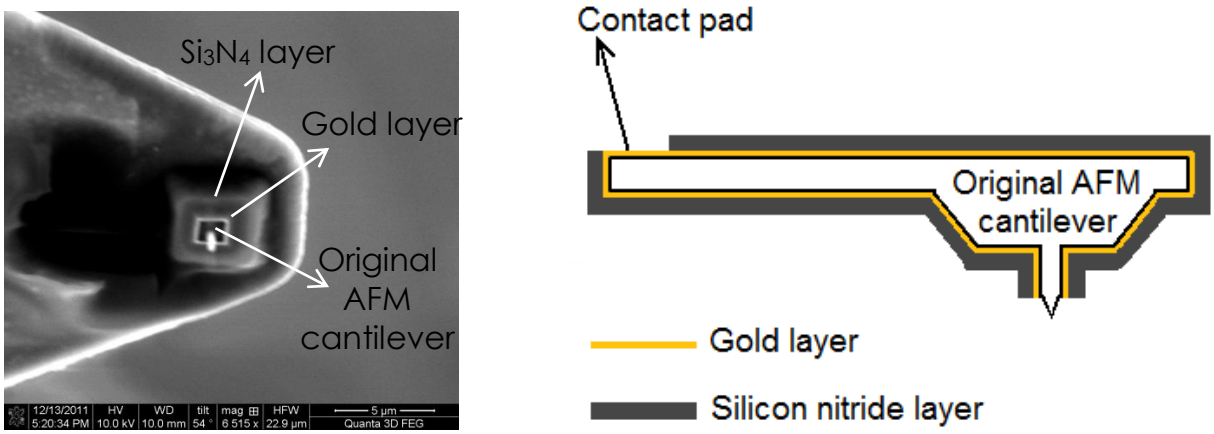

Figure 3.4.1. SEM image (left) and sketch (right) of the AFM-SECM cantilever.

Initial tests conducted for the characterization of the nitrite oxidation waves in chloride containing media, were performed with a CH-660A potentiostat (CH-Instruments, Austin, TX, USA). Gold disk microelectrode of 25 µm diameter size was employed as working electrode. Platinum counter electrode and Ag/AgCl (sat.) reference electrode completed the cell, which contained around 3 mL of solution. The solution was naturally aerated and contained 0.1 M NaCl with and without 0.1 M $NaNO_2$.

Three different operation procedures for inducing local pitting using AFM-SECM in contact mode were employed, with the goal to establish the smallest pit size that could be monitored. Nitrite oxidation was performed at applying a constant potential of +0.95 V vs. Ag/AgCl (sat.). The first procedure (*rastering* method) consisted in recording a small AFM scan with the tip constantly biased. In this manner, scans ranging from 0.25 x 0.25 to 3 x 3 μm^2 were performed at a scan rate of 3.84 µm s^{-1}. A second procedure, named *steady state* method, was performed by applying the positive potential to the tip while the tip remained stationary at a certain position in contact with the substrate. Consecutively, results from both experiments were analyzed with AFM, by increasing the scan area, around the positions of the pit formation. A third experimental series consisted of applying a sequence of short positive potential pulses followed by a relaxation time of the same duration while scanning again small areas, similarly to the previously described *rastering* method. However, with this third approach no visible corrosion pits could be achieved, at least with the applied pulses of 0.5 s duration. Characterization of the formed pits was always done directly after corrosion induction, but neither tip substitution nor solution refreshment was needed.

3.4.5. Results and discussion

3.4.5.1. Electrochemical behaviour of gold electrodes in nitrite solution

Initial experiments investigating the generation of nitric acid were performed by sweeping the potential applied at the gold microdisk electrode in 0.1 M sodium chloride either with sodium nitrite solutions or without the nitrite species. The resulting current response is given in Figure 3.4.2A. The black curve shows the recorded current obtained in nitrite free solution, where the only visible signal corresponds to water oxidation at potential values higher than +1.0 V vs. Ag/AgCl (sat.). When nitrite is present in solution, the current profile shows an additional oxidation process at less positive potential values, around approximately +0.7 V vs. Ag/AgCl (sat.), which clearly indicates the onset of half-reaction (3.4.1). Therefore, a constant potential of +0.9 V vs. Ag/AgCl (sat.), sufficiently anodic to ensure nitrite oxidation but preventing water electrolysis, was selected to investigate the formation of nitric acid at the gold surface. The current vs. time response was recorded for one minute. As expected, inspection of Figure 3.4.2B shows that the current determined after one minute was around 1 μA when the solution contained nitrite salt, whereas in the sodium chloride background solution the measured current was three magnitude orders smaller. This current range involves, considering that all the faradaic response comes from nitrite oxidation to nitrate and proton generation (cf. equation (3.4.1)), a nitrate generation of $5.12 \cdot 10^{-12}$ mol s^{-1}, and twice this amount, $1.04 \cdot 10^{-11}$ mol s^{-1}, for proton production. The precise data for the increment in concentration that this production supposes ought to be calculated using simulations. However, it would neither be comparable nor extrapolated to any result obtained using the AFM-SECM probes, since they show different active surface area even from one tip to another. As a rough estimation, it has been considered the 25 μm diameter hemisphere surrounding the active gold microdisk as the total volume in which these species are dissolved. This would lead to a concentration increase of 1.27 and 2.53 mol L^{-1} s^{-1} for nitrates and protons, respectively, if diffusion of these species towards bulk solution is neglected. These rough data point out that possible damage to the gold surface has to be taken into consideration, since high concentrations of nitrate and chloride anions in acidic media might etch it (actually, for metallurgical purposes, mixtures of HNO_3 and HCl are commonly employed for gold extraction). Therefore, the active area of the probes was determined in hexaaminruthenium (III) solution at the beginning and at the end of each experimental series in order to ensure that the gold electrodes were not damaged during the experiments.

3.4.5.2. Induction of pitting corrosion on iron surfaces

As explained above, characterization of the AFM-SECM tip was done by recording cyclic voltammograms in hexaaminruthenium (III) containing solution. In addition, the applied potential at the probes were also swept in the sodium nitrite test solution employed during measurements. Results for both tests are given in Figure 3.4.3. Plotted CVs obtained in hexaaminruthenium (III) solution from Figure 3.4.3A

were recorded at the beginning and at the end of one complete experimental series, which included the local induction of 5 pits of dimensions ranging from 7 to 12 µm in diameter. The stability of the AFM tip-integrated gold electrode is demonstrated by the overlay of two CV scans (recorded before and after the pitting experiments), which indicates that no relevant etching occurred at the gold surface due to the nitric acid formation in chloride media. The formation of nitric acid is indeed observed during nitrite oxidation at positive potentials, as shown in Figure 3.4.3B.

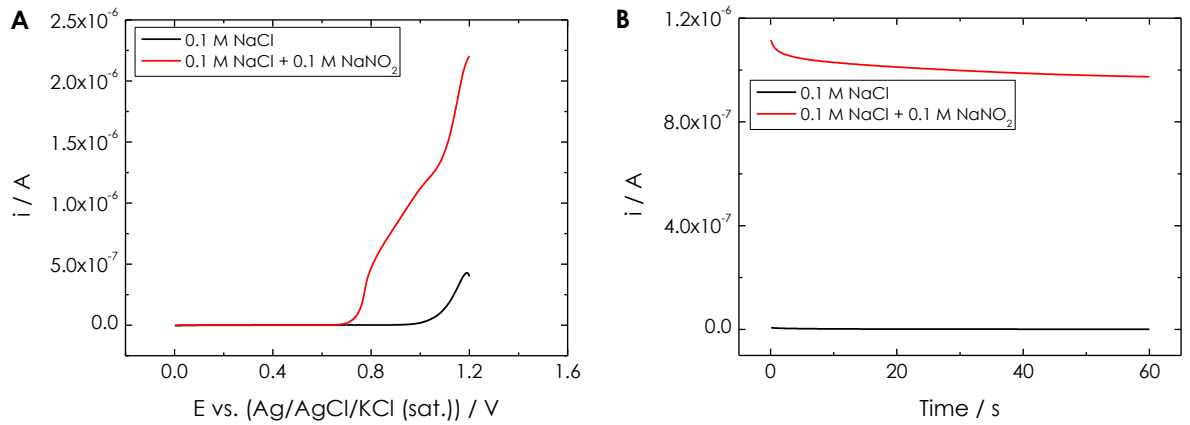

Figure 3.4.2. Current response recorded at the 25 µm diameter gold microdisk in 0.1 M NaCl + x M $NaNO_2$ (x = 0, 0.1). (A) Linear sweep voltammetry between 0 and +1.2 V; (B) potentiostatic measurement at +0.9 V vs. Ag/AgCl (sat.).

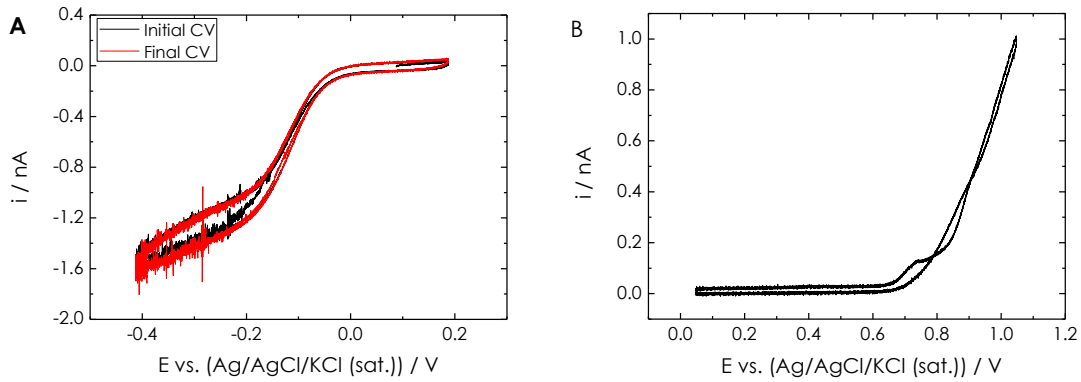

Figure 3.4.3. Cyclic voltammograms recorded at the AFM-SECM electrode: (A) in 0.1 M KCl + 10 mM $[Ru(NH_3)_6]Cl_3$ at the beginning and at the end of one experimental series consisting of 5 different pitting tests performed over iron surface, which resulted in pit dimensions between 7 and 12 µm in diameter; and (B) in 0.5 M NaCl + 0.1 M $NaNO_2$ before the experimental series.

Iron surfaces were locally attacked and AFM images were recorded before and after pitting. Figure 3.4.4 presents a typical topography obtained from an iron surface before and after inducing local pitting. Pitting formation in the presented experiment was induced by rastering a 3 µm x 3 µm area of the surface at 3.84 µm s^{-1} while applying +0.95 V vs. Ag/AgCl (sat.) to the AFM tip-integrated electrode. The

area of pitting was located in the center of the increased scan area given in Figure 3.4.4A. The topography after pitting is shown in Figure 3.4.4B and clearly shows a circular hole that corresponds to the nucleation of a single pit. No post-data treatment such as levelling correction has been applied for any of the scans displayed in this Thesis, in order to present the actual height differences. Only shifts in Z coordinates were performed to set the Z axis to zero at the minimum Z measured. Initial size of the formed pit was ca. 8.5 μm in width, though, considering the 3 μm x 3 μm scan done for this purpose plus the 1.07 μm length of the square ring electrode, only a 4.07 μm diameter pit would be expected as maximum assuming that only the area placed just below the active gold surface of the cantilever is under attack. This feature clearly indicates that diffusion of the consumed and produced species during the local corrosion induction promotes the attack to be extended at larger distances. Thus, diffusion is not constrained in spite of the short tip-sample distance motivated by the relatively short length of the thorn of the cantilever (ca. 460 nm).

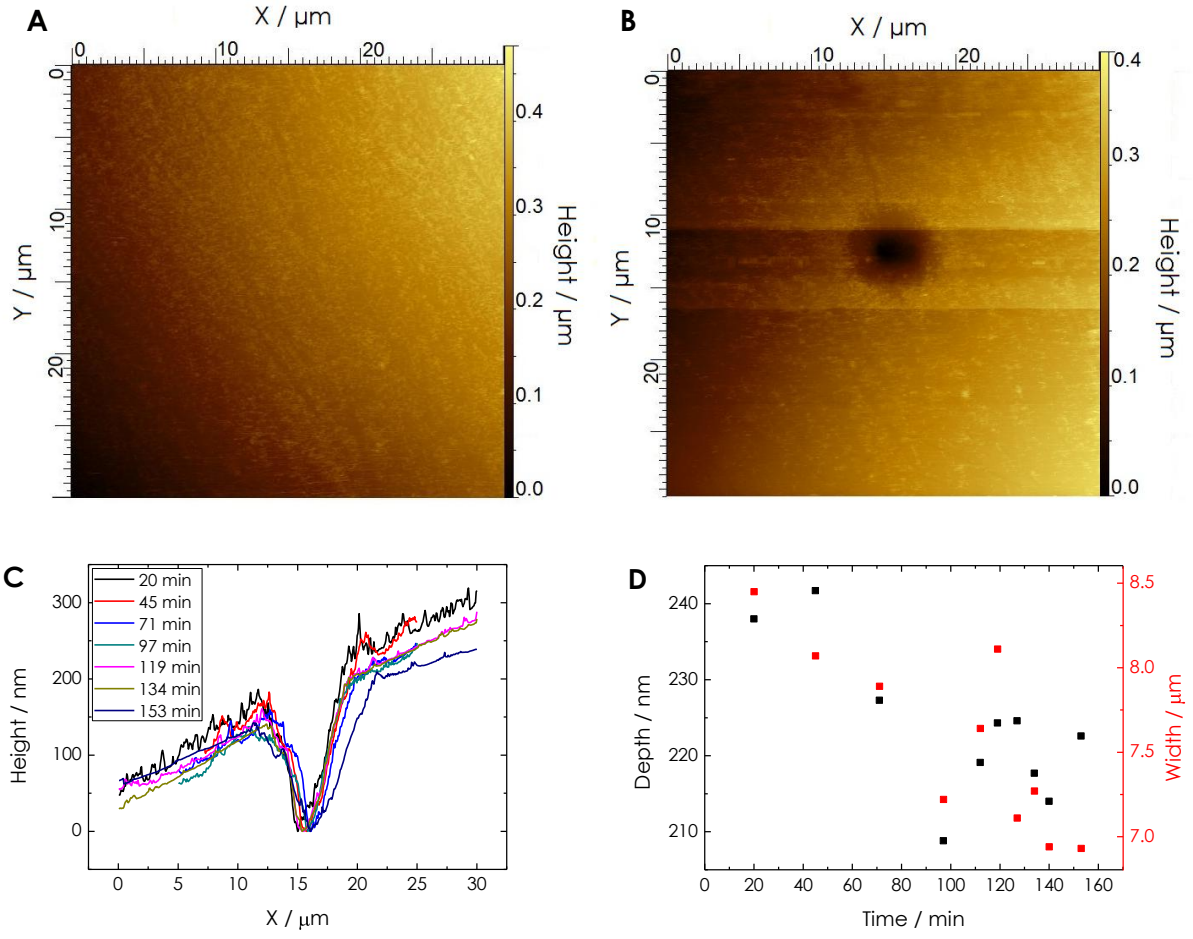

Figure 3.4.4. Topographical information obtained (A) before and (B, C, D) after producing a localized pits at the center of the scanned area under study. (A, B) Topographic scans; and topographic evolution displayed as (C) subsequent linear scans in Y coordinates where minimum height was found, and (D) depth and width of the generated pit. Scan rate: 20 μm s^{-1}.

A series of scan lines were subsequently recorded over a single generated pit in order to monitor its evolution in the chloride-nitrite medium. This was done by moving the probe along the *X* axis in the *Y* position where maximum depth was observed in the previous map. A selection of these 1-D scans is given in Figure 3.4.4C. No significant evolution with time could be observed in these scans, apart from slight changes in the shape of the height profile, or noise level decrease attributed to small particles remaining at the tip and finally being released. It is assumed that a rapid repassivation of the surface occurred, faster than further pit formation, within few minutes, probably motivated by refreshment of the nitrite content by diffusion of this species after the attack was finished and tip was moved far from the attack site. Moreover, ongoing pit formation should lead to a progressing growth of the hole with time, yet the evolution in depth and width as displayed in Figure 3.4.4D did not change over time, supporting the hypothesis of a heterogeneous growth of an oxide layer, which is apparently more pronounced inside the hole.

Since combined AFM-SECM also enables the electrochemical characterization towards the constituents of the medium in close proximity to the surface, it is in principle possible to image the release of soluble iron (II) ions from their oxidation to iron (III) at the AFM tip integrated electrode. This strategy has been extensively employed in conventional SECM for corrosion analysis of iron-based materials [10,11,45-47]. Thus, eventual iron (II) dissolution was monitored over the induced single pit once it was generated. This was attempted just by switching the tip potential from +0.95 to +0.55 V vs. Ag/AgCl (sat.), positive enough to oxidize the ferrous ion into their ferric state without promoting undesirable reactions involving the generation of nitrate anions. Both, the local corrosion and the iron (II) detection were performed by rastering a 3 µm x 3 µm area in the same spot, located at the center of the previously imaged larger region (AFM image). However, no local iron (II) concentration could be detected, and the only background current recorded at the AFM tip-integrated electrode corresponded to the slow homogeneous corrosion in the passive regime (not shown). It must be noticed that tip was neither withdrawn nor moved away from the 3 µm x 3 µm area in between the performance of these two small scans. Consecutively, a large scan was recorded after the tip potential was switched to -0.55 V vs. Ag/AgCl (sat.), negative enough to drive the oxygen reduction reaction, as oxygen was continuously consumed during the corrosion process, so its depletion over the cathodic areas of the surface might be monitored [46,48,49]. Again, only homogeneously distributed faradaic current was registered this time, and no evidence of localized oxygen consumption was observed. However, the topography recorded over this large area revealed changes following the induction of pitting corrosion. Figure 3.4.5A shows the initial topography scan when no localized pitting had been induced, and Figure 3.4.5B shows the topography of the same area after performing the pitting experiments as described above. In this case, instead of a hole, precipitations at the surface were observed, which probably consisted of corrosion products. This result may be explained in terms of the electrochemical phenomena occurring in the small confined volume below the AFM-SECM tip, which forms a "leaky" thin layer cell. The electrochemical nature of

this layer is actively modified by the reactions occurring in the square gold ring while rastering a 3 µm x 3 µm area at such close distance. Moreover, diffusion of the inhibitor into, and/or diffusion of ferrous out of this volume into the solution are prevented as long as the tip is not retrieved from the surface. As a result, oxidation of iron (II) at the AFM tip-integrated electrode leads to the accumulation of ferric cations. This latest species is more prone to undergo water hydrolysis, so ferric hydroxides may precipitate, allowing a layer of corrosion products to be formed. The reduction of oxygen during subsequent scans may also contribute to this process, since alkalization occurs during its reduction at the tip, and surface passivation is favoured in alkaline environments. Yet, probably the hydroxyl formation might have only a minor effect as the iron (II) species might have already diffused away by the time when this scan started with the electrode biased at E_{tip} = -0.55 V vs. Ag/AgCl (sat.), and hence no further iron (III) hydroxide precipitation was occurring. The final diameter of the observed precipitate is 5.15 µm, comparable to what would be expected only considering the above mentioned dimensions of the active area and scan for attack. This feature supports that the discussed diffusion limitation is one of the main motivations for the formation of that precipitate, since larger protrusions would otherwise have been observed.

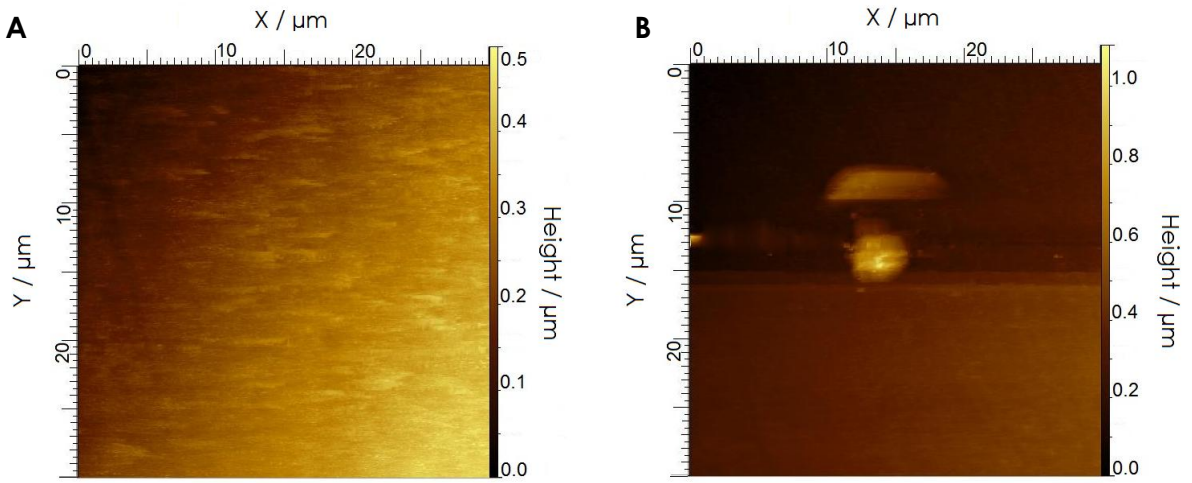

Figure 3.4.5. AFM Topography of the iron surface obtained in contact mode with an AFM-SECM probe, (A) before and (B) after the locally induced pitting experiment using E_{tip} = +0.95 V vs. Ag/AgCl (sat.), and consecutive scans for iron (II) detection (E_{tip} = +0.55 V vs. Ag/AgCl (sat.)) and oxygen detection at (E_{tip} = -0.55 V vs. Ag/AgCl (sat.)). Topographic images A and B (same scan as employed for eventual oxygen detection) were performed by scanning an area of 30 µm x 30 µm, whereas localized corrosion and iron detection steps were performed by scanning a 3 µm x 3 µm area at the center. Scan rate 20 µm s^{-1}.

The reproducibility of the pit formation on iron was confirmed by repeating such experiments with decreasing sizes. A freshly polished iron sample was firstly imaged by AFM over a 50 µm x 50 µm area, and then used to produce an artificial hole in this area, similarly to what was previously shown in Figure 3.4.4B, by rastering the cantilever over a 3 µm x 3 µm area with E_{tip} = +0.95 V vs. Ag/AgCl (sat.). Subsequently, the procedure was repeated at a different location within the same

50 µm x 50 µm area, though decreasing the scan size down to 1 µm x 1 µm. Next, the cantilever was positioned at three other locations while maintaining the same tip potential, but now the pit formation was induced without moving the tip. Three different duration of the polarization experiments were chosen. Results from these two sets of experiments, so called *rastering* and *steady state* regime, are depicted in Figure 3.4.6. AFM images recorded before and after the indicated sequence are displayed in Figure 3.4.6A and 3.4.6B, respectively. It could be demonstrated that the longer the scan duration and therefore the more aggressive the conditions, the deeper and wider was the resulting pit. For the three experiments performed in the *steady state* regime, zoomed views of the corresponding pits are shown in Figure 3.4.6C, and their characteristic widths and depths are listed in Table 3.4.1. The features shown in Figure 3.4.6B were produced after the sample was immersed in the solution for 103-125 min.

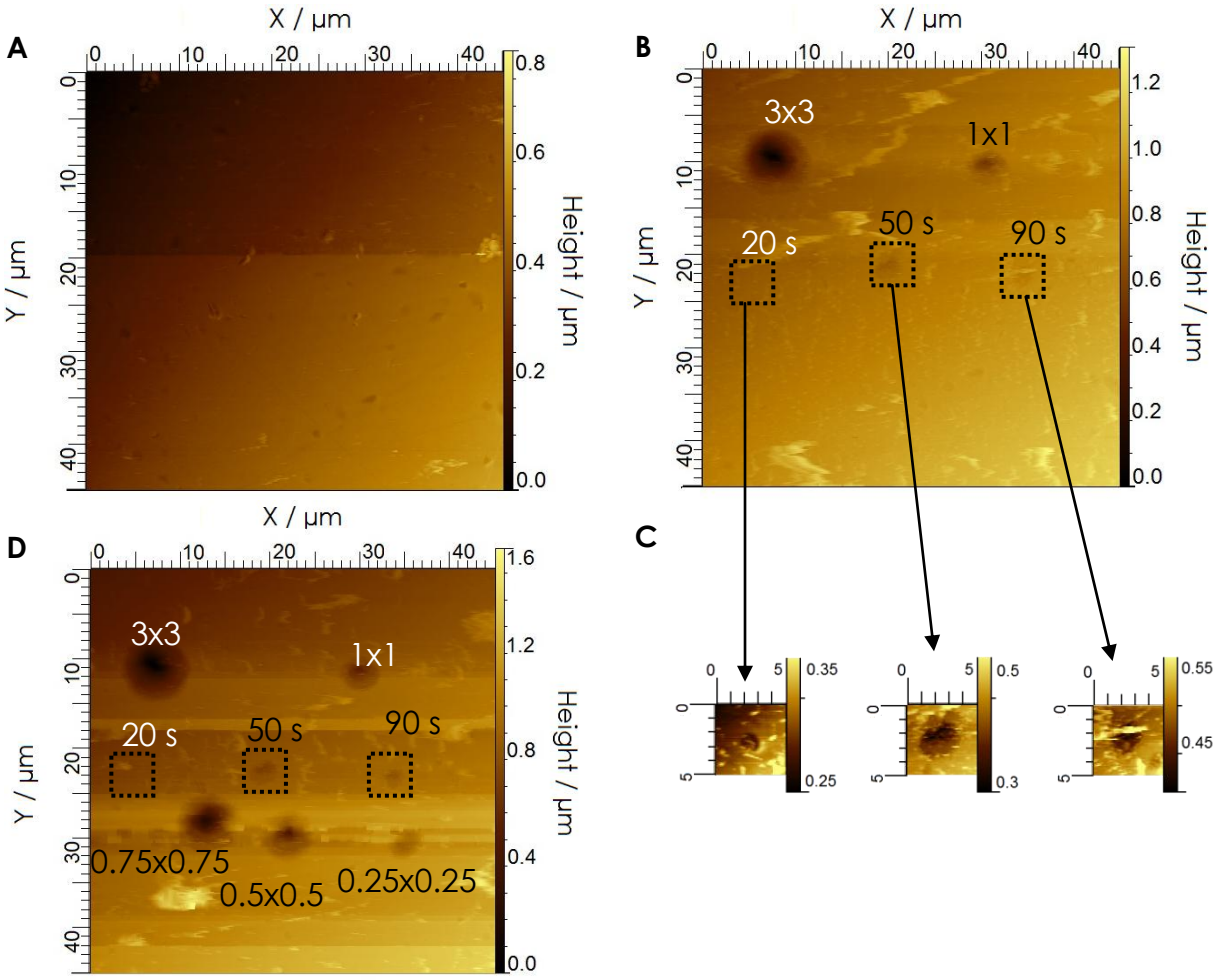

Figure 3.4.6. AFM topography images obtained from an iron surface (A) before and (B) after one series of localized attacks at various locations with E_{tip} = +0.95 V vs. Ag/AgCl (sat.) using the *rastering* or the *steady state* regimes. *Rastering* attacks: scan dimensions given in µm. *Steady state* attacks: time for tip potential application indicated in seconds. (C) Zoomed view of the three attacks performed using the steady state regime in B. (D) Topographic image after the second series of localized attacks performed using the *rastering* strategy; corresponding dimensions indicated in µm. Scan rate 33 µm s^{-1}.

Some concerns regarding adverse effects due to the duration of the exposure of the sample in the test solution remained at this stage. The hypothesis was that longer exposure times produced larger pits, possibly resulting from an increase of the chloride concentration due to solvent evaporation. Therefore, a similar series of experiments was performed in the same sample after 180-186 minutes total exposure using the *rastering* regime, but with even smaller scan sizes, namely 0.75 μm x 0.75 μm, 0.5 μm x 0.5 μm and 0.25 μm x 0.25 μm. The obtained topography after these experiments is shown in Figure 3.4.6D, where the last generated pits formed by scanning sub-micron sized areas are comparable in size to those obtained for the 3 μm x 3 μm or the 1 μm x 1 μm scans of pit formation. Table 3.4.1 also gives the width and depth of the generated pits using smaller scan sizes, supporting the hypothesis. Actually, corrosion pits formed at longer exposure times are typically deeper and wider for the similar conditions of surface induced alteration, that is, for pits formed after 180 minutes immersion, less time and smaller scan sizes for the attacks were needed to produce pits with similar size. As an example, the 0.75 μm x 0.75 μm attack, compared to that previously obtained with 3 μm x 3 μm area scan, resulted in similar pit widths (7290 and 8100 nm) and depths (834 nm and 754 nm). Similar comparison could be established between pits induced by rastering the tip at scan dimensions of 0.25 μm x 0.25 μm and 1 μm x 1 μm done over the same sample in the same solution.

Table 3.4.1. Depth and width of the artificially induced pits shown in Figure 6D started at the given immersion time. They were generated either using the *rastering* (*Rast.*) or the *steady state* (*St. st.*) strategies.

	Depth / nm	Width / nm	Immersion time / min
Rast. 3000 x 3000	754	8100	103
Rast. 1000 x 1000	283	4850	117
Rast. 750 x 750	834	7290	180
Rast. 500 x 500	601	6070	184
Rast. 250 x 250	235.4	4080	186
St. st. (time = 90 s)	85.4	3330	122
St. st. (time = 50 s)	143	2730	124
St. st. (time = 20 s)	48.2	1464	125

Nitrite diffusion and fast repassivation apparently occurred once the tip is moved far from the attack site, as derived from results shown in Figure 3.4.4. To corroborate these observations, a further strategy for pitting corrosion was developed. Now the potential was applied in short pulses of 0.5 s, followed by relaxation time sequences at 0 V vs. Ag/AgCl (sat.) of the same period of time, every time using the *rastering* strategy with different scan dimensions. In order to compare the results obtained from constant and pulsed polarization of the tip electrode, similar scans were taken using the same rate and dimensions for local modification with the two different procedures, namely constant potential and pulsed potential application regimes. Resulting topographical images are depicted in Figure 3.4.7. The left side of the imaged area reflects the area under constant tip potential pitting,

and the right side display experiments for the pulsed pitting. No evidence of local degradation was found for the locations where pulse polarization was used, and only pits were generated in the left half, which reflects the constant potential experiments. This observation points out that only if continuous inhibitor consumption is maintained, accompanied by local formation of the aggressive species, the attack can progress. The dimensions of the generated holes are consistent with the scan size employed during local pitting, as it was expected.

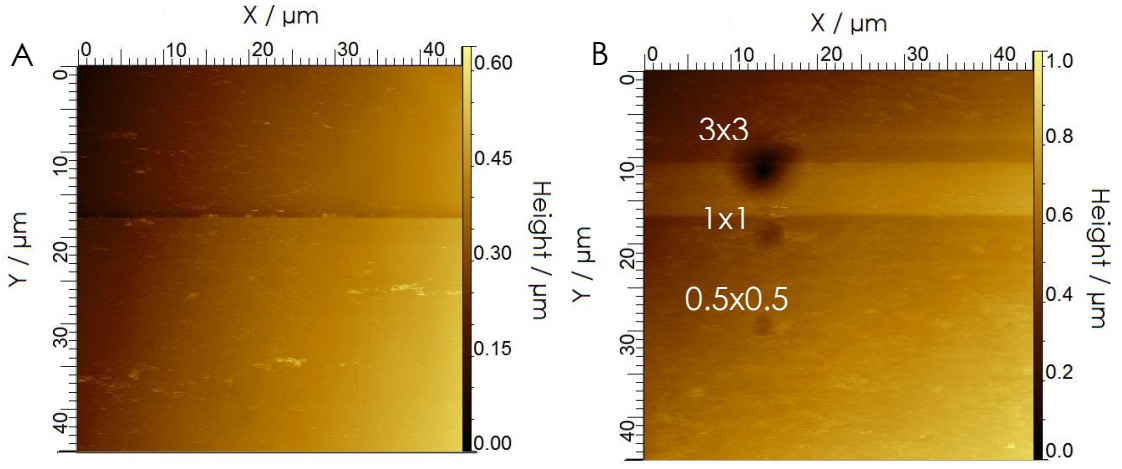

Figure 3.4.7. Topographic images obtained from an iron surface (A) before and (B) after localized pitting induced by E_{tip} = +0.95 V vs. Ag/AgCl (sat.) using the *rastering* method while applying either constant potential or potential pulses. Scan dimensions for *rastering* experiments are given in µm, and indicated next to the corresponding position. Only constant potential attacks are indicated in (B). Scan rate 33 µm s^{-1}.

3.4.6. Conclusions

Localized corrosion can be purposely induced on otherwise passive surfaces by using the AFM-SECM probe to generate the pitting precursor, and to diminish the passivating agent. The presence of an inorganic corrosion inhibitor in bulk solution diffuses sufficiently into the area of pit formation and promotes re-passivation once pitting induction has stopped (no further potential applied to the probe). Pit formation only occurs as long as the inhibiting species is consumed at the AFM-SECM probe and hence prevents the restoration of inhibitive conditions in the selected area, where an aggressive environment has being created, permitting the local attack to progress. Different experimental conditions may lead to the fast accumulation of corrosion products, which blocks the created defect and eventually protrude from the surface.

The applicability of various experimental procedures for the induction of sufficiently large pits has been explored. It was found that the pitting strategy involving surface scanning while producing the reactive species allowed greater

control of pit dimensions. Furthermore, the continuous application of a sufficiently positive potential is required to generate conditions aggressive enough for the nucleated pit to grow in depth. Besides, using AFM-SECM technique, dimensions of the generated pits can be as small as 1.5 µm in width. These ranges are beyond the limits of the previously reported pit induction procedures, conducted by only using the SECM, due to the usual electroactive areas of the tip.

3.4.7. References

1. J. Li, D. Lampner. Colloids and Surfaces A: Physicochemical and Engineering Aspects 154 (1999) 227.
2. R.E. Williford, C.F. Windisch Jr., R.H. Jones. Materials Science and Engineering: A 288 (2000) 54.
3. Q. Zhang, R. Wang, M. Kato, K. Nakasa. Scripta Materialia 52 (2005) 227.
4. F.A. Martin, C. Bataillon, J. Cousty. Corrosion Science 50 (2008) 84.
5. F. Zhang, J. Pan, C. Lin. Corrosion Science 51 (2009) 2130.
6. Y. Li, R. Hu, J. Wang, Y. Huang, C.-J. Lin. Electrochimica Acta 54 (2009) 7134.
7. C. Pan, L. Liu, Y. Li, F. Wang. Corrosion Science 73 (2013) 32.
8. T.E. Lister, P.J. Pinhero. Analytical Chemistry 77 (2005) 2601.
9. K. Fushimi, K.A. Lill, H. Habazaki. Electrochimica Acta 52 (2007) 4246.
10. Y. Yin, L. Niu, M. Lu, W. Guo, S. Chen. Applied Surface Science 255 (2009) 9193.
11. Y. Yuan, L. Li, C. Wang, Y. Zhu. Electrochemistry Communications 12 (2010) 1804.
12. C.-Q. Ye, R.-G. Hu, Y. Li, C.-J. Lin, J.-S. Pan. Corrosion Science 61 (2012) 242.
13. B. Vuillemin, X. Philippe, R. Oltra, V. Vignal, L. Coudreuse, L.C. Dufour, E. Finot. Corrosion Science 45 (2003) 1143.
14. H. Krawiec, V. Vignal, R. Oltra. Electrochemistry Communications 6 (2004) 655.
15. V. Vignal, H. Krawiec, O. Heintz, R. Oltra. Electrochimica Acta 52 (2007) 4994.
16. K. Eckhard, M. Etienne, A. Schulte, W. Schuhmann. Electrochemistry Communications 9 (2007) 1793.
17. K. Eckhard, T. Erichsen, M. Stratmann, W. Schuhmann. Chemistry A European Journal 14 (2008) 3968.
18. J. Zhou, D.O. Wipf. Journal of the Electrochemical Society 144 (1997) 1202.
19. M.A. Amin, S.S.A. El-Rehim. International Journal of the Electrochemical Science 7 (2012) 7600.
20. M.A. Amin, S.S.A. El-Rehim, F.D.A. Aarão Reis, I.S. Cole. Ionics 20 (2014) 127.
21. C. Gabrielli, S. Joiret, M. Keddam, H. Perrot, N. Portail, P. Rousseau, V. Vivier. Electrochimica Acta 52 (2007) 7706.
22. C. Gabrielli, S. Joiret, M. Keddam, N. Portail, P. Rousseau, V. Vivier. Electrochimica Acta 53 (2008) 7539.
23. N. Aouina, F. Balbaud-Célérier, F. Huet, S. Joiret, H. Perrot, F. Rouillard, V. Vivier. Electrochimica Acta 56 (2011) 8589.

24. N. Aouina, F. Balbaud-Célérier, F. Huet, S. Joiret, H. Perrot, F. Rouillard, V. Vivier. Electrochimica Acta 104 (2013) 274.
25. D. Battistel, S. Daniele, R. Gerbasi, M.A. Baldo. Thin Solid Films 518 (2010) 3625.
26. J. Ufheil, F.M. Boldt, M. Börsch, K. Borgwarth, J. Heinze. Bioelectrochemistry 52 (2000) 103.
27. J. Ufheil, C. Heß, K. Borgwarth, J. Heinze. Physical Chemistry Chemical Physics 7 (2005) 3185.
28. A.I. Marshakov, V.E. Ignatenko. Jorunal of Applied Electrochemistry 29 (1999) 201.
29. M. Reffass, R. Sabot, M. Jeannin, C. Berziou, Ph. Refait. Electrochimica Acta 52 (2007) 7599.
30. A.A. Al-Refaie, J. Walton, R.A. Cottis, R. Lindsay. Corrosion Science 52 (2010) 422.
31. M. Hayyan, S.A. Sameh, A. Hayyan, I.M. AlNashef. International Journal of the Electrochemical Science 7 (2012) 6941.
32. C. Kranz, G. Friedbacher, B. Mizaikoff, A. Lugstein, J. Smoliner, E. Bertagnolli. Analytical Chemistry 73 (2001) 2491.
33. A. Lugstein, E. Bertagnolli, C. Kranz, B. Mizaikoff. Surface and Interface Analysis 33 (2002) 146.
34. A. Lugstein, E. Bertagnolli, C. Kranz, A. Kueng, B. Mizaikoff. Applied Physics Letters 81 (2002) 349.
35. A. Kueng, C. Kranz, B. Mizaikoff, A. Lugstein, E. Bertagnolli. Applied Physics Letters 82 (2003) 1592.
36. H. Shin, P.J. Hesketh, B. Mizaikoff, C. Kranz. Sensors and Actuators B: Chemical 134 (2008) 488.
37. A. Davoodi, J. Pan, C. Leygraf, S. Norgren. Electrochemical and Solid-State Letters 8 (2005) B21.
38. A. Davoodi, J. Pan, C. Leygraf, S. Norgren. Applied Surface Science 252 (2006) 5499.
39. A. Davoodi, J. Pan, C. Leygraf, S. Norgren. Electrochimica Acta 52 (2007) 7697.
40. A. Davoodi, J. Pan, C. Leygraf, S. Norgren. Journal of the Electrochemical Society 155 (2008) C138.
41. A. Davoodi, J. Pan, C. Leygraf, S. Norgren. Journal of the Electrochemical Society 155 (2008) C211.
42. L. Dhouibi, Ph. Refait, E. Triki, J.M.R. Génin. Journal of Materials Science 41 (2006) 4928.
43. P. Garcés, P. Saura, A. Méndez, E. Zornoza, C. Andrade. Corrosion Science 50 (2008) 498.
44. M.B. Valcárcel, M. Vázquez. Materials Chemistry Physics 115 (2009) 313.
45. Y. González-García, G.T. Burstein, S. González, R.M. Souto. Electrochemistry Communications 6 (2004) 637.
46. A.C. Bastos, A.M. Simões, S. González, Y. González-García, R.M. Souto. Electrochemistry Communications 6 (2004) 1212.
47. M. Zhao, Z. Qian, R. Qin, J. Yu, Y. Wang, L. Niu. Corrosion Engineering Science and Technology 48 (2013) 270.
48. R.M. Souto, L. Fernández-Mérida, S. González. Electroanalysis 21 (2009) 2640.

49. R. Sánchez-Tovar, M.T. Montañés, J. García-Antón. Corrosion Science 73 (2013) 365.

3.5

Main conclusions

1. Substrate generation – tip collection mode in the SECM was implemented for the analysis of the corrosion of 304 and 316 stainless steel surfaces under aggressive conditions. Its combination with the SVET technique allowed the characterization of the reactivity of the material.

2. Initial reduction of the passive layer is mandatory in neutral pH containing media for the localized corrosion process to occur in the 304 stainless steel, as observed by conventional measurements simultaneously with local SVET imaging.

3. Speciation of the iron species spontaneously generated from materials exposed to different media and under applied polarization was successfully performed by adequately setting the SECM tip potential during the measurements. Iron (II) production is mostly observed in 0.1 M HCl electrolyte for the 304 surfaces. In contrast, iron (III) generation is promoted in hydrochloric acid solution for the 316 steel, and in 0.1 M NaCl media for the 304 steel surfaces.

4. The AFM-SECM technique has been applied for the first time to induce localized corrosion on otherwise passive surfaces. The procedure involves simultaneous generation of the pitting precursor species and the removal of the passivating agent added in the solution, effectively leading to the nucleation and propagation of single pits on iron. Further electrochemical modification of the surrounding media may induce the precipitation of corrosion products giving rise to the observation of topographic protrusions around the pits.

3.6

Conclusiones

1. El modo de operación del SECM generación en substrato – recolección en la punta ha sido implementado para el análisis de los procesos corrosivos sobre superficies de acero inoxidable 304 y 316 bajo condiciones agresivas. Su combinación con la técnica SVET ha permitido la caracterización de la reactividad del material.

2. Se requiere la reducción inicial de la capa pasiva formada sobre el acero inoxidable 304 para que ocurran los procesos de corrosión localizada en disoluciones de pH neutro, como se observa por medidas electroquímicas convencionales paralelamente a las imágenes de SVET.

3. Se ha analizado la especiación de los iones de hierro generados espontáneamente a partir de muestras de acero 304 y 316 para diferentes medios y polarizaciones aplicadas, mediante la adecuada selección de los potenciales de la punta durante las medidas. Se ha observado una producción de hierro (II) mayoritaria en el electrolito HCl 0.1 M para las superficies de 304. Por el contrario, la generación de hierro (III) se favorece para el acero 316 en disoluciones de ácido clorhídrico, así como en el medio NaCl 0.1 M para las superficies de acero 304.

4. La técnica AFM-SECM ha sido aplicada por primera vez a la inducción de corrosión localizada en superficies que de otra manera estarían pasivadas. La generación del precursor de picado, simultáneamente a la eliminación del agente pasivante, conlleva a la nucleación y propagación de picaduras singulares en hierro puro. Modificaciones adicionales en la naturaleza electroquímica del medio circundante pueden inducir la precipitación de productos de corrosión alrededor de las picaduras hasta la formación de una protrusión.

CHAPTER 4

Material selection and surface treatment for biomaterial application

Index

4.1

Prologue to the experiments

4.1.1. Introduction

Metallic materials including stainless steels, CoCr-based alloys, titanium and its alloys, have found wide application in restorative surgery as basic biomaterials for the manufacturing of implant prostheses for skeletal replacements and fixtures. In this case, materials are chosen which combine good mechanical characteristics, high corrosion resistance and good compatibility with biological materials. Titanium and titanium-based alloys are very widely employed in biomedical applications due to their low elasticity modulus, high corrosion resistance and excellent biocompatibility [1-3].

Compact and stable oxide layers are formed on titanium and its alloys because of their state of passivity in physiological environments [4]. The domain of thermodynamic stability of titanium dioxides encompasses that of water in the absence of complexants [5], and as determined by the conventional polarization curve, titanium is an extremely passive metal. It exhibits a typical active-passive transition in strongly acidic solutions, but active dissolution does not appear to take place in less acidic, neutral and alkaline solutions [6,7]. The onset of passivity is observed even in solutions which are fairly concentrated in chloride, where many other metals fail through pitting corrosion. Passive current densities on titanium are low and pitting potentials in chloride solutions are high [8,9], well above the equilibrium oxygen potential. The metal is nevertheless a base metal thermodynamically, with a low redox potential in aqueous solutions, and such powerful passivity is conferred by the very stable and tenaciously adherent passivating oxide film spontaneously formed over the surface [10-13], and it reforms very rapidly if removed or mechanically damaged. The actual composition of the passive film is still rather controversial, but most investigators agree that the film consists of titanium dioxide, TiO_2.

Though commercially pure titanium (CP Ti) and Ti6Al4V are the major materials for manufacture of orthopaedic implants, the poor shear strength of these materials has effectively led to restrict their effective service life to 10-15 years. Furthermore, despite the adherence and reforming skills exhibited by the passive film, titanium corrosion products (e.g. in the form of submicron particles) are often observed in tissues adjacent to implant prosthesis [18-23]. Though titanium appears to be tolerated in the body in minute amounts, the long term effect of its accumulation and the fact that it is not excreted remains of biological concern. Though these

surface films are fairly unreactive, transient microscopic breakdown of the passive state induced by the presence of chloride ions in the environment has been observed *in vitro* on both titanium and Ti6Al4V [24-26]. When the prostheses are placed in the human body, the passive films undergo further transformations, namely thickening of the passivating film and stoichiometric changes, as well as metal dissolution [19,27-29]. Both passivation and metal dissolution are processes of an electrochemical nature.

Further studies have indicated that vanadium, used to stabilize the β-phase, produces harmful oxides for the human body [30,31]. Moreover there has been concern, not yet confirmed, about the association between Al and Alzheimer disease [32,33].

This has stimulated material scientists to develop titanium alloys with lower mechanical modulus, thus closer to bone, and to explore them as for biocompatibility and corrosion resistance [14,15]. Additionally, candidate biomaterials exhibiting non-toxic and non-allergenic properties [16,17] are titanium alloys containing β-stabilizing elements. In this way, alloys containing Nb [17,34-36], Ta [37-45], Mo [34,36,46-50], Hf [42,51], Zr [52], and combinations of these elements [53-59] are investigated. Among them, molybdenum is considered to be instrumental in regulating the pH balance in the body and act as a cofactor for a limited number of enzymes in humans [60,61]. Ti15Mo (wt%) alloy is actually standardized (ASTM F 2066) [62]. Another promising alloying element is zirconium. Alloys containing zirconium have demonstrated both the required mechanical strength and a high resistance to corrosion in biological fluids [63-65]. The biocompatibility of TiZr-based alloys indicates an improvement even over CP Ti [66,67], thus ZrTi alloys have been reported to be "at least as good as" pure titanium in terms of biocompatibility and osseointegration [68].

4.1.2. Research aims

The aim of the studies described in this Chapter was to investigate the corrosion resistance and electrochemical behaviour of new Ti-based alloys synthesized by the cold crucible levitation melting (CCLM) technique, as well as the effect of surface treatments. They were tested in saline and artificial physiological solutions. The influence of both acidities such as those met during inflammatory response of tissues, and electrical polarization at anodic conditions more positive than the highest monitored in the human body under infection conditions [69], were taken into account. Since these were newly developed materials, attention was also paid to their morphological, chemical and electrochemical characterization in addition to the actual microelectrochemical studies. Conventional electrochemical techniques, namely potentiodynamic polarization and electrochemical impedance spectroscopy (EIS), were employed to characterize the corrosion resistance of the

materials, whereas surface analytical techniques (SEM, EDX, and XPS) were employed to determine the surface morphology and the chemical composition of the surface layers responsible for their passivity. The surface layers formed on these materials may vary in thickness from a few molecules to microns, producing major changes in their chemical behaviour, chemical composition, crystallinity and electronic properties. Heterogeneities and defects in these layers usually pass undetected using either conventional electrochemical or surface analysis techniques, but small variations in the thickness of insulating oxide layers are sufficient to produce variations in the mechanism of electron transfer kinetics at those surfaces [70,71]. The scanning electrochemical microscope (SECM) has already been employed to detect precursor sites for localized pitting corrosion on passivated titanium [72-74], and its ability to *in situ* image electron transfer reactions at metal-metal oxide surfaces [75,76], particularly in the case of thin films of TiO_2 and Ta_2O_5 [75-78], has recently opened the way to analyze the effect of alloying elements and impurities on the localized reactivity of titanium alloys [79].

4.1.3. References

1. T. Albrektsson, P.-I. Branemark, H.-A. Hansson, B. Kasemo, K. Larsson, I. Lundstrom, D.H. McQueen, R. Skalak. Annals of Biomedical Engineering 11 (1983) 1.
2. ASM Handbook: Corrosion, Vol. 13, 9th edn. ASM International, Metals Park, 1987, p. 669.
3. M. Geetha, A.K. Singh, R. Asokamani, A.K. Gogia. Progress in Materials Science 54 (2009) 397.
4. R.J. Solar. In: Corrosion and Degradation of Implant Materials (Edited by S.C. Syrett, A. Acharya). ASTM Special Technical Publication STP 684, Philadelphia, 1979, p. 259.
5. M. Pourbaix. Atlas of Electrochemical Equilibria in Aqueous Solutions. NACE, Houston, 1974, p. 213.
6. A. Ammar, I. Kamal. Electrochimica Acta 16 (1971) 1539.
7. A. Ammar, I. Kamal. Electrochimica Acta 16 (1971) 1555.
8. J. Dugdale, J. B. Cotton. Corrosion Science 4 (1964) 397.
9. T.R. Beck. In: Localized Corrosion (Edited by R.W. Staehle, B.F. Brown, J. Kruger, A. Agrawal). NACE, Houston, 1974, p. 644.
10. M. Ask, J. Lausmaa, B. Kasemo. Applied Surface Science 35 (1989) 283.
11. C. Johansson, J. Lausmaa, M. Ask, H.-A. Hansson, T. Albrektsson. Journal of Biomedical Engineering 11 (1989) 3.
12. J. Lausmaa, B. Kasemo, H. Mattson, H. Odelius. Applied Surface Science 45 (1990) 189.
13. R.L. Reis, O.C. Paiva, J.D. Santos. Bioceramics 7 (1994) 125.
14. M. Niinomi. Journal of the Mechanical Behaviour of Biomedical Materials 1 (2008) 30.

15. M. Long, H.J. Rack. Biomaterials 19 (1998) 1621.
16. S.G. Steinemann. In: Evaluation of Biomaterials, (Edited by G.D. Winter, J.L. Leray, K. de Groot). Wiley, New York , 1980, p. 1.
17. M. Niinomi, D. Kuroda, M. Morinaga, Y. Kato, T. Yashiro. In: Non-Aerospace Applications of Titanium (Edited by F.H. Froes, P.G. Allen, M. Niinomi). The Minerals, Metals and Materials Society, Warrendale, 1998, p. 217.
18. G. Meachim, D.F. Williams. Journal of Biomedical Materials Research 7 (1973) 555.
19. K.E. Healy, P. Ducheyne. Journal of Biomedical Materials Research 26 (1992) 319.
20. P. Ducheyne, G. Willems, M. Martens, J. Helsen. Journal of Biomedical Materials Research 18 (1984) 293.
21. J.L. Gilbert, C.A. Bucley. Journal of Biomedical Materials Research 27 (1993) 1533.
22. R.M. Urban, J.J. Jacobs, J.L. Gilbert, J.O. Galante. Journal of Bone and Joint Surgery – American 76A (1994) 1345.
23. J.J. Jacobs, R.M. Urban, J.L. Gilbert, A.K. Skipor, J. Black, M. Jasty, J.O. Galante. Clinical Orthopaedics and Related Research 319 (1995) 94.
24. G.T. Burstein, R.M. Souto. Electrochimica Acta 40 (1995) 1881.
25. R.M. Souto, G.T. Burstein. Journal of Materials Science: Materials in Medicine 7 (1996) 337.
26. G.T. Burstein, C. Liu, R.M. Souto. Biomaterials 26 (2005) 245.
27. P. Ducheyne, G. Willems, M. Martens, J. Helsen. Journal of Biomedical Materials Research 18 (1984) 293.
28. J.-E. Sundgren, P. Bodo, I. Lundstrom. Journal of Colloid and Interface Science 110 (1986) 9.
29. K.E. Healy, P. Ducheyne. Journal of Colloid and Interface Science 150 (1992) 404.
30. T.I. Kim, J.H. Han, I.S. Lee, K.H. Lee, M.C. Shin, B.B. Choi. Bio-Medical Materials and Engineering 7 (1997) 253.
31. M.A. Khan, R.L. D.F. Williams. Biomaterials 17 (1996) 2117.
32. Y. Okazaki, Y. Ito, K. Kyo, T. Tateishi. Materials Science and Engineering A 213 (1996) 138.
33. S. Rao, Y. Okazaki, T. Tateishi, T. Ushida, Y. Ito. Materials Science and Engineering C 4 (1997) 311.
34. D. Bombac, M. Brojan, P. Fajfar, F. Kosel, R. Turk. RMZ Materials and Geoenvironment 54 (2007) 471.
35. R. Godley, D. Starosvetsky, I. Gotman. Journal of Materials Science: Materials in Medicine 17 (2006) 63.
36. Q. Yao, J. Sun, H. Xing, W. Guo. Transactions of Nonferrous Metals Society of China 17 (2007) 1417.
37. Y.L. Zhou, M. Niinomi, T. Akahori. Materials Science and Engineering A 371 (2004) 283.
38. Y.L. Zhou, M. Niinomi, T. Akahori, H. Fukui, H. Toda. Materials Science and Engineering A 398 (2005) 28.
39. E.A. Trillo, C. Ortiz, P. Dickerson, R. Villa, S.W. Stafford, L.E. Murr. Journal of Materials Science: Materials in Medicine 12 (2001) 283.
40. Y.L. Zhou, M. Niinomi, T. Akahori, H. Fukui. Materials Science Forum 479 (2005) 2309.
41. Y.L. Zhou, M. Niinomi. Journal of Alloys and Compounds 466 (2008) 535.

42. Y.L. Zhou, M. Niinomi, T. Akahori. Materials Science and Engineering A 483-484 (2008) 153.
43. D. Mareci, R. Chelariu, D.M. Gordin, G. Ungureanu, T. Gloriant. Acta Biomaterialia 5 (2009) 3625.
44. Y.L. Zhou, M. Niinomi. Materials Science and Engineering C 29 (2009) 1061.
45. D. Mareci, R. Chelariu, G. Ciurescu, D. Sutiman, T. Gloriant. Materials and Corrosion 61 (2010) 768.
46. V.R. Jablokov, M.J.Nutt. M.E. Richelsoph, H.L. Freese. Journal of ASTM international 2 (2005) 491.
47. S. Kumar, T.S.N. Sankara Narayanan. Journal of Dentistry 36 (2008) 500.
48. N.T.C. Oliveira, A.C. Guastaldi. Corrosion Science 50 (2008) 938.
49. N.T.C. Oliveira, A.C. Guastaldi. Acta Biomaterialia 5 (2009) 399.
50. D. Mareci, R. Chelariu, D.M. Gordin, M. Romas, D. Sutiman, T. Gloriant. Materials and Corrosion 61 (2010) 829.
51. Z. Cai, M. Koike, H. Sato, M. Brezner, Q. Guo, M. Komatsu, O. Okuno, T. Okabe. Acta Biomaterialia 1 (2005) 353.
52. W.F. Ho, W.K. Chen, S.C. Wu, H.C. Hsu. Journal of Materials Science: Materials in Medicine 19 (2008) 3179.
53. M. Niinomi. Materials Science and Engineering A 243 (1998) 231.
54. X. Tang, T. Ahmed, H.J. Rack. Journal of Materials Science 35 (2000) 1805.
55. R. Banerjee, S. Nag, J. Stechschulte, H.L. Fraser. Biomaterials 25 (2004) 3413.
56. M. Geetha, A.K. Singh, K. Muraleedharan, A.K. Gogia, R. Asokamani. Journal of Alloys and Compounds 384 (2004) 131.
57. N. Sakaguchi, M. Niinomi, T. Akahori, J. Takeda, H. Toda. Materials Science and Engineering C 25 (2005) 363.
58. S. Nag, R. Banerjee, H.L. Fraser. Materials Science and Engineering C 25 (2005) 357.
59. I. Cvijović-Alagić, Z. Cvijović, S. Mitrović, V. Panić, M. Rakin. Corrosion Science 53 (2011) 796.
60. K.V. Rajagopalan. Annual Review of Nutrition 8 (1988) 401.
61. S. Kumar, T.S.N. Sankara Narayanan. Journal of Dentistry 36 (2008) 500.
62. ASTM F 2066, Standard Specification for Wrought Titanium-15 Molybdenum Alloy for Surgical Implant Applications (UNS R58150). ASTM International, West Conshohocken, 2011.
63. M.A. Khan, R.L. Williams, D.F. Williams. Biomaterials 20 (1999) 765.
64. N. Bernhard, S. Berner, M. De Wild, M. Wieland. Forum Implantologicum 5 (2009) 30.
65. Y.M. Zhang, F. Chai, J.C. Hornez, C.L. Li, Y.M. Zhao, M. Traisnel, H.F. Hildebrand. Biomedical Materials 4 (2009) 1.
66. T. Naganawa, Y. Ishihara, T. Iwata, A. Koide, M. Ohguchi, Y. Ohguchi, Y. Murase, H. Kamei, N. Sato, M. Mizuno, T.J. Noguchi. Journal of Periodontology 75 (2004) 1701.
67. Y. Ikarashi, K. Toyoda, E. Kobayashi, H. Doi, T. Yoneyama, H. Hamanaka, T. Tsuchiya. Materials Transactions 46 (2005) 2260.
68. H.M. Grandin, S. Berner, M. Dard. Materials 5 (2012) 1348.

69. T.P. Hoar, D.C. Mears. Proceedings of the Royal Society London A 294 (1966) 486.
70. H. Morisaki, H. Ono, K. Yazawa. Journal of the Electrochemical Society 135 (1988) 381.
71. H. Morisaki, H. Ono, K. Yazawa. Journal of the Electrochemical Society 136 (1989) 1710.
72. N. Casillas, S.J. Charlebois, W.H. Smyrl, H.S. White. Journal of the Electrochemical Society 140 (1993) L142.
73. N. Casillas, S.J. Charlebois, W.H. Smyrl, H.S. White. Journal of the Electrochemical Society 141 (1994) 636.
74. L.F. Garfias-Mesias, M. Alodan, P.I. James, W.H. Smyrl, Journal of the Electrochemical Society 145 (1998) 2005.
75. S.E. Pust, D.Scharnweber, C.N. Kirchner, G. Wittstock. Advanced Materials 10 (2007) 878.
76. S.E. Pust, D.Scharnweber, S. Baunack, G. Wittstock. Journal of the Electrochemical Society 154 (2007) C508.
77. S.B. Basame, H.S. White. Analytical Chemistry 71 (1999) 3166.
78. S.B. Basame, H.S. White. Proceedings of the Electrochemical Society 99-5 (1999) 15.
79. R. Zhu, Z. Qin, J.J. Noël, D.W. Shoesmith, Z. Ding. Analytical Chemistry 80 (2008) 1437.

4.2

Electrochemical characterization of ZrTi alloys for biomedical applications

4.2.1. Abstract

The electrochemical behaviour of three ZrTi alloys (Zr5Ti, Zr25Ti and Zr45Ti) in Ringer's solution has been investigated. Their resistance against localized corrosion has been determined from cyclic potentiodynamic polarization (CPP) and electrochemical impedance spectroscopy (EIS) measurements, whereas scanning electrochemical microscopy (SECM) was applied to investigate the local reactivity of the passive films developed on the materials, and scanning electron microscopy (SEM) was employed to characterize the surface morphology of the alloys subjected to anodic polarization. An increased reactivity could be detected with SECM when the metal samples were polarized at +0.50 V vs. NHE, though the extent of this feature greatly depended on the nature of the metallic material. At 37 ^{0}C, the Zr5Ti alloy was susceptible to localized corrosion. Though Zr25Ti alloy presented rather low pitting potential, the spontaneous corrosion potential of the material was sufficiently negative to require overpotentials around 600 mV for breakdown to occur. Finally, the Zr45Ti alloy exhibited a larger passive range in the polarization curve, and it was resistant to localized corrosion.

4.2.2. Resumen

Se ha investigado el comportamiento electroquímico de tres aleaciones ZrTi (Zr5Ti, Zr25Ti y Zr45Ti) en disolución Ringer. Su resistencia frente a la corrosión se ha determinado mediante el empleo de la polarización potenciodinámica cíclica (CPP) y espectroscopía electroquímica de impedancia electroquímica (EIS), mientras que la microscopía electroquímica de barrido (SECM) ha sido aplicada para investigar la reactividad local de la película pasiva desarrollada sobre las distintas aleaciones, y la microscopía electrónica de barrido (SEM) fue empleada para caracterizar la morfología superficial de las aleaciones sujetas a polarización anódica. Pudo detectarse un incremento de la reactividad con el SECM cuando las muestras se polarizaban a +0.50 V vs. NHE aunque la extensión de este hecho dependió fuertemente de la aleación ensayada. A 37 °C, la aleación Zr5Ti era susceptible a la corrosión localizada. Aunque la aleación Zr25Ti presentó un potencial de picado relativamente bajo, el potencial de corrosión espontáneo del material fue suficientemente negativo como para requerir un sobrepotencial de en torno a 600 mV para que la rotura de la capa pasiva pudiera ocurrir. Finalmente, la aleación Zr45Ti mostró un rango de pasividad mayor en su curva de polarización, resultando resistente a la corrosión localizada.

4.2.3. Introduction

Titanium and its alloys (especially Ti6Al4V) are widely used in restorative surgery due to their good biocompatibility and excellent corrosion resistance in physiological media [1-3]. Yet corrosion remains a concern because the protective passivating oxide layers that separate the metal from the environment are not perfect insulating barriers. Transient events related to localized depassivation have been observed for these materials in vitro [4-6], and they may release metal ions in the surroundings. There are reports in the literature describing several cases of extensive metallosis and necrosis in periprosthetic tissues of failed cemented Ti6Al4V prostheses [7,8], as well as local and systemic effects of corrosion products [9–14]. Thus, there is increasing awareness on the presence of vanadium in long term implants because this element is toxic both in the elemental state and in its oxides [15,16]. Additionally, the association between Al and Alzheimer disease has also been suggested [17,18].

The toxicity of vanadium pushes forward the development of new Ti-based alloys to replace Ti6Al4V. In particular, new β-type titanium alloys with biomechanical compatibility, low modulus and biochemical compatibility are sought [19,20]. β-stabilizing elements, such as Mo, Ta, Zr and Sn, are judged to be non-toxic and non-allergenic [21], and are thus selected as safe alloying elements to titanium. Zirconium and titanium are in the same group in the periodic table of elements, and are known to have similar chemical properties [22]. Both metals usually have their surfaces covered by passivating thin oxide films that are spontaneously formed in air or in electrolytes at open circuit [23,24]. Though Zr offers superior corrosion resistance over most other metals in different electrolytes [25], this metal is susceptible to localized corrosion induced by Cl^- ions [26,27]. In terms of biomaterial applications, the most inconvenient characteristics are related to degradation, which occurs due interaction of the material with body or physiological fluids that typically present concentrations of ca. 1 wt.% NaCl [28]. In this context, Yu and Scully have reported that Ti13Nb13Zr alloy has an extremely high resistance to active and passive dissolution in oxidizing acids [29]. The binary ZrTi system exhibits complete solid solution, thus efforts can be directed to finding an adequate ratio for the alloying of Zr with Ti that would produce a material with decreased or even hindered susceptibility to localized corrosion compared to pure zirconium. Electrochemical characterization of the new materials in simulated physiological environments is an important tool for this material selection process.

The current Section reports on the susceptibility to localized corrosion exhibited by various ZrTi alloys with different compositions during exposure to Ringer's solution. For the sake of comparison, titanium grade 1 was also investigated in the same experimental conditions. Electrochemical characterization was performed using cyclic potentiodynamic polarization (CPP) and electrochemical impedance spectroscopy (EIS) techniques with the objective to determine the potential ranges for the stability of the materials, and to quantify the resistance of the passive films

developed on them. Additionally, scanning electrochemical microscopy (SECM) was applied to monitor the local reactivity of the passive films exposed to the test environment. Probe approach curves and scan arrays were recorded at selected areas for this investigation.

4.2.4. Materials and methods

4.2.4.1. Materials and sample preparation

Three ZrTi experimental alloys were investigated. The code names and chemical compositions of the alloys are shown in Table 4.2.1. For comparison, titanium grade 1 was also considered. The non alloyed Ti samples were obtained from a bar stock in annealed state. The structural characterization of this metal was detailed elsewhere [30].

Table 4.2.1. Chemical composition* and supplier of Ti and ZrTi samples.

Sample	Composition / wt.%	Supplier
Ti	Ti: 99.9	IMNR**, Bucharest, Romania
Zr45Ti	Zr:55, Ti: 45	Zirom S.A., Giurgiu, Romania
Zr25Ti	Zr: 75, Ti: 25	Zirom S.A., Giurgiu, Romania
Zr5Ti	Zr: 95, Ti: 5	Zirom S.A., Giurgiu, Romania

*The information included in the Table was supplied by the manufacturers.
** National Institute of Research & Development for Non-ferrous and Rare Metals, Bucharest, Romania.

The samples were ground with a sequence of 400 to 4000 grit emery paper and subsequently polished with alumina suspension to attain mirror-appearance, washed with Milli-Q deionised water (18.2 MΩ), ultrasonically cleaned and degreased in ethanol, and dried in air. Tests specimens were embedded in a polytetrafluoroethylene (PTFE) holder specifically designed to facilitate connection to a rotating disc electrode holder (model EDI 101T, Radiometer Analytical). A polymeric resin was used to ensure a tight seal between the specimen and the PTFE holder, in order to avoid the occurrence of crevice corrosion [31]. The exposed surface of the materials to the test environments were discs of 0.196 cm^2 area. The same arrangement was employed for the SECM experiments, though in this case the mount containing the metals was placed at the bottom of the small electrochemical cell with the metal facing upwards to the electrolyte. In this way, scans could be performed both vertically (approach curves) and parallel (array scans) to the sample surface.

4.2.4.2. Test corrosion medium

Electrochemical tests were conducted in aerated physiological Ringer's solution whose composition was: NaCl: 8.6 g/L, KCl: 0.3 g/L, $CaCl_2$: 0.48 g/L. The pH of this solution was 6.8. SECM experiments were performed in Ringer's solution containing 0.5 mM ferrocene-methanol as the redox mediator. Electrolyte solutions were prepared using analytical grade chemicals and Milli-Q deionised water.

4.2.4.3. Electrochemical measurements

The test specimens were placed in a glass corrosion cell, which was filled with freshly-prepared electrolyte. A saturated calomel electrode was used as the reference electrode, and a platinum coil as the counter electrode. The potentials in this Section are reported versus the normal hydrogen electrode (NHE). The temperature of the electrochemical cell was maintained at 37 ^{0}C.

Electrochemical measurements were performed using a potentiostat manufactured by PAR (Model 263A, Princeton Applied Research, Princeton, NJ, USA). The instrument was controlled by a personal computer and specific software (Electrochemistry Power Suite, PAR, USA). The open circuit potentials of the materials attained stable values after 1 hour immersion in Ringer's solution (E_{corr}). Therefore, measurement of cyclic potentiodynamic polarization curves (CPP) was initiated after 1 hour exposure to the test environment. The tests were conducted by scanning the potential at 0.5 mV s^{-1} from -0.76 to +1.24 V vs. NHE, followed by scanning the potential in the negative direction down to -0.26 V vs. NHE. Using *PowerCorr* software (PAR, USA), the cyclic potentiodynamic polarization curves were plotted, and the corresponding values for the open circuit potential (E_{corr}) and the corrosion current density (j_{corr}) were determined. From the cyclic potentiodynamic polarization curves, the passivation current density (j_{pass}), breakdown potential (E_{bp}), and repassivation potential (E_{rp}) values were also obtained, which are indicators of the stability of the passive regime of the materials.

Electrochemical impedance spectroscopy (EIS) measurements were performed on the samples subjected to various potential conditions while immersed in Ringer's solution. A lock-in amplifier (Model 5210, Princeton Applied Research, Princeton, NJ, USA) was employed for EIS measurements using 10 mV amplitude of sinusoidal voltage over a frequency range extending from 100 kHz to 10 mHz. First, EIS spectra were acquired at the open circuit potential attained by the samples after 1 hour immersion in Ringer's solution. Next, the potential of the sample was set at +0.54 V vs. NHE for 30 min before recording the EIS data of the polarized sample. The EIS experimental data were analyzed in terms of equivalent circuits (EC) using *ZsimpWin 2.00* software [32].

All electrochemical tests were repeated three times to ensure reproducibility of the measurements.

4.2.4.4. *Scanning electrochemical microscopy (SECM)*

The SECM experiments were performed using a Model 900 Scanning Electrochemical Microscope from CH Instruments (Austin, TX, USA), controlled with a personal computer. The specimens were mounted horizontally facing upwards at the bottom of a cell made of polytetrafluoroethene, which was equipped with an Ag/AgCl/KCl (3M) reference electrode and a platinum counter electrode, all set up in. For the sake of comparison, potential values were referred to the normal hydrogen electrode (NHE). The electrochemical cell was located inside a Faraday cage. Tip microelectrodes were made from 10 µm platinum wires sealed in glass. 0.5 mM ferrocene-methanol was added to the Ringer's solution to act as electrochemical mediator at the tip. To enable the oxidation of the ferrocene-methanol the tip was kept at a constant potential of +0.70 V vs. NHE. In some experiments the metal specimens were polarized using the bipotentiostat associated with the SECM.

The micromanipulator stand of the SECM instrument was used to hold the microelectrode in place. Measurements were performed both vertically (approach and retreat curves), and parallel (array scans) to the sample surface at a height of 10 µm. Temperature control was not performed in the SECM, and data were recorded at ambient temperature (around 20 ^{0}C).

4.2.4.5. *SEM*

The surface morphology of the specimens after electrochemical testing was observed by scanning electron microscopy. SEM observations were made using a Quanta 200 (FEI, Hillsboro, OR, USA) operated at an accelerating voltage of 30 kV.

4.2.5. Results and discussion

Figure 4.2.1 shows typical cyclic potentiodynamic polarization curves for pure Ti and the ZrTi alloys plotted in a semi-logarithmic presentation. They were recorded after 1 hour immersion in Ringer's solution at 37 ^{0}C. Average open circuit potential (E_{corr}) and corrosion current density (j_{corr}) values determined from the polarization curves are listed in Table 4.2.2 for the various materials tested.

None of the materials exhibited a distinctive active-passive transition in the polarization curves following the Tafel region, but they entered directly into a stable passive regime. Next, the polarization curves measured for the three ZrTi alloys (namely Zr45Ti, Zr25Ti and Zr5Ti) exhibited positive hysteresis loops in the cyclic polarization curves, indicating that these materials are susceptible to localized corrosion (cf. Figure 4.2.1). In contrast, the pure titanium specimen showed no positive hysteresis loop in the cyclic polarization curve.

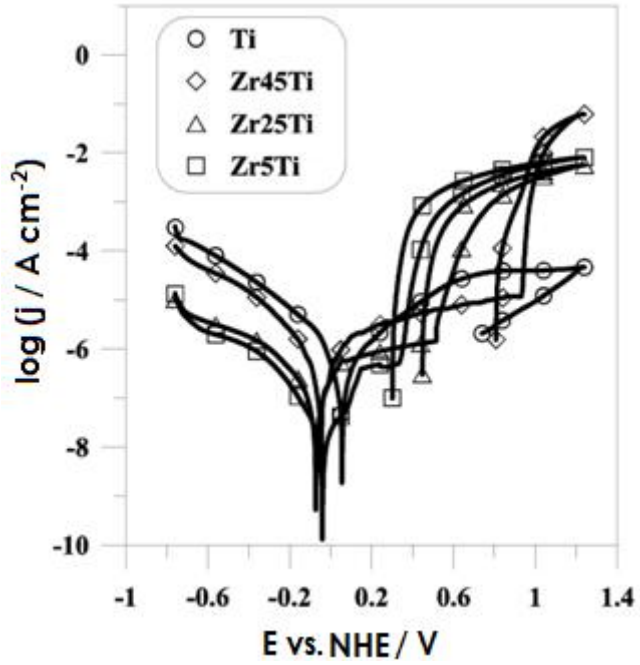

Figure 4.2.1. Cyclic potentiodynamic polarization curves of the Ti and ZrTi alloy samples in aerated Ringer's solution at 37 ^{0}C. Scan rate: v = 0.5 mV s^{-1}.

Table 4.2.2. Electrochemical parameters determined from the cyclic polarization curves measured for Ti and ZrTi alloys in aerated Ringer's solution at 37 ^{0}C.

Sample	E_{corr} / V vs. NHE	j_{corr} / nA cm^{-2}	j_{pass} / µA cm^{-2}	E_{bp} / V vs. NHE	E_{rp} / V vs. NHE	E_{bp} - E_{corr} / mV	E_{rp} - E_{corr} / mV
Ti	+0.056	560	36	-	-	-	-
Zr45Ti	-0.042	240	6.1	+0.942	+0.815	984	857
Zr25Ti	-0.075	125	0.9	+0.527	+0.455	602	530
Zr5Ti	-0.039	55	0.4	+0.342	+0.308	381	347

Though the ZrTi alloys exhibited common features in their CPP, it must be noticed that their corrosion resistance greatly varied between them as result of the different content of titanium in the materials. The susceptibility of an alloy to localized corrosion in a given environment can be characterized in terms of the breakdown potential (E_{bp}) and repassivation potential (E_{rp}), relative to the corresponding open circuit potential value (E_{corr}). The potential range comprised between the open circuit potential and E_{bp} represents the passivity zone, where corrosion is small or even insignificant. Thus, the difference $E_{bp} - E_{corr}$ can be adopted as a measure of the passive range of the material [33-35]. Additionally, the extent of the area covered by the hysteresis loop (i.e., the difference between E_{rp} and E_{corr} values) is a direct measure of the susceptibility of the material to localized corrosion [34].

Table 4.2.2 lists the values of the breakdown (E_{bp}), and repassivation (E_{rp}) potentials found for the materials under investigation, together with the values calculated for the differences $E_{bp} - E_{corr}$ and $E_{rp} - E_{corr}$. Based on these data, the

corrosion resistance of the various ZrTi alloys immersed in Ringer's solution can be characterized. The CPP for the alloy Zr5Ti exhibits both the more negative breakdown potential value and the narrowest potential range for passivity. These facts indicate that this alloy exhibits the greater susceptibility to localized corrosion. The electrochemical behaviour of Zr5Ti resembles that of pure zirconium [36], and the titanium content in the alloy is not enough to produce a significant improvement in the resistance of the material against localized corrosion in Ringer's solution at 37 ^{0}C.

Alloys containing higher amounts of titanium exhibit longer potential ranges for the passive regime, due to the shift of their breakdown potentials towards more positive values. This feature is readily observable for the Zr25Ti alloy as compared to Zr5Ti. Yet the more positive potential for breakdown of the passive film attained by Zr25Ti in Ringer's solution is not be regarded safe enough for this material to be proposed for biomedical application. The reason for this consideration arises from reports describing the exposure of Ti to positive potentials up to +0.64 V vs. NHE in the human body [37]. Though similar information regarding the ZrTi alloys is not available in the scientific literature yet, it can be estimated that similar potential values may occur as well. Thus, further addition of titanium to zirconium is still necessary to obtain a zirconium-based material that may be considered for biomedical application. The electrochemical behaviour of Zr45Ti is more promising. The passive zone now extends for almost 1.0 V, and a higher positive breakdown potential (ca. +0.94 V vs. NHE) is exhibited by this alloy, that is, 0.30 V more positive than the highest value recorded in the human body until now [37].

Though the trend exhibited by the pitting potential values can be related to the susceptibility of the material to localized corrosion, the possible occurrence of breakdown also depends on the surface condition of the metal in the environment, which results in variations in the value of the open circuit potential. In this way, the values of $E_{bp} - E_{corr}$ provide a more reliable measure of the breakdown resistance [34]. Indeed, an alloy with a particular surface condition may exhibit a small E_{bp} and yet have a sufficiently negative E_{corr}, that the difference between them is big. This was the case for Zr25Ti alloy exposed to Ringer's solution, namely it exhibited a small E_{bp} value (around +0.53 V vs. NHE), but the difference $E_{bp} - E_{corr}$ exceeded 0.60 V. In this study, larger passive ranges and more positive corrosion potentials were found for the alloys with a higher titanium contents. In fact, pure titanium exhibited the more positive value for E_{corr}, and no breakdown potential of the passive film was found for potential excursions up to +1.24 V vs. NHE.

The values of the passive current density (j_{pass}) were also determined from the potentiodynamic polarization curves. They were taken from the anodic branch of the potential-current density plots at around the middle of the corresponding passive regions for each material, and they are listed in Table 4.2.2. They were small for the Zr5Ti and Zr25Ti alloys, namely in the range of 0.5 - 1 μA cm^{-2}, whereas for Zr45Ti greater passivity currents were found, possibly related to the development of a thicker oxide film. Estimates of the thickness of the passive films have been derived from electrochemical impedance data.

Electrochemical impedance spectroscopy (EIS) measurements were performed both under open circuit potential conditions and under polarization at +0.54 V vs. NHE. This polarization value was chosen to account for the eventual development of positive potentials in the human body as described before. The EIS spectra of the non-polarized samples was measured after they attained a stable open circuit potential in Ringer's solution, whereas the measurements for the polarized samples were initiated after application of the potential value *E* = +0.54 V vs. NHE for 30 min.

Figure 4.2.2 depicts the Bode impedance plots for titanium and the ZrTi alloys under open circuit potential conditions in aerated Ringer's solution at 37 ^{0}C. From a cursory observation of the spectra it can be deduced that they exhibit behaviours consistent with the formation of a thin passive oxide film on the surface of the materials, i.e., a near capacitive response illustrated by a phase angle greater than -45^0 over a wide frequency range.

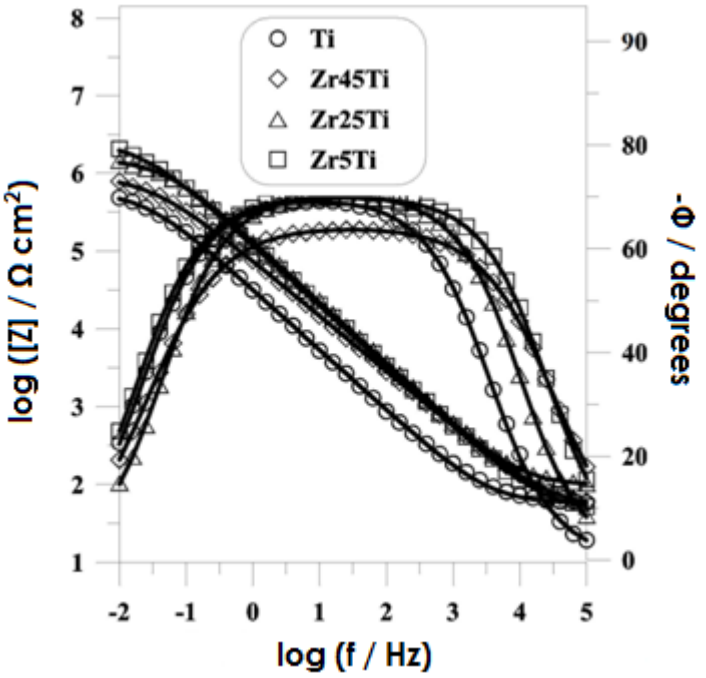

Figure 4.2.2. Measured (discrete points) and fitted (solid lines) impedance spectra typical for Ti and ZrTi alloy samples recorded at their open circuit potentials during exposure to aerated Ringer's solution at 37 ^{0}C.

The passive behaviour of pure titanium in Ringer's solution can be described by one time constant. The shape and the values obtained are very similar to those values previously reported for titanium grade 1 immersed in phosphate buffer solution by Pan et al. [38]. In their work they extended the low frequency range of the measurements down to 5 mHz, and though they fitted their spectra considering two time constants, the resistance of the outer layer was very small for its impact to be noticed on the shape of the Bode plots. The same system was later investigated by Aziz-Kerrzo et al. [39], though using high purity titanium (99.999%). In this case, two

time constants were observed for frequencies below 1 Hz, and higher resistance values were estimated for the outer layer of the passive film. The variation could be assigned to the development of a more porous outer layer due to impurities in the material in this case.

ZrTi alloys observed by EIS at their open circuit potential values can also be described by one time constant. Since the low frequency range limit of these measurements was set at 10 mHz, the occurrence of a second time constant below that frequency cannot be discarded. Yet, it should be noticed that most Ti-based alloys exhibiting two time constants have the transition between them in the 0.1-1.0 Hz range [39]. Therefore, the spectra were analyzed in terms of the equivalent circuit proposed for a sealed passive layer [38] that is depicted in Figure 4.2.3A. It assumes that the corrosion of the passive metal is hindered by an oxide film that acts as a barrier-type compact layer. The equivalent circuit consists of the parallel combination terms (R_{ox} Q_{ox}) in series with the resistance of the solution (R_{sol}) occurring between the sample and the reference electrode. The parameters R_{ox} and Q_{ox} describe the properties of the passive films formed on these metallic materials, respectively the resistance and capacitance of the compact oxide layers.

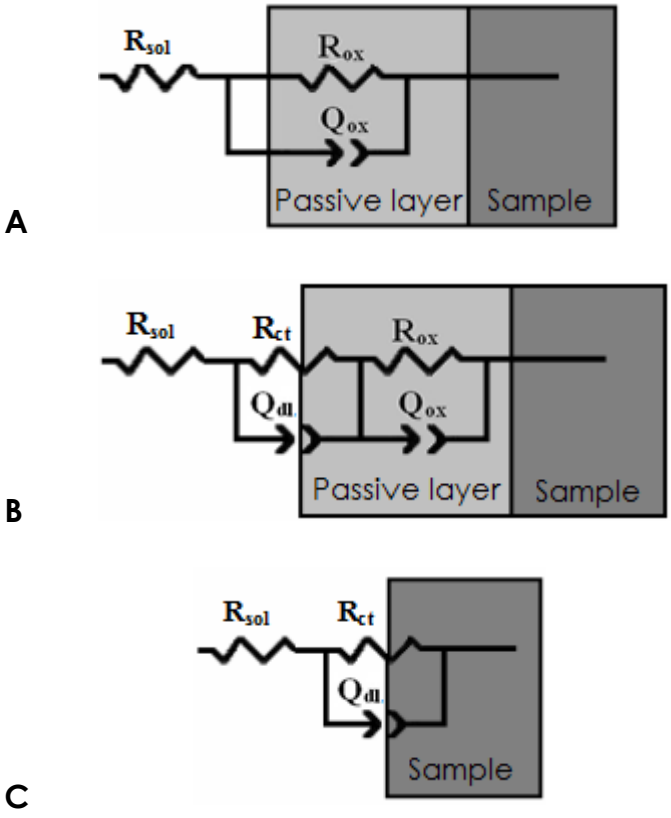

Figure 4.2.3. Equivalent circuits (ECs) used for the interpretation of the measured impedance spectra: (A) one-layer model of a barrier-type compact oxide surface film with one time constant; (B) two-layer model of an sealed porous surface film with two time constants; and (C) simplified Randles' circuit of a corroding metal.

For fitting the spectra, a constant phase element (CPE) was used instead of a pure capacitance because of the non-ideal capacitive response due to the distributed relaxation feature of the passive oxide films, which is observed as a depressed semicircle when the spectra are plotted in the corresponding Nyquist diagrams (not shown here). The impedance representation of CPE is given as:

$$Z_{(CPE)} = \frac{1}{Y_0 (j\omega)^n} \qquad (4.2.1)$$

where ω is the angular frequency and Y_0 is a constant, and the value of the exponent n indicates the deviation from ideal capacitive behaviour (e.g., when n = 1). In general, the CPE is given as both capacitance C, given in units s^n S, and factor n. Exponent values smaller than 1 arise from surface roughness of the oxide films. Yet the values were always greater than 0.8, which may indicate a rather smooth surface of the passive layers. Analysis of the impedance spectra in terms of this equivalent circuit allowed for the parameters R_{ox} and Q_{ox} to be determined, and they are presented in Table 4.2.3. The fits provided similar values for R_{sol} in all cases, namely 70 ± 5 Ω cm^2. The high quality of the fitting is readily seen from the good match between the measured and the fitted spectra, which are presented as solid lines together with experimental data on the Bode plots in Figure 4.2.2.

Table 4.2.3. Impedance parameters of Ti and ZrTi alloys in aerated Ringer's solution at 37 ^{0}C.

Sample	R_{ct} / kΩ cm^2	10^5 Q_{dL} / S cm^{-2} s^{-n}	n_{dL}	R_{ox} / kΩ cm^2	10^5 Q_{ox} / S cm^{-2} s^{-n}	n_{ox}
	***E* = E_{corr}**					
Ti	-	-	-	500	1.2	0.81
Zr45Ti	-	-	-	800	1.1	0.81
Zr25Ti	-	-	-	1200	0.8	0.82
Zr5Ti	-	-	-	2100	0.7	0.82
	***E* = +0.54 V vs. NHE**					
Ti	85	2.7	0.88	2900	1.0	0.85
Zr45Ti	7	2.7	0.87	1400	0.9	0.82
Zr25Ti	2	2.6	0.83	500	0.7	0.86
Zr5Ti	31	2.4	0.85	-	-	-

From the capacitance value, the oxide film thickness can be known using the parallel-plate capacitor equation:

$$C = \frac{\varepsilon \varepsilon_0 A}{d} \qquad (4.2.2)$$

where ε is the dielectric constant of the oxide and ε_0 the dielectric permittivity of vacuum, A is the effective area, and d the thickness of the oxide layer [40]. Since the values of the capacity of the passive oxide layer can be derived from CPE parameters using the following equation [11]:

$$C = R^{1-n}Q^{1/n} \quad (4.2.3)$$

the thickness of the oxide films formed on the titanium alloys could be estimated. To that end, ε = 65 was assumed, which is the value for TiO_2 [41], and the surface roughness factor as unity. The thicknesses of the oxide films formed on the different materials are given in Table 4.2.4. The value obtained for pure titanium (namely 4.5 nm) agrees well with previous reports in the literature [41]. Thinner films are formed when less Ti is present in the alloy, and the thickness for Zr5Ti, 2.9 nm, is close to that of pure zirconium spontaneously covered in air (2.5 nm) [42,43]. Therefore, the values reported in Table 4.2.4 are regarded to be a good estimate of the effect of composition on the thickness of the oxide films, though they were based on the assumption of ε = 65 to apply to the zirconium alloys, which may not be the case.

Table 4.2.4. Film thickness estimated from EIS results measured for Ti and ZrTi alloys in aerated Ringer's solution at 37 ^{0}C. A dielectric constant value of 65 was assumed [41].

Sample	Film thickness / nm
Ti	4.5
Zr45Ti	3.3
Zr25Ti	3.2
Zr5Ti	2.9

High impedance values, in the order of 10^6 Ω cm^2, were obtained in the medium and low frequency ranges for ZrTi alloys, suggesting high corrosion resistance of the materials in the Ringer's solution. The presence of protective passive layer provided the high corrosion resistance of the materials in this aqueous environment. The contribution of charge transfer resistance on the impedance data is regarded negligible for all the alloys. Additionally, it can be observed in Table 4.2.3 that the value of the passive layer resistance obtained at open circuit potential, R_{ox}, increases as the contents of Ti in the alloys are made smaller (i.e., 500 kΩ cm^2 for pure Ti, and 2100 kΩ cm^2 for Zr5Ti). This feature demonstrates that the spontaneously formed passive layer on ZrTi alloys becomes more resistant when the amount of titanium in the alloy decreases.

EIS measurements were also performed when the samples were polarized at +0.54 V vs. NHE, and the corresponding spectra are given in Figure 4.2.4. In this case, differences can be observed between the spectra which vary significantly among the tested materials. Two different situations can be distinguished by considering the resistance values attained in the low frequency range, namely: (1) pure Ti and the Zr45Ti alloy display higher resistances under anodic polarization than at the open circuit potential (respectively 2900 and 500 kΩ cm^2 for Ti, and 1400 and 800 kΩ cm^2 for Zr45Ti); and (2) Zr25Ti and Zr5Ti present the opposite trend (polarized Zr25Ti exhibits a value of 500 kΩ cm^2 whereas it amounted 1200 kΩ cm^2 at the OCP, and it could not be determined for the polarized Zr5Ti). Enhanced resistance is displayed by both Ti and the alloy with the highest titanium content, which is an indication of additional

growth of the oxide films favoured by anodic polarization. In this case, the Bode-phase plots show two relaxation constants, i.e. two peaks are observed in the Bode-phase plots. They can be satisfactorily fitted with the equivalent circuit shown in Figure 4.2.3B, which can be regarded as an electrical representation of a two-layer model of the oxide film consisting of a barrier-type compact inner layer and a relatively porous outer layer [44]. The new components in the EC are the resistance and the capacitance associated with the outer layer.

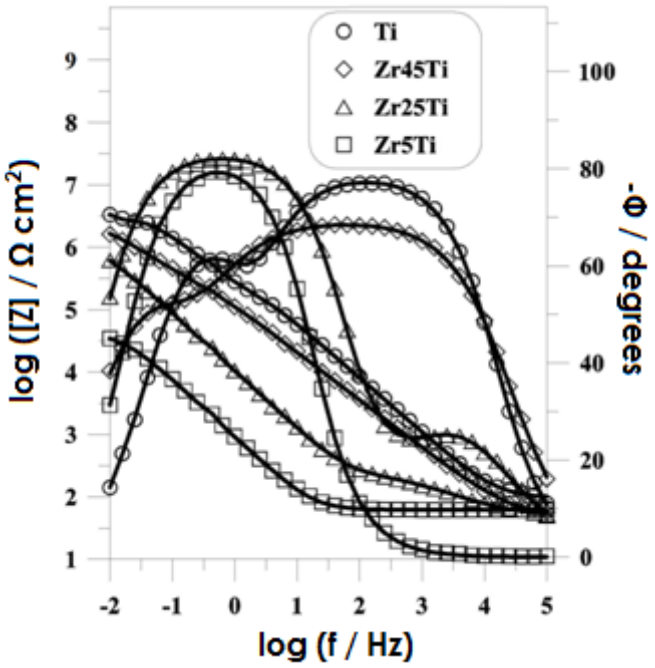

Figure 4.2.4. Measured (discrete points) and fitted (solid lines) impedance spectra typical for Ti and ZrTi alloy samples polarized at +0.54 V vs. NHE during exposure to aerated Ringer's solution at 37 ^{0}C.

Conversely, smaller resistances are exhibited by Zr5Ti and Zr25Ti when polarized at this anodic potential, indicating a thinning of the oxide film or even losses of the film continuity due to localized breakdown. Yet some differences can be observed between the two materials. The two time constants remain observable in the spectrum measured for polarized Zr25Ti, and the reported decrease in the resistance value determined in the low frequency limit is rather small. Conversely, Zr5Ti shows only one time constant and the resistance is decreased by almost 2 orders of magnitude. It is interesting to notice that the remarkable difference in shape between the spectra for this alloy and the other materials could be correlated with variations in the morphology of the samples retrieved after recording the EIS spectra. Figure 4.2.5 shows the corresponding SEM micrographs for the three ZrTi alloys and for pure titanium. The extent of the corrosion reaction on the polarized Zr5Ti sample spanning over the time required to record the EIS data becomes observable in Figure 4.2.5A. The surface roughening developed for this material was enough for the polishing lines not to be observed any longer. That is, the oxide film spontaneously formed over the surface of this alloy at the OCP during immersion in Ringer's solution,

became unstable upon application of an anodic potential of +0.54 V vs. NHE. The underlying metal is then directly exposed to the electrolyte and corrodes in the aqueous environment.

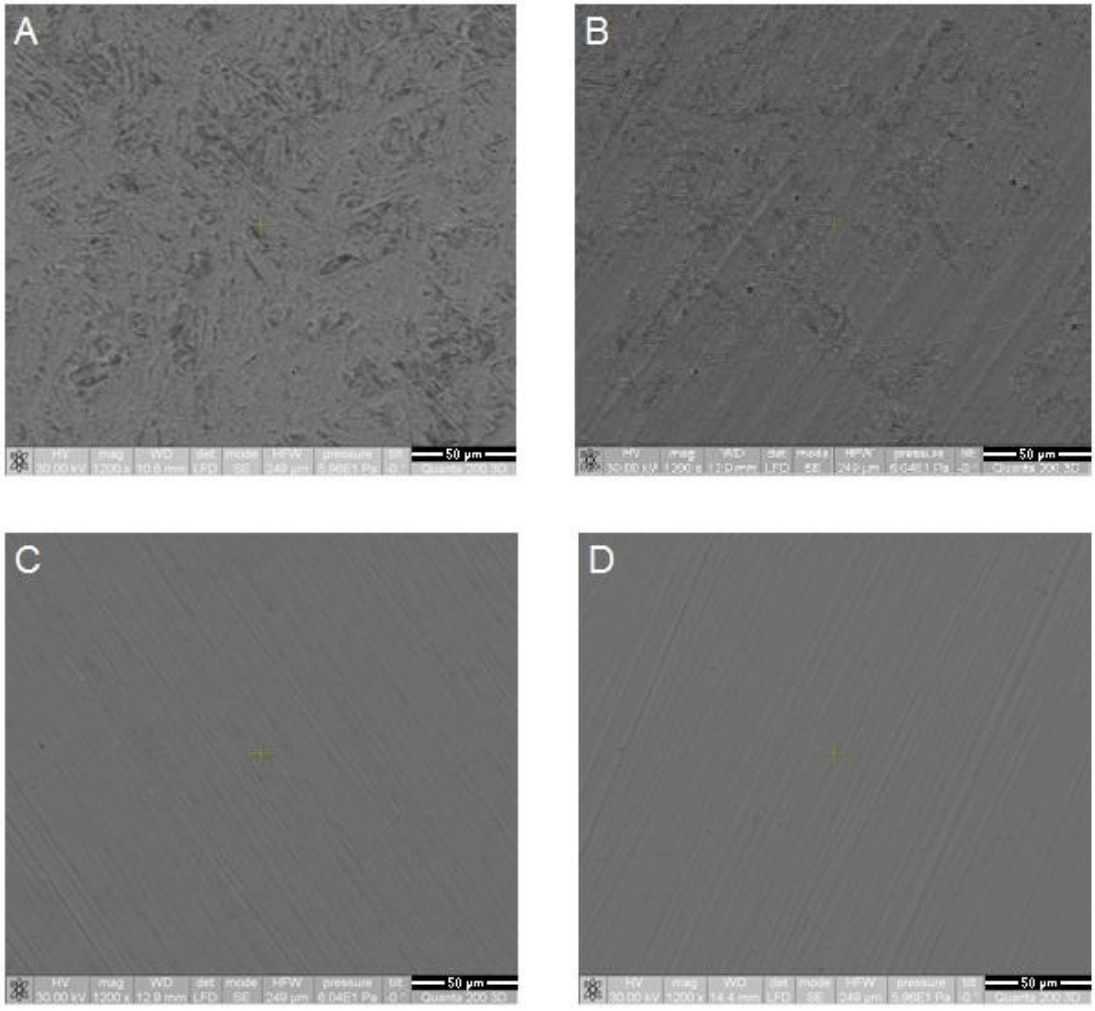

Figure 4.2.5. Surface morphology of: (A) Zr5Ti alloy; (B) Zr25Ti alloy; (C) Zr45Ti alloy; and (D) Ti, after EIS tests at +0.54 V vs. NHE in aerated Ringer's solution at 37 ^{0}C.

The onset of corrosion during anodic polarization at +0.54 V vs. NHE in Ringer's solution also occurred in the case of Zr25Ti, though in this case the polishing lines can still be observed (see image in Figure 4.2.5B). The nucleation of corrosion pits of micrometric dimensions is observed, as well as some roughening of the surface, though certainly in a smaller scale than for Zr5Ti. Therefore, the protective oxide film is still present on the surface of the material, though localized breakdown leading to pitting corrosion occurs, which is a very dangerous type of degradation process because the corrosive attack effectively penetrates in the bulk of the material. Conversely, no attack was observed in the case of Zr45Ti and pure titanium (see micrographs C and D in Figure 4.2.5). The passive films formed on the surface of these two materials effectively protect the underlying metallic matrix even at the

anodic polarization of +0.54 V vs. NHE. In summary, addition of titanium to zirconium leads to the formation of oxide films on the surface of the metallic material that more efficiently resist the onset of localized forms of corrosion.

The EIS spectrum measured for Zr25Ti while polarized at +0.54 V vs. NHE could still be satisfactorily fitted with the two-layer model presented in Figure 4.2.3B, though the less resistant system is evidenced by the smaller value determined for R_{ox}, the resistance of the inner passive layer. Finally, a different electrical model was required to fit the spectrum obtained for the polarized Zr5Ti alloy. In this case, the equivalent circuit is presented in Figure 4.2.3C, which is typical for a corroding metal. Thus, under such condition, the inner compact passive layer was no longer present to protect the metal from the environment. Extensive degradation of the passive layer occurred for Zr5Ti alloy polarized at +0.54 V vs. NHE in Ringer's solution.

In general, a very good agreement between the fitted and the experimental data was also achieved for the polarized samples. Table 4.2.3 shows the results of the fits. The parameters R_{ct} and Q_{dL} account for the properties of the reactions at the passive layer/solution interfaces and determine the impedance behaviour in the high frequency range of the spectrum. The capacitance values associated with Q_{dL} for all the samples are typical of those related to the double layer capacitance of passive oxide layers [45-48]. Therefore R_{ox} and Q_{ox} parameters describe the properties for passive layer. The resistance of passive layer of ZrTi alloys polarized at +0.54 V vs. NHE in Ringer's solution gradually decreases with the Zr content, implying that the corrosion resistance of ZrTi alloy decreases for greater Zr contents.

Scanning microelectrochemical measurements were also performed to spatially resolve different electrochemical properties of the oxide films originating from their heterogeneous composition. Scanning electrochemical microscopy (SECM) in the feedback mode, using ferrocene-methanol as redox mediator, was chosen for this purpose. In this operation mode, the current arising from the oxidation of the ferrocene-methanol to the ferrocinium ion at the SECM tip was monitored. To secure that the tip would always operate under diffusion-controlled regime, the tip potential was set at +0.70 V vs. NHE for the SECM measurements.

The tip-sample distance was established by recording Z-approach curves towards the surface of the metallic materials, while they were effectively maintained at their OCP value in the test electrolyte. Once located the surface, the tip was retracted 10 μm from the surface, and scan arrays covering an area of 250 x 250 μm^2 were registered by moving the microelectrode in an *X-Y* plane parallel to the sample. The microelectrode was subsequently moved back to the bulk solution while still measuring the current response related to ferrocene oxidation, and the retracting curve was obtained. This procedure was then repeated while the metallic substrate was polarized at +0.50 V vs. NHE. Figure 4.2.6 displays the Z-approach and Z-retreat plots measured for Ti and the ZrTi alloys. Dimensionless tip currents are represented in the graphs as a function of the tip-substrate distance. i / i_{lim} values were obtained by dividing the currents, i, at each location by the diffusion-limited current, i_{lim}, measured in the bulk electrolyte (i.e. sufficiently far from the surface for geometrical effects to be experienced).

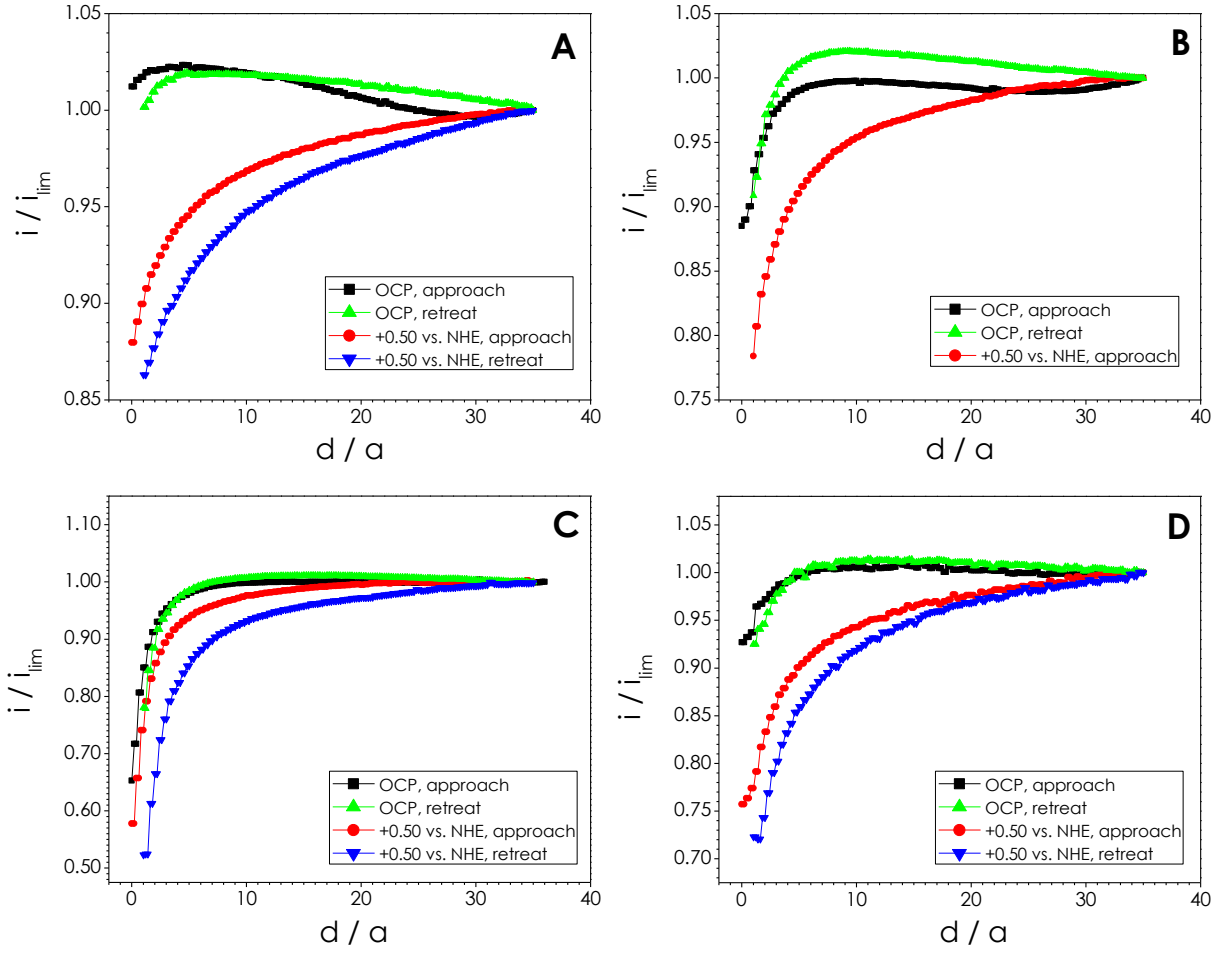

Figure 4.2.6. Z-approach and Z-retreat curves measured with the Pt microelectrode as the height of the tip is changed above: (A) Ti, (B) Zr45Ti, (C) Zr25Ti and (D) Zr5Ti. The metallic samples are either left unbiased at their corresponding OCP or polarized at +0.50 V vs. NHE during immersion in Ringer's + 0.5 mM ferrocene-methanol solution. Tip potential: +0.70 V vs. NHE. i / i_{lim} is the dimensionless tip current, and d / a is the dimensionless tip-sample distance.

Changes in the faradaic current measured at the tip are observed when it is located in close proximity to a surface under investigation. If the substrate is a conductive surface that can exchange electrons with the chemical species formed at the tip, the redox mediator species can be regenerated. Regeneration of the redox mediator would result in a fast increase of the currents measured at the tip when it approaches the surface of the substrate. Thus, this positive feedback effect would produce i / i_{lim} values greater than one. Conversely, a negative feedback effect is observed when the tip approaches an insulating substrate due to geometric hindrance for the diffusion of the reacting mediator. The tip current steadily diminishes when the tip approaches the substrate, and i / i_{lim} values smaller than one occur in this case.

There was a continuous decrease of the current measured at the tip as the tip moved towards the substrates for all the materials when they were polarized at +0.50 V vs. NHE. This negative feedback behaviour indicates that the oxide layers formed on the

surfaces act as a barrier towards electron transfer reactions. The same dependence between the tip current and the tip-substrate distance was observed when the tip was removed from the surface for all of the materials except Zr45Ti. For this alloy, activation of the surface was observed, and this effect will be discussed later.

Though a negative feedback regime also describes all the vertical lines measured at the OCP, some differences with the behaviour described for the polarized samples should be noticed. Firstly, the faradaic current measured at the tip initially increased with respect to the limiting diffusion value i_{lim} when the tip experienced the influence of the substrate. Such increase occurred rather slowly with variations in the tip-sample distance. In this way, dimensionless current values bigger than one were observed over a rather extended interval of normalized distances. Secondly, a fast decrease of the faradaic current occurs when the tip was located in a close proximity to the substrate, namely for $d / a \leq 3$. Therefore, at the smallest tip-sample distances, hindered diffusion of ferrocene-methanol towards the tip became the main contribution to the overall current. But at intermediate distances, some regeneration of the redox mediator occurred on the thinner oxide films formed at the more negative potentials corresponding to the OCP for each material. This behaviour has also been found for other titanium alloys containing either molybdenum or tantalum [49]. Regeneration of the redox mediator is more efficient on the oxide film formed on pure titanium, and the hindrance of diffusion occurring at the smallest tip-substrate distance is effectively overcome by the enhanced rate of ferrocinium ion reduction at the oxide covered metal. For this metal, $i / i_{lim} > 1$ at all tip-substrate distances. In summary, from the point of view of the shape of the Z-approach and Z-retreat curves, it can be deduced that the conductivity and the electrochemical reactivity of the passive films formed on these materials is influenced by their elemental composition because they affect the composition of the oxide film. Additionally, the behaviour of the alloys under spontaneously-developed electrical conditions can be significantly different from those generated during conventional electrochemical experiments, which are based on the application of a potential perturbation to the system under study, and this is applied to the overall material surface exposed to the test solution.

SECM images obtained for the samples either maintained at their corresponding E_{corr}, or under polarization at +0.50 V vs. NHE, are given in Figures 4.2.7 and 4.2.8, respectively. Titanium showed some heterogeneity even at the OCP (see Figure 4.2.7A). That is, tip currents greater than i_{lim} were observed at certain locations. This feature is due to facilitated regeneration of ferrocene-methanol at those areas, whereas hindered electron transfer occurs in the remaining surface. When the substrate was polarized at +0.50 V vs. NHE (cf. Figure 4.2.8A), no regions with normalized tip currents greater than 1 could be found. In this case, the SECM image exclusively reveals the topography of the sample. This result is not surprising, for the anodic potential applied to the substrate is already too positive for the electroreduction of ferrocinium ions. Then, the changes in the current values from top to bottom exclusively reflect some unavoidable tilt of the sample as observed in Figure 4.2.7A, though the main features in the image correspond to variations in the electrochemical reactivity of the investigated surface.

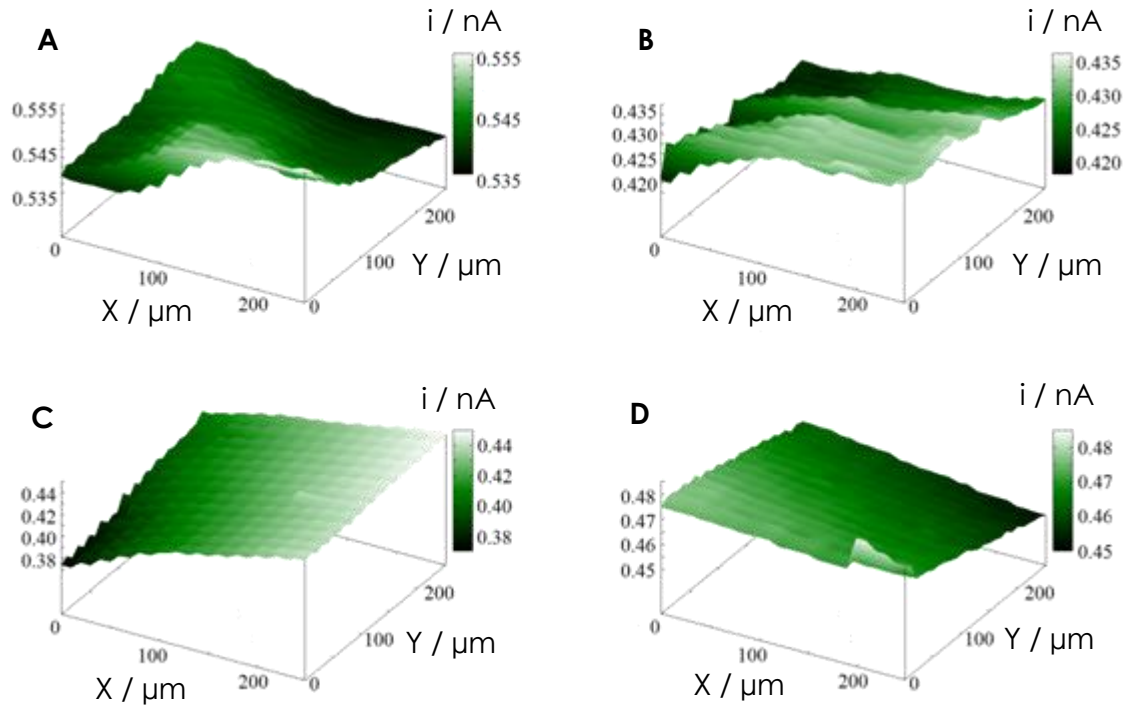

Figure 4.2.7. SECM images of: (A) Ti, (B) Zr45Ti, (C) Zr25Ti, and (D) Zr5Ti samples, maintained at their respective OCP, during immersion in Ringer's + 0.5 mM ferrocene-methanol solution. The *Z* scale is the tip current in nA. Tip potential: +0.70 V vs. NHE. Tip-substrate distance: 10 µm. Corresponding i_{lim} values for the maps: (A) 0.53 nA, (B) 0.51 nA, (C) 0.48 nA, and (D) 0.47 nA.

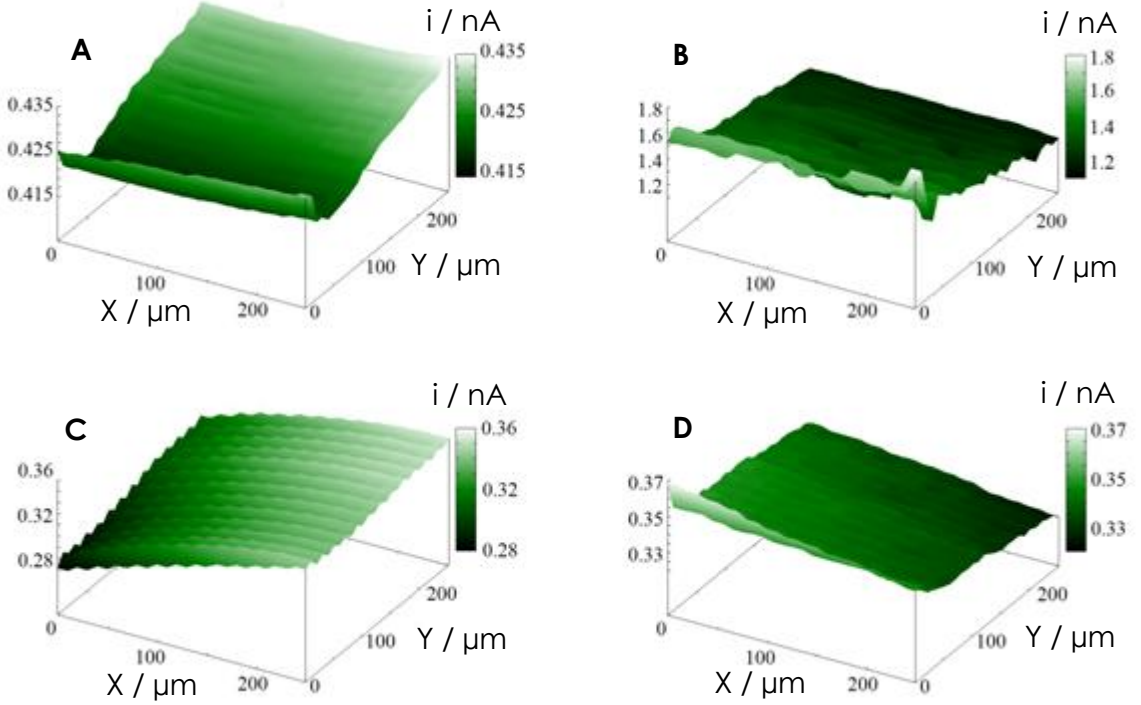

Figure 4.2.8. SECM images of: (A) Ti, (B) Zr45Ti, (C) Zr25Ti, and (D) Zr5Ti samples, polarized at +0.50 V vs. NHE, during immersion in Ringer's + 0.5 mM ferrocene-methanol solution. The *Z* scale is the tip current in nA. Tip potential: +0.70 V vs. NHE. Tip-substrate distance: 10 µm. Corresponding i_{lim} values for the maps: (A) 0.53 nA, (B) 0.51 nA, (C) 0.48 nA, and (D) 0.47 nA.

Featureless SECM images were obtained above Zr25Ti and Zr5Ti for both the unbiased and the polarized substrates (see Figures 4.2.7C, 4.2.7D, 4.2.8C, and 4.2.8D), thus they exclusively provide topographic information. The passive films formed on these alloys at the OCP are insulating enough for electron transfer not to occur at them. Yet, variations in the thickness of the passive films formed at the different potentials account for the variations in the average tip currents measured in each case. That is, higher faradaic currents for ferrocene-methanol oxidation are measured at the OCP of each metal, which corresponds to the less insulating surfaces resulting from thinner oxide films.

A special case is provided by the SECM maps measured for Zr45Ti alloy, which are displayed in Figures 4.2.7B and 4.2.8B. Negative feedback behaviour is clearly observed in the image recorded at the OCP for all the scanned area, though some locations are slightly more active (i.e. leading to higher tip currents). However, when the sample was polarized at +0.50 V vs. NHE, a sudden increase of the tip current values was observed, indicating that the metal surface became electrochemically activated. This new electrochemical behaviour was also observed in the Z-retreat curve subsequently registered, and remained during the measurement of a new Z-approach curve, (the two curves are shown in Figure 4.2.9). Even more striking is the observation that the apparent electrochemical activation of the surface affected the tip currents for tip-substrate distances as large as 200 μm. Because the potential applied to the substrate is not negative enough to reduce the ferrocinium ions, this phenomenon cannot be attributed to a positive feedback behaviour. Such a phenomenon has not been reported in the scientific literature yet, and its origin cannot be explained at this stage. It may arise from the electrochemical reaction of some active species generated from the surface undergoing corrosion, yet further investigations using other redox mediators must be undertaken to investigate this effect.

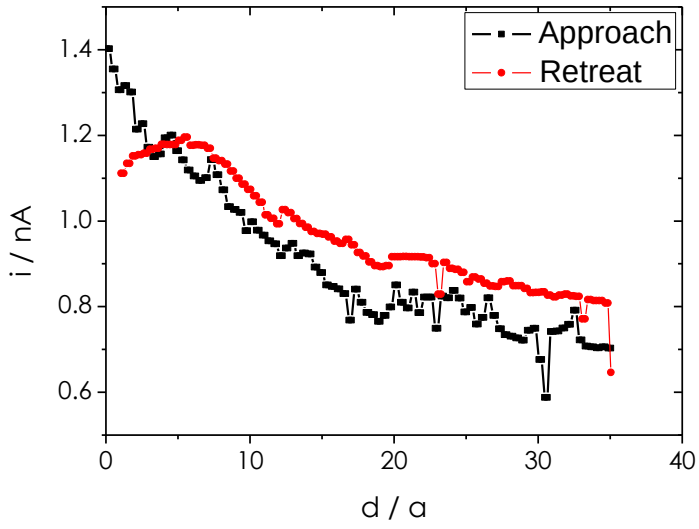

Figure 4.2.9. Z-retreat and Z-approach curves measured with the Pt microelectrode above of Zr45Ti alloy after recording the SECM image shown in Figure 4.2.8B. The metallic sample was polarized at +0.50 V vs. NHE during immersion in Ringer's + 0.5 mM ferrocene-methanol solution. Tip potential: +0.70 V vs. NHE. i / i_{lim} is the dimensionless tip current, and d / a is the dimensionless tip-substrate distance.

4.2.6. Conclusions

The electrochemical behaviour of three ZrTi alloys has been characterized in Ringer's solution (pH = 6.8) in order to investigate their potential use as biomaterials to replace Ti-based alloys containing Al and V. The development of passivity for all the materials could be deduced from the potentiodynamic polarization plots, and the corrosion resistance of ZrTi alloys in Ringer's solution results from the formation of a passive film on the surface of these materials. The current densities at the OCP, which are directly proportional to the corrosion rates of the materials, are observed to increase with greater titanium contents in the ZrTi alloys.

The addition of titanium to zirconium reduces the susceptibility of the later towards localized corrosion, as indicated by the shift of the breakdown potentials to more positive values. Though a sufficiently big overpotential (ca. +0.60 V) for film breakdown is already attained by Zr25Ti, the pitting potential of this alloy is more negative than the potential values that may occur in the human body [37]. Higher titanium contents in the alloys are required to ensure sufficient stability of the passive films developed on the ZrTi alloys for biomedical application.

EIS data show that the passive films behave as an insulating barrier towards electron transfer at the surface of the alloys, and this effect is more effectively provided by the ZrTi alloys compared to pure Ti when the oxide layers were spontaneously formed at their corresponding E_{corr} values. But this effect could not be effectively maintained for alloys with titanium contents smaller than 45 wt.% due to thickening and eventual breakdown of the passive oxide layers due to hazardous localized corrosion phenomena.

Localized differences in electrochemical reactivity of the materials could be established from SECM measurements. Though the passive films behave as an insulating barrier towards electron transfer at the surface of the alloys, this effect is more effectively provided by the ZrTi alloys compared to Ti when the oxide layers were spontaneously formed at their corresponding OCP values. Anodic polarizations at potentials reported to be achieved in the human body for Ti implants only led to thickening of the passive oxide layers without electrochemical activation due to hazardous localized corrosion reactions.

4.2.7. References

1. D.F. Williams. In: Biocompatibility of Clinical Impact Materials, Vol. 1(Edited by D.F. Williams). CRC Press, Boca Raton, 1981, p. 9.
2. P. Kovacs, J.A. Davidson. In: Medical Applications of Titanium and its Alloys: The Materials and Biological Issues (Edited by S.A. Brown, J.E. Lemons). ASTM, West Chonshohocken, 1996, p. 163.

3. M. Geetha, A.K. Singh, R. Asokamani, A.K. Gogia. Progress in Materials Science 54 (2009) 397.
4. G.T. Burstein, R.M. Souto. Electrochimica Acta 40 (1995) 1881.
5. R.M. Souto, G.T. Burstein. Journal of Materials Science: Materials in Medicine 7 (1996) 337.
6. G.T. Burstein, C. Liu, R.M. Souto. Biomaterials 26 (2005) 245.
7. C.P. Case, V.G. Langkamer, C. Jamec, M.R. Palmer, A.J. Kemp, P.F. Heap, L. Solomon. Journal of Bone and Joint Surgery 76B (1994) 701.
8. I. Milošev, V. Antolič, A. Minovič, A. Cör, S. Herman, V. Pavlovčič, P. Campbell. Journal of Bone and Joint Surgery 82B (2000) 352.
9. A. Balamurugan, S. Rajeswari, G. Balossier, A.H.S. Rebelo, J.M.F. Ferreira. Materials and Corrosion 59 (2008) 855.
10. M.V. Popa, E. Vasilescu, P. Drob, D. Mareci, J.M.C. Moreno, S. Ivanescu, C. Vasilescu, J.C.M. Rosca. Materials and Corrosion 60 (2009) 949.
11. B.I. Wang, Y.F. Zheng, I.C. Zhao. Materials and Corrosion 60 (2009) 330.
12. B.I. Wang, Y.F. Zheng, I.C. Zhao. Materials and Corrosion 60 (2009) 788.
13. I. Milosev, T. Kosec, H. H. Strehblow. Electrochimica Acta 53 (2008) 3547.
14. S.A. Shabalovskaya, G.C. Rondelli, A.L. Undisz, J.W. Anderegg, T.D. Burleigh, M.E. Rettenmayr. Biomaterials 30 (2009) 3662.
15. Y. Okazaki, E. Gotoh. Biomaterials 26 (2005) 11.
16. N.J. Hallab, S. Anderson, M. Caicedo, A. Brasher, K. Mikecz, J.J. Jacobs. Journal of Biomedical Materials Research 74A (2005) 124.
17. S. Piazza, G. Lo Biundo, M. C. Romano, C. Sunseri, F. Di Quatro. Corrosion Science 40 (1998) 1087.
18. S. Rao, Y. Okazaki, T. Tateishi, T. Ushida, Y. Ito. Materials Science and Engineering C 4 (1997) 311.
19. W.F. Ho, C.P Ju, J.H. Chern Lin. Biomaterials 20 (1999) 2115.
20. G. He, J. Eckert, Q.L. Dai, M.L. Sui, W. Löser, M. Hagiwara, E. Ma. Biomaterials 24 (2003) 5115.
21. M. Niinomi. Science and Technology of Advanced Materials 4 (2003) 445.
22. I. Halley-Demoulin, C. Valot, D. Ciosmak, M. Lallemant, J.J. Heizmann, C. Laruell. Materials Science Forum 157-162 (1994) 521.
23. C.V. D'Alkaine, L.M.M. Souza, F.C. Nart. Corrosion Science 34 (1993) 117.
24. M.M. Lohrengel. Electrochimica Acta 39 (1994) 1265.
25. N. Stojilovic, E.T. Bender, R.D. Ramsier. Progress in Surface Science 78 (2005) 101.
26. J. Fahey, D. Holmes, T.-L. Yau. Corrosion 53 (1997) 54.
27. F. Rosalbino, D. Maccio, A. Saccone, E. Angelini, S. Delfino. Materials and Corrosion 63 (2012) 580.
28. K.J. Bundy. In: Corrosion Tests and Standards: Application and Interpretation (Edited by R. Baboian). ASTM, Philadelphia, 1995, p. 411.
29. S.Y. Yu, J.R. Scully. Corrosion 53 (1997) 965.
30. D. Mareci, R. Chelariu, G. Ciurescu, D. Sutiman, T. Gloriant. Materials and Corrosion 61 (2010) 768.
31. D. Mareci, G. Ciurescu, R. Chelariu, I. Cretescu, D. Sutiman. Environmental Engineering and Management Journal 9 (2010) 81.

32. B. Yeum. Electrochemical Impedance Spectroscopy: Data Analysis Software. Echem Software, Ann Arbor, 2001.
33. B.E. Wilde, E. Williams. Electrochimica Acta 16 (1971) 1971.
34. J.R. Scully, R.G. Kelly. In: ASM Handbook, Vol. 13A (Edited by S.D. Cramer, B.S. Covino Jr.). ASM International, Materials Park, 2003, p. 68.
35. G.S. Frankel. In: ASM Handbook, Vol. 13A (Edited by S.D. Cramer, B.S. Covino Jr.). ASM International, Materials Park, 2003, p. 236.
36. N.T.C. Oliveira, S.R. Biaggio, R.C. Rocha-Filho, N. Bocchi. Journal of Biomedical Materials Research 74A (2005) 397.
37. G. Rondelli, B.Vicentini. Biomaterials 23 (2002) 639.
38. J. Pan, D. Thierry, C. Leygraf. Electrochimica Acta 41 (1996) 1143.
39. M. Aziz-Kerrzo, K.G. Conroy, A.M. Fenelon, S.T. Farrell, C.B. Breslin. Biomaterials 22 (2001) 1531.
40. J. Pan, D. Thierry, C. Leygraf. Journal of Biomedical Materials Research 30 (1996) 393.
41. J. Pan, D. Thierry, C. Leygraf. Journal of Biomedical Materials Research 28 (1994) 113.
42. N.T.C. Oliveira, E.A. Ferreira, L.T. Duarte, S.R. Biaggio, R.C. Rocha-Filho, N. Bocchi. Corrosion Science 51 (2006) 2068.
43. F. Rosalbino, D. Maccio, P. Giannoni, R. Quarto, A. Saccone. Journal of Materials Science: Materials in Medicine 22 (2011) 1293.
44. F. Mansfeld. In: Analysis and Interpretation of EIS Data for Metals and Alloys, Technical Report 26. Solartron-Schlumberger, Hampshire, 1993, Ch. 4.
45. M. Meticos-Hukovic, Z. Pilic, R. Babic, D. Omanovic. Acta Biomaterialia 2 (2006) 693.
46. T.P. Moffat, R.M. Latanision. Journal of the Electrochemical Society 139 (1992) 1869.
47. S. Haupt, H.-H. Strehblow. Corrosion Science 29 (1989) 163.
48. E.B. Castro, J.R. Vilche. Electrochimica Acta 38 (1993) 1567.
49. G. Ciurescu, J. Izquierdo, J.J. Santana, D. Mareci, D. Sutiman, S. González, R.M. Souto. International Journal of Electrochemical Science 7 (2012) 7404.

4.3

Electrochemical characterization of ZrTi alloys for biomedical applications. The effect of thermal oxidation

4.3.1. Abstract

Oxidation in air of ZrTi alloys at 500 ºC for 2 h produces oxide-covered materials with a very high corrosion resistance in Ringer's solution at 37 ºC. The oxide layers present a two-layer structure, comprised by a thin and very compact inner layer of ca. 5 nm thickness, and a less compact, more porous and thicker outer layer. The thickness of the outer layer greatly varies with the composition of the base ZrTi alloy, but has very little influence in the overall electrochemical behaviour of the material. The nature of the oxide layer is a mixture of ZrO_2 and TiO_2, and no evidence of higher oxidation states of the metal could be found using XRD and XPS data. The protective oxide film contains both TiO_2 and ZrO_2 in all cases, though titanium contents in the outer layer bigger than those in the base alloy are produced during the thermal oxidation process. Anodic dissolution through the passive layers formed on the oxidized alloys is greatly diminished compared to those measured from the untreated materials, allowing all the alloying ratios between Zr and Ti to be potentially considered for implant application. The combination of alloying with titanium and oxidation in air at 500 ºC resulted in the materials that do not exhibit the characteristic susceptibility of zirconium towards the initiation of localized corrosion processes in aqueous chloride-containing electrolytes even for anodic polarizations up to +1.00 V vs. SCE, a value well above the highest polarization experienced in the human body. Though all the oxidized alloys exhibited remarkable corrosion resistances, the best behaviour was found for oxidized Zr45Ti.

4.3.1. Resumen

La oxidación al aire de aleaciones ZrTi a 500 °C durante 2 horas produce una capa superficial de óxido con una resistencia a la corrosión muy elevada en disolución Ringer a 37 °C. Los óxidos formados presentan una estructura de dos capas, consistentes en una capa interna fina y muy compacta de aproximadamente 5 nm de espesor, y una capa externa menos compacta, más porosa y más gruesa. El espesor de la capa externa varía ampliamente con la composición de la aleación ZrTi de base, pero tiene poca influencia en el comportamiento electroquímico general del material. La naturaleza de esta capa de óxidos es una mezcla de ZrO_2 y TiO_2, y no se encuentran evidencias de estados de oxidación más altos de los metales en los datos de XRD y XPS. La película de óxidos protectores contiene tanto TiO_2 como ZrO_2 en todos los casos, aunque se obtiene mayor proporción de titanio en la capa externa respecto al presente en la aleación base durante el proceso térmico de oxidación. La disolución anódica a través de las capas pasivas formadas en las aleaciones oxidadas disminuye ampliamente en comparación con las obtenidas para el material sin tratar, permitiendo que todas las aleaciones ensayadas, independientemente de la relación Zr/Ti, puedan ser consideradas para su potencial aplicación como implante. La combinación de la presencia de titanio en la aleación conjuntamente con la oxidación al aire a 500 °C dio lugar a unos materiales que no mostraban la susceptibilidad característica del circonio hacia la iniciación de procesos de corrosión localizado en electrolitos conteniendo cloruros, incluso para polarizaciones anódicas de hasta +1.00 V relativo al SCE, un valor de polarización mucho más noble que el encontrado en el cuerpo humano. Pese a que todas las aleaciones oxidadas mostraban una considerable resistencia a la corrosión, el mejor comportamiento se encontró para el Zr45Ti oxidado.

4.3.3. Introduction

It was shown in Section 4.2 that alloying zirconium with titanium offers an attractive biomaterial alternative [1] for the replacement of commonly-employed titanium-based materials that contain toxic and allergenic elements such as vanadium and aluminium [2-5]. Though titanium and its alloys spontaneously passivate in air and in aqueous electrolytes with the formation of adherent and stable oxide films [6-8], they are susceptible to pitting corrosion in chloride-containing media [7,9-12] with the result that metal ions may be released to the surrounding tissues [5,13-16]. Zirconium is considered to be non-toxic and non-allergenic [17,18] and it stabilizes the β-phase of titanium [17]. It has been reported that zirconium influences the stability of passivating oxides and hinders the activation of metallic titanium exposed to reducing acids [19]. This effect has been justified by invoking that zirconium is a strong oxide former and likely produces Zr-O bonds of high strength [20]. Unfortunately, zirconium is susceptible to localized corrosion induced by chloride ions too [21,22]. In contrast, the addition of titanium to zirconium reduces the susceptibility of the latter towards localized corrosion, and the passive films developed by the ZrTi alloys provided a more insulating barrier towards electron transfer at the surface of the alloys compared to Ti when the oxide layers were spontaneously formed at their corresponding OCP values during immersion in Ringer's physiological solution [1]. But this protective effect could not be effectively maintained in ZrTi alloys with titanium contents smaller than 45 wt.% subjected to anodic polarization at potential values achieved in the human body [23] due to thickening and eventual breakdown of the passive oxide layers due to hazardous localized corrosion phenomena.

Surface modification treatments can greatly improve the passivation characteristics of oxide layers on titanium-based materials [24]. In particular, thermal oxidation at elevated temperature of metals and alloys leads to the rapid formation of oxide films on their surface, and they usually exhibit a multilayer structure [25,26]. This effect has been documented for high-temperature oxide films on a stainless steel [27] and nitinol [28] surfaces, and the electrical resistive and capacitive properties were correlated with the oxidation parameters. In the case of nitinol, low temperature treatment at 100 °C produced oxide layers only a few nanometers thick, whereas up to 500 °C a 20-fold thicker oxide film was observed, and these thermal oxide films always led to an improvement in the corrosion parameters for nitinol [28], a reduction in the release of Ni [29], and greater Ca and P precipitation from simulated physiological fluids [30] that is regarded to favour bioactivity for treatments. Though thicker films could also be formed at temperatures higher than 500 °C, poorer interaction of organic compounds with the resulting surface occurred, and consequently it has been regarded to be less bioactive [30]. Enhanced corrosion resistance after surface oxidation at 500 °C in air has also been reported for Ti48Al2Cr2Nb alloy, though treatment at higher temperatures, namely 800 °C was found to be detrimental due to the formation of very porous oxide films at high temperatures [31]. Finally, thermal oxidation in the case of Ti6Al4V, regardless the

temperature employed in the treatment, produces passive films with poor corrosion resistance characteristics [31]. Being corrosion products, high-temperature oxide films may present a distribution of defects, which might facilitate the penetration of the electrolyte into the passive film and consequently decrease the corrosion protection provided by the oxide layer [32,33].

It is the aim of this Section to investigate the corrosion behaviour of air-oxidized ZrTi alloys in Ringer's solution, used to simulate body fluids, at 37 °C. Electrochemical characterization was performed using potentiodynamic polarization (PP) and electrochemical impedance spectroscopy (EIS) techniques with the objective to determine the potential ranges for the stability of the materials, and to quantify the resistance of the passive films developed on them. In particular, EIS measurements assisted to establish the composition of the oxide layers developed on the materials in the thermal treatment. The formation of surface oxide layers with enhanced barrier characteristics would imply that ZrTi alloys can be considered as a biomaterial. In order to characterize the chemical properties of both non-treated and thermally-modified samples, X-ray diffraction analysis combined with X-ray photoelectron spectroscopy were used. These combined studies allowed relationships between the electrochemical behaviour in artificial physiological environment and the characteristics of the surface to be established.

4.3.4. Experimental

Three ZrTi alloys have been synthesized by electron beam melting method. The chemical compositions (wt.%) of experimental alloys are as follows: Zr-4.3%Ti-0.3%Nb-0.3%Mo (named Zr5Ti), Zr-23.8%Ti-0.4Nb%Zr-0.7%Mo (named Zr25Ti), and Zr-43.9%Ti-0.4%Nb-0.5%Mo (named Zr45Ti). The melting procedure was repeated three times in order to obtain chemically homogenized alloys. The chemical compositions have been determined by EDX analysis using a scanning electron microscope Quanta 3D (model AL99/D8229) equipped with EDX detector. The above mentioned percentages of alloying elements have been calculated as averages of ten values. The alloy specimens were cut into disks of 0.28 cm^2 surface area, and they were ground with SiC abrasive paper up to 2000 grit. The samples were next degreased with ethanol, followed by ultrasonic cleaning with deionized water, and finally dried under air stream. The oxidized samples involved heat-treatment in air at 500 °C for 2 hours. Both as cast (untreated), and oxidized samples of the ZrTi alloys were considered.

The test electrolyte was naturally-aerated physiological Ringer's solution at 37 ±1 °C. Ringer's solution was made to composition 8.6 g L^{-1} NaCl, 0.3 g L^{-1} KCl, and 0.48 g L^{-1} $CaCl_2$, in twice-distilled water. The pH of this solution was 6.8.

A three-electrode corrosion flow cell kit (C145/170, Radiometer, France) with platinum as counter electrode and saturated calomel reference electrode (SCE) as

reference electrode was employed for all the electrochemical measurements. The electrochemical cell contained a freely adjustable Luggin capillary to house the reference electrode. The sample was mounted in a PCTFE sample holder so that the exposed surface of the oxidized alloys to the test electrolyte was a disc of 0.95 cm^2.

All electrochemical measurements were carried out on a Princeton Applied Research potentiostat Model PARSTAT 4000 (Princeton Applied Research, Princeton, NJ, USA). The instrument was controlled by a personal computer and specific software (VersaStudio, PAR, Princeton, NJ, USA). Measurement of potentiodynamic polarization curves (PP) was initiated after 24 h exposure to the test environment. The potential was initiated at a potential value 0.20 V negative to the corresponding open circuit potential of the sample in the solution, and it was extended in the positive direction up to +1.00 V vs. SCE, at a sweep rate of 1 mV s^{-1}. The positive potential limit was chosen to be a value 0.50 V more positive than the highest value recorded in the human body until now [23]. The cyclic potentiodynamic polarization curves were plotted, and the corresponding values for the open circuit potential (E_{corr}), the corrosion current density (j_{corr}), and the passivation current density (j_{pass}), were determined from them.

Electrochemical impedance spectroscopy (EIS) measurements were also performed using the same instrumentation. The perturbation amplitude was 10 mV and the frequency ranging from 100 kHz down to 1 mHz. Five points were recorded for each frequency decade. The EIS spectra were obtained at different times after the electrode was immersed in the Ringer's solution. The EIS experimental data were analyzed in terms of equivalent circuits (EC) using *ZSimpWin 3.22* software [34].

All electrochemical tests begun with a new sample, and they were repeated three times to ensure reproducibility of the measurements.

The morphology of the oxidized ZrTi alloys, both before and after the electrochemical tests, was observed by scanning electron microscopy (SEM) using a Quanta 3D Model AL99/D8229 (FEI, Hillsboro, OR, USA) operating with beam energy 30 kV. In addition, the elemental analysis of the surfaces was done by energy dispersive X-ray spectroscopy (EDS).

X-ray diffraction (XRD) spectra were employed for the identification of oxides formed on the surface of the oxidized ZrTi samples. XRD spectra were recorded using an X'Pert PRO MRD (PANalytical, Almelo, The Netherlands) diffractometer equipped with a Cu Ka anode, and the XRD patterns were scanned in the $20 \leq 2\theta \leq 90$ degrees range at a rate of 1.8 degree min^{-1}.

X-ray photoelectron spectroscopy (XPS) was performed with an ESCALAB 250 spectrometer equipped with dual aluminum-magnesium anodes, using a monochromatized Al Ka X-ray radiation ($h\nu$ 1486.6 eV). The spectrometer energy calibration was performed using the Au $4f_{7/2}$ and Cu $2p_{3/2}$ photoelectron lines. For consistency, all binding energies are reported with reference to the binding energy of the C 1s core level spectrum corresponding to the carbon contamination layer at 284.6 eV.

4.3.5. Results

4.3.5.1. Electrochemical characterization

Potentiodynamic polarization techniques were employed to establish the potential ranges of the different electrochemical reactions occurring during the anodic polarization of oxidized ZrTi alloy specimens. The polarization curves recorded at a sweep rate of 1 mV s^{-1} in Ringer's solution at 37 ^{0}C are plotted in Figure 4.3.1. None of the three oxidized ZrTi alloys showed an active region in the polarization plots following the Tafel region but they entered directly into a stable passive regime. And the passive region extended over the whole complete range of potentials up to the anodic limit considered in this work. No rapid increases in the anodic current were observed that could be related to passivity breakdown as result of localized corrosion or transpassive processes. Therefore, breakdown potentials, E_b, are well above the range of potential the metals can experience in open circuit for all the samples tested. Therefore, the oxide layers formed on the surface of ZrTi alloys at 500 °C render these alloys passive and highly corrosion resistant in Ringer's solution at temperatures around those experienced in the human body.

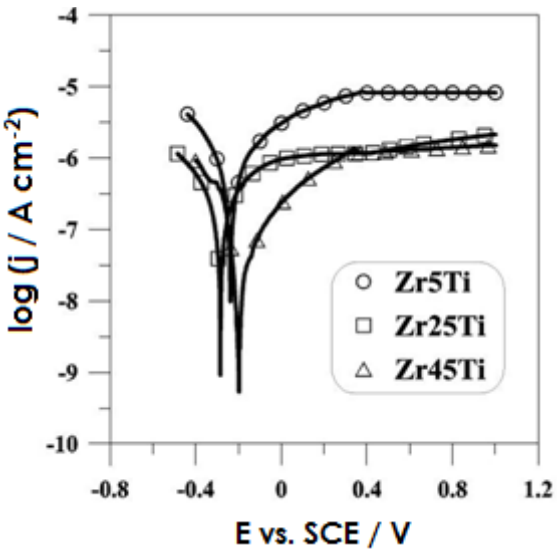

Figure 4.3.1. Cyclic potentiodynamic polarization curves for oxidized ZrTi samples immersed in aerated Ringer's solution at 37 °C. Sweep rate: 1 mV s^{-1}.

For the sake of comparison, the polarization curves were also analyzed to extract the values for the corrosion potential (E_{corr}), corrosion current density (j_{corr}), and the passive current density (j_{pass}), and they are given in Table 4.3.1. The formation of oxide on the ZrTi samples, resulting from surface treatments renders the three metal alloys passive in Ringer's solution at 37 °C. Yet some differences can be observed as corrosion and passivation current densities were found to depend on the alloy compositions. Oxidized Zr5Ti and Zr25Ti samples exhibited higher corrosion current densities than the oxidized Zr45Ti sample, possibly due to the presence of more porous mixed TiO_2/ZrO_2 layer. And the passivation current densities determined

for the Zr25Ti and Zr45Ti samples were approximately one order of magnitude smaller than that determined for the Zr5Ti sample. These results indicate that some electrodissolution through the passive film takes place for the latter. That is, the surface of the oxidized Zr5Ti sample is more reactive towards electron transfer than the surfaces of oxidized Zr25Ti and Zr45Ti when subjected to anodic polarization conditions. A clear beneficial effect can be attributed to the presence of titanium in the binary alloy, as both lower passivation and corrosion current densities are observed for the Zr45Ti alloy.

Table 4.3.1. Electrochemical parameters determined from the cyclic potentiodynamic polarization curves measured for oxidized ZrTi alloys in aerated Ringer's solution at 37 °C.

Sample	E_{corr} / V vs. SCE	j_{corr} / nA cm^{-2}	j_{pass} / μA cm^{-2}
Zr5Ti	-0.240 ± 0.011	690 ± 15	8.1 ± 0.2
Zr25Ti	-0.285 ± 0.008	210 ± 9	1.7 ± 0.1
Zr45Ti	-0.198 ± 0.006	60 ± 5	1.2 ± 0.1

The corrosion resistance and passivation characteristics of the oxidized alloys were quantified using electrochemical impedance spectroscopy (EIS). Impedance spectra were recorded for the oxidized Zr5Ti, Zr25Ti and Zr45Ti alloys exposed to Ringer's solution at 37 °C for different elapsed times up to 1 week. The samples were always investigated at their spontaneously-developed open circuit potentials. The measured impedance spectra are shown in Figure 4.3.2 and they are displayed in the form of Bode diagrams. The advantages of this procedure are that the data for all measured frequencies are shown and a wide range of impedance values can be displayed simultaneously. The frequency dependence of the impedance modulus and the phase shift indicate whether one or more time constants are present in the system.

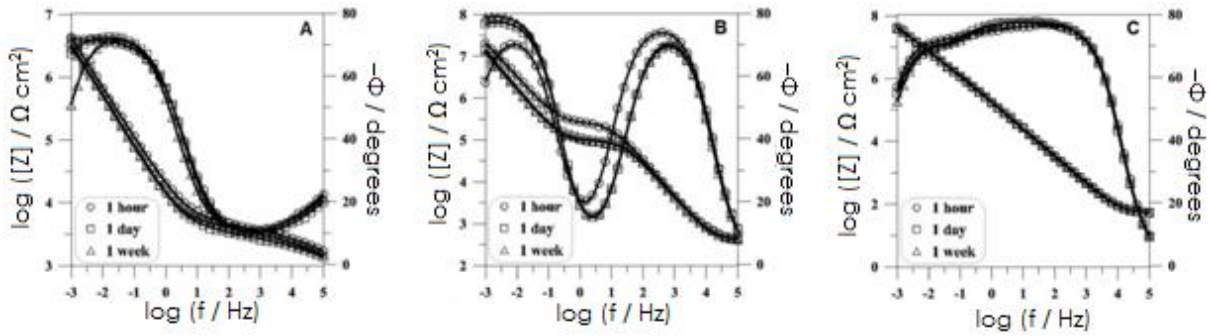

Figure 4.3.2. Measured (discrete points) and fitted (solid lines) impedance spectra for oxidized ZrTi alloy samples recorded at their open circuit potentials during exposure to aerated Ringer's solution at 37 °C: (A) Zr5Ti, (B) Zr25Ti, and (C) Zr45Ti. Exposure times are indicated in the plots.

From a cursory inspection of the spectra, it can be first observed that for a given material, they exhibited only very small changes with the elapse of time and they mainly occurred in the low-frequency region. The greater changes with time were exhibited by the oxidized Zr25Ti alloy. Secondly, the spectra look quite different for the various ZrTi alloys after oxidation in air at 500 °C. The spectra measured for oxidized Zr45Ti showed an extended frequency range of capacitive behaviour, characteristic of an effective barrier film, whereas oxidized Zr5Ti presented the narrowest capacitive regions. Therefore, the EIS spectra measured for oxidized ZrTi alloys and their variation with time of exposure demonstrate a significant influence of alloy composition on their electrochemical response during immersion in aerated Ringer's solution at 37 °C.

Though the spectra for each of the materials can be easily distinguished among the plots, they all contain two time constants, and they could be satisfactorily analyzed using the same equivalent circuit (EC). Figure 4.3.3 shows the equivalent circuit, which is based on a two-layer model of an oxide film [35]. It assumes that the corrosion of the passive metal is hindered by an oxide film that acts as a barrier-type compact layer. The equivalent circuit consists of the combination of two parallel *R*Q elements in series with the resistance of the solution (R_{sol}) occurring between the sample and the reference electrode. Constant phase elements (CPE) were used instead of pure capacitances because of the non-ideal capacitive response due to the distributed relaxation feature of the passive oxide films, which could be observed as a depressed semicircle when the spectra were plotted in the corresponding Nyquist diagrams (not shown here). The impedance representation of CPE, $Z_{(CPE)}$, is given by:

$$Z_{(CPE)} = \frac{1}{Y_0 (j\omega)^n} \qquad (4.3.1)$$

where ω is the angular frequency and Y_0 is a constant, and the value of the exponent *n* indicates the deviation from ideal capacitive behaviour (e.g., when *n* = 1). The high frequency R_{ct} and $Q_{dL,}$ parameters describe the properties of the reactions at the oxide layer/solution interface, whereas in the low frequency range the parameters R_{ox} and Q_{ox} describe the resistance and the capacitance of the compact oxide layers. A very good correlation was obtained between EIS data using the proposed equivalent circuit and the experimental impedance spectra of the solution interface/oxide layer/alloy. Figure 4.3.2 provides an evidence of fitting quality when applied to the measured spectra because all the solid lines corresponding to the fitted spectra passed through the measured data (discrete points).

Table 4.3.2 presents the corrosion parameters obtained for the three oxidized ZrTi alloys from the analysis of EIS data. Whereas charge transfer resistance values, $R_{ct,}$ in the range of kΩ cm^2 were determined for all the materials significantly higher values were obtained for the resistance of the oxide layers R_{ox} (they are quantified in MΩ cm^2). These results indicate that the corrosion protection of oxidized ZrTi samples is due to their oxide layer. Next, the impedance modulus was observed to decrease

during the exposure of the samples to Ringer's solution while they were left at their spontaneously-developed open circuit conditions, i.e. no polarization were applied to the systems. This effect is already noticeable from the observation of the EIS spectra given in Figure 4.3.2, and is more evident in the medium frequency range for the oxidized Zr25Ti alloy. Most of the change occurred already within the first 24 h. However, after one week of immersion time the R_{ox} of all three oxidized ZrTi samples remained high (around 10^6-10^7 Ω cm^2). The origin for the decrease in the values of R_{ox} during immersion may be related to the establishment of conductive electrolyte pathways inside pores existing in the oxide layers. The effect of alloy composition is also observed from the comparison of the resistance parameters obtained for each material. For the shortest exposure of 1 h, the R_{ox} value for the oxidized Zr45Ti alloy was approximately ten times higher than that determined for the oxidized Zr5Ti sample. The trend for R_{ox} with alloy composition is: Zr5Ti < Zr25Ti < Zr45Ti and this agrees well with the observations obtained from the polarization data.

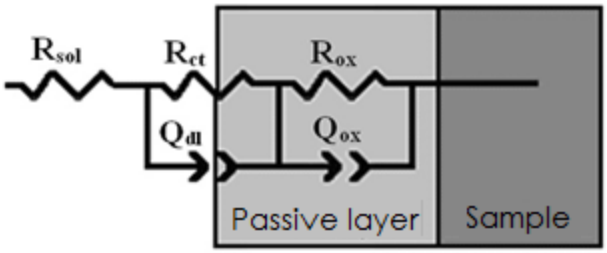

Figure 4.3.3. Equivalent electrical circuit (EC) used for the interpretation of the impedance spectra measured for ZrTi alloys oxidized in air at 500 °C for 2 h.

Table 4.3.2. Impedance parameters of oxidized ZrTi alloys immersed in aerated Ringer's solution at 37 °C.

Immersion time	R_{ct} / kΩ cm^2	10^5 Q_{dL} / S cm^{-2} s^{-n}	n_{ct}	R_{ox} / MΩ cm^2	10^5 Q_{ox} / S cm^{-2} s^{-n}	n_{ox}
	Zr5Ti alloy					
1 h	3.5	3.1	0.82	4.4	0.6	0.85
1 day	2.3	3.4	0.81	3.5	0.7	0.84
1 week	2.1	3.4	0.80	2.9	0.7	0.84
	Zr25Ti alloy					
1 h	25.2	2.2	0.84	21.5	0.3	0.88
1 day	19.5	2.3	0.83	14.8	0.4	0.87
1 week	17.8	2.3	0.83	12.4	0.4	0.87
	Zr45Ti alloy					
1 h	36.1	2.1	0.85	43.1	0.2	0.89
1 day	32.4	2.2	0.84	41.5	0.2	0.89
1 week	28.3	2.2	0.83	39.3	0.2	0.88

On the other hand, the impedance parameters related to the constant phase elements contained in the EC were almost invariant with the duration of the

exposures of the samples to Ringer's solution. Though exponent values *n* smaller than 1 were always found, yet the values were greater than 0.8, an indication of a rather smooth surface for the passive oxide layers. Capacitance values for both the compact oxide layers and the electrolyte/oxide interfaces could be extracted from the CPE parameters using [36]:

$$C = R^{1-n}Q^{1/n} \qquad (4.3.2)$$

In this way, the order of magnitude of the capacitance values determined for both C_{ox} and C_{dl} were found to correspond to those typical for a compact barrier layer and for an interface at which charge transfer occurs, respectively.

4.3.5.2. Surface analysis of ZrTi alloy surfaces after air-oxidation treatment

The oxides present on the three ZrTi alloys after oxidation in air for 2 h at 500 °C were characterized using a combination of two analytical techniques (SEM/EDX and XRD) to obtain some information on the morphology and composition of the films. The scanning electron microscope photographs given in Figure 4.3.4 showed that the surface of the oxide layers was apparently rather flat, though different distributions of pores and cracks on their surfaces could be clearly observed for the different alloys. In this way, the surface of oxidized Zr5Ti exhibited many pores and cracks, whereas a uniform oxide layer was only observed on the surface of the oxidized Zr45Ti sample, and the oxidized Zr25Ti specimen exhibited an intermediate situation. This variation in the topography of the oxide layers between the oxidized alloys can also be observed from the inspection of the SEM images taken from cross sections through the oxide films (cf. Figure 4.3.5). The formation of an oxide layer on ZrTi alloys can be identified in these micrographs due to their lighter contrast in the SEM images. It is observed that the thickness of the oxide layer formed on the alloys as result of the oxidation process in air at 500 °C during 2 h greatly diminishes for higher titanium contents in the ZrTi alloys. The thickest layer (ca. 250 μm) was formed on Zr5Ti, it amounted roughly a third in the case of Zr25Ti, and it was comparatively very thin on Zr45Ti (around 35 μm). Despite this great variation in thickness, the most striking difference between the oxide layers formed on the different alloys is related to their densities. A more dense and compact oxide layer was formed on Zr45Ti by air oxidation, whereas the oxide layers formed on the other alloys presented many defects and voids.

No significant enrichment in any of the two alloying elements in the oxide layer can be deduced from EDX analysis (cf. Figure 4.3.6), whereas the XRD spectra displayed in Figure 4.3.7 demonstrate that TiO_2 and ZrO_2 are the only corrosion products resulting from air oxidation of the ZrTi alloys at 500 °C. That is, no higher oxidation states for titanium and zirconium occur during the oxidation process for any of the ZrTi alloys.

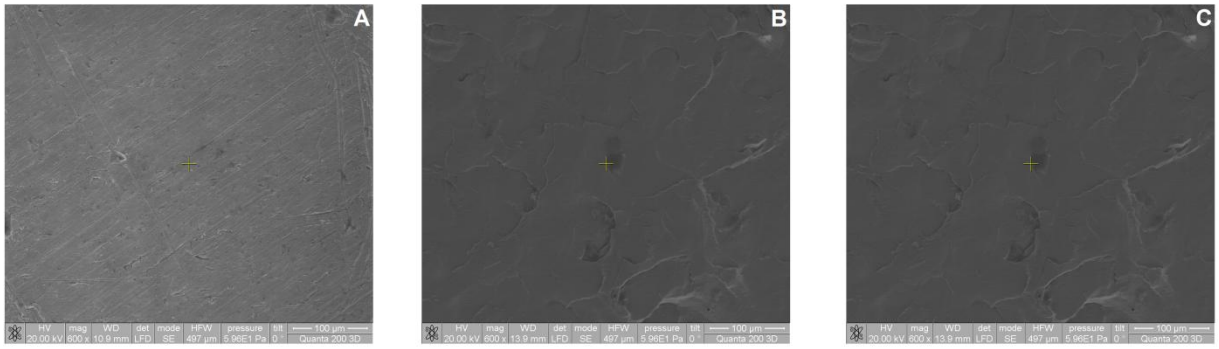

Figure 4.3.4. SEM photographs of the oxidized ZrTi alloys as obtained from the oxidation process in air at 500 °C for 2 h. (A) Zr5Ti, (B) Zr25Ti, and (C) Zr45Ti.

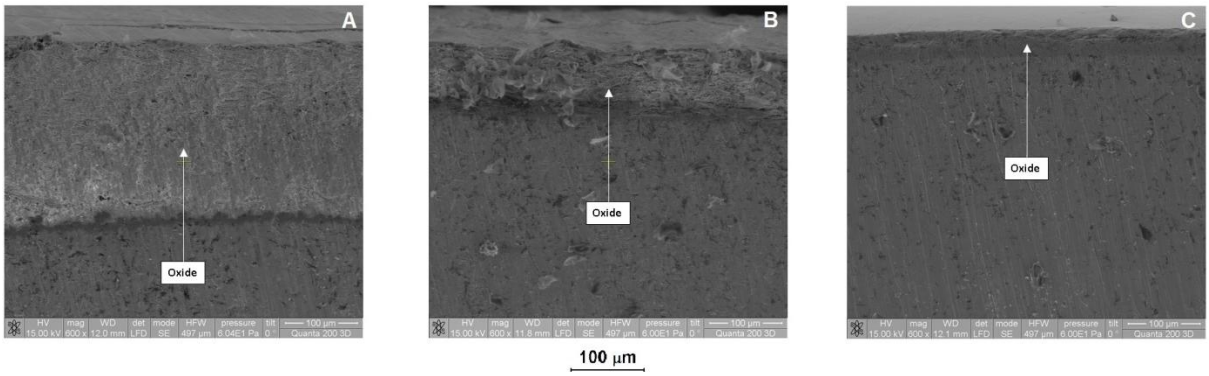

Figure 4.3.5. SEM photographs of cross sections through the oxide film of the oxidized ZrTi alloys as obtained from the oxidation process in air at 500 °C for 2 h. (A) Zr5Ti, (B) Zr25Ti, and (C) Zr45Ti.

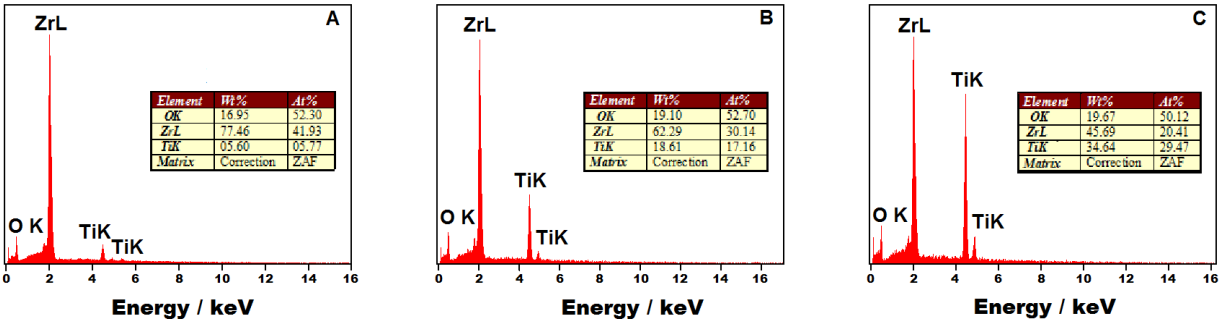

Figure 4.3.6. EDX spectra measured at the surface of the oxidized ZrTi alloys as obtained from the oxidation process in air at 500 °C for 2 h. (A) Zr5Ti, (B) Zr25Ti, and (C) Zr45Ti.

The effect of surface treatment was further investigated by XPS, focusing on the chemical composition of the oxide layers formed on the different ZrTi alloys under investigation. Figure 4.3.8 shows the XPS survey spectra recorded at the surface of the three ZrTi alloys prepared by thermal oxidation at 500 °C for 2 hours. The predominant elements detected at the surface of the alloys were C, O, Ti and Zr for

all three Zr/Ti ratios. Carbon concentration is related to air exposure with the formation of carbon-containing compounds at the outermost surface layer. Signals corresponding to Nb and Mo metals were not detected this time as they are contained in very small amounts in the samples.

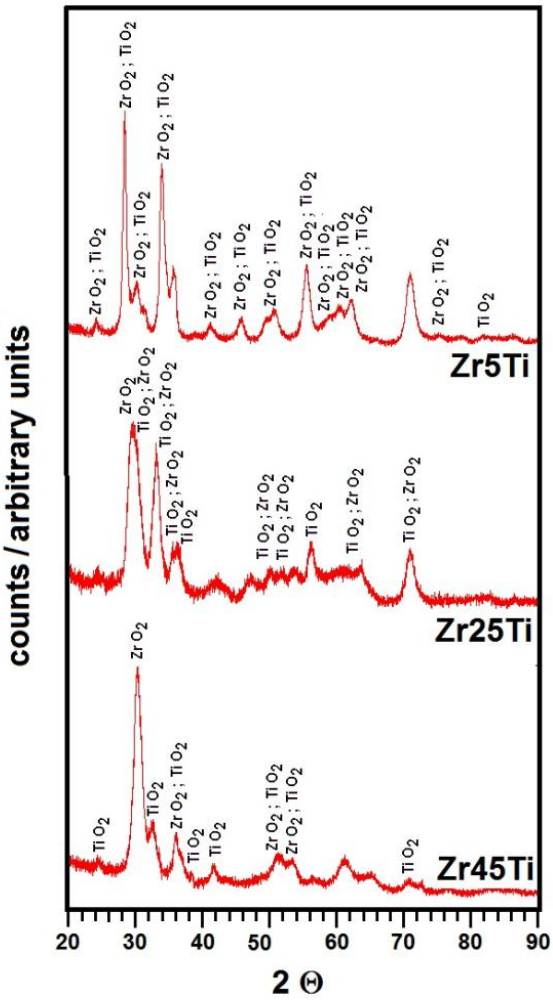

Figure 4.3.7. X-ray difractograms of the oxidized ZrTi alloys as obtained from the oxidation process in air at 500 ºC for 2 h.

Finally, Figure 4.3.9 presents the scanning electron micrographs of the three ZrTi samples after anodic polarization at +1.00 V vs. SCE in Ringer's solution at 37 ºC. No obvious variation in the surface morphology of the Zr45Ti sample as result of the anodic polarization tests compared to its condition prior to testing was observed, whereas rougher surfaces resulted for the other two alloys after electrochemical testing. This indicates that the anodic polarization tests had no major effect on the characteristics of the oxide layer of the Zr45Ti sample resulting from oxidation in air at 500 ºC for 2 hours.

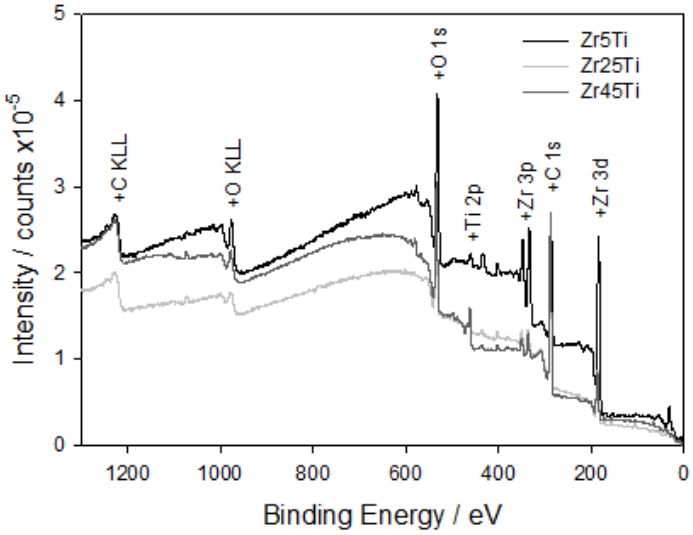

Figure 4.3.8. XPS survey spectra recorded at the surface of thermally-oxidized ZrTi alloys in air at 500 °C for 2 hours.

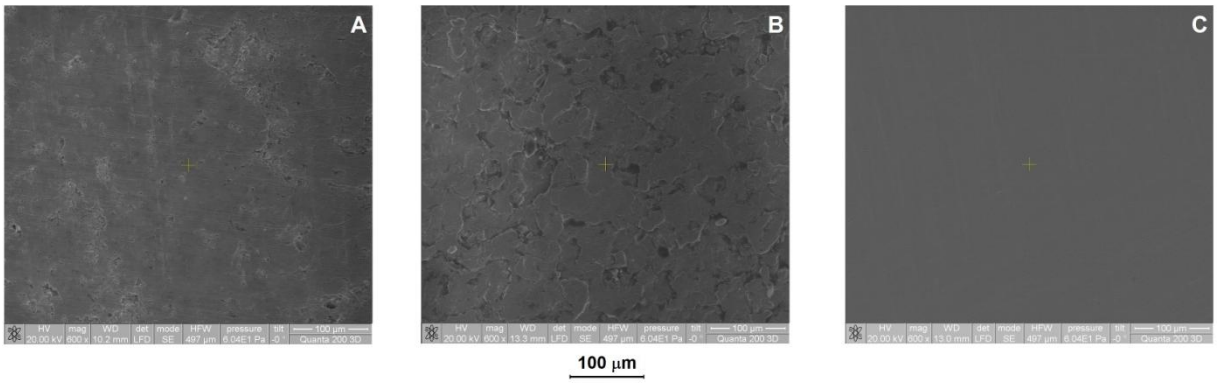

Figure 4.3.9. SEM photographs of the oxidized ZrTi alloys retrieved from Ringer's solution at 37 °C after recording the corresponding potentiodynamic polarization curves depicted in Figure 1. The samples were removed at the anodic potential value +1.00 V vs. SCE. (A) Zr5Ti, (B) Zr25Ti, and (C) Zr45Ti.

4.3.6. Discussion and conclusions

4.3.6.1. Effect of thermal oxidation

It was obvious that both Ti and Zr oxides are present in the protective film formed on the surface of the ZrTi alloys as result of the thermal oxidation treatment in air at 500 °C. The XPS peaks related to Zr metal are located between 182.0 and 184.4 eV, for Ti metal between 457.9 and 459.6 eV, and for O 1s between 535.0 and 530.9 eV, similar to reported values for Zr50Ti [37]. To reveal the surface distribution of the metals and oxide species, high-resolution spectra of elements were measured as a function of take-off angles, and they are given in Figures 4.3.10 and 4.3.11 for Zr and

Ti, respectively. Two spin-orbit components, corresponding to Zr $3d_{3/2}$ and Zr $3d_{5/2}$, are observed in Figure 4.3.10 for zirconium, and the corresponding peak energies after deconvolution of the XPS peaks are given in Table 4.3.3. The average separation between the signals is 2.4 eV, in good agreement with previous reports on Zr50Ti [37], and for other transition metal alloys subjected to similar thermal oxidation procedures [38]. The values of the binding energies increase with higher titanium contents in the alloy. In this way, the binding energies determined for the outermost oxide layer (given by takeoff angles of 20 degrees), are 182.0 eV for Zr5Ti, 182.9 eV in Zr25Ti, and 183.3 eV for Zr45Ti. These values are very close to that reported for Zr^{4+} $3d_{5/2}$ in ZrO_2 for passive layers formed on pure zirconium [39] and its alloys [37,40-43].

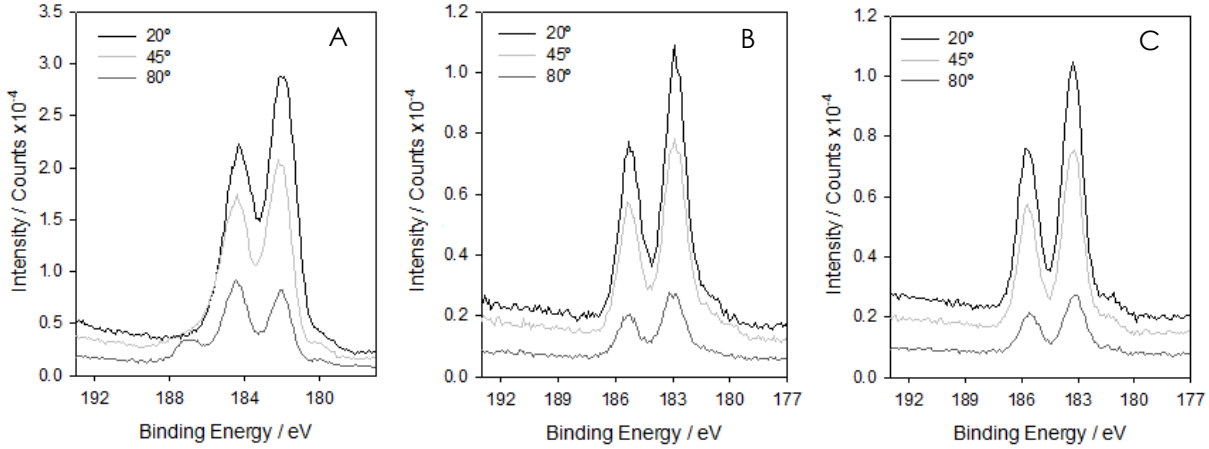

Figure 4.3.10. XPS zirconium Zr 3d spectra recorded at the surface of the thermally-oxidized ZrTi alloys at take-off angles 20, 45 and 80 degrees. Materials: (A) Zr5Ti, (B) Zr25Ti, and (C) Zr45Ti.

A similar trend between the binding energies and titanium contents in the alloy is also observed in the deconvoluted XPS peaks for Ti $2p_{3/2}$ shown in Figure 4.3.11. They shift from 458.3 eV in Zr5Ti to 459.5 eV in the alloys with higher Ti contents as for the outermost oxide layer. These values are in good agreement with the reported value of 458.8 eV for Ti^{4+} $2p_{3/2}$ [38], while the binding energy for TiO is 453.8 eV. Analogously, the binding energy for Ti $2p_{1/2}$ in the outermost oxide layer is 466 eV in the alloy with the lowest titanium content, and shifts to 465.0 eV for Zr25Ti and Zr45Ti. As result, the difference in binding energies between Ti $2p_{3/2}$ and Ti $2p_{1/2}$ signals amounts 5.7 eV in average, a value that supports the occurrence of Ti^{4+} state as TiO_2 in the surface films, in accordance to previous reports [37]. Higher contents in the ZrTi alloys originates a shift of the binding energies of the Ti 2p signals to higher values, progressively approaching the typical values for TiO_2 layers developed on pure titanium [38,39], and also for Zr50Ti [37]. Therefore, the oxide layers formed on the three ZrTi alloys under study are composed by a mixture of TiO_2 and ZrO_2.

As result, the difference in binding energies between Ti $2p_{3/2}$ and Ti $2p_{1/2}$ signals amounts 5.7 eV in average, a value that supports the occurrence of Ti^{4+} state as TiO_2 in the surface films, in accordance to previous reports [37]. Higher contents in the ZrTi alloys originates a shift of the binding energies of the Ti 2p signals to higher values,

progressively approaching the typical values for TiO_2 layers developed on pure titanium [38,39], and also for Zr50Ti [37]. Therefore, the oxide layers formed on the three ZrTi alloys under study are composed by a mixture of TiO_2 y de ZrO_2.

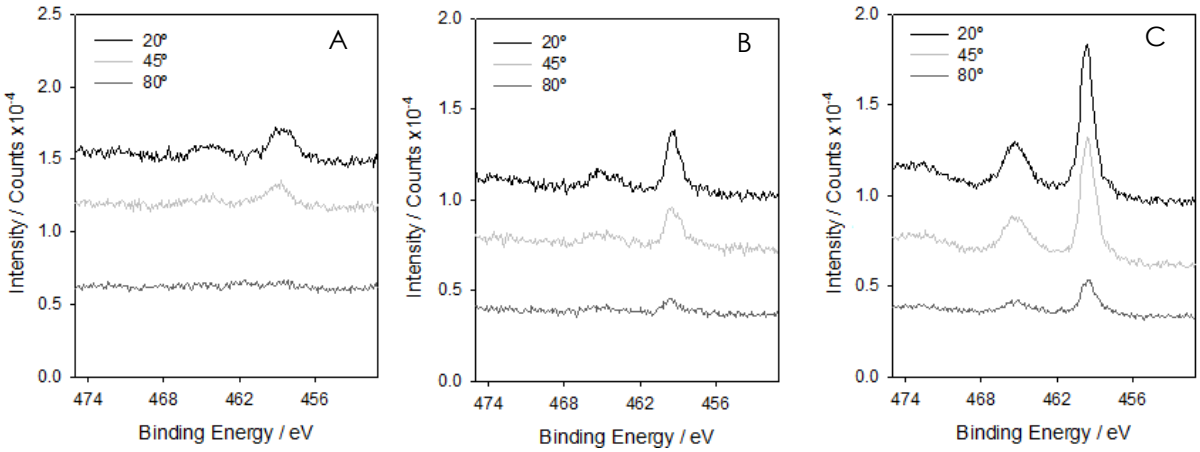

Figure 4.3.11. XPS titanium Ti 2p spectra recorded at the surface of the thermally-oxidized ZrTi alloys at take-off angles 20, 45 and 80 degrees. Materials: (A) Zr5Ti, (B) Zr25Ti, and (C) Zr45Ti.

Table 4.3.3. Binding energies and atomic contents obtained by XPS for samples of zirconium and titanium oxides grown in air at 500 °C for 2 hours.

Samples		Binding energies / eV					Content / at. %		
		Ti $2p_{1/2}$	Ti $2p_{3/2}$	Zr $3d_{3/2}$	Zr $3d_{5/2}$	O 1s	Ti	Zr	O
Zr5Ti	20°	466	458.30	184.3	182.0	535.0	1.07	12.83	36.82
	45°	464.2	458.98	184.6	182,2	534.5	1.45	11.82	35.26
	80°	-	-	184.4	182.1	533.1	0	10.05	26.65
Zr25Ti	20°	465.1	459.4	185.2	182.9	530.9	1.02	3.85	19.8
	45°	465.2	459.5	185.4	182.9	530.9	1.45	4.25	20.41
	80°	-	459.6	185.2	182.9				
Zr45Ti	20°	465.3	459.6	185.7	183.3	531.2	1.93	2.77	18.32
	45°	465.2	459.4	185.5	183.1	531.0	2.57	3.07	20.79
	80°	465.3	459.5	185.7	183.3	531.2	1.41	1.76	15.82

The distribution of these two metal oxides through the protecting surface films can be analyzed in semi-quantitative terms by comparing the XPS data obtained using different take-off angles. In this way, internal chemical composition can be derived from the measurements taken at 45 and 80 degrees, and their comparison with those from the outermost layer obtained at 20°. A summary of the data is provided in Table 4.3.3. It is found that enrichment in TiO_2 occurred in the outermost layer for the oxides formed on the ZrTi alloys with the higher titanium contents. Whereas no significant TiO_2 could be detected on Zr5Ti in the innermost layers, the amount of ZrO_2 decreases as we move towards the surface of the material. The same trends are observed for Zr25Ti. Quantification of TiO_2 from the data measured

using 80 degrees take-off angle was only achieved from Zr45Ti, the alloy with highest titanium content. It should also be noticed that the Zr/Ti ratios in the thermally-formed oxide layers are always smaller than in the bulk alloy. That is, there is more titanium in the outermost layer of the surface oxide than in the bulk of the material. Since the diffusion rate of zirconium is about 75% of the corresponding rate for titanium due to the high interaction energy of Zr^{4+} - O^{2-} [43], the surface preparation procedure produces an enrichment in TiO_2, which is known to be more corrosion resistant than ZrO_2 in acidic environment, and less susceptible to pitting corrosion.

4.3.6.2. Electrochemical stability of protecting oxide layers in Ringer`s solution

Experiments described in this Section correspond to the electrochemical behaviour of previously oxidized ZrTi alloys in naturally-aerated Ringer's solution at 37 ºC. In this environment, these alloys are covered by an oxide film that was characterized using SEM, EDX and XRD.

The electrochemical behaviour of the oxidized ZrTi alloys corresponds to materials covered by oxide layers with barrier characteristics typical of a protective passive film. They are highly stable in Ringer's solution at 37 ºC, and the potential range for either localized corrosion or transpassivity lie well beyond the values that can be experienced in the human body. Indeed, no signs for passivity breakdown could be observed from the inspection of the polarization curves depicted in Figure 4.3.1, though the anodic potential limit was fixed at a high positive value (namely +1.00 V vs. SCE). The current densities related to the passive state of oxidized ZrTi alloys immersed in Ringer's solution at 37 ºC are 2-3 orders of magnitude smaller than those determined for the untreated alloys (see Figure 4.2.1 in Section 4.2). The occurrence of metal dissolution through the passive layers has been decreased accordingly, which should greatly favour the biocompatibility of these materials as potential biomaterials for implant applications. Furthermore, alloys with low titanium contents such as Zr5Ti can also be considered for biomedical use after air oxidation at 500 ºC for 2 h, because the polarization curve for this material almost completely matches that determined for the untreated Zr45Ti alloy in the same environment, which was then regarded a good electrochemical characteristic for that material as to be considered for biomaterial application.

Tenacious and adherent oxide layers are produced on the ZrTi alloys by the air-oxidation procedure described in this Section. The susceptibility to localized corrosion has been greatly reduced for the materials even for low titanium contents, and they remain practically unaffected both electrochemically and morphologically when subjected to rather high anodic potential values (cf. Figures 4.3.1, 4.3.4 and 4.3.9). High impedance values (around 10^6-10^7 Ω cm^2) were measured in the low frequency range of the spectra for all the oxidized ZrTi samples. This is an evidence of the rather high corrosion resistance of these materials in Ringer's solution at 37 ºC which has been conferred by the oxide layers formed during oxidation of the alloys in air at 500 ºC for 2 h. For all the oxidized ZrTi alloys, the impedance modulus values are 1 order of magnitude greater than the corresponding values for the untreated

materials (cf. Figure 4.2.2 in Section 4.2). A more corrosion resistant oxide layer film has been thus formed during the oxidation pretreatment in air.

The impedance parameters in Table 4.3.2 can be employed to obtain estimates of the oxide film thickness. The procedure is based on the application of the parallel-plate capacitor model to these systems, as described by:

$$C_{ox} = \frac{\varepsilon \varepsilon_0 A}{d} \qquad (4.3.3)$$

In order to determine the thickness of the oxide layer, d, the values of the dielectric constants of the oxides for each alloy, ε, would be required. Unfortunately, those values are not available in the scientific literature, and only the dielectric constants corresponding to the oxides of the pure metals, namely ε = 65 for TiO_2 [44] and ε = 22 for ZrO_2 are available[45]. Due to the big difference between these two values, and because ZrO_2 is the main component in the oxide films considered in this work, only the value for this oxide was employed in the calculations instead of adopting an intermediate value. A unity surface roughness factor was also adopted. The thicknesses of the oxide films formed on the different materials after air-oxidation at 500 °C, and the capacitance values of the inner oxide film employed in their calculation, are given in Table 4.3.4. For the sake of comparison, the thickness of the oxide films on untreated materials were also calculated using the dielectric constant of ZrO_2 from the EIS data reported in Table 4.2.2, and they are listed in Table 4.3.5.

In general, these values are almost twice those determined for the non-oxidized materials using the same procedure. Therefore, thicker inner oxide layers occur on the ZrTi alloys subjected to thermal oxidation than those formed on non-treated materials during exposure to Ringer's solution. On the other hand, these values are very similar for the three oxidized ZrTi alloys, and they are very thin compared to the surface films discovered using SEM from cross sections through the oxide films given in Figure 4.3.5. Corrosion protection is mainly conferred to the alloys by the thin compact inner oxide layer, which amounts ca. 2 nm and directly in contact with the metallic crystalline lattice, whereas a less compact outer layer is formed film of the oxidized ZrTi alloy on top of it. From the comparison of the values of R_{ox} listed in Table 4.3.2, it can be concluded that the corrosion resistance of oxidized Zr45Ti sample was better than for the oxidized Zr5Ti sample, and slightly better than oxidized Zr25Ti sample. This means that a relatively more compact and less porous inner TiO_2/ZrO_2 layer was formed on Zr45Ti sample for the oxidation treatments at 500 °C though the thickness is very similar in all the cases. And these inner compact layers are thicker when the alloys are subjected to thermal oxidation. As for the outer oxide layer, this was thickest for oxidized Zr5Ti, and the thinnest for oxidized Zr45Ti. Yet, the outer oxide layer formed during thermal oxidation in air must not be very compact, and due to the occurrence of a distribution of pores and defects, the corrosion protection ability of the oxide film formed on ZrTi alloys almost exclusively depends on the characteristics of the inner compact layer, which effectively operates as a barrier film towards electron transfer reactions.

Table 4.3.4. Film thickness estimated from EIS results measured for oxidized ZrTi alloys in aerated Ringer's solution at 37 ºC. A dielectric constant value of 22 was assumed in the calculation [45].

Sample	Capacitance of the inner oxide layer / μF cm^{-2}	Film thickness / nm
Zr5Ti	10.69	2.0
Zr25Ti	12.87	1.7
Zr45Ti	12.42	1.6

Table 4.3.5. Film thickness estimated from EIS results in Table 4.2.2 corresponding to non-oxidized ZrTi alloys in aerated Ringer's solution at 37 ºC. A dielectric constant value of 22 was assumed in the calculation [45].

Sample	Film thickness / nm
Zr5Ti	1.0
Zr25Ti	1.1
Zr45Ti	1.1

The increase of titanium contents in the alloys produces more corrosion resistant materials. Though this effect was already reported for the untreated alloys [1], it also applies to air-oxidized samples. Indeed, EDX data suggest that the passive oxide layers are enriched in titanium compared to the substrates, and XRD data indicate that they consist exclusively of mixed TiO_2/ZrO_2, without the occurrence of higher oxidation states of the metals, as it was expected because TiO_2 and ZrO_2 are the most stable oxides of these elements.

4.3.7. References

1. G. Bolat, J. Izquierdo, J.J. Santana, D. Mareci, R.M. Souto. Electrochimica Acta 88 (2013) 447.
2. S. Rao, Y. Okazaki, T. Tateishi, T. Ushida, Y. Ito. Materials Science and Engineering C 4 (1997) 311.
3. S. Piazza, G. Lo Biundo, M.C. Romano, C. Sunseri, F. Di Quatro. Corrosion Science 40 (1998) 1087.
4. N.J. Hallab, S. Anderson, M. Caicedo, A. Brasherm K. Mikecz, J.J. Jacobs. Journal of Biomedical Materials Research A 74 (2005)124.
5. Y. Okazaki, E. Gotoh. Biomaterials 26 (2005) 11.
6. R.J. Solar. In: Corrosion and Degradation of Implant Materials (Edited by B.C. Syrett, A. Acharya). American Society for Testing and Materials, Philadelphia, 1979, p. 259.
7. R.W. Schutz, D.E. Thomas. In: Metals Handbook, Vol. 13, 9th edn. ASM International, Metals Park, 1987, p. 669.

8. M.M. Lohrengel. Electrochimica Acta 39 (1994) 1265.
9. G.T. Burstein, R.M. Souto. Electrochimica Acta 40 (1995) 1881.
10. R.M. Souto, G.T. Burstein. Journal of Materials Science: Materials in Medicine 7 (1996) 337.
11. G.T. Burstein, C. Liu, R.M. Souto. Biomaterials 26 (2005) 245.
12. G.T. Burstein, M. Carboneras, B.T. Daymond. Electrochimica Acta 55 (2010) 7860.
13. R.M. Urban, J.J. Jacobs, M.G. Tomlinson, J. Gavrilovic, J. Black, M. Peoc'h. Journal of Bone and Joint Surgery A 82 (2000) 457.
14. I. Milošev, V. Antolič, A. Minovič, A. Cör, S. Herman, V. Pavlovčič, P. Campbell. Journal of Bone and Joint Surgery B 82 (2000) 352.
15. A.V. Rousslle, D. Heymann, D. Demais, C. Charrier, N. Passuti, M.F. Basle. Histology and Histopathology 17 (2002) 1025.
16. A. Balamurugan, S. Rajeswari, G. Balossier, A.H.S. Rebelo, J.M.F. Ferreira. Materials and Corrosion 59 (2008) 855.
17. M. Niinomi. Science and Technology of Advanced Materials 4 (2003) 445.
18. H.M. Grandin, S. Berner, M. Dard. Materials 5 (2012) 1348.
19. S.Y. Yu, C.W. Brodrick, M.P. Ryan, J.R. Scully. Journal of the Electrochemical Society 146 (1999) 4429.
20. P. Marcus. Corrosion Science 36 (1994) 2155.
21. J. Fahey, D. Holmes, T.-L. Yau. Corrosion 53 (1997) 54.
22. F. Rosalbino, D. Maccio, A. Saccone, E. Angelini, S. Delfino. Materials and Corrosion 63 (2012) 580.
23. G. Rondelli, B.Vicentini. Biomaterials 23 (2002) 639.
24. M.C. García Alonso, L. Saldaña, G. Valles. Biomaterials 24 (2003)19.
25. P. Kofstad. In: High Temperature Corrosion, 2nd edn. Ellis Horwood, 1986.
26. I. Saeki, H. Konno, R. Furuichi. Corrosion Science 38 (1996) 19.
27. J. Pan, C. Leygraf, R.J. Petterson, J. Linden. Oxidation Metals 50 (1998) 431.
28. I. Milošev, B. Kapun. Materials Science and Engineering C 32 (2012) 1068.
29. W. Chrzanowski, E.A. Abou Neel, D.A. Armitage, J.C. Knowles. Journal of Materials Science: Materials in Medicine 19 (2008) 1553.
30. W. Chrzanowski, E.A. Abou Neel, D.A. Armitage, J.C. Knowles. Acta Biomaterialia 4 (2008) 1969.
31. C. Delgado-Alvarado, P.A. Sundaram. Acta Biomaterialia 2 (2006) 701.
32. S. Becker, A. Rahmel, M. Schorr, M. Schütze. Oxidation Metals 38 (1992) 425.
33. J.W. Fergus. Materials Science and Engineering A 338 (2002) 108.
34. B. Yeum. Electrochemical Impedance Spectroscopy: Data Analysis Software. Echem Software, Ann Arbor, 2001.
35. J. Pan, D. Thierry, C. Leygraf. Electrochimica Acta 41 (1996) 1143.
36. B.I. Wang, Y.F. Zheng, I.C. Zhao. Materials and Corrosion 60 (2009) 330.
37. N.T.C. Oliveira, S.R. Biaggio, P.A.P. Nascente, S. Piazza, C. Sunseri, F. Di Quarto. Electrochimica Acta 51 (2006) 3506.
38. L.Z. Zao, S.H. Liu, D.H. Wang, C.H. Pan. Journal of Electron Spectroscopy 52 (1990) 571.

39. C.D. Wagner, W.M. Riggs, L.E. Davies, J.F. Moulder, G.E. Muilenberg. Handbook of X-ray Photoelectron Spectroscopy. Perkin-Elmer, Eden Prairie, 1979, p. 68-9, p. 100-1.
40. D.Q. Peng, X.D. Bai, X.W. Chen, Q.G. Zhou, X.Y. Liu, R.H. Yu. Applied Surface Science 227 (2004) 73.
41. X.-Y. Li, E. Akiyama, H. Habazaki, A. Kawashima, K. Asami, K. Hashimoto. Corrosion Science 39 (1997) 1365.
42. C. Monticelli, A. Bellosi, M. Dal Colle. Journal of the Electrochemical Society 151 (2004) B331.
43. E.A. Ferreira, R.C. Rocha-Filho, S.R. Biaggio, N. Bocchi. Corrosion Science 52 (2010) 4058.
44. J. Pan, D. Thierry, C. Leygraf. Journal of Biomedical Materials Research 28 (1994) 113.
45. P.J. Harrop, J.N. Wanklin. British Journal of Applied Physics 18 (1967) 739.

4.4

Electrochemical behaviour of ZrTi alloys in artificial physiological solution simulating in vitro inflammatory conditions

4.4.1. Abstract

The effect of surface treatment on the corrosion resistance of ZrTi alloys (Zr5Ti, Zr25Ti, and Zr45Ti) in acidified Ringer's solution (pH = 3) was evaluated to ascertain their stability for biomedical application. All the samples were examined using electrochemical techniques: electrochemical impedance spectroscopy (EIS), potentiodynamic polarization curves (PP), and scanning electrochemical microscopy (SECM). In addition, scanning electron microscopy (SEM) was employed to observe the surface morphology of the retrieved specimens after the polarization tests. The electrochemical corrosion parameters obtained from the EIS and potentiodynamic polarization curves indicated a typical passive behaviour for untreated and thermal oxidized ZrTi alloys. Though rather high impedance values were observed for all untreated alloys, they were higher for oxidized ZrTi. More compact and electrically insulating oxide films were produced on the alloys by thermal oxidation treatment in air as revealed by SECM. The onset of localized pitting corrosion was not observed for the alloy with the highest titanium contents, namely 45 at.%.

4.4.2. Resumen

Se ha evaluado el efecto del tratamiento superficial en la resistencia frente a la corrosión de aleaciones ZrTi (Zr5Ti, Zr25Ti, and Zr45Ti) inmersas en disolución Ringer acidificada (pH = 3) con la finalidad de comprobar su estabilidad durante su posible aplicación biomédica. Todas las muestras se examinaron usando técnicas microelectroquímicas: espectroscopía de impedancia electroquímica (EIS), curvas de polarización potenciodinámica (PP), y microscopía electroquímica de barrido (SECM). Además, se empleó la microscopía electrónica de barrido (SEM) para observar la morfología de las superficies tras los experimentos de polarización. Los parámetros de corrosión electroquímica obtenidos de las curvas de EIS y de polarización indicaron un comportamiento típicamente pasivo para las aleaciones ZrTi no tratadas y las térmicamente oxidadas. Se han observado altos valores de impedancia en todos los casos, siendo éstos mayores para las aleaciones ZrTi oxidadas. Se generaron películas de óxidos más compactas y aislantes eléctricamente en las aleaciones bajo tratamiento de oxidación térmica al aire, tal como revela el SECM. El inicio de la corrosión localizada por picado no llega a observarse en la aleación más rica en titanio, con contenido del 45%.

4.4.3. Introduction

Metallic biomaterials play an essential role in repair or replacement of diseased or damaged bone tissue. The metals are more suitable for load-bearing applications compared with ceramics or polymeric materials because they combine high mechanical strength with fracture toughness [1-4]. In recent years, surgical alloys are investigated with a strong emphasis on their corrosion behaviour and biocompatibility due to reports of metallosis and necrosis [5-7]. Particularly, corrosion resistance is very important due to the hostile environments they experience in service. Different parts of the human body present different pH and oxygen concentration [8]. Ideally, metallic materials should be inert for implant application, but they react with components in the organic fluids, and they experience electrochemical activity to some extent. Although metals and alloys spontaneously undergo oxidation in air and aqueous environments, certain metals and alloys can form adherent and tenacious oxide films on their surface, which render them passive. Yet, this passive regime is actually a dynamic state, and passivity breakdown and reforming occurs [9], though in degrees that greatly vary between the different materials [10,11]. Additionally, for a given material, this transient behaviour is also influenced by the composition of the environment [12]. Metal release into the surrounding tissues may be the outcome from those transient passivity breakdowns [11]. Implant corrosion caused by the reaction with body fluids and tissues seems to affect the fatigue life as well [13]. Furthermore, immediately after implantation, fibrin and chloride ions surround the metallic biomaterials, with the subsequent decrease of the local pH [14]. Acidification is harmful to the stability of the passive regime [15-17]. In summary, for medical implant materials, it is important to minimize corrosion and the release of the metal ions [18]. In vitro evaluation of corrosion behaviour constitutes the first stage in the procedure to establish the successful applicability of metallic biomaterials [19]. The corrosion of a metal implant in the human body is primarily driven by electrochemical reactions. Consequently, electrochemical methods can be employed to evaluate the corrosion resistance of new implant alloys.

Titanium and its alloys present a high corrosion resistance under severely corrosive environments [20], and they exhibit excellent biocompatibility and osseointegration characteristics [21]. Because of its adequate mechanical properties, high corrosion resistance and excellent hemocompatibility, zirconium is believed to be an ideal alloying metal for titanium in biomedical applications [22-25]. The good corrosion resistance of zirconium, titanium, and their alloys is mainly due to a very good stable oxide grown spontaneously on their surface [26,27]. Additionally, the corrosion protection characteristics of the oxide films formed on these metals can be improved by using surface modification techniques. Thus, there are some works reporting an improvement in the corrosion resistance of Ti alloys treated by thermal oxidation [28,29]. In this Section, thermal oxidation at 500 °C was applied to Zr5Ti, Zr25Ti and Zr45Ti alloys with the aim to produce thicker oxide layers, as well as to enhance their corrosion resistance. The electrochemical behaviour of both

untreated and thermally oxidized ZrTi alloys was investigated in acidified Ringer's physiological solution of pH = 3 at ambient temperature.

4.4.4. Materials and methods

4.4.4.1. Materials

Three ZrTi alloys were fabricated by electron beam melting method. The melting procedure was repeated three times in order to obtain chemically homogenized alloys. The chemical compositions have been determined by EDX analysis, using a scanning electron microscope Quanta 3D (model AL99/D8229) equipped with an EDX detector. Chemical compositions (wt.%) of the alloys are as follows: Zr-4.3%Ti-0.3%Nb-0.3%Mo (named Zr5Ti), Zr-23.8%Ti-0.4Nb%Zr-0.7%Mo (named Zr25Ti), and Zr-43.9%Ti-0.4%Nb-0.5%Mo (named Zr45Ti). Discs of 0.28 cm^2 area were cut from the ingots. The surface of the specimens were ground with SiC abrasive paper up to 2000 grit, followed by polishing with 1 µm alumina suspension, and then cleaned ultrasonically in ethyl alcohol and in deionised water, and finally dried under a cold air stream. After preparing the surface, selected specimens were treated by thermal oxidation: the samples were oxidized in air atmosphere in an oven for 2 h at 500 °C.

4.4.4.2. Electrochemical measurements

Potentiodynamic polarization and electrochemical impedance tests were performed using a potentiostat (PARSTAT 4000, Princeton Applied Research, NJ, USA) controlled by a computer for data acquisition using specific software (VersaStudio, PAR, USA). A glass corrosion cell, which was filled with Ringer's solution acidified with hydrochloric acid at pH = 3, was employed. The sample was mounted in a PTCFE sample holder so that the exposed surface was one circular side of the disc. A saturated calomel electrode (SCE) was used as the reference electrode, and a platinum coil as the counter electrode. The temperature of the electrochemical cell was 25 °C. Upon immersion, the samples were left unpolarized for 1 h to spontaneously attain their open circuit potential (OCP) in the electrolyte. Electrochemical impedance spectroscopy (EIS) measurements were carried out subsequently at the OCP with an AC amplitude of 10 mV, and a scan frequency ranging from 100 kHz to 1 mHz. Two electrochemical impedance spectra were determined at different times since the specimen was immersed in the modified Ringer's solution, namely 1 hour and 1 day. EIS data were analyzed in terms of equivalent circuits (EC) using *ZSimpWin 3.22* software [30]. After completing the EIS measurements, potentiodynamic polarization curves were recorded from -0.8 to +1.0 V vs. SCE using a scan rate of 0.5 mV s^{-1}. Electrochemical tests were repeated three times to verify the reproducibility of the results.

Scanning electrochemical microscopy (SECM) was performed using Sensolytics SECM (Bochum, Germany). A 10 µm diameter Pt microelectrode, Ag/AgCl/KCl (3M), and a Pt strip were used as working, reference and auxiliary electrodes, respectively. Ringer's solution, containing 0.5 mM ferrocene-methanol as redox mediator at the tip, was acidified with HCl just before starting the experiments. The distance between the tip and the substrate was fixed at 10 µm after measuring the *Z*-approach curves towards the surface. 3D images in constant height mode were obtained by scanning the tip in the *X-Y* plane at 25 µm s^{-1}, and recording the tip current as a function of tip location. An area of 250 µm x 250 µm was examined in each specimen.

4.4.4.3. Surface characterization

A scanning electron microscope (SEM) Quanta 200 (FEI, Hillsboro, OR, USA) operated at an accelerating voltage of 20 kV was employed to characterize any morphological changes produced to the specimens after anodic polarization treatment in acidified Ringer's solution at 25 ºC.

4.4.5. Results and discussion

Corrosion resistance of zirconium-titanium alloys is due to the formation of a protective passive layer [25]. The surface oxide layer acts as a dielectric barrier hindering metal release. The stronger is the passive layer, greater corrosion resistance is achieved. Impedance spectra of the three untreated ZrTi alloys in acidified Ringer's solution at the OCP are presented as Bode phase and Bode magnitude plots in Figure 4.4.1. They were measured either 1 hour (A) or 1 day (B) after exposure of the specimens to the simulated artificial solution. Two time constants were clearly found in all cases, one corresponding to the thin native oxide film, and the other to the charge transfer process at the surfaces of the alloys. Quantitative data to assist the interpretation of the EIS results can be obtained by using an electrical analogue representing the physicochemical processes occurring at the alloys.

Impedance parameters were then determined by adopting the equivalent circuit (EC) presented in Figure 4.4.2. The model consisted of two parallel constant phase elements/resistor pairs, Q_{dL}/R_{ct} and Q_{ox}/R_{ox}, corresponding to the time constants found in the low and the high frequency ranges, respectively. Good agreement between the measured spectra (discrete points) and the fitted spectra (solid lines) is observed in Figure 4.4.1, and Table 4.4.1 gives the values of the calculated impedance parameters. Comparison of the spectra measured for each material at the two exposures illustrates that the corrosion resistance of the materials slowly decrease with the elapsed time in the acidic Ringer's solution. Next, the impedance determined for the Zr45Ti alloy is higher than those of the Zr25Ti and Zr5Ti alloys.

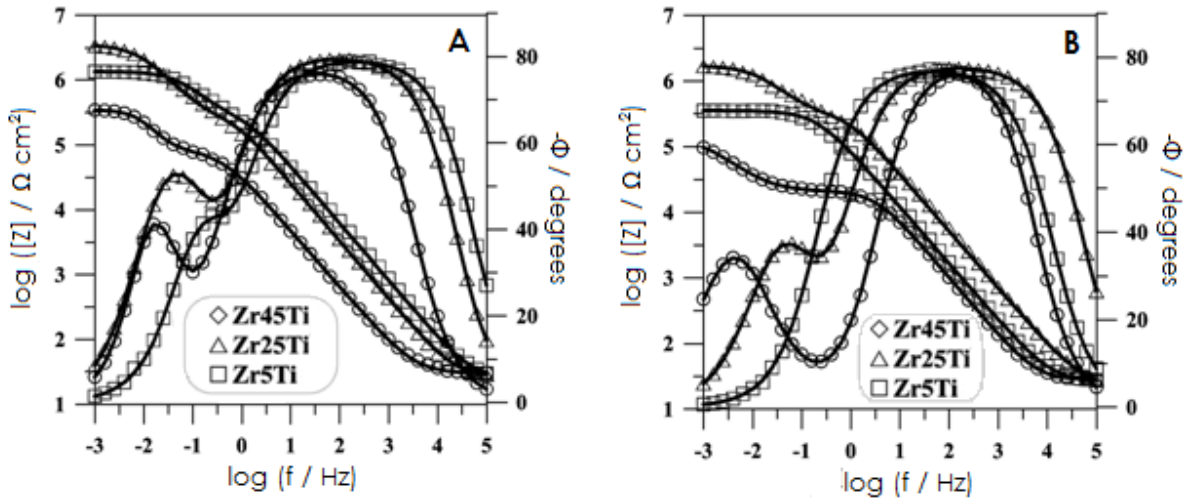

Figure 4.4.1. Measured (discrete points) and fitted (solid lines) impedance spectra for untreated ZrTi alloys recorded at their open circuit potentials during exposure to acidified Ringer's solution at 25 °C for: (A) 1 hour, and (B) 1 day.

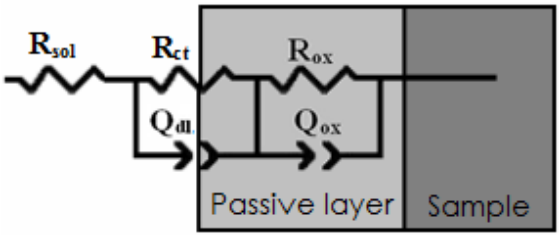

Figure 4.4.2. Equivalent circuit (EC) used for the interpretation of the impedance spectra.

Table 4.4.1. Impedance parameters of untreated ZrTi alloys immersed in acidified Ringer's solution according to the equivalent circuit given in Figure 4.4.2.

Sample	Immersion time / h	$10^5 Q_{dL}$ / S cm^{-2} s^n	n_{dL}	R_{ct} / kΩ cm^2	$10^6 Q_{ox}$ / S cm^{-2} s^n	n_{ox}	R_{ox} / MΩ cm^2
Zr5Ti	1	2.4	0.85	12.4	13	0.82	0.4
	24	2.5	0.84	8.3	15	0.81	0.1
Zr25Ti	1	2.4	0.85	14.6	10	0.83	1.4
	24	2.4	0.85	9.7	13	0.82	0.4
Zr45Ti	1	2.4	0.87	15.9	9	0.86	3.8
	24	2.4	0.86	11.5	10	0.84	1.4

Figure 4.4.3 shows the Bode plots from the thermally oxidized ZrTi alloys measured after 1 hour and 1 day exposure to acidified Ringer's solution. The two time constant model of the alloy/oxide/solution interface also held in this case, and good quality fits were obtained.

The values of the corresponding impedance parameters are listed in Table 4.4.2. Increase of the impedance modulus for the oxidized specimens compared to those untreated indicate an increase in corrosion resistance of the resulting oxide films. Meanwhile, the phase angle shifted to values ca. -90° in a wider frequency

range at both intermediate and low frequency ranges for oxidized Zr45Ti, which is an indication of more stable passive films. Indeed, the values of both R_{ct} and R_{ox} are bigger for oxidized Zr45Ti than for the untreated alloy, this increase being especially relevant in the case of R_{ox}, which is almost 10 times bigger.

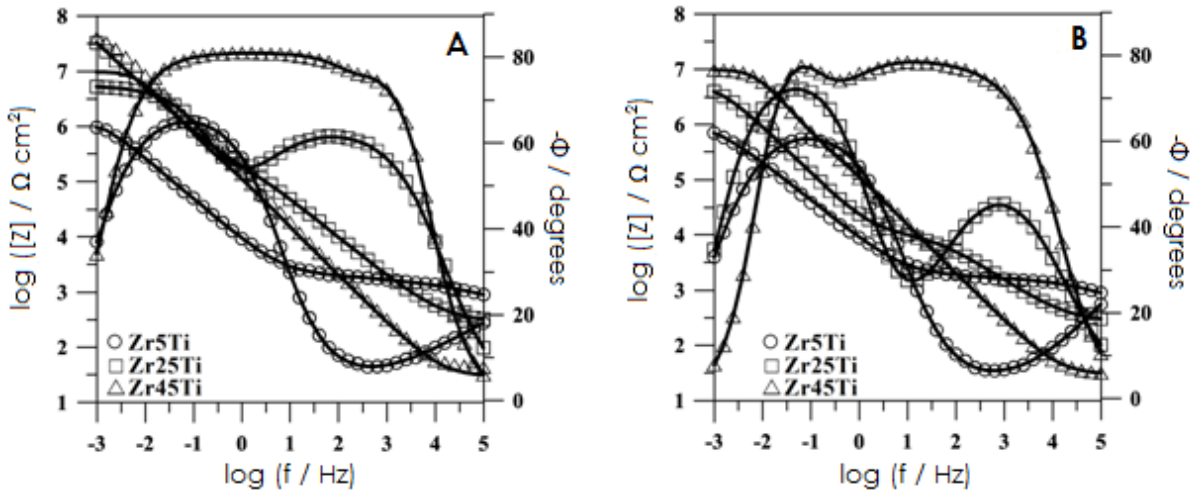

Figure 4.4.3. Measured (discrete points) and fitted (solid lines) impedance spectra for oxidized ZrTi alloys recorded at their open circuit potentials during exposure to acidified Ringer's solution at 25 °C for: (A) 1 hour, and (B) 1 day.

Table 4.4.2. Impedance parameters of oxidized ZrTi alloys immersed in acidified Ringer's solution according to the equivalent circuit given in Figure 4.4.2.

Sample	Immersion time / h	$10^5 Q_{dL}$ / S cm^{-2} s^n	n_{dL}	R_{ct} / kΩ cm^2	$10^6 Q_{ox}$ / S cm^{-2} s^n	n_{ox}	R_{ox} / MΩ cm^2
Zr5Ti	1	3.5	0.81	3.2	9.8	0.83	1.1
	24	3.6	0.80	1.8	10.3	0.80	0.7
Zr25Ti	1	3.3	0.82	8.6	7.8	0.85	19.3
	24	3.3	0.81	5.4	8.9	0.83	5.1
Zr45Ti	1	3.1	0.84	16.5	6.9	0.87	31.8
	24	3.2	0.82	12.1	8.5	0.86	10.3

Therefore, the improved corrosion resistance of the oxidized alloy arises mostly from the growth of the inner oxide layer directly attached to the underlying metal, and this was accompanied by a slightly less porous outer oxide layer leading to the obtainment of a sealed barrier to protect the metal.

The oxidation process also produces an improvement on the corrosion resistance of the other two alloys. Though the beneficial effect arises almost exclusively from the thin inner oxide layer in this case (i.e., higher values are only observed for R_{ox}), whereas a more porous outer layer is observed. Indeed, the Bode phase plots show a poor dielectric behaviour for these materials as indicated by the smaller phase angles occurring in the intermediate and low frequency ranges.

Therefore, they are expected to resist the aggressive attack of the simulated physiological solution for shorter exposures.

Polarization curves recorded for untreated and treated ZrTi alloys are presented in Figure 4.4.4. None of the specimens displayed an active region in the curves because of the passive oxide layer formed on their surface. The corrosion potential (E_{corr}) and corrosion current density (j_{corr}) values were determined by Tafel analysis from the anodic and cathodic branches of the polarization plots. Average values for these parameters are presented in Table 4.4.3. It must be noticed that untreated Zr5Ti and Zr25Ti exhibit dangerously low breakdown potentials in acidified Ringer's solution (cf. Figure 4.4.4A). This feature evidences that these materials are susceptible to the nucleation of localized corrosion. The addition of titanium to zirconium reduces the susceptibility of the later towards this form of corrosion, as indicated by the shift of the breakdown potentials to more positive values. This is in agreement with the report on the corrosion behaviour of ZrTi alloys in conventional Ringer's solution pH = 6.8, given in Section 4.3. However, the values encountered for j_{corr} and j_{pass} are higher in acidified Ringer's solution. Zr corrodes in acidic solutions and the area of oxide stability lies between pH 3.5 and 13 [31]. If passivation does not occur, Zr will react with the surrounding chemical species such as chloride and will be transformed into its ionic form [17].

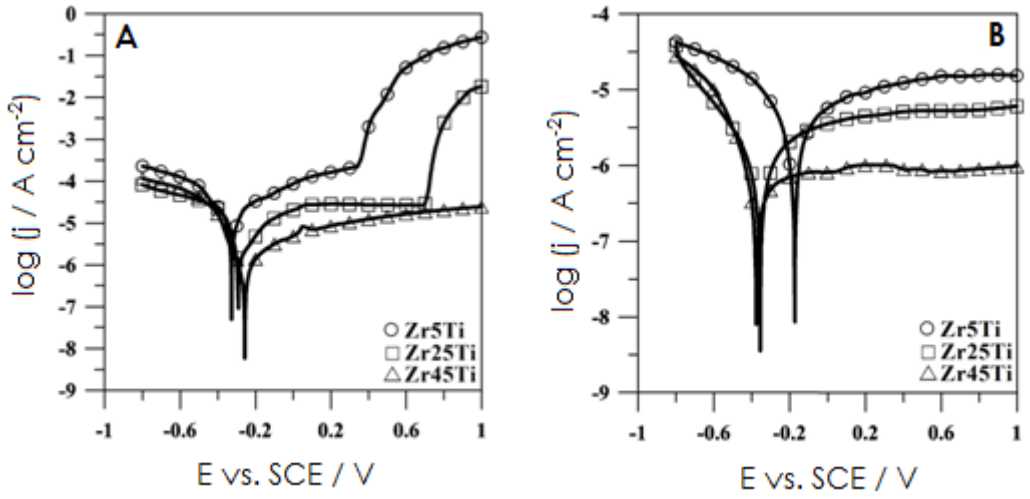

Figure 4.4.4. Potentiodynamic polarization curves for (A) untreated, and (B) oxidized ZrTi alloys immersed in acidified Ringer's solution at 25 °C. Scan rate: 0.5 mV s^{-1}.

The presence of chloride ions in acidic Ringer' solution (pH = 3) is detrimental to the protection properties of ZrO_2 surface film on Zr-based materials [17]. Figure 4.4.5 shows characteristic SEM micrographs of the untreated ZrTi samples retrieved from acidic Ringer's solution after anodic polarization tests that were terminated at +1.0 V vs. SCE. Inspection of the SEM images reveals the occurrence of localized corrosion at the surface of Zr5Ti and Zr25Ti alloys, whereas a rather uniform topography could be observed for the Zr45Ti alloy instead. Indeed, for the latter, the

only defects observable in the micrographs correspond to small scratches remaining from the prior polishing of the surfaces. These results confirm the observations derived from the electrochemical tests.

Table 4.4.3. Electrochemical parameters determined from the polarization curves measured for the untreated and the oxidized ZrTi samples immersed in acidified Ringer's solution.

Sample	E_{corr} / V vs. SCE	j_{corr} / μA cm^{-2}	j_{pass}^{*} / μA cm^{-2}
Untreated samples			
Zr5Ti	-0.256	14.5	200
Zr25Ti	-0.291	5.3	31.6
Zr45Ti	-0.325	1.4	10.0
Oxidized samples			
Zr5Ti	-0.172	2.4	11.0
Zr25Ti	-0.354	0.9	4.7
Zr45Ti	-0.376	0.4	1.0

*Measured at +0.30 V vs. SCE

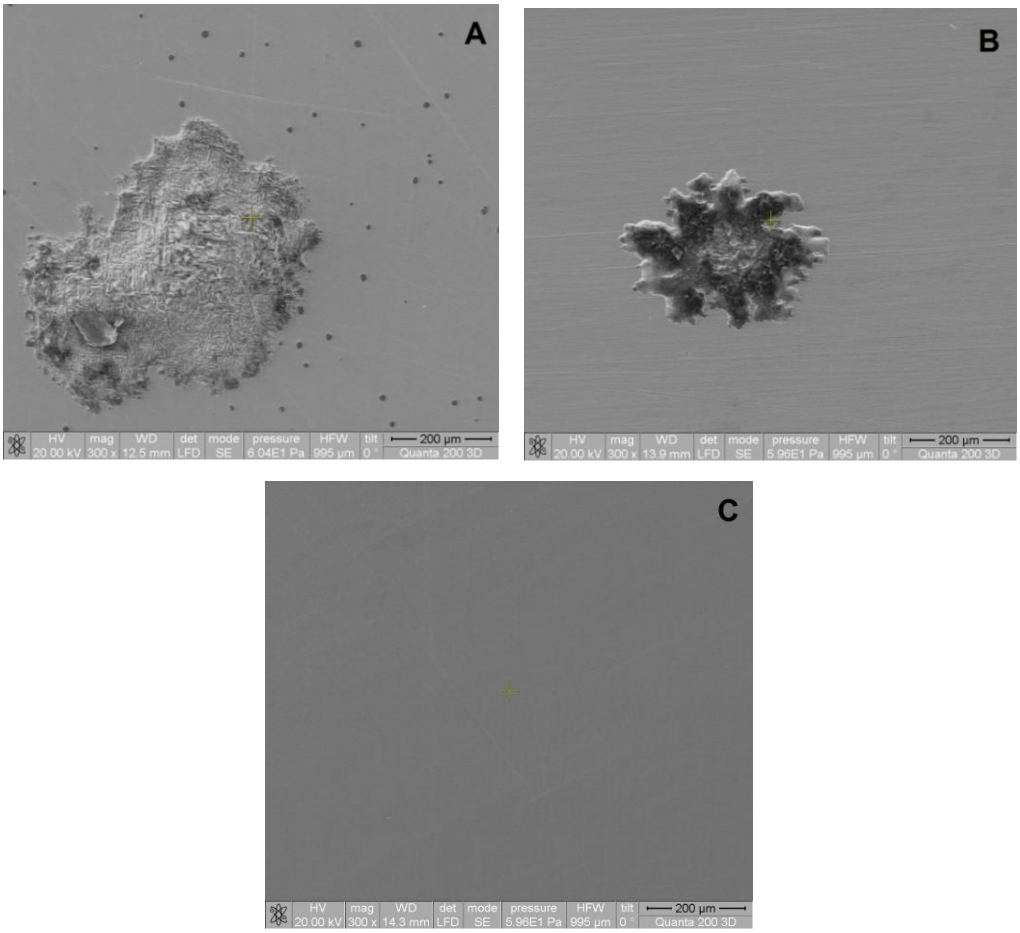

Figure 4.4.5. SEM images of the untreated ZrTi alloys retrieved at +1.0 V vs. SCE from acidified Ringer's solution at 25 °C surface after recording the corresponding potentiodynamic polarization curve given in Figure 4.4.4A. (A) Zr5Ti, (B) Zr25Ti, and (C) Zr45Ti alloys.

Potentiodynamic polarization curves were also measured for the oxidized ZrTi alloys, and they are displayed in Figure 4.4.4B. In comparison with the corresponding curves determined from the untreated ZrTi alloys, the oxidized ZrTi alloys exhibited smaller corrosion currents, confirming the improved corrosion resistance of the treated alloys. Addition of titanium is observed to significantly contribute to a decrease in both the corrosion and the passivation currents (cf. Table 4.4.3). The SEM micrographs of the retrieved oxidized samples show the formation of cracks on the surface in the case of Zr5Ti and Zr25Ti alloys (see Figures 4.4.6A and B), whereas a uniform surface is offered by the Zr45Ti (Figure 4.4.6C).

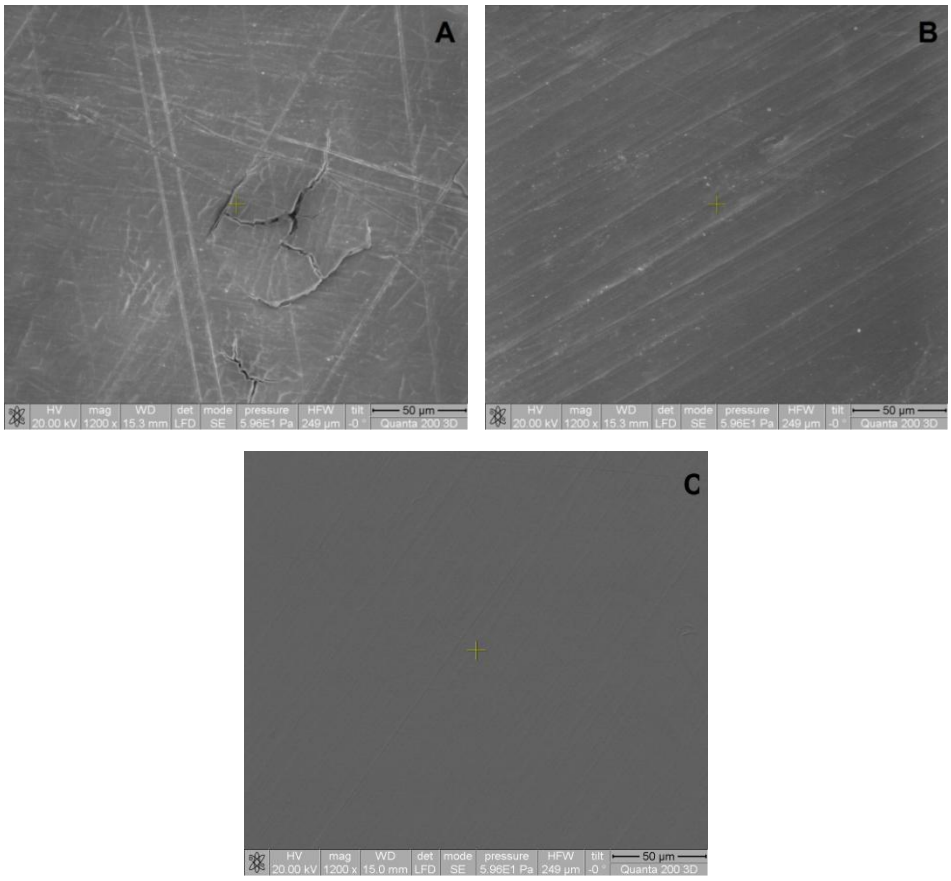

Figure 4.4.6. SEM images of the oxidized ZrTi alloys retrieved at +1.0 V vs. SCE from acidified Ringer's solution at 25 °C surface after recording the corresponding potentiodynamic polarization curve given in Figure 4B. (A) Zr5Ti, (B) Zr25Ti, and (C) Zr45Ti alloys.

The above discussed findings reflect the resistance towards passivity breakdown exhibited by the oxidized ZrTi samples in the acidified Ringer's solution. Surface characterization of these materials is then expected to inform only about the topography of the substrates, following the arguments stated in Section 4.3 of this Thesis. However, there is a greater chance to observe eventual localized surface activation over the insulating oxide layers in this acidified medium than in the previously used neutral Ringer's solution. In order to explore the insulating characteristics of these oxide films formed on the ZrTi alloys and their stability, scanning electrochemical microscopy (SECM) operated in the feedback mode was

employed. Ferrocene-methanol was used as redox mediator through its oxidation to ferrocinium ion at the Pt microelectrode tip under diffusion-limited conditions by applying a potential value of +0.48 V vs. SCE. Negative feedback behaviour should be expected if the oxide layers formed on the substrate would behave as barrier to electron transfer reactions, either ferrocene-methanol regeneration or metal dissolution from the metal substrate. This effect is better illustrated by recording the Z-approach curves by progressively moving the tip towards the surface with the positioning motors of the SECM, while recording the faradaic current at the tip. The specimens were left unbiased in the acidified Ringer's solution. For the sake of normalization, the dimensionless tip current, i / i_{lim}, was employed throughout. Normalized tip-substrate distances were obtained by dividing the absolute distance, d, by the diameter of the active Pt area of the tip microelectrode, a.

By approaching the substrate with the SECM tip, a progressively smaller volume of electrolyte is comprised in the volume gap between them. For the faradaic reaction to be maintained at the Pt tip, diffusion of the redox mediator from the electrolyte must occur. Due to increased hindrance to transport in the reduced amount of electrolyte available, the measured faradaic current must decrease steadily as the tip approaches an insulating surface. But the Z-approach curves illustrated in Figure 4.4.7A measured for the untreated ZrTi alloys first exhibit an increase of the measured current as the tip moved into the near-field range of the technique (i.e., normalized currents greater than one were measured). After describing a current maximum for normalized distances around 2-3, the current decreases and eventually negative feedback is observed for the smallest tip-sample distances. The findings observed in the Z-approach curves measured at OCP of the alloys indicate that the oxide films show partial insulating characteristics as some regeneration of the redox mediator occurs at their surface, an effect already described for Ti-Mo and Ti-Ta alloys [32]. More insulating are the oxide layers formed on the alloys after thermal oxidation as illustrated by the corresponding Z-approach curves displayed in Figure 4.4.7B.

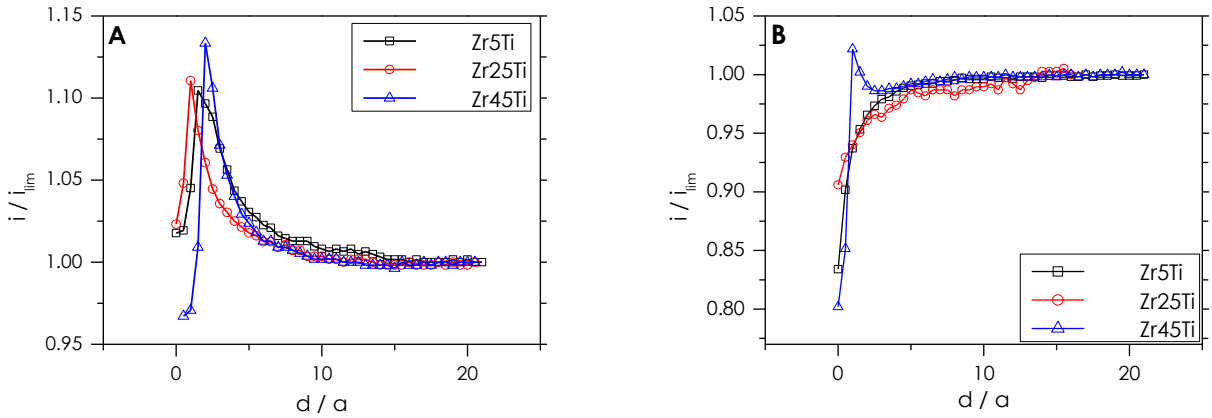

Figure 4.4.7. Z-approach curves recorded by moving the SECM tip towards the surface of ZrTi alloys immersed in acidified Ringer's solution containing 0.5 mM ferrocene-methanol. i / i_{lim} is the dimensionless tip current and d / a is the dimensionless tip-substrate distance. Tip potential: +0.48 V vs. SCE; scan rate: 10 μm s^{-1}; (A) untreated, and (B) oxidized TiZr alloys of the compositions given in the graphs. Samples were left unbiased at their corresponding OCP.

The electrochemical activity of the oxide layers was further investigated by imaging a random surface of 250 µm x 250 µm on the specimens. Figure 4.4.8 shows 3D images taken from the untreated samples immersed in acidified Ringer's solution. Weak positive feedback (e.g. electrochemical activity) was observed in regions of the Zr5Ti surface, as well as on the majority of the scanned surface in the case of Zr25Ti. Conversely, all the Zr45Ti remained electrochemically inactive as characterized by normalized currents smaller than 1. The images do not show any topographic heterogeneities on the surface of the materials, and the observed variations in the measured currents can be ascribed to small unavoidable tilt of the samples.

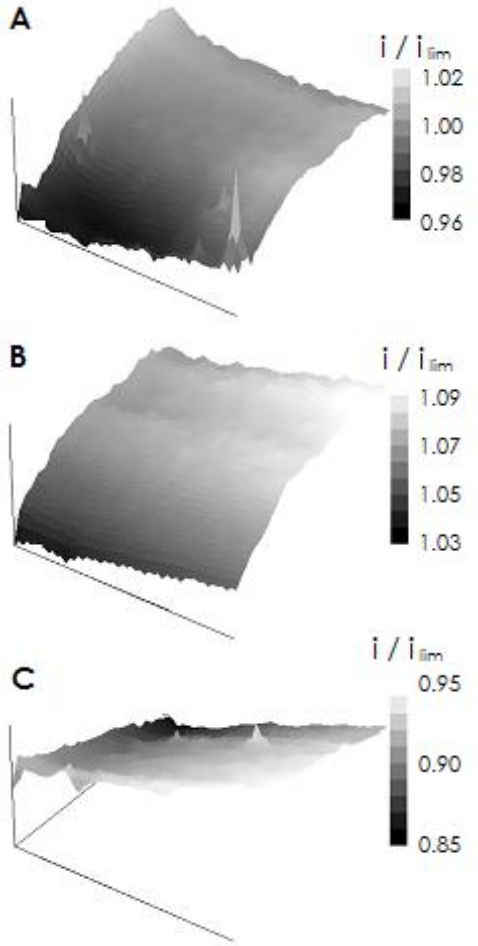

Figure 4.4.8. SECM images of untreated ZrTi alloys immersed in acidified Ringer's solution containing 0.5 mM ferrocene-methanol. The Z scale is the dimensionless tip current. Tip potential: +0.48 V vs. SCE; scan rate: 30 µm s^{-1}; (A) Zr5Ti, (B) Zr25Ti, and (C) Zr45Ti. Images represent an area of 250 µm x 250 µm. Samples were left unbiased at their corresponding OCP.

SECM images of the oxidized samples are given in Figure 4.4.9. Negative feedback behaviour was observed in all the cases, corresponding to electrically insulating surfaces, in good agreement with the observations from the Z-approach curves. Therefore, more compact and electrically insulating oxide films were produced on ZrTi alloys by thermal oxidation treatment in air.

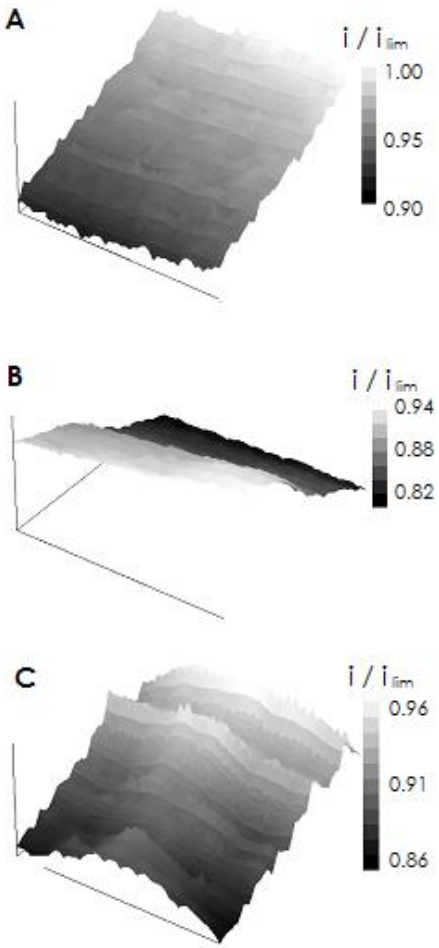

Figure 4.4.9. SECM images of oxidized ZrTi alloys immersed in acidified Ringer's solution containing 0.5 mM ferrocene-methanol. The Z scale is the dimensionless tip current. Tip potential: +0.48 V vs. SCE; scan rate: 25 μm s^{-1}; (A) Zr5Ti, (B) Zr25Ti, and (C) Zr45Ti. Images represent an area of 250 μm x 250 μm. Samples were left unbiased at their corresponding OCP.

4.4.6. Conclusions

The electrochemical behaviour of ZrTi alloys has been characterized in acidified Ringer's solution at pH = 3 in order to investigate their potential use as biomaterials. The development of passivity for all the ZrTi alloys was characterized from potentiodynamic polarization and EIS measurements. Electrochemical data show that the oxidized ZrTi alloys have better corrosion resistance than the untreated ZrTi alloys due to the formation of thicker inner oxide layers that act as dielectric barriers towards further electrodissolution of the underlying metals. Addition of titanium to zirconium assist the formation of more compact oxide layers, and at sufficiently high titanium contents (namely 45 at%), the onset of localized pitting corrosion is suppressed.

4.4.7. References

1. B. Kasemo. Surface Science 500 (2002) 656.
2. M.P. Staiger, A.M. Pietak, J. Huadmei, G. Dias. Biomaterials 27 (2006) 1728.
3. M. Geetha, A.K. Singh, R. Asokamani, A.K. Gogia. Progress in Materials Science 54 (2009) 397.
4. R. Bosco, J. van den Deuken, S. Leeuwenburgh, J. Jansen. Coatings 2 (2012) 95.
5. R.M. Urban, J.J. Jacobs, M.G. Tomlinson, J. Gavrilovic, J. Black, M. Peoc'h. The Journal of Bone and Joint Surgery A 82 (2000) 457.
6. I. Milošev, V. Antolič, A. Minovič, A. Cör, S. Herman, V. Pavlovčič, P. Campbell. The Journal of Bone and Joint Surgery B 82 (2000) 352.
7. N.J. Hallab, S. Anderson, M. Caicedo, A. Brasherm, K. Mikecz, J.J. Jacobs. Journal of Biomedical Materials Research A 74 (2005) 124.
8. H. Mutlu, E. Oktay. Materials Science and Engineering: C 33 (2013) 1125.
9. G.T. Burstein, C. Liu, R.M. Souto, S.P. Vines. Corrosion Engineering, Science and Technology 39 (2004) 25.
10. G.T. Burstein, C. Liu C, R.M. Souto. Electrochimica Acta 40 (1995) 1881.
11. R.M. Souto, G.T. Burstein. Journal of Materials Science: Materials in Medicine 7 (1996) 337.
12. G.T. Burstein, C. Liu, R.M. Souto. Biomaterials 26 (2005) 245.
13. M. Geetha, U.M. Kamachi, A.K. Gogia, R. Asokamani, R. Baldev. Corrosion Science 46 (2004) 877.
14. D.A. López, L. Durán, S.M. Cere. Journal of Materials Science: Materials in Medicine 19 (2008) 2137.
15. R.J. Solar. In: Corrosion and Degradation of Implant Materials (Edited by B.C. Syrett, A. Acharya). American Society for Testing and Materials, Philadelphia, 1979, p. 259.
16. P.I. Marshall, G.T. Burstein. Corrosion Science 23 (1983) 1219.
17. C.T. Kwok, P.K. Wong, H.C. Man, F.T. Cheng. Journal of Nuclear Materials 394 (2009) 52.
18. Y. Okazaki, E. Gotoh. Biomaterials 26 (2005) 11.
19. F.X. Xie, X.B. He, S.L. Cao, X. Lu, X.H. Qu. Corrosion Science 67 (2013) 217.
20. ASM Handbook: Corrosion, Vol. 13, 9th edn. ASM International, Metals Park, 1987, p. 725.
21. P. Kovacs, J.A. Davidson. In: Medical Applications of Titanium and its Alloys: The Materials and Biological Issues (Edited by S.A. Brown, J.E. Lemons). ASTM, West Conshohocken, 1996, p. 163.
22. Y.F. Zheng, D. Liu, X.L. Liu, L. Li. Applied Surface Science 255 (2008) 512.
23. Y. Ikarashi, K. Toyoda, E. Kobayashi, H. Doi, T. Yoneyama, H. Hamanaka, T. Tsuchiya. Materials Transactions 46 (2005) 2260.
24. H.M. Grandin, S. Berner, M. Dard. Materials 5 (2012) 1348.
25. G. Bolat, J. Izquierdo, J.J Santana, D. Mareci, R.M. Souto. Electrochimica Acta 88 (2013) 447.

26. E.A. Ferreira, N.T.C. Oliveira, S.R. Biaggio, P.A.P. Nascente, R.C. Rocha-Filho, N. Bocchi. Surface and Interface Analysis 38 (2006) 417.
27. E.A. Ferreira, R.C. Rocha-Filho, S.R. S.R. Biaggio, N. Bocchi. Corrosion Science 52 (2010) 4058.
28. I. Vaquila, L.I. Vergara, M.C.G. Passeggi Jr, R.A. Vidal, J. Ferrón. Surface and Coatings Technology 122 (1999) 67.
29. C. Delgado-Alvarado, P.A. Sundaram. Acta Biomateriala 2 (2006) 701.
30. B. Yeum. Electrochemical Impedance Spectroscopy: Data Analysis Software. Echem Software, 2001.
31. D.A. Jones. In: Principles and Prevention of Corrosion, 2nd edn. Prentice-Hall, Upper Saddle River, 1996, p. 62.
32. G. Ciurescu, J. Izquierdo, J.J Santana, D. Mareci, D. Sutiman, S. González, R.M. Souto. International Journal of Electrochemical Science 7 (2012) 7404.

4.5

Investigation of the electrochemical behaviour of TiMo alloys in simulated physiological solutions

4.5.1. Abstract

This paper addresses on the electrochemical behaviour of three TiMo alloys exposed to simulated physiological environments. Their stability and corrosion resistance was characterized in order to explore the potential application for the manufacturing of implant materials. Ringer's solution together with an acidic modification of the Ringer's solution (pH = 3.1) at room temperature were considered. Both electrochemical methods (namely, potentiodynamic polarization curves and electrochemical impedance spectroscopy, EIS), and spatially-resolved scanning electrochemical microscopy (SECM), were used. Additionally, surface characterization was made employing optical microscopy and scanning electron microscopy (SEM). The oxide films formed on the TiMo alloys in neutral and acidic Ringer's solutions effectively protect the metal from dissolution in these environments, and no breakdown of the passive layer occurs in the potential range up to +1.00 V vs. SCE. SEM micrographs of retrieved samples do not show corrosion pits, cracks, or any other defects despite the rather high positive potential values reached during the potential excursion. EIS data reveal that two-layer oxide films are formed, consisting of a porous outer layer and a compact inner layer (approximately 5-6 nm thick), the latter accounting almost completely for the corrosion resistance of the materials. The corrosion resistance of the inner compact film towards metal dissolution is smaller in the acidic environment, whereas it increases with higher Mo contents in the alloy. The passive oxide films exhibit dielectric characteristics towards charge transfer when they are imaged by scanning electrochemical microscopy.

4.5.2. Resumen

SE ha evaluado el comportamiento electroquímico de tres aleaciones TiMo expuestas a entornos fisiológicos simulados. Se ha caracterizado la estabilidad y resistencia a la corrosión de estas aleaciones para su la aplicación potencial en la fabricación de implantes. Para ello se ha considerado disolución Ringer más una versión acidificada de la misma (pH = 3.1). Se han empleado dos métodos electroquímicos (curvas de polarización potenciodinámicas y espectroscopía de impedancia electroquímica, EIS), además de la microscopía electroquímica de barrido (SECM) como técnica con resolución espacial. Además, se ha realizado la caracterización de las superficies empleando microscopía óptica y microscopía electrónica de barrido (SEM). Las películas de óxidos formadas en las aleaciones de TiMo en disoluciones Ringer neutra y ácida protegen de forma efectiva el metal de su disolución en estos ambientes, no produciéndose rotura de la capa pasiva incluso a potenciales de +1.00 V respecto al SCE. Las micrografías SEM de las muestras analizadas tras su medición no revelan la formación de picaduras, fracturas u otros defectos a pesar del relativamente alto valor de potencial alcanzado durante el barrido anódico. Los datos de EIS revelan que se forma una doble película de óxidos, consistente en una capa externa y una capa interna (de aproximadamente 5-6 nm), siendo esta última la que influye casi por completo en la resistencia a la corrosión del material. Dicha resistencia a la corrosión de la capa interna es menor en el medio ácido, incrementándose con el mayor contenido de Mo en la aleación. La película de óxidos pasivos muestra características dieléctricas con respecto a la transferencia de carga cuando se visualiza por microscopía electroquímica de barrido.

4.5.3. Introduction

Titanium-based materials pose a combination of properties that make them adequate for biomedical structural application as orthopaedic and dental implants [1-5]. The low elastic modulus, high strength, and the affinity and reactivity in contact with oxygen or aqueous solutions, which lead to form a compact and strong adherent oxide layer on their surface, all of these result in a good biological and mechanical compatibility. Although titanium-based materials are among the most corrosion-resistant materials in human body fluids, and they have been extensively employed in implantology, there still remains some concern in the scientific literature regarding their use because of the observation of corrosion processes in retrieved prosthesis, as well as reports on the occurrence of metallosis [6]. Metal ion release into peri-prosthetic tissues has been found from bone fixation implants [7], and in serum in ionic states [8] and bound to proteins [9]. More interestingly, distributed metal has been recently found in inflamed tissues adjacent to commercially pure titanium skin-penetrating devices despite the absence of wear or loads [10]. In the latter, release of titanium into the body could only be attributed to either micro-motion [10] or localized corrosion [11,12]. To diminish the impact of these limitations, a main research trend is the development of β-type (body-centered cubic) titanium alloys with biomechanical compatibility, low modulus and biochemical compatibility due to their greater corrosion resistance [13,14]. The stability of the β-phase in the case of titanium alloys is expressed as the sum of the weighted averages of the alloying elements in wt.% known as the Mo equivalent [15,16]. A value of Mo equivalent in the range 8-24 wt.% relates to β-metastable titanium alloys because the contents of β-stabilizers is high enough to prevent any martensitic transformation in the β phase from quenching to room temperature [15,16].

Molybdenum is used as alloying element for titanium because it has good thermodynamic stability [17,18]. Molybdenum is considered to be instrumental in regulating the pH balance in the body, and acts as a cofactor for a certain number of enzymes in humans [19,20]. The biocompatibility and corrosion resistance of TiMo alloys has already been described in the scientific literature [21-23]. It is considered that the addition of Mo to pure Ti, up to 15 wt.% content, improves the protection characteristics of the oxide films spontaneously formed on the materials oxides. Therefore, the Ti15Mo (% wt.) alloy has been recently approved for the manufacture of devices for implantation in humans, with composition allowances fixed under norm ASTM F 2066 [24]. Nevertheless, it was recently observed that Ti20Mo alloy possess better corrosion resistance than commercially pure Ti when exposed to artificial saliva [25]. Therefore, it was thought that Mo contents greater than 15 %wt. might lead to the production of TiMo alloys with even better corrosion resistance for implant application.

The present communication concerns a report on *in vitro* electrochemical characterizations of three TiMo alloys exposed to simulated physiological environments as to investigate their chemical activity and corrosion resistance. Two

alloys with Mo contents just below and above the composition given by the ASTM F 2066 norm were considered (namely Ti12Mo and Ti20Mo), in order to investigate the eventual occurrence of a deleterious effect on the corrosion resistance of the materials due to the higher Mo content. Additionally, a TiMo alloy with significantly higher Mo addition (Ti40Mo) was also explored. The work was carried out using Ringer's solution together with an acidic modification of the Ringer's solution (pH = 3.1) at room temperature. Both conventional and localized electrochemical techniques have been employed, including DC potentiodynamic polarization methods (PPM), electrochemical impedance spectroscopy (EIS), and scanning electrochemical microscopy (SECM).

4.5.4. Materials and methods

4.5.4.1. Materials

Experiments were carried out on three TiMo alloys with different composition (12, 20 and 40 wt.% of Mo) that have been synthesized by cold crucible levitation melting in an induction furnace (Fives Celes, Lautenbach, France), following the procedure described before [26]. The samples in the form of rods were cut into disks of 0.28 cm^2 circular area. They were ground with SiC abrasive paper up to 2000 grit, followed by a final polishing stage using 1 µm alumina suspension. In the case of the specimens investigated using scanning electrochemical microscopy, an additional polishing stage using 0.3 µm alumina suspension was employed to diminish the surface roughness in order to image the samples at a shorter distance for greater spatial resolution. The polished samples were degreased with ethyl alcohol, ultrasonically cleaned in deionized water, and finally dried under air stream.

Specimens were embedded in a polytetrafluoroethylene (PTFE) holder specifically designed to facilitate connection to a rotating disc electrode holder (model EDI 101T, Radiometer Analytical, Lyon, France). A polymeric resin was used to ensure a tight seal between the specimen and the PTFE holder, in order to avoid the occurrence of crevice corrosion [27]. The exposed surface of the materials to the test environments were discs of 0.28 cm^2 area.

4.5.4.2. Electrochemical measurements

The tests were conducted in two artificial physiological solutions based on the Ringer's solution. All components were of analytical grade, and Milli-Q deionised water. Ringer's solution was made from: 8.6 g/L NaCl, 0.3 g/L KCl, and 0.48 g/L $CaCl_2$. The pH of Ringer's solution was 6.9 in the naturally aerated solution. An acidified version of Ringer's solutions was also made by adding HCl to bring the pH down to 3.1. This addition caused only a minor change in the concentrations of the other components. The acid pH was chosen because the tissue adjacent to an implant

under distress is considered to become acidic [28]. Measurements were performed at room temperature (22 ± 3 ºC).

Conventional electrochemical measurements on the TiMo alloys were conducted employing a three-electrode configuration. The specimens were taken as the working electrode. They were placed in a glass corrosion cell, which was filled with the artificial physiological solution. A saturated calomel electrode (SCE) was used as the reference electrode, and a platinum coil as the counter electrode. Electrochemical techniques were performed using a PARSTAT 4000 potentiostat supplied by Princeton Applied Research (PAR, Princeton, NJ, USA). The instrument was controlled by a personal computer and specific software (*VersaStudio*, PAR, USA). The samples were immersed into the artificial physiological solution for an hour in order to attain their spontaneous open circuit potential values (OCP). Electrochemical impedance spectra (EIS) were carried out in the frequency range of 100 kHz down to 1 mHz by applying an alternating sinusoidal potential with an amplitude of 10 mV. EIS spectra were first recorded at their open circuit potential values, and subsequently the potential of the sample was set at +0.40 V vs. SCE for 30 min before recording the EIS data of the polarized sample. This potential value was chosen to be more positive than any reported in the human body for Ti implants [29]. The EIS experimental data were fitted and analyzed in terms of equivalent circuits (EC) using a non-linear least squares fit method (*ZSimpWin 2.00* software [30]) to obtain the relevant impedance parameters. Potentiodynamic measurements were also carried out on freshly polished samples. These measurements were conducted by stepping the potential from -0.80 to +1.00 V vs. SCE using a scanning rate of 0.5 mV s^{-1}. Before recording the potentiodynamic polarization curves, the TiMo samples were left unpolarized into the test solution for 1 hour. The electrochemical tests were made in triplicate.

A SECM equipment supplied by Sensolytics (Bochum, Germany), was employed for spatially-resolved characterization of the electrochemical reactivity of the TiMo alloys. The instrument was built around a PalmSens (Utrecht, The Netherlands) electrochemical interface, all controlled with a personal computer. The alloy specimens were either tested at their open circuit potentials in the test solutions, or polarized using the bipotentiostat in the electrochemical interface. The specimens were mounted horizontally facing upwards at the bottom of a cell made of polytetrafluoroethene, which was equipped with an Ag/AgCl/KCl (3M) reference electrode and a platinum counter electrode. For the sake of consistency, potentials in this Section are expressed in relation to the standard calomel electrode by taking in account the potential difference between the two reference electrodes. The electrochemical cell was located inside a Faraday cage. Tip microelectrodes were made from 10 µm dia. platinum wires sealed in glass. 0.5 mM ferrocene-methanol was added to the artificial physiological solution to act as electrochemical mediator at the tip. The tip was kept at a constant potential of +0.46 V vs. SCE to ensure the diffusion-limited oxidation of ferrocene-methanol [31]. The establishment of the operating tip distance over the sample was performed by slowly approaching the surface of the TiMo alloy sample with the tip, and simultaneously recording the

measured current at the microelectrode vs. *Z* displacement, until the measured current was equal to 30% of the steady-state value in the bulk of the electrolyte. Subsequently, the tip was withdrawn 10 μm from the sample surface, and SECM images were obtained with a scan rate of 30 μm s^{-1} by scanning the tip at constant height over an arbitrary area of 250 μm x 250 μm of the exposed alloy. For the sake of normalization, SECM data are represented as dimensionless tip currents, i / i_{lim}, where (i) is the feedback current measured at the tip while scanning the substrate, and i_{lim} is the limiting current determined when the tip is far from the surface. Values greater than unity occur when the redox mediator is regenerated on the electrochemically-active substrate (positive feedback behaviour), whereas an insulating substrate hinders the diffusion the redox species leading to values smaller than one (negative feedback behaviour). SECM imaging was first performed while the samples were still at their corresponding OCP. Next, imaging was performed on the polarized samples, starting from -0.54 V vs. SCE, and subsequently at increasingly more positive potentials.

4.5.4.3. Surface analysis

The structural characterization of the as-received TiMo alloys was performed by optical microscopy. An inverted metallographic microscope (XJP-6A, Chongqing Optical & Electrical Instrument Co., Chongqing, China) controlled using dedicated software (*Materials Plus*). The samples were mechanically polished to a final level of 0.02 μm alumina suspension and subsequently etched in a solution of water, hydrofluoric acid, and nitric acid [32].

Scanning electron microscopy (SEM, Quanta 3D Model AL99/D8229, FEI, Hillsboro, OR, USA), operating with beam energy 20 kV, was employed to characterize the topography of samples retrieved from the test solutions after the electrochemical experiments were completed.

4.5.5. Results and discussion

4.5.5.1. Microstructure

The microstructures of Ti12Mo, Ti20Mo and Ti40Mo alloys are shown in Figure 4.5.1. They mainly consist of an acicular microstructure with small non oriented grains, which is more noticeable the higher the molybdenum content in the alloy. The increase of Mo content led to a different morphology of the primary β-phase dendrites. Preferential growth of primary β-phase dendrites with smaller sizes is observed with increasing Mo content in the alloys.

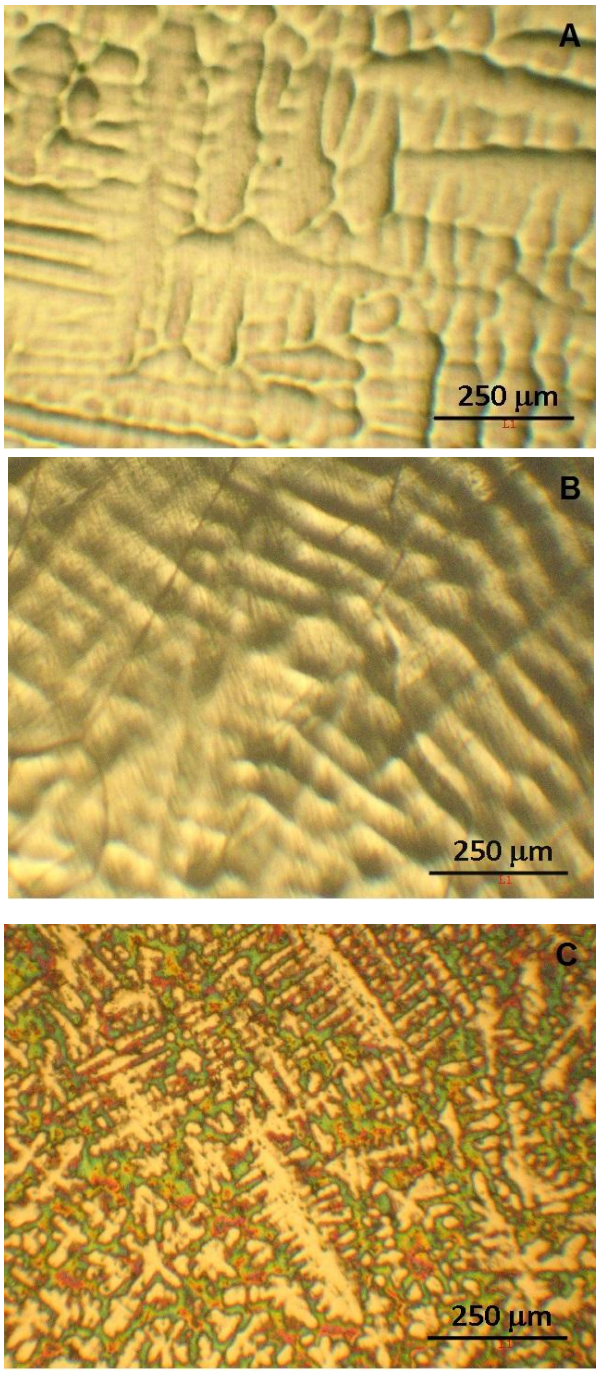

Figure 4.5.1. Optical micrographs of the TiMo alloys: (A) Ti12Mo, (B) Ti20Mo, and (C) Ti40Mo.

4.5.5.2. Potentiodynamic polarization and immersion

Open circuit potential (OCP) values of the three TiMo alloys in conventional and acidic Ringer's solutions after 1 hour immersion are listed in Table 4.5.1. It was found that Ti40Mo alloy exhibited the most positive values, while the Ti12Mo alloy showed the most negative ones. The more aggressive character of the acidic solution towards corrosive attack is evidenced by the shift of the open circuit potential values of the alloys in the negative direction. This feature evidences that the oxide films spontaneously developed on the samples are less protective against

corrosion when they were exposed to a lower pH. It is well known that the corrosion resistance of a given material depends on several factors such as composition, environment and microstructure [33]. Since the three TiMo alloys exhibit a common basic microstructure, the addition of Mo to Ti leads to the improvement of the protection characteristics of the passive oxide layers formed in the two environments.

Table 4.5.1. Open circuit potential values attained by the TiMo alloys immersed in the artificial physiological solutions at room temperature after 1 hour.

Alloy	OCP / V vs. SCE	
	Ringer´s solution	Acidified Ringer's solution
Ti12Mo	-0.221 ± 0.027	-0.305 ± 0.053
Ti20Mo	-0.148 ± 0.024	-0.281 ± 0.061
Ti40Mo	-0.104 ± 0.019	-0.252 ± 0.050

Figure 4.5.2 displays the potentiodynamic polarization curves of the TiMo alloys in the two artificial physiological solutions. Due to the common charge transfer control for the oxygen reduction reaction in the three materials, the cathodic branches of the polarization curves measured in Ringer's solution merged at ca. -0.80 V vs. SCE.

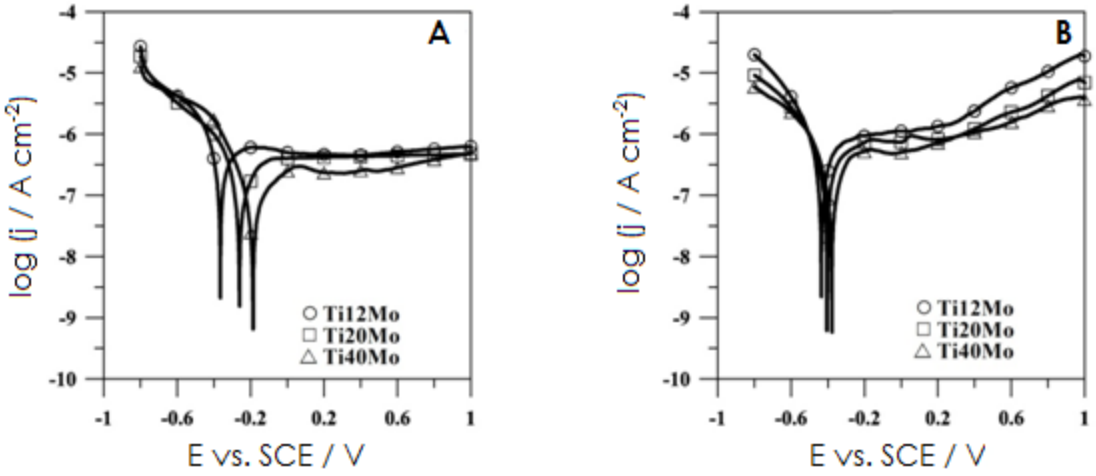

Figure 4.5.2. Potentiodynamic polarization curves of TiMo alloys in (A) Ringer's solution, and (B) acidified Ringer's solution at room temperature. v = 0.5 mV s^{-1}. Curves determined from individual samples.

Though slightly different rates for the same reduction reaction of hydrogen ions were observed when the alloys were exposed to the acidic solution, the cathodic branches of the corresponding polarization curves were found to be sufficiently close as to choose the potential value -0.80 V vs. SCE as the starting point for the potentiodynamic polarization experiments. On the other hand, the anodic limit potential (i.e., +1.00 V vs. SCE) was selected significantly higher than polarization

values ever measured in the human body [29]. The shape of the anodic branches revealed the onset of passivity for the alloys in both solutions, which is evidenced by the presence of an active-passive transition in all the curves at potentials more positive than their corresponding corrosion potential values (E_{corr}). Tafel analysis of both the anodic and cathodic branches of the polarization plots delivered values for E_{corr} and corrosion current densities (j_{corr}). Table 4.5.2 gives the average values determined for these parameters. In all cases the values determined for E_{corr} are more negative than the spontaneous open circuit potentials (cf. Table 4.5.1). This behaviour arises from the reduction of the oxide layer spontaneously formed on the surface of the alloys upon immersion in the solution that occurs during application of the cathodic polarization at -0.80 V vs. SCE. This oxide layer was evidenced by the shift of the open circuit potential of the samples towards more positive potentials upon immersion in the test solutions (cf. Figure 4.5.3). Yet, the variation in the E_{corr} values with alloy composition determined from polarization measurements agrees well with that exhibited by the open circuit potential (OCP) values in the two environments. According to Blackwood et al. [34], the shift to positive values shows an increase of the passive film thickness and correspondingly, a decrease of the corrosion rate. In Ringer´s solution, further excursion of the potential in the positive direction led to the measurement of a current density plateau extending up to the limiting anodic potential value. The oxide films formed on the TiMo alloys in Ringer's solution effectively protect the metal from dissolution in this environment, and no breakdown of the passive layer occurs in all the potential range under consideration. A somewhat different situation is found from inspection of the potentiodynamic polarization curves measured in the acidic Ringer's solution. In this case, the passive current densities increased with the excursion of potential for E > +0.20 V vs. SCE, which indicates that metal dissolution occurs through the oxide film in this more aggressive environment. Yet, no indications of localized breakdown of the passive film in the acidic solution are observed in these curves, which would have appeared as an abrupt increase of the current in the *log (j) - E* plots. Average passive current densities were determined for the alloys in the two solutions, and they are also given in Table 4.5.2.

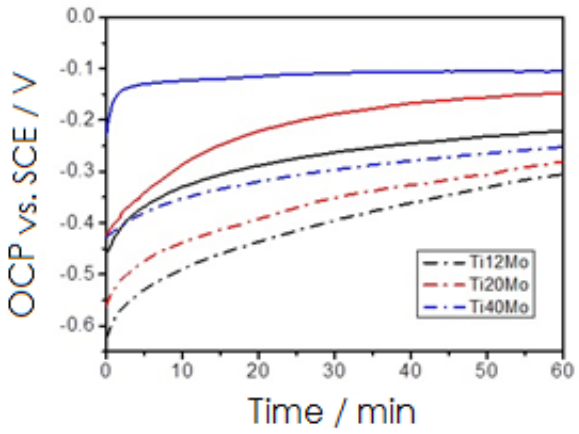

Figure 4.5.3. OCP as a function of time for TiMo alloys in (solid) Ringer's solution, and (dashed) acidified Ringer's solution at room temperature. Curves determined from individual samples.

Table 4.5.2. Electrochemical parameters determined from the potentiodynamic polarization curves measured for the TiMo alloys in aerated the artificial physiological solutions at room temperature.

Alloy	E_{corr} / V vs. SCE	j_{corr} / nA cm^{-2}	j_{pas}* / μA cm^{-2}
Ringer's solution (pH = 6.9)			
Ti12Mo	-0.365 ± 0.071	190 ± 16.7	0.600 ± 0.148
Ti20Mo	-0.260 ± 0.064	130 ± 12.5	0.500 ± 0.201
Ti40Mo	-0.185 ± 0.050	80 ± 16.5	0.300 ± 0.090
Acidified Ringer´s solution (pH = 3.1)			
Ti12Mo	-0.435 ± 0.060	250 ± 24.0	2.1 ± 0.180
Ti20Mo	-0.404 ± 0.092	160 ± 8.2	1.2 ± 0.130
Ti40Mo	-0.377 ± 0.076	110 ± 8.5	0.9 ± 0.127

*Values determined at +0.4 V vs. SCE

The stability of the oxide films formed on the TiMo alloys after potentiodynamic polarization up to +1.00 V vs. SCE was confirmed using scanning electron microscopy. Typical SEM micrographs of the retrieved TiMo specimens are shown in Figure 4.5.4. They revealed that uniform surfaces occurred on all TiMo alloys, and no signs of features other than the scratches due to polishing during preparation of the surfaces could be observed. That is, no corrosion pits, cracks, or any other defects were formed despite the rather high positive potential values reached during the potential excursion in the aggressive acidified Ringer's solution, thus supporting the observations from electrochemical experiments. Conversely, other titanium-based materials, such as nitinol [5,35] and TiZr alloys [36], experience pitting corrosion under these conditions.

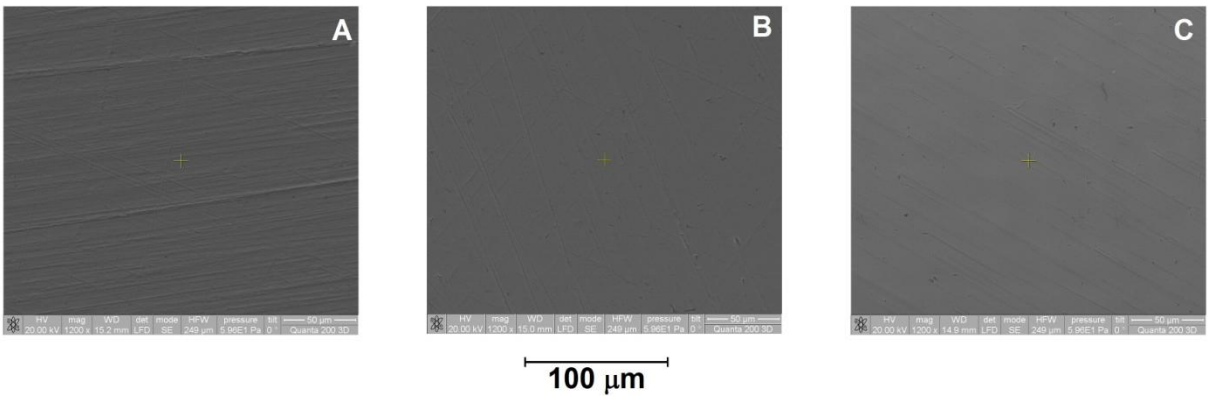

Figure 4.5.4. The morphologies of the surfaces of the TiMo alloys retrieved from acidified Ringer's solution after potentiodynamic polarization to +1.00 V vs. SCE. (A) Ti12Mo, (B) Ti20Mo, and (C) Ti40Mo.

4.5.5.3. Electrochemical impedance spectroscopy

Impedance spectra of Ti12Mo, Ti20Mo and Ti40Mo alloys in the two electrolytes at their OCP are presented as Nyquist, Bode-phase and Bode-magnitude plots in Figure 4.5.5. It is observed that these alloys present similar spectra

in conventional and acidic Ringer's solutions, and they correspond to systems exhibiting two time constants as revealed by the presence of two maxima in the Bode-phase diagrams. That is, they can be divided into two distinct frequency ranges: the time constant in the high-frequency part, which arises from the uncompensated ohmic resistance due to the electrolytic solution and the impedance characteristics resulting from the penetration of the electrolyte through a porous film, and the low-frequency part accounting for the processes taking place at the substrate/electrolyte interface. This agrees with the general understanding that passive films formed on most metals [37], including titanium and its alloys [38,39], consist of two layers, a thin compact oxide in direct contact with the base unoxidized metal, and the thicker and more porous outer layer that is in direct contact with the environment. The thicknesses of the two layers may be different and depend on the nature of the metal substrate and the environment. They typically amount a few nanometers in the case of the inner layer, whereas the outer layers may even extend over a few micrometers in some systems. High impedance values (in the order of 10^6 Ω cm^2) were determined in the low-frequency region, indicating high corrosion resistance at the substrate/electrolyte interface in both Ringer's solutions, typical of a compact inner oxide layer with barrier characteristics towards the passage of current through it.

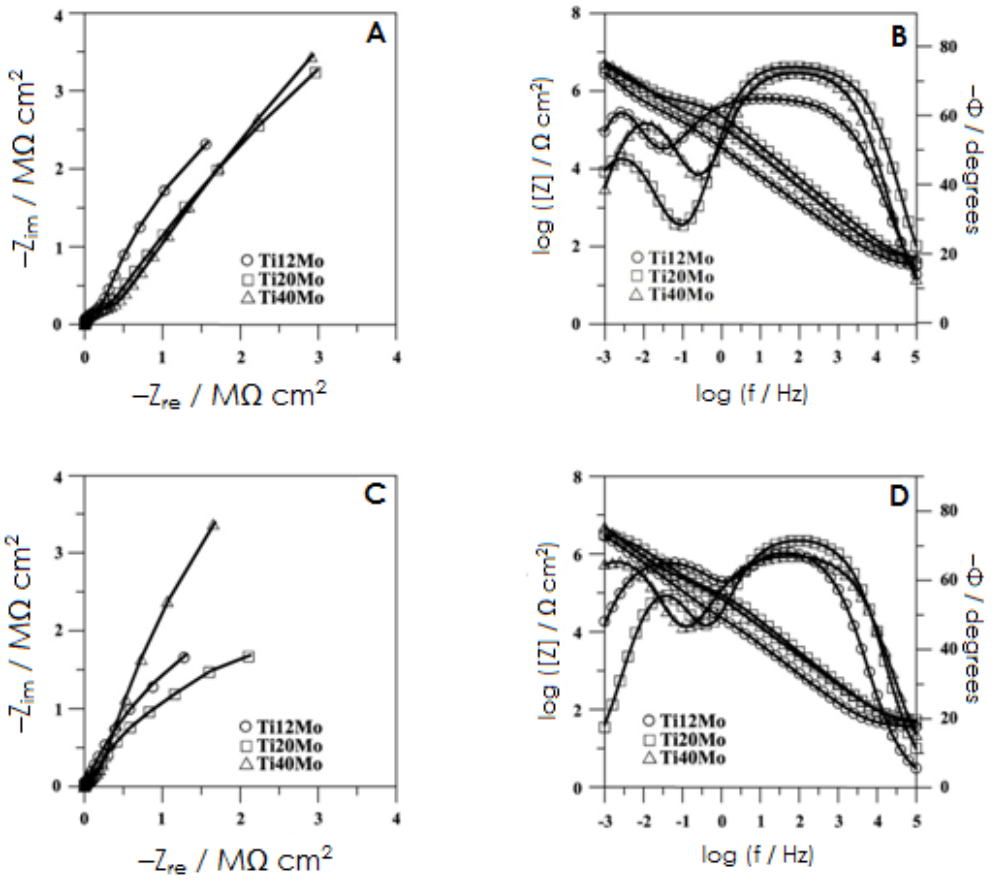

Figure 4.5.5. Measured (discrete points) and fitted (solid lines) impedance spectra for TiMo alloys at their corresponding OCP during exposure to: (A) Ringer's solution, and (B) acidified Ringer's solution at room temperature.

The presence of these two time constants can be described by means of an equivalent circuit (EC) with two RC components as shown in Figure 4.5.6. This has been proposed to give the electrical representation of two-layer surface films consisting of a barrier-type compact inner layer and a relatively porous outer layer formed on titanium [38,39] and titanium-rich alloys, such as Ti6Al4V [40-42], Ti6Al7Nb [41,43,44], Ti13Nb13Zr [41], and Ti29Nb13Ta4.6Zr [45]. It has also been found applicable to alloys with lower Ti contents including Ti35Nb [46], TiNbSn [47], TiNbHf [48] alloys, nitinol [49], and even to ZrTi alloys [36,50].

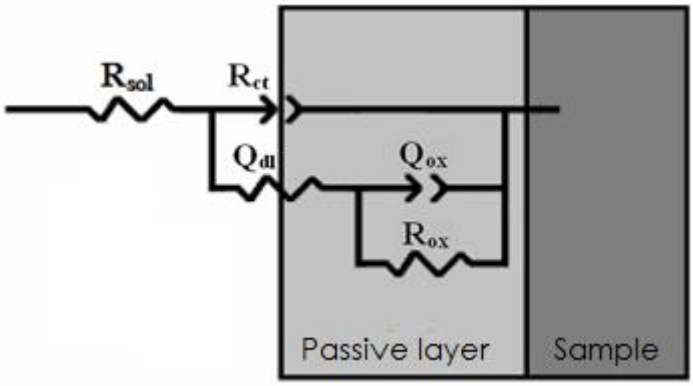

Figure 4.5.6. Equivalent circuit (EC) used to fit the impedance data.

The following elements are considered: a solution resistance R_{sol} of the test electrolyte, electrical leads, etc., the additional resistance R_{ct} of the solution inside the pores, the capacitance of the pore wall C_{dl}, and the resistance and the capacitance of the inner barrier layer (R_{ox}, C_{ox}). Constant phase elements (CPE, Q) were used in the EC instead of capacitors, allowing for the effects of deviations to ideality related to electrode roughness and heterogeneities of the surface films to be considered. In fact, the impedance of a CPE is defined as:

$$Z_{(CPE)} = \frac{1}{Y_0 (j\omega)^n} \qquad (4.5.1)$$

where ω is the angular frequency and Y_0 is a constant, and the value of the exponent n, ranging $-1 \leq n \leq 1$, indicates the deviation from ideal capacitive behaviour (e.g., when $n \approx 1$). The impedance results were obtained with the *ZSimpWin* software and the quality of the fits was evaluated by their Chi-squared values. A very good correlation was obtained between EIS data using the proposed equivalent circuit and the experimental impedance spectra, as it is evidenced by the solid lines corresponding to the fitted spectra passing through the measured data (discrete points) in Figure 4.5.5.

The values of fitted parameters of the EC are listed in Table 4.5.3. High values of R_{ox} (in the order of 10^6 Ω cm^2) are determined at their open circuit potential values for the three TiMo alloys in both simulated physiological solutions, confirming the formation of an inner compact layer with high corrosion protection ability for all the

systems. It can be observed that the variation in the values for R_{ox} with the nature of the alloy and the aggressiveness of the electrolyte closely matches both the trend and the magnitude of change in the values of j_{corr} determined from the polarization curves given in Table 4.5.2, thus supporting the consistency of the electrochemical data obtained using two different techniques.

From the fitted values of Table 4.5.3, some differences between the characteristics of the oxide films in both solutions are observed. In fact, the R_{ox} values determined for each alloy are smaller in the acidic electrolyte, thus indicating that the inner film is less protective in this environment. The opposite trend is shown by the impedance parameter related to the constant phase elements *ox* which can be related to the thickness of this inner layer.

Table 4.5.3. Parameters of the equivalent circuit for TiMo alloys in Ringer's solution and acidified Ringer's solution at room temperature. AC polarization was applied around their corresponding open circuit potential values in the electrolytes.

Alloy	$10^5\ Q_{dL}$ / S cm^{-2} s^n	n_{dL}	R_{ct} / kΩ cm^2	$10^6\ Q_{ox}$ / S cm^{-2} s^n	n_{ox}	R_{ox} / MΩ cm^2
Ringer's solution (pH = 6.9)						
Ti12Mo	2.1	0.86	26	8.8	0.83	2.9
Ti20Mo	1.9	0.87	29	7.4	0.85	4.3
Ti40Mo	1.9	0.87	35	7.1	0.85	5.4
Acidified Ringer's solution (pH = 3.1)						
Ti12Mo	1.9	0.86	59	9.1	0.82	2.6
Ti20Mo	1.6	0.87	72	7.7	0.84	3.3
Ti40Mo	1.6	0.88	85	7.3	0.84	4.8

Though exponent values *n* smaller than 1 were always found, yet they were greater than 0.8, thus *Q* values can be considered to represent a non-ideal capacitor. Then, capacitance values for both the compact oxide layer and the electrolyte/oxide interfaces could be extracted from the CPE parameters using [51]:

$$C = R^{1-n}Q^{1/n} \qquad (4.5.2)$$

Assuming that the capacitance may be related to the thickness as $C = \varepsilon\varepsilon_0 A/d$, where ε is the dielectric constant of the oxide, ε_0 the vacuum permittivity, *A* the geometric area, and *d* is the thickness. Higher values of capacitance correspond to smaller thicknesses. To that end, the Ti/Mo ratio in the metal matrix was assumed to hold also in the oxide layer, using $\varepsilon = 114$ for TiO_2 [52,53] and $\varepsilon = 16$ for MoO_3 [54], and the surface roughness factor as unity. The thicknesses of the inner oxide films formed on the different materials are given in Table 4.5.4. It is found that the thickness of the inner compact layer remains almost invariant for a given TiMo alloy with the change in pH of the Ringer´s solution, though the resistance of this layer towards metal dissolution is smaller in the acidic environment. This observation is also supported by

the bigger values of j_{pas} determined from the potentiodynamic polarization curves measured in the acidic solution (cf. Table 4.5.2). Next, the thickness of the inner compact layer is significantly smaller for Ti40 alloy compared to the other two alloys (namely ca. 25% reduction compared to Ti20Mo). A more compact inner oxide layer must be formed on this alloy to account for its higher resistance (see Table 4.5.3).

Table 4.5.4. Film thickness estimated from EIS results measured for TiMo alloys in Ringer's solution and acidified Ringer's solution at room temperature. Dielectric constant values of 114 for TiO_2 [52,53] and 16 for MoO_3 [54] were assumed in the calculation.

Sample	Capacitance of the inner oxide layer / μF cm^{-2}	Film thickness of the inner oxide layer / nm
Ringer's solution, *E* = OCP		
Ti12Mo	19.0	5.7
Ti20Mo	17.4	6.6
Ti40Mo	17.9	5.4
Ringer's solution, *E* = +0.40 V vs. SCE		
Ti12Mo	19.4	5.4
Ti20Mo	16.3	6.4
Ti40Mo	16.7	5.0
Acidified Ringer's solution, *E* = *OCP*		
Ti12Mo	18.0	5.7
Ti20Mo	17.9	6.4
Ti40Mo	18.2	5.2
Acidified Ringer's solution, *E* = +0.40 V vs. SCE		
Ti12Mo	14.4	5.5
Ti20Mo	13.5	5.3
Ti40Mo	14.2	5.0

EIS measurements were also performed on TiMo alloy samples polarized at +0.40 V vs. SCE in both simulated physiological solutions, and the corresponding spectra are given in Figure 4.5.7. Again the Bode-phase plots correspond to a physicochemical system characterized by two time constants. The chi-square value (χ^2) between 5 × 10^{-4} and 10^{-5} points to excellent agreement between the experimental data and simulated values. The values of fitted parameters of the EC are listed in Table 4.5.5. Higher polarization resistance values in the low frequency range of the Bode-modulus plots are observed in all cases compared to the spectra measured at their OCP, which demonstrates that after polarization of the samples at +0.40 V vs. SCE, the passive layer formed on the surface of the TiMo alloys in Ringer's solution is either more compact or more homogeneous than that formed in acidic Ringer's solution. This happens though a slightly thinner passive film is produced in the acidic environment as indicated by the thickness values given in Table 4.5.4.

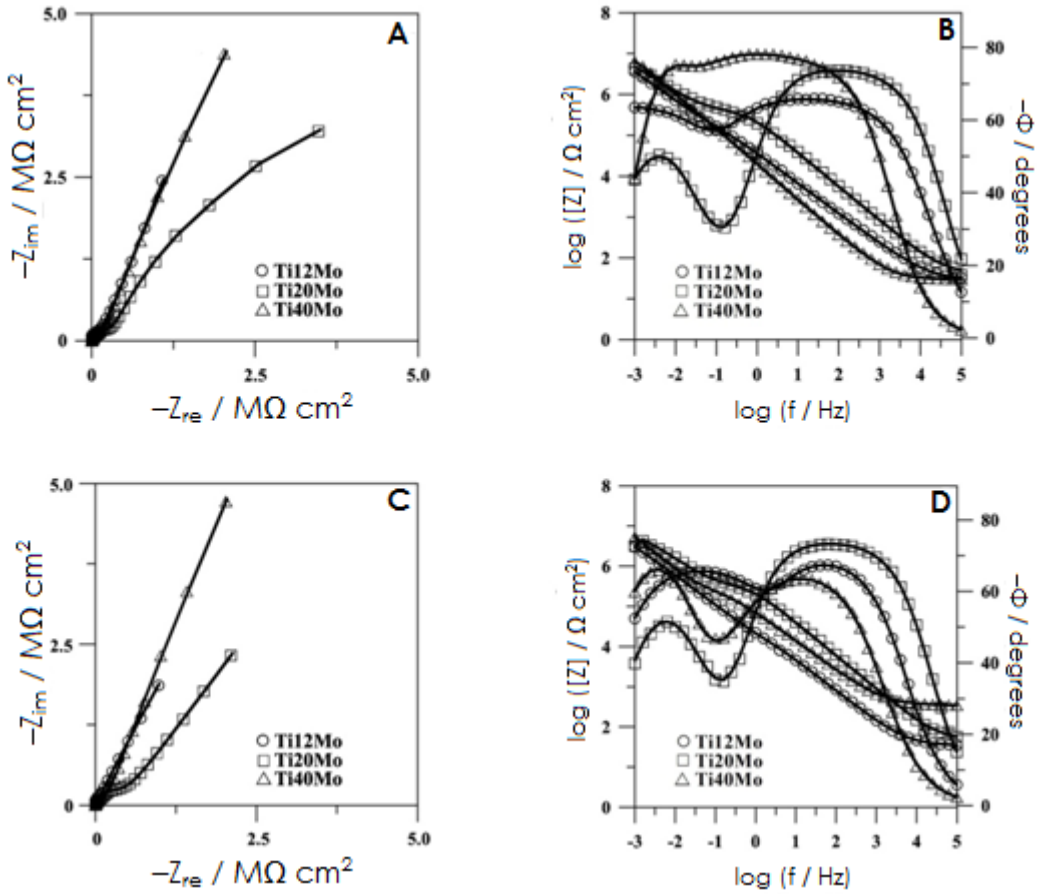

Figure 4.5.7. Measured (discrete points) and fitted (solid lines) impedance spectra for TiMo alloys polarized at +0.40 V vs. SCE during exposure to: (A) Ringer's solution, and (B) acidified Ringer's solution at room temperature.

Table 4.5.5. Parameters of the equivalent circuit for TiMo alloys in Ringer's solution and acidified Ringer's solution at room temperature. AC potential signal was applied to the samples polarized at +0.40 V vs. SCE.

Alloy	$10^5\ Q_{dL}$ / S cm^{-2} s^n	n_{dL}	R_{ct} / kΩ cm^2	$10^6\ Q_{ox}$ / S cm^{-2} s^n	n_{ox}	R_{ox} / MΩ cm^2
Ringer's solution (pH = 6.9)						
Ti12Mo	1.9	0.87	36	8.8	0.84	3.6
Ti20Mo	1.8	0.88	53	7.5	0.85	4.9
Ti40Mo	1.8	0.88	61	7.1	0.85	6.2
Acidified Ringer's solution (pH = 3.1)						
Ti12Mo	1.4	0.88	88	9.1	0.83	3.1
Ti20Mo	1.3	0.89	102	8.9	0.84	3.5
Ti40Mo	1.3	0.89	154	7.2	0.84	5.2

4.5.5.4. Scanning electrochemical microscopy

Since the above discussed electrochemical studies provide electrochemical information that is averaged over the exposed area of the material, scanning

electrochemical microscopy (SECM) was employed to detect local changes in the chemical reactivity of the passive layers formed on the alloys [31,55,56].

Figures 4.5.8-4.5.10 depict the SECM images measured for the TiMo alloys immersed in the two artificial physiological solutions while they were subjected to different electrical conditions. Normalized tip currents greater than 1 were usually obtained when the alloys were polarized at -0.54 V vs. SCE (cf. images (B) in Figures 4.5.8-4.5.10). Yet some variations are observed that depend on the nature of the alloys and the composition of the test solution. The highest normalized tip currents were found for Ti40Mo, followed by Ti20Mo, whereas the smallest were found for Ti12Mo, and they were smaller than one for the latter (see Figure 4.5.8B-left). That is, the surface of this alloy does not facilitate the regeneration of ferrocene-methanol despite the negative potential applied to the sample. This variation in the electrochemical activity of the cathodically-polarized alloys in Ringer's solution closely matches the variation in their open circuit potentials as listed in Table 4.5.1, the nobler value exhibited by Ti40Mo, and the more active for Ti12Mo. That is, polarization of the sample at -0.54 V vs. SCE corresponds to a greater cathodic overvoltage for the alloys with higher Mo contents, which exhibit the more positive OCP values. Therefore, only partial reduction of the oxide film has occurred for the Ti12Mo sample at this cathodic potential. These observations are thus in good agreement with the spontaneous formation of an insulating oxide film on the alloys upon immersion in Ringer's solution.

On the other hand, increased normalized tip currents were always observed in acidic Ringer's solution, supporting that the oxide films spontaneously formed on the surface of the alloys at their OCP are more easily reduced at this potential when immersed in the acid environment. Yet no evidence of a heterogeneous activation of the alloy surfaces can be observed in the images, which depict a rather featureless surface apart from the systematic variations in a random direction that arise from the unavoidably tilted surfaces. More stable passive films are formed at the OCP when the alloys are immersed in neutral Ringer´s solution, and polarization at -0.54 V vs. SCE. The reduction of the spontaneously-formed passive oxide film appears to be more difficult when the alloys are exposed in the neutral Ringer's solution.

An insulating surface towards regeneration of ferrocene-methanol was found when the alloys were polarized anodically as deduced from the inspection of images (C) in Figures 4.5.8-4.5.10. Normalized tip currents smaller than unity were measured in both physiological solutions for the three alloys while polarized at +0.16 V vs. SCE. No clear differences between the insulating characteristics of the passive films formed on each alloys could be distinguished at this time from the SECM maps obtained for each alloy in the tested environments. This observation agrees with the results from EIS data that indicated that the passive layers formed under anodic polarization on the three alloys and in both Ringer's solution and acidic Ringer's solution exhibit similar thicknesses and resistivities.

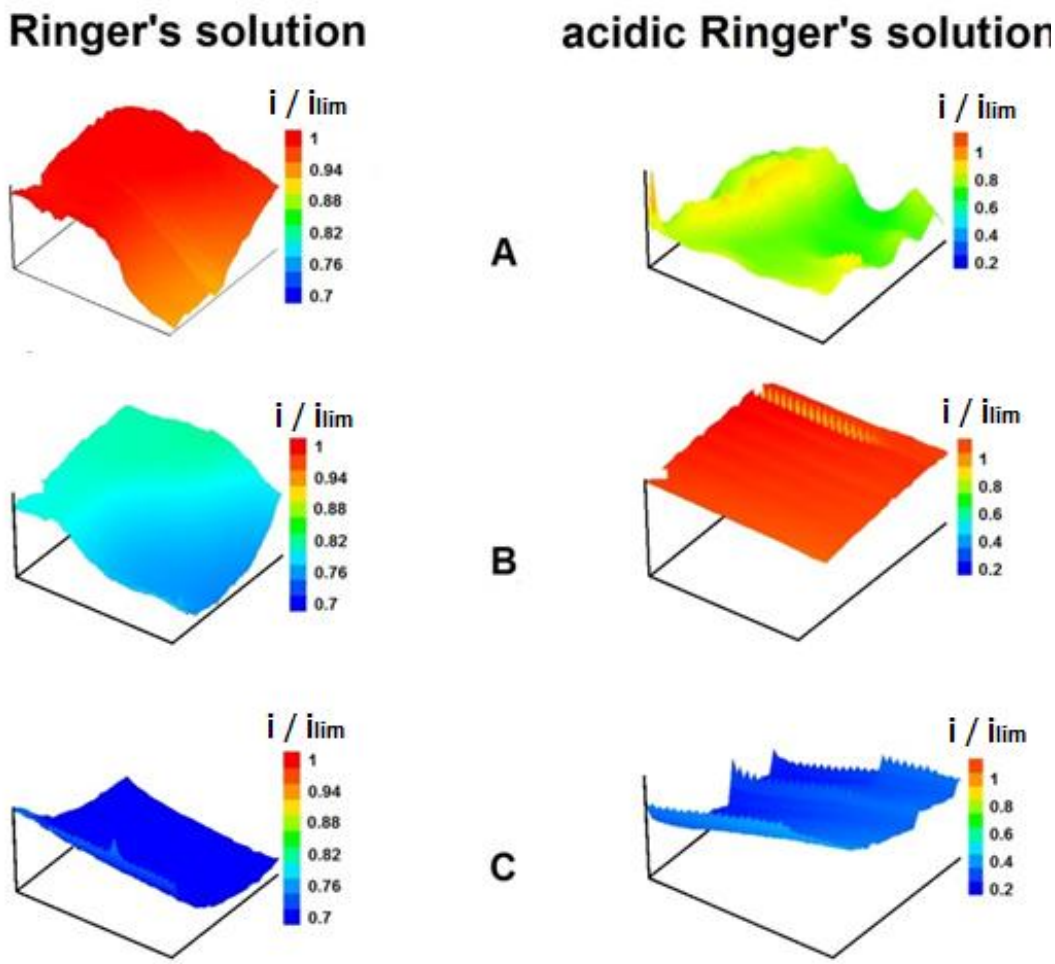

Figure 4.5.8. Images generated by SECM of Ti12Mo alloy during exposure to (left) Ringer's solution, and (right) acidic Ringer's solution at room temperature. The *Z* scale is the dimensionless tip current. Electric condition of the samples: (A) unbiased, and (B-C) under polarization. Applied potential values: (B) -0.54, and (C) +0.16 V vs. SCE. Tip-sample distance: 10 μm. Tip potential: +0.46 V vs. SCE. Scan rate: 30 μm s^{-1}. The figures represent an area of 250 μm × 250 μm in *X* and *Y* directions.

A more complex situation is observed from the inspection of the SECM images recorded at open circuit potential for each alloy. In this case, the dynamic process of oxide film formation could be followed through the maps labelled (A) in Figures 8.4.5-4.5.10 in some cases. This was possible because imaging of the surface was initiated shortly after immersion of the specimens in the electrolyte, that is, without waiting until a stable open circuit potential reading was attained. In this way, passivation of the surface was progressively advancing while the SECM probe was scanning the samples for image recording. Earlier times correspond to the location indicated by the axes origin in the figures, and tip movement advanced from left to right in the scan lines, and from the front to the back in consecutive lines. It can be observed that oxide film formation, which is related to the surface becoming an insulator for ferrocene-methanol regeneration, does not advance in a homogeneous manner, neither at the same rate in each system. Both local microcathodes and

microanodes must be distributed on the surface during oxide film formation, because an oxidant species from the electrolyte must consume the electrons left in the metal during its oxidation. This action is performed by dissolved oxygen molecules in the electrolyte in Ringer's solution, whereas hydrogen ions are preferentially reduced in the acidic electrolyte.

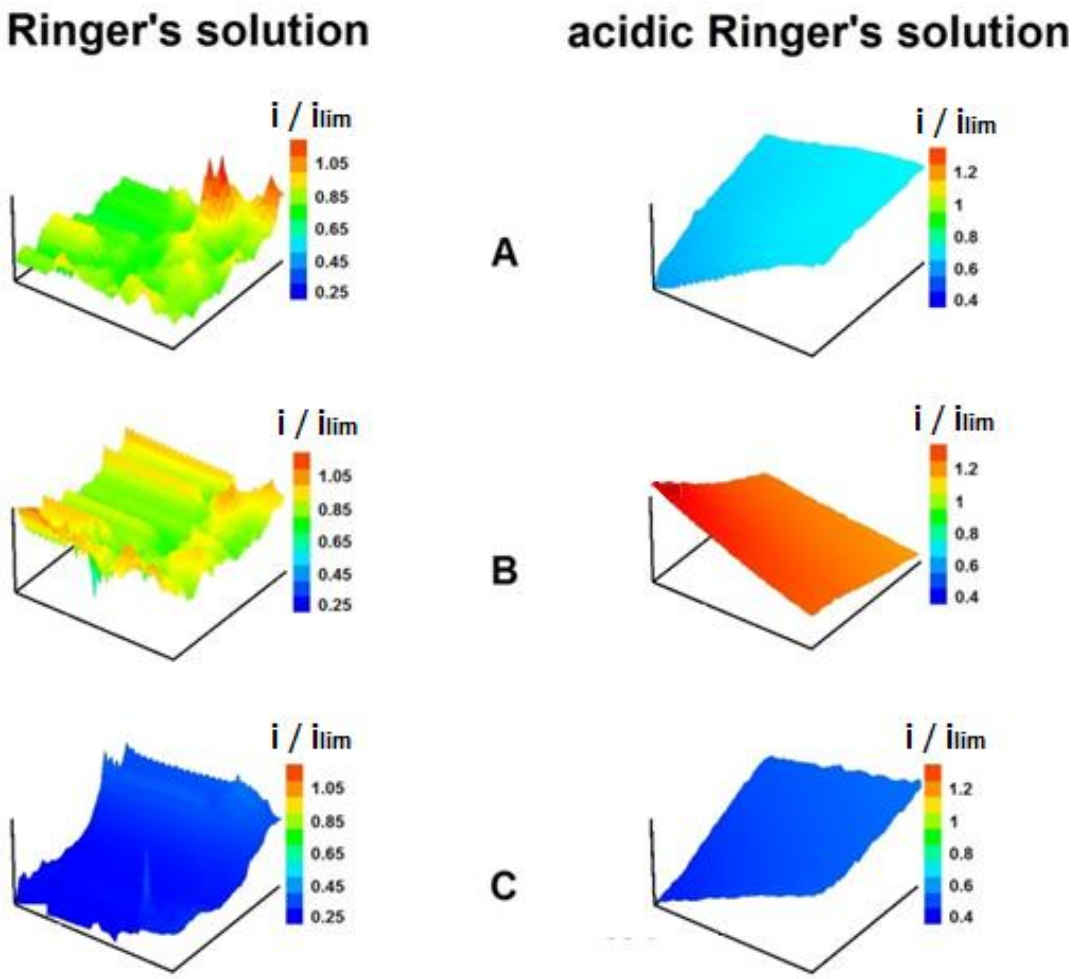

Figure 4.5.9. Images generated by SECM of Ti20Mo alloy during exposure to (left) Ringer's solution, and (right) acidic Ringer's solution at room temperature. The *Z* scale is the dimensionless tip current. Electric condition of the samples: (A) unbiased, and (B-C) under polarization. Applied potential values: (B) -0.54, and (C) +0.16 V vs. SCE. Tip-sample distance: 10 µm. Tip potential: +0.46 V vs. SCE Scan rate: 30 µm s^{-1}. The figures represent an area of 250 µm × 250 µm in *X* and *Y* directions.

A more active surface is imaged at earlier exposures in the case of the Ti40Mo alloy immersed in the acidic electrolyte, and the transition from positive to negative feedback behaviours occurs at longer exposures. Normalized currents greater than one are observed all over the surface, indicating the Ti40Mo alloy is not yet covered by a protective passive oxide layer at short exposures in the acidic environment (see Figure 4.5.10A-right). On the contrary, negative feedback effects are observed for

the other two alloys in this environment even at the beginning of the experiment, and further growth of the oxide film occurs with the elapse of time as evidenced by the continuous decrease of the values of the normalized currents as the tip continues scanning the surface (cf. Figure 4.5.8A-right). This trend in the insulating characteristics of the passive films spontaneously formed on the TiMo alloys at the OCP when exposed to acidic Ringer's solution is just the opposite to what it happens in the neutral solution. That is, an electrically-insulating passive film is formed on Ti40Mo in Ringer's solution that is characterized by normalized currents around 0.25 (Figure 4.5.10A-left). The dynamics of passive film formation is still evident at these early exposures, as indicated by the spikes that correspond to local sites in the surface of the passivating metal where the oxide film is still thinner. Average higher currents are measured in the images corresponding to lower Mo contents in Ringer´s solution, which correlates well with the measurement of bigger j_{corr} values from the potentiodynamic curves (cf. Table 4.5.2). In summary, local electrochemical activity for Ti12Mo and Ti20Mo alloys is smaller in acidic Ringer's solution compared to the neutral environment, whereas the opposite occurs for Ti40Mo. This difference in behaviour may support that the passive layer formed on Ti40Mo is more protective, and no passive layer breakdown occurs in the neutral environment as to produce positive feedback effects for the regeneration of the redox mediator. This finding agrees with the proposal of a more compact and protective inner oxide layer formed on Ti40Mo that was made on the basis of the EIS data. Thus, a molybdenum content in TiMo alloys significantly greater than 15 wt.% leads to a material forming a more insulating passive film when exposed to Ringer's solution.

4.5.6. Conclusions

The effects of molybdenum content in the TiMo alloys, and of pH of the simulated physiological solution, on the corrosion behaviour of these materials has been characterized using electrochemical and scanning microelectrochemical techniques. These materials show a high corrosion resistance in both neutral and acidic environments, even when subjected to anodic polarizations higher than those experienced in the human body [29]. Therefore, alloys with Mo contents higher than 15 wt.% should be further investigated for biomedical applications. The pH value of the Ringer's solution has a minor effect on the corrosion behaviour of TiMo alloys.

TiMo alloys form passive oxide films that are not affected by localized corrosion processes when polarized anodic with respect to their corresponding open circuit potential. A two-layer surface film is produced in all cases, though corrosion resistance is mainly conferred by the thin compact inner oxide layer as evidenced by electrochemical impedance spectroscopy.

The EIS analysis has shown that the resistance of passive layer increased with the content of Mo in TiMo alloys. Also, from potentiodynamic polarization results, the values of corrosion and passive current density decrease with increasing Mo

contents in the alloys. Consequently, surface stability increased with increasing Mo content. TiMo alloys did not show susceptibility to localized corrosion in these two simulated physiological solutions, though they have been tested at bigger anodic polarizations and acidities than those observed in the human body.

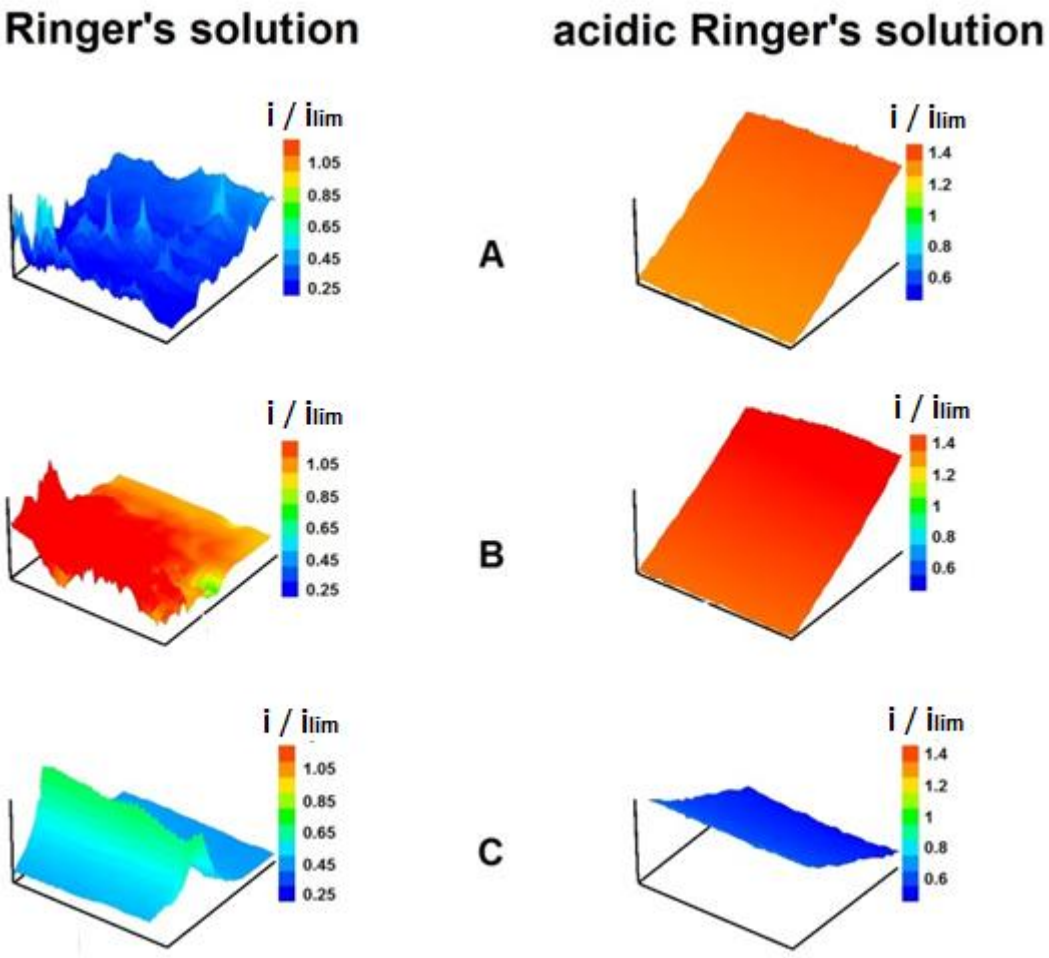

Figure 4.5.10. Images generated by SECM of Ti40Mo alloy during exposure to (left) Ringer's solution, and (right) acidic Ringer's solution at room temperature. The *Z* scale is the dimensionless tip current. Electric condition of the samples: (A) unbiased, and (B-C) under polarization. Applied potential values: (B) -0.54, and (C) +0.16 V vs. SCE. Tip-sample distance: 10 μm. Tip potential: +0.46 V vs. SCE. Scan rate: 30 μm s^{-1}. The figures represent an area of 250 μm × 250 μm in *X* and *Y* directions.

The passive oxide films formed on TiMo alloys exhibit dielectric characteristics towards charge transfer, and they were imaged as insulators by scanning electrochemical microscopy, even when imaged at their corresponding OCP values in the electrolyte. Eventual activation of the surfaces requires the reduction of the passive surface films under cathodic polarization.

Greater corrosion resistance of Ti40Mo alloy than alloys with composition close to surgical alloy F 2066 (Ti-15 wt.% Mo) was found during exposure to artificial

physiological solution, even in acidic environment. This behaviour arises from the formation of a more compact inner oxide layer at the metal-oxide interface for this alloy. Therefore, Ti40Mo is regarded a very promising material for the manufacture of implant devices.

4.5.7. References

1. H.M. Grandin, S. Berner, M. Dard. Materials 5 (2012) 1348.
2. M. Niinomi, M. Nakai, J. Hieda. Acta Biomaterialia 8 (2012) 3888.
3. Biesiekierski, J. Wang, M.A.H. Gepreel, C. Wen. Acta Biomaterialia 8 (2012) 1661.
4. M. Atapour, A.L. Pilchak, G.S. Frankel, J.C. Williams. Materials Science and Engineering C 31 (2011) 885.
5. M. Aziz-Kerrzo, K.G. Conroy, A.M. Fenelon, S.T. Farrell, C.B. Breslin. Biomaterials 22 (2001) 1531.
6. M. Geetha, A.K. Singh, R. Asokamani, A.K. Gogia. Progress in Materials Science 54 (2009) 397.
7. S. Ichinose, T. Muneta, I. Sekiya, S. Itoh, H. Aoki, M. Tagami. Journal of Materials Science 14 (2003) 79.
8. Sarmiento-González, J.M. Marchante-Gayón, J.M. Tejerina-Lobo, J. Paz-Jiménez, A. Sanz-Medel. Analytical and Bioanalytical Chemistry 391 (2008) 2583.
9. Y. Nuevo-Ordóñez, M. Montes-Bayón, E. Blanco-González, J. Paz-Aparicio, J.D. Raimundez, J.M. Tejerina, M.A. Peña, A. Sanz-Medel. Analytical and Bioanalytical Chemistry 401 (2011) 2747.
10. O. Addison, A.J. Davenport, R.J. Newport, S. Kalra, J.W.F. Mosselmans, D. Proops, R.A. Martin. Journal of the Royal Society Interface 9 (2012) 3161.
11. R.M. Souto, G.T. Burstein. Journal of Materials Science: Materials in Medicine 7 (1996) 337.
12. G.T. Burstein, C. Liu, R.M. Souto. Biomaterials 26 (2005) 245.
13. M. Niinomi. Journal of the Mechanical Behaviour of Biomedical Materials 1 (2008) 30.
14. X. Zhao, M. Niinomi, M. Nakai, J. Hieda. Acta Biomaterialia 8 (2012) 1990.
15. T. Zhou, M. Aindow, S.P. Alpay, M.J. Blackburn, M.H. Wu. Scripta Materialia 50 (2004) 343.
16. L.C. Zhang, T. Zhou, M. Aindow, S.P. Alpay, M.J. Blackburn. Journal of Materials Science 40 (2005) 2833.
17. L. De Rosa, C.R. Tomachuk, J. Springer, D.B. Mitton, S. Saiello, F. Bellucci. Materials and Corrosion 55 (2004) 602.
18. C.R. Tomachuk, L. De Rosa, J. Springer, D.B. Mitton, S. Saiello, F. Bellucci. Materials and Corrosion 55 (2004) 665.
19. K.V. Rajagopalan. Annual Review of Nutrition 8 (1988) 401.
20. S. Kumar, T.S.N. Sankara Narayanan. American Journal of Dentistry 36 (2008) 500.

21. M.C.R. Alvez Rezende, A.P. Rosifini Alvez, E.N. Codaro, C.A. Matsumoto Dutra. Journal of Materials Science: Materials in Medicine 18 (2007) 149.
22. N.T.C. Oliveira, A.C. Gustaldi. Corrosion Science 50 (2008) 938.
23. N.T.C. Oliveira, A.C. Gustaldi. Acta Biomaterialia 51 (2009) 399.
24. ASTM F 2066, Standard Specification for Wrought Titanium-15 Molybdenum Alloy for Surgical Implant Applications (UNS R58150). ASTM International, West Conshohocken, 2011.
25. D. Mareci, R. Chelariu, I. Dan, D.M. Gordin, T. Gloriant. Journal of Materials Science: Materials in Medicine 21 (2010) 2907.
26. D.M. Gordin, E. Delvat, R. Chelariu, G. Ungureanu, M. Besse, M. Laille, T. Gloriant. Advanced Engineering Materials 10 (2008) 714.
27. D. Mareci, G. Ciurescu, R. Chelariu, I. Cretescu, D. Sutiman. Environmental Engineering and Management Journal 9 (2010) 81.
28. P. Ducheyne, G. Willems, M. Martens, J. Helsen. Journal of Biomedical Materials Research 18 (1984) 293.
29. T.P. Hoar, D.C. Mears. Proceedings of the Royal Society A 294 (1966) 486.
30. B. Yeum, Electrochemical Impedance Spectroscopy: Data Analysis Software. Echem Software, Ann Arbor, 2001.
31. G. Ciurescu, J. Izquierdo, J.J. Santana, D. Mareci, D. Sutiman, S. González, R.M. Souto. International Journal of Electrochemical Science 7 (2012) 7404.
32. W.F. Ho, C.P. Hu, J.H.C. Lin. Biomaterials 20 (1999) 2115.
33. M. Geetha, U.M. Kamachi, A.K. Gogia, R. Asokamani, R. Baldev. Corrosion Science 46 (2004) 877.
34. D.J. Blackwood, A.W.C. Chua, K.H.W. Seah, R. Trampuran, S.H. Teoh. Corrosion Science 42 (2003) 481
35. M.H. Wong, F.T. Cheng, H.C. Man. Materials Letters 61 (2007) 3391.
36. G. Bolat, J. Izquierdo, J.J. Santana, D. Mareci, R.M. Souto. Electrochimica Acta 88 (2013) 447.
37. D.D. Macdonald, G.R. Engelhardt. ECS Transactions 28 (14) (2010) 123.
38. J. Pan, D. Thierry, C. Leygraf. Electrochimica Acta 41 (1996) 1143.
39. J.E.G. Gonzalez, J.C. Mirza Rosca. Journal of Electroanalytical Chemistry 471 (1999) 109.
40. M.C. García Alonso, L. Saldaña, G. Valles. Biomaterials 24 (2003) 19.
41. S.L. Assis, S. Wolynec, I. Costa. Electrochimica Acta 51 (2006) 1815.
42. V. Barranco, M.L. Escudero, M.C. García-Alonso. Electrochimica Acta 52 (2007) 4374.
43. I.C. Lavos-Valereto, S. Wolynec, I. Ramires, A.C. Guastaldi, I. Costa. Journal of Materials Science: Materials in Medicine 15 (2004) 55.
44. Milosev, T. Kosec, H.H. Strehblow. Electrochimica Acta 53 (2008) 3547.
45. V. Raman, S. Nagarajan, N. Rajendran. Electrochemistry Communications 8 (2006) 1309.
46. Cremasco, W.R. Osorio, C.M.A. Freire, A. Garcia, R. Caram. Electrochimica Acta 53 (2008) 4867.
47. F. Rosalbino, D. Maccio, G. Scavino, A. Saccone. Journal of Materials Science: Materials in Medicine 23 (2012) 865.

48. B.I. Wang, Y.F. Zheng, I.C. Zhao. Materials and Corrosion 60 (2009) 330.
49. N. Figueira, T.M. Silva, M.J. Carmezim, J.C.S. Fernandes. Electrochimica Acta 54 (2009) 921.
50. G. Bolat, J. Izquierdo, D. Mareci, D. Sutiman, R.M. Souto. Electrochimica Acta 106 (2013) 432.
51. J.R. Macdonald. Solid State Ionics 13 (1984) 147.
52. L.J. Berberich, M.E. Bell. Journal of Applied Physics 11 (1940) 681.
53. R.A. Parker. Physical Review 124 (1961) 1719.
54. G.S. Nadkarni, J.G. Simmons. Journal of Applied Physics 41 (1970) 545.
55. S.E. Pust, D. Scharnweber, S. Baunack, G. Wittstock. Journal of the Electrochemical Society 154 (2007) C508.
56. R. Zhu, Z. Qin, J.J. Noël, D.W. Shoesmith, Z. Ding. Analytical Chemistry 80 (2008) 1437.

4.6

Main conclusions

1. The resistance towards corrosion of several titanium based passivating materials, namely TiMo and ZrTi alloys, have been characterized in vitro using artificial physiological solutions. The motivation was to explore the risk of eventual hazardous corrosion processes while being used as biomedical implants. They were tested under even more aggressive conditions than those encountered in the human body.

2. Materials characterization was performed using a combination of conventional electrochemical methods and local surface analysis, supplemented by acquiring their specific microelectrochemical response by SECM.

3. Potentiodynamic polarization provided valuable information regarding the susceptibility of the materials towards corrosion in a given environment. Corrosion resistance is provided by the formation of surface oxide layers, whose nature and behaviour was established from electrochemical impedance measurements.

4. Surface conductivity and susceptibility towards electron transfer was studied by SECM for each material under immersion in the solutions of interest. Positive and negative feedback effects were further observed by adequately selecting the potential sequence applied to the substrate. Heterogeneous electrochemical reactivity distributions was found for the materials, though the spontaneously formed passive films globally behave as insulating barriers towards electron transfer at the surface of the alloys in most cases. Greater electrical insulation is achieved by increasing the molybdenum content in Ti-Mo, and by decreasing Zr content in the Zr-Ti series, respectively. Thermal oxidation pretreatment in air enhances the stability of surface oxide films.

4.7

Conclusiones

1. Se ha caracterizado la resistencia a la corrosión de varias aleaciones pasivas de base titanio, TiMo y ZrTi, usando disoluciones fisiológicas artificiales *in vitro*. La motivación de este trabajo fue la de estudiar el riesgo de los posibles procesos corrosivos durante su empleo como implantes biomédicos. Estos materiales fueron analizados bajo condiciones aún más agresivas que las halladas en el cuerpo humano.

2. La caracterización del comportamiento de estas aleaciones se ha desarrollado usando una combinación de métodos electroquímicos convencionales y de análisis superficial, complementada por la adquisición de su respuesta microelectroquímica específica mediante SECM.

3. La polarización potenciodinámica facilitó información valiosa sobre la susceptibilidad de estos materiales hacia la corrosión en los ambientes dados. La resistencia a la corrosión es aportada por las capas superficiales de óxidos que se generan, cuyo comportamiento y naturaleza pudieron establecerse a través de medidas de impedancia electroquímica.

4. Mediante SECM se ha estudiado la conductividad y susceptibilidad a la transferencia electrónica de cada aleación inmersa en la disolución de interés. Se han observado efectos de retroalimentación positiva y negativa mediante la adecuada selección del potencial aplicado al substrato. Se ha encontrado una distribución heterogénea de la reactividad del material, pese a que la película pasiva formada espontáneamente actúa como barrera aislante, impidiendo la transferencia electrónica en su superficie en la mayoría de los casos. Los mayores aislamientos eléctricos se han conseguido mediante el incremento del contenido en molibdeno en las series Ti-Mo, y mediante la disminución del contenido en Zr en las series de Zr-Ti. El tratamiento de oxidación térmica al aire ha demostrado ser capaz de aumentar la estabilidad de la película superficial de óxidos.

CHAPTER 5

In situ characterization of metal dissolution in galvanic corrosion processes using scanning microelectrochemical techniques

Index

5.1

Prologue to the experiments

5.1.1. Introduction

In situ information on the chemistry and structure at the metal/electrolyte interface is necessary to know the corrosion behaviour of metals and alloys in aqueous environments, and to develop and test efficient protection strategies for longer corrosion resistance of the materials. Nowadays, there are a quite large number of techniques that can be used for corrosion studies, and the choice of the most suitable one to be employed in the investigation depends on various factors, including the surface condition of the materials, dimensions of films and layers on the metal surfaces, and physicochemical characteristics of the aggressive environment. In this way, structural and chemical composition data, as well as surface imaging have been achieved, though, often, measurement procedures involved *ex situ* operations, thus generally quite different from those met by the materials in their environment. Moreover, time-resolved analysis is very difficult at their best, thus making the dynamics of structure modifications produced by the corrosion processes practically impossible to follow. The advent of scanning electrochemical techniques has opened up new opportunities in this field, and among them, scanning electrochemical microscopy (SECM) is conceiting most prospects due to its versatility to examine, with high spatial resolution, the surface topography and the electrochemical reactivity of many metal substrates subjected to corrosion processes [1-4]. Despite the variety of systems characterized by this technique, major limitations have been found for the investigation of a number of technologically interesting metal materials, such as zinc and magnesium. In fact, direct monitoring of the corresponding metal ions could not be investigated because either their corresponding standard redox potentials occur in the range of hydrogen evolution on platinum microelectrodes, usually employed as the SECM probe, or they would require the electroreduction of the metal ions to the zero oxidation state, thus effectively modifying the electrochemical response of the SECM tip. On the other hand, those materials are receiving major attention because of light weighting in areas of automotive and aerospace applications, or as components for active corrosion protection through galvanic coupling and cathodic protection mechanisms. In fact, zinc has been employed in the galvanizing of steels since long ago, but it is also present in modern coating formulations for metal protection designed for offshore conditions, where zinc-rich primers are widely employed.

Therefore, the development of operation procedures based on scanning electrochemical techniques, opening ways to investigate zinc reactivity *in situ*, is

currently a topic of major interest. This is even more the case of scanning electrochemical microscopy, since direct monitoring of zinc dissolution has not been possible yet with the use of typical SECM tips [5,6]. The introduction of Hg microelectrodes as SECM tips has opened new possibilities in corrosion research [7]. In fact, Hg probes offer a wider negative potential range than bare platinum tips allowing for the reduction of zinc ions at the tip to be investigated with low interference from oxygen reduction or hydrogen evolution from aqueous solutions [7]. Hg microelectrodes can be fabricated by electrodeposition of liquid mercury onto Pt microdisks [8-11], and adopt a sphere cap geometry, whose size depends on the plating time. Theory to predict diffusion-controlled steady state currents [12-14] and approach curves at sphere-cap tips for both negative and positive feedback conditions [15] is also available. In this way, the corrosion processes related to zinc dissolution that take place in a naturally corroding zinc sample and in a zinc-iron galvanic pair exposed to a chloride solution were successfully investigated by scanning electrochemical microscopy (SECM) using a mercury-coated platinum microelectrode as SECM tip [16,17]. Both the release of zinc ions and the consumption of dissolved oxygen that occur in separate sites at the zinc-iron galvanic pair were monitored. Zinc ion quantification could be performed by stripping the zinc metal collected at the Hg-coated tip using linear sweep voltammetry [17].

The objective of this Chapter is to develop new operation modes in SECM for monitoring of galvanic coupling reactions involving zinc dissolution capable of further miniaturization and chemical selectivity, as to characterize systems of practical interest such as constituted by cut edges of polymer coated galvanized steels. In this Chapter, proof of concept is illustrated for a model zinc-iron galvanic couple immersed in a naturally-aerated aqueous sodium chloride solution. Additionally, the observed discrepancies between the experimental results obtained using SECM with those derived from the use of the scanning vibrating electrode technique (SVET), were investigated and resolved.

5.1.2. References

1. S.E. Pust, W. Maier, G. Wittstock. Zeitschrift für Physikalische Chemie 222 (2008) 1463.
2. L. Niu, Y. Yin, W. Guo, M. Lu, R. Qin, S. Chen. Journal of Materials Science 44 (2009) 4511.
3. Y. González-García, J.J. Santana, J. González-Guzmán, J. Izquierdo, S. González, R.M. Souto. Progress in Organic Coatings 69 (2010) 110.
4. R.M. Souto, S. Lamaka, S. González. In: Microscopy: Science, Technology, Applications and Education, Vol. 3 (Edited by A. Méndez-Vilas, J. Díaz). Formatex Research Center, Badajoz, 2010, p. 1769.
5. R.M. Souto, Y. González-García, S. González. Corrosion Science 47 (2005) 3312.

6. A.M. Simões, A.C. Bastos, M.G. Ferreira, Y. González-García, S. González, R.M. Souto. Corrosion Science 49 (2007) 726.
7. S. Daniele, M.A. Baldo, C. Bragato. Current Analytical Chemistry 4 (2008) 215.
8. K.R. Wehmeyer, R.M. Wightman. Analytical Chemistry 57 (1985) 1989.
9. A.S. Baranski. Analytical Chemistry 59 (1987) 662.
10. S. Daniele, M.A. Baldo, P. Ugo, G.A. Mazzocchin. Analytica Chimica Acta 219 (1989) 9.
11. M.A. Baldo, S. Daniele, M. Corbetta, G.A. Mazzochin. Electroanalysis 7 (1995) 980.
12. A.M. Bond, K.B. Oldham, C.G. Zoski. Analytica Chimica Acta 216 (1989) 177.
13. K.B. Oldham. Journal of Electroanalytical Chemistry 313 (1991) 3.
14. S. Daniele, I. Ciani, D. Battistel. Analytical Chemistry 80 (2008) 253.
15. G. Lindsey, S. Abercrombie, G. Denuault, S. Daniele, E. De Faveri. Analytical Chemistry 79 (2007) 2952.
16. R.M. Souto, Y. González-García, D. Battistel, S. Daniele. Chemistry, A European Journal 17 (2011) 230.
17. R.M. Souto, Y. González-García, D. Battistel, S. Daniele. Corrosion Science 55 (2012) 401.

5.2

Spatially-resolved measurement of electrochemical activity and pH distributions in corrosion processes by scanning electrochemical microscopy using antimony microelectrode tips

5.2.1. Abstract

A new method for the spatially-resolved measurement of pH during corrosion processes with the scanning electrochemical microscope (SECM) is presented. Antimony tips are employed because the dual-function characteristics of this material allow the combined potentiometric/amperometric operation of the SECM. The applicability of this technique is illustrated by considering the galvanic corrosion of a model zinc-iron pair immersed in 0.1 M NaCl aqueous solution. Spatially resolved images of pH and oxygen concentration above the metal specimens could be obtained in the same experiment.

5.2.2. Resumen

Se presenta un nuevo método para la adquisición de medidas de pH con resolución espacial durante procesos corrosivos empleando el microscopio electroquímico de barrido (SECM). Se emplearon puntas de antimonio debido a la característica función dual de este material, lo cual permite la operación combinada amperométrica/potenciométrica para el SECM. La aplicabilidad de esta técnica se ilustra considerando la corrosión galvánica del par cinc-hierro inmerso en disolución acuosa de NaCl 0.1 M. Se han podido obtener imágenes de pH y de concentración de oxígeno sobre las muestras metálicas en el mismo experimento.

5.2.3. Introduction

Local microcells are formed during the spontaneous corrosion of metals exposed to aqueous environments. That is, spatial distributions of anodes and cathodes on the metallic surface are developed when the material is left at its open circuit potential. The metal is oxidized at the anodes, whereas the corrosion process is maintained by the reduction of some species from the environment at the cathodes (for instance, oxygen in neutral and moderately alkaline media, or protons in acidic solutions). Because the corroding metal usually produces M^{z+} cations transferred under diffusion control at the anodic sites, the system can be studied by SECM [1-3]. This fact has been exploited to image metastable pits on austenitic steel *in situ* by SECM at the open circuit potential [4], and to detect metal dissolution either from inclusions in alloys [5-7] or from defects in polymer-coated metals [8-10]. On the other hand, in a neutral aqueous environment, oxygen from the electrolyte is consumed at the cathodic areas, and the reaction may be detected by the scanning tip as local depletion of the oxygen concentration in the electrolyte adjacent to cathodic sites [11-15]. These studies have gathered new spatially-resolved information on the mechanisms of localized corrosion reactions in overwhelming cases employing metal microdisks as the tip and the amperometric operation of the SECM. That is, the electrochemical information is obtained from the measurement of the faradaic current flowing in the ultramicroelectrode tip as a function of either time or its location above the sample.

Corrosion processes are very sensitive to pH, and the progress of the corrosion reactions may produce changes in the pH of the environment too. Cathodic half-cell reactions often involve a progressive alkalization of the electrolyte, either by consuming protons if the electrolyte is originally acidic, or by releasing hydroxyl ions in the case of neutral or alkaline solutions. Additionally, the corrosion of the metal at the anodic sites results in the generation of metal ions, and some of them undergo hydrolysis reactions with the aqueous environment, producing local acidification of the medium. Thus, the measurement of pH in the vicinity of a corroding surface and its visualization as a function of the location at the surface, and its evolution with time are of major interest to a better understanding of the corrosion processes in micrometric and submicrometric scales.

Though pH imaging is possible by using SECM in potentiometric operation since an antimony tip was developed for ion-selective potentiometric microscopy in 1993 [16], this method has not been applied in Corrosion Science yet. The electric potential of this material changes in response to variations in the acidity of the environment due to its tendency to be coated by a Sb_2O_3 film. Thus, antimony tips have been employed as pH sensor in SECM for the characterization of a variety of systems [17-19], as well as microsensors for other techniques [20-28]. Due to the metallic properties of antimony, tips from this material can also be employed in amperometric SECM to image the topography of the substrates under investigation [16,18], thus allowing more information to be gained from these systems. That is,

antimony tips are dual-function microelectrodes applicable for both amperometric and potentiometric SECM. This is a major advantage compared to other ISMEs employed for pH monitoring in SECM which can only be employed for the potentiometric operation [29-34] or with the scanning ion-selective electrode technique (SIET) [35,36]. This dual-function property has application not only for SECM, because it has been employed for the detection of heavy metals with square-wave voltammetry when carbon-based microelectrodes were coated with antimony thin films [37-39].

This Section reports results obtained from SECM measurements with an antimony tip to characterize a model corrosion reaction. The experimental system selected for this work was the galvanic corrosion of a zinc-iron pair, an experimental system previously characterized by amperometric SECM [12], scanning vibrating electrode technique (SVET) [12,40], and SIET [36]. The dual function of the tip material was explored for the combined potentiometric monitoring of pH distributions and the amperometric detection of dissolved oxygen employed as redox mediator [13].

5.2.4. Experimental

Antimony microelectrodes were made of two parts as shown in Figure 5.2.1. The outer glass-capillary provides the electric connection, whereas the actual antimony tip is inserted into the lumen of the first. High purity antimony in powder presentation (266329, Aldrich) and borosilicate glass capillaries (B200-116-10, Sutter Instruments, Novato, CA, USA) were used.

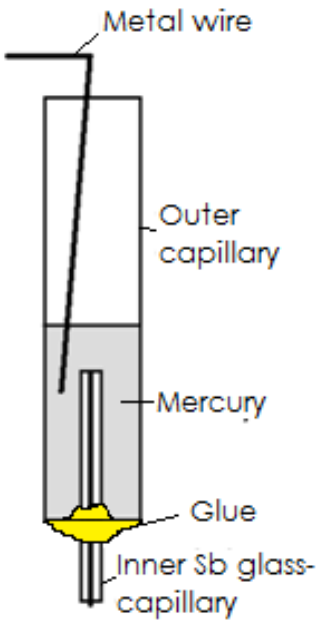

Figure 5.2.1. Sketch of the antimony microelectrode.

The fabrication of the microelectrode is initiated by heating the antimony powder in a melting pot with the help of a gas flame. When antimony melts, one glass-capillary is filled with it using syringe suction. The filled capillary is then pulled using metallic tweezers to produce a smaller size glass capillary filled with antimony. Further pulling with a micropipette puller (mod. P-30/P, Sutter) allowed one section of this conic tip, with an approximate diameter of 15 – 20 μm, to be fabricated. A second glass-capillary was also pulled to produce at its end a capillary of dia. 100 μm, and the antimony tip was next inserted in its lumen with the tip reaching out for about 15 mm, and about 20 mm long staying in the lumen. Mercury metal and the copper wire were then inserted into the lumen of the thicker capillary to provide electrical contact. Loctite adhesive was used to seal both ends. The resulting microelectrode had a *RG* value about 5.

In this Section, the corrosion behaviour of a zinc-iron galvanic pair was investigated. The samples were prepared from high purity strips of each metal supplied as sheets by Goodfellow Materials Ltd. (Cambridge, UK), with nominal purities of 99.5% for iron and 99% for zinc. The metals were cut into 1 x 1 mm^2 strips, and mounted in an Epofix epoxy sleeve (Struers, Ballerup, Denmark) with a separation of ca. 1 mm between them. The mounts with the samples were polished with silicon carbide paper down to 800 grit, and subsequently polished with alumina micropolish of 1 and of 0.3 μm particle size. The resulting surfaces were thoroughly rinsed with Millipore deionised water, dried with acetone and finally surrounded laterally by Sellotape, thus creating a small container for the test electrolyte solution. The two metals were electrically connected at the back of the epoxy mount to form a galvanic couple. The electrochemical cell was completed with an Ag/AgCl/KCl (3M) reference electrode, and a platinum wire as the counter electrode.

A home-built SECM system was employed [17], using a 3D positioning device driven by precision step motors with 75 nm minimal step size. A video camera was used to further assist positioning of the tip close to the surface. The distance between the tip and the substrate was established by allowing the probe to gently rest on the sample, and subsequently the probe was retreated to the chosen operation distance with the aid of the *Z*-positioning motor. Tip-surface distance was also estimated using the negative feedback function measured for the oxygen reduction current when the tip was located over the epoxy part. Selected experiments were also performed using a platinum microelectrode of 25 μm diameter to check the effect of the metal used to build the tip in amperometric SECM.

Reagents of analytical grade and twice-distilled water were employed to prepare all the solutions. The pH calibration of the antimony microelectrodes was made using various buffer solutions to cover the $3.0 < pH < 11.5$ range. The chosen buffer systems were phosphate, carbonate, ammonia and acetate. They were prepared from 0.1 M solutions of the basic species, and the pH was adjusted by adding HCl. Corrosion tests were carried out in aqueous 0.1 M NaCl solution.

5.2.5. Results and discussion

5.2.5.1. Calibration of the antimony microelectrode

Antimony microelectrodes were calibrated by measuring their open circuit potentials in the buffer solutions. The typical calibration procedure was performed by introducing the microelectrode in a sequence of buffer solutions initiated with the most alkaline solution. In this way, the tip was exposed to solutions of increased acidity as shown in Figure 5.2.2. The overpotential values observed in the plot occurred upon electrolyte exchange, and next the electrode attained a steady potential value in each solution. No steady value of the electrode potential could be observed when it was introduced in the buffer solution of pH 3.07, because the antimony electrode was not stable in this medium due to acid attack. In this medium, the initial potential value in the transient was taken for calibration purposes. Finally, the electrode was reintroduced in the most alkaline buffer solution to check the reproducibility of its potential response. The potential value measured after a quite short stabilization period was the same as that recorded at the beginning of the experiment within experimental error of 1.5 mV. With the potential values taken from each buffer solution, the calibration plot shown in the inset of the figure was drawn. It can be observed that there is a linear relationship between the potential of the antimony tip and the solution pH in the interval between 3 and 11.5. The slope of the plot amounts 46.1 mV (pH unit)$^{-1}$.

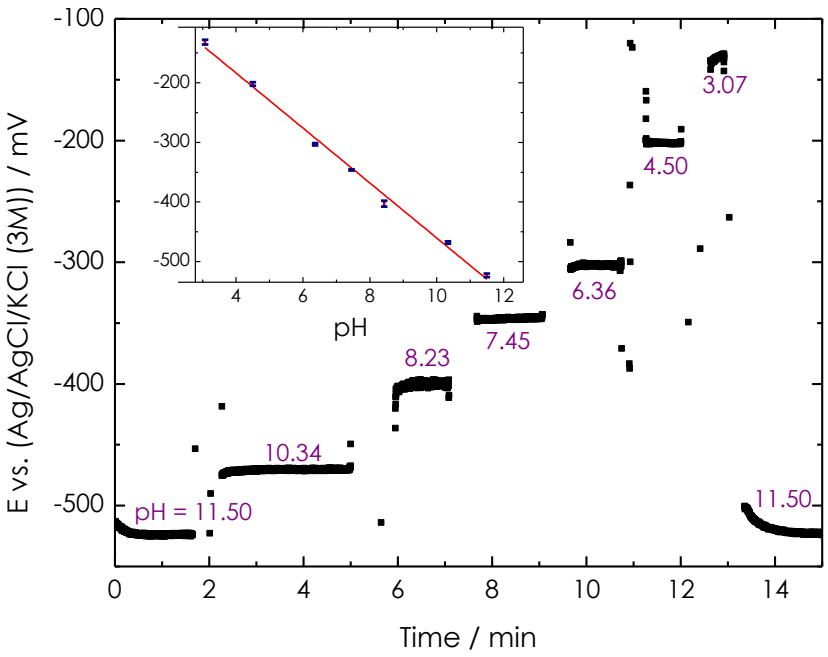

Figure 5.2.2. Dynamic response transients of the antimony microelectrode to pH. The pH changes were made by replacing the buffer solutions described in Section 5.2.4. The inset depicts the resulting calibration plot.

5.2.5.2. SECM visualization of pH and oxygen concentration distributions during the galvanic corrosion of a zinc-iron pair

The dual function of the antimony microelectrode used as tip in scanning electrochemical microscopy was explored on a zinc-iron galvanic pair immersed in naturally aerated 0.1 M NaCl solution at ambient temperature. The tip-sample distance was established by allowing the antimony tip to gently rest on the surface of the epoxy sleeve half way between the two metals. After the tip was retreated to a height of 25 μm, SECM scan lines or arrays were registered above the zinc-iron specimen by scanning the tip parallel to the surface.

Figure 5.2.3 displays the pH values measured with the antimony tip operated in potentiometric mode while scanning a line passing above the center of the two metals after they have been immersed in the test solution for about 120 min.

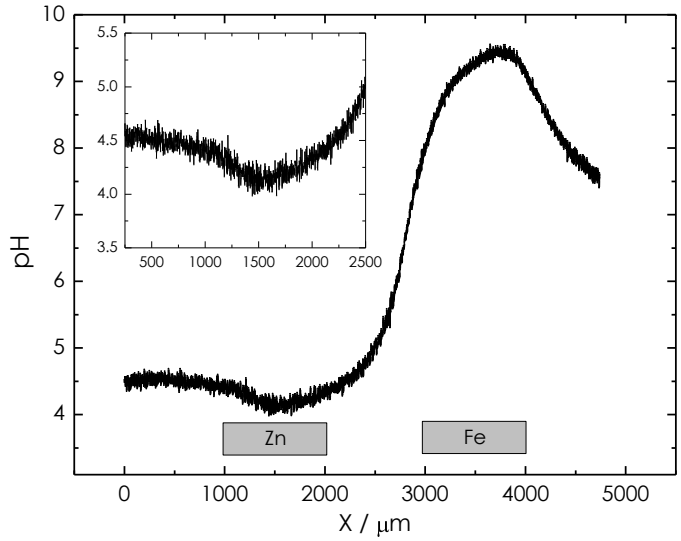

Figure 5.2.3. Potentiometric scan line of the antimony probe tip above the zinc-iron galvanic couple after 2 hours immersion in 0.1 M NaCl. The inset shows the pH variation measured above the zinc sample with greater resolution. Tip-sample distance: 25 μm; scan rate: 5 μm s^{-1}.

Alkalization of the electrolyte occurred in the proximity of the iron sample, which is the nobler metal in the galvanic pair. Thus, the cathodic process takes place on this metal. In an acidic electrolyte, protons are removed from the electrolyte as they are electroreduced to hydrogen at the cathodic sites:

$$2H^+ + 2e^- \rightarrow \uparrow H_2 \qquad (5.2.1)$$

whereas in neutral and alkaline environments, the electroreduction of dissolved oxygen releases hydroxide ions into the solution according to:

$$O_2 + 4H_2O + 4e^- \rightarrow 4OH^- \qquad (5.2.2)$$

Since the initial electrolyte is slightly acidic, equation (5.2.1) could be considered to occur first on the surface of iron, followed by the electroreduction of oxygen at a later stage. Yet, the simultaneous occurrence of oxygen electroreduction can be

checked by using the antimony microelectrode as conventional tip in amperometric SECM. In this case, the potential of the tip was set at -0.65 V vs. (Ag/AgCl/KCl (3M)) to detect the concentration distribution of dissolved oxygen above the iron sample. The same feature is clearly observed when the current value normalized to the bulk current (i / i_{lim}) during a scan line taken over the center of the image, was determined with the antimony microelectrode (see Figure 5.2.4A). In the later, the *Y* axis has been inversed to show smaller cathodic faradaic currents to fall lower in the graph, thus effectively corresponding to lower oxygen contents. In order to check the validity of this method, a platinum tip was also employed. The scan array given in Figure 5.2.4B displays a region of depleted oxygen concentration extending over the dimensions of the iron sample as recorded with the platinum microelectrode. In summary, oxygen is consumed at the cathodic sites through equation (5.2.2) at a higher rate than diffusion can supply it from the bulk of the electrolyte. Thus, the consumption of oxygen can be monitored by amperometric SECM with antimony tips as they provide the same results than conventional platinum microelectrodes.

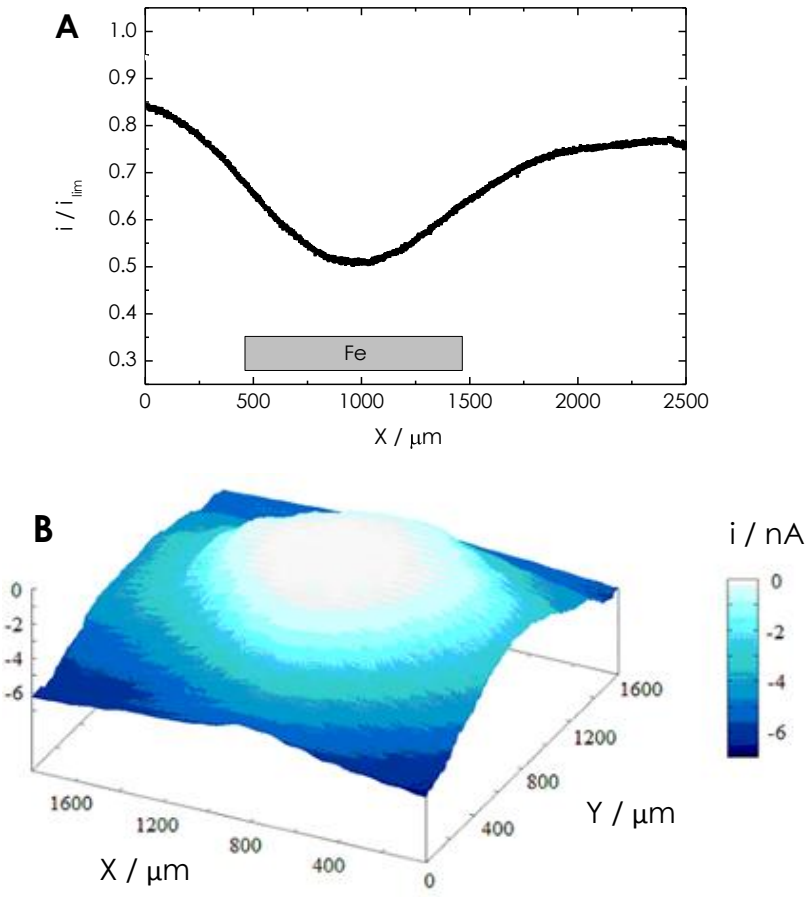

Figure 5.2.4. Distribution of oxygen concentration above the iron sample immersed in 0.1 M NaCl for 7 hours. SECM operating amperometrically by setting the tip potential at -0.65 V vs. (Ag/AgCl/KCl (3M)). Tip-sample distance: 25 µm. (A) Scan line depicting the normalized current (i / i_{lim}) for a trip of the antimony tip along *X* axis passing over the center of the sample; scan rate: 5 µm s^{-1}. (B) SECM map depicting the absolute current measured at a platinum microelectrode; scan rate: 30 µm s^{-1}. The *Z* scale in (B) is the tip current in nA.

The alkalization process continues with the elapse of time for the duration of the experiment, and even higher pH values are measured after 26 hours immersion of the galvanic pair in the electrolyte. The distribution of pH from the surface towards the bulk of the electrolyte can be obtained simply by stepwise changing the tip-sample distance during the measurements. This procedure is illustrated in Figure 5.2.5A which corresponds to the tip positioned directly above the center of the iron specimen. The tip was first removed from the vicinity of the surface to a distance of 900 μm, and then the direction of the tip movement was reversed for the probe to approach the surface again. The pH drops by almost 4 units during the retreating movement from the iron surface, whereas a stationary value is observed in the approach scan for distances in excess of 400 μm. This pH value corresponds to the bulk electrolyte after the galvanic corrosion process has proceeded for 26 hours.

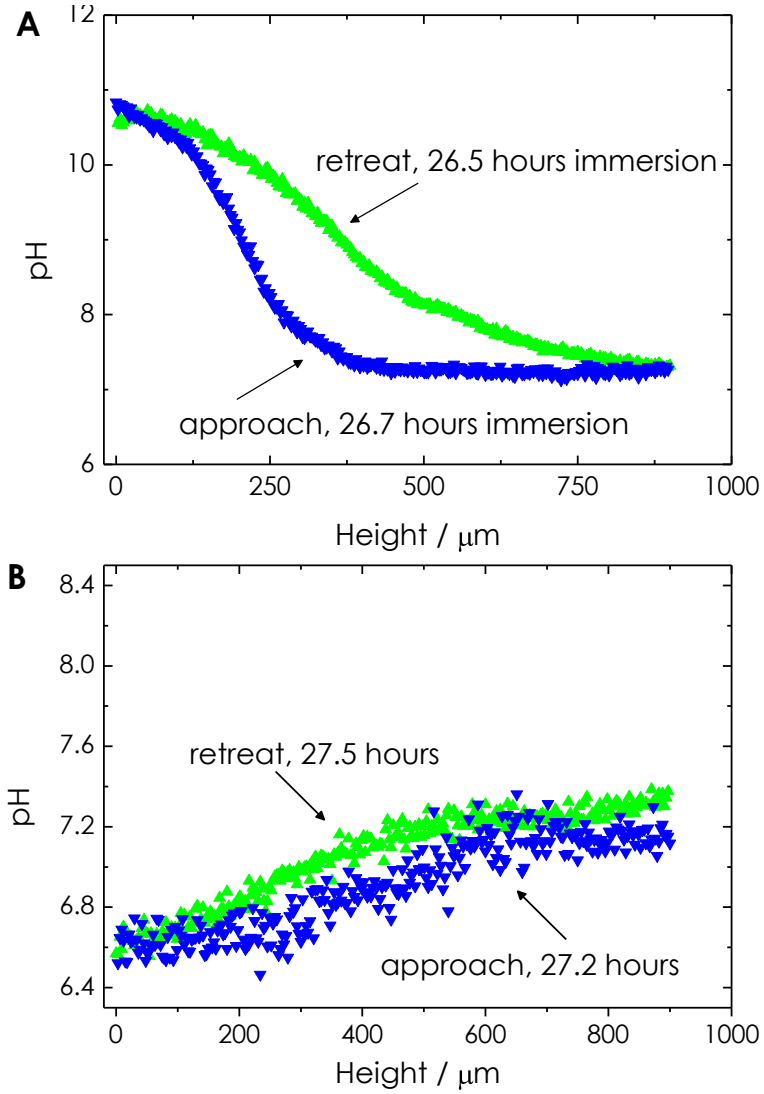

Figure 5.2.5. pH distributions above (A) iron and (B) zinc specimens measured with the antimony tip as the height of the tip is changed relative to the surface. The zinc-iron galvanic pair has been immersed in 0.1 M NaCl for the immersion times given in the graphs.

At shorter distances, a fast increase of pH values is observed as the tip continues approaching the iron surface until the initial value on the proximity of the metal is measured again. The two pH-distance curves obtained during retreat and subsequent approach of the tip to the surface thus describe a hysteresis loop. The origin of this feature can be attributed to the movement of the antimony tip that produces convective effects in the electrolyte. The slower decay of pH from the surface to the bulk electrolyte during the retreating movement happens because the tip leaves a hydroxide-rich region that constitutes the confined electrolyte volume formed between the tip and the iron surface for the previous 26 hours, and thus its movement is accompanied by a portion of this electrolyte that dilutes slower than the tip moves from the surface. This effect is less pronounced during the approach movement as the tip moves from a volume with very small concentration of hydroxide ions to much richer concentrations. The response time of most sensors is smaller in direction of concentration increase than in the opposite direction. The dilution effects due to tip movement are below the detection limit of the experimental technique in this case.

The spatial distribution of pH can be imaged when scan arrays are measured instead. They can be recorded either in a plane parallel to the surface, the arrays effectively being a composition of scan lines as that constituting Figure 5.2.3, or in a plane perpendicular to the surface. In the later case, the distribution of pH from the surface into the electrolyte is imaged instead. Figure 5.2.6 shows the pH distribution obtained above the iron sample. The map is composed by scan lines registered at different distances from the surface. Since the distance covered in each scan line is rather long to allow the pH distribution to be appreciated over a large area of the system, rather long acquisition times were required to measure each scan line, and they were registered only at some selected heights. Yet the spatial distribution of pH values from the surface into the bulk electrolyte can be clearly observed from the inspection of this image.

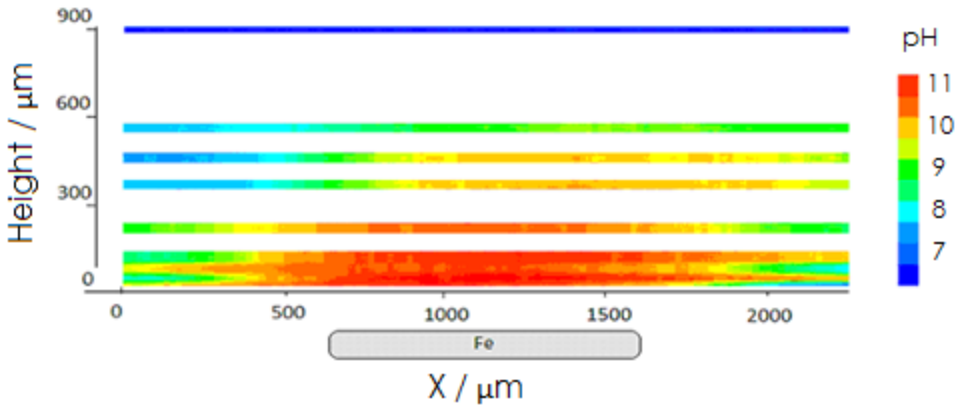

Figure 5.2.6. pH distribution in a plane perpendicular to the surface of the iron specimen 22 hours registered after the zinc-iron pair has been immersed in 0.1 M NaCl solution. Lateral scanning rate 5 µm s^{-1}. In order to shorten experimental time only 8 lateral scans at different distances were performed.

The pH distribution over the zinc sample was also investigated. The pH distribution over this metal looks almost homogeneous from the observation of the scan arrays, even for the longest exposures as shown in Figure 5.2.7. Nevertheless, some distribution of pH values occurs above the zinc sample when the data are plotted with greater resolution (cf. inset in Figure 5.2.3). Thus, some acidification happens in this case, though the magnitude of this effect is significantly smaller than the alkalization process occurring at the cathode.

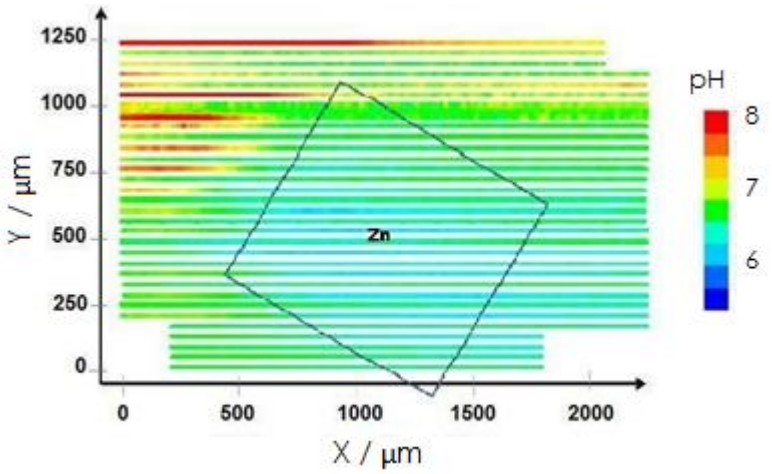

Figure 5.2.7. pH distribution in a plane parallel to the surface of the zinc specimen registered after the zinc-iron pair has been immersed in 0.1 M NaCl during 7 hours.

Furthermore, the pH distribution over the metal remains quite homogeneous over its whole surface. It is concluded that metal dissolution occurs at the surface of the zinc specimen according to reaction:

$$Zn \rightarrow Zn^{2+} + 2e^{-} \qquad (5.2.3)$$

The dissolution process does not produce a variation in the pH of the electrolyte as given by equation (3), unless a certain amount of the released metal ions undergo hydrolysis in the electrolyte as given by:

$$Zn^{2+} + nH_2O \rightarrow Zn(OH)_n^{2-n} + nH^{+} \qquad (5.2.4)$$

In this case, local acidification of the electrolyte would happen in the proximity of the zinc electrode.

Though the bulk electrolyte becomes progressively more alkaline with the elapse of time as shown above, the zinc surface remains slightly more acidic than the bulk even after 27 hours. This fact can be easily observed from the retreat and subsequent approach plots shown in Figure 5.2.5B, which were measured with the tip located above the center of the zinc specimen. The small concentration variations occurring in this case are not significantly affected by the mechanical movement of the tip, and both plots lie very close to each other.

5.2.6. Conclusions

The use of an antimony microelectrode as tip in a scanning electrochemical microscope greatly enhances the information gathered on corrosion reactions by allowing the spatial distribution of pH to be imaged (quasi) simultaneously to the conventional amperometric operation of the instrument in the generation-collection mode. This new methodology can be used to investigate a wide variety of corrosion systems, though its most immediate application can be found in the characterization of the sacrificial protection imparted by zinc to iron-base alloys in general, and to galvanized steels in particular.

5.2.7. References.

1. S.E. Pust, W. Maier, G. Wittstock. Zeitschrift für Physikalische Chemie 222 (2008) 1463.
2. L. Niu, Y. Yin, W. Guo, M. Lu, R. Qin, S. Chen. Journal of Materials Science 44 (2009) 4511.
3. R.M. Souto, S. Lamaka, S. González. In: Microscopy: Science, Technology, Applications and Education, Vol. 3 (Edited by A. Méndez-Vilas, J. Díaz). Formatex Research Center, Badajoz, 2010, p. 2162.
4. Y. González-García, G.T. Burstein, S. González, R.M. Souto. Electrochemistry Communications 6 (2004) 637.
5. C.H. Paik, H.S. White, R.C. Alkire. Journal of the Electrochemical Society 147 (2000) 4120.
6. C.H. Paik, R.C. Alkire. Journal of the Electrochemical Society 148 (2001) B276.
7. K. Fushimi, M. Seo. Electrochimica Acta 47 (2001) 121.
8. R.M. Souto, Y. González-García, S. González. Corrosion Science 47 (2005) 3312.
9. A.M. Simoes, D. Battocchi, D.E. Tallman, G.P. Bierwagen. Corrosion Science 49 (2007) 3838.
10. S. González, J.J. Santana, Y. González-García, L. Fernández-Mérida, R.M. Souto. Corrosion Science 53 (2011) 1910.
11. A.C. Bastos, A.M. Simões, S. González, Y. González-García, R.M. Souto. Electrochemistry Communications 6 (2004) 1212.
12. A.M. Simões, A.C. Bastos, M.G. Ferreira, Y. González-García, S. González, R.M. Souto. Corrosion Science 49 (2007) 726.
13. R.M. Souto, L. Fernández-Mérida, S. González. Electroanalysis 21 (2009) 2640.
14. J.J. Santana, J. González-Guzmán, L. Fernández-Mérida, S. González, R.M. Souto. Electrochimica Acta 55 (2010) 4488.
15. Y. Gonzalez-Garcia, J.M.C Mol, T. Muselle, I. De Graeve, G. Van Assche, G. Scheltjens, B. Van Mele, H. Terryn. Electrochemistry Communications 13 (2011) 169.

16. B. Horrocks, M.V. Mirkin, D.T. Pierce, A.J. Bard, G. Nagy, K. Toth. Analytical Chemistry 65 (1993) 1213.
17. B. Kovács, B. Csóka, G. Nagy, I. Kapui, R.E. Gyurcsányi, K. Tóth. Electroanalysis 11 (1999) 349.
18. B. Liu, W. Cheng, S.A. Rotenberg, M.V. Mirkin. Journal of Electroanalytical Chemistry 500 (2001) 590.
19. B. Csóka, B. Kovács, G. Nagy. Biosensors and Bioelectronics 18 (2003) 141.
20. T. Honda, K. Murase, T. Hirato, Y. Awakura. Journal of Applied Electrochemistry 28 (1998) 617.
21. F.L. Rosenfeldt, R. Ou, J.A. Smith, D.E. Mulcahy, J.T. Bannigan, M.R. Haskard. Journal of Medical Engineering and Technology 23 (1999) 119.
22. A.N. Ivanov, G.A. Evtugyn, R.E. Gyurcsányi, K. Tóth, H.C. Budnikov. Analytica Chimica Acta 404 (2000) 55.
23. F. Sjöberg, G. Nilsson. Acta Anaesthesiologica Scandinavica 44 (2000) 32.
24. Y. Tsuru, M. Nomura, F.R. Foulkes. Journal of Applied Electrochemistry 32 (2002) 629.
25. Y. Ha, M. Wang. Electroanalysis 18 (2006) 1121.
26. M. Wang, Y. Ha. Biosensors and Bioelectronics 22 (2007) 2718.
27. A. Avdić, A. Lugstein, C. Schöndorfer, E. Bertagnolli. Applied Physics Letters 95 (2009) 223106.
28. W. Vonau, W. Oelßner, U. Guth, J. Henze. Sensors and Actuators B 144 (2010) 368.
29. N. Radić, H.B. Mark Jr. Analytica Chimica Acta 144 (1982) 253.
30. P.J. Kinlen, J.E. Heider, D.E. Hubbard. Sensors and Actuators B 22 (1994) 13.
31. R.E.F. Einerhand, W.H.M. Visscher, E. Barendrecht. Electrochimica Acta 34 (1989) 345.
32. L.J. Bloor, D.J. Malcolme-Lawes. Journal of Electroanalytical Chemistry 278 (1990) 161.
33. M.J. Tarlov, S. Semancik, K.G. Kreider. Sensors and Actuators B 1 (1990) 293.
34. K. Yamamoto, G. Shi, T. Zhou, F. Xu, M. Zhu, M. Liu, T. Kato, J.-Y. Jin, L. Jin. Analytica Chimica Acta 480 (2003) 109.
35. M.F. Montemor, W. Trabelsi, S.V. Lamaka, K.A. Yasakau, M.L. Zheludkevich, A.C. Bastos, M.G.S. Ferreira. Electrochimica Acta 53 (2008) 5913.
36. S.V. Lamaka, M. Taryba, M.F. Montemor, H.S. Isaacs, M.G.S. Ferreira. Electrochemistry Communications 13 (2011) 20.
37. E. Tesarova, L. Baldrianova, S.B. Hocevar, I. Svancara, K. Vytras, B. Ogorevc. Electrochimica Acta 54 (2009) 1506.
38. V. Guzsvany, H. Nakajima, N. Soh, K. Nakano, T. Imato. Analytica Chimica Acta 658 (2010) 12.
39. H. Sopha, L. Baldrianova, E. Tesarova, S.B. Hocevar, I. Svancara, B. Ogorevc, K. Vytras. Electrochimica Acta 55 (2010) 7929.
40. R.M. Souto, Y. González-García, A.C. Bastos, A.M. Simões. Corrosion Science 49 (2007) 4568.

5.3

Development of solid contact micropipette Zn-ion-selective electrode for corrosion studies

5.3.1. Abstract

Micron-size ion-selective micropipettes can be used in scanning electrochemical microscopy (SECM). They can provide excellent spatial resolution. Unfortunately the resistance of these small sensors is high. Their application needs special shielding and slow scanning rates. Usually their lifetime hardly exceeds a few days.

Zinc layer or dispersed zinc particles containing films are often used for providing cathodic protection against corrosion in case of metal surfaces. Therefore in corrosion studies measurements of local zinc ion concentration can give important information about the nature of the process. SECM measuring tips are needed in corrosion studies to image concentration profiles of the Zn^{2+} ions evolved in surface processes. Solid contact micropipettes for selective measurements of Zn^{2+} ion concentration were prepared with tip size of a few micrometers following earlier work by Nagy and co-workers. The properties of the micropipettes were investigated. They were also used in SECM imaging. In this Section details of Zn^{2+} ion-selective microelectrodes preparation are described. Data about their properties, lifetime, resistance and ion activity response are shown. Preliminary findings using them in SECM imaging of zinc ion concentration profiles are shown. The improvement of scanning rate achieved by lowering tip resistance is a main advantage in potentiometric SECM.

5.3.2. Resumen

La microscopía electroquímica de barrido (SECM) permite el uso de micropipetas de ion selectivo de tamaño micrométrico como microelectrodos sensores. Éstas pueden aportar excelente resolución espacial. Desafortunadamente, la resistencia de estos pequeños sensores es alta. Sus aplicaciones requieren un blindaje especial y bajas velocidades de barrido. Normalmente su vida media apenas supera unos pocos días.

Con frecuencia las superficies metálicas se protegen catódicamente contra la corrosión mediante capas de cinc o películas que incluyen partículas de cinc. Por tanto, las medidas de la concentración local de iones cinc pueden dar información importante acerca de la naturaleza del proceso. Para los estudios de corrosión se necesitarían sondas que permitieran visualizar los perfiles de concentración de iones Zn^{2+} generados en los procesos superficiales. Con base a trabajos anteriores elaborados por el grupo del profesor Nagy en Pécs (Hungría), se han preparado micropipetas de contacto sólido de un tamaño de unos pocos micrómetros para medidas selectivas de ion Zn^{2+}. Se han investigado las propiedades de estas micropipetas y se han implementado en el microscopio SECM como sensores. En esta sección se describen los detalles de la preparación de estos microelectrodos selectivos de ion Zn^{2+}. Se muestran datos sobre sus propiedades, tiempos de vida, resistencia y respuesta frente a la actividad del ión. Se muestran también resultados preliminares de perfiles de concentración de ion cinc empleando estos sensores para su determinación por SECM. La mejora de la velocidad de barrido conseguida por la reducción de la resistencia del sensor es una ventaja primordial en el SECM potenciométrico.

5.3.3. Introduction

Zinc is a transition metal that has important roles in living organisms as well as in human technology. The functions of zinc in living objects are mainly related to enzymatic processes and DNA replication. In particular, the human hormone insulin contains zinc, and the human body contains a relatively high amount of zinc (ca. 2.3 g). Zinc is an important trace metal in human dietary. On the other hand, zinc is also contained in many technological applications including paints, batteries, pharmaceutical and other industrial products. And zinc-containing pollutants are often found in environmental samples. Therefore, analytical methods are needed for assessment of zinc concentration of dietary, environmental, industrial or biological samples. Numerous different methods developed for the analysis of zinc in various samples are available. Among them atom spectroscopic methods seem most popular. The zinc ion can be reduced on different electrodes, therefore voltammetric methods have also been successfully employed.

Due to the simplicity and cost effectiveness of potentiometry, several attempts have been made to develop zinc ion-selective electrodes (ISE). A zinc ISE made of plasticized PVC membrane containing 5,6-benzo-4,7,13,16,21,24-hexaoxa-1,10-diazabicyclo[8,8,8]hexacos-5-ene (BHDE) cryptandionophore has been reported [1]. This electrode was used for end point detection in complexometric titration as well as in the monitoring zinc ion occurrence in industrial wastewaters resulting from zinc electroplating processes. Another zinc electrode was fabricated using a porphyrin-based ionophore incorporated in a PVC matrix [2]. Up to now, most research groups working on the development of ion-selective zinc electrodes aimed the environmental, clinical or dietary analysis as potential application fields for their new sensors. But due to the complexity and low zinc concentration of these matrices it has been a difficult task to find appropriate ionophores to produce zinc ISEs that will function well for those samples. Therefore, still further work is needed in this area in order to improve the selectivity and dynamic range of analysis properties of the resulting zinc-selective electrodes.

An emerging field for the application of zinc ion-selective electrodes is found in Corrosion Science [3]. Zinc layers or films containing dispersed zinc particles are often used for providing cathodic protection against corrosion in case of metal surfaces. Indeed, spatially-resolved investigations of the corrosion processes occurring when iron and zinc surfaces are put in galvanic contact have already been performed by using the scanning vibrating electrode technique (SVET) [4-6], and the scanning electrochemical microscope (SECM) [7]. By carrying out experiments in different ionic solutions, consistent results were obtained for the corrosion of iron, but significant differences were observed concerning the detection of zinc corrosion. This arises from the low overpotential for oxygen reduction and water decomposition exhibited by the materials used as tips in SECM, and these reactions overlap the amperometric reduction of zinc ions [8]. It is thus expected that

the use of a selective zinc concentration detecting tip could be very helpful in these corrosion studies.

Scanning electrochemical microscopy (SECM) is a powerful technique for the local investigation of reactions occurring at surfaces as those responsible for corrosion [9-12]. The technique is based on the combined application of high-resolution measurement tip positioning devices, appropriate computer controlled measurement and data collection routines, and computerized image formation or evaluation software. The SECM can provide high-resolution images containing chemical information on surface processes [3,13,14] and concentration profiles of different species in the liquid phase in close vicinity to interfaces [15-17]. So far, most of the SECM studies employ a voltammetric ultramicroelectrode as data collecting measuring tip while the electrochemical system operates in amperometric mode. However in many cases, an ion-selective electrode measuring tip and operation of the SECM in the potentiometric mode would be a better choice. The local concentration of a species presenting no electroactivity in the accessible potential window can be measured with the appropriate ion-selective electrode. And its greater selectivity, which is superior to amperometry, is also often required. In an earlier work [18], images displaying zinc ion concentration profiles over small size zinc ion diffusion sources as well as over electrochemical zinc ion sinks were recorded with a micropipette type zinc ISE. Very recently, a new Zn^{2+}-selective microelectrode developed for the determination of the Zn^{2+} species released in the course of corrosion processes has been described [19].

Ion-selective micropipette electrodes are well known sensors and are broad scale used in experimental life sciences [20,21]. Their main advantage is that they can be made with very small measurement tip with diameter often in the nm range. Their preparation procedure is quite universal, and depending on the composition of the measurement "cocktail", several types of electrodes can be prepared by the same procedure. Unfortunately, the ion-selective micropipettes are very fragile devices sensitive to mechanic effects and electric shocks. Their lifetime is seldom longer than a few days. They need special care during handling, and noise filtering during measurements. Furthermore, their very high electrical resistance severely hinders them to be used in SECM. In this technique, the measuring probe travels stepwise at a programmed scan rate over the surface under study. At each location it takes a signal reflecting the ion activity there. The higher the resistance the longer time is needed for achieving steady signal at each place. Slower scanning rates are thus needed to attain reliable images when the resistance is higher. Additionally, bigger resistances result in more electric noise disturbing the measurements. For the interested reader, a detailed discussion concerning the problems and difficulties of ion-selective SECM can be found elsewhere [22].

On the other hand, a novel type of micropipette ion-selective electrodes has been recently developed [23,24]. In this electrode, the internal reference electrode has been replaced by a thin carbon fiber coated by a conductive polymer film, which is dipped into the ion-selective cocktail. In this way, the resistance of the electrode was greatly reduced at the same time that its lifetime was dramatically

improved. The properties of these novel ammonium [23] and potassium [24] selective micropipettes and their application in SECM have been reported. These new micropipette ISEs may be considered for the use of potentiometric SECM in the investigation of processes of interest in Corrosion Science. This Section describes the preparation of ion-selective zinc micropipettes provided with solid contact, together with the results obtained during the investigation of their properties. Preliminary data on the corrosion of zinc obtained with the SECM technique using these zinc ion-selective electrode tips are also given.

5.3.4. Experimental

5.3.4.1. Materials, instruments and methods

Chemicals in this Section were used as received, namely: high molecular weight poly(vinyl chloride), potassium tetrakis(4-chlorophenyl)borate (KTFPB), and 2-nitrophenyl octyl ether (OPOE) from Fluka; tris(hydroxymethyl)aminomethane buffer from Merck; tetrahydrofuran from Interkemia. The conductive polymer used to coat the carbon fiber was produced from the monomer, 3,4-ethylenedioxythiophene (EDOT) supplied by H.C. Starck. The electropolymerization process was carried out in 1-butyl-3-methylimidazolium hexafluorophosphate (BMIM PF_6^-) ionic liquid solvent from Solvent Innovation. The other chemicals not mentioned here were of analytical grade. The N-phenyliminodiacetic acid bis-N',N'-dicyclohexylamide zinc ionophore used in the ISMEs was synthesized as described elsewhere [25]. All solutions were prepared using deionized water.

The 33 µm diameter carbon fibers were a generous gift of Specialty Materials (Massachusetts, USA), and borosilicate glass capillaries (types: B100-50-10 and B200-116-10) were purchased from Sutter Instrument (Novato, CA, USA).

A battery-powered voltage follower based on TL082 operational amplifier was used for all potentiometric measurements. Its output was connected to a digital multimeter (METEX M-3630D Digital Multimeter). The cell voltage data were collected with a PC through a multimeter using the commercial program supplied for the METEX. A home built scanning electrochemical microscope was employed in this [26]. It is based on a 3D positioning device driven by precision step motors with 75 nm minimal step size. The distance between the ISME and the substrate was established by allowing the probe to gently rest on the sample, and subsequently the probe was retracted to the chosen operation distance with the aid of the Z-positioning motor.

Ag/AgCl reference electrodes in quasi-reference configuration were employed in the polymerization, potentiometric and SECM experiments, whereas a platinum wire was used as the auxiliary electrode during the preparation of the electropolymerized coating for the carbon fiber.

5.3.4.2. Preparation of the micropipette electrodes

The micropipette electrodes were made of two parts as shown in Figure 5.3.1. The glass pipette with broader internal diameter holds the cocktail, and the thinner one is inserted into the lumen of the first. The carbon fiber that provides the internal contact is inside at the tip of the thinner pipette, whereas a thin copper wire is inserted into the lumen. Mercury or silver epoxy paste provides electric contact between the carbon fiber and the copper wire. The internal part of the electrode assembly is reusable, i.e. it can be inserted into a new outer part when the previously used gets damaged.

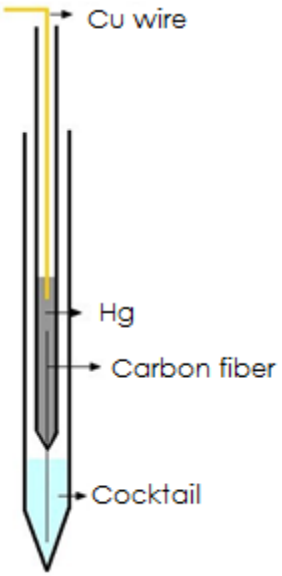

Figure 5.3.1. The structure of the micropipette electrode.

In preparation of the micropipette electrodes, borosilicate glass capillaries of two different internal diameters (types: B100-50-10 and B200-116-10, Sutter Instruments) were selected and checked that their diameters would fit. The capillaries were soaked in "piranha solution" of concentrated sulfuric acid: hydrogen peroxide (30%) 1:1 volume. Next, they were thoroughly washed with double deionized water and ethanol, and dried in oven at 105 °C. Micropipettes were pulled from both sizes of capillaries by using a pipette puller (Sutter Instruments, type P-30, Novato, CA, USA). The 33 μm diameter carbon fiber was inserted in the lumen of the thinner capillary with the fiber reaching out for about 15 mm, and about 20 mm long in the lumen. Loctite adhesive was used for sealing. Mercury metal or Amepox silver epoxy paste (Amepox Microelectronics, Ltd. Poland) and the copper wire were then inserted into the lumen of the thin pipettes as shown in Figure 5.3.1. At this point the inner section of the electrode assembly is ready for the electropolymerization of EDOT over the portion of the carbon fiber reaching out from the tip.

The tip of the larger diameter pipette was provided with a hydrophobic layer using dichlorodimethylsilane (Fluka) by using a simple procedure. Namely, the tip of the micropipette is introduced into a small amount quantity of 5% solution of

dichlorodimethylsilane in carbon tetrachloride into the tip of the micropipettes, and they were subsequently kept in oven (80 °C) for about half an hour inside a closed Petri dish. The finished pipettes were stored on the Petri dish at room temperature until use. The zinc ion-selective cocktail can be backfilled into the tip shortly before the assembly of the electrodes in the measuring device. In this way, a 5-10 mm long cocktail column is formed at the tip end of the pipettes.

The zinc ion-selective cocktail was made having the following composition: 5% zinc ionophore, 1.8% K-tetrakis (4-chlorophenyl) borate hydrophobic additive, 13% PVC matrix, 80% 2-nitrophenyloctylether (2-NPOE) plasticizer solvent, and 0.2% tetrahydrofurane diluting solvent 0.2%. Mechanical stability was attained with further additions of PVC in the case of bigger pipette orifices.

5.3.5. Results and discussion

The voltage divider method was used to measure the internal resistance (R_{ISME}) of the cell containing the zinc micropipettes. A high ohmic resistance resistor (R_k, 100 MΩ) was selected for these studies, and the OCP of the cell containing the quasi reference and the zinc ion-selective electrodes was recorded. After attaining a steady reading, resistance R_k was switched in as a load, and the transient of the voltage drop,

$$\Delta U = OCP \; - \; U_k \tag{5.3.1}$$

was determined. Assuming that R_k and R_{ISME} are much bigger than any other resistances in the circuit, equation (5.3.2):

$$R_{ISME} = \frac{\Delta U \cdot R_k}{U_k} \tag{5.3.2}$$

can be used to calculate R_{ISME}, where U_k is the steady voltage value established after switching in the resistor R_k. The average of three $\Delta U/U_k$ data pairs was used in every case. Values in the range of 40.9 MΩ mm^{-1} were found for the resistance R_{ISME}, and they depended on the tip diameter of the electrode. As it was observed earlier with potassium [24] and ammonium [23] micropipettes, the resistance of the solid contact micropipettes were just a fraction of those exhibited by micropipettes of the same size fabricated using the "conventional" procedures. In this Section, the new Zn ion-selective electrodes were fabricated using the optimized design for minimum internal resistance developed in previous work [23].

Figure 5.3.2 shows a typical recording obtained during the resistance measurements for an ISE electrode presenting a tip diameter of about 3 µm. When the resistor was connected in parallel to the cell is indicated by "on" in the figure, whereas the instant when it was disconnected has been indicated by "off", respectively. The shape of the curve corresponds to the initial purely resistive

response of the system, whereas a non-linear behaviour is observed from the transport characteristics of the membrane when the external resistor was switched off. This behaviour was also observed for potassium [24] and ammonium [23] selective electrodes, and corresponds to one of the two situations described in the pioneer work of ref. [27].

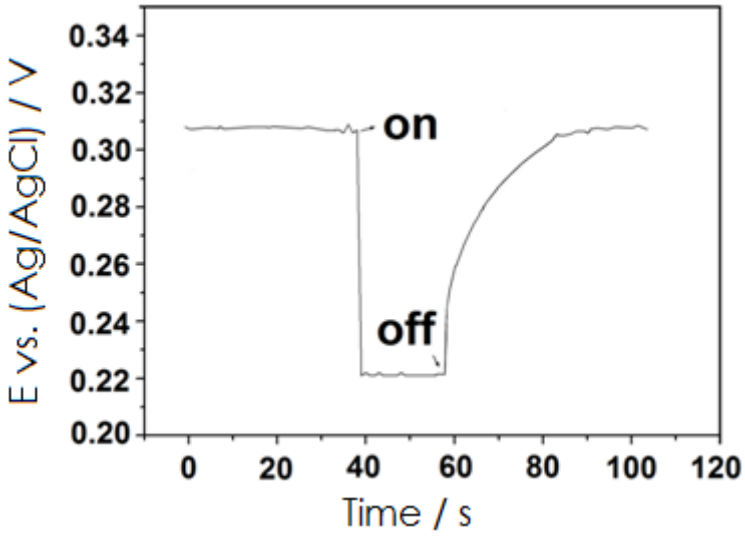

Figure 5.3.2. Cell voltage vs. time recording obtained during the measurement of the electrode resistance.

The concentration dependence of the electrode potential was checked using solutions of varying concentration. The obtained calibration curve is shown in Figure 5.3.3. As it can be seen the response exhibits close Nernstian slope in the concentration range of 10^{-4} to 10^{-1} M. In order to investigate the potential stability of the zinc micropipettes, the freshly made electrodes were inserted in the measurement cell containing 0.1 M tris(hydroxymethyl)aminomethane buffer with the different zinc ion concentrations. By monitoring the cell potential, the electric noise sensitivity and the potential stability were also observed. When the measurements were made outside the Faraday cage, the electric noise sensitivity was checked. The drift was then determined as the slope ΔE / Δt of the electrode potential - time dependence. Usually a 0.05-0.08 mV min^{-1} drift was observed for the freshly prepared electrodes when measured after a few minutes of their introduction in the solutions for zinc concentrations between 0.1-10 mM.

The applicability of the zinc micropipettes in SECM studies was checked after a small size zinc ion source was prepared and introduced through a hole in the bottom of the SECM measurement cell. This was prepared from a glass micropipette, the tip of which was blocked by an agar gel plug. The pipette was filled with 0.1 M $ZnSO_4$ solution and the measuring cell was filled with a 0.1 M KCl supporting electrolyte solution. The zinc ion-selective tip was moved upwards and downwards in relation to the investigated sample, and also parallel to the surface both above and

in the vicinity of the diffusion zinc source. In this way, the local electrode potential values were recorded at different locations. The variation of the electrode potential with the tip-substrate distance recorded above the center of the source in case of tip traveling in vertical direction can be seen in Figure 5.3.4. At 0 µm distance the tip almost touched the source plug. Calibration curve was used for transforming the electrode potential readings to concentration values. The corresponding zinc ion concentration vs. distance plot is depicted in Figure 5.3.4 as well.

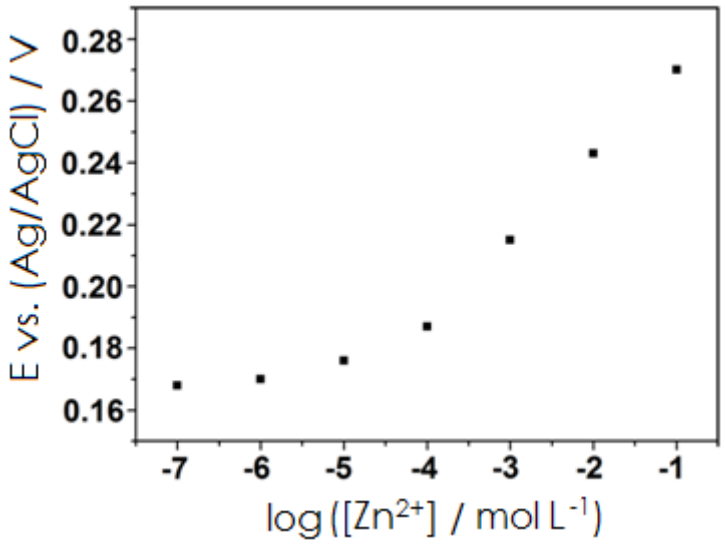

Figure 5.3.3. Plot of the electrode potential vs. log zinc concentration obtained with a solid contact zinc ion-selective electrode. Electrode tip diameter: 7 µm; slope in the 10^{-4} to 10^{-1} range: 27.7 mV decade^{-1}.

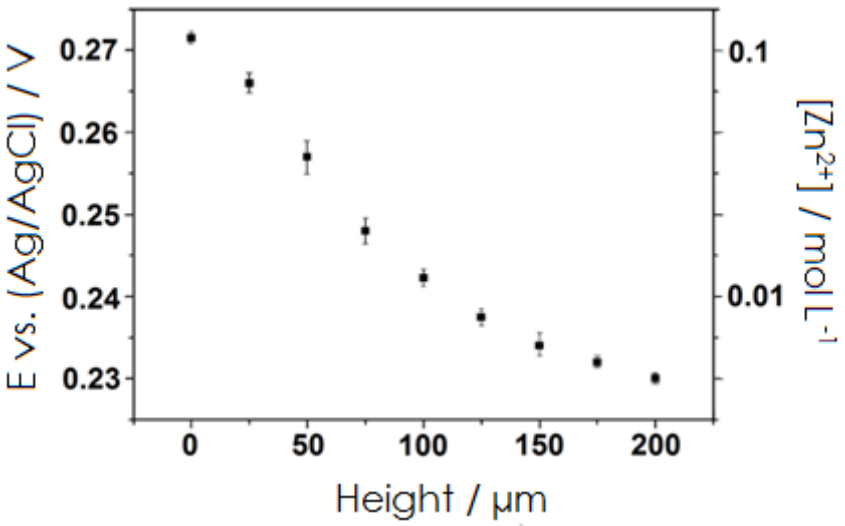

Figure 5.3.4. Effect of the tip-substrate distance on the electrode potential and the corresponding Zn ion concentration when a zinc ion-selective measuring tip (diameter 7 µm) was scanned above the center of a disc-shaped diffusing zinc source.

Analogously, Figure 5.3.5 shows the electrode potential recorded when an ISE tip (about 7 µm diameter) was scanned at the constant height of 150 µm above a 50 µm diameter source disc acting as the source for zinc ions. Though the potential curve shows some broadening beyond the limits of the ion source due to the smaller size of the probe compared to the active area of the metal, and it is sensed at the rather large distance between the measuring tip and the surface employed, the actual location of the source is satisfactorily imaged.

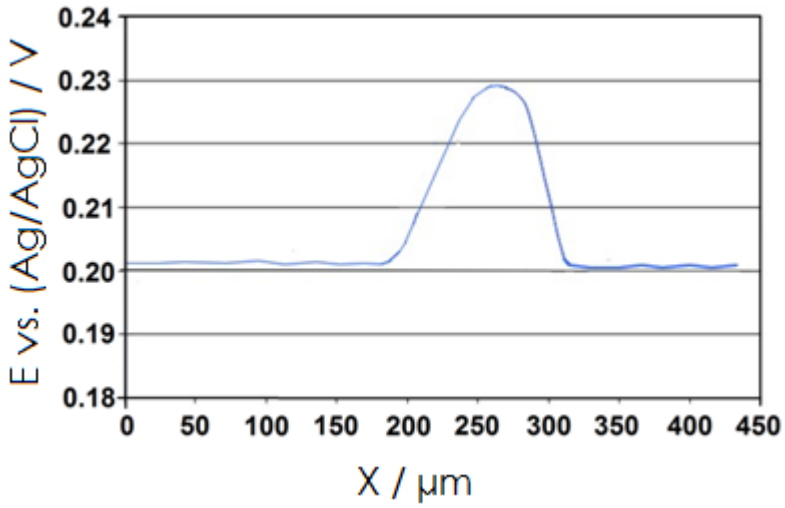

Figure 5.3.5. Electrode potential versus lateral distance plot recorded with a zinc ion-selective measuring tip (diameter 7 µm) scanned over a disc shaped diffusion zinc source of 50-100 µm. Scan rate: 5 µm s^{-1}.

The low resistance ion-selective measuring tip was developed for application in corrosion studies. In those studies SECM images are recorded over electrically connected as well as insulated iron and zinc surfaces. An one-dimension zinc electrode potential - horizontal distance image is shown in Figure 5.3.6. This curve was recorded when the electrode was scanned over a flat surface containing a small size zinc disc in direct electric contact with an iron surface disc, both inserted in an epoxy resin holder. Electric contact was established at the back of the sample. The detection of Zn ionic species is clearly detected when the ISE tip passed above the zinc disc, whereas no signal could be measured either above the surrounding epoxy resin or the iron disc. A more detailed analysis of the zinc-iron galvanic corrosion with the use of these zinc ISMEs will be presented in Section 5.4 of this Thesis. The relevance of this observation towards further use of SECM in corrosion investigations can be understood when it is considered that previous studies based on the amperometric operation of the SECM only allowed for the detection of the cathodic half reaction occurring over the iron sample measured as the local depletion of dissolved oxygen in the vicinity of the metal [7].

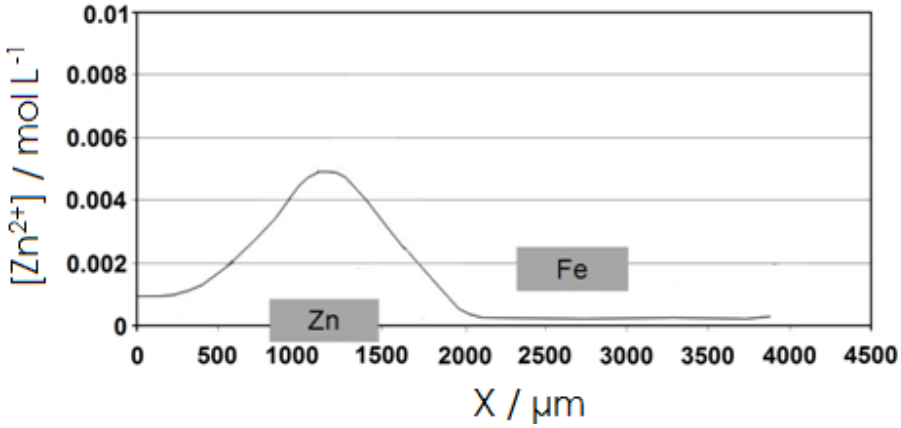

Figure 5.3.6. Horizontal line scan displaying the variation of the zinc concentration obtained by evaluating electrode potential values measured at the ISE tip when travelling above a Zn-Fe galvanic couple immersed in 0.1 M KCl. Scan rate: 5 µm s^{-1}.

5.3.6. Conclusion

Low resistance zinc ion-selective micropipette electrodes were prepared for corrosion studies. The electrodes contain electrochemically prepared PEDOT conductive polymer coated carbon fiber as solid contact. Using this design the electrode resistance could be significantly lowered, which allows faster scanning rates to be used in SECM applications. It is expected that the operation and storage stability of these newly developed zinc electrodes will be much higher than those of the "conventional" micropipettes based on the improved behaviour shown by similar regarding similar potassium and ammonium selective electrodes [23,24]. These electrodes can be prepared with tip sizes of a few micrometers. The preliminary results obtained in studying their analytical properties and their use as probes in potentiometric SECM operation proved their applicability.

5.3.7. References

1. H.A. Zamani, M.R. Ganjali, M.J. Pooyamanesh. Journal of the Brazilian Chemistry Society 17 (2006) 149.
2. V.K. Gupta, D.K. Chauhan, V.K. Saini, S. Agarwal, M.M. Antonijevic, H. Lang. Sensors 3 (2003) 223.
3. S.V. Lamaka, R.M. Souto, M.G.S. Ferreira. In: Microscopy: Science, Technology, Applications and Education, Vol. 3 (Edited by A. Méndez-Vilas, J. Díaz). Formatex Research Center, Badajoz, 2010, p. 2162.
4. K. Ogle, S. Morel, D. Jacquet. Journal of the Electrochemical Society 153 (2006) B1.

5. R.M. Souto, Y. González-García, A.C. Bastos, A.M. Simões. Corrosion Science 49 (2007) 4568.
6. A.M. Simões, J. Torres, R. Picciochi, J.C.S. Fernandes. Electrochimica Acta 54 (2009) 3857.
7. A.M. Simões, A.C. Bastos, M.G. Ferreira, Y. González-García, S. González, R.M. Souto. Corrosion Science 49 (2007) 726.
8. Y. González-García. Degradation of Anticorrosive Polymeric Coatings Applied on Metallic Materials: Electrochemical and Nanoscopic Research. Ph.D. Thesis, University of La Laguna, 2007, Ch. 5.
9. S.E. Pust, W. Maier, G. Wittstock. Zeitschrift für Physikalische Chemie 222 (2008) 1463.
10. L. Niu, Y. Yin, W. Guo, M. Lu, R. Qin, S. Chen. Journal of Materials Science 44 (2009) 4511.
11. Y. González-García, J.J. Santana, J. González-Guzmán, J. Izquierdo, S. González, R.M. Souto. Progress in Organic Coatings 69 (2010) 110.
12. R.M. Souto, S.V. Lamaka, S. González. In: Microscopy: Science, Technology, Applications and Education, Vol. 3 (Edited by A. Méndez-Vilas, J. Díaz). Formatex Research Center, Badajoz, 2010, p. 1796.
13. Y. González-García, G.T. Burstein, S. González, R.M. Souto. Electrochemistry Communications 6 (2004) 637.
14. J.J. Santana, J. González-Guzmán, L. Fernández-Mérida, S. González, R.M. Souto. Electrochimica Acta 55 (2010) 4488.
15. A.C. Bastos, A.M. Simões, S. González, Y. González-García, R.M. Souto. Electrochemistry Communications 6 (2004) 1212.
16. C. Gabrielli, E. Ostermann, H. Perrot, V. Vivier, L. Beitone, C. Mace. Electrochemistry Communications 7 (2005) 962.
17. E. Volker, C.G. Inchauspe, E.J. Calvo. Electrochemistry Communications 8 (2006) 179.
18. Ch. Wei, A.J. Bard, G. Nagy, K. Tóth. Analytical Chemistry 67 (1995) 1346.
19. A.C. Bastos, M.G. Taryba, O.V. Karavai, M.L. Zheludkevich, S.V. Lamaka, M.G.S. Ferreira. Electrochemistry Communications 12 (2010) 394.
20. M.A. Messerli, L.P. Collis, P.J.S. Smith. Biophysical Journal 96 (2009) 1597.
21. M.A. Messerli, L.P. Collis, P.J.S. Smith. Electroanalysis 21 (2009) 1906.
22. G. Denuault, G. Nagy, K. Toth. In: Scanning Electrochemical Microscopy (Edited by A.J. Bard, M.V. Mirkin). Marcel Dekker, New York, 2001, Ch. 10.
23. G. Gyetvai, S. Sundblom, L.Nagy, A. Ivaska, G. Nagy. Electroanalysis 19 (2007) 1116.
24. G. Gyetvai, L. Nagy, A. Ivaska, I. Hernadi, G. Nagy. Electroanalysis 21 (2009) 1970.
25. E. Lindner, M. Horváth, K. Tóth, E. Pungor, I. Bitter, B. Ágai, L. Tõke. Analytical Letters 25 (1992) 453.
26. B. Csóka, B. Kovács, G. Nagy. Biosensors and Bioelectronics 18 (2003) 141.
27. D. Amman, E. Pretsch, W. Simon, E. Lindner, E. Bezegh, E. Pungor. Analytica Chimica Acta 171 (1985) 119.

5.4

Scanning electrochemical microscopy for the investigation of corrosion processes: measurement of Zn^{2+} spatial distribution with ion-selective microelectrodes

5.4.1. Abstract

Ion-selective microelectrodes can be employed as tips in scanning electrochemical microscopy (SECM) for chemical imaging of corrosion processes. They present higher chemical selectivity than conventional amperometric microdisks, and may be the only effective option to visualize the dissolution of metals with negative redox potentials in aqueous environments when the use of Pt microelectrodes is limited by the onset of oxygen reduction and hydrogen evolution reactions. A robust micro-sized ion-selective electrode has been developed which allows the spatial distribution of Zn^{2+} during galvanic corrosion of a model Zn-Fe couple to be investigated using SECM. Owing to the low internal contact potential achieved with the novel design, the resistance of the micropipette electrodes is only fractions of the resistance of conventional micropipette electrodes of the same size. As a result, no special shielding of the microelectrodes is required and higher scanning rate can be used for scanning in the potentiometric modes using these micropipette tips. Concentration profiles over corroding surfaces measured with this technique will be presented.

5.4.2. Resumen

Los microelectrodos de ion selectivo pueden ser empleado como sensores (puntas) en microscopía electroquímica de barrido (SECM) para la visualización de procesos corrosivos. Éstas presentan mayor selectividad química que los microdiscos amperométricos convencionales, y pueden ser la única opción efectiva cuando el uso de microelectrodos de Pt está limitado en ambientes acuosos debido al inicio de las reacciones de reducción de oxígeno y generación de hidrógeno, cuando es necesario recurrir a potenciales redox muy negativos para la visualización de la disolución del metal de interés. Se ha desarrollado un electrodo de ión selectivo de escala micrométrica que permite investigar la distribución de Zn^{2+} durante la corrosión galvánica de un par Zn-Fe usando SECM. Debido al bajo potencial de contacto interno conseguido con el nuevo diseño, la resistencia del microelectrodo de ion selectivo es sólo una fracción de la resistencia de electrodos de micropipeta convencional de tamaño similar. Como resultado, no se requiere una especial protección de estos microelectrodos y pueden usarse velocidades de barrido mayores en modo potenciométrico. Se presentan aquí los perfiles de concentración medidos con esta técnica sobre superficies bajo corrosión.

5.4.3. Introduction

Scanning electrochemical microscopy (SECM) has become a powerful technique for studying the complex processes involved in Corrosion Science due to its ability to image the topography and to probe chemical reactivity in micrometer- and submicrometer-sized dimensions [1-4]. The use of an ultramicroelectrode (UME) that is scanned across the surface of a sample, allows interfaces to be characterized with spatial resolution whereas almost any kind of electrochemical measurement can be performed at the SECM tip and at the substrate surface. To date, SECM has found application in the detection of precursor sites [5-7] and the visualization of metastable regime [8] for pitting corrosion, the characterization of the chemical stability of thin surface films [9-12] and organic coatings applied on metals [13-26], the detection of metal and inclusion dissolution [25-27], the recognition of anodic and cathodic areas [28,29], hydrogen permeation [30], etc. These studies have supplied valuable information using metal microdisks as the tip, and amperometric operation of the SECM. That electrochemical information is derived from the measurement of the faradaic current flowing through the ultramicroelectrode tip as a function of either time or its position above the sample. Yet, limited application of this technique occurs when more than one chemical species can simultaneously react at the microdisk tip, thus compromising chemical selectivity [31], and when the species sensed at the tip reacts with it, giving rise to changes in the surface condition and composition of the material. Thus, there is need for new techniques and procedures in SECM that may provide greater selectivity for chemical imaging of corrosion processes.

Scanning electrochemical microscopy can also be operated in a potentiometric mode by employing an ion-selective microelectrode (ISME) as the tip [32-35]. They present higher chemical selectivity than conventional amperometric microdisks, and may be the only effective option to visualize the dissolution of metals with negative redox potentials in aqueous environments when the use of Pt microelectrodes is limited by the onset of oxygen reduction and hydrogen evolution reactions [36,37]. However a quick survey of the scientific literature concerning the use of SECM, serves to observe that the potentiometric method has been applied rather scarcely compared to conventional amperometric modes. The reason for this situation arises from the fragility, very high resistance and limited stability exhibited by the ISMEs, which require careful shielding of the electrochemical cell to improve the signal to noise ratio, and very slow scanning rates to account for their rather long response time. The resistance value in an ISME arises from the relatively thick organic cocktail layer and liquid contact between the ionophore containing cocktail and the filling solution of the inner reference. This is the reason that the potentiometric SECM has been almost completely limited to pH monitoring by using solid state microelectrodes based on the characteristics of certain oxides of transition metals, or solid state chloride electrode [32,38-40].

The situation has greatly changed due to the development of robust micro-sized ion-selective electrode containing a solid contact between the ionophore and the inner reference solution [41,42]. Owing to the low internal contact potential and smaller membrane thickness achieved with the novel design, the resistance of the micropipette electrodes are only fractions of the resistance of conventional micropipette electrodes of the same size. As a result, no special shielding of the microelectrodes is required and higher scanning rate can be employed in the potentiometric mode using micropipette tips. In the previous Section 5.3, the fabrication of a novel solid contact micropipette ion-selective microelectrode for Zn^{2+} ions has been presented. Since zinc is a metal widely employed in our technological society, the corrosion of this metal in aqueous environments has been extensively investigated up to now. In particular, the role of corrosion products to inhibit the cathodic reaction and the possibility of additional self-healing effects for corrosion protection due to additives in the composition of the metal alloy or arising from surface treatments, are a hot research topic in the case of galvanized steels [43-46]. To understand the role of corrosion products of galvanized steels, it is necessary to measure the concentration distributions of Zn^{2+} and OH^- ions in the solution above the surface. Whereas pH monitoring is already available using the SECM [38-40], the measurement of the distribution of the metal ions was not possible with this technique until now.

The present study investigated the applicability of a solid contact Zn^{2+}-ISME to measure the spatial concentration distribution of dissolved zinc over corroding surfaces measured with SECM operated in potentiometric mode

5.4.4. Experimental

5.4.4.1. Samples

The substrate consisted of 99.5% purity iron and 99.95% purity zinc surfaces mounted into an epoxy resin sleeve, such that only an 1 x 1 mm^2 square end surface formed the testing metal substrates. The separation between the two metals was 5 mm. These metals were supplied as sheets of thickness 1 mm by Goodfellow Materials Ltd. (Cambridge, UK). The front side of the mounts was grinded with silicon carbide paper down to 4000 grit, and followed by a polishing step with 0.3 μm alumina slurries. Samples were then washed thoroughly with ultra-pure deionized water and allowed to dry in air. The corrosive medium was 10 mM NaCl solution in contact with air, quiescent and at ambient temperature.

5.4.4.2. Zn^{2+}-ion selective microelectrodes

The ion-selective cocktail was prepared using was N-phenyliminodiacetic acid bis-N',N'-dicyclohexylamide as zinc ionophore, potassium tetrakis(4-

chlorophenyl)borate (KTCPB), 2-nitrophenyl octhyl ether (NPOE) and PVC in tetrahydrofurane (THF). The composition of the mixture was: 57.7 wt.% NPOE, 3.6 wt.% Zn ionophore, 3.4 wt.% PVC, 1.3 wt.% KTCPB, and 34.0 wt.% THF. The synthesis of N-phenyliminodiacetic acid bis-N',N'-dicyclohexylamide zinc ionophore can be found in ref. [47].

Two different kinds of zinc ion-selective microelectrodes were prepared using micropipettes pulled from acid washed, and dried borosilicate glass-capillaries (B100-50-10 and B200-116-10; Sutter Instruments, Novato, CA, USA), namely solid contact and conventional microelectrodes. The conventional micropipette ion-selective electrodes were fabricated according to the established methodology [48,49], whereas the solid contact ion-selective microelectrodes were manufactured with the new procedure described in refs. [41,50]. In brief, these novel micropipette electrodes were made of two parts as shown in Figure 5.4.1A. Two micropipettes were pulled from glass-capillaries using a pipette puller, and subsequently silanized by introducing inside their tip a few microliters of 5% dimethyldichlorosilane solution in carbon tetrachloride. The hydrophobic layer was completed after heating the pipettes at 80 °C in an oven for about 30 min. The cocktail was backfilled into the tip through a very thin glass-capillary attached to the syringe needle used. The internal solid contact is provided by a PEDOT-coated carbon fiber of 33 µm diameter (obtained as a generous gift from Specialty Materials, Lowell, Massachusetts, USA) dipped in the cocktail. To ensure electric contact between the inner fiber and the copper wire for the connection of the ISME with the measuring instrument, mercury was introduced in the inner capillary as shown in Figure 5.4.1A. Conventional micropipette electrodes used an internal filling solution (0.25 M potassium chloride containing 10 mM $ZnCl_2$) in contact with the cocktail and a chloride coated silver wire introduced as internal reference electrode as depicted in Figure 5.4.1B.

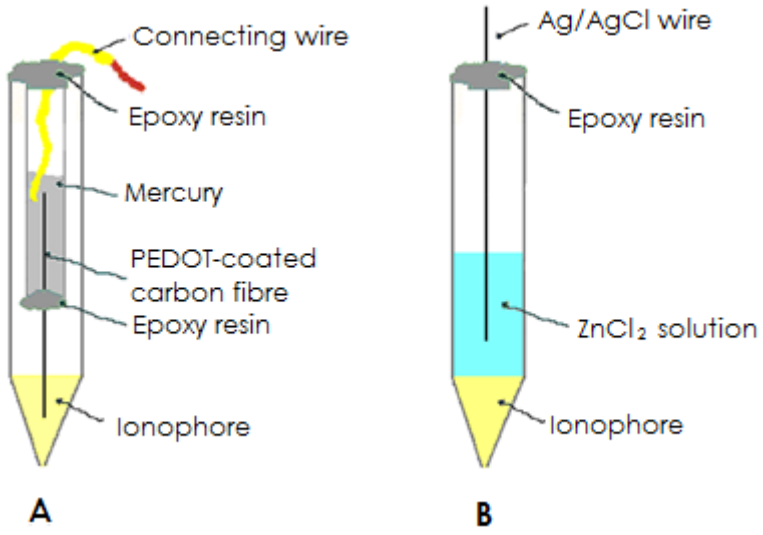

Figure 5.4.1. Sketches of the two configurations of Zn^{2+}-ISMEs employed in the experiments: (A) solid contact, and (B) conventional liquid contact. The diameter of the pipette tips used in the studies ranged between 10-50 µm.

5.4.4.3. Instrumentation

The SECM instrument has been described previously [51]. Main components are a 3D positioning stage driven by stepper motors (MFN 25PP; Newport, Irvine, CA, USA), a battery-powered voltage follower based on an operational amplifier (TL082; National Semiconductor, Santa Clara, CA; USA), a digital multimeter (M-3630D; METEX, Seoul, Korea) and home-built control software. A video camera was used to further assist positioning of the tip close to the surface. The electrochemical cell was composed by the ISME as tip, and an Af/AgCl/KCl (3M) as reference electrode. The complete set-up is schematically shown in Figure 5.4.2.

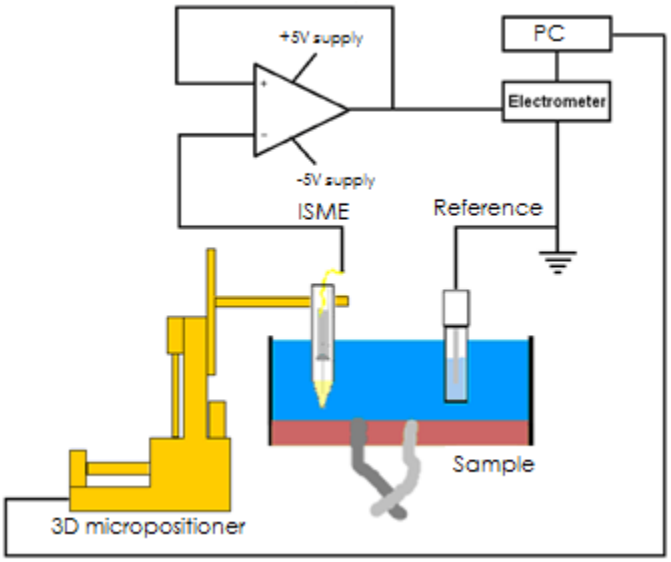

Figure 5.4.2. Diagram showing the main components of the SECM instrument.

5.4.5. Results and discussion

5.4.5.1. Characterization of the Zn^{2+}-ion selective electrodes

Following the fabrication of the zinc ion-selective microelectrodes, they were calibrated for operation in SECM. The calibration procedure consisted in the introduction of the microelectrode in a sequence of $ZnSO_4$ solutions with 10^{-x} molar concentration, with $6 \leq x \leq 1$. The procedure was initiated with the most diluted solution and subsequently exposed to solutions of increased concentration. After a brief period overpotential values occurring upon electrolyte exchange, the electrode always attained a steady potential value in each solution.

With the potential values taken from each solution, the calibration plot shown in Figure 5.4.3 was drawn. It can be observed that there is a linear relationship between the potential of the ISME and the minus logarithm of concentration of zinc

ions, and the slope of the plot is 29.8 mV decade^{-1}. The activity coefficients were calculated using the Debye-Hückel approximation.

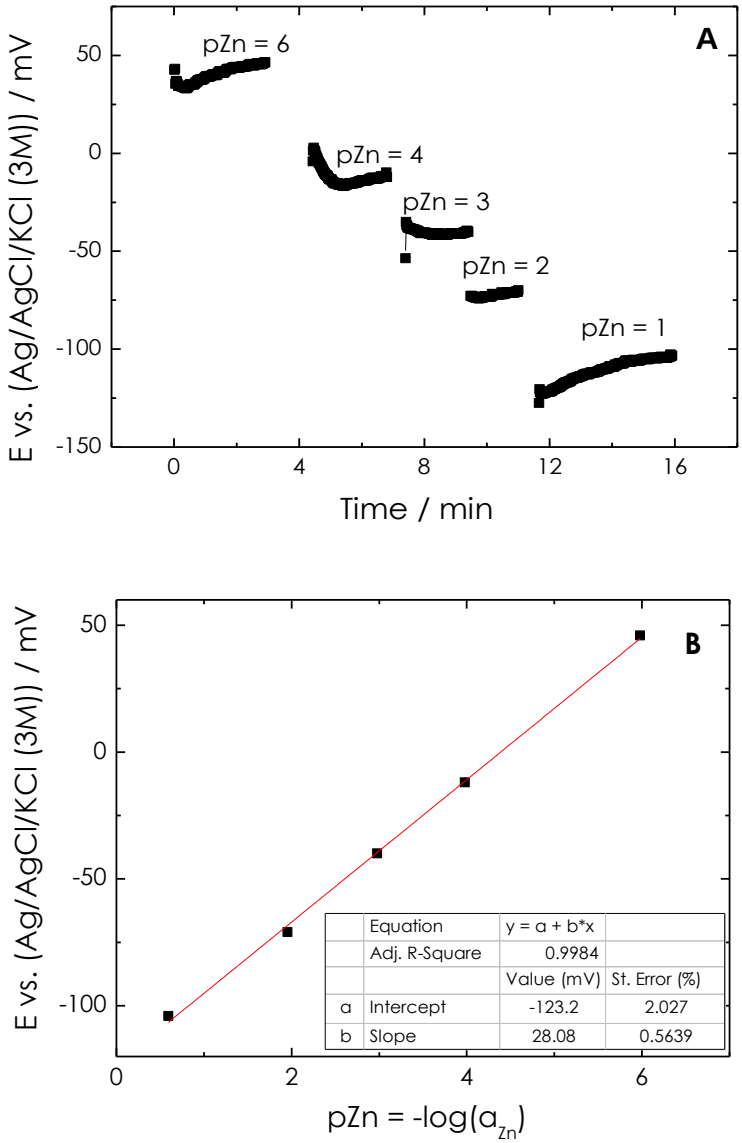

Figure 5.4.3. Calibration of the potentiometric response of the solid contact Zn^{2+}-ion-selective microelectrode to solutions of varying Zn^{2+} concentration. (A) Dynamic response transients of the Zn ISME to metal concentration; and (B) calibration plot.

5.4.5.2. Potentiometric SECM

The performance of the solid contact Zn^{2+}-ISME to image metal ion concentrations originating from a corroding surface using SECM was explored on a zinc-iron galvanic pair exposed to a 10 mM NaCl aqueous solution, open to air and at ambient temperature. Figure 5.4.4A depicts SECM scan lines obtained above the zinc specimen for different exposure times ranging from 1 to 177 minutes. That is, the ISME tip is moved in the *X* direction at a constant vertical distance of 25 μm from the

substrate, starting from a position on the resin sleeve close to the zinc squared strip. Indeed, the probe scans the zinc surface for 220 < *X* < 1460 μm, and subsequently continues its movement on the epoxy sleeve in direction towards the location of the iron sample.

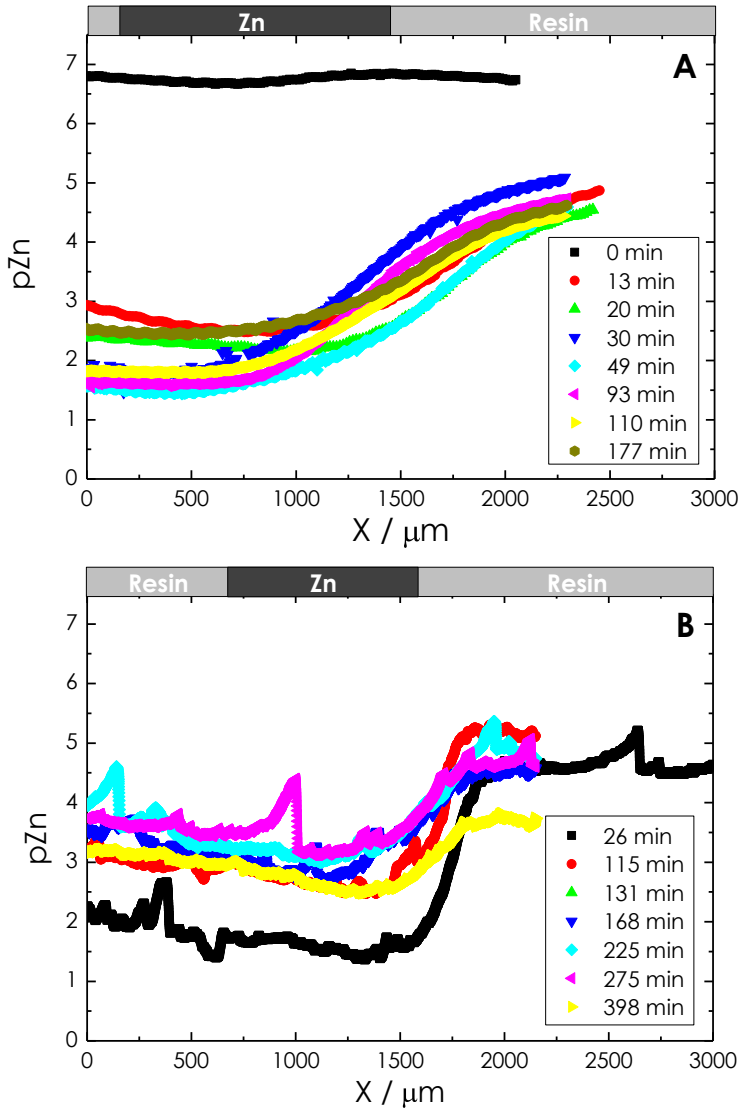

Figure 5.4.4. Potentiometric SECM scan lines measured above the zinc specimen in a zinc-iron galvanic pair immersed in 10 mM NaCl after different times as indicated in the plots. Two different Zn^{2+}-ISMEs were employed as SECM tips, namely: (A) the novel solid-contact micropipette system described in Sections 5.3 and 5.4, and (B) a conventional micropipette ISME having a liquid contact. Vertical tip-surface distance: 25 μm.

The tip movement was stopped before reaching the iron surface in this case, though a sufficiently long excursion above the insulating resin was made as to allow the probe to travel in a portion of the electrolyte with a concentration distribution characteristic of the bulk electrolyte. All the line scans were taken on the same line passing through the center of both metal samples, in order to unambiguously

monitor changes related to the advancement of the corrosion process. The onset of galvanic corrosion leads to the oxidation of zinc with the release of Zn^{2+} ions, whereas the cathodic process is located on the iron surface (not shown in the figure).

The first scan line recorded just after the electrolyte was added to the cell container and the chosen probe-substrate distance was attained, closely describes the initial conditions of the system. The potential recorded at the ISME shows an almost constant reading below the lower limit of detection of the microelectrode as from the calibration curve in Figure 5.4.3), regardless the probe travelling above either the zinc strip or the insulating resin. This condition is described in the graph by pZn values close to 7.

Yet, a more detailed inspection of the plot corresponding to this initial condition does exhibit some trends consistent with the dynamics of the corroding system. The pZn values show a tendency to decrease from left to right while the probe is passing above the zinc strip. Though zinc concentrations are below the range for their quantitative determination, the progress of the corrosion reaction and the subsequent release of Zn^{2+} ions, leads to the probe travelling into positions of greater metal concentrations during the time period of the scan. The situation changes after the other side of the zinc square is reached for X = 1460 μm, and the concentration values derived from the potential recording at the ISME returns to those found at the beginning of the scan line. And the situation remains almost constant until the end of the probe travel.

Quantitative determinations of the concentration of Zn^{2+} ions in the system are attained in all the subsequent line scans plotted in Figure 5.4.4A. They all show a clear accumulation of metal ions above the zinc strip, which quickly fades away as the probe moves on the resin sleeve to greater distances from the metal. This is already the case for the line scan measured after 13 min, which shows the progressive enrichment of the electrolyte in metal ions above the zinc strip during the duration of the probe travel as well. This feature is not observed in the scan lines measured for longer exposures, because the higher metal concentrations existing at those times are not significantly modified by the metal fluxes leaving the corroding surface below. The concentration of metal ions continue to increase with the elapse of time until about 30 min after immersion, and a stationary is observed for the rest of the experiment duration. This behaviour is more clearly observed by inspection of Figure 5.4.5, which gives the maximum metal ion concentration obtained from each line scan, thus effectively plotting the variation of Zn^{2+} concentration with exposure time. It is interesting to notice the development of a maximum concentration of metal ions after ca. 30 min, and the concentration remains practically unchanged for the remaining of the experiment.

Since it is unlikely that the corrosion process might have stopped after this short exposure when the metal is galvanically coupled to iron in 10 mM NaCl aqueous solution, the attainment of a maximum concentration for Zn^{2+} ions in the electrolyte must be due to the combined effect of the corrosion reaction (that

should lead to further increase of zinc ion concentration), and the consumption of the metal ions during the precipitation of corrosion products through reaction [52]:

$$Zn^{2+} + nH_2O \rightarrow [Zn(OH)_n]^{(2-n)} + nH^+, \quad pK_1 = 7.96 \qquad (5.4.1)$$

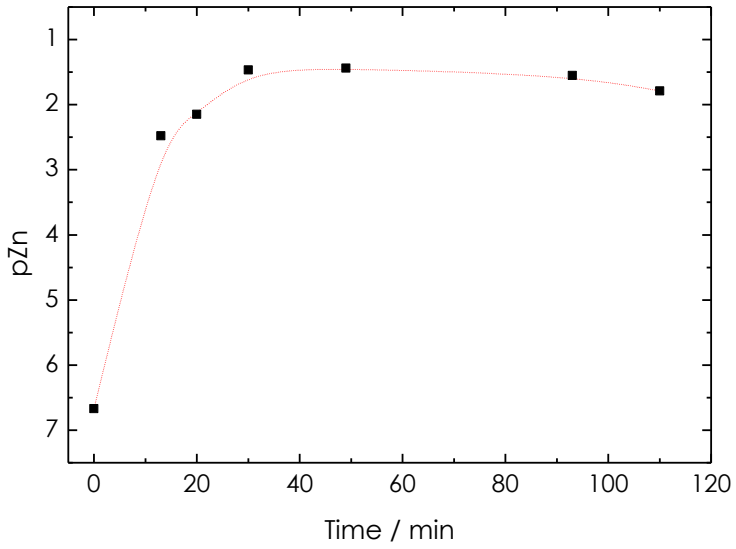

Figure 5.4.5. Time evolution of the Zn^{2+} concentration measured above the zinc specimen from the potentiometric scan lines depicted in Figure 5.4.4A.

Accordingly, the local pH of the electrolyte in contact with the surface of zinc should be ca. 3.9, a value that agrees well with the pH values observed for the same system when a pH-sensitive antimony electrode was employed as the SECM tip instead (cf. Figure 5.2.3). Though from the inspection of the Pourbaix diagram of zinc [53], precipitation of corrosion products would not be expected for pH values below 7, the calculations given in ref. [52] may support these observations. Furthermore, similar results were recently reported using SIET as observed during the self-repair processes occurring in a defective coating applied on galvanized steel [46].

Another feature is that the greater change in metal ion concentrations when departing from the corroding sample occurs within a short distance from the metal limit (in excess of two decades in the values of pZn), which is followed by a rather slow asymptotic decay to the values characteristic of the bulk electrolyte for the furthest distance covered in this experiment. All these observations are consistent with previous studies based on the measurement of ionic fluxes in the electrolyte adjacent to the same zinc-iron galvanic system made by SVET [29].

The behaviour of the novel solid contact Zn^{2+} ISME was compared with that exhibited by conventional micropipette electrodes by conducting a similar set of experiments on the same experimental system. Figure 5.4.4B shows a selection of the line scans recorded after different exposures. In this case, the ion-selective electrode does not provide data with enough stability and reproducibility to record quantitative data in potentiometric SECM. The plots exhibit big oscillations, and they are greatly affected by the scan direction for this scan rate, whereas the solid

contact ISME did not show these limitations. In this way, the superiority of a solid contact ISME for the potentiometric operation of the SECM could be established.

The distribution of Zn^{2+} species in the electrolyte phase over a corroding sample could also be monitored as a function of the distance from the surface. In this case, the ISME probe moved over the specimen until it was placed approximately above the center of the Zn sample, and subsequently retracted from the surface by means of the *Z* positioner. Figure 5.4.6 depicts the corresponding plot measured whereas the ISME was moved from the distance of closest approach in this work (i.e. 25 μm) until a distance of 1200 μm. The concentration of Zn^{2+} ions diminished steadily during this operation. The stability of the microsensor is further evidenced by switching the scan direction in order to measure the corresponding approach curve. Both plots are well superimposed, a further evidence of a robust and stable potentiometric probe. Thus, the distribution of metal ions can be imaged by scanning in the *X*-*Z* plane as it is shown in Figure 5.4.7. This image is effectively a composition of scan lines recorded in the *X* direction in a movement parallel to the surface of the sample. In this way, each scan line extends for 2500 μm.

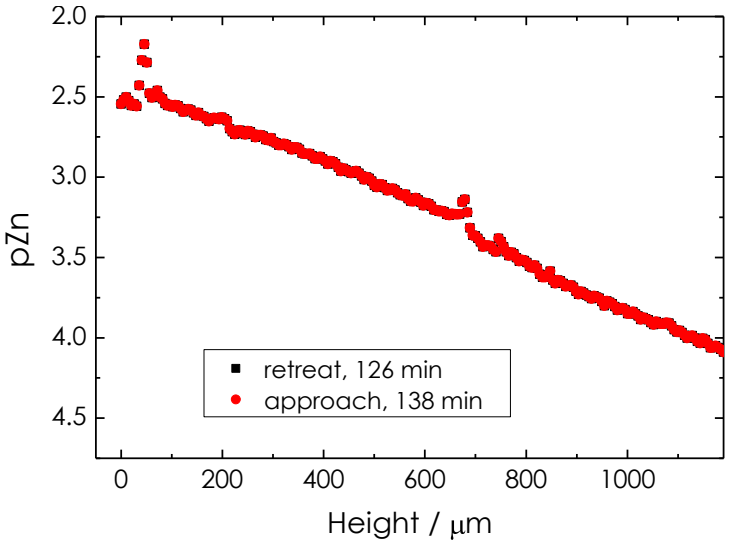

Figure 5.4.6. Distribution of Zn^{2+} ion concentration above the zinc specimen measured with the solid contact Zn^{2+}-ISME as the height of the tip is changed. The zinc-iron galvanic pair has been immersed in 10 mM NaCl for the immersion times given in the graph. The approach and retreat lines closely match each other.

Once the scan line has been completed, the probe is retracted on the *Z* axis to a new height, and the next scan line was recorded. In order to reduce the time required to acquire a complete map up to a distance of 1000 μm, well inside the bulk of the electrolyte. That is, scan lines have been recorded only at a selection of probe-surface distances, and the composed map given in Figure 5.4.7 shows some blank lines accordingly. Yet, the concentration profiles in both the *X* and *Z* directions can be clearly deduced from the observation of this image.

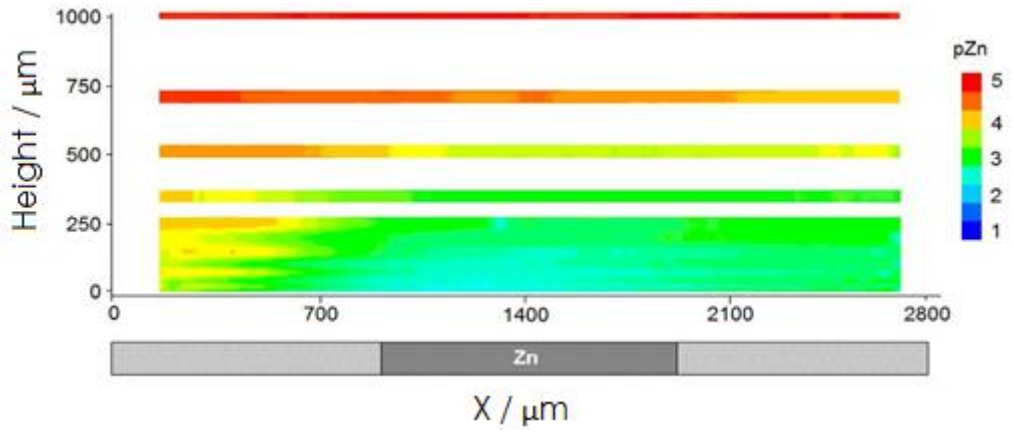

Figure 5.4.7. Distribution of Zn^{2+} ion concentration in a plane perpendicular to the surface of the zinc specimen registered after the zinc-iron pair has been immersed in 10 mM NaCl for 5 hours. *Y* axis indicates the height position of the ISME in relation to the substrate surface at which each line was recorded.

5.4.6. Conclusions

This study reveals that solid contact Zn^{2+} ion sensor microelectrodes can be used to monitor concentration distribution of zinc cations in a corroding system and the influence of corrosion products precipitation with the scanning electrochemical microscope operating using rastering conditions similar to those employed with the amperometric modes.

The formation of zinc soluble species is identified in the anodic zone covering the zinc strip coupled to iron when exposed to an aqueous 10 mM NaCl solution. The time evolution of the corroding system could thus be monitored.

SECM images depicting the concentration distribution of Zn^{2+} species over the reactive system can be obtained by recording scan lines in the *X-Y* plane parallel to the investigated surface, or as depth profiles when the *X-Z* plane (i.e. perpendicular to the surface) is taken instead.

Summarizing, this Section demonstrates the complementary use of the potentiometric operation of the scanning electrochemical microscope to detect local changes of the ion activity as result of corrosion reactions.

5.4.7. References

1. S.E. Pust, W. Maier, G. Wittstock. Zeitschrift für Physikalische Chemie 222 (2008) 1463.

2. L. Niu, Y. Yin, W. Guo, M. Lu, R. Qin, S. Chen. Journal of Materials Science 44 (2009) 4511.
3. Y. González-García, J.J. Santana, J. González-Guzmán, J. Izquierdo, S. González, R.M. Souto. Progress in Organic Coatings 69 (2010) 110.
4. R.M. Souto, S. Lamaka, S. González. In: Microscopy: Science, Technology, Applications and Education, Vol. 3 (Edited by A. Méndez-Vilas, J. Díaz). Formatex Research Center, Badajoz, 2010, p. 2162.
5. N. Casillas, S. Charlebois, W.H. Smyrl, H.S. White. Journal of the Electrochemical Society 141 (1994) 636.
6. S.B. Basame, H.S. White. Journal of Physical Chemistry 99 (1995) 16430.
7. Y.Y. Zhu, D.E. Williams. Journal of the Electrochemical Society 144 (1997) L43.
8. Y. González-García, G.T. Burstein, S. González, R.M. Souto. Electrochemistry Communications 6 (2004) 637.
9. K. Mansikkamäki, P. Ahonen, G. Fabricius, L. Murtomäki, K. Kontturi. Journal of the Electrochemical Society 152 (2005) B12.
10. S. Hocevar, S. Daniele, C. Bragato, B. Ogorevic. Electrochimica Acta 53 (2007) 555.
11. D. Battistel, S. Daniele, R. Gerbasi, M.A. Baldo. Thin Solid Films 518 (2010) 3625.
12. J. Izquierdo, J.J. Santana, S. González, R.M. Souto. Electrochimica Acta 5 (2010) 8791.
13. R.M. Souto, Y. González-García, S. González, G.T. Burstein. Corrosion Science 46 (2004) 2621.
14. A.C. Bastos, A.M. Simões, S. González, Y. González-García, R.M. Souto. Progress in Organic Coatings 53 (2005) 177.
15. R.M. Souto, Y. González-García, S. González. Corrosion Science 47 (2005) 3312.
16. A.M. Simoes, D. Battocchi, D.E. Tallman, G.P. Bierwagen. Corrosion Science 49 (2007) 3838.
17. R.M. Souto, Y. González-García, S. González. Corrosion Science 50 (2008) 1637.
18. R.M. Souto, Y. González-García, S. González. Progress in Organic Coatings 65 (2009) 435.
19. R.M. Souto, Y. González-García, S. González, G.T. Burstein. Electroanalysis 21 (2009) 2569.
20. R.M. Souto, L. Fernández-Mérida, S. González. Electroanalysis 21 (2009) 2640.
21. E. Salamifar, M.A. Mehrgardi, M.F. Mousavi. Electrochimica Acta 54 (2009) 4638.
22. R.M. Souto, Y. González-García, J. Izquierdo, S. González. Corrosion Science 52 (2010) 748.
23. J.J. Santana, J. González-Guzmán, J. Izquierdo, S. González, R.M. Souto. Corrosion Science 52 (2010) 3924.
24. J.J. Santana, J. González-Guzmán, L. Fernández-Mérida, S. González, R.M. Souto. Electrochimica Acta 55 (2010) 4488.
25. C.H. Paik, H.S. White, R.C. Alkire. Journal of the Electrochemical Society 147 (2000) 4120.
26. C.H. Paik, R.C. Alkire. Journal of the Electrochemical Society 148 (2001) B276.

27. K. Fushimi, M. Seo. Electrochimica Acta 47 (2001) 121.
28. A.C. Bastos, A.M. Simões, S. González, Y. González-García, R.M. Souto. Electrochemistry Communications 6 (2004) 1212.
29. A.M. Simões, A.C. Bastos, M.G. Ferreira, Y. González-García, S. González, R.M. Souto. Corrosion Science 49 (2007) 726.
30. S. Modiano, J.A.V. Carreño, C.S. Fugivara, R.M. Torresi, V. Vivier, A.V. Benedetti, O.R. Mattos. Electrochimica Acta 53 (2008) 3670.
31. S. González, J.J. Santana, L. Fernández-Mérida, R.M. Souto. Electrochimica Acta 56 (2011) 9596.
32. B. Horrocks, M.V. Mirkin, D.T. Pierce, A.J. Bard, G. Nagy, K. Toth. Analytical Chemistry 65 (1993) 1213.
33. G. Nagy, L. Nagy. Fresenius Journal of Analytical Chemistry 366 (2000) 735.
34. G. Denuault, G. Nagy, K. Tóth, In: Scanning Electrochemical Microscopy (Edited by A.J. Bard, M.V. Mirkin). Marcel Dekker, New York, 2001, Ch. 10.
35. G. Nagy, L. Nagy. Analytical Letters 40 (2007) 3.
36. S. González, J.J. Santana, Y. González-García, L. Fernández-Mérida, R.M. Souto. Corrosion Science 53 (2011) 1910.
37. R.M. Souto, Y. González-García, D. Battistel, S. Daniele. Chemistry - A European Journal 18 (2012) 230.
38. D.O. Wipf, F. Ge, T.W. Spaine, J.E. Baur. Analytical Chemistry 72 (2000) 4921.
39. E. Klusmann, J.W. Schultze. Electrochimica Acta 8 (2003) 3325.
40. J. Izquierdo, L. Nagy, Á. Varga, J.J. Santana, G. Nagy, R.M. Souto. Electrochimica Acta 56 (2011) 8846.
41. G. Gyetvai, S. Sundblom, L. Nagy, A. Ivaska, G. Nagy. Electroanalysis 19 (2007) 1116.
42. G. Gyetvai, L. Nagy, A. Ivaska, I. Hernadi, G. Nagy. Electroanalysis 21 (2009) 1970.
43. K. Ogle, S. Morel, D. Jacquet. Journal of the Electrochemical Society 153 (2006) B1.
44. F. Thébault, B. Vuillemin, R. Oltra, K. Ogle, C. Allely. Electrochimica Acta 53 (2008) 5226.
45. R.M. Souto, B. Normand, H. Takenouti, M. Keddam, Electrochimica Acta 55 (2010) 4551.
46. M. Taryba, S.V. Lamaka, D. Snihirova, M.G.S. Ferreira, M.F. Montemor, W.K. Wijting, S. Toews, G. Grundmeier. Electrochimica Acta 56 (2011) 4475.
47. E. Lindner, M. Horváth, K. Tóth, E. Pungor, I. Bitter, B. Ágai, L. Tõke. Analytical Letters 25 (1992) 453.
48. R.C. Thomas. Ion-selective Intracellular Microelectrodes: How to Make and Use Them. Academic Press, London, 1978.
49. D. Ammann. Ion-selective Microelectrodes. Principles, Design and Application. Springer-Verlag, Berlin, 1986.
50. Á. Varga, L. Nagy, J. Izquierdo, I. Bitter, R.M. Souto, G. Nagy. Analytical Letters 44 (2011) 2876.

51. B. Kovács, B. Csóka, G. Nagy, I. Kapui, R.E. Gyurcsányi, K. Tóth. Electroanalysis 11 (1999) 349.
52. Y.Y. Lur'e. Spravochnik po Analiticheskoi Himii, 6th edn. Himiya, Moscow, 1989.
53. M. Pourbaix, Atlas of Electrochemical Equilibria in Aqueous Solutions. NACE, Houston, 1974.

5.5

Resolution of the apparent experimental discrepancies observed between SVET and SECM for the characterization of galvanic corrosion reactions

5.5.1. Abstract

A new approach for studying the local distribution of anodic and cathodic sites in a corroding system is presented in this Section. Using the scanning vibrating electrode technique (SVET), experiments are performed at closer distances to the investigated surface in order to monitor the electrochemical activity of a sample with enhanced spatial resolution. This new approach allowed the detection of cathodic sites on the active metal in a galvanic couple when it corroded in a localized manner (e.g. pitting corrosion). This is the case for zinc coupled to iron. Differences between the ionic fluxes related to cathodic activity on zinc and iron were detected. But no cathodic activity could be detected on zinc when SVET was operated at the usual tip-sample distances. The new results agree with recent observations of local cathodic activity on the more active metal in a galvanic couple provided by scanning electrochemical microscopy (SECM), thus allowing for a greater complementarity of these techniques.

5.5.2. Resumen

Se presenta en esta sección una nueva aproximación microelectroquímica para el estudio de las distribuciones locales de sitios anódicos y catódicos. Usando la técnica de barrido del electrodo vibrante (SVET), se han desarrollado experimentos a distancias muy cercanas a las superficies investigadas con objeto de determinar la actividad electroquímica de una muestra con elevada resolución espacial. Esta nueva aproximación ha permitido la detección la formación de de sitios catódicos sobre un metal activo conectado galvánicamente durante un proceso de corrosión localizada (esto es, corrosión por picadura). Se trata del caso del cinc acoplado al hierro. Se han detectado diferencias entre los flujos iónicos relacionados con la actividad catódica en el cinc y el hierro. Sin embargo, no se ha podido detectar actividad catódica en el cinc a las distancias muestra-sonda del SVET habituales. Estos nuevos resultados se relacionan con observaciones recientes de actividad catódica en el metal más activo de un acoplamiento galvánico, obtenidas por microscopía electroquímica de barrido (SECM), aportándose por tanto una complementariedad entre estas técnicas.

5.5.3. Introduction

The application of scanning microelectrochemical techniques in Corrosion Science has contributed to a major advancement in the understanding of many corrosion reactions and mechanisms because earlier stages of these processes have been made available to the researcher. Despite their diversity and the differences in operating principles involved, their outcomes have been demonstrated to be usually greatly complementary, thus helping to gain new insights of the reactions with high spatial and electrochemical resolution [1-4].

The real introduction of scanning microelectrochemical techniques to corrosion studies can be dated back to the work by Isaacs initially employing the scanning reference electrode technique (SRET) [5], later followed by the scanning vibrating electrode technique (SVET) [6,7]. He also developed the concept of the local electrochemical impedance spectroscopy (LEIS) and used a dual microelectrode for sensing the local AC-potential gradient for the first time [8]. Among these techniques, SVET has become quite extensively employed in corrosion laboratories nowadays, whereas LEIS is regaining new interest [9]. Due to the development of microelectrodes, scanning probe microscopy was adapted to monitor the electrochemical reactivity of a metal/electrolyte interface [10,11] leading to the development of the scanning electrochemical microscopy (SECM) [12,13]. Amperometric SECM is based on the reaction that occurs at a mobile ultramicroelectrode tip (UME) immersed in an electrolyte solution, and rastered in close vicinity of a surface in order to characterize the topography and/or the redox activity of the solid/liquid interface. A faradaic current is measured at the tip which serves as a local probe. Alternately, SECM can also be operated potentiometrically, allowing for the selective detection of ion distributions in the vicinity of the anodic and cathodic sites [14].

Among the numerous corrosion processes investigated using scanning microelectrochemical techniques, the zinc-iron galvanic pair has been frequently considered [15-30]. This experimental system has been chosen both in order to investigate its mechanism, with a special application to galvanized steel, and to explore the validity of new experimental methods and techniques. Firstly, SVET has been employed to investigate the effect of ambient parameters on the galvanic process [17,18], to screen the efficiency of corrosion inhibitors [19,20], and to characterize delamination effects from cut edges [21-23] or defects on coated galvanized steels [24,25]. On the other hand, most of the operation modes currently available for the corrosion researcher with SECM have been developed using the zinc-iron galvanic pair as model system. In this way, the determination of concentration distributions from amperometric generation-collection operation [26], the monitoring of oxygen using the redox competition mode [27], tip modification and stripping voltammetry for quantitative metal dissolution determination [28], local pH and ion-selective detection using potentiometric operation [29,30], were demonstrated. And in many of those studies, the spatial resolution and the

consistency of the results provided by the new methods were compared to those obtained using SVET.

Though good agreement between the results provided by SVET and the new operation modes in SECM used to be the rule, certain important discrepancies were discovered arising from the localized nature of the dissolution process occurring on the zinc metal. Furthermore, there were new evidences of a more extended distribution of the cathodic activity in the system that cannot be regarded any longer to occur exclusively on the iron metal.

In this contribution observations of local cathodic activity on the more active metal within the zinc-iron galvanic couple are reported. They were detected using the new operation modes of SECM available for the characterization of corrosion processes, which allow enhanced spatial and chemical resolution of the system. Next, the same experimental features were successfully monitored by SVET when the operation conditions of the technique were carefully controlled to ensure greater spatial resolution.

5.5.4. Experimental

The test specimen was the same employed before that is described in ref. [18]. In brief, 99.5% purity iron and 99.95% purity zinc cut into square specimens of 1 x 1 mm^2 dimensions were mounted into an epoxy resin sleeve (dia. 4 cm). The separation between the two metals was ca. 1 mm, thus electric connection between them was made at the rear of the resin mount. The front side of the mounts was ground with silicon carbide paper down to 4000 grit and subsequently polished with 0.3 μm alumina before the experiments. The resulting surface was rinsed with Millipore deionized water and allowed to dry in air. The front side of the mount was placed upwards and surrounded laterally by Sellotape, thus creating a small container for the electrolyte solution. The electrochemical cells for both SVET and SECM were completed with the inclusion of their corresponding microelectrodes. Testing was carried out in aqueous 0.01 M NaCl solution made from analytical grade reagent and Millipore deionized water. The solution was naturally aerated and experiments were conducted at ambient temperature.

The SVET instrument used in this Section was manufactured by Applicable Electronics (New Haven, CT, USA). The vibrating probe was prepared from a Pt/Ir (80%/20%) wire insulated with paralene C® and arced at the tip to expose the metal. The microelectrode was platinized in order to produce a spherical platinum black deposit of 20 μm diameter. The measurements were made with the electrode tip vibrating in a plane perpendicular to the sample.

A home-built SECM system was employed [31]. For the potentiometric operation, a 10^{12} Ω input impedance operational amplifier was introduced in the

measuring circuit [30]. An antimony tip was employed both as amperometric tip and pH sensor, having a 25 μm diameter active disk surface and an RG value of about 5. The procedures employed both in the fabrication of the antimony microelectrode, and for the determination of its pH sensing performance are described in detail elsewhere [32]. A linear relationship between the potential of the antimony tip and the solution pH was observed in the $3 < pH \leq 11.5$ range, and the slope of the calibration plot amounted 46.1 mV $(pH\ unit)^{-1}$. The SECM cell was completed with an Ag/AgCl/KCl (3M) reference electrode, and a Pt wire as counter electrode for the amperometric measurements.

5.5.5. Results and discussion

Figure 5.5.1 shows the ionic current flows over a zinc-iron couple as measured by SVET. The cathodic and anodic activities were well separated and located on iron and zinc, respectively, as anticipated in a galvanic couple with zinc oxidizing sacrificially and preventing the corrosion of iron. The cathodic activity corresponded to an upward flow of OH^- anions emerging from the surface as a consequence of the reduction of dissolved oxygen given by:

$$O_2 + H_2O + 4e^- \rightarrow 4\ OH^- \qquad (5.5.1)$$

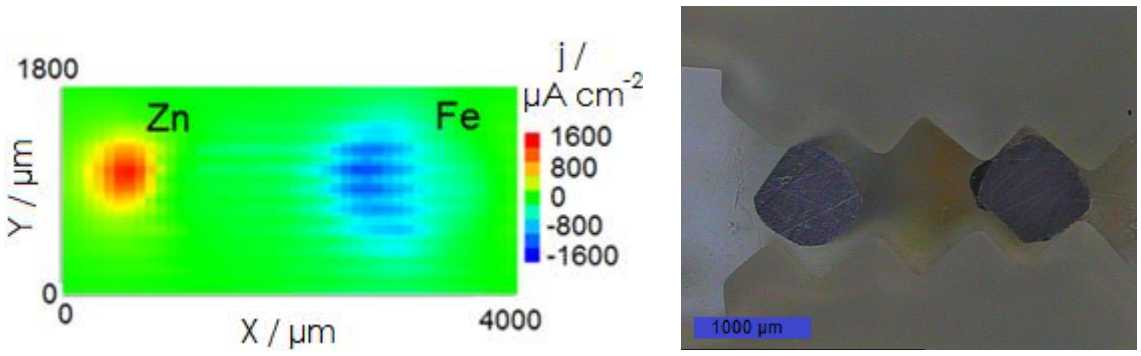

Figure 5.5.1. Ionic current map (left) and video image (right) of a zinc-iron galvanic pair immersed in 0.01 M NaCl. Tip-sample distance: 150 μm.

According to reaction (5.5.1), the amount of O_2 dissolved in solution should be lower near this cathodic region, simultaneously to local alkalinization of the electrolyte. The ionic flows related to cathodic activity arise from a large cathode that covers the complete surface of iron. Conversely, a small anode was observed on the zinc wire related to the development of one corrosion pit. Anodic currents were detected only above the pit corresponding to the flow of cations produced during the oxidation of zinc according to:

$$Zn \rightarrow Zn^{2+} + 2e^- \qquad (5.5.2)$$

pH changes also occur due to the hydrolysis of the metal ions:

$$Zn^{2+} + H_2O \xrightarrow{K^1_{hyd}} Zn(OH)^+ + H^+ \qquad (5.5.3)$$

This process leads to weak acidification in the solution around the anodic sites [33]. Additionally, the diffusion fronts of OH^- anions and Zn^{2+} cations could eventually merge leading to the precipitation of zinc hydroxide corrosion products, though the separation produced between the two metal strips in the mount should be enough to prevent the occurrence of this process provided the OH^- anions are only produced on the more noble metal.

These observations described above are in full agreement with those reported in the scientific literature from previous investigations on this system performed using SVET [16,18].

The consumption of dissolved oxygen related to cathodic activity can be imaged *in situ* using the amperometric mode of the SECM, provided a sufficiently negative potential is applied to the antimony microelectrode (namely -0.65 V vs. Ag/AgCl/KCl (3M)) [32]. Figure 5.5.2 displays a series of scan lines measured with the tip travelling above the center of the two metals after they have been immersed in the test solution for different times. The first line recorded after 28 min effectively depicts a region of depleted oxygen concentration extending over the dimensions of the iron sample, and the concentration steadily tends to the values in the bulk electrolyte when the tip is placed over the resin sleeve.

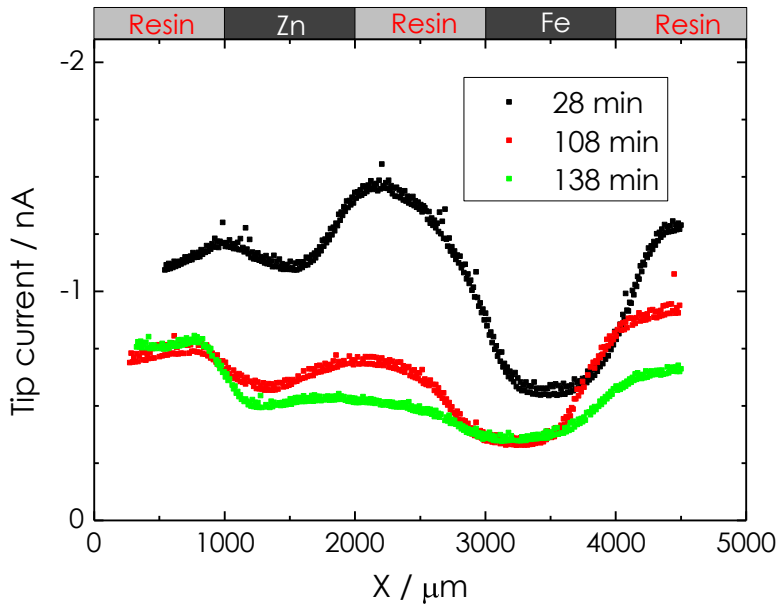

Figure 5.5.2. Distribution of oxygen concentration above the zinc-iron galvanic couple after immersion in 0.01 M NaCl for the times indicated in the figure. SECM operating amperometrically by setting the tip potential at -0.65 V vs. Ag/AgCl/KCl (3M) of the antimony probe tip above the zinc-iron galvanic couple alter immersion in 0.01 M NaCl for the exposures indicated in the figure. Tip-substrate distance: 25 μm.

Though concentration values for oxygen close to those initially present in the electrolyte are equally observed at both sides of the iron strip independently of the location of the zinc anode. But further excursion of the antimony tip above the zinc strip reveals the development of a new region of depleted oxygen concentration in the solution. With the elapse of time, the faradaic currents measured at the tip were even smaller, indicating that oxygen was consumed on both metals and it became exhausted from the surrounding bulk electrolyte. In fact, at the largest exposure considered (e.g. 138 min), oxygen concentration was almost the same above both metals and the resin between them, and only increased above the insulator beyond the two metal strips. It is also important to notice that the region of depleted oxygen above zinc had smaller dimensions that the zinc sample, an evidence that the reduction of oxygen occurs only on the otherwise inactive surface of the metal outside the corroding pit.

Further evidence on the occurrence of localized cathodic activity on the zinc strip was gained from the pH distribution maps determined with potentiometric SECM. The resulting 2D image is shown in Figure 5.5.3. Though the electrolyte was slightly acidic originally due to carbonation of the naturally aerated solution, alkalinization is observed on both metals. Analogously to the depletion of oxygen, higher pH values are observed over the dimensions of the iron sample, whereas it occurs only over a fraction of the zinc strip. Moreover, the higher pH values recorded over zinc amount to ca. 10, whereas they are 1-2 units higher on iron. These results are consistent with the observation that most of the cathodic activity indeed occurred on the nobler metal in the galvanic couple. Yet, some measurable cathodic activity could be detected above the zinc metal, at those regions of the surface that do not undergo anodic oxidation.

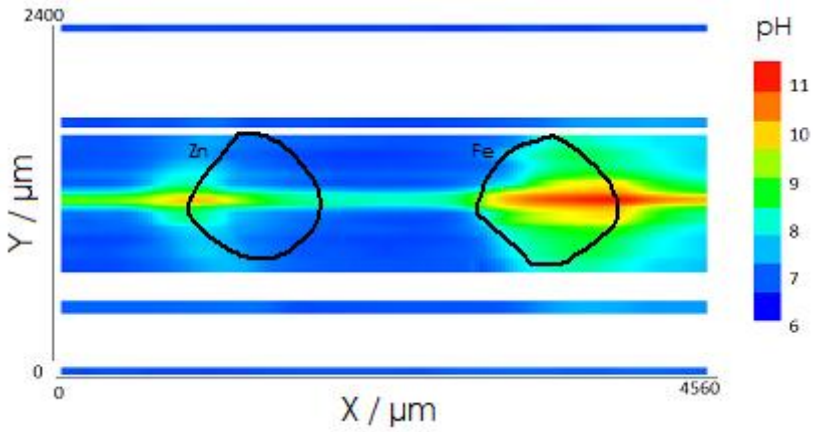

Figure 3. Potentiometric SECM using the antimony probe tip to record the pH distribution in a plane parallel to the surface of the zinc-iron galvanic couple after immersion in 0.01 M NaCl for 4 h. Tip-sample distance: 25 µm.

The features described above have not been described in the scientific literature until now. Furthermore, they seem to be directly in conflict with the

observations based on images taken by SVET such as Figure 5.5.1. With a view to explore if SVET measurements would be consistent with the occurrence of some cathodic activity also on the zinc metal when galvanically-coupled to iron, new experiments were conducted. In this case, the experimental procedure was modified in two ways.

Firstly, the tip-sample distance was changed from that employed to record Figure 5.5.1. Usually, tip-sample distances in excess of 100 μm are chosen for vibrating probes of 20 μm diameter, and successful imaging of ionic currents may even be attained for a height of 500 μm, though at the expense of resolution [26]. On the other hand, artefacts can occur in SVET measurements at shorter distances from coupling currents [34], tip inclination [35], and large-amplitude vibrations [36], which severely hinder the accessibility of the limits predicted by the theory [37,38] (ideally equivalent to 1 tip diameter). From the foregoing, a tip-sample distance of 80 μm was regarded to be an adequate choice for this work. Secondly, the electrochemical activity above each metal was recorded in separated images, to improve the detection of the highest and lowest ionic currents on each metal.

The map measured above the zinc strip using SVET operated in these conditions is shown in Figure 5.5.4A. Inspection of the image leads to the observation of a large anodic activity localized on the left half of the image, simultaneously to the occurrence of a significantly smaller cathodic activity on the remaining metal surface. The localization of the current flow related to the release of Zn^{2+} ions from the metal surface closely matches the position of the corrosion pit observed in the micrograph given in Figure 5.5.4B. On the other hand, the unmodified portion of the surface outside the pit serves as corrosion sites for oxygen electroreduction with the generation of a small flow of OH^- ions into the electrolyte solution. Most importantly, these results validate the previous observations obtained by SECM, thus resolving the apparent discrepancies observed between different scanning microelectrochemical techniques for the characterization of galvanic corrosion reactions.

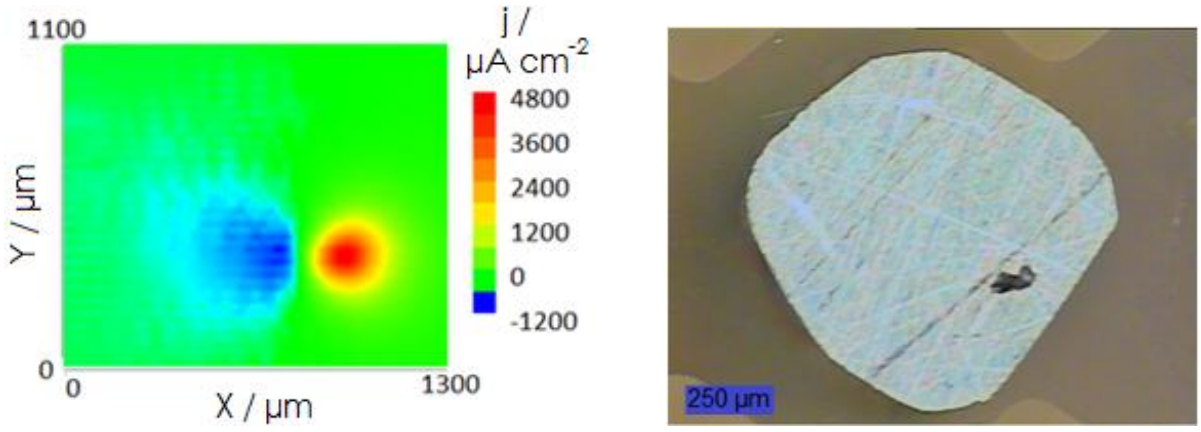

Figure 4. Ionic current map (left) and video image (right) of the zinc sample in a zinc-iron galvanic pair immersed in 0.01 M NaCl. Tip-sample distance: 80 μm.

5.5.6. Conclusion

The use of scanning microelectrochemical techniques has led to the experimental observation of cathodic activity on the more active metal in a zinc-iron galvanic couple. The greatly localized nature of the anodic reaction of zinc, with the formation of corroding pits, leaves the remaining surface of the metal available for oxygen electroreduction by the electrons released by the oxidation of the metal. The cathodic activity on both iron and the non-corroding zinc originates both the depletion of dissolved oxygen and the alkalization of the electrolyte solution around the cathodic sites. Changes on the oxygen concentration and the pH in the solution can be spatially resolved using a dual potentiometric/amperometric antimony microelectrode as the tip in SECM. Additionally, the fluxes of the OH- anions on both metals can be detected by SVET if the operating conditions for the measurements are optimized for enhanced resolution. In this way, it has been shown that SECM and SVET are highly complementary techniques for the investigation of corrosion processes.

5.5.7. References

1. P. Marcus, F. Mansfeld. Analytical Methods in Corrosion Science and Engineering. CRC Press, Boca Raton, 2006.
2. R. Oltra, V. Maurice, R. Akid, P. Marcus. Local Probe Techniques for Corrosion Research. Woodhead, Cambridge, 2007.
3. L. Niu, Y. Yin, W. Guo, M. Lu, R. Qin, S. Chen. Journal of Materials Science 44 (2009) 4511.
4. M.B. Jensen, D.E. Tallman, In: Electroanalytical Chemistry, Vol. 24 (Edited by A.J. Bard, C.G. Zoski). CRC Press, Boca Raton, 2012, p. 171.
5. H.S. Isaacs, B. Vyas, In: Electrochemical Corrosion Testing (Edited by F. Mansfeld, U. Bertocci), ASTM STP 727. ASTM, Baltimore, 1987, p. 3.
6. H.S. Isaacs. Corrosion Science 28 (1988) 547.
7. H.S. Isaacs. Corrosion Science 29 (1989) 313.
8. H.S. Isaacs, M.W. Kendig. Corrosion 36 (1980) 269.
9. V.M. Huang, S.-L. Wu, M.E. Orazem, N. Pébère, B. Tribollet, V. Vivier. Electrochimica Acta 56 (2011) 8048.
10. R.C. Engstrom, M. Weber, D.J. Wunder, R. Burgess, S. Winquist. Analytical Chemistry 58 (1986) 844.
11. R.C. Engstrom, T. Meaney, R Tople, R.M. Wightman. Analytical Chemistry 59 (1987) 2005.
12. A.J. Bard, F.R.F. Fan, J. Kwak, O. Lev. Analytical Chemistry 61 (1989) 132.
13. A.J. Bard, F.-R. Fan, M. Mirkin. In: Physical Electrochemistry: Principles, Methods, and Applications (Edited by I. Rubinstein). Marcel Dekker, New York, 1995, p. 209.

14. B.R. Horrocks, M.V. Mirkin, D.T. Pierce, A.J. Bard, G. Nagy, K. Tóth. Analytical Chemistry, 65 (1993) 1213.
15. A.C. Bastos, A.M. Simões, M.G. Ferreira. Electrochimica Acta 21 (2003) 371.
16. E. Tada, S. Satoh, H. Kaneko. Electrochimica Acta 49 (2004) 2279.
17. A.P. Yadav, H. Katayama, K. Noda, H. Masuda, A. Nishikata, T. Tsuru. Electrochimica Acta 52 (2007) 3121.
18. R.M. Souto, Y. González-García, A.C. Bastos, A.M. Simões. Corrosion Science 49 (2007) 4568.
19. A.C. Bastos, M.G.S. Ferreira, A.M. Simões. Progress in Organic Coatings 52 (2005) 339.
20. S. Kallip, A.C. Bastos, M.L. Zheludkevich, M.G.S. Ferreira. Corrosion Science, 52 (2010) 3146.
21. K. Ogle, S. Morel, D. Jacquet. Journal of the Electrochemical Society, 153 (2006) B1.
22. J. Elvins, J.A. Spittle, J.H. Sullivan, D.A. Worsley. Corrosion Science 50 (2008) 1650.
23. F. Thébault, B. Vuillemin, R. Oltra, K. Ogle, C. Allely. Electrochimica Acta 53 (2008) 5226.
24. D.A. Worsley, H.N. McMurray, A. Belghazi. Chemical Communications (1997) 2369.
25. R.M. Souto, B. Normand, H. Takenouti, M. Keddam. Electrochimica Acta 55 (2010) 4551.
26. A.M. Simões, A.C. Bastos, M.G. Ferreira, Y. González-García, S. González, R.M. Souto. Corrosion Science 49 (2007) 726.
27. J.J. Santana, J. González-Guzmán, L. Fernández-Mérida, S. González, R.M. Souto. Electrochimica Acta 55 (2010) 4488.
28. R.M. Souto, Y. González-García, D. Battistel, S. Daniele. Corrosion Science 55 (2012) 401.
29. J. Izquierdo, L. Nagy, Á. Varga, J.J. Santana, G. Nagy, R.M. Souto. Electrochimica Acta 56 (2011) 8846.
30. J. Izquierdo, L. Nagy, Á. Varga, I. Bitter, G. Nagy, R.M. Souto. Electrochimica Acta 59 (2012) 398.
31. B. Kovács, B. Csóka, G. Nagy, I. Kapui, R.E. Gyurcsányi, K. Tóth. Electroanalysis 11 (1999) 349.
32. J. Izquierdo, L. Nagy, Á. Varga, J.J. Santana, G. Nagy, R.M. Souto. Electrochimica Acta 56 (2011) 8846.
33. S.V. Lamaka, R.M. Souto, M.G.S. Ferreira. In: Microscopy: Science, Technology, Applications and Education, Vol. 3 (Edited by A. Méndez-Vilas, J. Díaz). Formatex Research Center, Badajoz, 2010, p. 2162.
34. N. Murer, R. Oltra, B. Vuillemin, O. Néel. Corrosion Science 52 (2010) 130.
35. B.P. Wilson, J.R. Searle, K. Yliniemi, D.A. Worsley, H.N. McMurray. Electrochimica Acta 66 (2012) 52.
36. H.N. McMurray, D. Williams, D.A. Worsley. Journal of the Electrochemical Society 150 (2003) B567.
37. H.S. Isaacs. Journal of the Electrochemical Society 138 (1991) 722.
38. R. Akid, M. Garma. Electrochimica Acta 49 (2004) 2871.

5.6

Main conclusions

1. A model zinc-iron galvanic couple was employed to test the applicability of potentiometric microsensors for SECM monitoring in Corrosion Science, as to detect key chemical species participating in corrosion processes that could not be detected using conventional amperometric operation modes in SECM. In this way, concentration distributions of highly reactive metals and pH have been monitored with high chemical selectivity for the first time.

2. Use of antimony tips in SECM allows quasi-simultaneous imaging of pH gradients in the electrolyte phase and chemical reactivity distributions in the investigated surface. The local pH distribution over corroding surfaces, known to be both the cause as well as the consequence of localized corrosion processes, can be determined with this combined potentiometric/amperometric operation of the SECM.

3. Low internal resistance zinc ion-selective micropipette electrodes, intended to operate as quantitative sensors for the monitoring of the sacrificial dissolution of zinc in galvanic processes, were successfully developed and characterized. The new design allowed faster scanning rates to be implemented in SECM, significantly overcoming the limitation imposed by the rapid evolution of surfaces experiencing active corrosion.

4. Both types of potentiometric sensors greatly extend the range of information gathered on corrosion reactions, providing new methodologies for better understanding the involved mechanisms. This conclusion has been supported by the quantitative characterization of the evolution of an active metal during its degradation.

5. Investigation of the Zn-Fe model galvanic pair allowed resolution of the apparent discrepancies previously encountered by using different microelectrochemical techniques for the characterization of this system, mainly the conflicting observations of some cathodic activity on the surface of the more active metal even under galvanic connection to a nobler one.

5.7

Conclusiones

1. Se ha empleado un par galvánico cinc-hierro para comprobar la aplicabilidad de los microsensores en SECM para estudios de Ciencia de Corrosión, permitiendo la detección de especies químicas que participan en los procesos de corrosión imposibles de determinar mediante los modos convencionales de operación amperométrica del SECM. De esta manera se han visualizado por primera vez, con elevada selectividad química, las distribuciones de pH y de concentración de metales altamente reactivos.

2. El uso de puntas de antimonio en SECM permite la visualización casi simultánea de gradientes de pH en la fase del electrolito y de distribuciones de reactividad química en la superficie investigada. La distribución local de pH sobre superficies bajo corrosión, producida como consecuencia de los procesos corrosivos, ha podido determinarse con la operación combinada potenciométrico/amperométrica del SECM.

3. Se han desarrollado y caracterizado con éxito electrodos de micropipeta selectivos de ion cinc de baja resistencia interna, fabricados para operar como sensores cuantitativos en la determinación de la disolución de ánodos de sacrificio de cinc en procesos galvánicos. El nuevo diseño ha permitido implementar mayores velocidades de barrido en SECM, superando significativamente las limitaciones impuestas por la rápida evolución de las superficies activas cuando experimentan procesos de corrosión.

4. Ambos tipos de sensores potenciométricos han extendido ampliamente el rango de información adquirible en relación a las reacciones de corrosión, aportando nuevas metodologías para el mejor entendimiento de los mecanismos involucrados. Esta conclusión se fundamenta a partir de la caracterización de la evolución de un metal activo durante su degradación.

5. La investigación del par galvánico Zn-Fe ha permitido la resolución de discrepancias aparentes en la caracterización del sistema que previamente se habían encontrado usando diferentes técnicas microelectroquímicas, principalmente por observaciones conflictivas que mostraban cierta actividad catódica en la superficie del metal más activo incluso bajo conexión galvánica con uno más noble.

CHAPTER 6

Scanning electrochemical microscopy for the investigation of the corrosion mechanism of magnesium-based materials

Index

6.1

Prologue to the experiments

6.1.1. Introduction

Despite the favourable properties of magnesium resulting from specific strength combined with light weight, utility of magnesium and magnesium alloys is still limited to low corrosively environments due to their high reactivity in aqueous environments. Corrosion processes are characterized by the highly negative potential of magnesium (ca. -2.38 V vs. NHE) [1], and the nature of the cathodic reaction, namely water reduction for pH values up to 11, that is not subjected to mass transport limitations [2]:

$$2\,H_2O + 2\,e^- \rightarrow \uparrow H_2 + 2\,OH^- \qquad (6.1.1)$$

Therefore, magnesium dissolution in aqueous environments is accompanied by gas evolution (i.e. hydrogen evolution reaction, HER) at all pH values, even under open circuit conditions [1-3]. More interestingly, HER also occurs when the magnesium sample is anodically polarized respect to its corrosion potential [4-7], a feature usually named "anomalous hydrogen evolution" or "anodic hydrogen evolution" [8]. Contrary to the expectations derived from the conventional Tafel equation, an apparent "negative difference effect" (NDE) occurs that is characterized by an increase in the rate of hydrogen production with increasing applied potential [9].

A further complication arises from the difficulties experienced to improve the corrosion resistance of magnesium by alloying. Indeed, most additions lead to even poorer corrosion performances, because higher corrosion rates occur when elements such as Cu, Fe and Ni exist as impurities [10]. Second phases that serve as intense local cathodes are formed, promoting anodic dissolution because magnesium is a poor cathode with one of the lowest exchange current densities of all metals [11,12].

The particular behaviour of corroding magnesium related to NDE, together with the fast dissolution of the metal in aqueous environment accompanied with vigorous gas evolution, have received major interest since the 1950's [13,14]. Yet, the corrosion mechanism could not be established until now, and conflicting views and controversial proposals have been presented. The main issues under debate include the eventual formation of Mg(I) intermediate species, the apparent evolution of hydrogen at both anodic and cathodic sites on the corroding metal, and the possible localization of the corrosive attack. In brief, the scientific community seems

to be divided between those assuming that magnesium may be ionized with a stoichiometry n = 1 (i.e., unipositive Mg^+ is involved as an early step in the electrochemical oxidation of magnesium and reacts chemically with other available species) [15-18], and those supporting that magnesium dissolution occurs with n = 2 [19-23].

6.1.2. Research aims

A goal of the research presented in this Chapter was to develop a new experimental procedure to investigate the corrosion of mechanism of magnesium and its alloys in aqueous solution based on the potentiometric operation of the scanning electrochemical microscope, using ion-selective electrodes as probes. Section 6.2 describes the work devoted to the fabrication of a Mg-based microelectrode capable of operation in the SECM to monitor the concentration distributions of Mg(II) species from a model corroding magnesium source. A micropipette based on a suitable chromophore and containing a liquid internal reference solution was thus developed. The following Section 6.3 focused on the characterization of the electrochemical behaviour of a magnesium sample corroding in chloride-containing aqueous solution at either its open circuit potential or galvanically-coupled to iron, in order to modify the rate of the corrosion reaction. Combined potentiometric/amperometric operation of the SECM allowed for additionally monitoring the distribution of pH and the consumption of oxygen as to identify the cathodic and anodic sites operating in the system. The high internal resistance and slow response time of the ion-selective electrodes with a liquid internal contact imposed slow scanning rates for SECM operation, effectively limiting the total area that could be scanned in each experiment to the obtainment of scan lines. Additional developments are presented in Section 6.4 after ion-selective microelectrodes with an internal solid contact were designed, thus allowing to obtain concentration maps of the species participating in the process, and to follow their evolution with time. The procedure was also extended to the characterization of magnesium alloys in Section 6.5 as to extract new information regarding the corrosion mechanism of magnesium and its alloys in aqueous solutions containing chloride ions.

6.1.3. References

1. G.L. Makar, J. Kruger. International Materials Reviews 38 (1993) 138.
2. M. Pourbaix. Atlas of Electrochemical Equilibria in Aqueous Solutions. National Association of Corrosion Engineers, Houston, 1974.

3. J.A. Boyer. The Corrosion of Magnesium and of the Magnesium Aluminum Alloys Containing Manganese; Report-248. American Magnesium Corporation, Niagara Falls, 1927.
4. G.L. Makar, J. Kruger. Journal of the Electrochemical Society 137 (1990) 414.
5. N.T. Kirkland, J. Lespagnol, N. Birbilis, M.P. Staiger. Corrosion Science 52 (2010) 287.
6. A.D. Sudholz, N. Birbilis, C.J. Bettles, M.A. Gibson. Journal of Alloys and Compounds 471 (2009) 109.
7. F. Cao, Z. Shi, G.-L. Song, M. Liu, A. Atrens. Corrosion Science 76 (2013) 60.
8. G. Song. Advanced Engineering Materials 7 (2005) 563.
9. G.L. Song, A. Atrens. Advanced Engineering Materials 1 (1999) 11.
10. N. Birbilis, G. Williams, K. Gusieva, A. Samaniego, M.A. Gibson, H.N. McMurray. Electrochemistry Communications 34 (2013) 295.
11. J.O'.M. Bockris, A.K.N. Reddy. Modern Electrochemistry 2B: Electrodics in Chemistry, Engineering, Biology and Environmental Science. Springer, New York, 2001.
12. G.S. Frankel, A. Samaniego, N. Birbilis. Corrosion Science 70 (2013) 104.
13. R.L. Petty, A.W. Davidson, J. Kleinberg. Journal of the American Chemical Society 76 (1954) 363.
14. P. Brouillet, I. Epelboin, M. Froment. Comptes Rendus de l'Académie des Sciences (1954) 239.
15. G. Song, A. Atrens, D. St John, J. Nairn, Y. Li. Corrosion Science 39 (1997) 855.
16. G. Song, A. Atrens, D. St John, X. Wu, J. Nairn. Corrosion Science 39 (1997) 1981.
17. A. Atrens, W. Dietzel. Advanced Engineering Materials 9 (2007) 292.
18. T.R. Thomaz, C.R. Weber, T. Pelegrini, L.F.P. Dick, G. Knörnschild. Corrosion Science 52 (2010) 2235.
19. G. Williams, H.N. McMurray. Journal of the Electrochemical Society 155 (2008) C340.
20. N.T. Kirkland, G. Williams, N. Birbilis. Corrosion Science 65 (2012) 5.
21. G.S. Frankel, A. Samaniego, N. Birbilis. Corrosion Science 70 (2013) 104.
22. S. Lebouil, A. Duboin, F. Monti, P. Tabeling, P. Volovitch, K. Ogle. Electrochimica Acta (2013) doi.: http://dx.doi.org/10.1016/j.electacta.2013.07.131.
23. G. Williams, N. Birbilis, H.N. McMurray. Electrochemistry Communications 36 (2013) 1.

6.2

Progress in scanning electrochemical microscopy by coupling potentiometric and amperometric measurement modes

6.2.1. Abstract

Scanning electrochemical microscopy (SECM) with coupled potentiometric and amperometric measurement modes is used to study corrosion reactions in aqueous environments. Whereas conventional electrochemical techniques lack spatial resolution and provide little information on behaviour at sites of corrosion initiation or at defects, the advent of scanning electrochemical microscopy is contributing to overcome these limitations when applied to the investigation of corrosion processes *in situ*. Ion-selective microelectrodes (ISME) and dual potentiometric/amperometric probes have been developed that can be employed as SECM tips as they exhibit sufficiently low resistances and response times. The applicability of this experimental approach is demonstrated by chemically imaging the behaviour of a magnesium-iron galvanic couple immersed in a diluted aqueous electrolyte. The dissolution of metal ions from anodic sites, the consumption of oxygen at the cathodic sites, and the local pH changes associated with both half-cell reactions can be effectively monitored.

6.2.2. Resumen

Se ha empleado la microscopía electroquímica de barrido (SECM) con un acoplamiento de modos amperométrico y potenciométrico para el estudio de procesos corrosivos en ambientes acuosos. Mientras que las técnicas electroquímicas convencionales carecen de resolución espacial y aportan muy poca información sobre el comportamiento de los sitios de iniciación a la corrosión o defectos, el avance de la microscopía electroquímica de barrido puede contribuir a superar tales limitaciones al aplicarse *in situ* en la investigación de los procesos corrosivos. Se han desarrollado microelectrodos de ión selectivo (ISME) y puntas con carácter dual amperométrico/potenciométrico para que puedan ser empleadas como puntas de SECM al mostrar resistencias y tiempos de respuesta relativamente bajos. Se demuestra la aplicabilidad de esta aproximación experimental mediante la visualización química del comportamiento de un par galvánico magnesio-hierro inmerso en electrolito acuoso agresivo. De esta manera ha sido posible el análisis de la disolución de los iones metálicos desde los sitios anódicos, el consumo de oxígeno en los sitios catódicos, y los cambios de pH local asociados con ambas semirreacciones.

6.2.3. Introduction

Microelectrodes positioned in the vicinity of a sample can be employed as probes in scanning microscopies to achieve chemical sensitivity. The probe is moved parallel to the sample's surface inside an electrochemical cell and changes in the probe response are related to local chemical reactivity. Local variations of the substrate potentials are the measuring principle in the scanning reference electrode technique (SRET) [1], whereas technical developments either employ a vibrating probe for enhanced resolution of ionic current fluxes in the electrolytic phase (scanning vibrating electrode technique, SVET) [2], or introduce ion-selective microelectrodes for the monitoring of concentration changes related to surface dynamics (scanning ion-selective electrode technique, SIET) [3]. These techniques can measure changes related to either membrane-transport processes in biological systems [4], or ionic-transport processes in corrosion reactions [5]. It must be noticed that these methods are not able to modify any surfaces, and they exclusively monitor chemical heterogeneities at the sample's surface related to on-going chemical processes.

A different approach involved the introduction of microelectrodes to scanning probe microscopies, particularly modifying the scanning tunnelling microscope (STM) to monitor the electrochemical reactivity of a metal/electrolyte interface leading to the development of the scanning electrochemical microscopy (SECM) [6]. Conversely to other electrochemical scanning probe techniques, SECM needs a redox mediator in solution. That is, a reaction occurring at the microelectrode tip with an active species in the liquid electrolyte is the measuring principle (i.e., amperometric operation). Under steady-state operation, changes in the faradaic current measured at the tip due to the proximity of the sample's surface can be related to local electrochemical properties of the sample and to the distance towards the tip [7]. Since SECM operation requires chemical changes in redox species to occur due to the tip operation, it can be employed to modify surfaces or inside surface films by delivering electrolytically generated reagents to different locations in a controlled time [8].

Despite the major success of SECM operated amperometrically to monitor corrosion reactions [9,10], based on the conversion of the M^{z+} ions released at the anodic sites [11,12], or the depletion of oxygen content in the solution volume adjacent to the cathodic sites [13], there are still some relevant systems in Corrosion Science that cannot be investigated by this technique. Namely, in certain corroding samples, especially for metals with sufficiently negative redox potentials in aqueous environments, the use of noble metal microelectrodes is limited by the onset of oxygen reduction and hydrogen evolution reactions. On the other hand, Pt microelectrodes are not able to detect pH alterations, though the corrosion processes are dramatically affected by this parameter. Furthermore, some metal ions may undergo hydrolysis at the anodic sites, and consequently reduce the pH, a feature that usually accelerates the corrosive attack. Though scarcely applied, these

physicochemical parameters may be studied using ion-selective electrodes (ISME) as tips. In this case, the SECM should be operated in the potentiometric mode, which gives greater chemical selectivity for sensing species generated at the substrate without their consumption [14]. The most usual potentiometric probes are ion-selective reference microelectrodes [15], and pH microsensors [16]. Ion-selective micropipette electrodes are widely employed in experimental life sciences [17]. They are also employed in SIET to investigate some corrosion systems [3]. Ion-selective electrodes can be fabricated using a well-established procedure [18], because they depend on the chosen "ionophore cocktail" for selectivity. However, three main drawbacks were encountered when they were considered for use in SECM, namely, the resistivity and the fragility of the probe, and its time-response [14]. A new opportunity has been offered by the recent development of ion-selective micropipettes containing a solid internal contact [19]. Owing to this design, the resistances of these solid-contact micropipette electrodes are only fractions of the resistance of conventional micropipette electrodes of the same size, which have a liquid contact, and may offer improved SECM performance. Their advantageous performance was also probed *in vivo* in both plant and animal tissue experiments [20].

6.2.4. SECM operation

A SECM built by Sensolytics (Bochum, Germany) was employed. In amperometric operation, the microelectrode tip and the substrate form part of an electrochemical cell which is also constituted by reference and auxiliary electrodes, and sometimes by a second working electrode, and a bipotentiostat (Autolab, Utrecht, The Netherlands) is the actual electrochemical interface. The microelectrode is a microdisk, in which the electrode material is surrounded by an insulating shield. The most common procedure for its fabrication is the encapsulation of the electrode material (carbon fibers or noble metal wires) in glass capillaries and the subsequent polishing of the tips to expose the microdisk surface. Details on the geometric characterization of the tip and on the operation procedures in amperometric SECM are given in ref. [10]. Tip displacement and its position relative to the substrate are controlled with a three-dimensional microstage that provides independent and accurate control in the *X-Y-Z* axis. The remaining component is the data acquisition and display system, usually conformed by a computer, an interface and a display system.

The same SECM instrument was employed for the potentiometric measurements, though in this case a 10^{12} Ω input impedance operational amplifier was introduced in the measuring circuit. The cell voltage data were collected with a PC through the electrometer included in the electrochemical interface (Autolab potentiostat/galvanostat). The distance between the ISME and the substrate was

established by allowing the probe to gently rest on the sample, using a video microscope to assist the process. Subsequently, the probe would be retracted to the chosen operation distance with the aid of the Z-positioning motor.

6.2.5. Preparation and characterization of the micropipette ion-selective electrodes

The ionophore cocktail used in the construction of the Mg^{2+}-selective microelectrode was composed by tetrahydrofurane (THF) as solvent, poly(vinyl chloride) (PVC), bis-N,N-dicyclohexyl-malonamide, potassium tetrakis(4-chlorophenyl)borate (KTFPB), and 2-nitrophenyl octyl ether (2-NPOE). The optimum ratios of these components were established using the methodology described elsewhere [18,21], and the composition of the mixture required for the fabrication of 500 µm thick membranes [22] is given in Table 6.2.1.

Table 6.2.1. Composition of the mixture employed to produce the ionophore cocktail for the Mg^{2+} ion-selective microelectrodes.

Component	Quantities for 200 µL of the mixture	
	Content	wt.%
Tetrahydrofurane (THF)	100 µL	-
Poly(vinyl chloride) (PVC)	7.68 mg	5.06
bis-N,N-dicyclohexyl-malonamide	2.23 mg	1.47
Potassium tetrakis(4-chlorophenyl)borate (KTFPB)	2.13 mg	1.40
2-nitrophenyl octyl ether (2-NPOE)	139.79 mg	92.07

6.2.5.1. Preparation of the micropipette ion-selective electrode

The micropipettes of desired size were built from borosilicate glass-capillaries, previously soaked in "piranha" solution and thoroughly washed with twice deionized water. The ionophore cocktail was then introduced in the micropipette under suction. A carbon fiber was employed to ensure the internal contact with the cocktail, whereas the other end of the fiber was soldered to a copper wire to produce the electrical connection between the ISME and the external equipment. The portion of the carbon fiber to be inserted in the cocktail was previously coated with the conductive polymer PEDOT in an electrochemical cell composed by the carbon fiber as working electrode, an Ag/AgCl wire immersed in the electrolyte as reference electrode, and a Pt wire as the auxiliary electrode. The monomer employed was 3,4-ethylenedioxythiophene dissolved in $BMIM^+$ PF_6^- ionic liquid [22]. Finally, Loctite® adhesive was used to seal the rear of the ISME. A micrograph of the tip of this solid contact micropipette electrode is shown in Figure 6.2.1A.

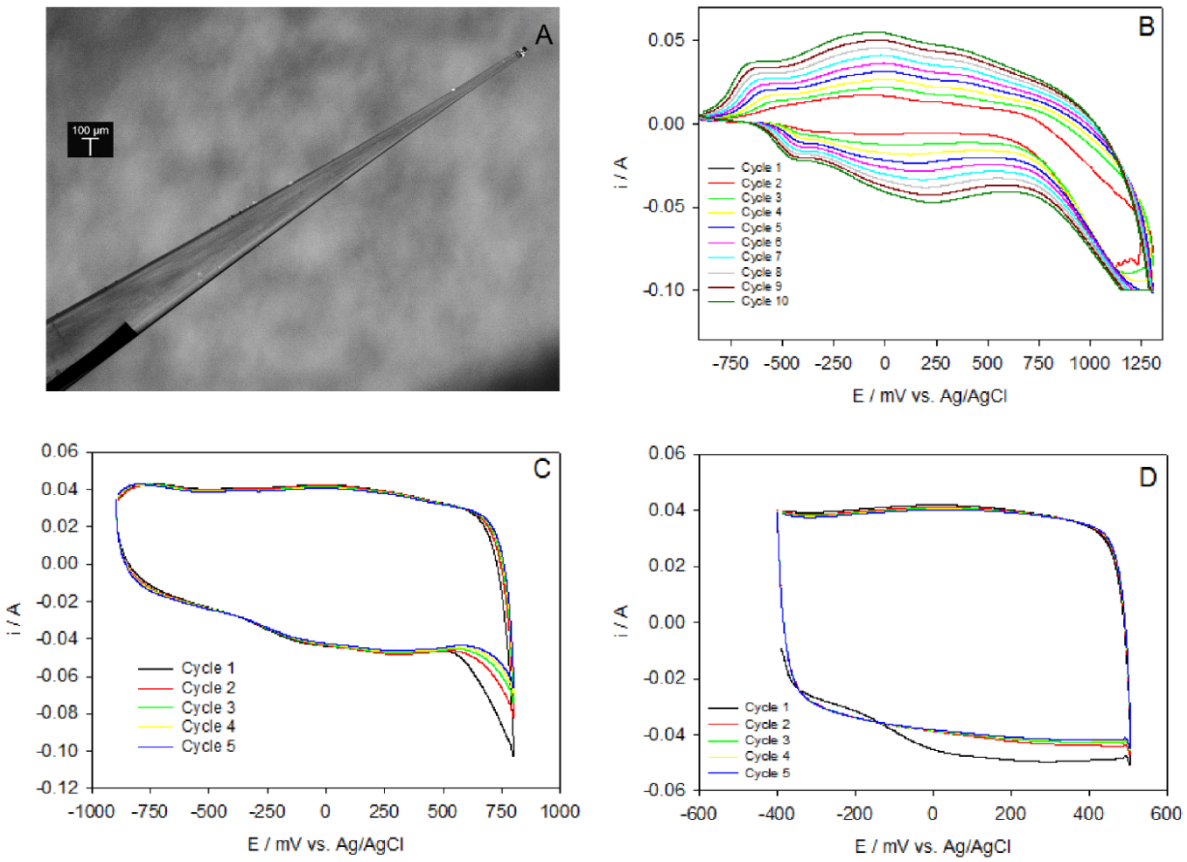

Figure 6.2.1. (A) Micrograph of the solid contact Mg^{2+}-ISME. (B-D) Cyclic voltammograms recorded during the preparation of the solid contact micropipette ISME. The goal and the electrolyte of the three steps described in the figure are, respectively: (B) coating of the carbon fiber by polymerization, with 3,4-ethylenedioxythiophene dissolved in $BMIM^+$ PF_6^- ionic liquid; (C) doping, in $BMIM^+$ PF_6^- ionic liquid free of the monomer; and (D) testing, in 0.1 M KCl. v = 0.05 V s^{-1}.

6.2.5.2. Electropolymerization of the carbon fiber

The carbon fiber was electrochemically coated by PEDOT prior to insertion in the ionophore cocktail in order to ensure good electrical contact. The electro-polymerization process was performed by subjecting the coated carbon fiber to ten potential cycles between -0.90 and +1.30 V vs. Ag/AgCl pseudo-reference. Potential cycling was performed at a sweep rate of 0.05 V s^{-1}, and Figure 6.2.1B depicts the current-potential response of the system recorded during this process. Subsequently, the cell electrolyte was replaced by $BMIM^+$ PF_6^- ionic liquid free from EDOT, and doping of the polymer film on the carbon fiber was done by potential cycling from -0.90 to +0.80 V vs. Ag/AgCl pseudo-reference. Five potential cycles with 0.05 V s^{-1} scanning rate were completed at this stage as shown in Figure 6.2.1C. The stability of the working electrode immersed in 0.1 M KCl was checked by recording five cyclic voltammograms (CV) scanning between -0.40 and +0.50 V vs. Ag/AgCl pseudo-reference (see Figure 6.2.1D).

The micropipette electrode was silanized using 5% dimethyldichlorosilane in heptane. This process was performed by inserting a few microliters of silinizing solution inside the tip of the pipette and then kept in 80 ºC oven for 30 min. Next, the membrane cocktail was introduced into the tip of this pipette by using a very thin glass-capillary attached onto the end of a syringe needle to produce back filling. The solid contact micropipette preparation was completed by placing the thinner pipette inside its lumen trying to position the carbon fiber inside the cocktail close to the orifice of the tip.

6.2.5.3. Calibration of the Mg^{2+}-ion selective microelectrode

Firstly, the novel membrane cocktail must show good selectivity and resolution towards monitoring the activity of Mg^{2+} dissolved ions in aqueous environments as result of corrosion reactions from either magnesium-based or magnesium-containing alloy materials. A silver chlorinated wire was inserted into the internal solution as the inner reference electrode. The open circuit potential of the resulting sensor with respect to an external reference electrode arises from the potential difference between both sides of the membrane, which depends on the activity of the electrolyte in the tested solution with linear Nernstian response following equation (6.2.1):

$$E = E_0 + \frac{RT}{nF} \ln\ a_{M^{z+}} \qquad (6.2.1)$$

were $a_{M^{z+}}$ is the activity of the ion to be detected. The concentration range with linear Nernstian response will be conditioned by the composition of the ionophore cocktail, that includes other compounds such as solvents, plasticizers or polymer resin, in order to improve the mechanical properties and selectivity against other ions.

The Mg^{2+}-ISME was calibrated using 1 mM NaCl as base electrolyte, with standard solutions of $MgCl_2$ of concentrations 10^{-1} to 10^{-5} M as shown in Figure 6.2.2A. The ISME was washed between different measurements. A linear response was found in Figure 6.2.2B for the range $1 \leq pMg \leq 3$. The observed slope (25.6 mV $decade^{-1}$) is sufficiently close to the expected Nernstian value of 29.6 mV $decade^{-1}$ as to employ this electrode for quantitative measurements.

6.2.6. Preparation and characterization of dual potentiometric/amperometric electrodes

Electrodes made of antimony and coated by the metal oxide have the ability to behave as a double function electrodes. That is, they can be used as

amperometric SECM tip for the measurement of faradaic currents when antimony is in the metallic state, whereas its oxidized state allows pH monitoring [16].

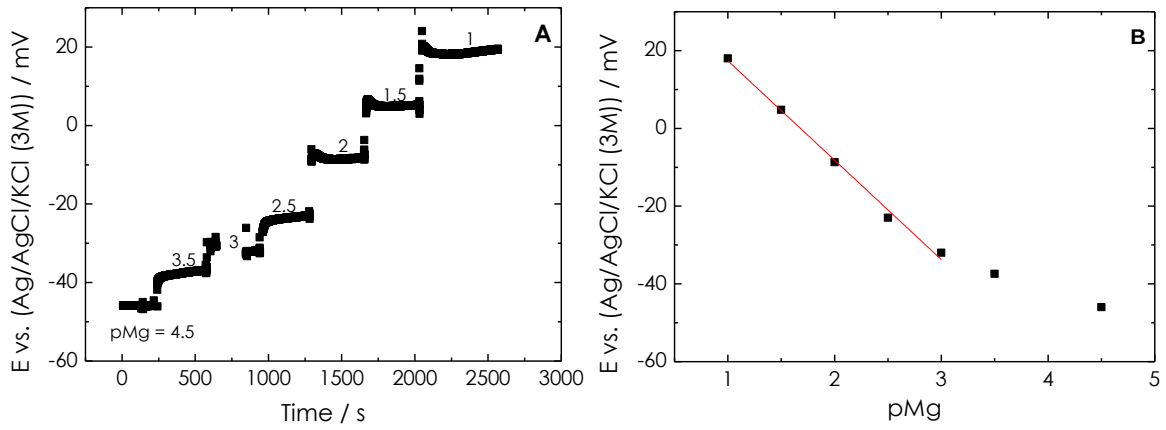

Figure 6.2.2. (A) Transient response and, (B) resulting calibration plot for the Mg^{2+} ion selective micropipette electrode in 1 mM NaCl solutions containing varying amounts of $MgCl_2$ (pMg= -log [Mg^{2+}]).

6.2.6.1. Characterization of the antimony microelectrode for amperometric operation

The preparation of the antimony electrode has already been described in Section 5.2. A micrograph of the resulting antimony microelectrode tip is shown in Figure 6.2.3A. Geometric characteristics greatly determine the amperometric operation of a disk-shaped tip in amperometric SECM. The dimensions of the active metal surface, and the effect of the insulating glass shield, can be characterized by CV. A simple redox reaction is employed for this end. Figure 6.2.3B shows a CV of the electrode immersed in naturally aerated 1 mM NaCl solution, giving an almost diffusive behaviour for oxygen reduction at potentials between -0.60 and -0.80 V vs. Ag/AgCl/KCl (3M), as depicted in the inset. Analogously, the CV of the electrode in a deoxygenated $[Ru(NH_3)_6]Cl_3$ solution is presented in Figure 6.2.3C, showing a reduction peak at around -0.20 V vs. Ag/AgCl/KCl (3M). Though this is not exactly the typical behaviour presented by microelectrodes, it still can be considered in the limit between macroscopic- and microscopic-sized electrodes because it exhibits a nearly diffusive response. The electrochemical data are consistent with the dimensions of an antimony disk electrode with dia. 175 μm, and RG = 2.9.

6.2.6.2. Calibration of the antimony microelectrode as pH sensor

Antimony microelectrodes were calibrated by measuring their open circuit potentials in nine buffer solutions. The typical calibration procedure was performed by introducing the microelectrode in a sequence of buffer solutions initiated with the most alkaline solution. In this way, the tip was exposed to solutions of increased acidity as shown in Figure 6.2.4A. The overpotential values observed in the plot

occurred upon electrolyte exchange, and next the electrode attained a steady potential value in each solution. With the potential values taken from each buffer solution, the calibration plot shown in Figure 4B was drawn. It can be observed that there is a linear relationship between the potential of the antimony tip and the solution pH in the interval between 4 and 11. The slope of the plot amounts to 42.3 mV (pH unit)$^{-1}$. Though this value is not fully Nernstian, this behaviour has also been observed for other antimony-based sensors like those employed in previous Chapter.

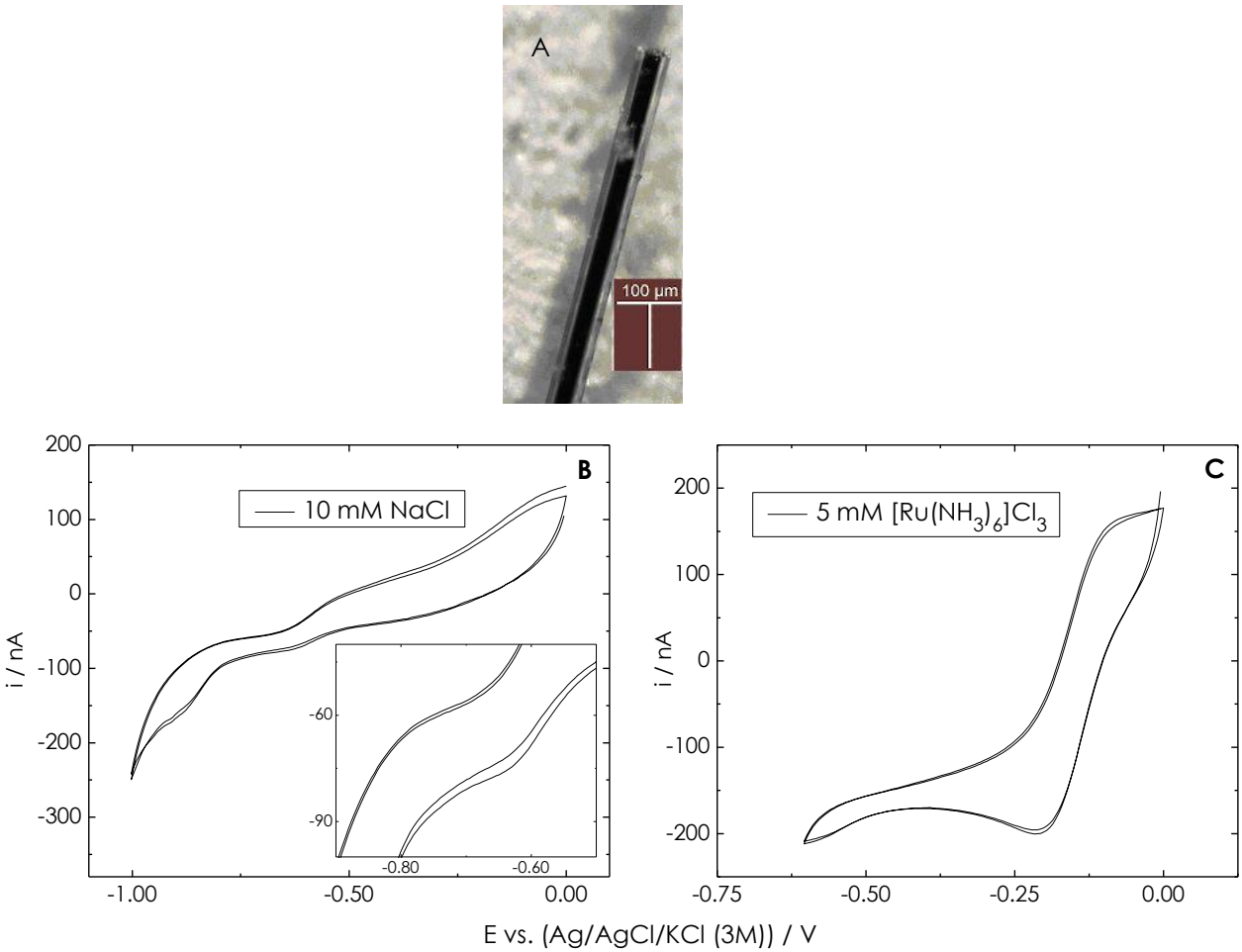

Figure 6.2.3. (A) Micrograph of the antimony microelectrode. (B-C) Cyclic voltammograms recorded at this electrode in: (B) aerated 1 mM NaCl solution, and (C) deaerated 5 mM $[Ru(NH_3)_6]Cl_3$ + 0.1 M NaCl solution. v = 0.01 V s^{-1}. Tip parameters: a = 87 µm, RG = 2.9.

6.2.7. Experimental investigation of galvanic corrosion

Galvanic corrosion can occur when two dissimilar metallic materials are in electrical contact with each other for electron transfer and are exposed to an electrolytic environment. A material with a lower free corrosion potential in a galvanic couple becomes more active and corrodes preferentially. The corrosion

rate of a galvanic couple in electric or direct contact is a technological challenge which can only be estimated with conventional electrochemical techniques. In this context, spatially-resolved chemically-sensitive microelectrochemical techniques may open a new route for quantitative characterization of those systems. In this Section, a model galvanic couple was selected as a test system for the applicability of highly selective tips in scanning electrochemical microscopy for corrosion research.

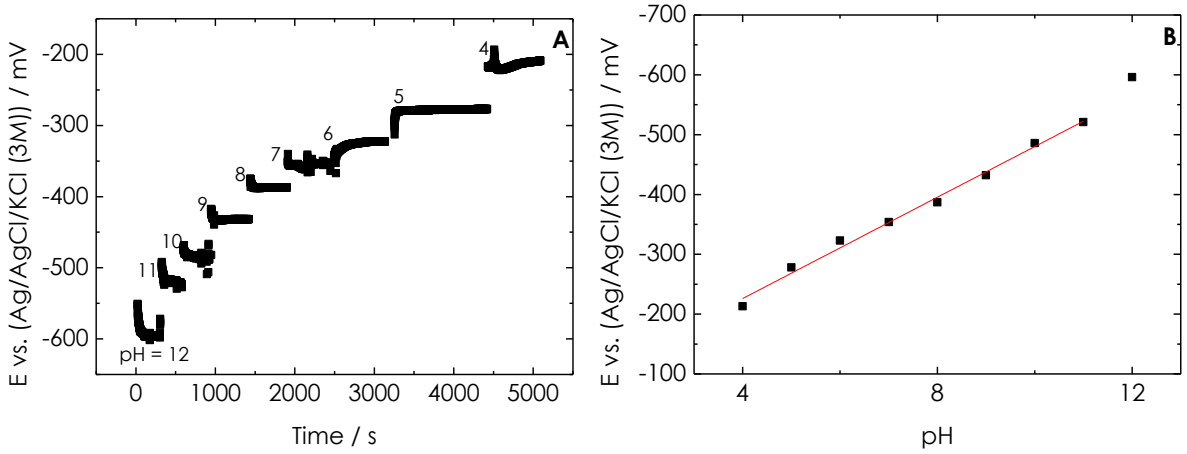

Figure 6.2.4. (A) Transient response, and (B) corresponding calibration plot for the antimony electrode in buffered pH solutions.

Magnesium-steel galvanic pairs can be encountered in aerospace and automobile applications, thus providing a corrosion problem of technological interest. For the sake of simplicity, iron could be considered instead of steel at this preliminary stage. The galvanic Mg-Fe couple employed for this study consisted on one sheet of magnesium and either a wire or a strip of iron immobilized in *Epofix*® resin. Both metals were fixed vertically in the resin, facing up their rectangle cross sections as the active surfaces to be analyzed. The separation between the two metals was ca. 5 mm. The resulting mount containing the embedded metals had a circular top surface of 3 cm diameter. The surface of the specimen was wrapped around laterally by Sellotape. Thus a small container for about 5 mL of electrolyte was created for use in the microelectrochemical measurements. The test electrolyte was 1 mM NaCl aqueous solution.

SECM experiments consisted in recording the distribution of concentrations for the chemical species involved in the galvanic corrosion process. The mount containing the two metals was scanned with the relevant SECM tips in close proximity to the surface, thus allowing chemical activity to be mapped. Initially, the two metals were left without electric contact between them, thus actually attaining their corresponding open circuit potentials in the test electrolyte. After recording the relevant SECM images over the insulated metals, the galvanic coupling effect was subsequently achieved by connecting the two metals at the rear of the mould.

The ability of the ISME to respond to changes in the concentration of magnesium soluble species as result of the onset of corrosion reactions, was first investigated using the magnesium strip as a source of its ions. In this case, the ISME tip of the SECM was placed just above the center of the magnesium sample, and its potential was monitored with the elapse of time. A steady reading was obtained as long as the metal was maintained without galvanic coupling with iron. After a selected time, galvanic coupling of the metals was imposed, and enhanced dissolution of magnesium occurred as result of it. This resulted in potential oscillations in the recording of the tip as shown in Figure 6.2.5 which depicts the behaviour in the case of two such experiments. Less negative values of the potential at the ISME are observed because a higher amount of magnesium ions have been released into the solution from the metal surface. Vigorous hydrogen gas evolution over the magnesium strip was also observed through the videocamera. It has been demonstrated that the tip responds to variations in the activity of magnesium ions due to an increase in the rate of corrosion of the metal.

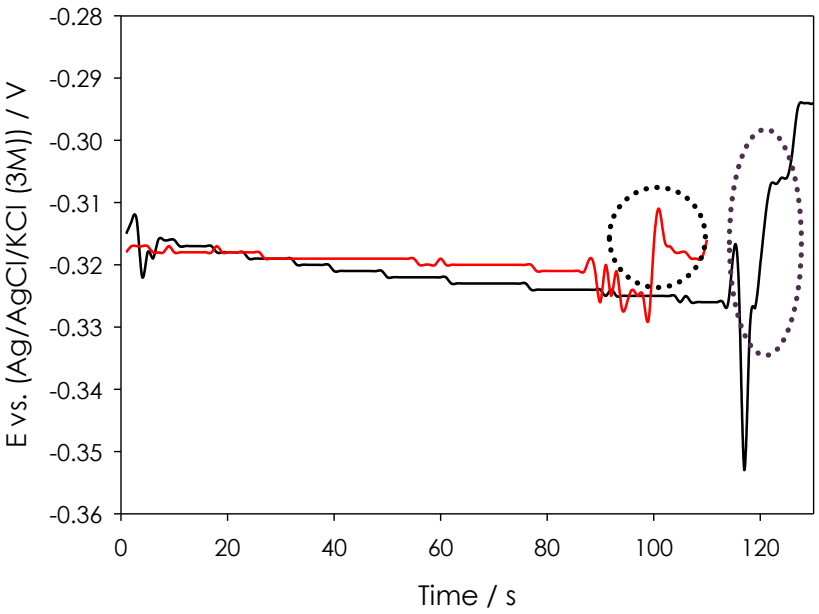

Figure 6.2.5. Potentiometric SECM measurement of the potential variation with time occurring at a solid contact Mg^{2+}-ISME placed just above the magnesium strip in a magnesium-iron galvanic pair immersed in 10 mM NaCl. The two wires were maintained electrically-disconnected until connected for the times indicated by the circles in the plot.

Figure 6.2.6 shows the SECM maps related to the spatial distribution of magnesium ions that were recorded using the solid contact Mg^{2+}-ISME. In the case of the uncoupled metal (cf. Figure 6.2.6A), active corrosion of the magnesium strip is observed to occur in this electrolyte, leading to the release of metal ions into the solution. Nevertheless, the anodic activity is observed to concentrate on a portion of the metal strip (located in the upper part of the image). Thus, the remaining surface of the metal actually acts as a cathode to maintain the corrosion process, as

indicated by the pMg values close to zero that are measured in the lower part of the exposed sample. Upon galvanic coupling of the two metals, enhanced dissolution of the magnesium strip occurs, resulting in pMg values almost three orders of magnitude greater than those recorded for the uncoupled metal. Furthermore, the metal dissolution process now extends over all the length of the exposed metal strip, though the process occurs heterogeneously, with anodes shifting positions over the exposed metal (see Figure 6.2.6B).

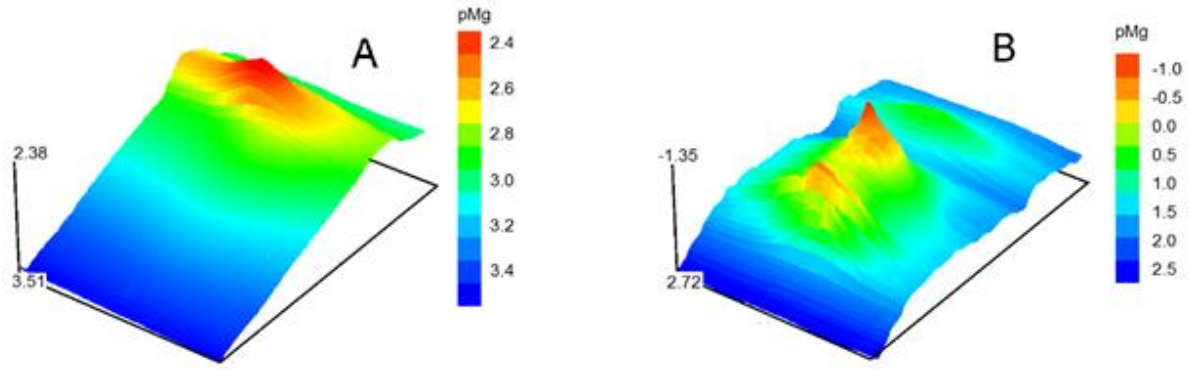

Figure 6.2.6. Potentiometric SECM images measured with the Mg^{2+}-ISME depicting the magnesium ion concentration over the magnesium strip when the magnesium-iron sample was immersed in 1 mM NaCl. The *Z* scale is the measured magnesium activity in pMg. The metals were: (A) without, and (B) with galvanic connection. The figures represent an area of 1000 µm x 1500 µm in *X* and *Y* directions, respectively.

Changes in the solution pH close to the mount, which are associated with the corrosion process, could be monitored when the antimony microelectrode was employed for the potentiometric operation of the SECM. Figure 6.2.7 depicts the pH distributions occurring over the magnesium strip for the uncoupled (image A) and the coupled (image B) metal. For the uncoupled metal, alkalization of the electrolyte volume close to the surface occurs. In this case, an almost homogeneous distribution of pH is found over the metal, whereas the pH decreases as the tip scans about the epoxy mount surrounding the metal strip. Conversely, upon galvanic coupling, the magnesium surface becomes less alkaline, because the cathodic activity is now moved to the iron wire (image C). Yet, the pH distribution above the magnesium strip is heterogeneous, and the less alkaline areas correspond to sites where dissolution occurs preferentially.

Finally, the antimony tip could also be employed to monitor the corresponding cathodic process by measuring oxygen consumption with the SECM in amperometric operation. The images given in Figure 6.2.8 show the regions with depleted oxygen in the electrolyte adjacent to the iron strip, as those where the tip recorded smaller faradaic currents [10]. Again, a major change is observed in the SECM images when the two metals are coupled, as illustrated by the higher peak in Figure 6.2.8B. In this case, tip currents close to 0 nA were measured over the metal, thus showing that oxygen was absent from the thin electrolyte volume comprised

between the tip and the iron strip. This proves that the whole metal was behaving as a cathode when galvanically-coupled to magnesium. Therefore, the iron strip is effectively protected from corrosion through its connection with the sacrificial anode of magnesium.

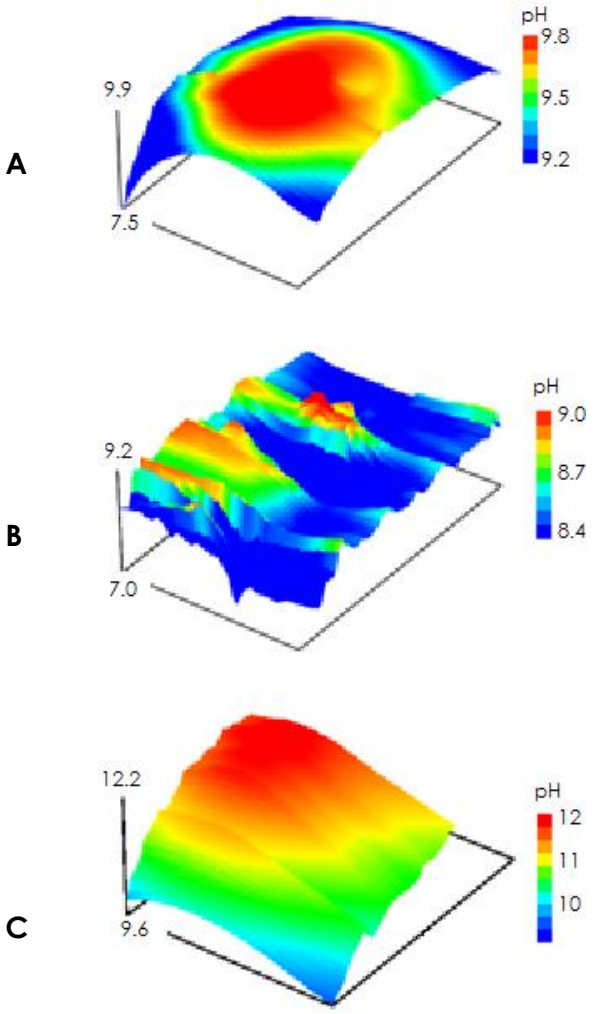

Figure 6.2.7. Potentiometric SECM images measured with the antimony electrode depicting pH distribution over the magnesium strip and iron wire when the magnesium-iron sample was immersed in 1 mM NaCl. The *Z* scale is the measured magnesium activity in pMg. The metals and electrical conditioning were: (A) uncoupled magnesium, (B) galvanically-coupled magnesium, and (C) galvanically-coupled iron. The figures represent an area of: (A,B) 1000 µm x 1500 µm, and (C) 1500 µm x 1500 µm in *X* and *Y* directions, respectively.

6.2.8. Conclusions

Significant improvement in SECM for the investigation of corrosion processes is achieved by combining amperometric and potentiometric operations in the instrument. Dual potentiometric/amperometric tips based on the special properties of certain oxides of transition metals such as antimony allow conventional SECM

operation and pH detection in the same experiment. Furthermore, ion-selective microelectrodes based on micropipettes with an internal solid contact, are robust enough to be employed as SECM tips for selective detection of relevant chemical species. Thus, combinations of operation modes in SECM can be employed for more sensitive applications of SECM imaging in Corrosion Science.

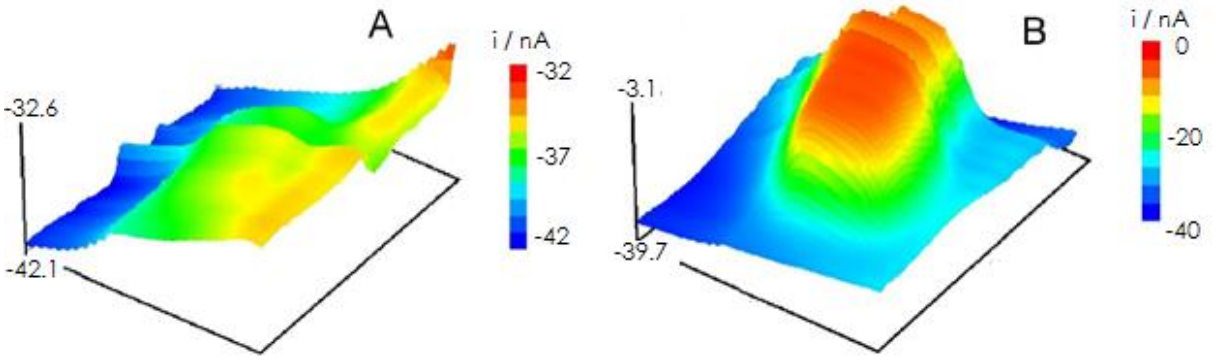

Figure 6.2.8. Amperometric SECM images measured with the antimony tip depicting oxygen consumption over the iron strip when the magnesium-iron sample was immersed in 10 mM NaCl. The *Z* scale is the tip current in nA. The metals were: (A) without, and (B) with galvanic connection. Tip potential: -0.70 V vs. Ag/AgCl/KCl (3M). The figures represent an area of 2500 µm x 3000 µm in *X* and *Y* directions, respectively.

6.2.9. References

1. R.S. Lillard. In: Analytical Methods in Corrosion Science and Engineering (Edited by P. Marcus, F, Mansfeld). Taylor and Francis, Boca Raton, 2006, p. 571.
2. L.F. Jaffe, R. Nuccitelli. Journal of Cell Biology 63 (1974) 614.
3. S.V. Lamaka, R.M. Souto, M.G.S. Ferreira. In: Microscopy: Science, Technology, Applications and Education. Vol. 3 (Edited by A. Méndez-Vilas, J, Díaz). Formatex, Badajoz, 2010, p. 2162.
4. P.J.S. Smith, R.H. Sanger, M.A. Messerli. In: Electrochemical Methods for Neuroscience (Edited by A.C. Michael, L.M. Borland LM). CRC, Boca Raton, 2007, p. 373.
5. S. Rossi, M. Fedel, F. Deflorian, M.C. Vadillo. Comptes Rendue Chimie 11 (2008) 984.
6. A.J. Bard, F.-R.F. Fan, J. Kwak, O. Lev. Analytical Chemistry 61 (1989) 132.
7. J. Kwak, A.J. Bard. Analytical Chemistry 61 (1989) 1221.
8. A.J. Bard, G. Denuault, C. Lee, D. Mandler, D.O. Wipf. Accounts of Chemical Research 23 (1990) 357.
9. L. Niu, Y. Yin, W. Guo, M. Lu, R. Qin, S. Chen. Journal of Materials Science 44 (2009) 4511.

10. R.M. Souto, S.V. Lamaka, S. González. In: Microscopy: Science, Technology, Applications and Education. Vol. 3 (Edited by A. Méndez-Vilas, J, Díaz). Formatex, Badajoz, 2010, p. 1769.
11. Y. González-García, G.T. Burstein, S. González, R.M. Souto. Electrochemistry Communications 6 (2004) 637.
12. R.M. Souto, Y. González-García, S. González. Corrosion Science 47 (2005) 3312.
13. S. González, J.J. Santana, Y. González-García, L. Fernández-Mérida, R.M. Souto. Corrosion Science 53 (2011) 1910.
14. G. Denuault, G. Nagy, K. Tóth. In: Scanning Electrochemical Microscopy (Edited by A.J. Bard, M.V. Mirkin). Marcel Dekker, New York, 2001, p. 397.
15. G. Nagy, L. Nagy. Analytical Letters 40 (2007) 3.
16. B.R. Horrocks, M.V. Mirkin, D.T. Pierce, A.J. Bard, G. Nagy, K. Tóth. Analytical Chemistry 65 (1993) 1213.
17. M.A. Messerli, L.P. Collis, P.J.S. Smith. Biophysics Journal 96 (1999) 1597.
18. A. Craggs, G.J. Moody, J.D.R. Thomas. Journal of Chemical Education 51 (1974) 541.
19. G. Gyetvai, S. Sundblom, L. Nagy, A. Ivaska, G. Nagy. Electroanalysis 19 (2007) 1116.
20. G. Gyetvai, L. Nagy, A. Ivaska, I. Hernadi, G. Nagy. Electroanalysis 21 (2009) 1970.
21. E. Lindner, R.E. Gyurcsányi, R.P. Back. Electroanalysis 11 (1999) 695.
22. S. Bodor, J.M. Zook, E. Lindner, K. Tóth, R.E. Gyurcsányi. Analyst 133 (2008) 635.

6.3

Potentiometric scanning electrochemical microscopy for the local characterization of the electrochemical behaviour of magnesium-based materials

6.3.1. Abstract

The applicability of scanning electrochemical microscopy for the local detection and quantification of relevant species participating in the corrosion of magnesium-based materials is presented. The magnesium-iron galvanic pair exposed to aqueous NaCl solution was adopted as model system for this purpose. Mg^{2+} ion concentration and pH profiles were investigated using ion-selective electrodes, containing a liquid membrane and Sb/Sb_2O_3 as sensor elements, respectively. Oxygen consumption at the substrate related to the cathodic reaction was also monitored with the antimony-based electrode though operated amperometrically. Data show a major production of hydroxyl anions at the cathodic sites as result of the oxygen reduction half-reaction, whereas in the vicinity of the magnesium surface pH is greatly affected by the anodic dissolution process instead. The later produces the release of metal cations accompanied by hydrogen evolution.

6.3.2. Resumen

Se presenta la aplicabilidad de la microscopía electroquímica de barrido para la detección y cuantificación local de especies relevantes que participan en la corrosión de materiales de base magnesio. Se ha adoptado para este propósito el par galvánico hierro-magnesio expuesto a disolución acuosa de NaCl. Se han investigado los perfiles de concentración de Mg^{2+} y de pH, utilizando como elementos sensores electrodos de ion selectivo con membrana líquida, y de Sb/Sb_2O_3, respectivamente. También se ha analizado el consumo de oxígeno en el substrato, relacionado con la reacción catódica, con el electrodo de base antimonio pero operado amperométricamente. Los datos demuestran una elevada producción de aniones hidróxido en los sitios activos como resultado de la semirreacción de reducción del oxígeno, mientras que en la proximidad de la superficie de magnesio el pH se ve ampliamente afectado por los procesos de disolución anódica. Esto último da lugar a la generación de cationes metálicos junto con el desprendimiento de gas hidrógeno.

6.3.3. Introduction

Electrochemical corrosion is one major cause of economic losses in the industrialized countries [1]. Despite their attractive mechanical properties, most metals and alloys spontaneously undergo corrosion if certain conditions occur, especially in aqueous environments. Particularly, due to its high strength-to-weight ratio, magnesium and its alloys are attractive materials for several applications in the automotive, aerospace, electronics and energy-production industries [2-5]. And they are often found in unavoidable contact with other metals such as aluminum or steel [5]. However, these materials lack stability against corrosion and usually require additional protection. In fact, thanks to its tendency to degrade in aqueous environments, it has been considered as a potential biodegradable and biocompatible material for non permanent implants [6-9]. Moreover, its position in the galvanic series has allowed magnesium to be evaluated for the protection of other metals by acting as sacrificial anode, either as a component of a protective coating, or via direct galvanic connection [10-14]. Besides, several Mg-containing alloys like those aluminum-based ones, tend to suffer from preferential dissolution of this component, usually the most active in the material [5,15,16].

Local microcells are originated in a metallic material subjected to corrosion, with the subsequent spatial distributions of anodes and cathodes on its surface when left at its open circuit potential (OCP). In this way, dissolution occurs as result of metal oxidation at the anodes, whereas this process is maintained by the reduction of some species from the environment at the cathodes, usually oxygen in neutral and moderately alkaline media, or protons in acidic solutions. Since these local cells are originally formed within the range of micrometers and nanometers, a comprehensive understanding of the mechanistic aspects of corrosion requires the synthesis of data in those scales. Unfortunately, conventional electrochemical techniques lack spatial resolution and provide little information on behaviour at sites of corrosion initiation or at defects. The recent advent of a variety of local probe techniques is greatly contributing to overcome these limitations when applied to the investigation of corrosion processes *in situ*. Following this trend, researchers are exploring a wide variety of methods to characterize local electrochemical processes, which range from the design of microelectrochemical cells and setups, to the use of scanning probe techniques [17]. Among the later scanning electrochemical microscopy (SECM) has become one of the most powerful local techniques for corrosion research due to the wide variety of operation modes which contribute to give a great versatility to the technique [18-20].

The corrosion of metals produces local changes in the concentrations of ionic and molecular species present in the adjacent liquid phase. Thus, the M^{z+} ions produced at the anodic sites are transferred under diffusion control to the bulk, and the system can be studied by amperometric SECM [21]. This feature has been exploited to image the generation of specific metal cations in several studies that include visualization of metastable pits on austenitic steel *ex situ* by SECM at the

open circuit potential [22], to the detection of metal dissolution either from inclusions in alloys [23-25] or from defects in polymer-coated metals [10,26,27]. On the other hand, in a neutral aqueous medium, the reaction of dissolved oxygen from the electrolyte at the cathodic areas may be analyzed through monitoring of the subsequent depletion of oxygen content in the solution volume adjacent to the cathodic sites [28-32]. However, for the detection of concentration distributions in certain corroding samples, especially for metals with sufficiently negative redox potentials in aqueous environments, the use of Pt microelectrodes is limited by the onset of oxygen reduction and hydrogen evolution reactions [10,27,31]. Thus, for effective amperometric operation of the SECM, it becomes necessary to either purge out oxygen and to use modified electrodes to avoid early evolution of hydrogen gas [33,34]. Yet, more robust and selective procedures are to be developed for the analysis of these metal cations in order to gain a better understanding of the mechanisms involved in corrosion and passivation. As it is well known, corrosion processes are dramatically affected by pH too. Furthermore, both corrosion half-cell reactions may lead to local changes in pH of the surrounding environment. On one hand, alkalization always occurs in the cathodic sites due to either H^+ consumption or OH^- release, depending on nature of sample and electrolyte, and it may facilitate the formation of passive films. On the other hand, some corrosion-produced metal ions may undergo hydrolysis at the anodic sites, and consequently reduce the local pH, a feature that usually accelerates the corrosive attack. Though the extent of pH variation associated with the hydrolysis of metal ions mainly depends on the equilibrium constant for their hydrolysis process [35], thus greatly varying from one metal to another, it may become a major feature affecting the onset of local corrosion microcells. Therefore, the measurement of the local alterations of pH in the vicinity of a corroding system and their time evolution is a matter of major interest.

In contrast, though rather scarcely applied, these physicochemical parameters may be studied using ion-selective electrodes (ISEs) as tips. In this case, the SECM is operated in the potentiometric mode [36-38], which gives greater chemical selectivity. The applicability of Zn^{2+} ion-selective microelectrodes (ISMEs) for the study of model corrosion systems with SECM [39,40] has been recently demonstrated, similarly to what has already been achieved with the Scanning Ion Electrode Technique (SIET) [41]. In studies applying SIET, a variety of ion-selective systems has been investigated [42-50], including Mg^{2+} species released during corrosion of the buried metal from defects operated on coated magnesium alloys [42,45,48]. Yet investigations of magnesium substrates with SECM have only been carried out in amperometric mode [51,52] or for measurements of the electrolyte resistance between the tip and the substrate [53], using always Pt microelectrodes as the probe. In those studies, visualization of active regions in the surface was accomplished, however selective potentiometric detection of the local concentration of the corrosion produced Mg^{2+} ions was not attempted.

Most often liquid type microelectrodes have been employed for studying pH distributions above corroding metal surfaces [42-50]. Nevertheless, for corrosion

purposes using SECM, it would be preferable to use microelectrodes based on the characteristics of certain oxides of transition metals such as antimony [54-56] and iridum [57]. These solid state microelectrodes are much more robust than ion selective micropipettes. Furthermore they have the ability to behave as double function electrodes. This means that while in potentiometric mode they detect local pH, they can also function as amperometric SECM tip to detect electroactive species.

This Section reports preliminary results on the characterization of a model corrosion system formed by a magnesium-iron galvanic couple which were obtained from SECM measurements using antimony and Mg^{2+}-ion selective electrodes as the tips. The concentration distributions of dissolved oxygen and Mg^{2+} ions, as well as the pH distributions that result of the galvanic corrosion process, were measured and analyzed in terms of the reactions occurring in the system.

6.3.4. Experimental section

6.3.4.1. Chemicals and solutions

High purity antimony in powder presentation (Aldrich) was employed for the fabrication of the antimony electrode. Solutions were prepared from Millipore deionised water and analytical grade chemicals. The inner reference solution employed in the lumen of the Mg^{2+}-ion selective microelectrode (ISE) was 10 mM $MgCl_2$ + 0.25 M KCl. Different concentrations of the same magnesium salt, dissolved in 10 mM NaCl solution, were employed for calibration of the ISE.

The ionophore employed in the fabrication of the Mg^{2+} ISE was bis-N,N-dychlohexyl-malonamide, which was synthesized following the method described in ref. [58]. The composition of the ion selective cocktail was the following: 2.1 wt.% ionophore, 34.0 wt.% high molecular weight poly(vinyl-chloride), and 63.9 wt.% o-nitrophenyloctylether. 70 mol.% potassium tetrakis(p-chlorophenyl)borate was subsequently added. All the components in the ionophore membrane were supplied by Sigma-Aldrich. Ion-selective microelectrodes were prepared using micropipettes pulled from borosilicate glass capillaries B200-116-10 (Sutter, Novato, CA, USA). The inner wall of the pipette tips were hydophobized exposing them to a solution of dimethyldichlorosilane in carbon tetrachloride.

6.3.4.2 . Samples and instruments

The galvanic Mg-Fe couple employed for this study consisted on one sheet of each metal immobilized in *Epofix* resin (Struers, Ballerup, Denmark). Iron was cut from 1 mm thick sheet of 99.99% purity purchased from Goodfellow Materials Ltd. (Cambridge, UK), in order to obtain a 1 mm x 2 mm strip. For the magnesium surface, metal ribbon of 99% purity supplied by Panreac (Barcelona, Spain), with a cross

section of 200 μm x 3 mm, was employed. The metal was not analysed, but typical impurity levels (in ppm) were cited by the supplier as: Cu 5, Fe 50, Ni 5, Pb 5, Zn 20. Both metal strips were fixed vertically in the resin, facing up their rectangle cross sections as the active surfaces to be analyzed. The separation between the two metals was ca. 5 mm, which was assumed to be enough distance to avoid alterations in either of the active metal areas due to the reactions taking place on the other one for the duration of the tests performed in this study. The resulting mount with the embedded metals had a circular top surface of 3 cm diameter. The surface of the specimen was flat ground with abrasive SiC paper up to 4000 grit, rinsed with ethanol, dried in air, and finally wrapped around laterally by Sellotape that reached over the mount surface for about 6 mm. Thus a small container of approximately 5 mL of electrolyte was created for the microelectrochemical measurements.

The antimony electrode employed in SECM for combined potentiometric/amperometric operation was fabricated following the procedure described in Section 5.2 of this Thesis. In brief, the fabrication was initiated by heating the antimony powder in a melting pot with a gas flame. When antimony melted, it was introduced in a thick glass Pyrex capillary using syringe suction. The resulting, antimony filled capillary was then pulled manually with standard glass blowers technique using metallic tweezers. This resulted in a small diameter glass fiber filled with antimony. A pipette with 500 μm tip diameter was prepared from borosilicate glass-capillary and a section of the previously prepared antimony fiber was inserted in its lumen with the tip reaching out for about 15 mm, whereas ca. 20 mm long staying in the lumen. Mercury metal and a copper wire were then inserted into the lumen of the thicker capillary to provide electrical contact resulting in the assembly shown in Figure 6.3.1A. Loctite® adhesive was used to seal both ends. The final microelectrode had an antimony disk of 175 μm with an *RG* value of 2.9. The electrochemical response of the antimony microelectrode for amperometric operation was tested in two electrolytes, namely aerated 10 mM NaCl, and deaerated 5 mM $[Ru(NH_3)_6]Cl_3$ + 0.1 M NaCl solutions. Potentiometric operation was directed to monitor the effect of pH on the potential of the electrode. Calibration was performed using 9 buffer solutions covering the range $4 \leq pH \leq 12$. A linear relationship between the potential of the antimony tip and the solution pH was observed between 4 and 11, and the slope of the calibration plot amounted 42.3 mV $(pH\ unit)^{-1}$.

Potentiometric ion-selective operation was performed using a conventional micropipette type Mg^{2+}-ISE, that was prepared with liquid internal filling solution and a silver chloride coated silver wire of 250 μm diameter, as internal reference electrode. Schematic drawing of the micropipette electrode is shown in Figure 6.3.1B. It was fabricated according to well established procedures [59,60]. In brief, two micropipettes were first pulled from one glass-capillary, and subsequently silanized by introducing inside a few microliters of 5 vol.% dimethyldichlorosilane solution in carbon tetrachloride. The hydrophobic layer was obtained by keeping the micropipettes at 80^0C in an oven for about 30 min.

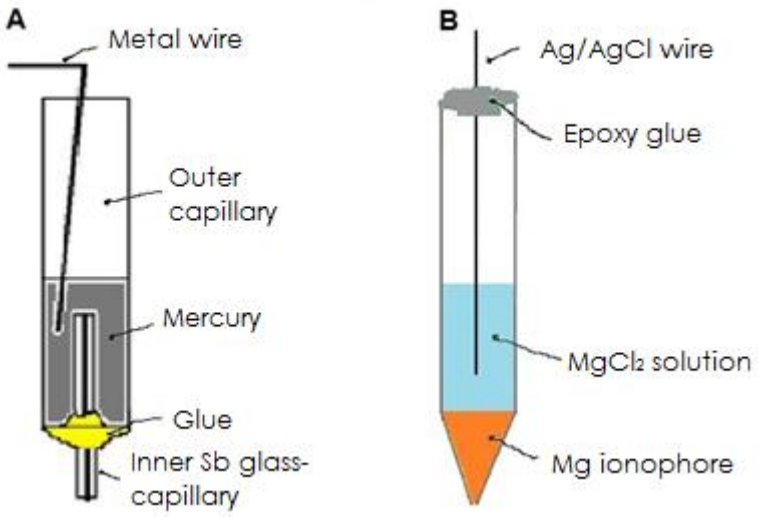

Figure 6.3.1. Sketches of the two types of potentiometric tips employed in the SECM measurements: (A) antimony electrode, and (B) micropipette-based Mg^{2+}-ISE (containing 10^{-2} M $MgCl_2$ + 0.25 M KCl as the internal solution).

The ionophore cocktail was then filled into the micropipette by applying vacuum from the back side with an attached syringe. Finally, the internal solution was backfilled with the assistance of a very thin capillary attached to a syringe, and the Ag/AgCl was placed and fixed with Loctite® adhesive. Due to the relatively big size of the metal samples employed in this study, micropipettes with about 180 µm tip diameter were prepared and used. As it is well known micropipette ISEs can be easily prepared with submicron diameter, however it was not justified to use so small tips in this work, because they present bigger resistance and high noise picking up character.

6.3.4.3. Instruments

Measurements were performed in an SECM equipment built by Sensolytics (Bochum, Germany), controlled with a personal computer. The electrochemical interface employed in the amperometric operation was an Autolab bipotentiostat provided with a frequency response analyzer (Metrohm, Herisau, Switzerland). In this case, the electrochemical cell was completed with an Ag/AgCl/KCl (3M) electrode as reference, and a Pt wire as counter electrode. Alternating current (AC) mode was also performed using these instrument and cell configurations. AC voltage signals of 10 mV_{pp} amplitude around the open circuit potential of the tip in the electrolyte were applied. A total of 26 frequency values in the 351 to 55493 Hz frequency range were used, and the values spaced logarithmically. The same SECM instrument was employed for the potentiometric measurements using ion-selective electrodes, though in this case a home-made voltage follower based on a 10^{12} Ω input impedance operational amplifier was interconnected between the cell and the potentiometric input of the system.

6.3.5 . Results

6.3.5.1. Mg^{2+} distribution over the magnesium surface

In order to study the distribution of Mg^{2+} concentration in the electrolyte from metal corrosion, SECM in potentiometric operation was employed with a Mg^{2+}-ISE as probe. The metal sample was placed at the bottom of the small electrochemical cell, and the Mg-ISE tip was fastened onto the tip holder. Before the test electrolyte was added to the cell, the tip was placed over the center of Mg metal surface using the *X-Y* motors of the instrument. A video camera was employed to assist the process. Next, the tip was carefully moved towards the metal surface by means of the *Z*-motor until ca. 75 µm vertical tip-substrate distance was reached. At this stage, the test solution was added to the measuring cell, the reference electrode was introduced, and the two metals in the sample were electrically connected at the rear of the sample by means of a copper wire. The evolution of the EMF of the cell was monitored with the elapse of time. After a few minutes, a steady voltage was attained. Then the tip was slowly removed from the metal surface, at a speed of 5 µm s^{-1} moved upward, while recording the electrode potential at the ISE. Once the chosen maximum tip-substrate distance was reached, the tip-substrate distance was kept constant for two minutes, and subsequently the tip was moved down at the same rate, 5 µm s^{-1}, to approach the Mg metal surface again. The electrode potential vs. tip-substrate distance curves could be converted into pMg – tip-substrate distance plots using the calibration curve of the electrode. Normalized tip-substrate distances were used by determining the ratio between the tip radius, *a*, and the vertical tip-substrate distance, *d*. The pMg – *d* / *a* curves measured during the initial withdraw (black curve) and the subsequent approach (red curve) steps are shown in Figure 6.3.2. Next, the electric connection between the Fe and Mg metals was removed, and a new retreat pMg – *d* / *a* curve was registered for the electrically-disconnected magnesium metal (cf. the blue curve in Figure 6.3.2).

As it was expected, the Mg^{2+} ion concentration was higher when the tip was placed closer to the substrate. Nevertheless, the approaching (black) and the withdrawing (red) experimental curves for the galvanically-coupled metals are quite different. This difference can be attributed to unavoidable convection in the electrolyte produced by the motion of the tip. That is, as the tip is moved, it displaces some electrolyte from the Mg^{2+}-rich surroundings of the metal to the bulk solution, resulting in the measurement of bigger values for ion concentration during the retreat movement. And the opposite behaviour is observed when recording the approach curve.

Higher pMg data were determined when the two metals were disconnected. This indicates that magnesium dissolves less vigorously in the environment when it is not acting as sacrificial anode for iron. From the plots given in Figure 6.3.2, it is also obvious that when magnesium was galvanically-coupled to iron, the curves were rougher than the one determined over the unconnected metal. The origin of this fact could be explained with the assistance of the video camera, because gas evolution

occurred on the surface of magnesium when the two metals were electrically connected. That is, gas evolution was not exclusively restricted to the iron strip, but it was even more vigorous over magnesium. It is known from basic chemistry that the gas evolving at the magnesium - water interface must be hydrogen resulting from the reaction between this metal and water. Interestingly the magnesium acts as an anode in the Mg-Fe couple, but hydrogen is reduced during its corrosion protecting function, a distinctive feature for this metal and its alloys [5].

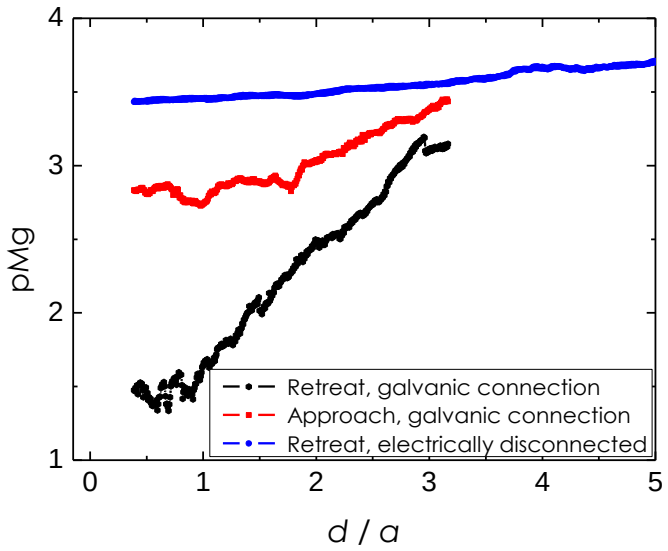

Figure 6.3.2. Distribution of Mg^{2+} ion concentration above the magnesium strip measured with the Mg^{2+}-ISE as the height of the tip is changed. The magnesium-iron sample was immersed in 10 mM NaCl solution, whereas the two metals were either connected electrically (i.e. galvanic coupling) or disconnected. Both the direction of the tip movement and the electrical condition of the metal are given in the graph. *d / a* is the dimensionless distance between the sample and the tip. Scan rate: 5 µm s^{-1}.

The electric connection of the two metals originates the development of a high negative potential on the iron metal. It was observed to be more negative than -1.60 V vs. Ag/AgCl/KCl (3M) at all times. These potential values lay outside the stability range of water. And hydrogen gas evolution is also occurring at the iron surface.

Concentration profiles of Mg^{2+} ions were also determined by rastering the ISE parallel to the surface. Line scans were measured along the 200 µm cross section of the Mg area, both with (red curve) and without (black curve) galvanic connection between the two metals. Results are given in Figure 6.3.3 for single scan lines determined when the tip was maintained at ca. 75 µm vertical distance from the surface. As it was observed before, the signal registered near the corroding metal indicated higher Mg^{2+} concentration when the metal was acting as sacrificial anode in the magnesium-iron galvanic pair, than those measured when the two metals were disconnected. The maximum dissolution of magnesium was detected when the

tip passed over the central position of the metal strip, which supports that the whole area was behaving anodically. Conversely, this maximum over the center of the Mg strip surface was not observed when the metals were not in electrical contact. In this case, the shape of the concentration profile was not symmetric over the metal, and a separation between the portion acting as the anode (at the left side of the line scan), and the area functioning as hydrogen-reducing cathode (right side), could be noticed.

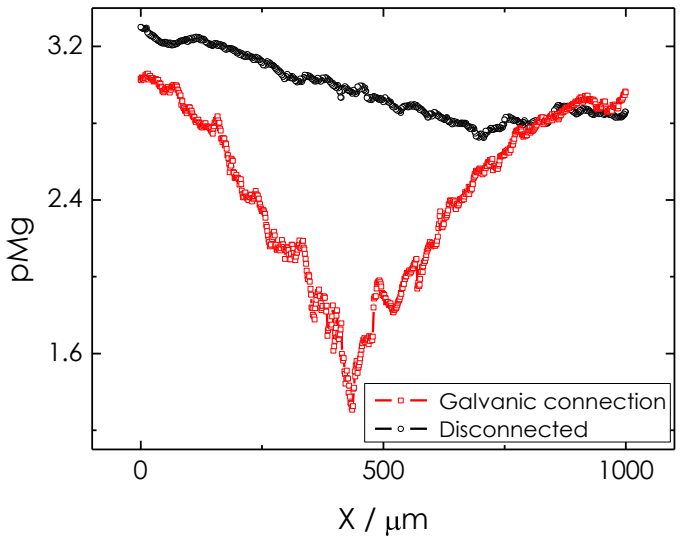

Figure 6.3.3. Potentiometric SECM scan lines measured above the magnesium strip in the magnesium-iron sample during immersion in 10 mM NaCl. Vertical tip-substrate distance: 75 µm; scan rate: 5 µm s^{-1}.

Additionally, several concentration profiles were measured at different locations over the Mg strip while the metal was under galvanic connection. In this way, heterogeneities in the location of the corrosion process over the metal could be detected. Figure 6.3.4 depicts six concentration profiles measured when the tip was moved along the *X* axis at different *Y* positions, covering a total length of 100 µm in the *Y* axis, whereas keeping the same scan direction used to record Figure 6.3.3. That is, scanned *X* lines correspond to several of the cross sections taken in the 200 µm width direction of the magnesium area, which were measured over a central region of the larger 3 mm side. Despite the fact that the tip is actually too large to spatially resolve the system in these dimensions, the concentration profile measured for *Y* = 20 µm shows the highest values, indicating a region in the anodic surface of the metal displaying greater electrochemical activity. Further studies would be necessary to determine the actual heterogeneity of the whole system and its possible relationship to any microstructural features as the nucleation sites for the eventual generation of corrosion pits as result of it.

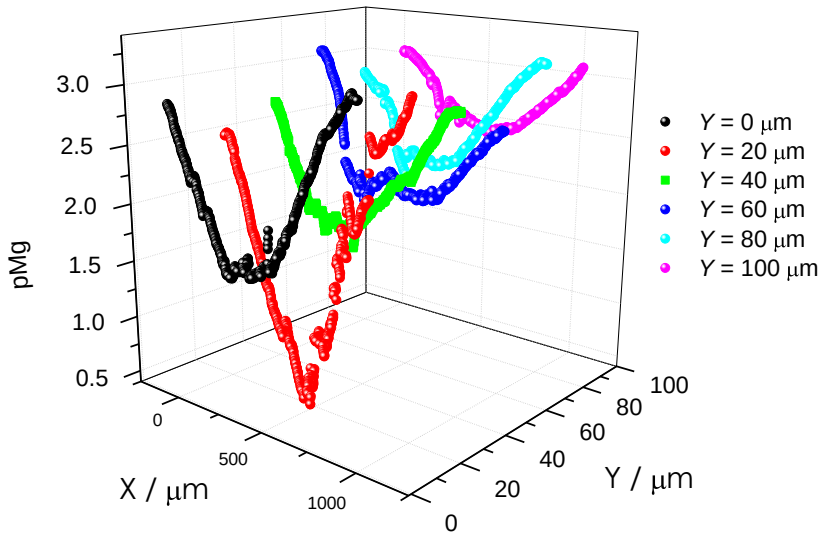

Figure 6.3.4. Potentiometric SECM scan lines measured when the tip crossed crossing (*X* direction) over the magnesium strip in the magnesium-iron galvanic pair immersed in 10 mM NaCl, taken in a plane parallel to the surface of the metal. The different curves were obtained after shifting the tip in the *Y* direction in 20 μm steps. Tip-substrate distance: 75 μm; scan rate: 5 μm s^{-1}.

6.3.5.2. Oxygen consumption

When a sacrifice anode is used for corrosion protection, oxygen consumption occurs at the cathodic sites of the protected metal surface if these metals are placed in non-acidic environments. In order to study the oxygen concentration profile over the protected iron surface, an antimony microelectrode was employed as the SECM measuring tip while the technique operated in the amperometric mode. Since the SECM was operated in the amperometric mode, the tip-substrate distance could be adjusted using the negative feedback effect when approaching a zone of the resin sleeve located between the two metals. Furthermore, variations in the local oxygen concentration can also be visualized. For this purpose, the electrode was placed as close to the surface of the iron strip as possible with the assistance of a video camera, and subsequently retracted 1000 μm in the *Z* direction. Next, the tip was shifted horizontally 1.5 mm to be located above the resin sleeve. After the test electrolyte was added to the system, and while the two metals were kept electrically disconnected, the *Z*-approach curve was recorded. A constant potential of -0.70 V vs. Ag/AgCl/KCl (3M) was applied to the tip, a potential value at which oxygen reduction occurs. The closest tip-substrate distance in *Z*-approach curve shown in Figure 6.3.5 occurs for a negative feedback of ca. 60% (black curve). This reduction in the faradic current measured at the tip corresponds to a height of 85 μm over the surface for a microelectrode of 175 μm diameter with *RG* = 2.9 [61]. After this curve was recorded, the tip was lifted up, and moved parallel to the surface to a position located just above the center line of the iron strip to record the corresponding *Z*-approach curve. The same scan parameters were employed as before, still without

galvanic connection between the two metals. The corresponding approach plot is also given in Figure 6.3.5 (blue curve). Though it could be expected that the corrosion of the disconnected iron should result in some oxygen consumption, the negative feedback effect actually seemed to be smaller on iron than above the resin. This apparent discrepancy could be explained by considering differential polishing on the resin and the metal piece. That is, due to the difference in hardness between the materials, the metal sample can be expected to protrude above the surrounding resin holder. Indeed, the *Z*-approach curve measured above the iron strip could be superimposed over that obtained on the resin by slightly shifting the curve along the *X* axis of the graph. In the forecoming, this observed distance difference was taken into account in order to establish the actual tip-substrate distance. On the other hand, the fact that the *Z*-approach curves measured both on the resin and on the iron strip could be superimposed, indicates that the extent of iron corrosion in this environment does not lead to a significant depletion of the oxygen concentration at early exposures.

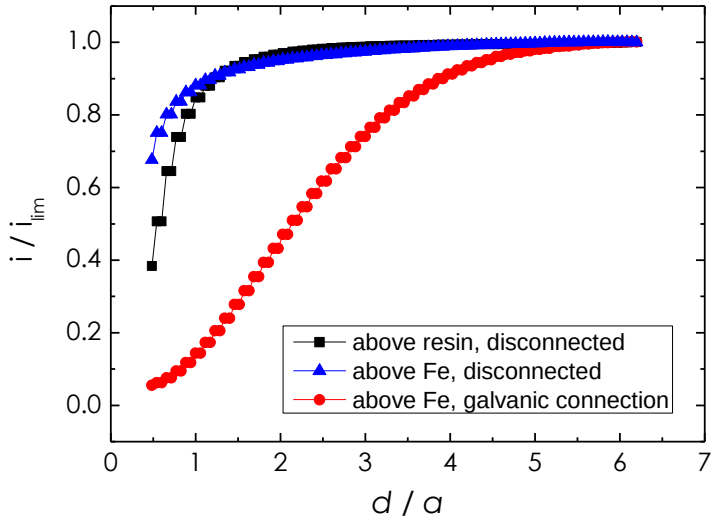

Figure 6.3.5. Normalized *Z*-approach curves measured with the antimony electrode in amperometric SECM operation using oxygen reduction at the tip as redox mediator reaction. The plots were measured above the resin sleeve or the iron strip as indicated in the graph. They were performed when the iron and the magnesium strips were either disconnected, or connected electrically during the experiments, as indicated in the legend. Test electrolyte: 10 mM NaCl. Tip potential: -0.70 V vs. Ag/AgCl/KCl (3M); scan rate: 10 μm s^{-1}; tip diameter: 175 μm; *RG* = 2.9. i / i_{lim} is the dimensionless tip current, and d / a is the dimensionless distance between the sample and the tip.

On the other hand, the red curve in Figure 6.3.5 shows the *Z*-approach curve measured above the same location on iron strip that was measured after the two metals were electrically connected. In this case, local depletion of oxygen is readily observed in the plot. Thus, the corrosion of Mg drives a very intensive electrochemical oxygen reduction at the iron surface. And oxygen diffusion from the bulk electrolyte could not compensate its consumption at the metal.

Two dimensional images of oxygen consumption were obtained when the antimony tip made was scanned surface in an *X-Y* plane set at 175 µm vertical tip-substrate distance, and they are shown in Figure 6.3.6. Image A was recorded when the two metals were disconnected, while image B was achieved when they were galvanically-coupled. In Figure 6.3.6A, the image of iron substrate shows up among the surrounding epoxy areas. Above the iron surface smaller current values were registered, corresponding to smaller oxygen concentrations that evidence the advancement of the corrosion of iron in this environment. On the other hand, the image of the iron strip shown in Figure 6.3.6B is much sharper. In this case, tip currents close to 0 nA were measured over the metal, thus showing that oxygen was absent from the thin electrolyte volume comprised between the tip and the iron strip. The dimensions of the area showing the lowest current values in the image closely match the dimensions of the iron surface (1 mm x 2 mm). This proves that the whole metal is behaving as a cathode. Therefore, the iron strip is effectively protected from corrosion through its connection with the sacrificial anode of magnesium.

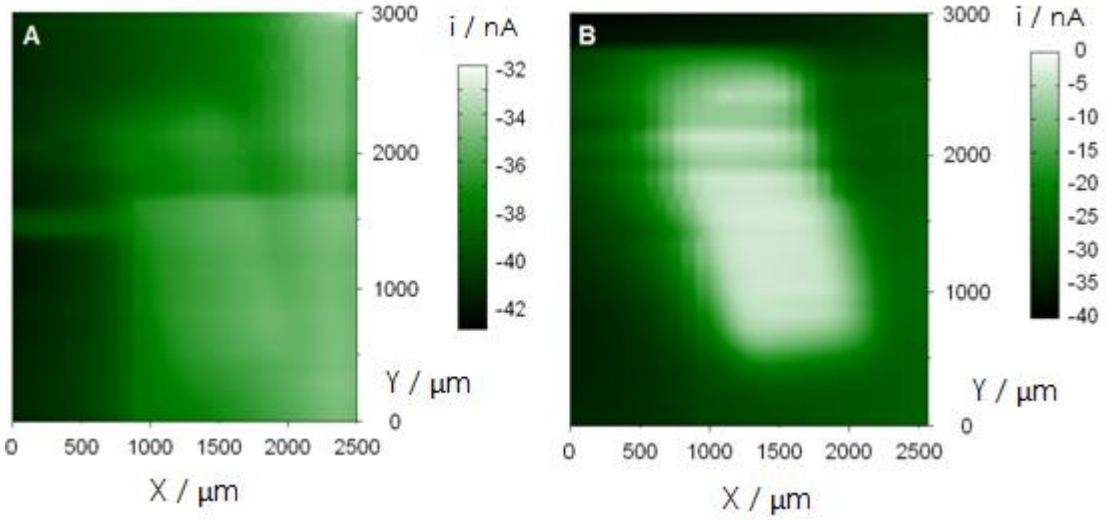

Figure 6.3.6. Amperometric SECM images depicting the absolute current measured at the antimony tip travelling over the iron strip when the magnesium-iron sample was immersed in 10 mM NaCl. The metals were: (A) without, and (B) with galvanic connection. Tip potential: -0.70 V vs. Ag/AgCl/KCl (3M); tip diameter: 175 µm; *RG* = 2.9; tip-substrate distance: 175 µm; scan rate: 30 µm s^{-1}. The figures represent an area of 2500 µm x 3000 µm in *X* and *Y* directions.

6.3.5.3. pH distributions

The antimony electrode was also employed to image pH distributions over the substrate during the corrosion reaction. Though the electrode was usually placed as close as possible to the investigated surface with the assistance of a video camera, the possibility to more precisely establish the tip-substrate distance by applying an alternating potential to the tip was investigated. In this way, the tip could remain unbiased, provided a sufficiently small excitation AC signal was employed. The

rationale for not polarizing the antimony tip was to avoid the chemical modification of the Sb/Sb_2O_3 surface of the electrode. Alternating-current (AC) operation of the SECM was employed, and the magnitude of the current and its phase shift with respect to the applied AC potential modulation were recorded as impedance values. The near-field interaction between the SECM tip and the surface could be employed to obtain AC Z-approach curves within the frequency range. A location above the insulating resin, approximately equidistant from both metal specimens, was chosen for the determination of the tip-substrate distance, and the result is given in Figure 6.3.7. The plots depict the variation of the normalized modulus (Figure 6.3.7A), and the phase shift (Figure 6.3.7B) of the impedance as the tip approached the substrate for a selection of frequencies of the AC perturbation. Modulus values have been normalized by dividing the value recorded at each point by that measured in the bulk solution (e.g., sufficiently far from the substrate to give a stationary value). The higher impedance observed at the end of the curve for every frequency and the decrease in phase angle, are indications of the greater resistance offered to ionic current flow when the tip approached the insulating surface due to the smaller electrolyte volume, though the extent of this blocking effect greatly depends on the frequency of the AC excitation signal. Greater contrast was observed in the low-frequency range, whereas the system became very noisy at 55 kHz.

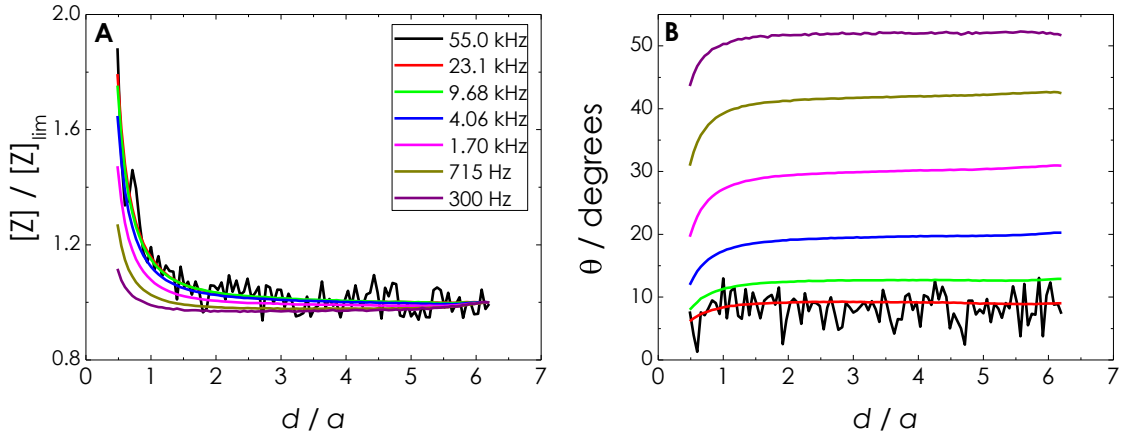

Figure 6.3.7. Normalized AC Z-approach curves towards the resin sleeve at a position located between the iron and the magnesium strips when the sample was immersed in 10 mM NaCl with the 175 µm antimony electrode. The tip was left at its spontaneous open circuit potential in the electrolyte (namely -0.44 V vs. Ag/AgCl/KCl (3 M)). The excitation signal amplitude was 10 mV_{pp}, and frequencies are indicated in the figure. (A) Normalized magnitude, and (B) phase of the impedance measured at the tip. *d / a* is the dimensionless distance between the sample and the tip. $[Z] / [Z]_{lim}$ is the dimensionless impedance.

Once the very close tip-substrate distance was established with AC mode of SECM, the antimony tip was removed to a height of 80 µm, and subsequently positioned over the center of the magnesium sample, or the iron strip by moving the tip in the *X-Y* plane. Then, the potentiometric operation mode was set in order to

monitor pH distributions over the metals. Vertical pH profiles were determined over the center line of each of the metals, both when they were disconnected, and when galvanic contact was established between them. In these experiments the following protocol was followed: First, the pH-sensitive ISE was removed from the surface to a distance of 600 μm. After 10 s waiting time at this height, the tip was moved down towards the surface until a tip-substrate distance of 0.5 normalized (*d* / *a*) units. After 10 s waiting time, the tip was removed again from the surface of the metal to the bulk. The potential of the ISE was continuously recorded during all the duration of the experiment. Tip movement in the vertical direction was always performed at the speed of 5 μm s^{-1}. In this way, vertical pH profiles could be obtained as a function of the normalized tip-substrate distance for both the approach and the retreat steps. The same protocol was employed while the two metals were electrically disconnected, and when they were galvanically coupled. Figure 6.3.8 shows the mentioned vertical pH profiles measured above Mg surface. As it can be seen, in the case of the free-corroding magnesium sample, higher alkalinity is detected in the vicinity of the Mg surface (see Figure 6.3.8A), which indicates that the cathodic half-reaction takes place on some regions of the metal due to its free corrosion. The pH values determined at the largest distances were close to the corresponding value for the bulk solution, which was measured to be 8.76 when registered with a conventional pH-meter. Though the approach and retreat curves exhibit a similar behaviour, they could not be overlapped, and they showed the biggest gap for normalized distances smaller than 1.5. This fact can be attributed to the forced convection effect produced by the tip during its movement to and from the surface. Higher pH values were measured during the retracting process in the major part of the displacement, because the electrode was departing from a portion of the electrolyte more concentrated in hydroxide anions during its movement from the surface towards the bulk of the solution.

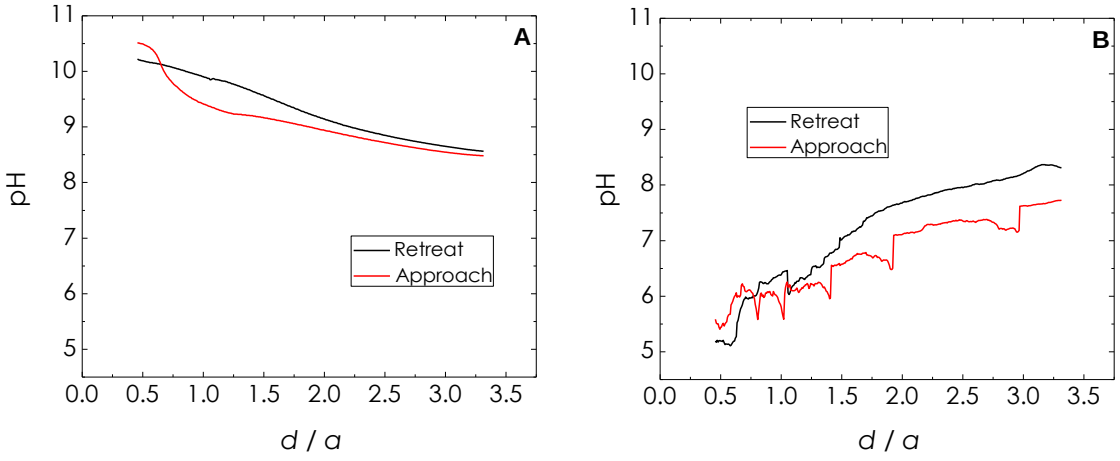

Figure 6.3.8. pH distributions above the magnesium strip measured with the antimony tip as its height was changed relative to the surface. The magnesium-iron sample was immersed in 10 mM NaCl, whereas the two metals were (A) disconnected, and (B) galvanically-coupled. The direction of the tip movement is indicated in the figures; scan rate: 5 μm s^{-1}. *d* / *a* is the dimensionless distance between the sample and the tip.

The opposite trend was observed when galvanic connection was ensured (cf. Figure 6.3.8B). The pH of electrolyte adjacent to the magnesium surface became smaller, than the pH of the bulk. Close to the metal surface, pH values as low as 5.5 could be detected. This shift to the acidic direction occurred despite hydrogen evolution could still be observed with the video camera, and thus a source of alkalization was still somehow active at the metal. However, the higher presence of protons is more difficult to evaluate due to the greater diffusion rate of this species and, in this specific case, also due to the noise in the system provoked by the evolution of hydrogen gas. The same effect was observed when the tip was moved parallel to the surface to record the scan line given in Figure 6.3.9. This latest measurement shows a clear pH decrease in a section of ca. 200 µm, which corresponds with the actual *X* portion of the magnesium strip used as target. It must be noticed that the onset of acidification could be detected at larger distances as a result of the diffusion of H^+ and Mg^{2+} ions.

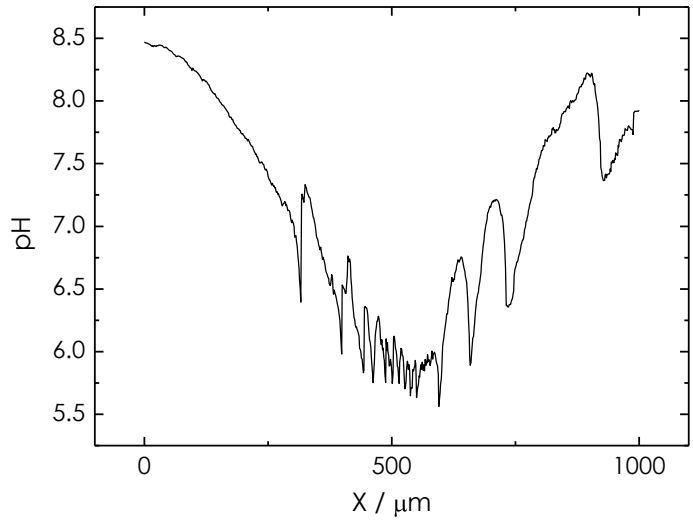

Figure 6.3.9. pH distribution during a scan line recorded with the antimony electrode over the magnesium strip. The magnesium-iron galvanic pair was immersed in 10 mM NaCl. Tip-substrate distance: 80 µm; scan rate: 5 µm s^{-1}.

Finally, Figure 6.3.10 displays pH-vertical vs. *d* / *a* plots obtained above iron surface when the two metals were connected. In both plots, namely approach and retreat curves, the alkalinization observed near the cathode is extensive, even at distances as large as 2 mm. It is interesting to compare this result with the amperometric curve recorded for oxygen detection, previously shown in Figure 6.3.6B, when the limiting current was attained at *d* / *a* values of ca. 5. That is, constant oxygen concentration in the electrolyte close to the bulk solution value could already be found at a tip-substrate distance of 900 µm. Certainly, the corrosion process originates an increase in the solution pH here through the reduction of oxygen. But in combination with the amperometric observations, if that was the only source of this effect, OH^- concentration should decrease down to the values in bulk

solution at much smaller tip-substrate distances than those found in Figure 6.3.10. Then, hydrogen evolution, probably resulting from the highly negative OCP experienced by the electrically connected system, is likely to be the additional factor that leads to this high pH in the proximity of the iron strip. It must be noted that pH values shown in Figure 6.3.10 for the volume of electrolyte in the vicinity of the iron surface are far beyond the dynamic measuring range of the antimony electrode. Therefore no quantitative information can be extracted from these curves.

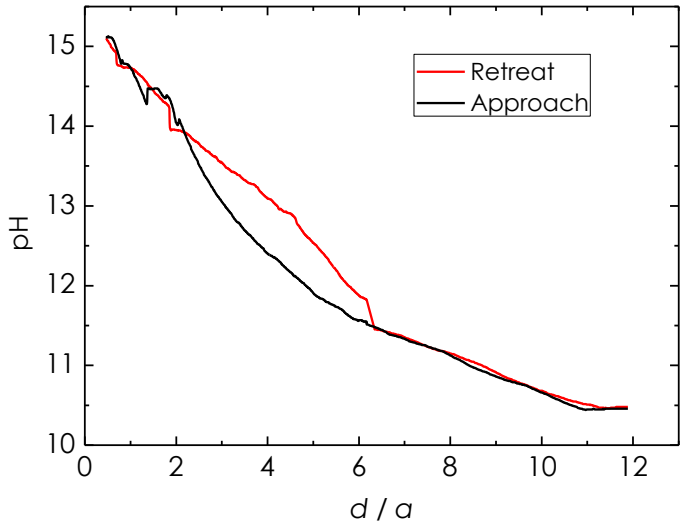

Figure 6.3.10. pH distributions above the iron strip measured with the antimony tip as its height was changed relative to the metal surface. The magnesium-iron galvanic pair was immersed in 10 mM NaCl. *d / a* is the dimensionless distance between the sample and the tip. The direction of the tip movement is indicated in the figures; scan rate: 5 μm s^{-1}.

6.3.6. Discussion

It is reported here that potentiometric operation of the SECM can be employed to locally measure concentration distributions of key species involved in the corrosion of magnesium in aqueous solution. This metal is very reactive in water, thus making difficult to design accurate experiments to study its corrosion mechanism. At present, despite the rather extensive literature on the corrosion of this metal and its alloys, the origin of the corrosion process is still obscure and subjected a big controversy, and a number of experimental observations are regarded by some researcher as dubious. Even experimental techniques are often put to their limits when investigating the electrochemical behaviour of magnesium in aqueous solutions due to joint operation of several features, namely:

1. The high dissolution rate of the metal in contact with an aqueous environment often leads to portions of the material being physically detached from the matrix. It

also makes difficult the safe removal of corrosion products from the uncorroded material. As a result, weight-loss measurements may bear big experimental errors. Furthermore, they are average measurements that give no information on the dynamics of the corrosion reactions.

2. The corrosion of the magnesium is accompanied by vigorous hydrogen evolution [3,4]. A "strange hydrogen evolution behaviour" has been described [5]. That is, more hydrogen is evolved when the anodic overvoltage is increased or a higher anodic current density is imposed, conversely to what happens with the other metals. This phenomenon is called the negative difference effect (NDE). Hydrogen evolution can greatly affect the efficiency of electrochemical probes either by blocking their surface or even modifying their surface state. Additionally, it causes convection effects in the electrolyte solution that affect the current distribution in the electrochemical cell. Conversely, experimental methods have been developed for the quantification of hydrogen evolving during the corrosion of magnesium and its alloys [62]. Though they may be regarded highly efficient techniques, and procedures have been designed to follow the variation with time of hydrogen evolution, they cannot distinguish whether the gas evolves from anodic or cathodic sites.

3. Magnesium hydrolysis is basically non-acidic. The equilibrium constant associated with the first deprotonation step of its aquo-complexes $[Mg(H_2O)_x]^{2+}$, has pK_a^1 = 11.4 [63]. The acidification caused by hydrolysis of Mg^{2+} can be calculated for given concentrations of the metal ion using the equation:

$$pH = -\log\sqrt{K_a^1 \cdot [Mg^{2+}]} \qquad (6.3.1)$$

Using $[Mg^{2+}]$ = 0.0001 and 0.1 M, the expected pH values would be 7.0 and 6.2, respectively [41]. That is, oxidation of magnesium is not capable of significantly changing the pH of a neutral corrosion medium. Conversely, either oxygen or proton electroreduction during the cathodic half-cell reaction produce strong alkaline environments. Strong alkaline environments are usually reported around corroding magnesium and magnesium alloys [5].

4. The formation of a passive film of magnesium hydroxide that exhibits some corrosion protection characteristics is considered to be formed on magnesium and its alloys, especially at high pH [64]. This passive film is unstable, and the onset of corrosion on magnesium is regarded to occur at film-free areas on the surface of the metal [5,53,65]. Indeed, the open circuit potential of fresh polished samples immersed in aqueous environments usually evolves towards more noble potentials [5,53], until a "pitting potential" is attained at which breakdown of the surface film occurs [3,66,67]. Though pitting potential and pit nucleation are terms frequently employed in the literature related to the corrosion of this metal, stable pit growth has not been described for magnesium and magnesium alloys [35]. Conversely, retrieved samples show that the entire exposed surface has been corroded [35].

Scanning electrochemical microscopy was selected as the experimental technique for this work as to gain new spatially-resolved information concerning the chemical reactions responsible for the corrosion of CP magnesium. A special concern was taken in relation to identify if alkalization occurred at both the anodic and cathodic microcells formed on the metal, or whether diffusion of the high concentration of hydroxyl ions formed in the cathodes were responsible for the alkalization of the electrolyte. Though a small electrolyte volume is typically employed in SECM experiments, the choice of a small magnesium strip insulated in a much bigger resin mount was considered to allow enough dilution of the formed OH^- species as to detect the source of these ions at least for the early stages of metal corrosion. Additionally, the mount contained also an iron strip, thus allowing some experiments to be conducted with galvanic coupling of the two metals, which can be simply attained by electrically connecting the two strips at the back of the mount. In this way, separation of the anodic and cathodic sites could be achieved if the two metal strips were separated enough in the mount, though at the cost of both an increase of the corrosion rate of magnesium and a greater ohmic loss in the electrolyte. Though the latter might be regarded to drive a fraction of the hydrogen evolution reaction from the iron to the magnesium strip in order to minimize the separation between both half-cell reactions, this would result in local alkalinization around those cathodic sites on magnesium. But no evidence of any local alkalinization around magnesium has been observed in the course of these experiments. Yet, additional experiments must be undertaken in order to completely rule out any eventual effects on the localization of the hydrogen evolution reaction directly related to the significant losses occurring in the electrochemical cell. Variations in both the distance comprised between the two metals in the holder and the ionic strength of the electrolyte are thus considered.

Figures 6.3.2 and 6.3.3 show significantly smaller pMg values in a thin electrolyte layer above the magnesium strip following the galvanic coupling of this metal to iron. That is, the use of a Mg^{2+} ion-selective microelectrode (ISME) allowed for concentration distributions of the dissolved metal to be measured. It must also be noticed that despite the enhancement of magnesium dissolution due to the galvanic-coupling to iron, the dimensions of the magnesium strip were sufficient for the amount of dissolved magnesium never to saturate the detection limit of the ISME. That is, the microelectrode probe was sensitive to changes in the concentrations of Mg^{2+} for the duration of the experiments, contrary to the expectations made by other Authors [5]. Another important outcome from this work is obtained from inspection of Figure 6.3.4. Though the magnesium strip was working as the anode in the Mg-Fe galvanic pair, dissolution of the metal does not occur simultaneously over the entire exposed surface. Indeed, it has been observed from a sequence of SECM measurements passing over the same scan lines (not shown), that the locations of high Mg^{2+} concentrations are shifted over the exposed magnesium strip. The experiments described in this Section, still of some preliminary nature, agree thus well with the previous observations made using SVET by Williams and McMurray [35]. In order to record maps instead of exclusively some selected scan lines, higher scan

rates for SECM would be required involving more robust ion-selective electrodes with smaller internal resistances, as it will be described in the following Section 6.4.

Another important outcome of this work was the observation of oxygen consumption when magnesium was galvanically connected to iron. This dissolved species in the solution was consumed in the thin electrolyte volume located over the iron strip when acting as the cathode during the corrosion of magnesium. Indeed, the amperometric SECM images in Figure 6.3.6 clearly demonstrate that the enhanced corrosion rate of magnesium when galvanically-coupled to iron directly corresponds to an enhancement in the consumption of oxygen, despite the occurrence of hydrogen evolution on the metal. Simultaneously, the pH in the thin electrolyte volume located above the magnesium strip becomes slightly acidic, attaining values between 5.5 and 6. These values are only slightly more acidic than those predicted by application of equation (6.3.1) considering the hydrolysis of Mg^{2+} ions in the electrolyte. Values as low as 5.3 have already been reported from SIET measurements on corroding AZ31 magnesium alloy, which was ascribed to the co-dissolution and hydrolysis of Al along with Mg, since this alloy contains ca. 3% aluminium. In the case of CP magnesium, the possible contribution of minute amounts of iron, even in small amounts in the order of ppm [68], may justify the more acidic values found in this work. Since the pK^1_a of Fe is more than two units smaller than that of Al (2.2 and 4.5, respectively) [63], a 0.0001 M Fe^{2+} solution of produces almost the same pH decrease than another 0.1 M in Al^{3+} [41]. Not only the pH values can be justified on the basis of the physicochemical response of CP magnesium, but they are well inside the linear response of the antimony microelectrode with pH [56]. Again the design of the experiment has satisfactorily served for pH monitoring of magnesium corrosion in an aqueous solution, without meeting the warnings raised in ref. [5]. This feature is very important when considering that no alkalinization was observed around the anodic sites in any of the experiments described in this Section. And alkalinization is a requirement for the occurrence of the chemical reaction suggested to account for the negative difference effect (NDE) [65,69]. In this model, formation of Mg^+ species and their direct reaction with water, is proposed:

$$2\,H^+ + 2\,e^- \rightarrow \uparrow H_2 \qquad \text{(cathodic partial reaction)} \qquad (6.3.2)$$

$$2\,Mg \rightarrow 2\,Mg^+ + e^- \qquad \text{(anodic partial reaction)} \qquad (6.3.3)$$

$$2\,Mg^+ + 2\,H_2O \rightarrow 2\,Mg^{2+} + 2\,OH^- + \uparrow H_2 \qquad \text{(chemical reaction)} \qquad (6.3.4)$$

From equation (6.3.4), both the consumption of protons and the production of OH^- are expected at the anodic sites on corroding magnesium. Another implication is that hydrogen gas evolution should occur at those sites. Yet, evolution of hydrogen gas from the corroding magnesium sample can be explained by taking in account the previous observations by Williams and McMurray [35]. In their work on the corrosion of magnesium in concentrated chloride solution investigated by SVET, they observed that the anodic sites occupy only a (small) fraction of the area exposed to the electrolyte, and that local cathodes can develop in very near proximity to them on the previously corroded surface. Therefore, hydrogen evolution do not necessarily must occur at the actual anodic microcell sites, but could occur on the surrounding

cathodic area. The results reported in this Section could be well described using the same interpretation. This explanation may hold even in the case of magnesium galvanically-coupled to iron. Though the major part of the cathodic reaction occurs on the separated iron strip, some cathodic areas might still develop on the magnesium sample in the close proximity to the corroding anodic sites. The development of such minute cathodic sites in the otherwise anodic metal in a galvanic couple has already been described in Section 5.5 of this Thesis for the Zn-Fe galvanic system using a combination of scanning microelectrochemical techniques. This interpretation also accounts for the electrolyte resistance SECM images given in ref. [53], in which the anodic activity on a free corroding magnesium sample occurred only on a small portion of the exposed surface.

6.3.7. Conclusion

The applicability of the Mg^{2+}-ISE to characterize magnesium-based materials by SECM has been demonstrated. The results show that anodic dissolution of magnesium anodes takes place preferentially in certain most active sites. The increase in Mg^{2+} ion concentration occurring in the vicinity of the magnesium strip, was found to be two orders of magnitude bigger when the nature of the degradation process changed from spontaneous self-corrosion to galvanic corrosion. Imaging of oxygen concentration distribution and pH detection were carried out with the antimony electrode, and it was possible to clearly distinguish anodic and cathodic behaviours occurring simultaneously on the same surface. Thus, the combination of measurements and electrodes presented here allowed to identify and to quantify the different reactions taking place during the corrosion process. Additionally, the results open a promising new route to the elucidation of certain characteristics of the mechanism involved in the corrosion and passivation of magnesium, which result from greatly localized reactions.

6.3.8. References

1. M.V. Biezma, J.R. San Cristóbal. Corrosion Engineering, Science and Technology 40 (2005) 344.
2. G.L. Makar, J. Kruger. International Materials Reviews 38 (1993) 138.
3. G. Song, A, Atrens. Advanced Engineering Materials 1 (1999) 11.
4. G. Song, A. Atrens. Advanced Engineering Materials 5 (2003) 837.
5. G. Song. Advanced Engineering Materials 7 (2005) 563.
6. F. Witte. Acta Biomaterialia 6 (2010) 1680.
7. N.T. Kirkland, J. Lespagnol, N. Birbilis, M.P. Staiger. Corrosion Science 52 (2010) 287.

8. S. Virtanen. Materials Science and Engineering: B 176 (2011) 1600.
9. N.T. Kirkland, N. Birbilis, M.P. Staiger. Acta Biomaterialia 8 (2012) 925.
10. A.M. Simões, D. Battocchi, D.E. Tallman, G.P. Bierwagen. Corrosion Science 49 (2007) 3838.
11. A.M. Simões, D. Battocchi, D.E. Tallman, G.P. Bierwagen. Progress in Organic Coatings 63 (2008) 260.
12. P.C.R. Varma, B. Duffy, J. Cassidy. Surface and Coatings Technology 204 (2009) 277.
13. D. Wang, G.P. Bierwagen. Progress in Organic Coatings 64 (2009) 327.
14. P. Volovitch, T.N. Vu, C. Allély, A.A. Aal, K. Ogle. Corrosion Science 53 (2011) 2437.
15. J. Wloka, G. Bürklin, S. Virtanen. Electrochimica Acta 53 (2007) 2055.
16. F.M. Queiroz, M. Magnani, I. Costa, H.G. de Melo. Corrosion Science 50 (2008) 2646.
17. P. Marcus, F. Mansfeld (Editors). Analytical Methods in Corrosion Science and Engineering. CRC Press, Boca Raton, 2006.
18. L. Niu, Y. Yin, W. Guo, M. Lu, R. Qin, S. Chen. Journal of Materials Science 44 (2009) 4511.
19. S.E. Pust, W. Maier, G. Wittstock. Zeitschrift für Physikalische Chemie 222 (2008) 1463.
20. R.M. Souto, S.V. Lamaka, S. González. In: Microscopy: Science, Technology, Applications and Education, Vol. 3 (Edited by A. Méndez-Vilas, J. Díaz). Formatex Research Center, Badajoz, 2010, p. 1769.
21. J.V. Macpherson, P.R. Unwin. In: Scanning Electrochemical Microscopy (Edited by A.J. Bard, M.V. Mirkin). Marcel Dekker, New York, 2001, p. 521.
22. Y. González-García, G.T. Burstein, S. González, R.M. Souto. Electrochemistry Communications 6 (2004) 637.
23. C.H. Paik, H.S. White, R.C. Alkire. Journal of the Electrochemical Society 147 (2000) 4120.
24. C.H. Paik, R.C. Alkire. Journal of the Electrochemical Society 148 (2001) B276.
25. K. Fushimi, M. Seo. Electrochimica Acta 47 (2001) 121.
26. R.M. Souto, Y. González-García, S. González. Corrosion Science 47 (2005) 3312.
27. S. González, J.J. Santana, Y. González-García, L. Fernández-Mérida, R.M. Souto. Corrosion Science 53 (2011) 1910.
28. A.C. Bastos, A.M. Simões, S. González, Y. González-García, R.M. Souto. Electrochemistry Communications 6 (2004) 1212.
29. A.M. Simões, A.C. Bastos, M.G. Ferreira, Y. González-García, S. González, R.M. Souto. Corrosion Science 49 (2007) 726.
30. R.M. Souto, L. Fernández-Mérida, S. González. Electroanalysis 21 (2009) 2640.
31. J.J. Santana, J. González-Guzmán, L. Fernández-Mérida, S. González, R.M. Souto. Electrochimica Acta 55 (2010) 4488.
32. Y. González-García, J.M.C. Mol, T. Muselle, I. de Graeve, G. van Assche, G. Scheltjens, B. van Mele, H. Terryn. Electrochemistry Communications 13 (2011) 169.
33. R.M. Souto, Y. González-García, D. Battistel, S. Daniele. Chemistry - A European Journal 18 (2012) 230.

34. R.M. Souto, Y. González-García, D. Battistel, S. Daniele. Corrosion Science 55 (2012) 401.
35. G. Williams, H.N. McMurray. Journal of the Electrochemical Society 155 (2008) C340.
36. G. Denuault, G. Nagy, K. Tóth. In: Scanning Electrochemical Microscopy (Edited by A.J. Bard, M.V. Mirkin). Marcel Dekker, New York, 2001, p. 397.
37. G. Nagy, L. Nagy. Fresenius' Journal of Analytical Chemistry 366 (2000) 735.
38. G. Nagy, L. Nagy. Analytical Letters 40 (2007) 3.
39. Á. Varga, L. Nagy, J. Izquierdo, I. Bitter, R.M. Souto, G. Nagy. Analytical Letters 44 (2011) 2876.
40. J. Izquierdo, L. Nagy, Á. Varga, I. Bitter, G. Nagy, R.M. Souto. Electrochimica Acta 59 (2012) 398.
41. S.V. Lamaka, R.M. Souto, M.G.S. Ferreira. Microscopy: Science, Technology, Applications and Education, Vol. 3 (Edited by A. Méndez-Vilas, J. Díaz). Formatex Research Center, Badajoz, 2010, p. 2162.
42. S.V. Lamaka, O.V. Karavai, A.C. Bastos, M.L. Zheludkevich, M.G.S. Ferreira. Electrochemistry Communications 10 (2008) 259.
43. M.F. Montemor, W. Trabelsi, S.V. Lamaka, K.A. Yasakau, M.L. Zheludkevich, A.C. Bastos, M.G.S. Ferreira. Electrochimica Acta 53 (2008) 5913.
44. S.V. Lamaka, G. Knörnschild, D.V. Snihirova, M.G. Taryba, M.L. Zheludkevich, M.G.S. Ferreira. Electrochimica Acta 55 (2009) 131.
45. S.V. Lamaka, M.G. Taryba, M.L. Zheludkevich, M.G.S. Ferreira. Electroanalysis 21 (2009) 2447.
46. A.C. Bastos, M.G. Taryba, O.V. Karavai, M.L. Zheludkevich, S.V. Lamaka, M.G.S. Ferreira. Electrochemistry Communications 12 (2010) 394.
47. D. Snihirova, S.V. Lamaka, M. Taryba, A.N. Salak, S. Kallip, M.L. Zheludkevich, M.G.S. Ferreira, M.F. Montemor. ACS Applied Materials and Interfaces 2 (2010) 3011.
48. O.V. Karavai, A.C. Bastos, M.L. Zheludkevich, M.G. Taryba, S.V. Lamaka, M.G.S. Ferreira. Electrochimica Acta 55 (2010) 5401.
49. S.V. Lamaka, M. Taryba, M.F. Montemor, H.S. Isaacs, M.G.S. Ferreira. Electrochemistry Communications 13 (2011) 20.
50. M. Taryba, S.V. Lamaka, D. Snihirova, M.G.S Ferreira, M.F. Montemor, W.K. Wijting, S. Toews, G. Grundmeier. Electrochimica Acta 56 (2011) 4475.
51. X. Liu, T. Zhang, Y. Shao, G. Meng, F. Wang. Corrosion Science 51 (2009) 1772.
52. M.D. Pereda, C. Alonso, M. Gamero, J.A. del Valle, M.F.L. de Mele. Materials Science and Engineering: C 31 (2011) 858.
53. G. Baril, G. Galicia, C. Deslouis, N. Pébère, B. Tribollet, V. Vivier. Journal of the Electrochemical Society 154 (2007) C108.
54. B. Horrocks, M.V. Mirkin, D.T. Pierce, A.J. Bard, G. Nagy, K. Toth. Analytical Chemistry 65 (1993) 1213.
55. J. Izquierdo, L. Nagy, Á. Varga, J.J. Santana, G. Nagy, R.M. Souto. Electrochimica Acta 56 (2011) 8846.
56. J. Izquierdo, L. Nagy, J.J. Santana, G. Nagy, R.M. Souto. Electrochimica Acta 58 (2011) 707.

57. D.O. Wipf, F. Ge, T.W. Spaine, J.E. Baur. Analytical Chemistry 72 (2000) 4921.
58. K. Tóth, E. Lindner, M. Horváth, J. Jeney, E. Pungor, I. Bitter, B. Ágai, L. Töke. Electroanalysis 5 (1993) 781.
59. R.C. Thomas. Ion-selective Intracellular Microelectrodes: How to Make and Use Them. Academic Press, London, 1978.
60. D. Ammann. Ion-selective Microelectrodes. Principles, Design and Application. Springer-Verlag, Berlin, 1986.
61. M.V. Mirkin. In: Scanning Electrochemical Microscopy (Edited by A.J. Bard, M.V. Mirkin). Marcel Dekker, New York, 2001, p. 145.
62. G.L. Song, A. Atrens, D. StJohn. Magnesium Technology 2001. TMS, New Orleans, 2001, p. 255.
63. Y.Y. Lur'e. Spravochnik po Analiticheskoi Himii, 6th edn. Himiya, Moscow, 1989.
64. A.-M. Lafront, W. Zhang, S. Jin, R. Tremblay, D. Dubé, E. Ghali. Electrochimica Acta 51 (2005) 489.
65. G. Song, A. Atrens. Advanced Engineering Materials 9 (2007) 177.
66. G. Song, A. Atrens, X. Wu, B. Zhang. Corrosion Science 40 (1998) 1769.
67. G. Song, A. Atrens, M. Dargush. Corrosion Science 41 (1999) 249.
68. Z. Qiao, Z. Shi, N. Hort, N.I.Z. Abidin, A. Atrens. Corrosion Science 61 (2012) 185.
69. A. Atrens, W. Dietzel. Advanced Engineering Materials 9 (2007) 292.

6.4

Spatially-resolved imaging of concentration distributions on corroding magnesium-based materials exposed to aqueous environments by SECM

6.4.1. Abstract

The spatial resolution of Mg^{2+} release from magnesium and its alloys during exposure to aqueous environments has been imaged using a new, solid contact, micropipette-based magnesium ion-selective electrode employed as potentiometric tip in SECM. The detection of metal dissolution is a crucial factor to detect the local microcells established on the surface of the metal, and distinguish the processes related to anodic and cathodic half-cell reactions. Concentration distribution images have been obtained for the magnesium-based alloy AZ63 when galvanically coupled to pure iron during exposure to 1 mM NaCl solution.

6.4.2. Resumen

Se ha visualizado la producción de Mg^{2+} con resolución espacial a partir de muestras de magnesio y sus aleaciones durante su exposición a ambientes acuosos, utilizando un nuevo electrodo de micropipeta de ion selectivo empleado como sonda en SECM. La detección de la disolución del metal es un factor crucial para poder analizar las microceldas locales que se establecen en la superficie del metal y distinguir los procesos relacionados con las semirreacciones catódica y anódica. Se han obtenido imágenes de la distribución de la concentración de ion Mg^{2+} sobre la aleación de base magnesio AZ63 durante su acoplamiento galvánico con hierro puro bajo exposición a disolución 1 mM de NaCl.

6.4.3. Introduction

Elucidation of the mechanism responsible for the degradation of magnesium and its alloys in aqueous environments is required to develop efficient protection procedures for these materials to be employed in various technological applications. At present, even the identification of the species participating in the local microcells distributed on the materials during their heterogeneous corrosion remains a matter of major discussion. Particularly, the identification of the actual sites for the evolution of hydrogen gas, and the speculative initiation of metal dissolution from the nucleation of corroding pits are two major problems associated to this reaction. In addition, contradictory experimental data are often reported on these processes, which account for the diversity of mechanisms proposed for the corrosion of magnesium. For instance, hydrogen gas evolution has been reported both to occur exclusively at the cathodic sites [1,2], and at anodic and cathodic sites simultaneously, though preferentially from the anodic ones [3,4]. In this context, some authors have claimed the existence of univalent magnesium intermediates to justify the apparent anomalous amounts of hydrogen collected in their experiments [5], whereas recent independent observations using the scanning electrode technique (SVET) [1], atomic emission spectroelectrochemistry [6] and video recording [4] are in conflict with the so-called "Negative Difference Effect" [7]. Additionally, pitting corrosion has also been proposed to account for the initiation of metal dissolution [3,8], but confined sites have never been imaged. Though chemically different, both problems have in common a highly localized nature. Thus, there was need for spatially-resolved electrochemical information on the system, and significant advances have been accomplished since the introduction of the scanning Kelvin probe (SKP) [9,10] and the scanning vibrating electrode technique (SVET) [1,11] to these studies. Yet these techniques exhibit some limitations for such investigation, namely the former actually operates *ex situ*, whereas the later can only measure ionic flows in the adjacent electrolyte at rather big distances from the corroding surface to avoid spurious convective effects on the system produced by the mechanical vibration of the probe. More recently, potentiometric mapping of specific cations has been achieved using the scanning ion electrode technique (SIET) [12]. Ion-selective micropipette electrodes with a liquid contact are employed there [13,14].

The scanning electrochemical microscope (SECM) has found no use in aerated aqueous electrolytes due to the high negative potentials related to the corrosion of magnesium thus hindering amperometric operation. Then, SECM can only be operated potentiometrically using ion-selective microelectrodes as the probe. Despite some promising results, its practical application to the investigation of magnesium degradation was still severely limited by the very slow response times of the liquid contact micropipette electrodes employed [15], that only allowed to record scan lines for the most. That is, the time required to image a relevant portion of the corroding sample would be too long, and major changes in the reactivity of the sites on the metal would already occur between consecutive lines in the image grid. In order to overcome this severe limitation, new ion-selective microelectrodes

with shorter response times and smaller internal resistances rates have been developed, suitable to be employed for SECM operation using faster scan rates. In this Section, data obtained using a new solid-contact micropipette-based design for magnesium ion-selective probes are reported for the first time. The obtained results were consistent with those obtained using the SVET.

6.4.4. Material and methods

Experiments were performed on an epoxy resin sleeve holding 760 μm diameter wires of pure iron and AZ63 magnesium alloy. The composition of the alloy was determined (in wt%) by emission spectrometry (ICP-OES): Al 5.74, Zn 2.88, Cu <0.005, Fe <0.005, Ni <0.005, Si <0.005, Mg balance. The mount with the samples was polished with silicon carbide paper down to 4000 grit, washed thoroughly with Millipore deionised water and dried with acetone. Specimens were placed horizontally facing upwards and surrounded laterally by a small piece of PVC plastic tube creating a container for approximately 5 mL of electrolyte solution. Tests were conducted in 1 mM NaCl solution, naturally aerated, and at ambient temperature.

The Scanning Electrochemical Microscope was manufactured by Sensolytics (Bochum, Germany). A voltage follower was introduced between the cell and the potentiometric input of the system to perform the potentiometric operation [17], and the probe was the Mg^{2+}-ion selective microelectrode (ISME). The reference electrode was an Ag/AgCl/KCl (3M). Concentration distributions over the corroding sample were determined with the ISME placed at a constant height of 100 μm above the sample; scan rate: 25 μm s^{-1}. The SVET instrumentation was manufactured by Applicable Electronics (New Haven, CT, USA), and operated a platinized platinum tip (20 μm dia.) placed at 150 μm from the sample and vibrating with an amplitude of 20 μm.

The micropipette for the microelectrode was pulled from a borosilicate glass-capillary type B100-50-10 (Sutter Instruments, Novato, CA, USA), and subsequently silanized by introducing inside a few microliters of 5 vol.% dimethyldichlorosilane solution in carbon tetrachloride. The hydrophobic layer was obtained by keeping the micropipette at 200 ^{0}C in an oven for about 30 min. The ionophore cocktail was then filled into the micropipette by applying vacuum from the back side with an attached syringe. It was fabricated using Selectophore-grade poly(vinyl chloride) (PVC), ortho-nitrophenyl octyl ether (2-NPOE), potassium tetrakis(4-chlorophenyl)-borate (PTCB), tetrahydrofurane (THF), and tris(hydroxymethyl)aminomethane (Tris) supplied by Fluka (Buchs, Switzerland), whereas the bis-N,N-dicyclohexyl-malonamide magnesium ionophore was synthesized at the Technical University of Budapest adapting the procedure described in ref. [16]. The internal contact was provided by a 33 μm diameter carbon fiber (supplied by Specialty Materials (Lowell, MA, USA) as a generous gift) inserted in the lumen of the ionophore cocktail. A copper wire was

attached to the free end of the carbon fiber using silver epoxy adhesive (Amepox Microelectronics, Lódz, Poland) to provide electric contact. Loctite adhesive was used to seal the back side. Figure 6.4.1 shows a scheme of the ion-selective micropipette electrode assembly and a micrograph of the obtained micropipette tip.

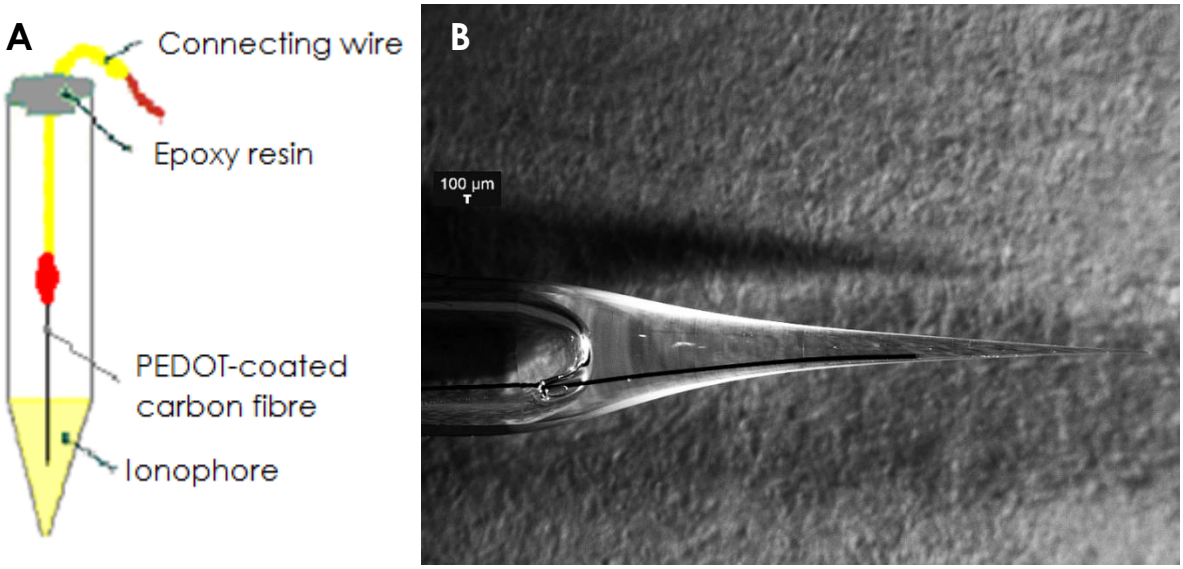

Figure 6.4.1. (A) Sketch and (B) micrograph of the micropipette electrodes fabricated for the selective detection of Mg^{2+} ions.

6.4.5. Results and discussion

The concentration dependence of the electrode potential for this novel Mg^{2+}-ion-selective microelectrode was calibrated using solutions of different concentration in $MgCl_2$, keeping 1 mM NaCl as the base electrolyte. Figure 6.4.2A depicts the dynamic response curve of the system, whereas the calibration curve derived from these data is plotted in Figure 6.4.2B. The response was linear in the concentration range of 10^{-5} to 10^{-1} M, and the slope was 21.7 mV $decade^{-1}$.

During galvanic corrosion, magnesium dissolves anodically to form Mg^{2+} ions that diffuse into the electrolyte. A heterogeneous concentration distribution of Mg^{2+} develops near the couple surface. 2D concentration distribution images were recorded by SECM when the Mg^{2+}-ISME was scanned over a flat sample containing a small disk of AZ63 alloy separated ca. 5 mm from an iron surface disk, both inserted in an epoxy resin holder. The experiment was initiated by placing the electrodes in the small electrochemical cell, and the tip-substrate height was fixed at 100 µm with the assistance of a video camera.

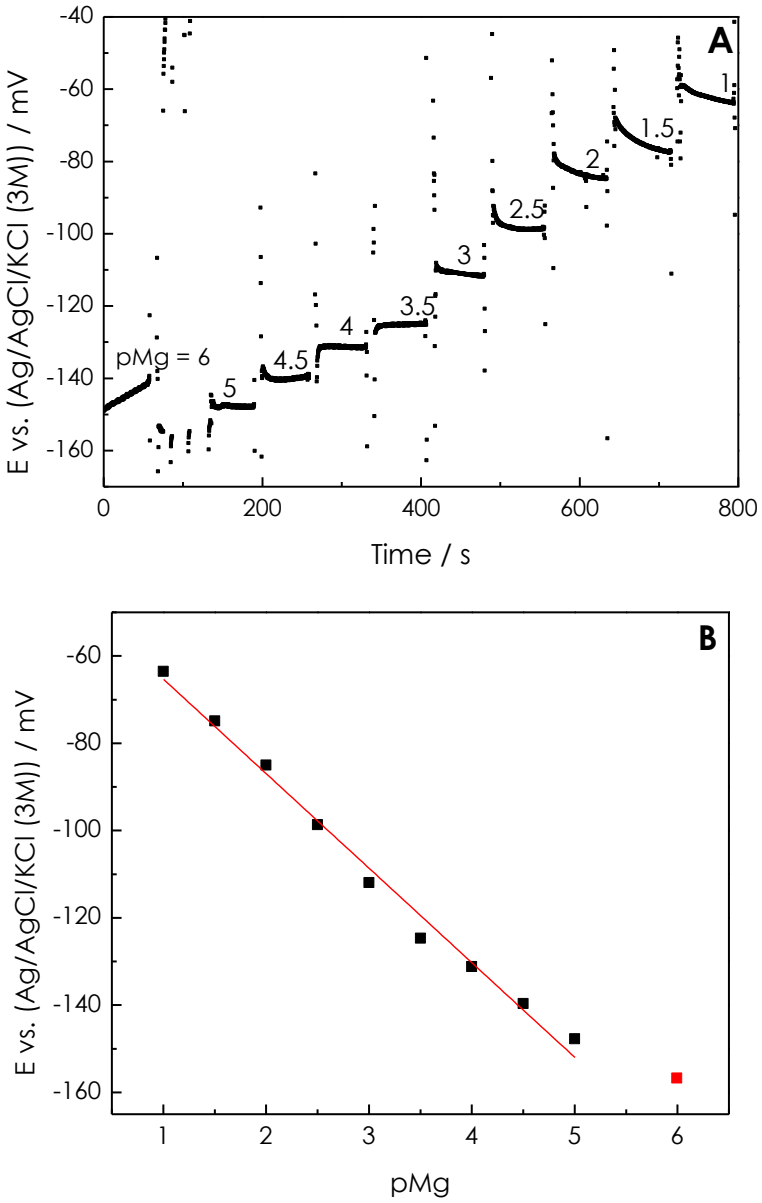

Figure 6.4.2. Calibration of the Mg^{2+}-ion selective micropipette electrode: (A) Dynamic response curves obtained for different $MgCl_2$ concentrations using 10^{-3} M NaCl as background electrolyte; and (B) calibration plot.

Subsequently, the test electrolyte was admitted in the electrochemical cell. At this stage, the two metals were still electrically disconnected, thus effectively achieving their corresponding open circuit potential values in 1 mM NaCl aqueous solution. The system was allowed to stabilize for 15 min, and then the concentration distribution map shown in Figure 6.4.3A above the AZ63 disk was obtained. The distribution of Mg^{2+} ions over the corroding closely matched the circular geometry of the alloy in this case. The higher concentration (pMg = 3.8) was found almost at the center of the disk, and it decayed smoothly as the ISME was moved from the center. Less than one pMg unit occurred between the highest and the lowest values in the figure.

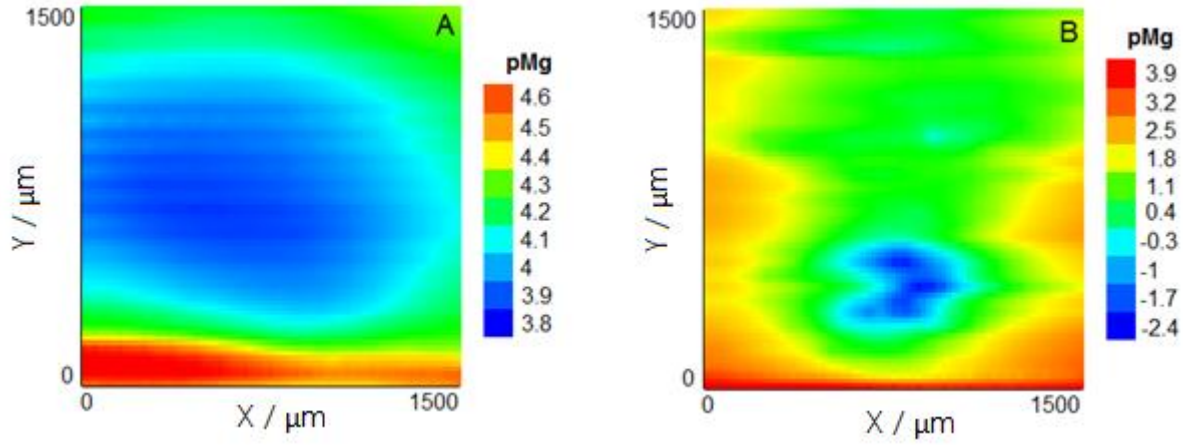

Figure 6.4.3. SECM images displaying the distribution of Mg^{2+} ion concentration above the AZ63 disk in the corrosion cell containing 1 mM NaCl. (A) Map recorded while the galvanic pair was disconnected, and (B) after electric contact between the two metals was produced. Tip-substrate distance: 100 µm; scan rate: 25 µm s^{-1}.

Next, the two metals were galvanically coupled by connecting the wires at the rear of the epoxy mount. Vigorous activation of the corrosion reaction occurred, and it was accompanied by an enhancement in the evolution of hydrogen gas from the system. An asymmetric distribution of Mg^{2+} ions was now measured with values apparently varying in excess of 5 pMg units above the corroding magnesium alloy. A quantitative measurement of the total change in the ionic concentration of the metal could not be established at this time, because the potential values measured at the ISME tip when it passed above the lower third of the image were indeed more negative than those plotted in the calibration curve (cf. Figure 6.4.2B). Therefore, pMg values smaller than 1 in Figure 6.4.3B resulted from the extrapolation of the calibration line to higher concentrations of Mg^{2+} ions, which is rarely to hold in the system. Despite this uncertainty, it can be concluded that heterogeneous activation of the magnesium alloy sample occurred when the corrosion of the metal proceeded with a higher rate.

The localized nature of anodic activity on the AZ63 sample galvanically-coupled to Fe was confirmed using the scanning vibrating electrode technique (SVET). Figure 6.4.4 shows the ionic current flows in the electrolyte solution above the two metals as result of the galvanic process. Whereas the cathodic activity is observed to be evenly distributed over the iron disk (see Figure 6.4.4B), the distribution of ionic currents above the magnesium alloy is heterogeneous (cf. Figure 6.4.4A), thus indicating the simultaneous occurrence of several local microanodes on the surface that do not cover the total exposed area of the alloy. This leaves space for some cathodic activity to occur on the regions of the metal surface next to the microanodes, which will account for hydrogen evolution without requiring the formation of unipositive magnesium species. The proposal of this minute cathodic activity on the magnesium alloy strip does not contradict that most of the cathodic reaction still occurs on the separated iron strip.

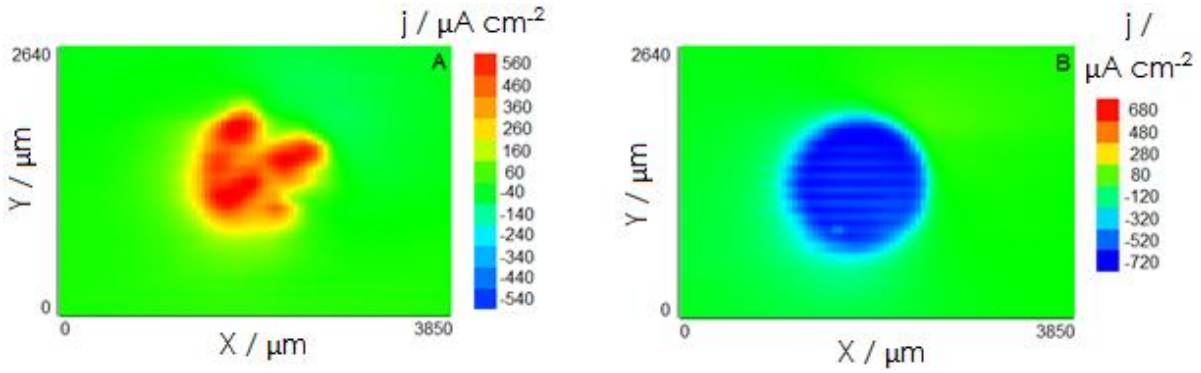

Figure 4. SVET images of the (A) AZ63 alloy and (B) Fe disks after the galvanic pair has been immersed in 1 mM NaCl for 4 hours.

6.4.6. Conclusion

Spatially-resolved images of concentration distributions of Mg^{2+} ions from a corroding magnesium alloy were recorded. The work herein is the first of its type using SECM, and is consistent with emerging studies that indicate Mg corrodes via the $Mg \rightarrow Mg^{2+} + 2e^-$ reaction. This independent validation is an important finding in itself. The new assembly for the fabrication of an Mg^{2+} ion-selective microelectrode with internal solid contact allows its use as probe in SECM. This is of general utility to the Mg-corrosion community, where Mg ionic species are clearly detected and quantified. Further miniaturization of the micropipette electrodes is possible, and this will be advantageous in elucidating localized corrosion mechanism of Mg-alloys that are microstructurally complex.

6.4.7. References

1. G. Williams, H.N. McMurray. Journal of the Electrochemical Society 155 (2008) C340.
2. N.T. Kirkland, G. Williams, N. Birbilis. Corrosion Science 65 (2012) 5.
3. G. Song, A. Atrens. Advanced Engineering Materials 9 (2007) 177.
4. T.R. Thomaz, C.R. Weber, T. Pelegrini, L.F.P. Dick, G. Knörnschild. Corrosion Science 52 (2010) 2235.
5. G.L. Song, A. Atrens, D. StJohn. Magnesium Technology 2001. TMS, New Orleans, 2001, p. 255.
6. J. Swiatowska, P. Volovitch, K. Ogle. Corrosion Science 52 (2010) 2372.
7. G. Song, A, Atrens. Advanced Engineering Materials 1 (1999) 11.
8. A.M. LaFront, W. Zhang, S. Jin, R. Tremblay, D. Dubé, E. Ghali. Electrochimica Acta 51 (2005) 489.

9. R. Hausbrand, M. Stratmann, M. Rohwerder. Journal of the Electrochemical Society 155 (2008) C369.
10. G. Williams, R. Grace. Electrochimica Acta 56 (2011) 1894.
11. A.F. Galio, S.V. Lamaka, M.L. Zheludkevich, L.F.P. Dick, I.L. Müller, M.G.S. Ferreira. Surface and Coatings Technology 204 (2010) 1479.
12. S. Lamaka, R.M. Souto, M.G.S. Ferreira. In: Microscopy: Science, Technology, Applications and Education, Vol. 3 (Edited by A. Méndez-Vilas, J. Díaz). Formatex Research Center, Badajoz, 2010, p. 2162.
13. S.V. Lamaka, O.V. Karavai, A.C. Bastos, M.L. Zheludkevich, M.G.S. Ferreira. Electrochemistry Communications 10 (2008) 259.
14. O.V. Karavai, A.C. Bastos, M.L. Zheludkevich, M.G. Taryba, S.V. Lamaka, M.G.S. Ferreira. Electrochimica Acta 55 (2010) 5401.
15. J. Izquierdo, L. Nagy, I. Bitter, R.M. Souto, G. Nagy. Electrochimica Acta 87 (2012) 283.
16. K. Tóth, E. Lindner, M. Horváth, J. Jeney, E. Pungor, I. Bitter, B. Ágai, L. Töke. Electroanalysis 5 (1993) 781.
17. J. Izquierdo, L. Nagy, Á. Varga, I. Bitter, G. Nagy, R.M. Souto. Electrochimica Acta 59 (2011) 398.
18. A.M. Simões, A.C. Bastos, M.G. Ferreira, Y. González-García, S. González, R.M. Souto. Corrosion Science 49 (2007) 726.

6.5

Development of Mg^{2+} ion-selective microelectrodes for potentiometric scanning electrochemical microscopy monitoring of galvanic corrosion processes

6.5.1. Abstract

The fabrication of a solid-contact, micropipette-based magnesium ion-selective micro-tipped electrode (ISME) suitable for scanning electrochemical microscopy is reported and compared against a conventional micro-tipped ISME having a conventional aqueous internal reference electrode. Measurements showed that the solid-contact ISME had a lower internal resistance and a faster response time than the one with a liquid-contact. These advantages increased the spatial distribution and improved 2D images depicting concentration distributions of Mg^{2+}. The ability of the microelectrode to image local ionic concentration has been tested over magnesium surfaces freely corroding or galvanically coupled to iron in aqueous chloride-containing solution. Scans of magnesium ion distribution, in the absence of corrosion currents, were also made over a micro-pipette source containing a concentrated magnesium chloride gel as a source of Mg^{2+} and over a current source in the absence of Mg^{2+}. From these measurements it was concluded that the potentiometric measurements over corroding surfaces were dominated by the changes in Mg^{2+} distributions with small electric potential contributions due to corrosion current.

6.5.2. Resumen

Se presenta la fabricación de un electrodo de micropunta selectiva de ion magnesio, con contacto sólido y de base micropipeta, aplicable para microscopía electroquímica de barrido, y se compara con las micropuntas ISME convencionales que presentan un electrodo de referencia interno en contacto con un medio acuoso. Las medidas mostraron que el ISME de contacto sólido tiene una menor resistencia interna y un tiempo de respuesta más rápido que el de contacto líquido. Estas ventajas aumentan la resolución de la distribución espacial y mejoran las imágenes en 2D a la hora de representar distribuciones de concentración de Mg^{2+}. La capacidad del microelectrodo para visualizar concentraciones locales de iones se ha comprobado sobre superficies de magnesio bajo corrosión espontánea o acoplamiento galvánico a hierro en disolución acuosa de cloruros. También se registraron los mapas de distribución iónica de magnesio, en ausencia de corrientes de corrosión, sobre una fuente micropipeta que contenía un gel concentrado en cloruro de magnesio como fuente de Mg^{2+} y sobre una fuente de corriente en ausencia de Mg^{2+}. De estas observaciones se concluye que las medidas potenciométricas sobre superficies bajo corrosión están dominadas por los cambios de la distribución de Mg^{2+}, con pequeñas contribuciones en potencial causadas a la componente eléctrica de la corriente de corrosión.

6.5.3. Introduction

Magnesium and its alloys have a major potential for use in many industrial sectors, particularly in automotive, aerospace and biomaterials industries, because of their high strength to weight ratio. Unfortunately, the resistance of magnesium and its alloys against corrosion in aqueous media is poor [1-4], thus requiring the development of improved corrosion-resistant alloys, inhibitor and protective coatings. Currently, understanding the characteristics of metal dissolution and passivity for these materials remains a major challenge, for conflicting ideas and results have been presented [5-10]. Oxide films formed on magnesium are less stable than the passive films formed on industrial metals and alloys owing to the low Pilling-Bedworth-ratio of $Mg(OH)_2$ [11], leading to pitting and general corrosion [12]. Indeed, Song and co-workers [13,14] suggested that corrosion of magnesium and its alloys is initiated from free-film region where the pitting corrosion is the main corrosion form. Additionally, these materials exhibit the behaviour that anodic polarization results in increased hydrogen production when they are exposed to chloride-containing electrolytes similar to what is observed during pitting of aluminium [15]. To account for this so-called "Negative Difference Effect" [3,16,17], it has been proposed that the poorly protective film developed on the surface of magnesium involves the formation of intermediate magnesium(I) species [7,18-21], which directly react with water leading to local alkalization and hydrogen gas evolution [20]. Though evidences for such a mechanism have been presented from the use of a variety of techniques [20,22,23], recent contributions claim that catalytic activation of the cathodic reaction can be induced by the anodic dissolution reaction [24-27], that is, Mg dissolves with a stoichiometry close to n = 2, and these reactions are highly localized.

Chemical imaging of reactive surfaces with high spatial resolution has become available with the introduction of scanning electrochemical microscopy (SECM). In fact, this technique has become a powerful tool in the study of a wide range of corrosion processes [28-30]. Despite the success of SECM in Corrosion Science, the investigation of dissolution processes in a number of technologically-relevant metals such as magnesium, aluminum and zinc, has not been monitored with the SECM using conventional amperometric microdisks due to their very negative redox potentials. The use of noble metal tips coated by metals that present wider stability potential ranges for water have allowed more negative potentials to be reached [31], yet still there are applications beyond those attained in this way. An alternate approach is the use of microsized ion-selective pipette electrodes as measuring tips because they provide the selectivity in chemical imaging [32], which is desirable to investigate the different stages of corrosion processes occurring in micrometric and submicrometric dimensions. As a result, scanning electrochemical microscopy will find an even wider application in materials science and corrosion technology. Unfortunately, ion-selective micropipette electrodes (ISME) are rather fragile tools, and operation lifetime of these probes is seldom longer than a few days. Mechanical contact or electrical shock easily can damage them. Furthermore, the

electrical resistances of these "conventional" ion-selective micropipettes are high necessitating special electric shielding and a very slow scanning rate. This often hinders their applicability to corroding systems.

An improved ISME performance has been found with electrodes of specially prepared carbon fiber that could be placed close to the orifice of the micropipette. The internal contact potential remains constant by applying a doped, electrochemically-prepared conductive polymer coating on the carbon fiber surface based from 3,4-ethylenedioxythiophene (EDOT) [33], thus accounting for reversibility. The life times of these new micropipettes were found surprisingly long; many performed well many months after their preparation. Application include an ammonium and a potassium ISME [33,34]. More recently, a zinc(II) ion-selective microelectrode was constructed. It allowed for the first time to image the local zinc ion concentrations during the galvanic corrosion of a Fe/Zn couple [35]. High spatial resolution was further developed employing a combined potentiometric/amperometric operation methodology for SECM [36] by using materials that exhibit a dual-function in different potential ranges as ultramicroelectrode tips [37,38]. This is the case with antimony as its open circuit potential responds to the pH of the environment [39].

Once the capability of these micropipette measuring tips in corrosion studies was demonstrated in the previous Chapter of this Thesis for Zn^{2+}-ISMEs, research was next focused on the fabrication of an Mg^{2+} ion-selective microelectrode. The first neutral carrier-based ion-selective electrodes for magnesium reported in the scientific literature were developed to monitor the hardness of water of different origins [40-42]. From those studies it was concluded that the best selectivity against sodium ion was achieved using amidic-based ionophores. Indeed, an amidic ionophore, octamethylenbis (N,N''-octamethylene-bis(N'-heptyl-N'-methyl-methylmalonamide) (ETH 5214), was used to build a liquid-contact magnesium ISME that was able to measure Mg^{2+} ion distributions over a Mg-based alloy in aqueous chloride-containing solution [43,44]. Another amidic ionophore, bis-N,N-dicyclohexyl-malonamide [45], was employed for the fabrication of a Mg^{2+}-ion selective electrode tip for ISME for the first time [46]. In that work, a liquid-contact ion-selective micropipette electrode configuration was employed. Spatially-resolved data showing a major production of hydroxyl anions at the cathodic sites as result of oxygen reduction and local acidification in the vicinity of magnesium dissolution sites were obtained. Yet, the rather slow response times of the ion-selective microelectrode tips employed in the work severely limited the mapping capabilities of the technique and only selected one-dimensional line scans could be recorded at that time as it was shown in Section 6.3.

In this Section, the fabrication and characterization of a new, faster, robust, solid-contact, micropipette-based magnesium ion-selective electrode suitable for use as an ISME is described. The electrodes were constructed using a carbon fiber coated by a conductive polymer as internal contact. These electrodes had a higher resolution with lower resistance. Conventional micropipette Mg^{2+}-selective electrodes were also fabricated for the sake of comparison. These results on the

galvanic corrosion of magnesium connected to iron in chloride solutions demonstrate that this Mg^{2+}-ISME with carbon fiber internal electrodes can be employed for corrosion studies.

6.5.4. Experimental

6.5.4.1. Reagents and samples

Selectophore grade poly(vinyl-chloride) (PVC), ortho-nitrophenyloctylether (2-NPOE), potassium tetrakis(4-chlorophenyl)borate (KTFPB), tetrahydrofurane (THF), and tris(hydroxymethyl)aminomethane (TRIS) were supplied by Fluka (Buchs, Switzerland). Carbon fiber of 33 μm diameter was provided by Specialty Materials (Lowell, MA, USA) as a generous gift. The carbon fibers were coated with a conductive polymer. Thus, 3,4-ethylenedioxythiophene (EDOT) (ref CH04M006) monomer obtained from Starck (Golar, Germany) was electropolymerized in 1-butyl-3-methyl-imidazoliumhexafluorophosphate ($BMIM^+$ PF_6^-) ionic liquid solvent from Solvent Innovation (Cologne, Germany). Analytical grade magnesium chloride hexahydrate Merck (Darmstadt, Germany). Chemicals were used as received. Aqueous solutions were prepared using ultra-pure deionized water.

A magnesium-iron galvanic couple was used as model corroding system. Iron wire 760 μm diameter and magnesium ribbon with 200 μm x 800 μm cross section were employed. The two metals were mounted in an *Epofix* resin disk (Struers, Ballerup, Denmark). Only their cross sections were exposed on the front side of the disk-shaped resin mounting (dia. 3 cm), and they extended about 15 mm at the rear of the mount for electric connection. The front side of the mounts was polished with silicon carbide paper down to 4000 grit. The surface was degreased with acetone, abundantly rinsed with ultra-pure deionized water and allowed to dry in air. When tested, the front side of the mount faced upwards surrounded laterally by a small section of PVC plastic tubing creating a small container holding 5 mL of 1 mM NaCl test electrolyte solution (Figure 6.5.1A) and an Ag/AgCl/KCl (3M) reference electrode.

Detection of Mg^{2+} in a solution free of electric currents was conducted in a validation cell, Figure 6.5.1B of similar construction to 6.5.1A. The cell held a small embedded glass micropipette with a diameter of 200 μm about 10 mm long. The micropipette was filled with 0.1 M $MgCl_2$ + 1mM NaCl contained in 4% agar-agar gel to establish a stable Mg^{2+} diffusion source and prevent the solution incursions when using only the $MgCl_2$ in a liquid aqueous solution.

The effect on the performance of the ion-selective microelectrodes due to electric fields with currents in the electrolyte was explored using two different arrangements with electrodes acting as point current sources. Firstly, a noble metal disk microelectrode was considered. In this case, two 100 μm diameter Pt-Ir wires

were employed. They were embedded in *Epofix* resin with only cross sections exposed to the electrolyte. One serving as current source was placed normal to the surface to offer a 100 μm diameter disk surface, whereas the other serving as counter electrode was placed with a certain tilt in order to offer a larger elliptical area. In the second arrangement, a glass micropipette with a tip diameter of 113 μm was employed as the current source and dipped into the electrolyte in a small container. A platinum electrode was inserted in the pipette. Another platinum wire was present in the electrolyte and acted as a counter electrode. Batteries and resistors were used to vary the current through the pipette which was measured with an ammeter.

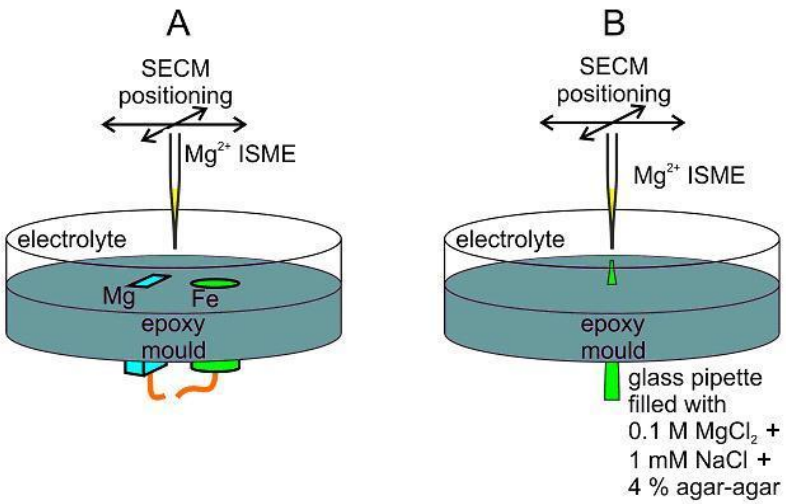

Figure 6.5.1. Sketches of the electrochemical cells employed: (A) galvanic Mg-Fe system; (B) validation cell supporting a glass pipette filled with $MgCl_2$ solution.

6.5.4.2. Preparation of the ion-selective magnesium micropipette electrodes

The ionophore employed for the fabrication of the Mg^{2+}-ISE was bis-N,N-dicyclohexyl-malonamide, which was synthesized following the method described in ref. [45]. Selectivity coefficients of this ionophore towards Na^+ and H^+ ions are also available there [45]. The composition of the ion-selective cocktail is given in Table 6.5.1. All the components in the ionophore cocktail were supplied by Sigma-Aldrich, except the home-made ionophore. Ion-selective microelectrodes were prepared using micropipettes pulled from borosilicate glass-capillaries B100-50-10 (Sutter, Novato, CA, USA). The glass-capillaries were first soaked in "piranha solution", then thoroughly washed with twice deionized water and ethanol, and dried in oven at 105 ^{0}C. Micropipettes were pulled from the capillaries by using a pipette puller (Sutter Instruments, type P-30, Novato, CA, USA). The inner wall of the pipette tips were hydrophobized by exposing them to a solution of dimethyldichlorosilane in carbon tetrachloride through capillary action, and baking them at 200 ^{0}C for 30 minutes in a closed petri dish.

Figure 6.5.2 shows the sketches and micrographs of the liquid-contact and solid-contact ion-selective microelectrodes employed in this Section, both using the same ion-selective cocktail but differing exclusively in the design of the electrochemical contact and the internal reference inside the micropipette electrode. The conventional micropipette Mg^{2+}-selective electrodes were prepared as described elsewhere [33]. The ionophore cocktail was filled into the micropipette tip under vacuum, whereas the internal solution was backfilled with the assistance of a microsyringe. The internal filling solution was 10 mM $MgCl_2$ + 0.25 M KCl, and the internal reference electrode was a chlorinated silver wire. The internal solution and the reference electrode were confined in the micropipette with *Loctite*® adhesive. A sketch and micrograph of the liquid-contact ion-selective microelectrode are shown in Figure 6.5.2A.

Table 6.5.1. Composition of the mixture employed to produce the cocktail for the Mg^{2+} ion-selective microelectrodes.

Component	Quantities for 200 µL of the mixture	
	Content	wt.%
Tetrahydrofurane (THF)	100 µL	-
Poly(vinyl chloride) (PVC)	7.68 mg	5.06
bis-N,N-dicyclohexyl-malonamide	2.23 mg	1.47
Potassium tetrakis(4-chlorophenyl)borate (KTFPB)	2.13 mg	1.40
2-nitrophenyl octyl ether (2-NPOE)	139.79 mg	92.07

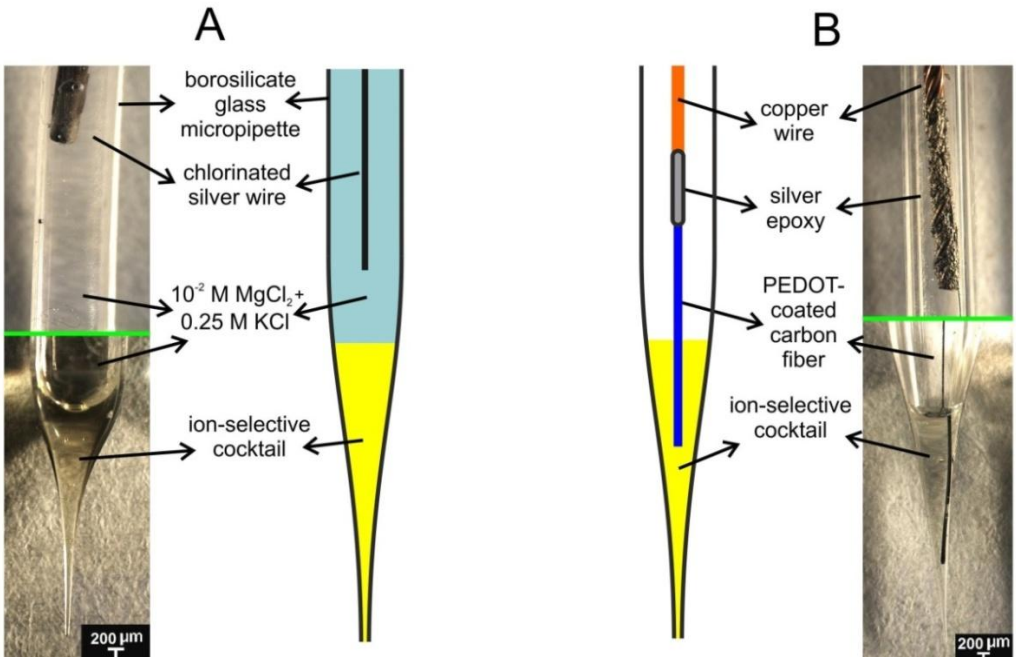

Figure 6.5.2. Sketches and micrographs of the micropipette electrodes fabricated for the selective detection of Mg^{2+} ions: (A) liquid-contact, and (B) solid-contact ISMEs.

The solid-contact ion-selective microelectrodes were built using the same components employed for the fabrication of the conventional ISME, though in this case the internal contact was provided by a 33 µm diameter carbon fiber cut to 35 mm length. A copper wire was previously attached to the carbon fiber using silver epoxy adhesive, to provide electric contact. The portion of the fiber to be contacting the ionophore cocktail was then coated with PEDOT conductive polymer in an electrochemical cell composed of the carbon fiber as working electrode, an Ag/AgCl wire immersed in the electrolyte as reference electrode, and a platinum wire as the auxiliary electrode. The monomer employed was 3,4-ethylenedioxythiophene dissolved in $BMIM^+$ PF_6^- ionic liquid [33].

Oxygen was purged from the EDOT-containing solution with nitrogen gas before and during the polymerization step. The resulting coated tip of the carbon fiber was immersed to a depth of 20 mm in the ionophore cocktail. The top of the micropipette electrode was sealed using Loctite® adhesive. A micrograph of the resulting microelectrode is depicted in Figure 6.5.2B.

A voltage divider method was employed to determine the resistance of the microelectrodes using 1 mM $MgCl_2$ + 1 mM NaCl solution. The electrochemical cell consisted of an Ag/AgCl/KCl (3M) reference electrode and a freshly prepared microelectrode. Their potentials were recorded with respect to the reference electrode. The electrodes were connected to the voltage follower as shown in Figure 6.5.3A. After a steady reading was achieved, then a precision resistor R_k was interconnected between the inputs of the voltage follower. The experiment was performed with two different precision resistors, namely 0.5 and 1.0 GΩ.

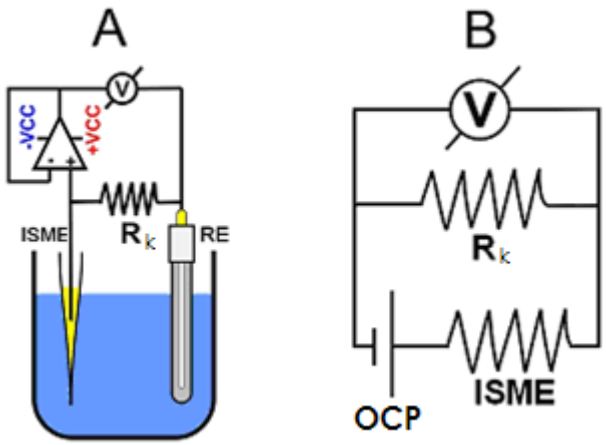

Figure 6.5.3. (A) Sketch of the electrochemical cell used for the measurement of the internal resistance of the ISME, and (B) equivalent circuit.

6.5.4.3. Instrumentation

High-resolution SECM equipment supplied by Sensolytics (Bochum, Germany), was employed. The instrument was built around an Autolab (Metrohm, Herisau, Switzerland) electrochemical interface, controlled with a personal computer. Amperometric, potentiostatic and potentiometric operations were available in this

configuration. For the potentiometric measurements where the Mg^{2+} sensing electrodes were employed, a voltage follower based on a 10^{13} Ω input impedance operational amplifier (TL071, Texas Instruments) was introduced in the measuring circuit [32], as shown in Figure 6.5.4. The cell voltages were measured with an electrometer and collected by the PC through the electrochemical interface. The scanning system (Applicable Electronics Inc) used a 3D micro-positioner driven by precision stepping motors. The distance between the scanning tip and the substrate was usually established by allowing the probe to gently touch the sample, and subsequently the probe was generally retracted to operation distance 100 μm with the aid of the *Z*-positioning motor. A video camera was used to further assist positioning of the tip close to the surface. Raster scanning was employed to record the consecutive scan lines composing the *X-Y* grid.

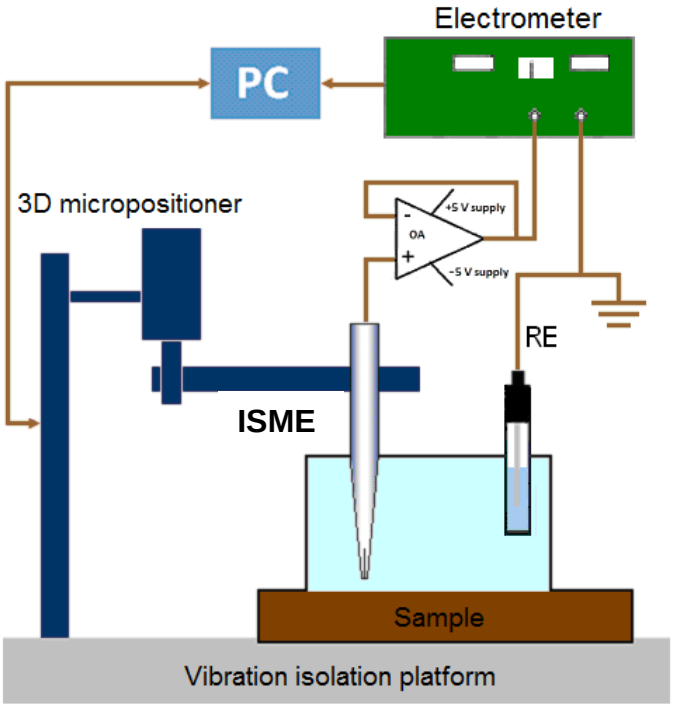

Figure 6.5.4. Sketch showing the main components of the instrument employed for ISME measurements, including the high input impedance operational amplifier (OA), and the ion-selective microelectrode (ISME).

6.5.5. Results and Discussion

The performances of the two types of Mg^{2+} ion-selective micropipette electrodes were compared concerning their calibration, resistance, response time, and imaging stability and reproducibility when used as potentiometric tips in SECM.

For their calibration, a series of $MgCl_2$ solutions containing 1 mM NaCl as base electrolyte was employed. The range covered extended between 10^0 and 10^{-5} M Mg^{2+}. As it can be seen in Figure 6.5.5, both microelectrodes maintain a linear relationship at the higher concentrations. The calibration equations for the linear portions of the curves obtained for the two ISMEs with the potentials were expressed in mV are:

$$E_{lc\text{-}ISME} = 87.75 - 29.12\ pMg \quad (6.5.1)$$

$$E_{sc\text{-}ISME} = -7.47 - 33.44\ pMg \quad (6.5.2)$$

The solid-contact microelectrode, Figure 6.5.5B, attained a wider approximately linearity range to lower concentration whereas the liquid-contact electrode appeared to be insensitive to the concentration. The slopes of the linear portions (29.1 mV decade^{-1} for the liquid-contact microelectrode, and interestingly 33.4 mV decade^{-1} for the solid-contact one) are sufficiently close to the expected Nernstian value of 29.6 mV decade^{-1} to employ these microelectrodes for quantitative measurements.

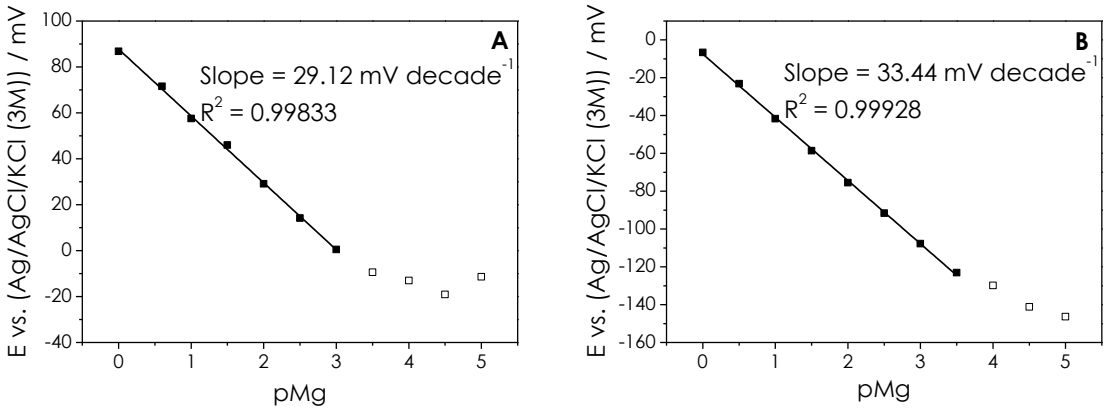

Figure 6.5.5. Calibration plots for the Mg^{2+} ISME in 1 mM NaCl solutions containing varying amounts of $MgCl_2$ (pMg = -log [Mg^{2+}]). (A) Liquid-contact, and (B) solid-contact

The noise present during potential measurements increases with increasing resistance of an ISME, and is therefore an indication of the expected performance of the sensors. The equivalent circuit (EC) for the resistance measurements is depicted in Figure 6.5.3B. Resistances of the solution and the reference electrode are also part of the system, but they are very small values compared to that of the ion-selective microelectrode. Therefore, they have not been included in the EC for the sake of simplicity. In contrast, the voltage follower has an impedance of the order of 10^{13} **Ω**, considerably larger than the precision resistors. Hence, once again this resistance has not been included in the EC.

Figure 6.5.6 shows the current transients recorded for the liquid-contact (A) and the solid-contact (B) ISMEs, respectively. After steady reading, U_k values were determined, and the resistance of the ISME was calculated using the equation describing the operation of a voltage divider:

$$R_{ISME} = R_k \frac{OCP - U_k}{U_k} \qquad (6.5.3)$$

where *OCP* is the open circuit potential value established between the ISME and the external reference electrode, and U_k is the potential value measured when the resistor load *R* was introduced inside the electrical circuit. Table 6.5.2 contains the resistance values obtained for micropipette electrodes of the two types. The resistance determined for the solid-contact ISME is about a seventh of that shown by that with a liquid-contact (0.56 and 4.80 GΩ, respectively). This observation is especially relevant when considering that the size of the micropipette openings were practically the same in both cases, thus the resistance values actually arose from differences in the interfacial resistance between the internal interfaces for each system.

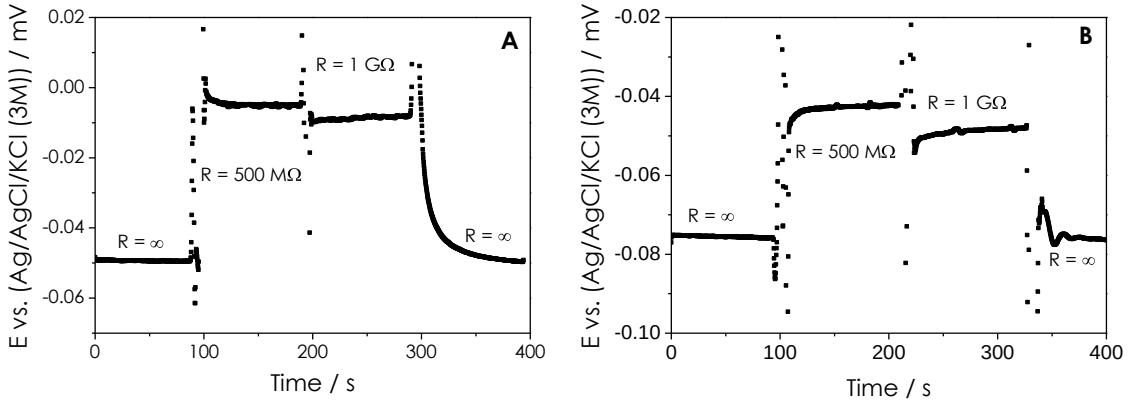

Figure 6.5.6. Response of ISME to shorting resistors for the voltage divider method: (A) Liquid-contact, and (B) solid-contact.

Table 6.5.2. Resistance measurements for the two kinds of Mg^{2+} ion-selective micropipette electrodes conducted in 1 mM $MgCl_2$ + 1 mM NaCl solution.

Parameter	ISME	
	Liquid-contact	Solid-contact
OCP / mV	-49.5	-75.7
R_k / GΩ	1	1
U_k / mV	-8.53	-48.41
R_{ISME} / GΩ	**4.80**	**0.56**

Another very important factor to be considered in the applicability of the Mg^{2+}-ISME is their response time, which severely limits the scan rates necessary to accurately record the concentration distribution maps of a given species. This issue is especially relevant in the case of corroding systems, where the location and size of the active sites continuously vary and are followed by changes in solution concentrations due to diffusion and convection. Ideally the scans must be recorded

in a sufficiently short time to ensure that the system has not changed significantly during the measurement.

The response time of the microelectrodes was measured following the method proposed by Lamaka et al. [44] with a dual drop cell. The electrodes were immersed in one drop of 0.1 M $MgCl_2$ + 1 mM NaCl and then move to the second drop of 0.01 M $MgCl_2$ + 1 mM NaCl after a stable potential was reached in 3 minutes. The time needed to reach 95% of the total potential change caused by the change in Mg^{2+} ion concentration was regarded as response time, τ_{95}.

Figure 6.5.7 depicts the potential changes recorded during these experiments. A visual inspection of the transients leads to the observation that the solid-contact micropipette electrode exhibits a more reproducible and stable response than the liquid-contact one. In fact, significantly shorter transient times were needed for the solid-contact ISME when quantified as τ_{95} values (namely, 71.1 s and 27.7 s were determined for the liquid-contact and the solid-contact microelectrodes, respectively).

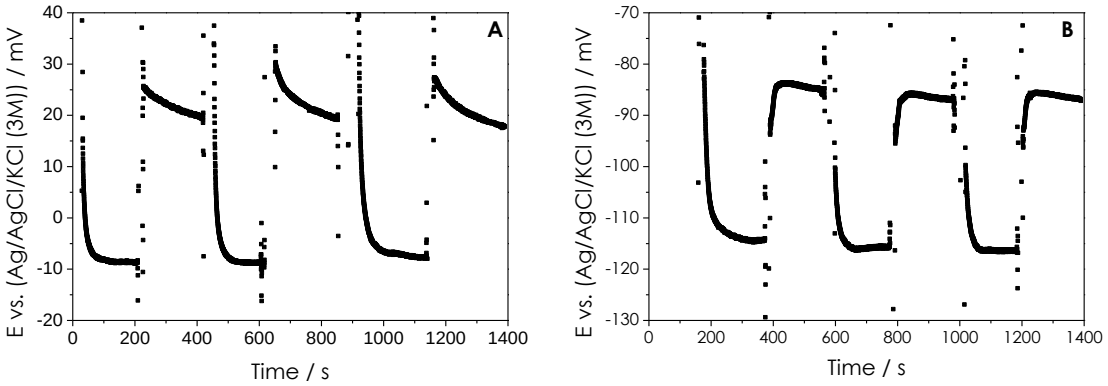

Figure 6.5.7. Dynamic response curves obtained for response time measurements to changes in $MgCl_2$ concentrations of 10^{-1} M and 10^{-2} M, in 10^{-3} M NaCl. (A) liquid-contact, and (B) solid-contact Mg^{2+}-ISME.

The performance of the two types of micropipette-based ion-selective electrodes for the imaging of Mg^{2+} ion concentration distributions was tested using the validation cell giving a source of Mg^{2+} ions 200 μm diameter pipette containing $MgCl_2$ in agar-agar. Figure 6.5.8 gives the ISME images obtained using a liquid-contact (A), and a solid-contact (B), micropipette electrode. Both 2D ISME maps were recorded at a scan rate of 12.5 μm s^{-1}. The same pipette holding the 0.1 M $MgCl_2$ agar solution was used in the measurements plotted in Figures 6.5.8A and 6.5.8B. The experiment was initiated using the solid-contact ISME The 2D array scan image in Figure 6.5.8B was recorded after about 5 to 10 minutes following immersion of the Mg^{2+} containing pipette. Subsequently, the solid-contact ISME was replaced by the liquid-contact, and array scan in Figure 6.5.8A was obtained ca. 150 minutes later. As a result of the sustained diffusion from the Mg^{2+} pipette source in the validation cell the flux of Mg^{2+} would have decreased by about 4 to 5 times

according to the Cottrell equation [47]. Additionally, some stirring of the aqueous solution takes place during the experiment because of unavoidable convection currents and gravitational effects due to the higher density of the $MgCl_s$ containing solution. Also the rather high scan rate employed for enhanced resolution could produce for some convective distortion. Nevertheless, the approximate circular shapes of the higher concentrations are the same as that of the pipette. Visual inspection of the two images clearly shows significant image distortion in the *X*-direction with the liquid-contact ISME (cf. Figure 6.5.8A) which possibly occurred because of its slower response.

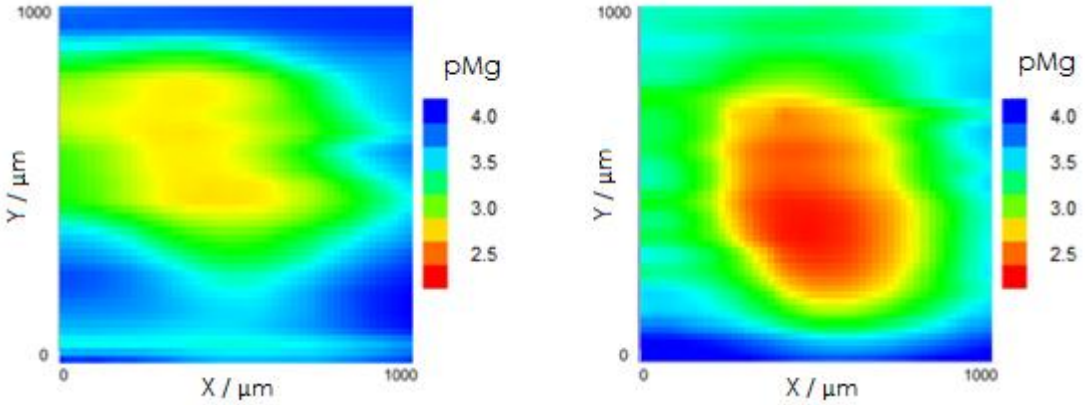

Figure 6.5.8. ISME images displaying the of Mg^{2+} ion concentrations 100 µm; above the tip of a centered pipette source (A) liquid-contact, and (B) solid-contact. Scan rate: 12.5 µm s^{-1}.

Differences in the performance of the two types of micropipette electrodes are more easily seen shown in the graphs depicted in Figure 6.5.9. They correspond to a sequence of scan lines taken from Figure 6.5.8 at the *Y*-positions indicated. It is seen that the liquid-contact microelectrode, exhibited a much boarder curve indicating a poorer electrode performance in accord with a slower response.

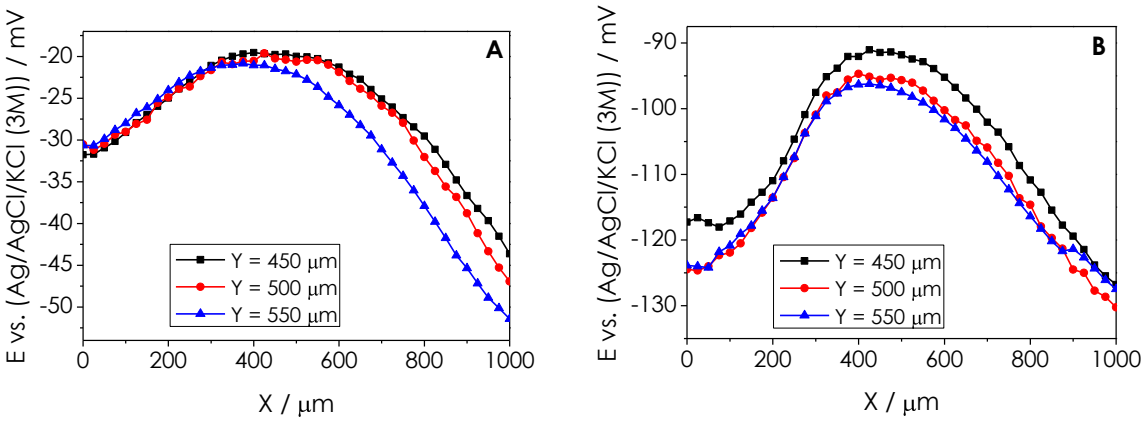

Figure 6.5.9. Line scans displaying the distribution of Mg^{2+} ion concentration close to the center of the magnesium ion-pipette source. (A) liquid-contact, and (B) solid-contact ISMEs. The scans were extracted from the middle of the ISME images given in Figure 6.5.8. Tip-substrate distance: 100 µm; scan rate: 12.5 µm s^{-1}.

On the other hand, these experiments with the validation cell clearly highlight the new opportunities opened by this new solid-contact micropipette-based ion-selective electrode for the monitoring of concentration distributions of species participating in corrosion with good spatial resolution using an ISME. This hypothesis was further checked by imaging the concentration distributions of Mg^{2+} ions over a corroding magnesium sample. Separate experiments were conducted on the magnesium strip galvanically coupled to iron and at open circuit when the two metals were electrically disconnected.

Freely corroding magnesium in the chloride-containing aqueous solutions leads to the release of metal ions that were detected in ISME measurements. The concentration distributions of Mg^{2+} are shown in Figure 6.5.10 for two separate experiments. The images of the concentrations of Mg^{2+} ions looked very different. In the case of the liquid-contact electrode, the ion concentration is rather homogeneously distributed which suggests a uniform corrosion process occurring over the entire metal strip. The morphology of the corrosive attack deduced from the inspection of Figure 6.5.10A seems to contradict the results previously reported in Section 6.3 using the same type of liquid-contact ISME tip. The observations derived from the analysis of a sequence of single scan lines supported the conclusion of a localized corrosive attack on the magnesium strip.

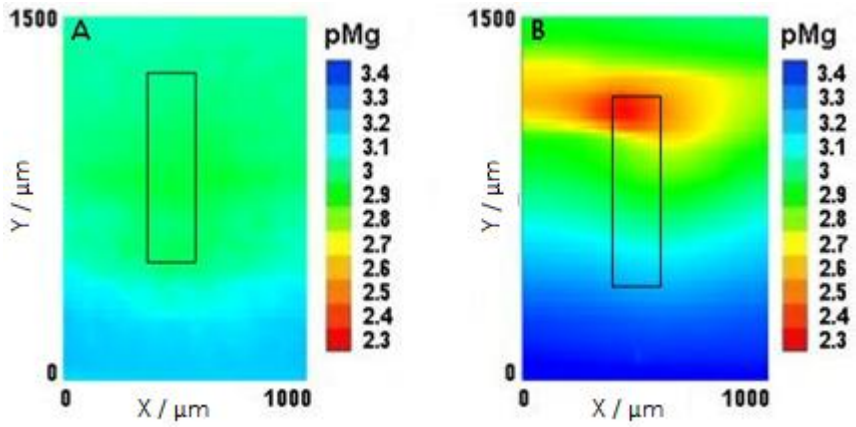

Figure 6.5.10. Mg^{2+} ion concentration images above freely corroding magnesium in 10 mM NaCl. (A) liquid-contact, and (B) solid-contact. Tip-substrate distance: 100 µm; scan rate: 12.5 µm s^{-1}. The location of the magnesium strip is drawn on the images.

The origin for such discrepancy must arise from the higher scan rates needed for recording a 2D map compared to the line scans in Figure 6.3.4 which may originate blurring effects that could not be satisfactorily resolved here because of the long response times of the microelectrode. A different situation is observed when the solid-contact ISME was employed however confirms the previous result. Metal dissolution is detected from a highly localized source over the metal strip (see Figure 6.5.10B), which only covers a small fraction of the exposed metal surface. Most of the metal is thus effectively in contact with an electrolyte either free from Mg^{2+} ions or

with a very low ion concentration originating from their diffusion in the electrolyte away from the actual source for the metal ions. This result is consistent with a corroding pit or crevice corrosion located at the upper end of the magnesium strip demonstrating that he time response of the solid-contact ISME is low enough to achieve the spatial resolution required for imaging the concentration distribution of Mg^{2+} ions in the system.

Similar localized features can be observed from the inspection of the images obtained for the magnesium strip galvanically coupled to iron shown in Figure 6.5.11. Despite the increased number of active anodes established on the surface of the metal with the higher concentration gradients in this system, the liquid-contact electrode also shows that the anodic activity on the metal strip occurs in a localized manner. That is, though blurring still affects the system, the high concentration met allows for better spatial resolution than in the case of the free-corroding magnesium in Figure 6.5.11A. Indeed, very high dissolution rates for magnesium are observed when the metal was connected to iron, which are related to potential differences beyond those used for calibration of the ISME. At this stage, the negative pMg values in Figure 6.5.11 should only be considered as semi-quantitative estimates of high local Mg^{2+} concentrations compared to lower releases over most of the metal coupon. In typical experiments, less aggressive conditions should be employed in order to detect earlier stages of the localized attack on the metal, and the linear range of the ISME calibration will thus be applicable.

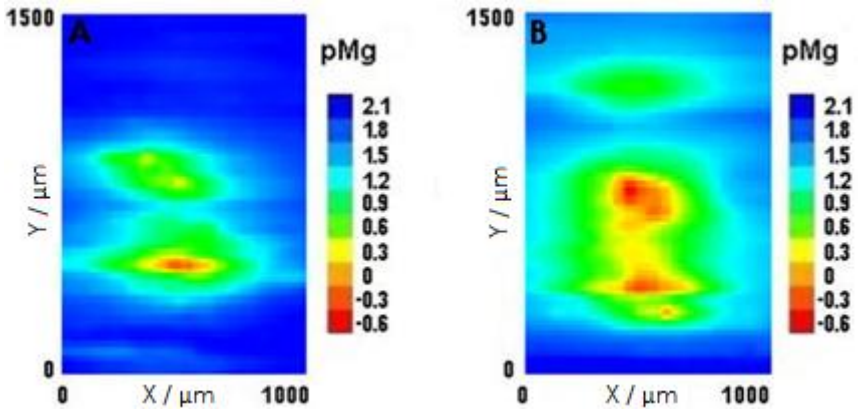

Figure 6.5.11. Mg^{2+} ion concentration images above a magnesium strip galvanically shorted to iron in 10 mM NaCl solution (A) liquid-contact, and (B) solid-contact. The position of the iron strip was 5 mm to the right of the magnesium strip in the images. Tip-substrate distance: 100 µm; scan rate: 12.5 µm s^{-1}.

In summary, from inspection of the ISME images in Figures 6.5.10B and 6.5.11B, the magnesium sample was observed to corrode in a heterogeneous fashion regardless the electrical condition imposed to it, as it was reported in Section 6.3. The main difference imposed by galvanic coupling this metal to iron is that metal dissolution greatly increases, as evidenced by the measurement of low pMg values for the electrically-connected condition, and the observation of more than one

anodic site simultaneously operating on the surface. However, general corrosion was also observed to occur.

In the preceding discussion it has been assumed that the potential measured by the ISME, above the corroding magnesium surface, was solely determined by the local Mg^{2+} concentration. But there might also be an additional contribution to the measured potential difference due to the electric field present above the corroding surface. These potential differences in the electrolyte arise ohmically as a consequence of the ionic current fluxes generated by the local corrosion cell, an effect that has been effectively exploited to visualize localized events in a corroding metal using the scanning reference electrode technique (SRET) [48]. Though the ISME employed in this Section are not conventional micro-tip reference electrodes, they nevertheless will be subject to such effect when positioned over a corroding surface. Also SRET is influenced by the concentration of the salts of the dissolving metal as it alters the solution conductivity reducing the electric potentials.

The measurement of the response of the solid-contact ISME over 100 μm diameter Pt-Ir current source embedded in an epoxy holder was first considered. However, the measurements were poor and attributable to the changes in pH and bubbles that formed on the surface due to water electrolysis during the experiment observation of vigorous gas evolution. The presence of bubbles and pH changes during these measurements was confirmed by video camera imaging with a pH indicator, phenolphthalein, added to the electrolyte. The indicator changes from colourless to purple at the concentrations used. The purple coloration is seen at the cathodes and a corresponding acidic formation occurs at the anode. The pH changes affect the offset potential of the ISME because the ionophore exhibits a Nernstian response towards protons activity in acidic solution [45]. The bubbles adhering to the electrodes also tended to adhere to the tip of the ISME and they distorted the current flow directions.

The effects due to pH changes and bubbles evolution were overcame using a glass micropipette. In this case, the solid-contact ISME was placed 100 μm from its tip. In Figure 6.5.12A it can be seen that the background potential of the ISME remains virtually constant throughout all the measurements as indicated by the drawn dotted lines. The application of different currents ranging from -0.57 to +2.86 μA produced potential changes in the ISME amounting 3-18 mV, respectively. Scan lines are shown in Figure 6.5.12B. The scans produced well defined potential peaks without perfect symmetry. This feature is attributed to the practical difficulties found in order to produce perfectly symmetrical glass capillary openings parallel to the scan direction. Despite these practical limitations, the potential changes occurring at the ISME clearly reflect the magnitude and the sign of the electric field developed from the glass micropipette current source. Next, a stable potential response of the ISME was found at the end of the experiment when it was scanned over the glass micropipette current source when no current was flowing in the cell. An important observation in Figure 6.5.12A is the rapid change following application or removal of the current flow. The changes, particularly those on disconnecting the current,

occurred too rapidly to be a result of interfacial effects. Delays in the response were less than about 20 s which were seen with the larger cathodic currents.

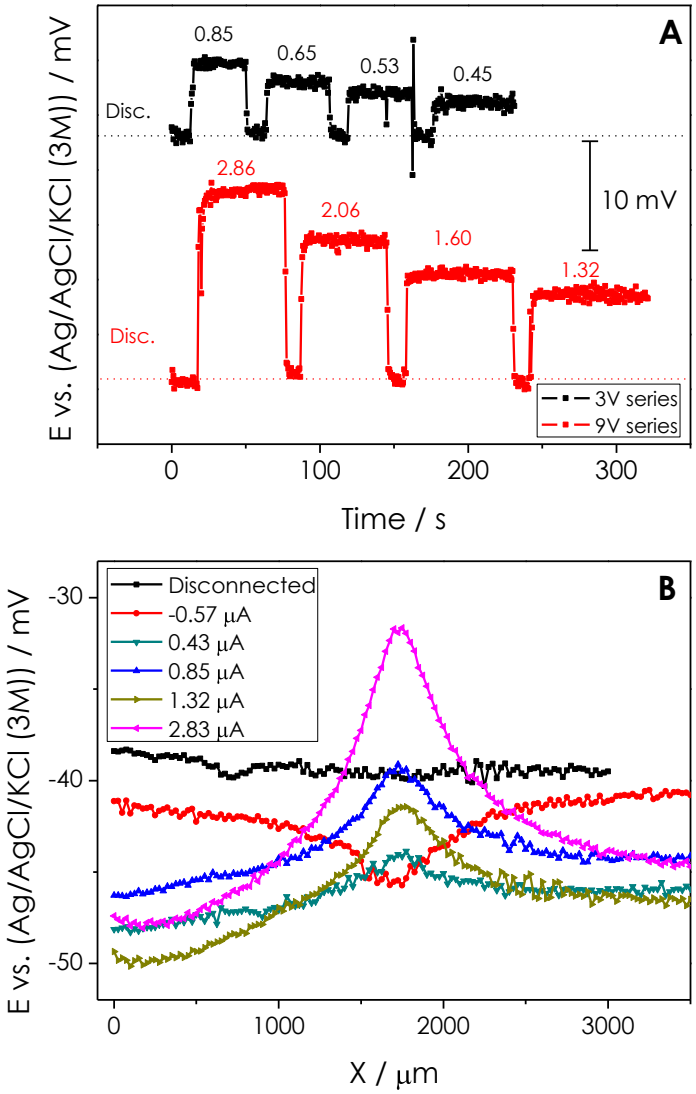

Figure 6.5.12. Potential response of a solid-contact Mg^{2+} ISME in 1 mM NaCl solution to the application of different currents from a glass micropipette current source. (A) The current was varied using batteries (namely 9 and 3 V, respectively) and resistors by using a sequence of connection/disconnection steps; the current values measured with an ammeter during each electrical connection, given in µA, are indicated in the figure; probe placed 100 µm above the center of the source. (B) Line scans taken 100 µm above the source for the indicated current values flowing through the pipette; scan rate: 12.5 µm s^{-1}.

The magnitude of the potential change produced by the applied currents in Figure 6.5.12A are plotted in Figure 6.5.13. A linear relationship was established between these two parameters, thus allowing the response of the ISME to be calibrated regarding an electric field operating in the solution where the concentration of the ion being monitored does not change.

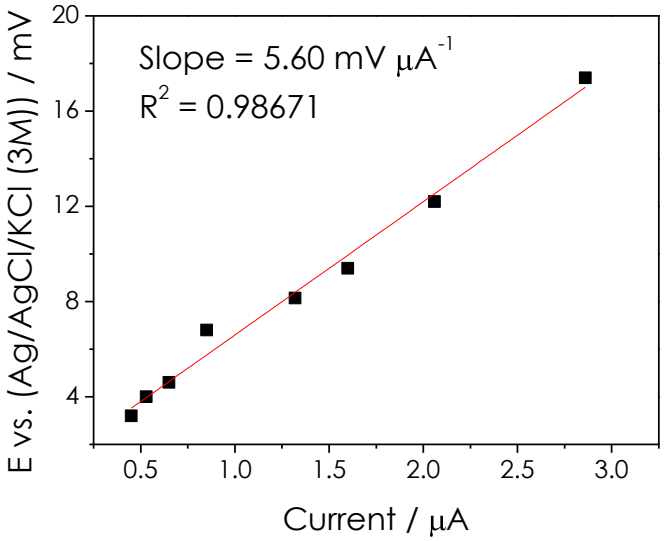

Figure 6.5.13. Calibration plot for the potential response of the solid-contact Mg^{2+} ion selective micropipette electrode with the amount of current flowing in the solution from a glass micropipette current source. The ISME was 100 μm above the glass micropipette current source.

The predicted variation is given by

$$V = \frac{i\rho}{2\pi r} \qquad (6.5.4)$$

where V is the electric potential at a point due to the flow of current i from a point source, at a distance r , in an electrolyte of resistivity ρ [49]. A very close fit of these results is obtained with a ratio of resistivity to probe distance (ρ / r) of 38 kΩ. This result is plotted in Figure 6.5.13. However, it must be pointed out that for a distance of r =100 μm, a resistivity of 380 Ω cm is obtained (although the measured resistivity was 6060 and a literature value of 8084 Ω cm was found for 1 mM NaCl [49]). The differences may in part be due to the source and probe having real diameters, and the distance between the two tips being approximately equal to these diameters so that ideal point to point conditions were not met or that the probe or that the distances between the tips were greater than measured. Because of these uncertainties and that experiment conditions were repeated for the different sets of measurements, more confidence is given to the experimental results rather than to the predictions based on equation (6.5.4). With these experimental conditions, currents in excess of 3 μA must flow from the current source located 100 μm from the probe in a 1.0 mM NaCl solution to produces a potential change of about 20 mV, which from Equation 6.5.1 and 6.5.2 would be equivalent to a change in the magnesium concentration smaller than one order of magnitude.

The external galvanic current was measured between the Mg and the Fe and found to be about 2.5 ± 1.0 μA. There were three active anodic areas detected with ISME in Figure 6.5.11A and about four in 6.5.11B in addition to activity over virtually its whole Mg area. The total anodic current flowing from the Mg surface producing these sites would be divided between them. The total anodic current, would in turn,

be made up of the external current flowing from the iron, and also that contribution supported by the cathodic current on the Mg. Generally, it would be expected that the external current would be the major contributor because of more rapid cathodic kinetics for water reduction on the Fe. There could also be a contribution to the pitting currents from the presence of hydrogen ions produced by hydrolysis of the Mg^{2+} as discussed by Bender [17] and Frankel [27] but the sites where the hydrogen reduction takes place must be at a sufficient distance from the pits for currents in solution to be detected. It is therefore difficult to extract the total anodic current. However, in order to compare possible contributions from (ohmic) electric potential contributions to the potential changes measured using an ISME over a corroding surface, an upper value of 2.5 µA flowing from a single site will be used. It should have a shape similar to that from the curves in 1mM NaCl solution (Figure 6.5.12B). The maximum potential for the 2.8 µA curve corresponds to a peak potential of less than 20 mV. However, the bulk solution in which the results in Figure 6.5.11 were obtained, was 10 mM NaCl which has a resistivity 9.7 times smaller than that of the calibration solution [50]. The lower resistivity would then give a peak potential of about 2 mV in the corroding solution. This potential is to be compared with the peak potential in Figure 6.5.11B which correspond a peak height above background of about 90 mV (using the calibration curve given by Equation 2, or taken from Figure 6.5.5B). Hence it is clear that the magnitudes of the ISME potential response, is dominated by the concentration changes of Mg^{2+}, and potential contributions due to corrosion currents are small in comparison. It is also important to note that the SRET potential measurements carried out over a corroding surface may also be influenced by the presence of dissolved corrosion products. This is especially true when the bulk solution is dilute, and rapid localized corrosion takes place that can reduce the resistivity and consequentially the ohmic potential.

6.5.6. Conclusion

A new ISME construction to investigate corrosion processes on magnesium-based or magnesium-containing materials with high spatial resolution has been presented. It is based on a robust solid-contact with the ionophore which exhibits smaller internal resistance and a faster response times compared to one with a conventional liquid-contact having the same tip dimensions. Both types of magnesium ion measuring micropipette probes were successfully employed to perform *in situ* experiments on model corroding systems. The solid-contact ISME with its greater stability and lower internal impedance had a marked impact on the ability to collect these images with a high spatial resolution needed to study early stages of localized corrosion. Most of the corrosion studies were due to localized pitting and crevice corrosion but examples of general corrosion were seen. In the corrosion experiments the observed potential changes with the ISME were possibly attributed to both changes in Mg^{2+} concentrations and to corrosion currents. The

Nernstian potential changes due to the Mg^{2+} concentrations were much larger than those produced by the ohmic electric potentials in solution.

6.5.7. References

1. M.M. Avedesian. In: ASM Handbook, Vol. 13, Corrosion, 4th edn. ASM International Metals Park, 1992.
2. D. Eliezer, E. Aghion, F.H. Froes. Advanced Performance Materials 5 (1998) 201.
3. G.L. Song, A. Atrens. Advanced Engineering Materials 1 (1999) 11.
4. R.C. Zeng, J. Chen, W. Dietzel, R. Zettler, J.F. Dos Santos, M. Lucia Nascimento, K.U. Kainer. Corrosion Science 51 (2009) 1738.
5. G. Song, A. Atrens, D. St John, J. Nairn, Y. Li. Corrosion Science 39 (1997) 855.
6. G.L. Song, A. Atrens, X.L. Wu, B. Zhang. Corrosion Science 40 (1998) 1769.
7. R. Ambat, N.N. Aung, W. Zhou. Corrosion Science 42 (2000) 1433.
8. S. Bender, J. Goellner, A. Heyn, E. Boese. Materials and Corrosion 58 (2007) 977.
9. T.R. Thomaz, C.R. Weber, T. Pelegrini, L.F.P. Dick, G. Knörnschild. Corrosion Science 52 (2010) 2235.
10. N.T. Kirkland, G. Williams, N. Birbilis. Corrosion Science 65 (2012) 5.
11. W.A. Ferrando. Journal of Materials Engineering 11 (1989) 299.
12. A.-M. Lafront, W. Zhang, S. Jin, R. Tremblay, D. Dubé, E. Ghali. Electrochimica Acta 51 (2005) 489.
13. M.C. Zhao, M. Liu, G.L. Song, A. Atrens. Corrosion Science 50 (2008) 3168.
14. G.L. Song, Z. Xu. Electrochimica Acta 55 (2010) 4148.
15. Z. Szklarska-Smialowska. Corrosion Science 41 (1999) 1743.
16. G. Song, A. Atrens. Advanced Engineering Materials 9 (2007) 177.
17. S. Bender, J. Goellner, A. Atrens. Materials and Corrosion 63 (2012) 707.
18. P. Brouillet, I. Epelboin, M. Froment. Comptes Rendus de l'Académie des Sciences 239 (1954) 1795.
19. R.L. Petty, A.W. Davidson, J. Kleinberg. Journal of the American Chemical Society 76 (1954) 363.
20. A. Atrens, W. Dietzel. Advanced Engineering Materials 9 (2007) 292.
21. D. Sadcheva. Corrosion Science 60 (2012) 18.
22. G.L. Song, A. Atrens, D. StJohn. In: Magnesium Technology 2001. TMS, New Orleans, 2001, p. 255.
23. G. Baril, G. Galicia, C. Deslouis, N. Pébère, B. Tribollet, V. Vivier. Journal of the Electrochemical Society 154 (2007) C108.
24. G. Williams, H.N. McMurray. Journal of the Electrochemical Society 155 (2008) C340.
25. J. Światowska, P. Volovitch, K. Ogle. *Corrosion Science* 52 (2010) 2372.
26. G. Williams, R. Grace. Electrochimica Acta 56 (2011) 1894.
27. G.S. Frankel, A. Samaniego, N. Birbilis. Corrosion Science 70 (2013) 104.

28. S.E. Pust, W. Maier, G. Wittstock. Zeitschrift für Physikalische Chemie (Muenchen Ger.) 222 (2008) 1463.
29. L. Niu, Y. Yin, W. Guo, M. Lu, R. Qin, S. Chen. Journal of Materials Science 44 (2009) 4511.
30. M.B. Jensen and D.E. Tallman. In: Electroanalytical Chemistry: A Series of Advances, Vol. 24 (Edited by A.J. Bard, C.G. Zoski). CRC Press, Boca Raton, 2012, p. 171.
31. R.M. Souto, Y. González-García, D. Battistel, S. Daniele. Chemistry - A European Journal 18 (2012) 230.
32. R.M. Souto, J. Izquierdo, J.J. Santana, A. Kiss, L. Nagy, G. Nagy. In: Current Microscopy Contributions to Advances in Sciences and Technology, Vol. 2 (Edited by A. Méndez-Vilas). Formatex Research Center, Badajoz, 2012, p. 1407.
33. G. Gyetvai, S. Sundblom, L. Nagy, A. Ivaska, G. Nagy. Electroanalysis 19 (2007) 1116.
34. G. Gyetvai, L. Nagy, A. Ivaska, I. Hernádi, G. Nagy. Electroanalysis 21 (2007) 1970.
35. J. Izquierdo, L. Nagy, Á. Varga, I. Bitter, G. Nagy, R.M. Souto, Electrochimica Acta 59 (2012) 398.
36. J. Izquierdo, L. Nagy, J.J. Santana, G. Nagy, R.M. Souto, Electrochimica Acta 58 (2011) 707.
37. B. Czoka, Z. Mekhalif. Electrochimica Acta 54 (2009) 3225.
38. J. Izquierdo, L. Nagy, J.J. Santana, R.M. Souto, G. Nagy. Electrochimica Acta 56 (2011) 8846.
39. B. Horrocks, M.V. Mirkin, D.T. Pierce, A.J. Bard, G. Nagy, K. Toth. Analytical Chemistry 65 (1993) 1213.
40. M.V. Rouilly, M. Badertscher, E. Pretsch, G. Suter, W. Simon. Analytical Chemistry 60 (1988) 2013.
41. U.E. Spichiger, R. Eugstrer, E. Haase, G. Rumpf, P.M. Gehrig, A. Schmid, B. Rusterholz, W. Simon. Fresenius' Journal of Analytical Chemistry 341 (1991) 727.
42. Z. Hu, D. Qi. Analytica Chimica Acta 248 (1991) 177.
43. S.V. Lamaka, O.V. Karavai, A.C. Bastos, M.L. Zheludkevich, M.G.S. Ferreira. Electrochemistry Communications 10 (2008) 259.
44. S.V. Lamaka, M.G. Taryba, M.L. Zheludkevich, M.G.S. Ferreira. Electroanalysis 21 (2009) 2447.
45. K. Tóth, E. Lindner, M. Horváth, J. Jeney, E. Pungor, I. Bitter, B. Ágai, L. Töke. Electroanalysis 5 (1993) 781.
46. J. Izquierdo, L. Nagy, I. Bitter, R.M. Souto, G. Nagy, Electrochimica Acta 87 (2013) 283.
47. A.J. Bard, L.R. Faulkner. Electrochemical Methods. John Wiley and Sons, New York, 1980, p. 143.
48. H.S. Isaacs, B. Vyas. In: Electrochemical Corrosion Testing (Edited by F. Mansfeld, U. Bertocci). ASTM, Baltimore, 1981, p. 3.
49. H.S. Isaacs. Journal of the Electrochemical Society 138 (1991) 772.
50. W.R. West (Editor). Handbook of Physics and Chemistry, 55th edn. CRC Press, Cleveland, 1974, p. D-132.

6.6

Main conclusions

1. Significant improvement in SECM for the investigation of corrosion processes is achieved by combining amperometric and potentiometric operations in the instrument. It is demonstrated that dual potentiometric/amperometric tips and ion-selective microelectrodes can be employed for more sensitive applications of SECM imaging in Corrosion Science.

2. The applicability of the conventional liquid contact and the newly-developed solid contact Mg^{2+} ion selective sensors for the determination of the evolution of magnesium-based materials by SECM has been demonstrated. By comparison, the solid contact ISME shows a marked impact on the ability to study localized corrosion phenomena in active materials.

3. Heterogeneous generation of Mg^{2+} cations was visualized during spontaneous corrosion and sacrificial anodic dissolution of magnesium based surfaces. Mostly localized corrosion processes were observed on magnesium, though situations corresponding to generalized corrosion were also found.

4. Relevant complementary information was acquired by taking advantage of the dual functionality of the antimony electrode. Local pH distributions, resulting from the involved reactions occurring at the surfaces under study, could be imaged quasi simultaneously with the observation of oxygen consumption.

5. The combination of measurements and electrodes presented here allowed identification and quantification of the different reactions taking place during the corrosion processes. Additionally, the results open a promising new route to the elucidation of certain characteristics of the mechanisms involved in the corrosion and passivation of magnesium.

6.7

Conclusiones

1. Se han logrado mejoras significativas en el SECM para la investigación de los procesos corrosivos mediante la combinación de las operaciones amperométrica y potenciométrica en dicho instrumento. Se demuestra que las puntas de operación dual amperométrica/potenciométrica y los microelectrodos de ion selectivo pueden emplearse con aplicaciones más sensibles para visualización en Ciencia de la Corrosión.

2. Se ha demostrado la aplicabilidad de los electrodos de contacto líquido y de los recientemente desarrollados sensores selectivos de ion Mg^{2+} de contacto sólido para SECM en el análisis de la evolución de materiales de base magnesio. En comparación, el ISME de contacto sólido aporta una destacada mejoría en su capacidad para estudiar fenómenos de corrosión localizada en materiales activos.

3. Se ha visualizado la generación heterogénea de cationes Mg^{2+} durante la corrosión espontánea y disolución anódica de sacrificio de superficies de base magnesio. La mayoría de los procesos observados en el magnesio han consistido en procesos de corrosión localizada, aunque también se encontraron situaciones que se corresponden con corrosión generalizada.

4. Se ha adquirido información complementaria relevante aprovechando la ventaja ofrecida por la doble funcionalidad del electrodo de antimonio. Se han podido visualizar distribuciones locales de pH, las cuales resultan de las reacciones involucradas que ocurren en las superficies bajo estudio, de manera casi simultánea con las observaciones de consumo de oxígeno.

5. La combinación de medidas y electrodos presentados aquí permite la identificación y cuantificación de las diferentes reacciones que tienen lugar durante los procesos de corrosión. Además, los resultados abren una nueva y prometedora ruta para la elucidación de ciertas características de los mecanismos involucrados en la corrosión y pasivación del magnesio.

CHAPTER 7

Detection of localized chemical heterogeneities in aluminium alloys

Index

7.1

Prologue to the experiments

7.1.1. Introduction

Aluminium is the third most abundant material element in the earth crust, and its alloys have gained increasing application as high strength and lightweight materials in aircraft and engineering structures [1-3]. Secondly, aluminium and its alloys are recognized to be one of the most suitable materials for future hydrogen production and there is a trend to utilize them as an energy material [4]. Although many aluminium alloys exhibit high corrosion resistance due to the presence of a protective oxide layer, most high strength alloys are microstructurally complex systems presenting a rather high number of individual phases, namely phase-pure intermetallic compounds found as particles distributed in the aluminium matrix [5,6]. For instance, aluminium alloy AA2024 (Al-4.4Cu-1.5Mg-0.6Mn) is regarded to have up to 10 or more individual phases that are important to alloy corrosion behaviour [7]. In the particular case of this alloy, three major types of intermetallic particles differing in composition are distinguished: AlCuFeMnSi (2nd phase) intermetallics and Al_2CuMg (S phase) and Al_2Cu (ϑ phase) precipitates [8]. Furthermore, it was shown that the 2nd phase particles of AA2024 can be heterogeneous in elemental composition [9]. The major impact of microstructure on the electrochemical resistance of a material can be anticipated by considering that the corrosion behaviour of an alloy is the result of the electrochemical behaviour of its constituent particles [7,8,10]. Selective particle dissolution and pitting corrosion of aluminium alloys are the main failure processes experienced by these materials. The role of synthetic intermetallics Al_2Cu and Al_2CuMg in an aluminium matrix was investigated [11], leading to the observation that the potential of the Al_2Cu is positive to that of Al and Al_2CuMg and it acts as the cathodic zone in the alloy. On the other hand, Al_2CuMg is the main anodic phase, but it was argued that preferential Mg dissolution may originate a noble Cu-rich residue that may become eventually cathodic with the result of dissolution of the aluminium matrix [11]. Indeed, copper redistribution on the alloy surface will also influence the local electrochemical activity towards cathodic oxygen reduction [12,13]. In summary, the corrosion behaviour of aluminium alloys remains under debate, and the application of localized electrochemical techniques may contribute to understand the roles of the different components and phases [14-17].

Further, the very negative value of the aluminium standard electrode potential (E^0 = -1.66 V vs. NHE) [18] is responsible for hydrogen co-evolution during metal dissolution. In this context, the anomalous occurrence of both cathodic

dissolution of the metal [19] (i.e., Al dissolution increases as the surface is polarized in the cathodic direction) and anodic hydrogen evolution analogously to corroding magnesium-based materials.

7.1.2. Research aims

In this Chapter, the applicability of some scanning microelectrochemical techniques to image the heterogeneous distribution of electrochemical activity occurring in high strength aluminium alloys with complex microstructures has been explored. Due to the noble character of Cu-containing inclusions compared to the aluminium matrix, two aluminium alloys were selected, namely AA2024 and AA6060, as these alloys present a high and a low copper content, respectively. Due to the localized nature of the corroding processes in these materials in aqueous solutions containing chloride ions, low conductivity solutions were employed to allow recording electrochemical activity images with sufficient resolution. Therefore, both the scanning vibrating electrode technique (SVET) and scanning electrochemical microscopy in the AC mode (AC-SECM) were chosen. The reactivity of the two alloys were first investigated by SVET in Sections 7.2 and 7.3, allowing some differences in the corrosion behaviour of the materials to be established. Furthermore, Section 7.3 also contains an investigation on the protecting ability of a zirconia layer applied on AA2024. High spatially-resolved monitoring of the local activation of inclusions in AA2024, and the dissolution processes related to their electrochemical activity, by using AC-SECM is presented in the following Section 7.4.

7.1.3. References

1. D.J. Altenpohl. Aluminium: Technology, Applications and Environment. The Aluminium Association and the Minerals, Metals and Materials Society, USA, 1998.
2. Aluminium and Aluminium Alloys (Edited by J.R. Davis). ASM International, Materials Park, 1993.
3. F.M. Queiroz, M. Magnani, I. Costa, H.G. de Melo. Corrosion Science 50 (2008) 2646.
4. H.Z. Wang, D.Y.C. Leung, M.K.H. Leung, M. Ni. Renewable and Susteinable Energy Reviews 13 (2009) 845.
5. N. Birbilis, R.G. Buchheit. Journal of the Electrochemical Society 155 (2008) C117.
6. R.R. Leard, R.G. Buchheit. In: Proceedings of the 8th International Conference on Aluminium Alloys (Edited by P.J. Gregson, S.J. Harris). Materials Science Forum, Cambridge, 2002, p. 1491.
7. R.G. Buchheit, N. Birbilis. Electrochimica Acta 55 (2010) 7853.

8. L.C. Abodi, J.A. DeRose, S. Van Damme, A. Demeter, T. Suter, J. Deconinck. Electrochimica Acta 63 (2012) 169.
9. A. Boag, A.E. Hughes, N.C. Wilson, A. Torpy, C.M. Glenn, T.H. Muster. Corrosion Science 51 (2009) 1565.
10. T. Suter, R.C. Alkire. Journal of the Electrochemical Society 148 (2001) B36.
11. J.F. Li, Z. Ziqiao, J. Na, T. Chengyu. Materials Chemistry and Physics 91 (2005) 325.
12. R.G. Buchheit, R.P. Grant, P.F. Hlava, B. McKenzie, G.L. Zender. Journal of the Electrochemical Society 144 (1997) 2621.
13. R.G. Buchheit, M.A. Martinez, L.P. Montes. Journal of the Electrochemical Society 147 (2000) 119.
14. N. Birbilis, M.K. Cavanaugh, L. Kovarik, R.G. Buchheit. Electrochemistry Communications 10 (2008) 32.
15. N. Birbilis, M.K. Cavanaugh, R.G. Buchheit. Corrosion Science 48 (2006) 4202.
16. H. Krawiec, Z. Szklarz, V. Vignal. Corrosion Science 65 (2012) 387.
17. G. Williams, A.J. Coleman, H.N. McMurray. Electrochimica Acta 55 (2010) 5947.
18. M. Pourbaix, Atlas of Electrochemical Equilibria in Aqueous Solutions. National Association of Corrosion Engineers, Houston, 1974.
19. Y. Baek, G.S. Frankel. Journal of the Electrochemical Society 150 (2003) B1.

7.2

In situ monitoring of the electrochemical reactivity of aluminium alloy AA6060 using the scanning vibrating electrode technique

7.2.1. Abstract

Localized electrochemical activation of aluminium alloy AA6060 surfaces during immersion in chloride-containing aqueous solution has been characterised using the scanning vibrating electrode technique (SVET). Ionic current flows in the electrolyte phase adjacent to corroding microcells are imaged *in situ*, allowing their evolution with time to be monitored with spatial resolution. A heterogeneous response due to the presence of intermetallic inclusions in the material occurred on AA6060 surfaces. The highly localized anodic activity was thus detected, which has been interpreted to result from galvanic coupling between the matrix and the intermetallic particles. Metallic inclusions behave cathodically whereas the aluminium matrix undergoes metal dissolution due to the activation of anodic sites in the proximity of those inclusions. Hydrolysis of aluminium ions leads to local acidification of the electrolyte adjacent to the anodic sites, accompanied by hydrogen evolution.

7.2.2. Resumen

Se ha caracterizado la activación electroquímica localizada en superficies de aleaciones de aluminio AA6060 durante su inmersión en disoluciones acuosas con cloruro usando la técnica de barrido del electrodo vibrante (SVET). Se han visualizado *in situ* los flujos de corriente iónica en la fase del electrolito adyacente a las microceldas de corrosión, permitiéndose así seguir con resolución espacial su evolución en el tiempo. Se ha observado una respuesta heterogénea en las superficies de AA6060 debida a la presencia de inclusiones metálicas en este material. Se ha detectado, por tanto, una actividad anódica altamente localizada, interpretada en términos de acoplamiento galvánico entre la matriz y las partículas intermetálicas. Las inclusiones metálicas se comportan catódicamente mientras que la matriz de aluminio se encuentra bajo disolución anódica al activarse anódicamente las regiones próximas a estas inclusiones. La hidrólisis de los iones de aluminio deriva en la acidificación local del electrolito adyacente a los sitios anódicos, acompañado por generación de hidrógeno.

7.2.3. Introduction

The wide use of aluminium and its alloys in a variety of applications arises from the combination of high strength and low density [1], while exhibiting a good corrosion resistance due to the development of a protective oxide layer. However, aluminium alloys are susceptible to localized corrosion in a variety of environments, particularly when chloride ions are present [2-4]. Though pitting corrosion in aluminium-based materials is a complex process that is affected by diverse environmental factors, the composition and microstructure of the alloy surfaces have also been found to significantly influence it [5-7]. The development of micro-galvanic differences between the aluminium matrix and the alloying elements would then trigger the corrosion process, leading to localized distributions of corroding sites on the surface of the material [7]. Since most metallic inclusions are nobler than aluminium, they should behave as local cathodes and subsequently induce the anodic dissolution of the metal around them [8-12]. Yet other metals such as Cu, Mg and Zn are less noble than pure aluminium and behave anodically, whereas the aluminium matrix might remain inert while acting as the cathode in the galvanic reaction [1,13-15]. Localized corrosion would also occur in this case, though leading to the removal of active inclusions from the exposed surface of the metal.

Scanning microelectrochemical techniques are increasingly employed to investigate the reactions occurring in corroding systems with high spatial resolution as to gain new insights into the mechanism of the participating reactions [16,17]. Among them, the scanning vibrating electrode technique (SVET) senses potential gradients in the electrolyte phase adjacent to the corroding surface with a high sensitivity [18]. In this way, distributions of micro-anodes and micro-cathodes related to localized corrosion processes can be detected *in situ*. Furthermore, the non-destructive character of the technique allows monitoring the time evolution of the systems, independently from the corrosion reactions either undergoing increased dissolution or progressively ceasing as the result of inhibitor action and/or corrosion products precipitation. In this Section, the SVET has been employed to spatially-resolve local differences in electrochemical activity on aluminium alloy AA6060 related to the anodic dissolution of the matrix when exposed to chloride-containing aqueous solution.

7.2.4. Experimental

7.2.4.1. Samples and solutions

AA6060 sheets of 1 mm thickness were employed. Table 7.2.1 gives the composition of the alloy. The samples were mounted into an epoxy resin sleeve such that only a 3.2 mm diameter circular end surface was free, forming the test metal

substrates. The surface of the samples was abraded with SiC paper up to grit 4000. The resulting surfaces were degreased with acetone, abundantly rinsed with ultra-pure deionised water, and allowed to dry in air. They were mounted facing up in the electrochemical cell, and immersed in 0.05 M NaCl solution as test media. Solutions were prepared with analytical grade reagents and ultra-pure water purified with a Milli-Q system from Millipore.

Table 7.2.1. Composition of AA6060 aluminium alloy (wt.%).

Al	Cu	Mg	Si	Fe	Mn	Ti	Cr	Zn	Pb
Bal.	< 0.02	0.4 – 0.45	0.4 – 0.45	0.15 – 0.22	< 0.03	< 0.02	< 0.02	< 0.02	< 0.02

7.2.4.2. Electrodes and instrumentation

The set-up for microelectrochemical measurements was assembled as it follows. The epoxy-sleeved metal specimen (diameter of ca. 4 cm), once polished and cleaned, was taken as the base for the electrochemical cell by placing it horizontally with the polished surface facing upwards. Then the specimen was surrounded laterally by Sellotape, thus allowing a volume for the electrolyte to be filled in.

The scanning vibrating electrode instrumentation was manufactured by Applicable Electronics Inc. (Forestdale, MA, USA) and controlled by dedicated software (Science Wares, Falmouth, MA, USA). A Micro Probe PI200101F microelectrode, which consisted of Pt/Ir (80%/20%) wires insulated with paralene C® and arced at the tip to expose the metal, was employed. The microelectrode was platinized in order to produce a spherical platinum black deposit of 10-20 μm diameter. The measurements were made with the electrode tip vibrating in a plane perpendicular to the sample, at an amplitude of 20 μm and with frequencies in the order of 200-400 Hz. A reference measurement with the microelectrode away from the active area was subtracted from the values measured during the scan. The electrochemical cell was completed by using a Pt-black wire as reference electrode. All the experiments were carried out at the free corrosion potential. A video camera connected to an optical microscope was introduced in the system to follow the movement of the vibrating electrode over the sample during operation as well as to establish the mean distance between the microelectrode and the sample surface. Additionally, changes in the exposed surface as result of the degradation reactions could be monitored by taking photographs just before and after each scan.

7.2.5. Results and discussion

Testing of the samples with the SVET technique was carried out on the abraded surfaces immediately following their immersion in the test solution. The development of electrochemical activity on the surface could be monitored by recording the current densities flowing in the solution. In this study, 2D maps were recorded by shifting the vibrating probe at constant height over the sample while the probe was vibrating perpendicular to the substrate. An example of the local current density maps which arise from electrochemical activation of the alloy in 0.05 M NaCl solution is shown in Figure 7.2.1. Additionally, micrographs showing the state condition of the explored surface just before and after recording the corresponding SVET map are also given in Figure 7.2.1. The actual scanned area has been marked by drawing a blue parallelogram on the photographs.

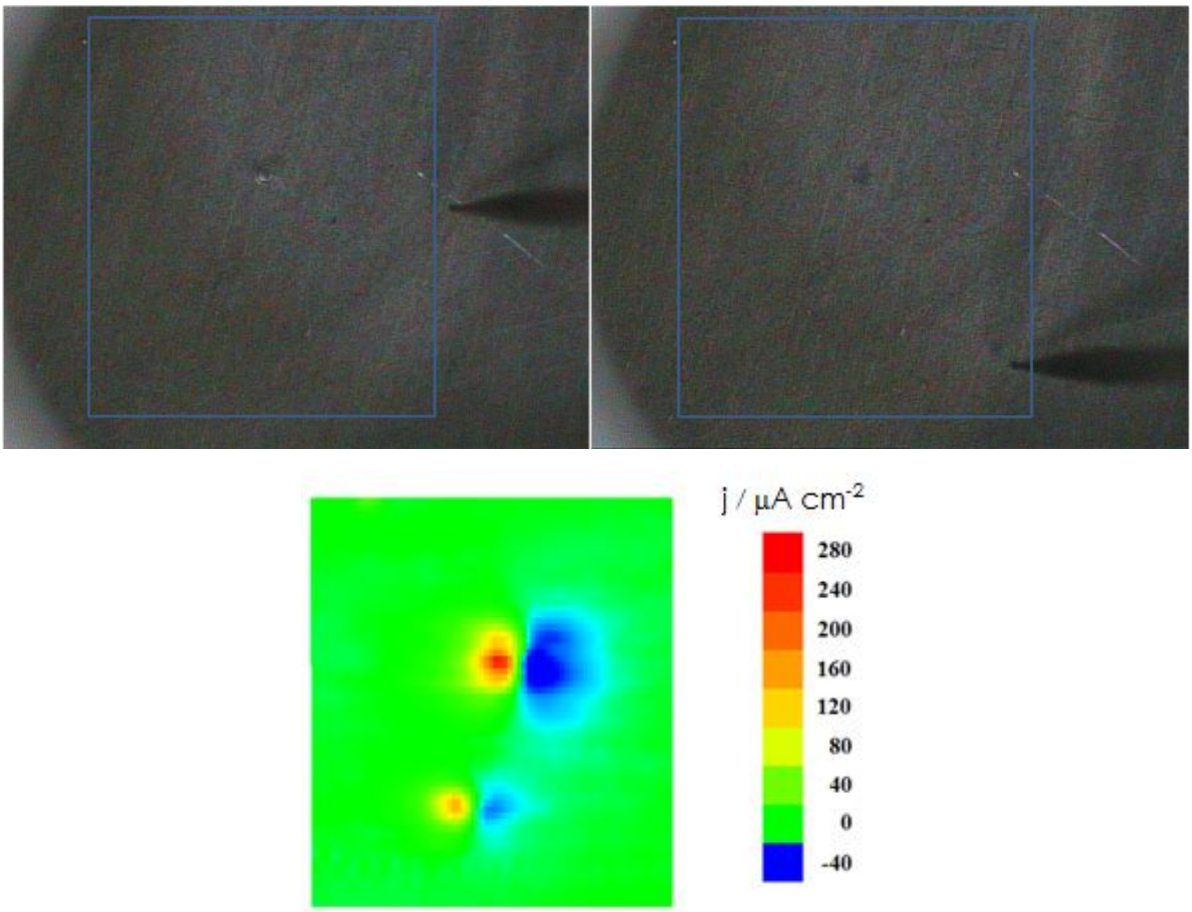

Figure 7.2.1. Micrographs and SVET image of AA6060 alloy immersed in 0.05 M NaCl aqueous solution for ca. 20 minutes. The micrographs were taken just before (left) and after (right) recording the SVET image. Values of *Z* axis: Ionic current, µA cm^{-2}. Mean probe-substrate distance: 50 µm. The images represent 2300 µm x 2600 µm in *X* and *Y* directions.

The activation of localized sites on the metal surface for metal dissolution appears as two local microanodes in the SVET image, whereas the cathodic activity is mainly concentrated in areas close to the anodic sites. It must also be noticed that the electrochemical activity at the anodes is quite different for the two sites monitored in this map. Ionic currents 2-3 times bigger occurred at the microanode found in the upper half of the image, which may be an indication of an independent development of electrochemical activity at each site with the elapse of time. The evolution of gas bubbles from the surface is also observed from inspection of the micrographs.

The time evolution of electrochemical activity on the surface was next monitored by recording a series of SVET maps at different elapsed times since immersion of the sample in the electrolyte. Smaller areas were scanned to reduce the time required for the acquisition of the maps. Figure 7.2.2 shows the SVET images and the micrographs of the scanned area obtained for the sample during 4 hours immersion in 0.05 M NaCl. Localization of reacting sites is observed at all times, though they are found to shift position on the surface, supporting that these sites are progressively activated and subsequently deactivated during the exposure to the aggressive environment. Inspection of the micrographs in Figure 7.2.2 allowed us to observe that corrosion products were deposited in those sites at which electrochemical activity occurred at earlier exposures.

Gas evolution was located at the anodic sites. Bubbles were often removed during the passage of the vibrating probe over the scanned substrate and thus they could not be usually observed in the micrographs taken just after recording the SVET images. Yet the active site remained producing gas evolution, and a new bubble might eventually become visible in the optical microscope as shown in Figure 7.2.3.

The observed features can be justified by considering the nucleation of corroding pits on the surface of the alloy, at which protons can be formed during the hydrolysis of metal ions released from the corroding anodic sites.

$$Al^{3+} + 2\ H_2O \rightarrow Al(OH)_2^{+} + 2\ H^{+} \qquad (7.2.1)$$

This reaction would also involve the formation of hydroxide species which may eventually lead to the precipitation of corrosion products. These compounds may either block the opening of the corroding pit or lead to the repassivation of the corroding site after some time.

The combination of a low pH around the anodic sites and a sufficiently negative mixed potential for the alloy immersed in the electrolyte are sufficient for hydrogen evolution reaction to occur from the anodic sites, similarly to the so-called "anomalous hydrogen evolution" effect described during the corrosion of magnesium and its alloys in aqueous environments [19]. Thus, only a fraction of the released protons can diffuse into the electrolyte, and it is detected by the SVET as a positive ionic current flowing from the pit. Outside the pit, the media is not acidic, so the reduction half reaction is still oxygen reduction. In the latter case, the formation of hydroxide ions is detected as a negative ionic current.

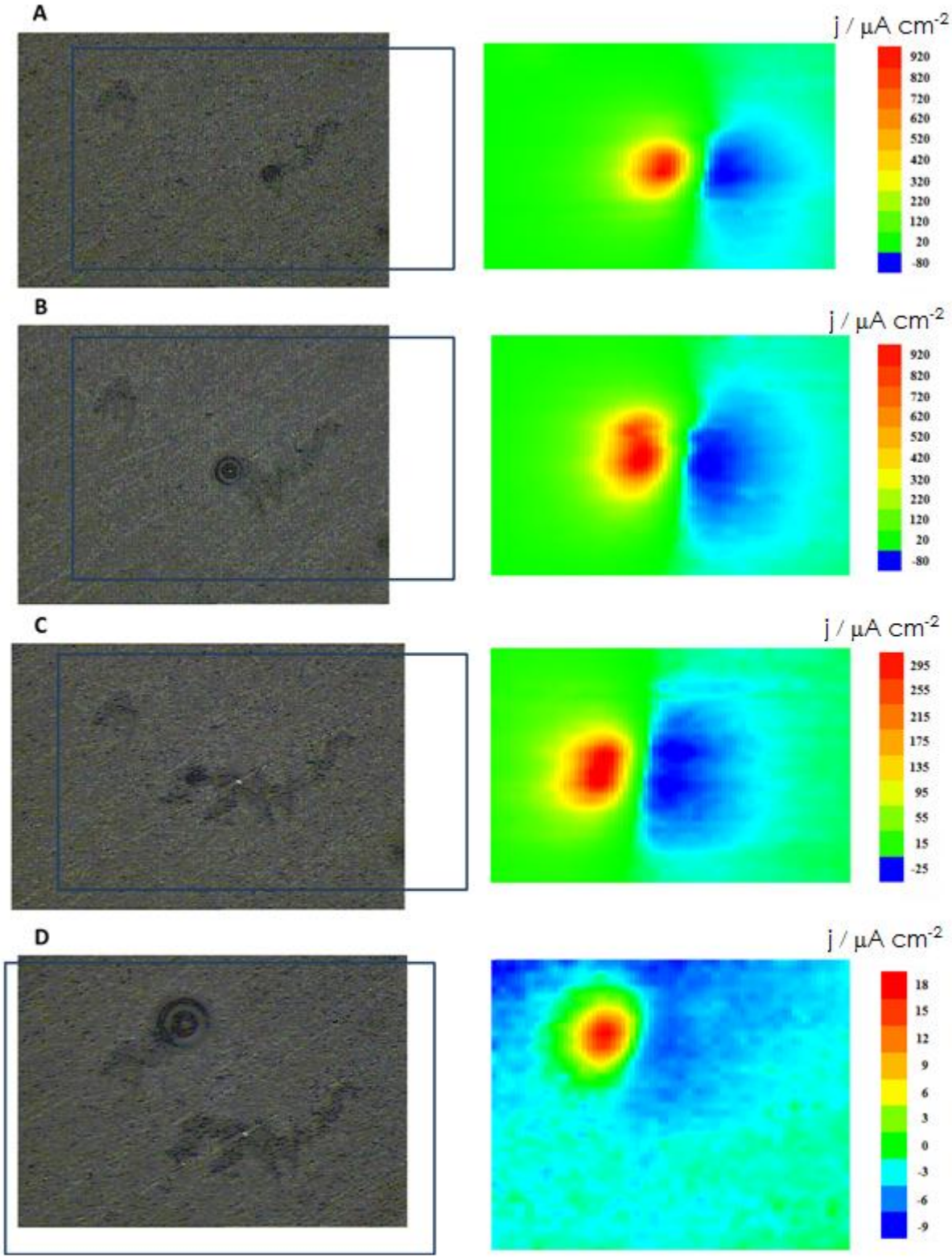

Figure 7.2.2. SVET images and micrographs of AA6060 alloy immersed in 0.05 M NaCl aqueous solution for: (A) 95, (B) 125, (C) 170, and (D) 270 minutes. Values of *Z* axis: Ionic current, µA cm^{-2}. Mean probe-substrate distance: 80 µm. The images represent 1500 µm x 1000 µm in *X* and *Y* directions.

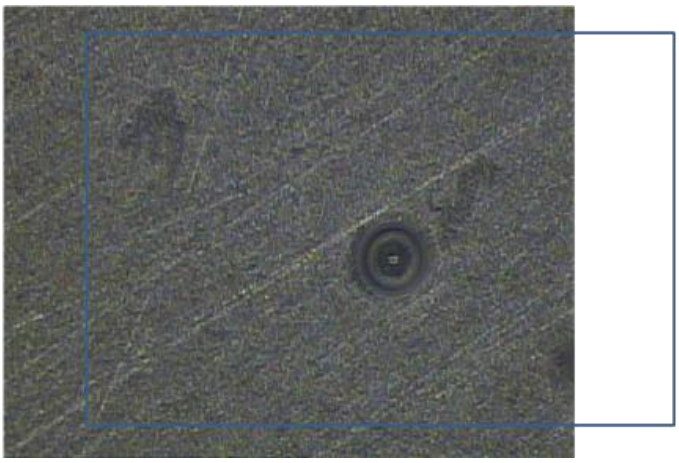

Figure 7.2.3. Micrograph of the AA6060 alloy immersed in 0.05 M NaCl aqueous solution taken after the SVET map in Figure 7.2.2A was recorded.

This passivation effect was further investigated by treating a sample in the following way. The sample was firstly immersed in 0.05 M NaCl for 24 hours. Upon removal from the solution, the complete surface of the alloy in the sample was covered by a black film layer considered to be formed by corrosion products. Subsequently, a portion of the surface was abraded to remove this precipitate layer, and it was then carefully cleaned with distilled water in order to not modify the remaining non-abraded surface of the alloy (see Figure 7.2.4 for a sketch of the substrate). The resulting substrate was introduced again in 0.05 M NaCl solution, and a series of SVET images were recorded by scanning the vibrating probe over both the abraded and the non-abraded portions of the surface. In this way, the time evolution of the substrate with two different surface finishes could be monitored *in situ*.

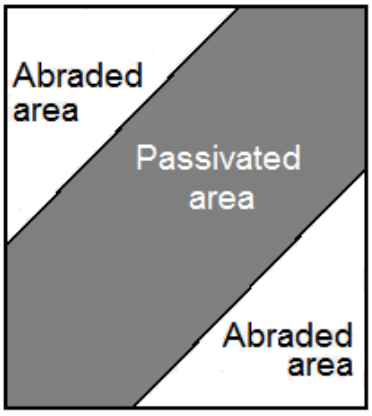

Figure 7.2.4. Sketch depicting sample preparation. The sample is corroded for 24 hours in 0.05 M NaCl. After retrieval, two portions of the surface are abraded with 4000 grit emery paper to remove the surface film from the metal sample, leaving an abraded area. The resulting sample is exposed again to 0.05 M NaCl. The surface scanned in order to record the SVET images covers both the abraded and the non-abraded portions of the sample.

SVET images were recorded over a period of 21 hours after immersion of the sample in the test electrolyte. Figure 7.2.5 shows selected SVET images and optical micrographs taken just before the maps were actually recorded. At all times, the active anodic sites were found in the abraded portion of the sample, thus confirming the passive state achieved by the surface alloy in the test electrolyte at long exposures. Therefore, a satisfactory explanation of the corrosion reaction of alloy AA6060 exposed to chloride-containing environments would involve the formation of corroding pits which may eventually be passivated through a precipitation mechanism, and the process is subsequently initiated at a different location. The formation of pits could also be confirmed from the inspection of retrieved samples under a microscope, as shown in Figure 7.2.6.

Oxidation of the aluminium matrix would imply the occurrence of metallic inclusions that behave cathodically as described in the sketch depicted in Figure 7.2.7. This behaviour can be expected for either Al(CuMnFe) or Al(MnSi) inclusions. In this case, the extent of the surrounding aluminium matrix undergoing oxidative dissolution processes has been proposed to be approximately 5 times greater than the cathodic sites (i.e., 200 – 250 μm) [19], and they could be monitored using SVET.

The microgalvanic mechanism also serves to describe the observed differences in time evolution of the corrosive process as monitored by SVET in terms of the microstructure and composition of the alloy. High strength aluminium alloys like AA6060 and AA2024 (Al-4.4Cu-1.5Mg-0.6Mn) are microstructurally complex materials presenting various individual phases that greatly influence the corrosion behaviour. Though nucleation of corrosion pits occur on AA6060 as well as on AA2024 aluminium alloys, despite their different composition and distribution of repassivation of the pits only occurs for the former, thus leading to the progressive displacement of anodic and cathodic sites over the surface with the elapse of time. Conversely, such repassivation process does not occur on the AA2024 alloy [20], and the dissolution process at the anodic sites continue progressing with time [20,21], probably due to self-corrosion of the aluminium matrix via hydrogen evolution, leading to significantly higher corrosion rates for this alloy.

7.2.6. Conclusion

The occurrence of localized electrochemical activation of complex systems such as aluminium alloys can be monitored using the scanning vibrating electrode technique (SVET) when the samples are immersed in an electrolytic corroding environment. The sizes of the anodic and cathodic sites observed here are much bigger than those typically corresponding to metallic inclusions in the alloy (namely, 20-50 μm), a feature that must be taken in account for mechanistic considerations.

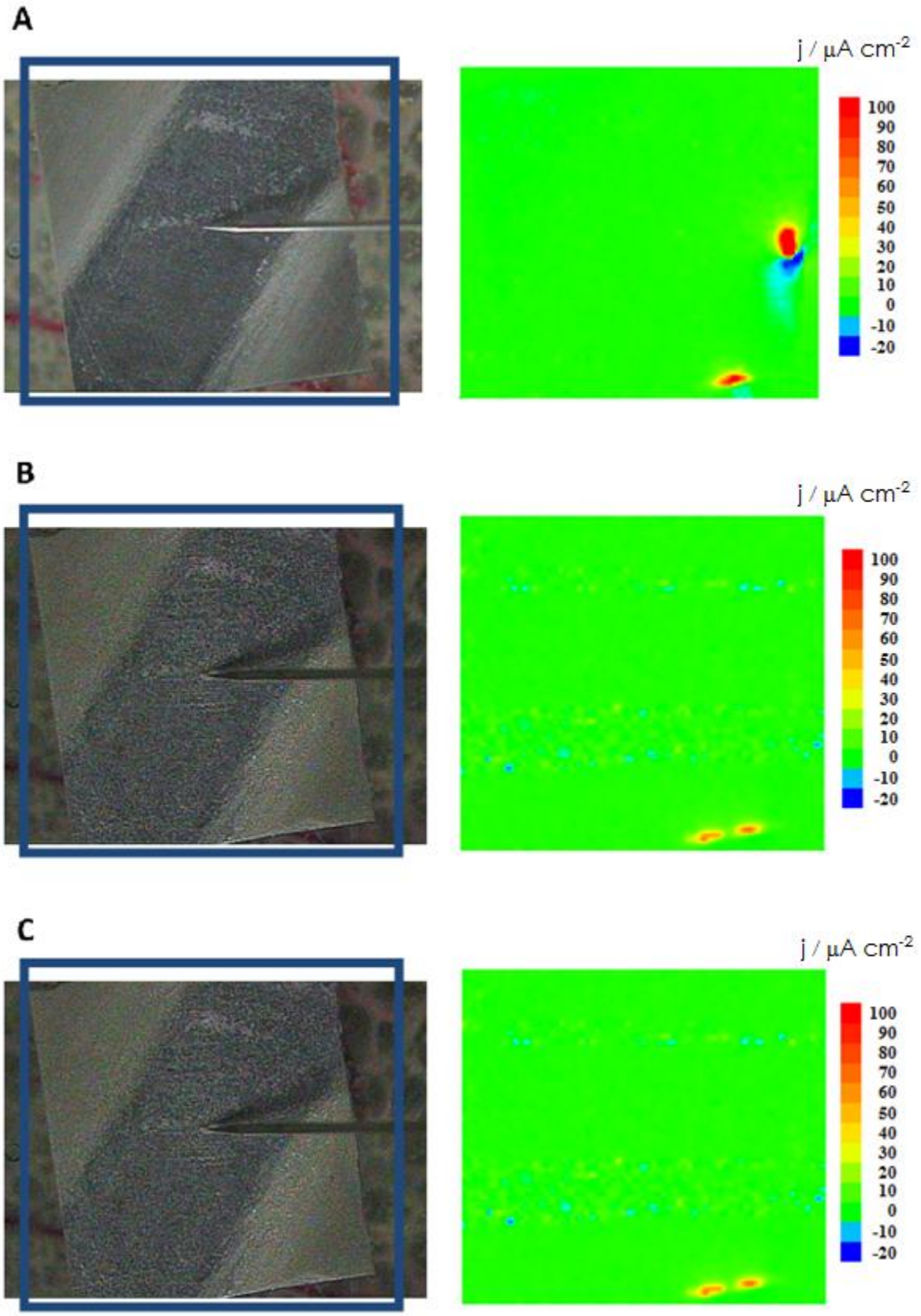

Figure 7.2.5. SVET images and micrographs on an abraded – passivated (24 hours treatment in 0.05 M NaCl) AA6060 alloy system (from bottom to top) during immersion in 0.05 M NaCl aqueous solution for: (A) 1, (B) 9, and (C) 21 hours. Mean probe-substrate distance: 40 µm. The images represent 1200 µm x 3400 µm in *X* and *Y* directions.

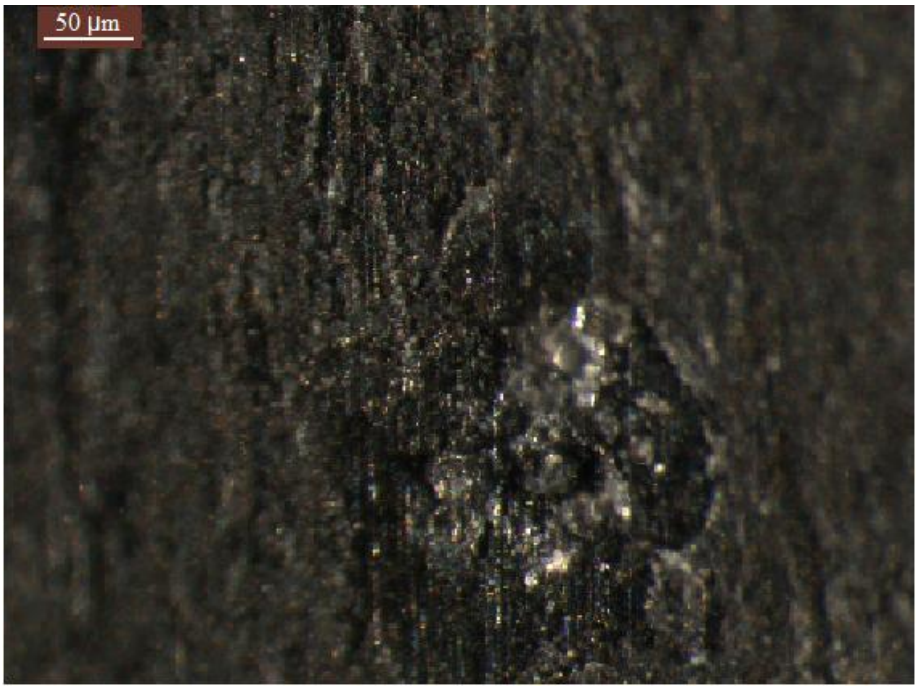

Figure 7.2.6. Optical micrograph of a retrieved AA6060 alloy sample after completing the tests presented in Figure 7.2.5.

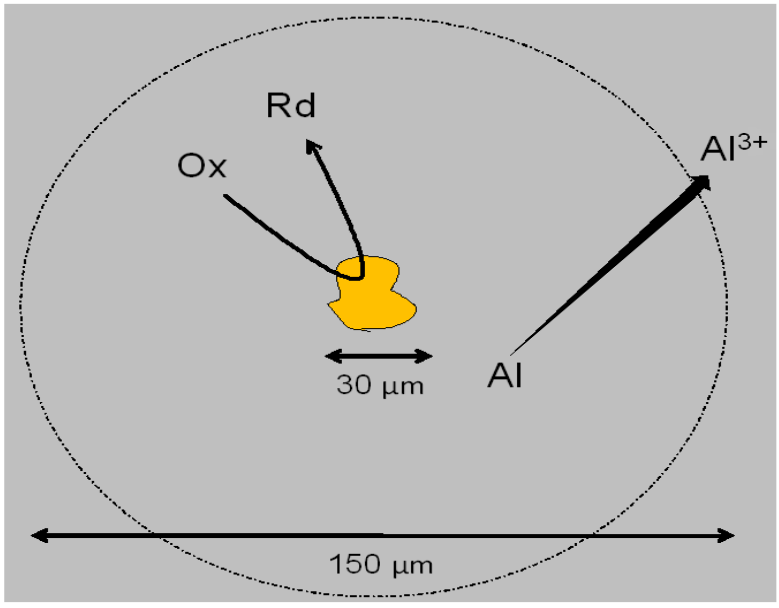

Figure 7.2.7. Sketch describing the corrosion process at aluminium alloys sustained by metallic inclusions with a cathodic behaviour.

Oxidation of the aluminium matrix would imply the occurrence of metallic inclusions that behave cathodically whereas the surrounding aluminium matrix undergoes oxidative dissolution processes. When protons are the chemical species reduced at the microcathodes, evolution of hydrogen gas occurs on the alloy surface.

7.2.7. References

1. F.M. Queiroz, M. Magnani, I. Costa, H.G. de Melo. Corrosion Science 50 (2008) 2646.
2. J.B. Bessone, D.R. Salinas, C.E. Mayer Ebert, W.J. Lorenz. Electrochimica Acta 37 (1992) 2283.
3. A.G. Muñoz, J.B. Bessone. Corrosion Science 41 (1999) 1447.
4. L.C. Abodi, J.A. DeRose, S. Van Damme, A. Demeter, T. Suter, J. Deconinck. Electrochimica Acta 63 (2012) 169.
5. A. Alavi, R. Cottis. Corrosion Science 27 (1987) 443.
6. K. Nisancioglu. Journal of the Electrochemical Society 137 (1990) 69.
7. M. Bethencourt, F.J. Botana, J.J. Calvino, M. Marcos, M.A. Rodriguez. Materials Science Forum 567 (1998) 289.
8. E.V. Koroleva, G.E. Thompson, G. Hollrigl, M. Bloeck. Corrosion Science 41 (1999) 1475.
9. Z. Szklarska-Smialowska. Corrosion Science 41 (1999) 1743.
10. P. Campestrini, E.P.M. van Vesting, H.W. van Rooijen, J.H.W. de Wit. Corrosion Science 42 (2000) 1853.
11. N. Birbilis, M.K. Cavanaugh, R.G. Bucheit. Corrosion Science 48 (2006) 4202.
12. R. Grilli, M.A. Baker, J.E. Castle, B. Dunn, J.F. Watts. Corrosion Science 52 (2010) 2855.
13. P. Campestrini, H.W. van Rooijen, E.P.M. van Westing, J.H.W. de Wit. Materials and Corrosion 51 (2000) 616.
14. J. Zhang, M. Klasky, B.C. Letellier. Journal of Nuclear Materials 384 (2009) 175.
15. A.E. Hughes, A. Boag, A.M. Glenn, D. McCulloch, T.H. Muster, C. Ryan, C. Luo, X. Zhou, G.E. Thompson. Corrosion Science 53 (2011) 27.
16 P. Marcus, F. Mansfeld (Editors). Analytical Methods in Corrosion Science and Engineering. CRC Press, Boca Raton, 2006.
17. M.B. Jensen, D.E. Tallman. In: Electroanalytical Chemistry: A Series of Advances, Vol. 24 (Edited by A.J. Bard, C.G. Zoski). CRC Press, Boca Raton, 2012, p. 171.
18. R.S. Lillard. In: Analytical Methods in Corrosion Science and Engineering (Edited by P. Marcus, F. Mansfeld). CRC Press, Boca Raton, 2006, p. 571.
19. G. Song. Advanced Engineering Materials 7 (2005) 563.
20. R.P. Wei, C.-M. Liao, M. Gao. Metallurgical Materials Transactions A 29 (1998) 1153.
21. R.M. Souto, J. Izquierdo, J.J. Santana, S. González. European Journal of Science and Theology 9 (2013) 71.
22. J. Izquierdo, S. González, R.M. Souto. International Journal of Electrochemical Science 7 (2012) 11377.

7.3

Sensing electrochemical activity in AA2024 coated with zirconia by means of the scanning vibrating electrode technique

7.3.1. Abstract

Application of scanning vibrating electrode technique (SVET) for corrosion studies of zirconia coatings formed by a sol-gel procedure on AA2024 aluminium alloy is presented. SVET was used to monitor the electrochemical processes both uncoated and zirconia-coated specimens immersed in 50 mM NaCl aqueous solution. The coated samples were also investigated after a scratch was operated through the zirconia layer down to the metal-substrate surface in order to simulate a defect across the coating. SVET imaging probes that the electrochemical behaviour of the system is different for a defect-free and a defective coating. Surface reactivity, without self-healing ability, occurred for the defective zirconia layer, closely resembling the behaviour of the uncoated substrate in the environment.

7.3.2. Resumen

En esta sección se ha empleado la técnica de barrido del electrodo vibrante (SVET) para estudios de corrosión en recubrimientos de óxido de circonio formados por procedimiento sol-gel en aleaciones de aluminio AA2024. Se ha empleado el SVET para seguir los procesos electroquímicos tanto en las muestras cubiertas de óxido de circonio como no cubiertas, inmersas en disolución acuosa de NaCl 50 mM. Las muestras recubiertas fueron también investigadas tras aplicar un rayado a través de la capa de óxido de circonio hasta descubrir la superficie del substrato metálico, con el fin de simular un defecto a lo largo del recubrimiento. La visualización por SVET prueba que el comportamiento electroquímico del sistema difiere para un recubrimiento con y sin defecto. La reactividad de la superficie tiene lugar en la zona defectuosa del recubrimiento, que no presenta capacidad de auto-curado, asemejándose su comportamiento al del substrato sin recubrir en el mismo medio.

7.3.3. Introduction

Organic coatings are applied to aluminium for corrosion protection. Actually, the main measure for achieving efficient corrosion control for application of aluminium alloys in the automotive, aerospace, construction and appliances industries is the application of organic coatings. The main function of organic coatings is to act as a barrier against access of water and ions to the interface and to inhibit electrochemical reactions at the interface. No coating is totally impermeable against water and ions and hence sooner or later some corrosive activity will occur at tiny interfacial defects which are always present and especially at larger defects with the coatings that are inflicted by the environment (scratches, stone impact…). Inhibitors can then extend the lifetime of the coated material by inhibiting the corrosion in these defects, at least as long as a steady supply of fresh inhibitors is provided by pigments added to the coating. The release of the inhibitors, however, does not occur in a controlled way. Instead, the inhibitors are continuously leached out of the coating. If corrosion in a defect occurs, they are then available for suppressing it. If there is no corrosion, they are fully released into the environment, continuously. Most of the current inhibitors are in discussion to be environmentally detrimental. The by far best corrosion inhibitor known up to now is chromate. However, it is harmful for the environment and toxic and hence its use is severely restricted and soon will be fully prohibited [1-4]. Since most other available inhibitors, which are not nearly as efficient as chromate, are under discussion to be problematic, new concepts are needed.

Coatings obtained with sol-gel technique might replace chromate conversion coatings proven that these sol-gel coatings can provide good adhesion and barrier properties. The sol-gel technique is widely used for the production of ceramic materials starting from metal-organic precursors or soluble metal salts. This technique is employed for deposition of mixed metal oxides and metal oxide-organic composites [5–7]. Oxide layers deposited by dip-coating and spin-coating from sol-gel systems improve the corrosion resistance of aluminium alloys [8,9]. Beccaria et al. [10,11] showed that silane treatment improves the resistance of aluminium to general and localized corrosion. Yang et al. [12] reported that mixed SiO_2 and ZrO_2 oxide layers deposited on AA2024 with sol-gel technique improve the resistance to localized attack in diluted Harrison solution. Besides, the sol-gel technique presents the possibility of introducing inhibitors in the oxide layer. Zheludkevich and co-workers [13] recently showed that the addition of ZrO_2 nanoparticles in sol-gel coatings could improve the corrosion resistance of AA2024. Fedrizzi et al. [14] deposited zirconia amorphous films on AA1050 with dip-coating technique. They showed that control of hydrolysis leads to the formation of pre-treatments, which promote adhesion of organic coatings [14]. Besides, the electrochemical behaviour of AA1050 coated with amorphous zirconia films is strongly dependent on the deposition parameters. Similar results were found for zirconia-coated AA6060 [15].

Herein the electrochemical performance of a ZrO_2 sol-gel coating for the corrosion protection of AA2024 is reported and characterized from experiments employing the scanning vibrating electrode technique. Specifically, SVET images of heterogeneous distribution of chemical reactivity occurring inside scratches operated through the zirconia coating where the metal substrate is exposed to the electrolytic environment are reported. For the sake of characterization, the behaviour of uncoated AA2024 substrates immersed in the same test electrolyte was recorded.

7.3.4. Experimental

7.3.4.1. Material and sample preparation

The substrate for the deposition of ZrO_2 films was AA20240 aluminium alloy. The alloy composition is given in Table 7.3.1. The surface preparation of the substrate consisted in degreasing in acetone for all samples. The samples underwent degreasing and pickling using commercial products from Chemetall (Gardoclean 515, Gardoclean 620 HP and Gardacid 65) before deposition of ZrO_2 on the sample surface. The deposition of the ZrO_2 layer was performed using dipping sol-gel technique. The starting solution was 0.1M $Zr(OBu\textit{n})_4$ in anhydrous *n*-butanol with addition of acetic acid as complexing agent where [AcH]/[Zr] = 0.6. The deposition of the film was performed by dipping the samples in the sol-gel solution. The samples were withdrawn with controlled rate of 1 mm s^{-1}. The dipping step was repeated one, two or three times in order to deposit overlapping zirconia layers on the samples. After each dip in the sol-gel solution, the samples were subjected to thermal treatment. The thermal treatment was performed at 150 °C for 1 h and at 250 °C for 4 min. This step was followed by drying at room temperature.

Table 7.3.1. Composition of AA2024 aluminium alloy (wt.%).

Cu	Mg	Si	Fe	Mn	Zr	Ti	Cr	Al
3.8-4.9	1.2-1.8	< 0.5	< 0.5	0.3-0.9	< 0.25	< 0.15	< 0.10	balance

In selected samples, a scratch of approximately 1 cm length and 1 mm width was produced in the ceramic coating to the metal substrate with a scalpel. A photograph of the resulting surface performed with an optical microscope is shown in Figure 7.3.1. The direct exposure of the underlying metal inside the scratch is observed through its characteristic metallic brilliance, a clear indication that the polymeric film has been completely removed inside the artificial defect operated through the zirconia coating.

Figure 7.3.1. Optical micrograph image of a scratched zirconia-coated AA2024 sample prior to immersion in the test electrolyte. The figure also shows the SVET probe placed above the electrochemical cell containing the investigated specimen at its bottom facing upwards.

Uncoated samples were mounted into an epoxy resin sleeve such that only a 3.2 mm diameter circular end surface was free, forming the test metal substrates. The surface of the samples was abraded with SiC paper up to grit 4000. The resulting surfaces were degreased with acetone, abundantly rinsed with ultra-pure deionised water and allowed to dry in air.

Samples were mounted facing up in the electrochemical cell, and immersed in 0.05 M NaCl solution as test media. Solutions were prepared with analytical grade reagents and ultra-pure water purified with a Milli-Q system from Millipore.

7.3.4.2. SVET measurement and data analysis

The scanning vibrating electrode instrumentation used was manufactured by Applicable Electronics Inc. (Forestdale, MA, USA) and controlled by dedicated software. The probe microelectrode consisted of Pt/Ir (80%/20%) wires insulated with paralene C® and arced at the tip to expose the metal, and they were platinized in order to produce a spherical platinum black deposit of 10-20 μm diameter. A video camera connected to an optical microscope was introduced in the system both to establish the probe-sample distance, and to follow the movement of the vibrating electrode over the sample during operation. The measurements were made with the electrode tip vibrating in a plane perpendicular to the sample at an amplitude of 20 μm and with frequencies in the order of 200-400 Hz. Operation at constant height was chosen, and the mean distance between the microelectrode and the sample surface was 50 μm.

7.3.5. Results and discussion

7.3.5.1. Detection of localized chemical heterogeneities at AA2024

For the SVET measurements, bare aluminium alloy was introduced in the Teflon cell and exposed to 50 mM NaCl as test environment. This technique is more sensitive at relatively low ionic strength solutions, as it is able to detect differences in potential due to the presence of extra amounts of ionic charges in the vicinity of the surface, and the lower the concentration, the higher the relative proportion of the extra ions is. On the other side, one needs to establish a compromise situation as sufficiently aggressive media is required to promote corrosion and thus to monitor results.

In situ SVET acquisitions in the electrolyte are displayed in Figure 7.3.2. The variations in the current density values are comparable to those encountered in the literature for the same media though measured at bigger distances from the substrate [16,17]. The smaller probe-substrate distance taken in this Section, in combination with the reduction of the amplitude vibration, allows us to better distinguish the reacting sites. It can be noticed that, while most of the metal surface is behaving slightly cathodic, some areas are activated anodically during the exposure to chloride anions, and they remain under attack for several hours. In fact, the location on the surface with the coordinates (X = 1120 µm, Y = 900 µm) appears anodically-activated in Figure 7.3.2B, recorded after 5 hours immersion of the sample in the electrolyte, and remains active in Figure 7.3.2C taken 4 hours later. The photographs taken just before each scan show the accumulation of corrosion products at that position.

The dimensions of the developed pits are in the order of 100 µm diameter, which is consistent with the SVET results found in the previous papers cited before. However, it was expected to detect the effect of the Al(CuMnFe) particles, which behave cathodic with respect to the matrix, yet what can be visualized consists on local anodic sites, that cover greater areas than those expected for any of the possible intermetallics. This feature can be justified in terms of two different options:

- Anodic dissolution occurs in the matrix via pitting corrosion, promoted by the galvanic connection with the noblest particles. The cathodic half-reaction on them is not easily detected since their size is too small to be spatially resolved by SVET. In that case, the dissolution of anodic intermetallics and its eventual removal from the surface may be acting as the initial stage of pit formation, leading to the exposure of a weaker area to the electrolyte.

- Cu-rich particles, either Al(CuMnFe) intermetallics or the s-phase of the base metal once lost its Mg content, mainly promote the dissolution of the surrounding material, resulting in the degradation of the matrix around them reaching active diameters up to 5 times greater than that of the original particle [17-24]. Conversely, SVET would detect the anodic current on their proximity, but probably it will not be able to resolve the anionic current emerging locally from the inclusion in the center of the active location.

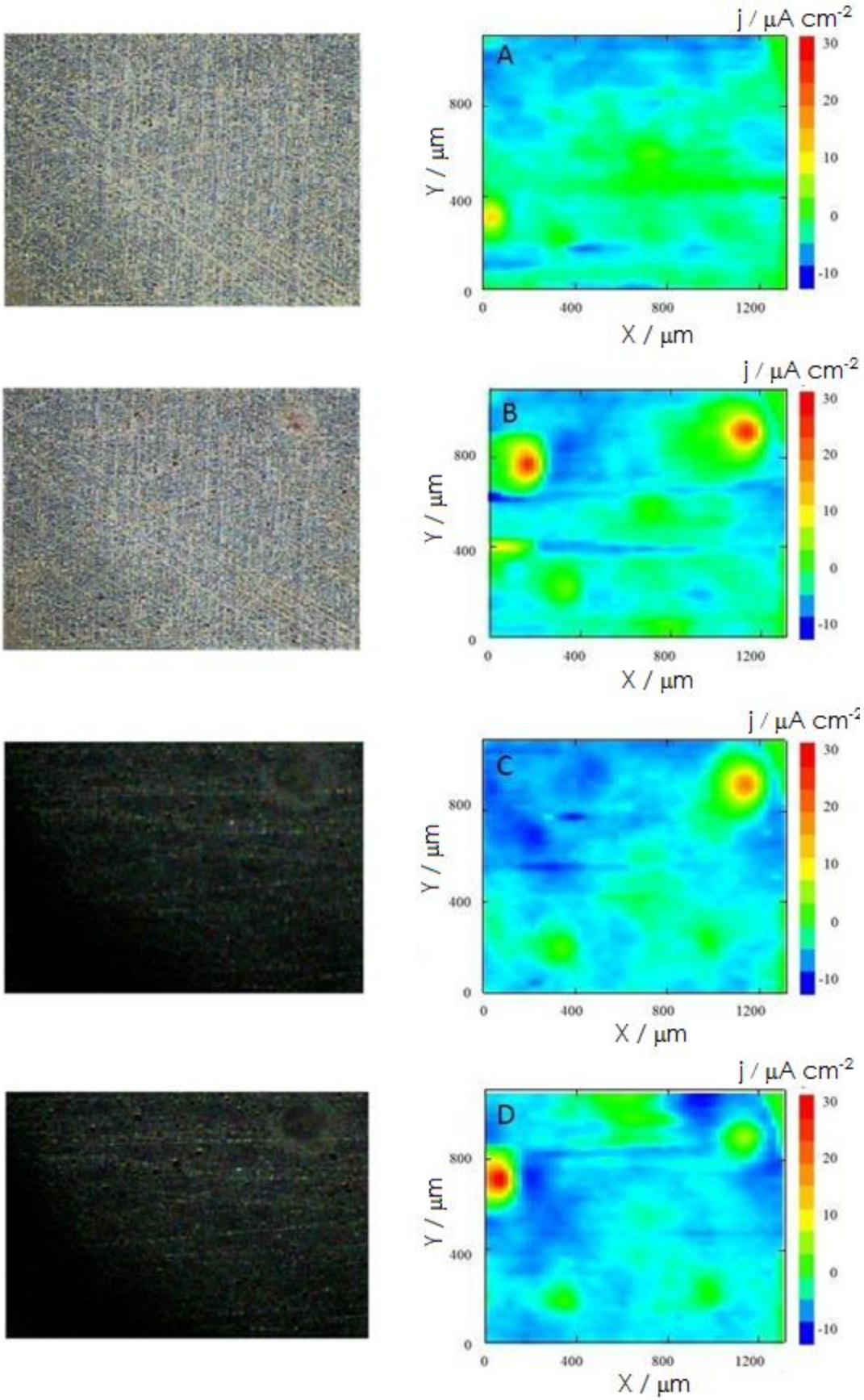

Figure 7.3.2. SVET images and micrographs of AA2024 alloy immersed in 50 mM NaCl aqueous solution for: (A) 4, (B) 5, (C) 9, and (D) 11 hours. Values of *Z* axis: Ionic current, µA cm^{-2}. Tip-substrate distance: 50 µm. The images represent 1000 µm x 1300 µm in *X* and *Y* directions.

The SVET results may well adjust to both explanations, though further discussion concerning degradation in the proximity of some active sites and subsequent topographic changes during deactivation of the surface will be offered in base of the AC-SECM that will be presented in Section 7.4, that seem better described by the second option. However, the media employed for the SVET measurements is more aggressive that the one employed in the forecoming Section, so the results described here may correspond to a later stage in the degradation of the material which corresponds to pit formation in the alloy. In fact, according to the literature, the corrosion process will lead to pit formation and intergranular corrosion [16,27,28].

7.3.5.2. Detection of localized chemical heterogeneities at ZrO_2-coated AA2024

The SVET images together with micrographs of the zirconia coated surface of AA2024 for various immersion times in 50 mM NaCl solution are shown in Figure 7.3.3. No electrochemical activity was detected by SVET when the coated samples were immersed in 50 mM NaCl aqueous solution for exposures up to 15 hours. It is found that aluminium alloys can be effectively protected from corrosion by coating the material with a zirconia layer.

7.3.5.3. Detection of localized chemical heterogeneities at scratched ZrO_2-coated AA2024

A new series of experiments was performed on a sample that was scratched until the underlying AA2024 alloy was exposed to the environment inside the defect (cf. Figure 7.3.4A). At the beginning of the experiment, only a very small electrochemical activity could be detected inside the scratch when recording the SVET image with high sensitivity.

With the elapse of time, onset of corrosion inside the defect is observed through the progressive development of two greatly localized anodic sites, whereas the remaining uncoated metal serves as the cathode for the consumption of the electrons liberated by the corroding metal (see Figures 7.3.4B and 7.3.4C). SVET has allowed the detection of distributed corrosion microcells inside the defect through the zirconia coating with great spatial resolution. That is, once the zirconia coating is perforated as to not longer effectively separate the underlying aluminium alloy from the environment, the corrosion mechanism operating in the uncoated material is also operating inside the defect. Therefore, an effective protection method for aluminium based on the use of zirconia as physical barrier film must also include self-healing mechanisms capable of repairing the perforated film, possibly through the controlled release of corrosion inhibitor compounds.

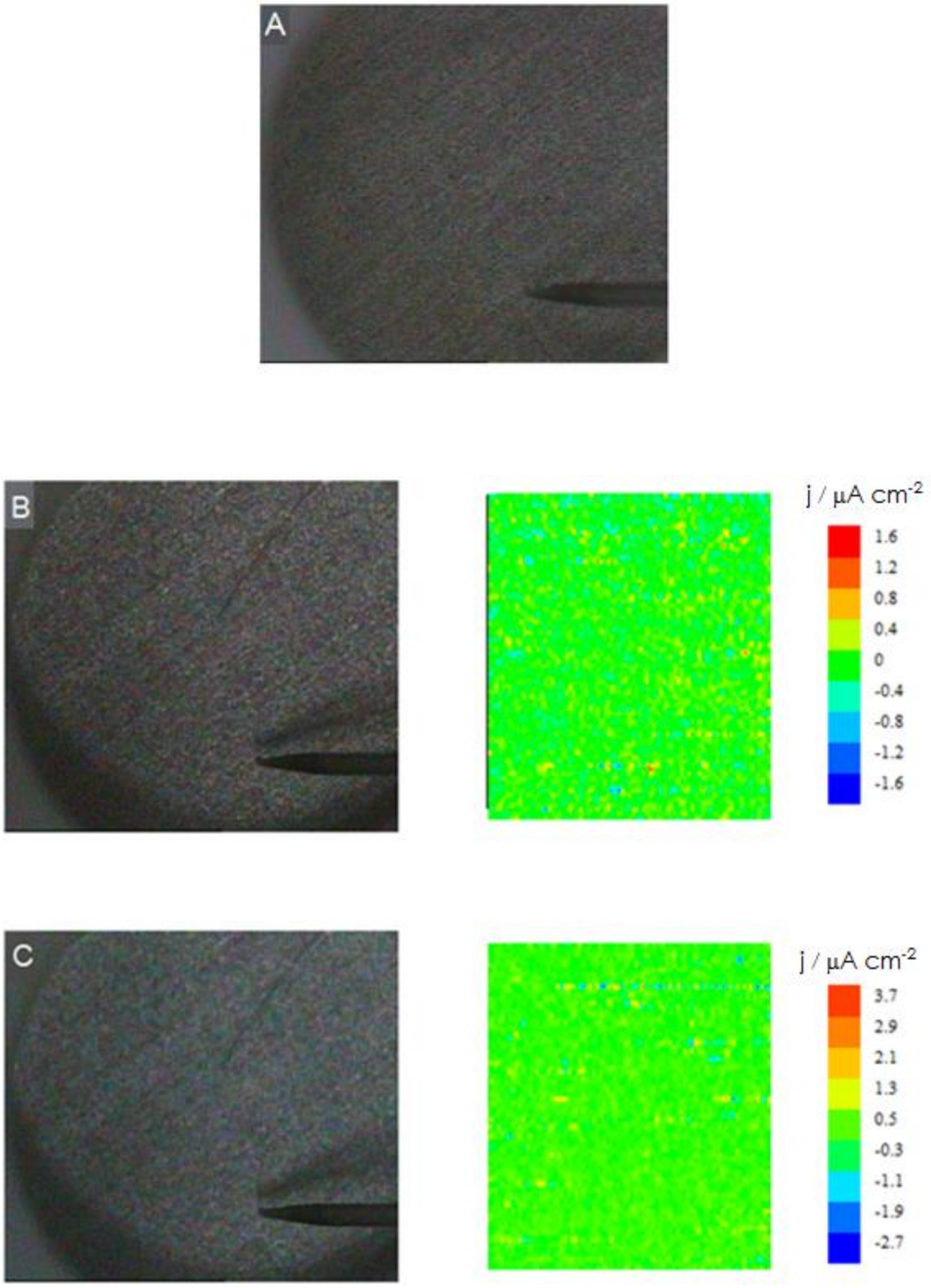

Figure 7.3.3. SVET images and micrographs of zirconia-coated AA2024 alloy immersed in 50 mM NaCl aqueous solution for: (A) 0, (B) 2, and (D) 15 hours. Values of *Z* axis: Ionic current, µA cm^{-2}. Tip-substrate distance: 50 µm. The images represent 1000 µm x 1300 µm in *X* and *Y* directions.

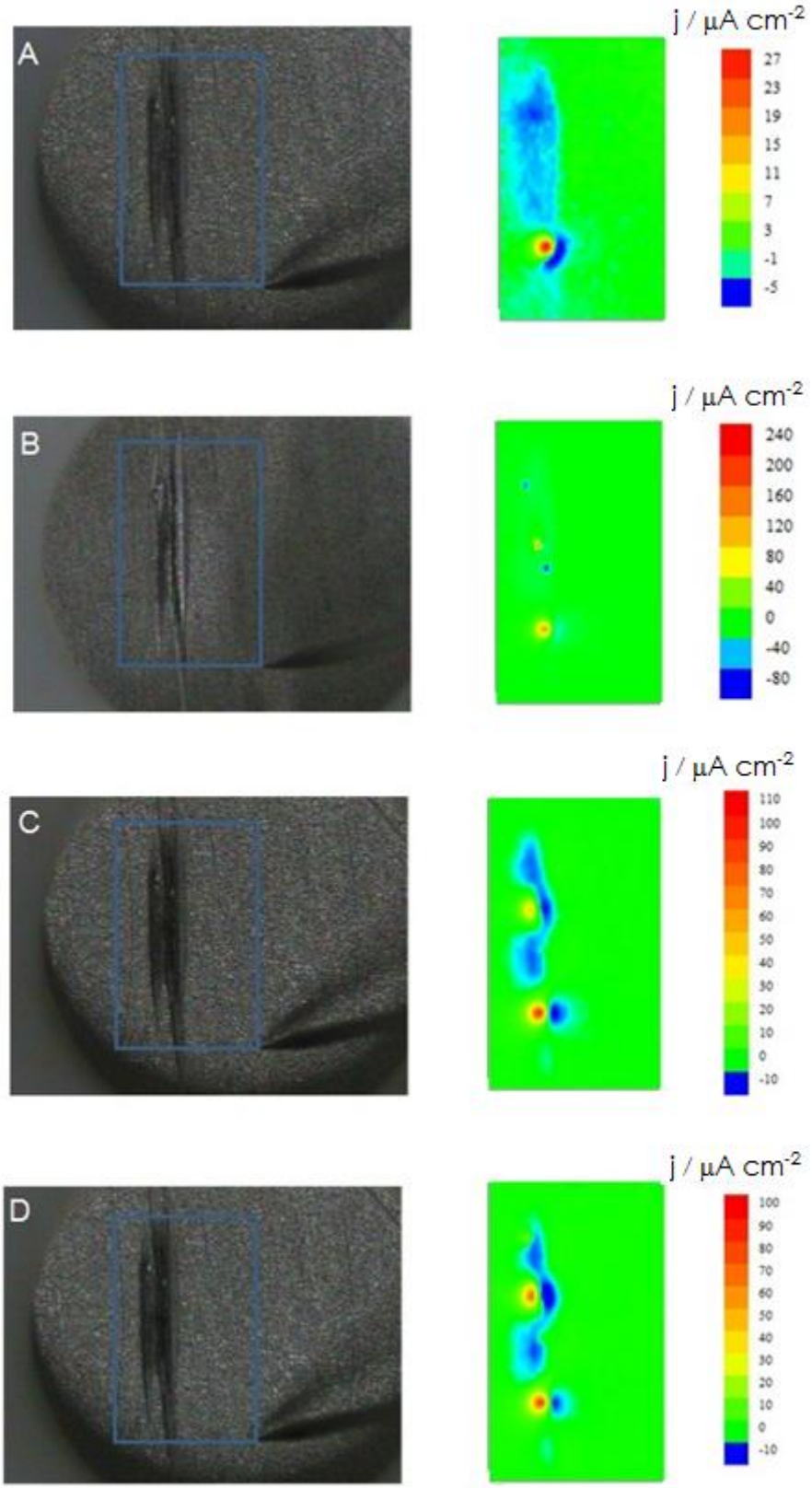

Figure 7.3.4. SVET images and micrographs of AA2024 alloy immersed in 50 mM NaCl aqueous solution for: (A) 4, (B) 5, (C) 9, and (D) 11 hours. Values of *Z* axis: Ionic current, µA cm^{-2}. Tip-substrate distance: 50 µm. The images represent 1000 µm x 1300 µm in *X* and *Y* directions.

7.3.6. Conclusions

The scanning vibrating electrode technique has been employed for the detection of ionic fluxes departing from the investigated samples originating from the development of localized redox process responsible for the corrosion of AA2024. The experimental procedure has been extended to the investigation of the efficiency of a ZrO_2 to produce a barrier layer on the alloy, and the evolution of the system after the onset of localized corrosion processes. High anticorrosion protection is provided by an intact zirconia coating. However, no self-healing ability is observed for defective ZrO_2 films applied on AA2024.

Due to the poor capacity of AA2024 for repassivation compared to other aluminium alloys such as AA6060, the zirconia coatings cannot be regarded an efficient corrosion protection procedure for this aluminium alloy unless self-healing repairing mechanisms of the perforated layer could be introduced by adding inhibitors into the zirconia layer, or by producing multilayer hybrid organic-inorganic coatings.

7.3.7. References

1. Gefahrstoffverordnung – GefStoffV vom 23. Dezember 2004; basiert auf der EUStoffrichtlinie RL 67/548/EWG, Anhang I, "Gefahrstoffliste" und EU-GHS-VerordnungVO (EG) Nr. 1272/2008 Anhang III.
2. AltfahrzeugV - Altfahrzeug-Verordnung - Verordnung über die Überlassung,Rücknahme und umweltverträgliche Entsorgung von Altfahrzeugen vom 21. Juni **2002**(BGBl. I S. 2214), zuletzt durch Verordnung vom 3. April 2009 (BGBl. I S. 738) geändert.
3. Richtlinie 2002/95/EG vom 27. Januar **2003** des Europäischen Parlaments und des Rates zur Beschränkung der Verwendung bestimmter gefährlicher Stoffe in Elektro- und Elektronikgeräten "Restriction of Hazardous Substances (ROHS)" (ABl. L Nr. 37 vom13.02.2003 S. 19); latest entry: 11. Juni 2009 (ABl. Nr. 148 vom: 11.06.2009 S.27).
4. Toxicological Profile for Chromium, http://www.atsdr.cdc.gov/toxprofiles/tp7.html (latest entry: 10.10.**2009**).
5. J.H. Osborn. Progress in Organic Coatings 41 (2001) 280.
6. M. Guglielmi. Journal of Sol-Gel Science and Technology 8 (1997) 443.
7. R.L. Ballard, J.P. Williams, J.M. Njus, B.R. Kiland, M.D. Soucek. European Polymer Journal 37 (2001) 381.
8. T.L. Metroke, R.L. Parkhill, E.T. Knobbe. Progress in Organic Coatings 41 (2001) 233.
9. N.N. Voevodin, N.T. Grebasch, W.S. Soto, F.E. Arnold, M.S. Donley. Surface and Coatings Technology 140 (2001) 24.

10. A.M. Beccaria, G. Padeletti, G. Montesperelli, L. Chiaruttini. Surface and Coatings Technology 111 (1999) 240.
11. A.M. Beccaria, L. Chiaruttini. Corrosion Science 41 (1999) 885.
12. X.F. Yang, D.E. Tallman, V.J. Gelling, G.P. Bierwagen, L.S. Kasten, J. Berg. Surface and Coatings Technology 140 (2001) 44.
13. M.L. Zheludkevich, R. Serra, M.F. Montemor, I.M. Miranda Salvado, M.G.S. Ferreira. Electrochimica Acta 51 (2005) 208.
14. L. Fedrizzi, R. Di Maggio, S. Rossi, L. Leonardelli. Benelux Metallurgie 43 (2003) 15.
15. F. Andreatta, P. Aldighieri, L. Paussa, R. Di Maggio, S. Rossi, L. Fedrizzi. Electrochimica Acta 52 (2007) 7545.
16. K.A. Yasakau, M.L. Zheludkevich, O.V. Karavai, M.G.S. Ferreira. Progress in Organic Coatings 63 (2008) 352.
17. S.M. Tamborim, S.L.P. Dias, S.N. Silva, L.F.P. Dick, D.S. Azambuja. Corrosion Science 53 (2011) 1571.
18. R.G. Buchheit, R.P. Grant, P.F. Hiava, B. Mckenzie, G.I. Zende. Journal of the Electrochemical Society 144 (1997) 2621.
19. R.P. Wei, C.-M. Liao, M. Gao. Metallurgical and Materials Transactions A 29 (1998) 1153.
20. P. Campestrini, H.W. van Rooijen, E.P.M. van Westing, J.H.W. de Wit. Materials and Corrosion 51 (2000) 616.
21. T. Suter, R.C. Alkire. Journal of the Electrochemical Society 148 (2001) B36.
22. K.A. Yasakau, M.L. Zheludkevich, S.V. Lamaka, M.G.S. Ferreira. Journal of Physical Chemistry B 110 (2006) 5515.
23. F.M. Queiroz, M. Magnani, I. Costa, H.G. de Melo. Corrosion Science 50 (2008) 2646.
24. A. Boag, A.E. Hughes, A.M. Glenn, T.H. Muster, D. McCulloch. Corrosion Science 53 (2011) 17.
25. A.E. Hughes, A. Boag, A.M. Glenn, D. McCulloch, T.H. Muster, C. Ryan, C. Luo, X. Zhou, G.E. Thompson. Corrosion Science 53 (2011) 27.
26. J. Izquierdo, S. González, R.M. Souto. International Journal of Electrochemical Science 7 (2012) 11377.
27. C.H. Paik, H.S. White, R.C. Alkire. Journal of the Electrochemical Society147 (2000) 4120.
28. F. Andreatta, H. Terryn, J.H.W. de Wit. Electrochimica Acta 49 (2004) 2851.

7.4

Application of AC-SECM in Corrosion Science: local visualization of heterogeneous chemical activity in AA2024 surfaces

7.4.1. Abstract

Aluminium alloy AA2024-T3 surfaces have been characterised by using a new microelectrochemical technique, frequency-dependent alternating current scanning electrochemical microscopy (AC-SECM), which does not require the addition of any redox active species to the electrolyte solution. Information regarding the topography and/or redox activity of the solid/liquid interface is obtained *in situ*, allowing their evolution with time to be monitored with high spatial resolution. By scanning the microelectrode over the surface, an image is generated, as well as information concerning reactions that take place in the solution space between the tip and the sample or on the surface of the scanned sample. A heterogeneous response due to the presence of intermetallic inclusions precipitated in the material is found on AA2024-T3 surfaces. The highly localized anodic activity was thus detected, which has been interpreted as a result of the galvanic coupling between the matrix and the intermetallic particles.

7.4.2. Resumen

En esta sección se ha caracterizado la superficie de una aleación de aluminio AA2024-T3 usando una nueva técnica microelectroquímica, la microscopía electroquímica de barrido en modo de corriente alterna con dependencia de la frecuencia (AC-SECM), la cual no requiere de la adición de especie redox alguna en la disolución electrolítica. Se ha obtenido información acerca de la topografía y/o actividad redox *in situ* en la interfase sólido/líquido, permitiendo el seguimiento de su evolución con el tiempo con alta resolución espacial. Mediante el barrido del microelectrodo sobre la superficie, se han obtenido imágenes con información sobre las reacciones que tienen lugar en la disolución que queda en el espacio entre la punta y la superficie de la muestra estudiada. Se ha encontrado una respuesta heterogénea debida a la presencia de inclusiones intermetálicas que han precipitado en la superficie de la aleación AA2024-T3. Se ha detectado, por tanto, una actividad anódica altamente localizada, la cual puede interpretarse como el resultado del acoplamiento galvánico entre la matriz y las partículas intermetálicas.

7.4.3. Introduction

Despite its considerably low standard reduction potential, aluminium is relatively resistant towards corrosion thanks to the passive layer formed on its surface [1-7]. In order to improve the mechanical properties of the metal for industrial applications, it becomes necessary to alloy it with other metals. In this way, alloy series AA2xxx and AA7xxx have found extensive use in several engineering and scientific applications, especially in the aerospace industries, because they exhibit high strength-to-weight ratios [7,8]. Improvement of the mechanical properties is achieved through the precipitation of metallic inclusions during optimized thermal treatments for each specific material. However, these particles, with different composition than the matrix, may promote galvanic coupling and subsequent highly localized corrosion [8-13], which is a major problem affecting other technological materials such as steels containing MnS precipitates [14-16].

During the corrosion process, local microcells are developed on the metal exposed to an aggressive electrolyte. These microanodes and microcathodes are distributed over the metallic surface due to different asymmetries existing in the material. At the anodic sites, evolution of metal cations and degradation of the material takes place by oxidation (7.4.1). This dissolution, when the substrate is an alloy, is more likely to be selective, with the most active elements being oxidized first. Electrons produced in this half-reaction flow to the cathodic sites, participating in the reduction of the oxidant, a role that, depending on the media, may be assumed by oxygen in aerated electrolytes at neutral and alkaline pH (7.4.2), or by protons at lower pH and/or poorly oxygenated solutions (7.4.3) [17]:

$$M \rightarrow M^{n+} + n\,e^- \qquad (7.4.1)$$

$$O_2 + H_2O + 4\,e^- \rightarrow 4\,OH^- \qquad (7.4.2)$$

$$2\,H^+ + 2\,e^- \rightarrow \uparrow H_2 \qquad (7.4.3)$$

In particular, the AA2024 alloy presents two main types of precipitates that compromise its corrosive susceptibility: Mg-rich particles or s-phase particles, with composition Al(MgCu), that behave anodic with respect to the matrix, and Cu-rich particles, with composition Al(CuMnFe), that, in contrast, behave cathodic [7,9,10,18-24]. The former are usually smaller than 5 μm diameter and selectively dissolve Mg, subsequently acting as cathodes, and promoting degradation of the surrounding matrix until they are released when no matrix sustains them. Concerning the Cu-rich ones, they are also released after enough time of attack to the proximal matrix, but its usual greater size (ca. 20-50 μm diameter), helps them to be retained for longer times. These phenomena have consequences in both topography and surface activity, and some aspects of the corrosion mechanism are still under discussion.

Conventional electrochemical methods for corrosion research, such as polarization or electrochemical impedance, gain information regarding electrochemical reactions taking place on the metal-electrolyte interface. However,

they only provide the average results of the whole surface under study, and lack the spatial resolution that would allow the proper analysis of the heterogeneity of samples responsible for their localized attack.

Chemical imaging of surfaces has been achieved with the development of scanning electrochemical microscopy (SECM) [25-27]. SECM is based on the reaction that occurs at a mobile ultramicroelectrode probe (UME) immersed in an electrolyte solution, and accurately rastered in close vicinity of a substrate surface in order to characterize the topography and/or redox activy of the solid/liquid interface. Measurements are performed recording electrochemical signals related to the interaction with the surface of a redox species in the solution phase [25,26]. Electrochemical operation is usually amperometric, applying a potential to the UME, and recording the current at the probe as the measuring signal. When a diffusion-controlled reversible redox reaction is used as electrochemical mediator, the faradaic current measured at the tip is affected by the nature of the surface under investigation and the tip-substrate distance. The surface may either block its diffusion towards the tip, or may facilitate a reaction site for it (i.e. being produced, consumed, etc.). Separate control of the electric state of the substrate can be attained by using a bipotentiostat as electrochemical interface in the system, allowing for the controlled polarization of the sample. Nevertheless, operation of the system under open circuit conditions is of a great advantage, especially when naturally corroding conditions are explored. Unfortunately, the need of a redox mediator in solution may affect the electrical state of the surface, because the electrochemical mediator can polarize the system. That is, the potential of the system is determined by the ratio between the two species involved in the redox couple, and can be determined by applying the Nernst equation [28]. Additionally, the possible interference of any of the redox species on the actual corrosion process under investigation cannot be discarded, particularly when thin surface films, such as those formed during the adsorption of corrosion inhibitors on metals, are involved [29].

This limitation of scanning electrochemical microscopy can be overcome by using a different technique, frequency-dependent alternating current scanning electrochemical microscopy (AC-SECM) [28]. In this case, an oscillating potential perturbation is applied to the tip, and the AC current flowing at the tip is measured for different frequencies of the perturbation signal [28,30]. This feature strongly amplifies the possibilities of the SECM, since results will also be conditioned by the parameters of the voltage oscillation whereas it does not require the addition of electrochemical mediators. It has been demonstrated that the alternating current response may be successfully used to monitor variations in the local chemical activity of a surface [30]. The applicability of this technique in Corrosion Science has already been found in the detection of corrosion pits [31,32], the monitoring of metal release [33,34], the imaging of the early stages of blistering under an organic coating applied on a metal [35], and the local visualisation of inhibitor films on active metals for corrosion protection [36,37]. At this stage, it was considered that a new

application of technological interest might be found in the visualization of chemical heterogeneities in reactive materials such as aluminium alloys.

7.4.4. Experimental

7.4.4.1. Samples and solutions

Measurements were performed on AA2024-T3 substrates of composition given in Table 7.4.1. The surface of the samples was abraded with SiC paper up to grit 4000. The resulting surfaces were degreased with acetone, abundantly rinsed with ultra-pure deionised water and allowed to dry in air. They were mounted facing up in the electrochemical cell, and immersed in NaCl solutions as test media. Ferrocene-methanol (Aldrich) was added as redox mediator when necessary in SECM experiments. All solutions were prepared with analytical grade reagents and ultra-pure water purified with a Milli-Q system from Millipore.

Table 7.4.1. Composition of AA2024 aluminium alloy (wt.%).

Cu	Mg	Si	Fe	Mn	Zr	Ti	Cr	Al
3.8-4.9	1.2-1.8	< 0.5	< 0.5	0.3-0.9	< 0.25	< 0.15	< 0.10	balance

7.4.4.2. Electrodes and instrumentation

The set-up for electrochemical measurements consisted on a Teflon cell with a circular orifice of 5 mm diameter at its bottom to facilitate the exposure of the sample to the test environment. Around 2 mL of solution was added in each case as electrolytic medium. A video microscope was used to aid microelectrode positioning and sample levelling using three thumbscrews arranged in a tripod configuration. An Ag/AgCl/KCl (3M) reference electrode and a stainless steel wire used as counter electrode were also introduced in the electrochemical microcell.

SECM measurements were carried out with a microscope built by Sensolytics (Bochum, Germany). A three electrode configuration was employed, with 10 µm Pt microelectrode as working electrode, stainless steel as auxiliary-electrode and Ag/AgCl/KCl (3M) as reference. Amperometric SECM measurements were carried out applying a constant potential of +0.50 V vs. Ag/AgCl/KCl (3M) in 0.50 mM ferrocene-methanol solution, ensuring oxidation of this species on the tip under diffusion control. 2-D motion was performed parallel to the surface of the substrate at 15 µm tip-substrate height.

For AC-SECM measurements, an EG&G Princeton Applied Research potentiostat, model 273A was connected to the SECM equipment, whereas

measurement of the AC current was performed using the lock-in amplifier available in the instrument for the high resolution operation. The same ultramicroelectrodes than in conventional SECM were employed for the alternating current operation. Data acquisition involved at least 4 dimensions, namely the 2-D related to the position in the X-Y plane in which the scan is recorded, AC current data and frequency. AC voltage signals of 10 mV_{pp} amplitude were applied around a constant base potential for 10 frequency values in 60000 to 1000 Hz range. The constant potential value was either +0.50 V vs. Ag/AgCl/KCl (3M) when ferrocene-methanol was added to the test electrolyte, or the open circuit potential (OCP) developed spontaneously in the solution. Measurements were performed in 1 mM NaCl.

7.4.5. Results and discussion

In a first series of experiments, the establishment of a correlation between the results obtained using conventional amperometric operation of SECM, and those delivered by the new alternating-current mode, was attempted. In order to locate the surface, the tip was progressively moved towards the surface and experimental approach curves were measured in a solution containing ferrocene-methanol. The corresponding plots for the two operation modes are shown in Figure 7.4.1. In both cases, the signals measured at the tip have been normalized by dividing the values at each tip-substrate distance by the corresponding value measured in the bulk of the solution, i_{lim} and $[Z]_{lim}$, respectively.

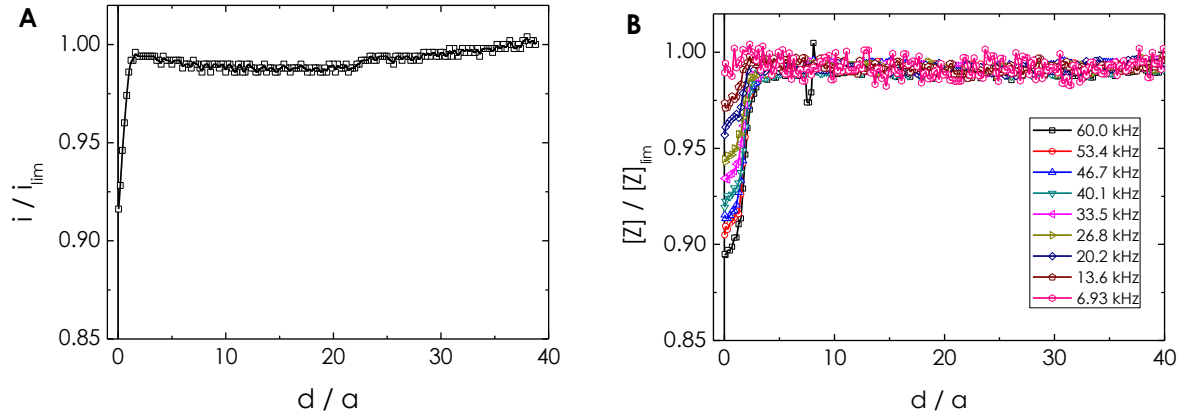

Figure 7.4.1. Normalized change in the current measured at the tip electrode as a function of distance from the AA2024 bare surface (i.e., approach curves). The SECM operation was: (A) amperometric, and (B) alternating-current modes. Test environment: 0.5 mM ferrocene-methanol. DC potential: +0.50 V vs. Ag/AgCl/(3M) KCl. Amplitude of the AC potential signal: 10 mV_{pp} for the frequencies indicated in the legend. Tip diameter: 10 µm. The non dimensional tip-substrate distance is given by d / a, where d is the actual distance, and a the diameter of the Pt microelectrode. i / i_{lim} is the dimensionless tip DC-current and $[Z]$ / $[Z]_{lim}$ is the modulus of the dimensionless tip AC-current.

A negative feedback effect is observed when applying a constant potential in Figure 7.4.1A, leading to a sudden decrease in current when the diffusion of the redox mediator towards the tip is hindered by the close proximity of the substrate. However, a small increase in current can be observed just before this decay, which probably arises from the partial reduction at the substrate of some ferrocinium ions produced during the oxidation of ferrocene-methanol at the UME. In this way, greater concentrations of the electroactive species are encountered at small tip-substrate distances.

Thus, a combined situation of positive and negative feedback is observed, indicating that this surface is active enough to allow some redox regeneration of the mediator, though the kinetics of this electronic exchange is not fast enough to overcome the limitation to diffusion imposed at smallest distances. This result can be justified considering that aluminium alloys are known to form a passive layer with lower conductivity than the metal, effectively slowing the rate of the electronic exchange reaction [17].

After completing the measurement of the approach curve under amperometric SECM operation, the same procedure was followed to measure a new approach curve above the same location of the surface, but under AC operation of the SECM. The corresponding approach curves for a selection of frequencies of the AC signal are given in Figure 7.4.1B. There exists a decrease in the value of the magnitude of the impedance when the tip approximates the substrate, which is consistent with the lower resistance offered by the surface to electric conduction, thus facilitating charge transfer towards the auxiliary electrode. This response is more pronounced at higher frequencies, whereas at 6.93 kHz the proximity of the surface is hardly noticeable. In the figure, the corresponding plot for 1.00 kHz has been omitted as the surface could not be distinguished at this frequency.

In the case of a metallic substrate, when the electrolyte concentration is low, the equivalent circuit that better fits to the system is depicted in Figure 7.4.2 and can be described as it follows [28]. When the tip is far enough from the surface, electric motion takes place through the electrolyte and the only term altering the obtained signal is the solution resistance. If the tip approaches the metal surface, electric charges find another alternative route through the substrate, now affecting the resistance and the capacitance at the metal-substrate interface, especially at the local position of the tip. In addition, electric motion in solution is reduced due to the blockage of diffusion. As a result, by approaching the UME to the sample, the impedance of the system will be altered, thus affecting the modulus and phase angle of the AC current, and this will be strongly dependent on the frequency. Conversely, on the tip approaching an insulator surface, a thinner electrolyte layer of the solution is left between the tip and the substrate, so the solution resistance increases and the current drops.

Therefore, inspection of Figure 7.4.1B indicates that the substrate behaves as an insulator at the highest frequency under consideration, thus the AC-SECM

response is solely determined by the tip-substrate distance. In this way, topographic information is obtained exclusively. A sufficiently high frequency value should be found that provides the greatest contrast for topographic imaging. On the other hand, it is also observed that the current measured at the distance of closest approach progressively grows with the decrease in the applied frequency. That is, the chemical characteristics of the surface affect the current response measured at the tip in the low frequency range of the AC signal. In this, local differences in chemical reactivity occurring in the investigated surface should be spatially resolved at lower frequency values.

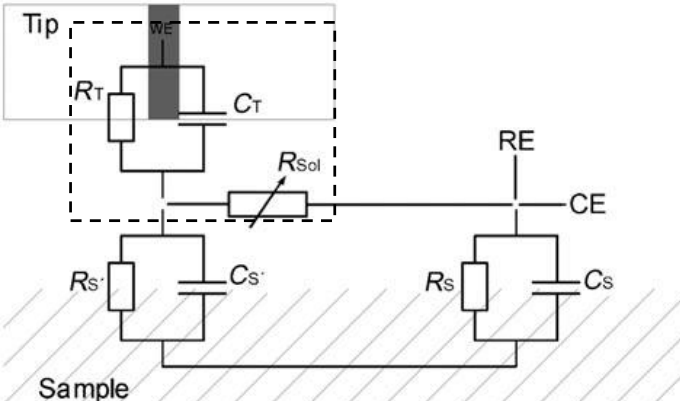

Figure 7.4.2. Equivalent circuit representing the impedance behaviour of the metal/electrolyte system [28]: R_T and C_T are resistance and capacitance of the tip, respectively; R_{SOL} is the solution resistance; R_S and C_S are the resistance and capacitance of the sample, being $R_{S'}$ and $C_{S'}$ these parameters at the specific area covered by the AC-SECM tip.

In order to image the chemical heterogeneity of the surface under study, scans measured at constant height were recorded under the same experimental conditions employed in Figure 7.4.1, and the resulting maps are depicted in Figure 7.4.3. The SECM image in Figure 7.4.3A, obtained with amperometric SECM, exhibits some areas with higher tip current values. They correspond to locations at which faster regeneration of the mediator occurs, a feature previously reported in the scientific literature [40,41]. These zones, assumed to correspond to intermetallic particles, present greater electronic exchange with species from the solution. This ability is generally due to either a less insulating passive layer that makes the specimen more electrically conductive, and/or different surface potential that facilitates the donation of electrons to the ferrocinium ion. However, the later would contradict the observations of scanning Kelvin probe force microscopy [20,32,34]. According to them, intermetallics that may be more easily observed thanks to their size and persistence on the surface are the Al(CuMnFe) ones, with nobler potential, so they are not so likely to donate electrons, and the hypothesis of the thinner passive layer above these particles seems to more adequately describe the observed results.

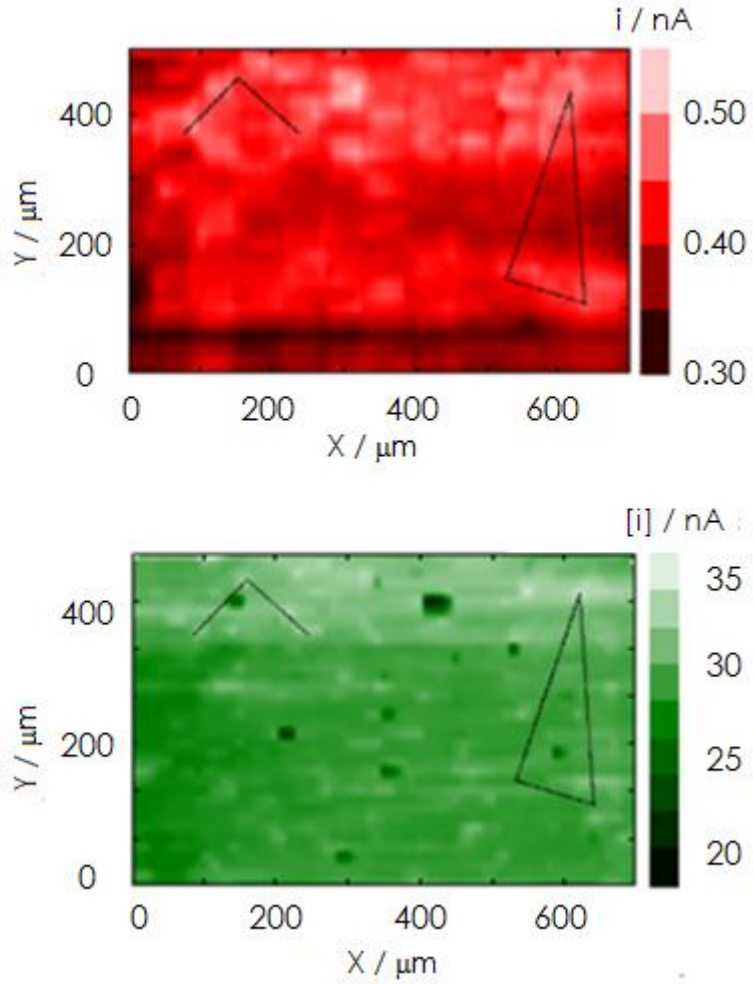

Figure 7.4.3. SECM images obtained over an AA2024 bare surface immersed in 0.5 mM ferrocene-methanol solution. The SECM operation was: (up) amperometric, and (down) alternating-current modes. DC potential: +0.50 V vs. Ag/AgCl/KCl (3M). Amplitude of the AC potential signal: 10 mV_{pp}, and frequency of 33.5 kHz. Tip diameter: 10 µm; tip-substrate distance: 15 µm.

After recording a map with conventional SECM, the same area of the surface was monitored using the alternating-current mode of SECM, and the image shown in Figure 7.4.3B was recorded. The image was obtained at the frequency of 33.5 kHz, which provided the greater contrast. It can be observed that certain active sites already detected using the conventional operation (cf. marks in the figure), are also seen in the AC-SECM map as regions of enhanced current modulus. Furthermore, the features occurring in the surface are resolved with greater sensitivity in the alternating current image. At this stage, it must be taken in account that these preliminary experiments were performed adding a redox mediator to the solution for imaging with conventional SECM, and this procedure may produce some drawbacks during measurements. Firstly, it cannot be discarded that the mediator would not affect the spontaneous evolution of the substrate, and there is no special application in studying the influence of ferrocene on these substrates as for real systems. Secondly, the tip showed a stable trend to produce decreasing currents

when biased at +0.50 V vs. Ag/AgCl/KCl (3M) in this solution, as if it was becoming progressively blocked either by some chemical species originating from the active metal and subsequently reacting at the microelectrode, or as if ferrocene concentration was effectively decreasing with time due by reaction of this species with the metal sample (i.e. being oxidized by oxygen present in the naturally aerated solution acting the metal as a catalyst). For this reason, a new sample was analysed in a mediator-free solution, and in the presence of a more aggressive media. For that purpose, AC-SECM scans were performed in 1 mM NaCl solutions. Figures 7.4.4 and 7.4.5 show the AC-SECM images of an AA2024 sample immersed in 10 mM NaCl for different exposures, as registered at two different frequencies, namely 55 and 7 kHz. They are given as both the modulus and phase angle components of the AC current flowing in the system.

The images of the current modulus imaged for different durations of the immersion in the electrolytic media shows an almost homogeneous surface at the early stages of the experiment (cf. Figure 7.4.4). However, the longer the time they are exposed to the electrolyte, the activation of specific sites in the surface are observed as regions of increased current modulus in the plots. This chemical activation effect is viewed in the development of small regions that appear lighter in the image recorded at the frequency of 55 kHz, which actually corresponds to higher current modulus values. That is, these areas are effectively located at a bigger distance from the tip than the surrounding surface when the tip scans over the sample at a constant height. Therefore, the development of holes in the surface has been imaged, which might correspond to detachment of the matrix material surrounding cathodic intermetallic particles. This observation agrees with reports in the literature based on *ex situ* analysis by scanning electron microscopy [10,18-24]. Additionally, the higher current modulus values recorded over the whole imaged surface at both frequency values after the sample has been exposed to the solution overnight, is an indication that the aged oxide layer is less insulating than at earlier exposures. The absence of features in the image taken in Figure 7.4.4D at the lower frequency of 6.93 kHz, supports that all the surface is covered likewise by this film. Yet, the different physicochemical properties if the surface oxide film is evidenced from the comparison of the current phase images for these two frequency values given in Figure 7.4.5.

Though they appear rather featureless at both frequency values, especially in the case of the longer exposures of the sample in the electrolyte solution, it is directly observable that low phase values are only observed in Figure 7.4.5D with the frequency of 6.93 kHz. This value corresponds to a resistive system, whereas higher phase values are more consistent with a dielectric barrier film displaying a somewhat capacitive behaviour towards the passage of AC current. Again the physicochemical characteristics of the surface have been viewed from the AC-SECM images taken at the lowest frequency, whereas the phase values are always high and almost invariable throughout the duration of the experiments in the images taken with the frequency of 55 kHz.

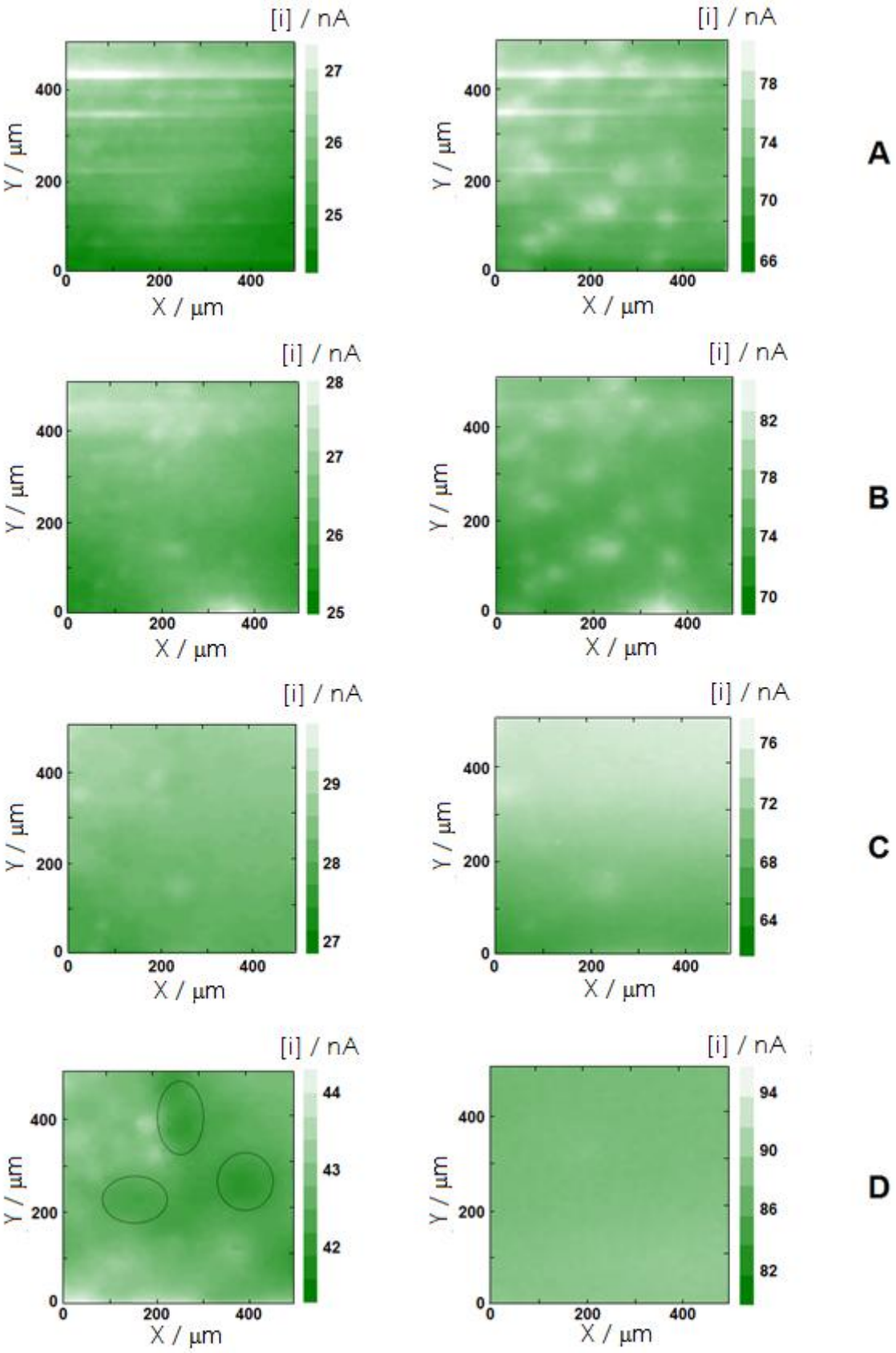

Figure 7.4.4. Change in the modulus of the tip AC current observed during scanning over an AA2024 bare surface immersed in 10 mM NaCl after: (A) 60 min, (B) 105 min, (C) 255 min, and (D) 17 hours immersion. Tip diameter: 10 µm; tip-substrate distance: 15 µm. Amplitude of the AC potential signal: 10 mV_{pp}. Frequency was: (left) 55.0 kHz, and (right) 6.93 kHz.

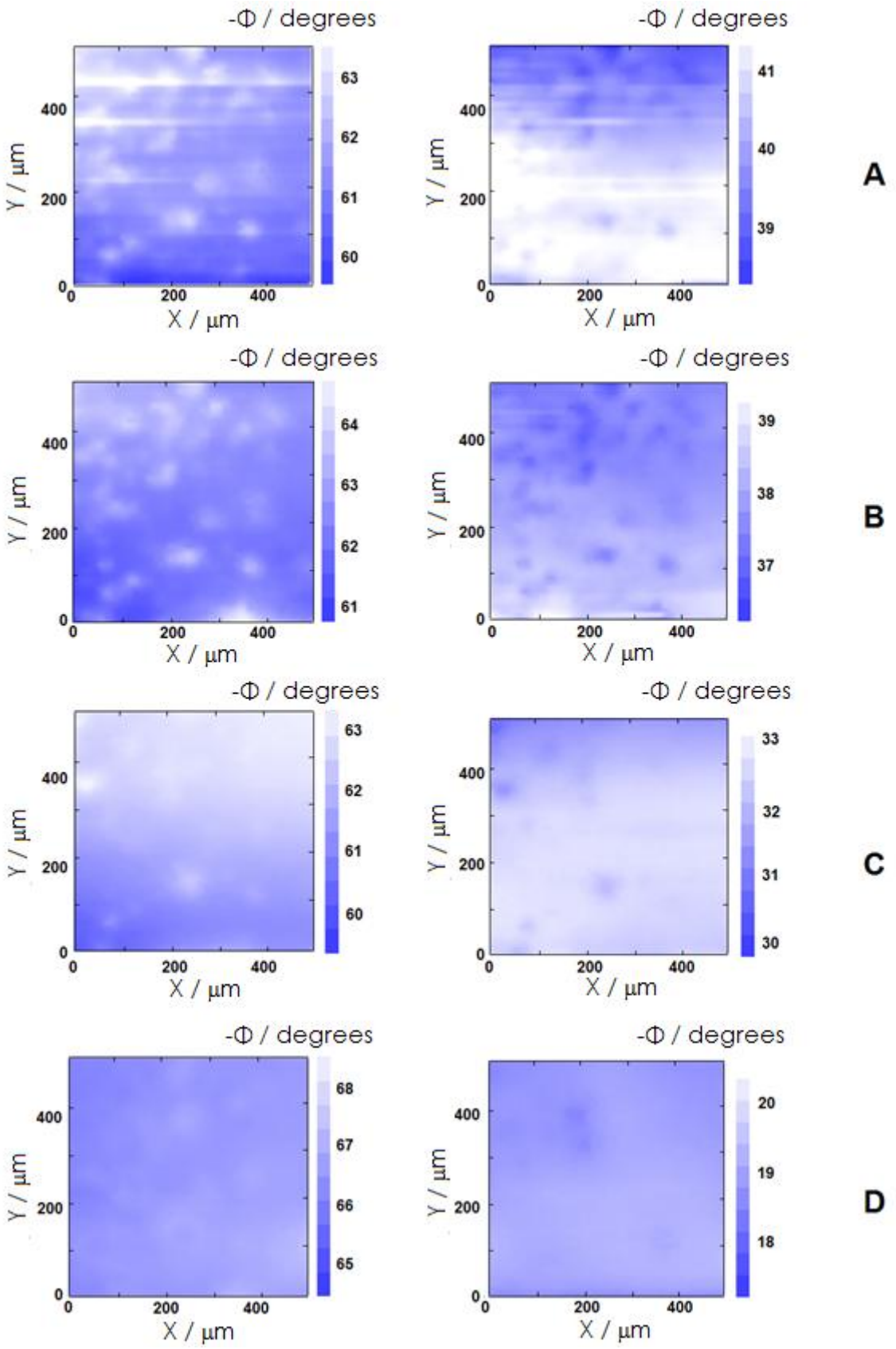

Figure 7.4.5. Change in the phase of the tip AC current observed during scanning over an AA2024 bare surface immersed in 10 mM NaCl after: (A) 60 min, (B) 105 min, (C) 255 min, and (D) 17 hours immersion. Tip diameter: 10 µm; tip-substrate distance: 15 µm. Amplitude of the AC potential signal: 10 mV_{pp}. Frequency was: (left) 55.0 kHz, and (right) 6.93 kHz.

7.4.6. Conclusion

The application of a new technique, alternating-current scanning electrochemical microscopy (AC-SECM), to the characterization of the electrochemical behaviour of AA2024 exposed to a dilute aqueous solution containing NaCl has provided new insights towards the elucidation of the surface processes related to the corrosion of this material. Spatially-resolved images combining topographic and chemical activity information could be obtained by adequately tuning the frequency of the AC current used as measuring signal. Local activation of inclusions and dissolution processes related to their electrochemical activity could be monitored both topographically and chemically. The evolution of physicochemical characteristics of the surface films spontaneously formed on the material during immersion in the electrolyte as a function of time could be determined as changes in its resistance to undergo charge transfer reactions through these layers.

7.4.7. References

1. C.A. Melendres, S. van Gils, H. Terryn. Electrochemistry Communications 3 (2001) 737.
2. J.C.S. Fernandes, R. Picciochi, M. da Cunha Belo, T.M. Silva, M.G.S. Ferreira, I.T.E. Fonseca. Electrochimica Acta 49 (2004) 4701.
3. F.J. Martin, G.T. Cheek, W.E. O'Grady, P.M. Natishan. Corrosion Science 47 (2005) 3187.
4. J. Bernard, M. Chatenet, F. Dalard. Electrochimica Acta 52 (2006) 86.
5. M.A. Amin, S.S. Abd El Rehim, E.E.F. El Sherbini. Electrochimica Acta 51 (2006) 4754.
6. D. Battistel, S. Daniele, G. Battaglin, M.A. Baldo. Electrochemistry Communications 11 (2009) 2195.
7. J. Zhang, M. Klasky, B.C. Letellier. Journal of Nuclear Materials 384 (2009) 175.
8. M. Morozov, G.Y. Tian, P.J. Withers. International Journal of Scientific and Technology Research 43 (2010) 493.
9. P. Campestrini, E.P.M. van Westing, H.W. van Rooijen, J.H.W. de Wit. Corrosion Science 42 (2000) 1853.
10. P. Campestrini, H.W. van Rooijen, E.P.M. van Westing, J.H.W. de Wit. Materials and Corrosion 51 (2000) 616.
11. B.A. Shaw, R.G. Buchheit, J. P. Moran (Editors). Corrosion and Corrosion Prevention of Low Density Metals and Alloys. The Electrochemical Society, Pennington, 2001.
12. F. Andreatta, M.M. Lohrengel, H. Terryn, J.H.W. de Wit. Electrochimica Acta 48 (2003) 3239.
13. F. Andreatta, H. Terryn, J.H.W. de Wit. Electrochimica Acta 49 (2004) 2851.

14. C.H. Paik, H.S. White, R.C. Alkire. Journal of the Electrochemical Society147 (2000) 4120.
15. V. Vignal, H. Krawiec, O. Heintz, R. Oltra. Electrochimica Acta 52 (2007) 4994.
16. F. Zhang, J. Pan, C. Lin. Corrosion Science 51 (2009) 2130.
17. D.A. Jones, Principles and Prevention of Corrosion. Maxwell Macmillan International Editions, New York, 1992.
18. R.G. Buchheit, R.P. Grant, P.F. Hiava, B. Mckenzie, G.L. Zende. Journal of the Electrochemical Society144 (1997) 2621.
19. R.P. Wei, C.-M. Liao, M. Gao. Metallurgical and Materials Transactions A 29 (1998) 1153.
20. T. Suter, R.C. Alkire. Journal of the Electrochemical Society148 (2001) B36.
21. K.A. Yasakau, M.L. Zheludkevich, S.V. Lamaka, M.G.S. Ferreira. Journal of Physical Chemistry B 110 (2006) 5515.
22. F.M. Queiroz, M. Magnani, I. Costa, H.G. de Melo. Corrosion Science 50 (2008) 2646.
23. A. Boag, A.E. Hughes, A.M. Glenn, T.H. Muster, D. McCulloch. Corrosion Science 53 (2011) 17.
24. A.E. Hughes, A. Boag, A.M. Glenn, D. McCulloch, T.H. Muster, C. Ryan, C. Luo, X. Zhou, G.E. Thompson. Corrosion Science 53 (2011) 27.
25. A.J. Bard, F.-R.F. Fan, J. Kwak, O. Lev. Analytical Chemistry 61 (1989) 132.
26. J. Kwak, A.J. Bard. Analytical Chemistry 61 (1989) 1221.
27. A.J. Bard, G. Denuault, C. Lee, D. Mandler, D.O. Wipf. Accounts of Chemical Research 23 (1990) 357.
28. K. Eckhard, W. Schuhmann. Analyst 133 (2008) 1486.
29. J. Izquierdo, J.J. Santana, S. González, R.M. Souto. Electrochimica Acta 55 (2010) 8791.
30. P.M. Diakowski, A.S. Baranski. Electrochimica Acta 52 (2006) 854.
31. K. Eckhard, M. Etienne, A. Schulte, W. Schuhmann. Electrochemistry Communications 9 (2007) 1793.
32. K. Eckhard, T. Erichsen, M. Stratmann, W. Schuhmann. Chemistry - A European Journal 14 (2008) 3968.
33. D. Ruhlig, W. Schuhmann. Electroanalysis 19 (2007) 191.
34. D. Ruhlig, H. Gugel, A. Schulte, W. Theisen, W. Schuhmann. Analyst 133 (2008) 1700.
35. J.J. Santana, M. Pähler, R.M. Souto, W. Schuhmann. Electrochimica Acta 77 (2012) 60.
36. M. Pähler, J. J. Santana, W. Schuhmann, R.M. Souto. Chemistry - A European Journal 17 (2011) 905.
37. J.J. Santana, M. Pähler, W. Schuhmann, R.M. Souto. ChemPlusChem 77 (2012) 707.

7.5

Main conclusions

1. Heterogeneous surface behaviour of complex materials containing metallic inclusions has been characterized using SVET and direct and alternating current modes of SECM. This was illustrated with aluminium-based alloys AA2024 and AA6060, widely employed for industrial applications but susceptible to localized corrosion.

2. Visualization of anodic and cathodic activities, resulting principally from the local corrosion of the matrix surrounding a nobler intermetallic particle, was imaged by SVET. The sizes of the active sites where resulting ionic fluxes occurred are much larger than those typically corresponding to metallic inclusions in the alloy (namely, 20-50 μm), a feature that must be taken in account for mechanistic considerations.

3. ZrO_2 coatings for the protection of AA2024 alloy provided high anticorrosion resistance while intact. However, no self-healing ability is observed for defective ZrO_2 films applied on AA2024. Thus, due to the poor repassivation characteristics of this material, application of zirconia coatings cannot be regarded as an efficient corrosion protection procedure for AA2024.

4. Spatially-resolved images, related to topographic and chemical activity changes on the AA2024 surface exposed to aggressive environments, could be obtained by using the AC-SECM technique. This was achieved by adequately tuning the frequency of the AC potential applied as perturbation to the microelectrode tip.

7.6

Conclusiones

1. Se ha caracterizado el comportamiento superficial heterogéneo de materiales complejos que contienen inclusiones metálicas utilizando el SECM en tanto en su modo de corriente continua como en corriente alterna, y el SVET. Ello se ha ilustrado con las aleaciones de base aluminio AA2024 y AA6060, ampliamente empleadas en la industria pero susceptibles de sufrir corrosión localizada.

2. Se han visualizado mediante SVET las actividades anódicas y catódicas que resultan principalmente de la corrosión localizada de la matriz circundante a partículas intermetálicas, de carácter más noble. Las dimensiones de los sitios activos donde se encontraron los flujos iónicos resultaron mucho mayores a los típicos de las inclusiones metálicas de la aleación (esto es, 20-50 μm), un hecho que debe tomarse en consideración al hacer consideraciones de los mecanismos.

3. Los recubrimientos de ZrO_2 como protección para la aleación de AA2024 aportan gran resistencia anticorrosiva mientras permanecen intactos. Sin embargo, no se observa capacidad de auto-curado en películas defectuosas de ZrO_2 aplicadas en AA2024. Por tanto, dada las pobres características repasivadoras de este material, la aplicación de los recubrimientos de óxido de circonio no puede considerarse como un procedimiento eficiente en la protección anticorrosiva para AA2024.

4. Se han podido obtener imágenes con resolución espacial, relacionadas con cambios topográficos y de actividad química en la superficie AA2024 expuesta a ambientes agresivos, mediante el uso de la técnica AC-SECM. Esto se ha logrado ajustando adecuadamente la frecuencia del potencial AC aplicado como perturbación a la punta microelectrodo.

CHAPTER 8

A microelectrochemical investigation of the microscopic aspects of metal dissolution and corrosion inhibition by surface films illustrated by copper metal

Index

8.1.

Prologue to the experiments

8.1.1. Introduction

Highly corrosion-resistant metallic materials are currently designed for a wide range of applications in our technologically-based society. Their resistance arises from the onset of passivity, that is, the protection of the metal from the aggressive environment is conferred by a stable and adherent passivating oxide film on the surface. These surface films maybe modified through the interaction of organic molecules which may operate as corrosion inhibitors when they form a thin passivating layer covering metal surfaces they should protect by adsorption or chemisorption. The organic compounds may either be dissolved in the electrolyte (conventional inhibitors) or adsorb on the metal surface. In this way, corrosion inhibitors contribute to the formation of more resistant surface films, or they effectively originate a barrier film on the surface of the material, effective separating it from the aggressive environment. Unfortunately, the breakdown of the passive regime to give localised corrosion can be stimulated from many causes, originating catastrophic failures of the materials. The organic compounds may either be dissolved in the electrolyte (conventional inhibitors) or adsorb on the metal surface.

A representative metal model for the study of the electrochemical behaviour of passivating materials is provided by copper, a base metal with a low redox potential in aqueous solutions [1]. Copper, as a metal or as an alloy, is a very important metal in the industry due to its resistance to some aggressive environments. Copper is generally a relatively noble metal, however, it is susceptible to corrosion by acids and strong alkaline solutions, especially in the presence of oxygen or oxidants. In the pH range between 2 and 5 the dissolution of Cu is very rapid and the formation of a stable surface oxide layer, which can passivate metal surfaces, is impossible. Copper can only passivate by forming an oxide surface layer in weak acid or alkaline solutions.

The electrochemistry of copper in alkaline aqueous solutions has been extensively investigated in relation to the protective characteristics of passive films [2-19]. The onset of passivity is related to the formation of copper oxide layers with a duplex structure, consisting in general terms of an inner Cu/Cu_2O porous and an outer CuO hydrated layers [7,8]. It was also found that the thickness, structure and protective properties of the passive layer depended on a number of variables, such as the solution composition, the copper surface treatment, the temperature and the potential routine employed in the experiments [5-8,11-19]. Thus, in aqueous

solutions containing either a carbonate [13,16,18,20,21] or a phosphate [14,18,21,22] salt the protectiveness of the passive layers is enhanced as the result of insoluble copper salts becoming a part of the anodic layer. Conversely, the high solubility of copper salts could favour a more extensive corrosive attack of copper eventually leading to pitting corrosion [8,13,15,17,23-26].

The behaviour of Cu in acidic media is extensively investigated and several schemes have been presented for the dissolution process [27-31]. In an acidic media where Cu is applied, corrosion attack is quite high and costly. The application of effective environment friendly inhibitors is one way to hinder corrosion of copper. There are only few materials that could be applied as effective inhibitors for copper corrosion in acidic media.

Aromatic heterocyclic compounds such as benzotriazole (BTAH), benzimidazole, mercaptobenzothiazole and others are well known inhibitors of copper corrosion [32-44]. The selection of inhibitors is often based on gravimetric determination of the metal-dissolution rate (mass losses), but this method provides very little information about the complex interactions between the metal, the inhibitor and the corrosive medium. For inhibition to be optimized, the mechanisms involved in such interactions must be known, which demands the use of electrochemical and surface analytical techniques in the corrosion laboratory. The major part of the current knowledge of corrosion inhibition processes has been gained from the use of conventional electrochemical methods such as cyclic voltammetry, chronoamperometry and electrochemical impedance spectroscopy (EIS). Whatever the measurable quantity, it reflects the reactivity of the whole electrode surface; in other words, its analysis is based on the assumption that the electrochemical behaviour of the interface is uniform, and the monitored signal corresponds to an average measurement over the whole electrode surface.

In this context, ability to provide *in situ* topographic and electrochemical reactivity information about the surface evolution at the micrometer and submicrometer scales in aqueous solution exhibited by the scanning electrochemical microscope (SECM) is attractive. Unfortunately, despite the various detection schemes developed for scanning electrochemical microscopy operation such as the amperometric feedback mode [20], generator-collector mode [21] or redox competition mode [22] among others, the technique always involves the measurement of faradaic current at the microelectrode tip. Thus, the addition of a freely diffusing redox species to the electrolytic phase is often employed. This may represent a problem in many systems, as it may modify the electrical state of the investigated surface either by affecting its corresponding Nernst potential in the electrolyte, or even shifting chemical and electrochemical equilibria occurring at the substrate [45]. Indeed, the addition of a redox mediator is always required for the investigation of metallic systems covered by insulating films or layers such as those employed for corrosion protection when they do not exhibit detectable flaws of continuity [46]. Such insulating films are found when the metal is coated with a polymeric film (i.e., anticorrosion paints and varnishes) resulting in the formation of inhibitor films due to the interaction of organic molecules with the metallic surface.

These layers introduce a physical barrier between the underlying metal and the electrolytic environment, and greatly hinder the investigation of such highly resistive systems. This is reflected by the scarce number of publications concerning the characterization of corrosion protection with inhibitors [47-49], though both are topics of major interest in Corrosion Science. And even then, the eventual transport of the added redox mediator through the surface layers into the polymeric matrix and towards the metal-organic film interface cannot be discarded to occur, at least for sufficiently long exposure times, thus greatly limiting the applicability of the method. An additional requirement of conventional amperometric SECM is that sufficiently high conductive electrolytes are employed to exclude the participation of the diffusing redox species in migration or convective transport processes, though many real corrosion processes actually occur in poorly conductive environments.

8.1.2. Research aims

This Chapter focus on the applicability of scanning microelectrode techniques to investigate the inhibition of metal corrosion. Copper surfaces partially modified with different organic inhibitors namely benzotriazole (BTAH), 5-methyl-benzotriazole (MBTAH), 2-mercaptobenzimidazole (MBI), and ethyl xanthate (KEX) were investigated. Benzotriazole (BTAH) is an established and widely explored inhibitor against copper corrosion [50]. It binds via chemisorption to Cu(I)-centres located on the surface [51], and the formed layer has a thickness of only a few nanometres depending on the time the metal was immersed in the inhibitor solution. 2-Mercaptobenzimidazole (MBI) has been found to be more effective than BTAH in the corrosion protection of copper in aerated aqueous HCl environment [52]. Its inhibitive action is exerted mainly on the anodic process. In general terms, both MBI and BTAH are regarded to exhibit excellent inhibitor characteristics for corrosion protection in many aggressive environments [53]. Finally, the mineral collector ethyl xanthate (KEX) offers high protection against copper corrosion in neutral and moderately alkaline aqueous NaCl solutions [54,55]. XPS data suggest that copper protection is achieved through the growth of a cuprous diethyl dixanthogen layer on the metal in which the oxidation state +1 of copper becomes stabilized [56].

Prior to investigating the effect of inhibitor compounds on the degradation of copper metal, monitoring of its dissolution process with enhanced spatial and chemical resolution was attempted using the combined AFM-SECM technique. In this way, topographic changes could be imaged simultaneously to collecting the ionic species released during the process, opening a new powerful method for the investigation of metal dissolution from active metals.

The possibilities and limitations of conventional amperometric operation of the SECM, as proposed by Kontturi and co-workers [47-49], were next considered in relation to the inhibitive effect of benzotriazole and 2-mercaptobenzimidazole. The

method was significantly improved to avoid polarization of the substrate allowing the material to corrode spontaneously, and reproducible results are presented in Sections 8.2 and 8.3. Yet, concern remained regarding the addition of ferrocene-methanol to the test electrolyte to serve as freely diffusing redox mediator, as it might influence the corrosion process on the metal surface. Therefore, Sections 8.4 and 8.5 describe new methods for the investigation of thin inhibitor films by SECM which do not require the addition of any redox active species to the electrolyte solution [57]. Firstly, the combined potentiometric/amperometric of the SECM using antimony microelectrodes was considered. The secondly alternative for the study of highly resistive surfaces consisted in frequency-dependent alternating-current scanning electrochemical microscopy (4D AC-SECM) [58]. By applying an alternating potential to a microelectrode used as SECM-tip and recording the alternating current response spatially-resolved information on the electrochemical behaviour of heterogeneous samples becomes available [59].

8.1.3. References

1. M. Pourbaix. Atlas of Electrochemical Equilibria in Aqueous Solutions. NACE, Houston, 1974.
2. D.W. Shoesmith, T.E. Rummery, D. Owen, W. Lee. Journal of the Electrochemical Society 123 (1976) 1790.
3. V. Ashworth, D. Fairhust. Journal of the Electrochemical Society 124 (197) 506.
4. J. van Muylder. In: Comprehensive Treatise of Electrochemistry, Vol. 4 (Edited by J.O'M. Bockris, B.E. Conway, E. Yeager, R.E. White). Plenum Press, New York, 1981.
5. M.R.G. de Chialvo, R.C. Salvarezza, A.J. Arvia. Journal of Applied Electrochemistry 14 (1984) 165.
6. H.H. Strehblow, H.D. Speckmann. Materials and Corrosion 35 (1984) 512.
7. H.D. Speckmann, M.M. Lohrengel, J.W. Schultze, H.H. Strehblow. Berichte der Bunsengesellschaft für Physikalische Chemie 89 (1985) 392.
8. M.R.G. de Chialvo, R.C. Salvarezza, D. Vásquez Moll, A.J. Arvia. Electrochimica Acta 30 (1985) 1501.
9. M.R.G. de Chialvo, J.E. Zerbino, S.L. Marchiano, A.J. Arvia. Journal of Applied Electrochemistry 16 (1986) 517.
10. M.G. Figueroa, R.C. Salvarezza, A.J. Arvia. Electrochimica Acta 31 (1986) 655.
11. M. Wanner, H. Wiese, K.G. Weil. Berichte der Bunsengesellschaft für Physikalische Chemie 92 (1988) 736.
12. J. Gómez Becerra, R.C. Salvarezza, A.J. Arvia. Electrochimica Acta 33 (1988) 613.
13. M. Pérez Sánchez, M. Barrera, S. González, R.M. Souto, R.C. Salvarezza, A.J. Arvia. Electrochimica Acta 35 (1990) 1337.

14. M.M. Laz, R.M. Souto, S. González, R.C. Salvarezza, A.J. Arvia. Electrochimica Acta 37 (1992) 655.
15. R.M. Souto, M. Pérez Sánchez, M. Barrera, S. González, R.C. Salvarezza, A.J. Arvia. Electrochimica Acta 37 (1992) 1437.
16. R.M. Souto, M. Pérez Sánchez, M. Barrera, S. González, R.C. Salvarezza, A.J. Arvia. Electrochimica Acta 38 (1993) 703.
17. R.M. Souto, S. González, R.C. Salvarezza, A.J. Arvia. Electrochimica Acta 39 (1994) 2619.
18. R.M. Souto, M.M. Laz, S. González. Anales de Química 93 (1997) 252.
19. S. González, M. Pérez, M. Barrera, A.R. González Elipe, R.M. Souto. Journal of Physical Chemistry B 102 (1998) 5483.
20. M. Drogowska, L. Brossard, H. Ménard. Journal of the Electrochemical Society 139 (1992) 39.
21. M. Drogowska, L. Brossard, H. Ménard. Journal of Applied Electrochemistry 24 (1994) 344.
22. C.-H. Lyun, S.-M. Park. Journal of the Electrochemical Society 133 (1986) 2024.
23. D. Vásquez Moll, R.C. Salvarezza, A.J. Arvia. Electrochimica Acta 30 (1985) 1011.
24. M.G. Figueroa, M.F.L. de Mele, R.C. Salvarezza, D. Vásquez Moll, A.J. Arvia. Electrochimica Acta 32 (1987) 231.
25. M.R.G. de Chialvo, M.F.L. de Mele, R.C. Salvarezza, A.J. Arvia. Corrosion Science 28 (1988) 121.
26. R.M. Souto, M. Pérez Sánchez, M. Barrera, S. González, R.C. Salvarezza, A.J. Arvia. Portugaliae Electrochimica Acta 9 (1991) 43.
27. F. Mansfeld (Editor). Corrosion Mechanisms. Marcel Dekker, New York, 1987, p. 119
28. G. Trabanelli. Corrosion 47 (1991) 410.
29. L. Kiss. Kinetics of Electrochemical Metal Dissolution. Elsevier, Amsterdam, 1988.
30. A. Shaban, E. Kálmán, J. Telegdi. Electrochimica Acta 43 (1998) 159.
31. A. Jardy, A. Legal Lasalle-Molin, M. Keddam, H. Takenouti. Electrochimica Acta 37 (1993) 2195.
32. J.B. Cotton, I.R. Scholes. British Corrosion Journal 2 (1967) 1.
33. G.W. Poling. Corrosion Science 10 (1970) 359.
34. P.G. Fox, G. Lewis, P.J. Boden. Corrosion Science 19 (1979) 457.
35. F. El-Taib Heakal, S. Haruyama. Corrosion Science 20 (1980) 887.
36. O. Holler, R.C. May. Corrosion 41 (1985) 39.
37. D. Kuron, A. Botta, M. Gräfen. Materials and Corrosion 36 (1985) 407.
38. J. Penninger, K. Wippermann, J.W. Schultze. Materials and Corrosion 38 (1987) 649.
39. R. Holm, D. Holtkamp, R. Kleinstück, H.-J. Rother, S. Storp. Fresenius' Zeitschrift für Analytische Chemie 333 (1989) 546.
40. R. Youda, H. Nishihara, K. Aramaki. Electrochimica Acta 35 (1990) 1011.
41. K. Aramaki, T. Kiuchi, T. Sumiyoshi, H. Nishihara. Corrosion Science 32 (1991), 593.
42. S. González, R.M. Souto, M. Pérez Sánchez, M.M. Laz, M. Barrera, R.C. Salvarezza, A.J. Arvia. Materials Science Forum 111-112 (1992) 103.

43. M.M. Laz, R.M. Souto, S. González, R.C. Salvarezza, A.J. Arvia. Journal of Applied Electrochemistry 22 (1992) 1129.
44. H.Y.H. Chan, M.J. Weaver. Langmuir 15 (1999) 3348.
45. V. Radtke, C. Heß, R.M. Souto, J. Heinze. Zeitschrift für Physikalische Chemie 220 (2006) 393.
46. R.M. Souto, Y. González-García, J. Izquierdo, S. González. Corrosion Science 52 (2010) 748.
47. K. Mansikkamäki, P. Ahonen, G. Fabricius, L. Murtomäki, K. Kontturi. Journal of the Electrochemical Society 152 (2005) B12.
48. K. Mansikkamäki, C. Johans, K. Kontturi. Journal of the Electrochemical Society 153 (2006) B22.
49. K. Mannsikkamäki, U. Haapanen, C. Johans, K. Kontturi, M. Valden. Journal of the Electrochemical Society 153 (2006) B311.
50. M. M. Antonijević, S. M. Milić, M. B. Petrovic. Corrosion Science 51 (2009) 1228.
51. S. L. Cohen, V. A. Brusic, F. B. Kaufman, G. S. Frankel, S. Motakef, B. Rush. Journal of Vacuum Science and Technology A 8 (1990) 2417.
52. D. Zhang, L. X. Gao, G. D. Zhou. Corrosion Science 46 (2004) 3031.
53. C. Monticelli, G. Brunoro, A. Frignani, A. Marchi. Surface and Coating Technology. 27 (1986) 175.
54. R.M. Souto, V. Fox, M. Laz, M. Pérez, S. González. Journal of Electroanalytical Chemistry 411 (1996) 16.
55. M. Scendo. Corrosion Science 47 (2005) 1738.
56. R.M. Souto, M.M. Laz, S. González. Journal of Physical Chemistry B 101 (1997) 508.
57. K. Eckhard, C. Kranz, H. Shin, B. Mizaikoff, W. Schuhmann. Analytical Chemistry 79 (2007) 5435.
58. K. Eckhard, W. Schuhmann. Analyst 133 (2008) 1486.
59. B. Ballesteros Katemann, A. Schulte, E.J. Calvo, M. Koudelka-Hep, W. Schuhmann. Electrochemical Communications 4 (2002) 134.

8.2

Uses of scanning electrochemical microscopy for the characterization of thin inhibitor films on reactive metals: The protection of copper surfaces by benzotriazole

8.2.1. Abstract

Scanning electrochemical microscopy (SECM) was used to study the film formation of benzotriazole towards corrosion of copper. SECM was operated in the feedback mode by using ferrocene-methanol as redox mediator, and the sample was left unbiased at all times to freely attain its open circuit potential in the test environment. Following exposure to aggressive electrolytes the anticorrosion abilities of the layers were characterised by image analysis and by an electrochemical method derived from the experimental approach curves. Changes in the shape of the approach curves were clearly observed during the inhibitor film formation process. They showed the transition from an active conducting behaviour towards ferrocinium reoxidation typical of unprotected copper, to a surface exhibiting insulating characteristics when the metal was covered by a surface film containing the inhibitor. This supports that SECM is a practical technique in the investigation of corrosion inhibitor performance. However, a consistent tendency for the characterization of inhibitor film formation using SECM measurements in the positive feedback mode for the copper-benzotriazole system was only found when the experiments were conducted when the inhibitor molecule was not present in the test solution. That is, inhibitor molecules were found to interact not only with the copper surface during the monitoring process, but to interact with the SECM tip as well, this effect being significantly enhanced when chloride ions were present in the electrolyte. Finally, a procedure to image the chemical activity of copper surfaces partially covered with the inhibitor film with SECM is proposed.

8.2.2. Resumen

En esta sección se ha empleado la microscopía electroquímica de barrido (SECM) para la caracterización de la formación de películas anticorrosivas de benzotriazol para la protección del cobre. Se ha operado con el SECM en modo de retroalimentación usando ferroceno-metanol como mediador redox, manteniendo la muestra sin polarizar en todo momento, permitiéndosele alcanzar su potencial de circuito abierto en el ambiente de ensayo. Se ha caracterizado la capacidad anticorrosiva de estas capas durante su posterior exposición a electrolitos agresivos, mediante el análisis de imágenes y métodos derivados de curvas de aproximación experimentales. Se han observado claramente cambios en la forma de las curvas de aproximación durante el proceso de formación de películas de inhibidor. Éstas mostraron una transición desde un comportamiento conductor con respecto a la reoxidación del ferroceno, típica del cobre sin proteger, a la aparición de unas características superficiales aislantes cuando el metal se encontraba cubierto por una película superficial de inhibidor. Los resultados ponen de manifiesto las capacidades del SECM como técnica práctica para la investigación del desarrollo de inhibidores de corrosión. Sin embargo, sólo cuando los experimentos se realizaban sin estar presente la molécula de inhibidor en la disolución de medida, se pudo encontrar una tendencia consistente con la caracterización de la formación de películas de inhibidor realizando medidas de SECM en el modo de retroalimentación positiva para este sistema cobre-benzotriazol. Esto es, se encontró que las moléculas interaccionan no sólo con la superficie del cobre durante el análisis, sino también con la punta del SECM, siendo este efecto especialmente significativo cuando los iones cloruro se encuentran presentes en el electrolito. Finalmente, se propone un procedimiento para visualizar la actividad química en superficies de cobre parcialmente recubiertas con películas de inhibidor.

8.2.3. Introduction

Microelectrochemical techniques are becoming essential tools in the study of corrosion reactions, because they provide new *in situ* information on the processes involved, which are resolved simultaneously in space and time [1,2]. Furthermore, new information concerning earlier steps in the corrosion mechanisms can be gained through the design of experimental methods which are based in operation modes of some of these techniques [3-7]. Among the microelectrochemical techniques, the scanning electrochemical microscope (SECM) [8] seems to be most especially suited for the investigation of such complex systems. It combines the local resolution characteristics of a scanning probe technique with the use of a microelectrode as sensing element, thus providing electrochemical resolution simultaneously. Thus, it is very appropriate to provide *in situ* topographic and electrochemical reactivity information about the surface evolution at the micrometer and submicrometer scales in aqueous solution. In addition, SECM has already been used in Corrosion Science for the detection of anodic and cathodic areas [9,10], the dissolution of metals [11], the investigation of the chemical stability of surface coatings [12,13], the degradation of organic films [14-22], the characterization of the metastable regime of pit nucleation [23], the detection of precursor sites for pitting inclusion dissolution [3,24,25], single pit generation [4-6,26-28], the monitoring of inclusion dissolution [29,30], and the imaging of surface changes during hydrogen permeation [31].

Another potential field of application for SECM in Corrosion Science is to study the film formation and destruction of corrosion inhibitor layers. Inhibition is one of the most important means for the protection of metals against corrosion. The effectiveness of organic inhibitors is related to the extent to which they adsorb and cover the metal oxide surface. The efficacy of inhibitors is normally investigated by gravimetric and electrochemical methods [32-39], including the electrochemical quartz crystal microbalance (EQCM) due to its ability to measure mass differences in the order of nanograms per surface area [40-45], and frequently assisted by surface analytical techniques such as X-ray photoelectron spectroscopy (XPS), Auger electron spectroscopy (AES), secondary ion mass spectrometry (SIMS), and laser micro mass analysis (LAMMA) [46-53]. Unfortunately, all these techniques exclusively provide global information as they lack enough spatial resolution, which is demanded to better understand the nature of the interactions and processes responsible for the inhibiting effect. Such knowledge is highly needed to elucidate the mechanisms involved, and it would facilitate inhibition to be optimized. This is the rationale behind the introduction of scanning probe microscopies (SPM) to this work. Yet its application has been reduced to investigate how metal dissolution in acids is influenced by the inhibitor films already produced on the metal samples from imaging the surface morphological changes occurring in micrometer and nanometer scales [52-57].

The aim of this Section is to explore the applicability of scanning electrochemical microscopy to the characterization of the formation and destruction of corrosion inhibiting films. The system copper/benzotriazole was chosen as an example of interface inhibition. Some investigation of this metal-inhibitor system with the SECM operated in the feedback mode has already been reported by Kontturi and co-workers [58-60], gaining information regarding the kinetics of film formation and on the effects of oxygen contents in the environment and of copper polarization in the inhibitive effect of benzotriazole. In those investigations, Z-approach curves were employed exclusively, and ferrocene-methanol had to be added to the electrolyte to serve as redox mediator at the ultramicroelectrode tip. Despite these antecedents, no attempts have yet been made either to obtain SECM images of the inhibitor-covered copper samples, or to investigate the behaviour of the inhibitor on unpolarized copper samples.

Copper is a metal with a low redox potential in aqueous solutions [61], and it constitutes a representative example for the study of the electrochemical behaviour of passive materials. Copper is extensively used in various industrial applications due to its interesting properties, namely high electrical and thermal conductivities. Moreover, it exhibits a high corrosion resistance due to the formation at its surface of an uniform and adherent oxide film by the corrosion process itself. This passive film protects copper from the aggressive medium. The onset of passivity has been related to the formation of copper oxide layers with a duplex structure, consisting in general terms of an inner Cu/Cu_2O porous and an outer CuO hydrated layers [62-65]. However, in spite of this self-protecting property, copper is susceptible to corrosion by acids and strong alkaline solutions, especially in the presence of oxygen or oxidants. An oxide surface layer can only be formed in weak acid or alkaline solutions.

Heterocyclic organic compounds containing nitrogen, sulphur or oxygen atoms are often used to protect metals from corrosion due to the ability of the heterocyclic atoms to easily form bonds with transition metals such as copper. Thus, several inhibitors like azoles, triazoles, and sulfoxide derivatives have been known and successfully been applied for the protection of copper [38,66], though until now, benzotriazole (BTAH) is probably the most efficient substance for the inhibition of copper corrosion in those environmental conditions, and it has become the most commonly used in practice.

The protecting effect of BTAH is based on the formation of a coordination polymer $[Cu(I)BTAH]_n$ on the surface of the metal featuring a Cu(I) center bridging between two BTAH molecules [67-69], and this layer inhibits the anodic reaction. Adsorption of BTAH is considered to be the initial step in the formation of the inhibiting layer, which is often represented as:

$$Cu\ (s) + BTAH\ (aq) = Cu{:}BTAH(ads) \qquad (8.2.1)$$

The adsorbed layer containing this molecule is insoluble in water, and its thickness varies with both pH and the concentration of BTAH [70]. Subsequent thickening of

the inhibiting layer is regarded to occur as Cu^+ species migrate through the Cu-BTAH layer which are necessary to form the Cu(I)-BTAH coordination polymer [71].

In this study the application of scanning electrochemical microscopy to study the film formation and the stability of the protective film formed on copper by benzotriazole (BTAH) is explored. The protection characteristics of the resulting layers against copper corrosion has been further investigated by considering the electrochemical behaviour of copper samples left unbiased at their open circuit potential in the aqueous environments containing either sulphate or chloride ions. SECM was operated in the feedback mode by using ferrocene-methanol as redox mediator, and the sample was left unbiased at all times to freely attain its open circuit potential in the test environment. Following exposure to aggressive electrolytes the anticorrosion protection abilities of the layers were characterised by image analysis and by an electrochemical method derived from the experimental approach curves. Additionally, the scanning vibrating electrode technique (SVET) [72,73] was employed in order to measure the local distribution of ionic current flows from both inhibitor-free and inhibitor-treated copper substrates, and complementary information to that obtained with the SECM could thus be obtained.

8.2.4. Experimental

8.2.4.1 Materials

The copper materials used in this study were available as copper sheets of thickness 1 mm and 99.99% purity supplied by Goodfellow (Cambridge, UK). They were cut into square specimens of area *ca*. 1 cm^2. The surface of the copper specimens was grounded mechanically with silicon carbide papers of 800 and 4000 grit and subsequently polished with aluminium micropolish (0.3 mm particle size). The resulting surfaces were degreased with acetone, abundantly rinsed with twice-distilled water and allowed to dry in air.

Benzotriazole (BTAH) (Avocado 15423) and ferrocene-methanol (Aldrich 335061) were used as received. Analytical grade potassium chloride (KCl), sodium chloride (NaCl) and sodium sulphate (Na_2SO_4) were employed to prepare the base aqueous electrolytes. All aqueous solutions were prepared using ultra-pure water purified with a Milli-Q system from Millipore. All measurements were performed at ambient temperature in the naturally aerated solutions.

SECM measurements were performed in both BTAH-free and BTAH-containing solutions, in order to establish eventual interactions between the organic molecule and the sensing platinum microelectrode. KCl and Na_2SO_4 solutions were employed as base electrolytes. Two different procedures were employed for the monitoring of the formation of inhibitor films on the copper surfaces, namely: (1) measurements in inhibitor-containing solutions (*in situ* experiments), BTAH was added to either base

electrolyte to attain a 0.33 mM concentration; and (2) measurements in inhibitor-free solutions (*ex situ* experiments), copper surfaces were first pretreated by immersing the metal plates in 0.1 M base electrolyte + 1 mM BTAH solutions for different immersion times between 2 to 70 min, subsequently removed and carefully rinsed with ultra-pure water, and finally immersed in 1 mM Na_2SO_4 solution to perform the SECM measurements.

On the other hand, SVET experiments were performed following the ex situ experimental procedure described above, with the only difference that the actual SVET measurements were performed in 10 mM NaCl solution, which provided an aggressive environment with low-conductivity to monitor the onset of corrosion reactions in the samples.

8.2.4.2 SECM instrumentation and experimental procedure

SECM experiments were carried out by using a Sensolytics scanning electrochemical microscope (Sensolytics, Bochum, Germany), controlled with a personal computer. All measurements were carried out in a three-electrode cell, located inside a Faraday cage. The electrodes were a 25 µm platinum microelectrode as the probe, an Ag/AgCl/KCl (3M) reference electrode and a platinum wire as counter electrode, all set up in a cell made of polytetrafluoroethene. Specimens were mounted horizontally facing upwards. In all experiments the copper sample was left unpolarized at its open-circuit corrosion potential. The micromanipulator stand of the SECM instrument was used to hold the microelectrode in place. Scans were conducted both vertically (Z-approach curves) and parallel (3D images) to the sample surface. The measurement of 3D images was performed with the microelectrode at a height of 15 µm over the specimen surface.

Ferrocene-methanol was added to the test electrolyte solutions to act as electrochemical mediator at the tip. The oxidation of this redox mediator at the microelectrode was used to establish the height of the tip over the coated surface as described elsewhere [20], and then to image the surface *in situ*. During the measurements, the potential of the tip was held at +0.50 V vs. the Ag/AgCl/KCl (3M) reference electrode to obtain a diffusion-limited tip current. In brief, the establishment of the operating tip distance over the sample was performed by slowly approaching the surface of an untreated copper sample with the tip and simultaneously recording the measured current at the microelectrode *vs. Z* displacement. In this way, the true distance between the tip and the substrate could be determined for the height at which the microelectrode displacement was stopped when recording the approach curve. The approaching microelectrode was stopped when the measured current either increased by 300% during the *in situ* tests, or decreased by 30% in the *ex situ* tests, with respect to the steady-state value in the bulk of the electrolyte (in the forecoming, this position of the tip relative to the sample will be referred as the closest distance attained during the measurement of the approach curves in the "*in situ* tests"). After the corresponding Z-approach

curve was obtained, it was modelled assuming that the reduction of the mediator at the surface was under kinetic control [74]. Subsequently, the tip was withdrawn to a distance of 250 μm from the sample surface, and the CV for the ferrocene-methanol/ferrocinium redox process was registered in order to monitor the surface state of the Pt microelectrode. After electrolyte exchange for the inhibitor-containing electrolyte to be placed in site, a new Z-approach curve could be measured by approaching the surface until the closest distance attained during the measurement of the approach curve for the untreated copper sample. When 3D images of the chemical reactivity of the surface were to be recorded, the tip was always withdrawn to a distance of 15 μm from the sample surface (i.e. constant height), and the positioning motors were employed to move the tip parallel to the surface at a scan rate of 30 μm s^{-1}. All the 3D maps shown were recorded by shifting the microelectrode tip from left to right (i.e., they were built as a composition of *X* displacement lines, which were stepwise shifted in the *Y* direction).

8.2.4.3. SVET instrumentation and experimental procedure

The SVET instrumentation was manufactured by Applicable Electronics Inc. (MA, USA) and controlled by dedicated software. Further details can be found in the literature [75]. The technique is based upon the measurement of small potential variations in solution, associated to the ionic fluxes that arise from active sites at the surface due to metal corrosion, which originate a very minute electric field within an electrolyte medium [76]. The distribution of potentials and currents on the surface of the sample can be theoretically determined from the application of Laplace's equations and Ohm's law [72,77]. The microelectrode had a platinum tip with a diameter of 20 μm, the amplitude of the probe vibration was 20 μm, both parallel and normal to the surface, and its main position was located at a distance of 100 μm from the sample. A calibration routine converts the measured potentials into current densities at the corroding surface [78]. The results are displayed as three-dimensional plots, with the current density (*Z*-direction) plotted as a function of the *X*-*Y* position in the probe scan plane. A video microscope was used to aid microelectrode positioning and sample levelling using three thumbscrews arranged in a tripod configuration before the test electrolyte was introduced in the electrochemical cell. Furthermore, video microscope images were taken *in situ* both before and after recording each SVET map to assist in the observation of the most significant features occurring on the substrate surface with the elapse of time.

8.2.5. Results and discussion

SECM was operated in the feedback mode to follow the kinetics of BTAH adsorption on copper, by monitoring the surface ability for electron transfer to ferrocinium species generated at the microelectrode tip. The eventual blockage of

the active sites due to the adsorption of the inhibitor was thus investigated. Both vertical *Z*-approach curves and *X-Y* scans were recorded for that purpose.

8.2.5.1. Use of ferrocene-methanol as redox mediator for SECM measurements

SECM operation in the feedback mode required a suitable redox mediator to be added to the test electrolyte. Special caution had to be taken in relation to the choice of this electrochemical species in order to secure no spurious effects could be caused on the investigated copper and copper-BTAH samples due to either direct reaction or potential modification. The second effect is especially relevant for the system under investigation since reversible redox couples would modify the potential at the interface as predicted by the Nernst equation [79]. That is, the potential of the substrate could be determined by the redox mediator species if both species are simultaneously present in the environment. Both reported effects could be avoided by selecting ferrocene-methanol as redox mediator in the investigation. The redox potential for ferrocene-methanol oxidation to ferrocinium ion occurs at potential values very positive compared to the open circuit potential of the copper samples, thus maintaining ferrocene-methanol as the only stable species from this redox couple present in the electrolyte. The Nernst equation can only apply if the open circuit potential of the system under investigation would shift positively beyond the onset of ferrocene-methanol oxidation, in which case both ferrocene-methanol and the ferrocinium ion will be present in the electrolyte, and the potential would be determined by their concentration ratio.

8.2.5.2. SECM Z-approach measurements

Approach curves are obtained when the SECM-microelectrode is moved towards the surface in a controlled motion, with the result of variations in the signal measured at the tip as result of the near field effect originating in the proximity of the sample. The potential of the tip is set at +0.50 V vs. Ag/AgCl/KCl (3M) [15] to attain the diffusion-controlled oxidation of ferrocene-methanol to ferrocinium. Different behaviours are observed in conventional amperometric SECM depending on the conductive or insulating characteristics of the sample, which originate positive or negative feedback effects, respectively. These feedback effects could be employed to image the surface under investigation provided the sample is chemically-homogeneous and thus changes in the faradaic current measured at the tip could be directly correlated to the topography of the scanned surface.

8.2.5.2.1. In situ experiments

Figure 8.2.1 shows selected Z-approach curves measured at different elapse times during the immersion of a copper sample in a sodium sulphate solution containing BTAH as corrosion inhibitor. All the plots were recorded by using the same maximum and minimum tip-substrate distances as chosen from the first approach

curve determined as soon as the electrolyte was introduced in the electrochemical cell. From the inspection of this first amperometric curve, the characteristic positive-feedback behaviour of free copper can be clearly observed whereas the SECM tip approaches the surface, which is due to the regeneration of the ferrocene-methanol species on the conductive copper substrate. But with the elapse of time, the extent of this effect progressively diminishes, and it becomes hardly noticeable from the approach curve recorded at the end of the experiment (i.e., 17 hours) under the same scale. Despite the decrease of the positive feedback effect for longer exposures, no negative feedback effect was observed at any time in the system under these experimental conditions.

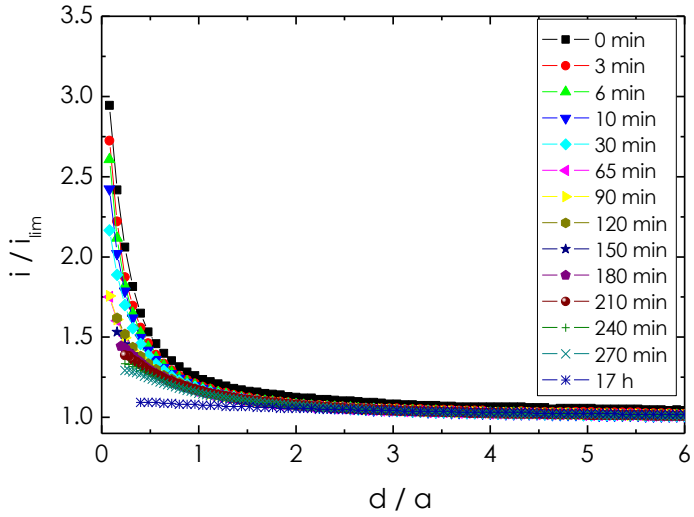

Figure 8.2.1. SECM normalized Z-approach curves towards a copper surface measured in BTAH-containing electrolyte (i.e. "*in situ* test"). Experiments were carried out in a 0.067 M Na_2SO_4 + 0.33 mM BTAH + 0.67 mM ferrocene-methanol solution with a 25 μm Pt electrode. Tip potential: +0.50 V vs. Ag/AgCl/KCl (3M). The sample was left at its spontaneous open circuit potential in the electrolyte and the curves were measured for the immersion times indicated in the figure. The time values indicate the moment when the approach curve was initiated in relation to electrolyte exchange as described in the text; *t*=0 corresponds to the inhibitor-free electrolyte. i / i_{lim} is the dimensionless tip current, and d / a is the dimensionless distance between the sample and the tip.

It has been shown that the formation and subsequent growth of the inhibitor-containing film adsorbed on the surface of the copper sample progressively hinders the regeneration of ferrocene-methanol at the substrate, whereas diffusion of the redox mediator from the bulk electrolyte is made difficult when the tip-substrate distance is below one tip diameter because it occurs in the thin-electrolyte column existing below the tip. The net outcome is that smaller faradaic currents are measured at the tip for a given tip-substrate distance with the increase of immersion time, which is due to the adsorption of BTAH and the subsequent formation of the coordination polymer Cu(I)BTAH on the metal surface, thus originating a less-conductive substrate. An alternate procedure to follow the formation of the inhibitor film with time from the SECM measurements consists in plotting the values of the

current measured at the distance of maximum approach employed in the work as a function of immersion time as depicted in Figure 8.2.2. In this way the major decrease in current is found to occur during the first 50 minutes of immersion, and it progressive levels off for longer exposures (for the sake of clarity, only the values determined during the first 300 min are shown in the plot).

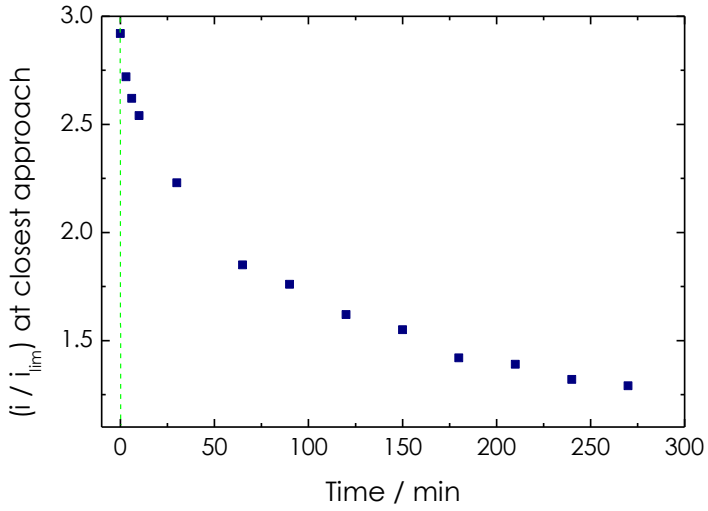

Figure 8.2.2. Time evolution of the normalized current values measured when the tip was placed at the closest distance attained during the measurement of the approach curves in the "*in situ* tests". Experiments were carried out in a 0.067 M Na_2SO_4 + 0.33 mM BTAH + 0.67 mM ferrocene-methanol solution with a 25 μm Pt electrode. Tip potential: +0.50 V vs. Ag/AgCl/KCl (3M).

Similar experiments were conducted when the electrolyte contained chloride ions instead of sulphate ions, though at the same concentration, and the measured Z-approach curves are depicted in Figure 8.2.3. Though the positive feedback behaviour also occurred when the Z-approach curves were measured in the chloride-containing solution, significant changes in both the shape and the time evolution of these plots could be observed when they were compared with those determined in the sulphate base electrolyte (cf. Figures 8.2.1 and 8.2.3).

Firstly, all the plots show normalized currents significantly smaller than those found for the sulphate-containing electrolyte (i.e., the current values of these approach curves are comparable to those obtained for exposures in excess of 240 min in Figure 8.2.1). Secondly, the approach curves in Figure 8.2.3 exhibit very similar relationships between the current and the tip-substrate distance regardless the exposure time in the test environment, and even compared to the inhibitor-free condition. These two features may indicate that the adsorption of BTAH at the copper surface in the presence of free chloride ions in the electrolyte occurs significantly faster than in sodium sulphate solution, and that the initially formed inhibiting film exhibits enhanced insulating characteristics towards charge transfer. On the other hand, details on the kinetics of film formation from the SECM measurements could be attempted by plotting the values of the current measured

at the distance of maximum approach as a function of immersion time, which is given in Figure 8.2.4.

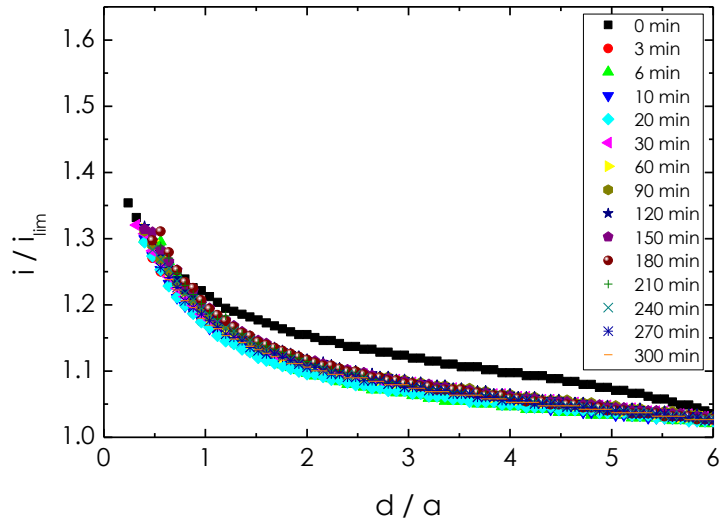

Figure 8.2.3. SECM normalized Z-approach curves towards a copper surface measured in BTAH-containing electrolyte (i.e. "*in situ* test"). Experiments were carried out in a 0.067 M KCl + 0.33 mM BTAH + 0.67 mM ferrocene-methanol solution with a 25 μm Pt electrode. Tip potential: +0.50 V vs. Ag/AgCl/KCl (3M). The sample was left at its spontaneous open circuit potential in the electrolyte and the curves were measured for the immersion times indicated in the figure. The time values indicate the moment when the approach curve was initiated in relation to electrolyte exchange as described in the text; t = 0 corresponds to the inhibitor-free electrolyte. i / i_{lim} is the dimensionless tip current, and d / a is the dimensionless distance between the sample and the tip.

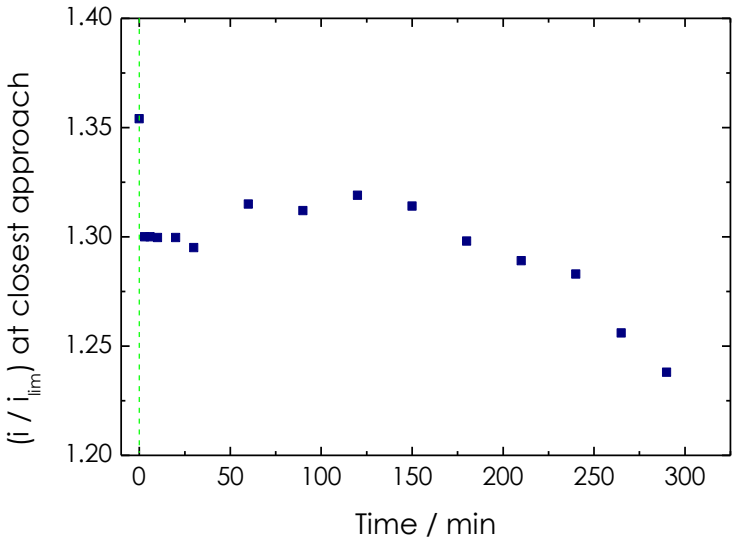

Figure 8.2.4. Time evolution of the normalized current values measured when the tip was placed at the closest distance attained during the measurement of the approach curves in the "*in situ* tests". Experiments were carried out in a 0.067 M KCl + 0.33 mM BTAH + 0.67 mM ferrocene-methanol solution with a 25 μm Pt electrode. Tip potential: +0.50 V vs. Ag/AgCl/KCl (3M).

The measurements seem to support that the protecting characteristics of the inhibitor film do not improve as compared to those formed during the first minute for exposures up to ca. 200 min, but rather to be slightly more conductive (i.e. less protective) during this period of time, with a maximum around 100 min. On the other hand, when the sample is exposed to the inhibitor-containing medium in excess of 200 min, the inhibitor film progressively improves as time elapses.

The rather striking behaviour of the Cu-BTAH system in a chloride-containing electrolyte just mentioned can be understood when the absolute current values measured at the SECM tip are considered instead. Tables 8.2.1 and 8.2.2 show the absolute current values measured at the distances of maximum and minimum approach from the Z-approach curves in either chloride or sulphate base electrolytes when they contain 0.33 mM BTAH. The following observations can be made for a given microelectrode geometry and redox mediator concentration, namely: (1) the diffusion-limited current for ferrocene-methanol oxidation, i_{lim}, is always smaller when benzotriazole is present in the test electrolyte; (2) the values of i_{lim} consistently decrease as time elapses for the SECM tip immersed in an electrolyte containing the inhibitor molecule; (3) the magnitude of the positive feedback effect, as determined from the current values (i_{max}) measured at the tip when the minimum tip-substrate distance is attained, strongly depends on the composition of the base electrolyte, which is an evidence of the different chemical characteristics of the passive film developed on copper in contact from each electrolyte; and (4) the i_{max} values decrease as time elapses in the inhibitor-containing electrolyte, though they do not show the progressive dependency that can be found for i_{lim} values instead.

Table 8.2.1. Time evolution of the absolute current values measured when the SECM tip was placed at the point of closest approach to the surface (i_{max}) and in the bulk electrolyte (i_{lim}) during "*in situ* tests" carried out in a 0.067 M Na_2SO_4 + 0.33 mM BTAH + 0.67 mM ferrocene-methanol solution with a 25 μm Pt electrode.

Time / min	i_{max} / nA	i_{lim} / nA
0	6.53	2.16
3	6.62	2.37
6	6.46	2.40
10	6.25	2.39
30	5.12	2.23
65	4.20	2.21
90	3.93	2.18
120	3.60	2.18
150	3.41	2.20
180	3.19	2.21
210	3.08	2.22
240	2.99	2.24
270	2.92	2.26
10200	1.77	1.61

Table 8.2.2. Time evolution of the absolute current values measured when the SECM tip was placed at the point of closest approach to the surface (i_{max}) and in the bulk electrolyte (i_{lim}) during "*in situ* tests" carried out in a 0.067 M KCl + 0.33 mM BTAH + 0.67 mM ferrocene-methanol solution with a 25 μm Pt electrode.

Time / min	i_{max} / nA	i_{lim} / nA
0	3.15	2.15
3	3.14	2.40
6	3.08	2.37
10	3.11	2.37
20	3.14	2.40
30	3.06	2.31
45	3.05	2.30
60	3.07	2.32
90	3.06	2.31
120	3.03	2.30
150	2.97	2.26
180	2.89	2.22
210	2.81	2.18
240	2.73	2.13
265	2.50	1.99
290	2.35	1.89

A satisfactory explanation for these facts must account for both the decrease in the diffusion-limited currents measured at the tip in the bulk electrolyte, and the smaller magnitude of the positive feedback effect during the *in situ* experiments when the base electrolyte contains chloride instead of sulphate. The steady decrease in the diffusion-limited currents with time measured when the tip is located far from the metal substrate is due to the interaction of the benzotriazole molecule with the platinum surface of the UME, which results in the partial blockage of the sensing tip, and hinders the application of SECM to characterize this reactive system. The decrease in the active area of the UME is clearly followed by measuring cyclic voltammograms for the ferrocene-methanol/ferrocinium system in benzotriazole-containing solutions just after recording the corresponding Z-approach curves. The CV's displayed in Figures 8.2.5 and 8.2.6 were measured when the tip was located at a height of 250 μm from the sample surface. It is directly observable that the magnitude of the diffusion-limited current for ferrocene-methanol oxidation in the chloride-containing electrolyte continuously decreased with the elapse of time, an indication that the active area of the Pt microelectrode was effectively reduced due to the interaction of the organic inhibitor molecule with the metal, whereas such an effect was significantly smaller when the sulphate-based electrolyte was employed instead and required longer exposures to be significant (cf. the CV measured after 1020 min exposure in the electrolyte).

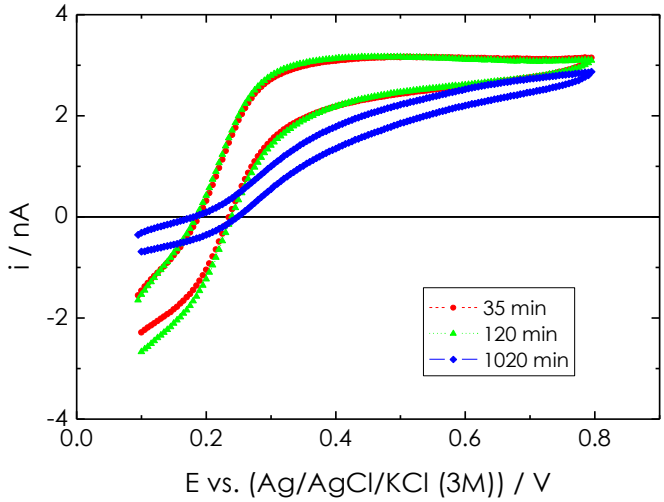

Figure 8.2.5. Cyclic voltammograms measured at the SECM-tip in a 0.067 M Na_2SO_4 + 0.33 mM BTAH + 0.67 mM ferrocene-methanol solution with a 25 μm Pt electrode. Tip-substrate distance: 250 μm. Scan rate: v = 0.10 V s^{-1}. The voltammograms were measured just before recording the Z-approach curves shown in Figure 8.2.1. The curves correspond to the immersion times indicated in the figure.

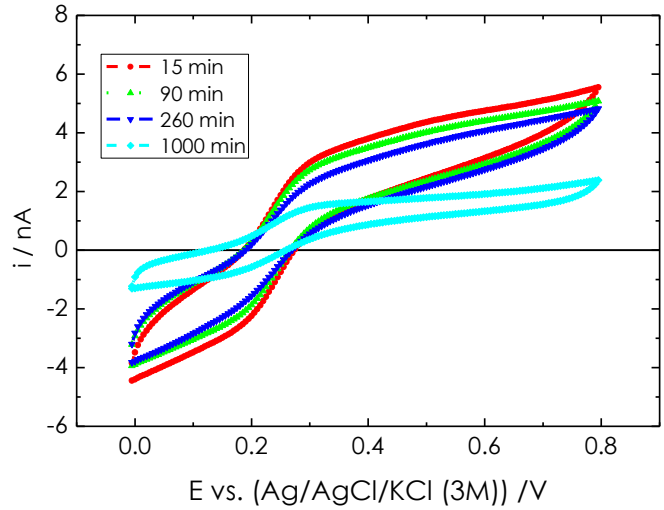

Figure 8.2.6. Cyclic voltammograms measured at the SECM-tip in a 0.067 M KCl + 0.33 mM BTAH + 0.67 mM ferrocene-methanol solution with a 25 μm Pt electrode. Tip-substrate distance: 250 μm. Scan rate: v = 0.10 V s^{-1}. The voltammograms were measured just before recording the Z-approach curves shown in Figure 8.2.3. The curves correspond to the immersion times indicated in the figure.

Therefore, the surface of the sensing microelectrode is sensitive to modification by the benzotriazole molecule, and the reported changes in the faradaic currents measured at the Pt tip cannot be exclusively attributed to variations in the tip-substrate distance and the chemical state of the copper substrate, hindering the SECM to be employed to monitor the Cu-BTAH films when the benzotriazole molecule is present in the electrolyte ("*in* situ tests"), and it would

require to search for a different electrode material that would show no interaction with BTAH for the fabrication of the SECM tip. Since this feature is less notorious for the samples immersed in the Na_2SO_4 base electrolyte, it may have passed unnoticed in previous investigations from another laboratory [58-60]. Nevertheless, the interaction between platinum and benzotriazole cannot be neglected from the observations gathered during this work. On the other hand, it is impossible to establish from these measurements whether the formation of an inhibiting film on the copper surface from a chloride-containing electrolyte is faster than in sulphate, due to the reported uncertainties in the active area of the measuring tip, and it would be further addressed on the basis of the *ex situ* experiments described next.

8.2.5.2.2. Ex situ experiments

In the previous Section 8.2.5.2.1, it has been demonstrated that the method to investigate the kinetics of inhibitor film formation based on the measurement of Z-approach curves with the SECM cannot be applied when the experiments are performed *in situ*, that is, in the inhibitor-containing electrolytes, because the adsorbing molecule will interact both with the metal surface to be protected and with the monitoring tip. To overcome this problem, *ex situ* experiments were next performed. The copper samples were treated by immersion in the inhibitor-containing electrolytes for selected times, subsequently removed and carefully rinsed with high-purity water, and the protection characteristics of the inhibitor films formed on the metal was investigated by SECM in an electrochemical cell containing a 1 mM Na_2SO_4 solution using 1mM ferrocene-methanol as redox mediator.

Figure 8.2.7 displays the Z-approach curves measured for copper samples pre-treated in 0.1 M Na_2SO_4 + 1 mM BTAH solution for different exposures as indicated. The positive feedback behaviour is clearly observed for those samples exposed to the inhibitor up to 70 min, whereas the apparent negative feedback effect is found for significantly longer immersion times. The reason for this apparent negative feedback behaviour originates from the slower kinetics for ferrocinium reduction at the surface due to the progressive coverage of the sample by BTAH. A consistent decrease in the values of the normalized current measured at the tip for given tip-substrate distances is observed due to the progress of BTAH adsorption leading to either a greater surface coverage or the thickening of the inhibitor-containing passivating film as the duration of the treatment increases. The insulating characteristics of the protecting surface film improve as the film thickens, and the regeneration of ferrocene-methanol on the substrate is progressively hindered. Regeneration of the redox mediator is eventually completely impeded when a certain thickness of the surface film is attained, and then only a negative feedback effect can be observed.

The same *ex situ* experiment was conducted for copper samples protected with benzotriazole through their immersion in a chloride-containing electrolyte, and the measured Z-approach curves are plotted in Figure 8.2.8.

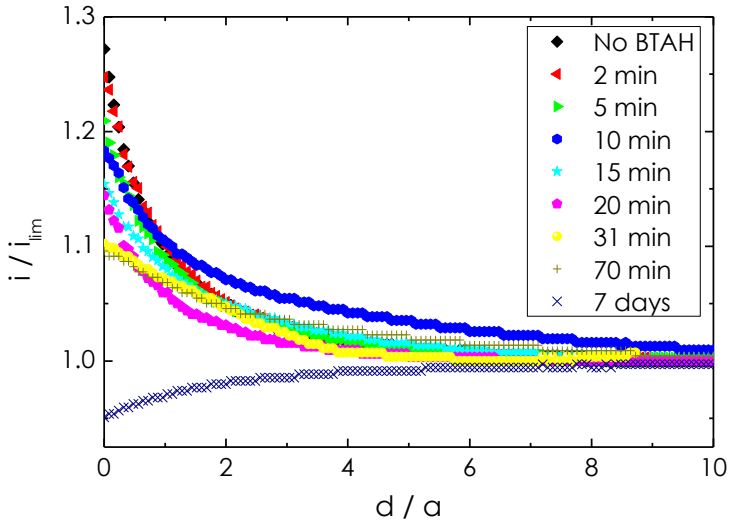

Figure 8.2.7. SECM normalized *Z*-approach curves towards a copper surface measured in an inhibitor-free electrolyte (i.e. "*ex situ* test"). The pre-treatment of the copper samples was conducted in 0.1 M Na_2SO_4 + 1 mM BTAH solution for different immersion times as indicated in the figure. SECM experiments were carried out in a 1 mM Na_2SO_4 + 1 mM ferrocene-methanol solution with a 25 μm Pt electrode. Tip potential: +0.50 V vs. Ag/AgCl/KCl (3M). The sample was left at its spontaneous open circuit potential in the electrolyte. i / i_{lim} is the dimensionless tip current, and d / a is the dimensionless distance between the sample and the tip.

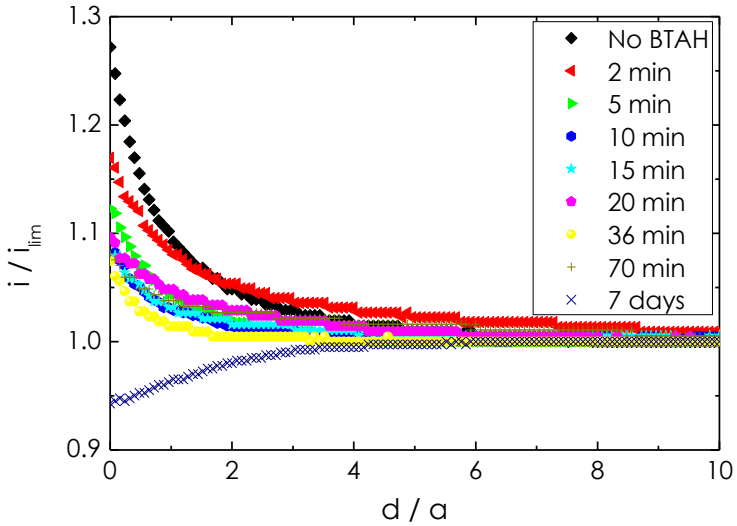

Figure 8.2.8. SECM normalized z-approach curves towards a copper surface measured in an inhibitor-free electrolyte (i.e. "*ex situ* test"). The pre-treatment of the copper samples was conducted in 0.1 M KCl + 1 mM BTAH solution for different immersion times as indicated in the figure. SECM experiments were carried out in a 1 mM Na_2SO_4 + 1 mM ferrocene-methanol solution with a 25 μm Pt electrode. Tip potential: +0.50 V vs. Ag/AgCl/KCl (3M). The sample was left at its spontaneous open circuit potential in the electrolyte. i / i_{lim} is the dimensionless tip current, and d / a is the dimensionless distance between the sample and the tip.

From the inspection of these figures, the same general trends reported above for the samples treated in sulphate environment are observed, though it must be noted that the decrease in the currents for the positive feedback effect occurs faster in the case of those samples preconditioned in the chloride-containing electrolyte. This feature is more pronounced for the samples subjected to the shorter exposures, especially during the first 5 minutes of the treatment, an observation which is consistent with previous observations [80]. Therefore, the adsorption of BTAH on the copper surface is favoured by chloride ions, as well as the subsequent growth of the inhibiting passive film as compared to the behaviour of the system in a sulphate base electrolyte containing the same concentration of the inhibitor molecule. With the objective to facilitate the comparison of these results, a plot displaying the time evolution of the normalized current values measured when the tip was placed at the closest distance attained during the measurement of the approach curves depicted in Figures 8.2.7 and 8.2.8 was prepared, and it is depicted in Figure 8.2.9. Significantly smaller values are found for the dimensionless currents measured during the *ex situ* experiments. Therefore, it can be concluded that the progressive blockage of the active surface of the SECM tip by the benzotriazole molecules led to an overestimation of the normalized currents plotted in Figures 8.2.2 and 8.2.4, and this variation was significant even during the period of time employed to record the approaching curve. Conversely, consistent time dependences are only observed for the inhibitive films formed *ex situ*, as observed from the comparison of Figures 8.2.2, 8.2.4 and 8.2.9.

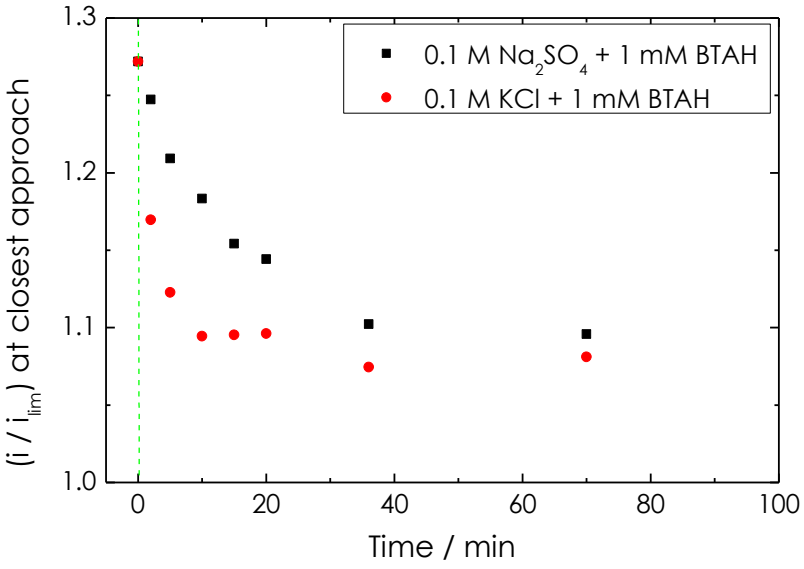

Figure 8.2.9. Time evolution of the normalized current values measured when the tip was placed at the closest distance attained during the measurement of the approach curves depicted in Figures 8.2.7 and 8.2.8 corresponding to "*ex situ* tests" following treatment in the solutions given in the plot.

8.2.5.3. SECM X-Y maps

The *ex situ* preconditioning procedure developed in Section 8.2.5.2.2 was next employed to prepare copper samples presenting various regions of different surface activity. The first set of experiments corresponds to that of bare copper and Cu-BTAH treated during different times in either sulphate- or chloride-base electrolytes. Inhibitor-modified regions were obtained by dipping a freshly-polished copper sample in the BTAH-containing solution a half of its length for the chosen pre-treatment times, and subsequently rotated 90º to dip a half of its width for another exposure. In this way, the resulting copper samples display four regions of different surface coverage by the inhibitor molecule, which correspond to bare copper, Cu-BTAH treated for 5 min, Cu-BTAH treated for 10 min, and Cu-BTAH treated for 15 min.

The samples were subsequently immersed in 1 mM Na_2SO_4 + 1 mM ferrocene-methanol test solution and were left at their spontaneous open circuit potential in the electrolyte. The SECM images were recorded by rastering the tip at a constant height of 15 μm selecting an area of the sample that would extend over portions of the 4 regions presenting different surface finishes, and the resulting SECM maps are depicted in Figures 8.2.10 and 8.2.11. In both cases, the highest currents were observed above the untreated copper regions due to the regeneration of ferrocene-methanol over the free metal, whereas significantly smaller currents were measured above the BTAH-modified portions. Indeed, differences in surface reactivity among the regions covered by the inhibitor can be found in both SECM maps, which can be directly related to the duration of the pre-treatment in the inhibitor-containing environment. Thus, the smallest currents were found above the Cu-BTAH portion pre-treated for 15 minutes, though the effect is already clear when the pre-treatment only lasted 5 minutes, because the currents measured from that region are only slightly bigger than those from the portion pre-treated for 15 minutes.

Though differences in surface activity could be readily observed among the Cu-BTAH films formed in a given environment due to the formation of thicker films at longer exposures, the direct comparison of the SECM maps depicted in Figures 8.2.10 and 8.2.11 do not allow possible changes in chemical reactivity due to the nature of the base electrolyte to be distinguished, i.e., to establish whether a specific effect of chloride ions towards the local chemistry of the resulting Cu-BTAH films occurs. To this end, a second set of experiments was conducted as described next. They consisted in a pre-treatment stage to form the Cu-BTAH film by dipping a freshly-polished copper sample in the inhibitor-containing solution for 7 days. After the sample was removed and gently rinsed with ultra-pure water, the stability of the Cu-BTAH films was investigated by exposing portions of the treated surface to an aggressive electrolyte solution such as 3 wt.% NaCl for various chosen exposure times. Four different conditions could be attained for each sample by following a procedure similar to that described in the previous paragraph. That is, about a half of the length of the sample was immersed for 16 hours, and subsequently rotated 90º to dip a half of its width for an extra 8 hours exposure. In this way, the Cu-BTAH samples would present four different zones corresponding to a non-exposed, and to exposures of 8, 16 and 24 hours duration to the chloride environment, respectively.

The samples were subsequently imaged in 1 mM Na_2SO_4 + 1 mM ferrocene-methanol test solution by rastering the SECM tip at a constant height of 15 μm selecting an area of the sample that would extend over portions of the 4 regions presenting different surface attacks.

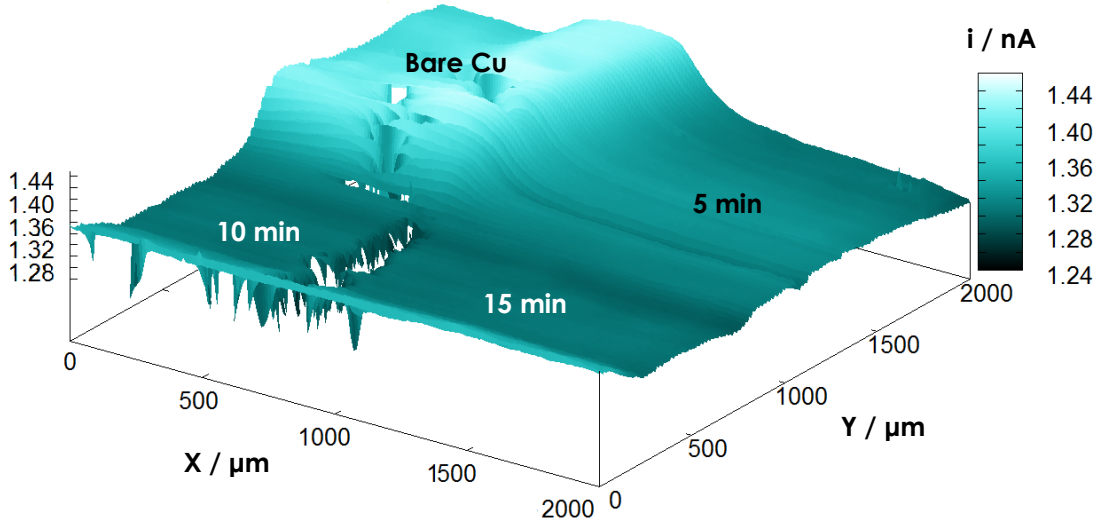

Figure 8.2.10. Image generated by SECM of an untreated Cu – Cu-BTAH (5 min pre-treatment) – Cu-BTAH (10 min pre-treatment) – Cu-BTAH (15 min pre-treatment) system immersed in 1 mM Na_2SO_4 + 1 mM ferrocene-methanol solution with a 25 μm Pt electrode. The pre-treatment of the copper samples was conducted in 0.1 M KCl + 1 mM BTAH solution. Tip-substrate distance: 15 μm. Tip potential: +0.50 V vs. Ag/AgCl/KCl (3M). The *Z* scale is the tip current in nA. The sample was left at its spontaneous open circuit potential in the electrolyte.

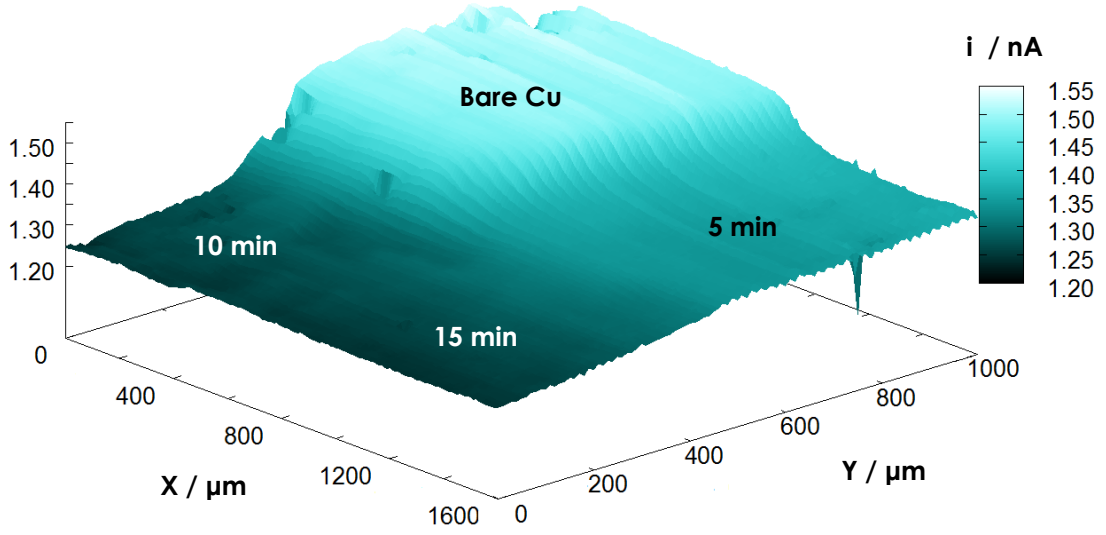

Figure 8.2.11. Image generated by SECM of a untreated Cu – Cu-BTAH (5 min pre-treatment) – Cu-BTAH (10 min pre-treatment) – Cu-BTAH (15 min pre-treatment) system immersed in 1 mM Na_2SO_4 + 1 mM ferrocene-methanol solution with a 25 μm Pt electrode. The pre-treatment of the copper samples was conducted in 0.1 M Na_2SO_4 + 1 mM BTAH solution. Tip-substrate distance: 15 μm. Tip potential: +0.50 V vs. Ag/AgCl/KCl (3M). The *Z* scale is the tip current in nA. The sample was left at its spontaneous open circuit potential in the electrolyte.

Figures 8.2.12 and 8.2.13 display the maps obtained for the Cu-BTAH films formed in sulphate- and chloride-containing environments, respectively. The extent of chloride attack towards the Cu-BTAH film can be seen as variations in the faradic current measured at the tip for ferrocene-methanol oxidation. The lowest currents are always observed for the zone that was not exposed to 3 wt.% NaCl solution, and bigger currents are measured when the tip passes over those regions that have been exposed for longer periods of time. Yet, a major difference can be observed from the comparison of Figures 8.2.12 and 8.2.13. The Cu-BTAH film formed in the presence of sulphate ions is less resistant against the attack of the chloride ions in the inhibitor-free test environment, and deteriorates quite significantly during the duration of the experiments as demonstrated from the measurement of currents above the zone exposed during 24 hours that are effectively twice those measured above the unexposed zone (namely 1.0 and 0.5 nA, respectively, in Figure 8.2.12). Conversely, the currents measured above the equivalent zones for the Cu-inhibitor film formed in a chloride-containing medium only amount to 0.68 and 0.58 nA, respectively. This observation agrees with previous observations that a key factor in the formation of a Cu-BTAH film is the concentration of chloride ions in solution [81]. Furthermore, this experiment allows variations in the chemical stability of surface films formed in different conditions to be distinguished when imaged with the SECM during their exposure to an aggressive environment.

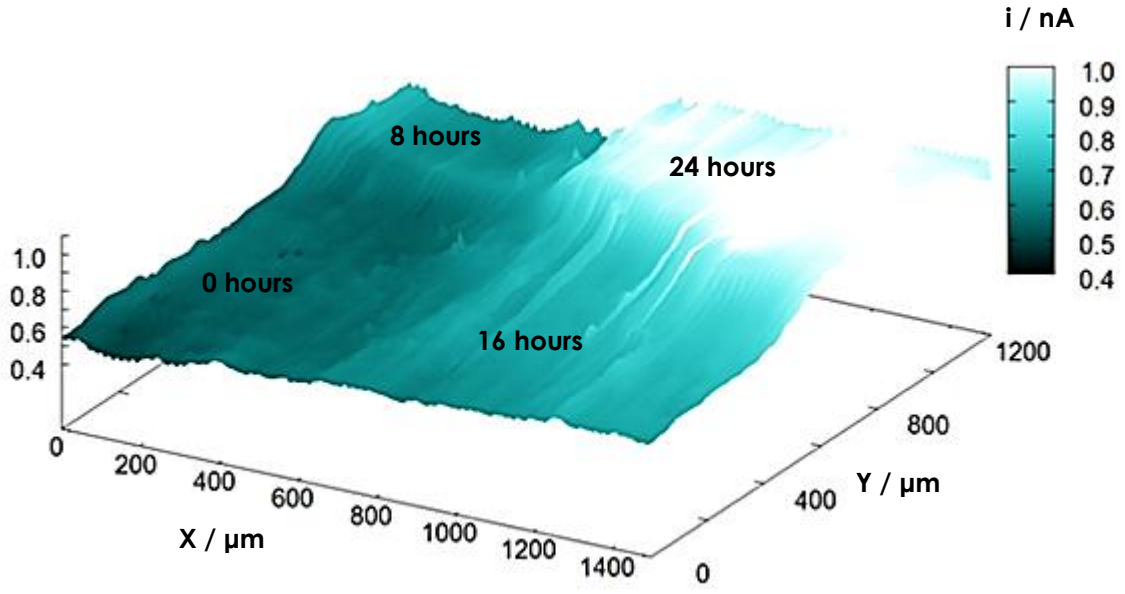

Figure 8.2.12. Image generated by SECM of a copper sample displaying 4 zones of different electrochemical activity during immersion in 1 mM Na_2SO_4 + 1 mM ferrocene-methanol solution with a 25 µm Pt electrode. The copper sample was first treated during 7 days in 0.1 M Na_2SO_4 + 1 mM BTAH solution to form a Cu-BTAH inhibitive film. The corrosion resistance characteristics of the Cu-BTAH inhibitive film was investigated by exposing the sample to 3 wt.% NaCl solution for the various times indicated on the figure. Tip-substrate distance: 15 µm. Tip potential: +0.50 V vs. Ag/AgCl/KCl (3M). The *Z* scale is the tip current in nA. The sample was left at its spontaneous open circuit potential in the electrolyte.

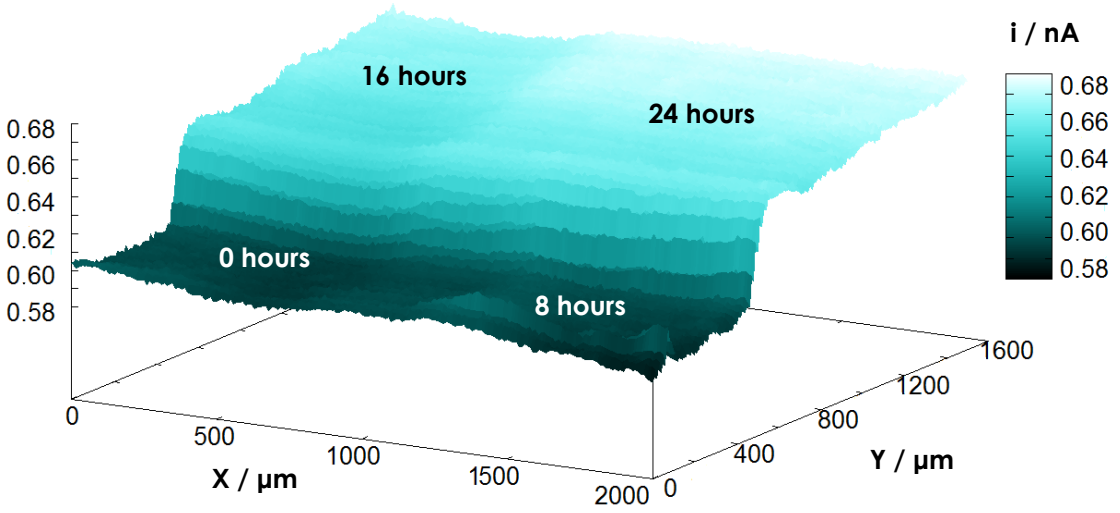

Figure 8.2.13. Image generated by SECM of a copper sample displaying 4 zones of different electrochemical activity during immersion in 1 mM Na_2SO_4 + 1 mM ferrocene-methanol solution with a 25 µm Pt electrode. The copper sample was first treated during 7 days in 0.1 M KCl + 1 mM BTAH solution to form a Cu-BTAH inhibitive film. The corrosion resistance characteristics of the Cu-BTAH inhibitive film was investigated by exposing the sample to 3 wt.% NaCl solution for the various times indicated on the figure. Tip-substrate distance: 15 µm. Tip potential: +0.50 V vs. Ag/AgCl/KCl (3M). The Z scale is the tip current in nA. The sample was left at its spontaneous open circuit potential in the electrolyte.

A final notice should be given in relation to the SECM images depicted in Figures 8.2.10-13. They do not provide any topographical information as to consider that certain areas of the surface may be more prominent than others. The thicknesses of the Cu-BTAH films formed in this Section are below the detection limit of the technique as it corresponds to thin layers. Yet, differences in the electrochemical activity among different regions on the samples due to variations in the thickness and the surface coverage of the Cu-inhibitor films are imaged by SECM. The occurrence of surface reactivity in these systems is further demonstrated when a Cu-BTAH system exhibiting two regions of different inhibitor coverages which was imaged with the scanning vibrating electrode technique (SVET) in a solution free from ferrocene-methanol. The system was produced by dipping in 0.1 M Na_2SO_4 + 1 mM BTAH a freshly-polished copper sample for about a half of its length from either side for the chosen pre-treatment times. Only a partial coverage of the metal surface was achieved when the sample was exposed for 3 seconds in the inhibitor-containing solution, whereas a rather continuous film occurred in the portion immersed during 60 minutes.

The SVET images given in Figure 8.2.14 show that corrosion of the metal occurs above the region that was exposed to BTAH during 3 seconds, with the development of a distribution of localized microanodes and microcathodes which are sources for the ionic flux of metal cations and hydroxyl anions, respectively. No evidence of electrochemical activity is observed at any times above the portion of the surface covered with the Cu-BTAH film in this mild corrosive medium.

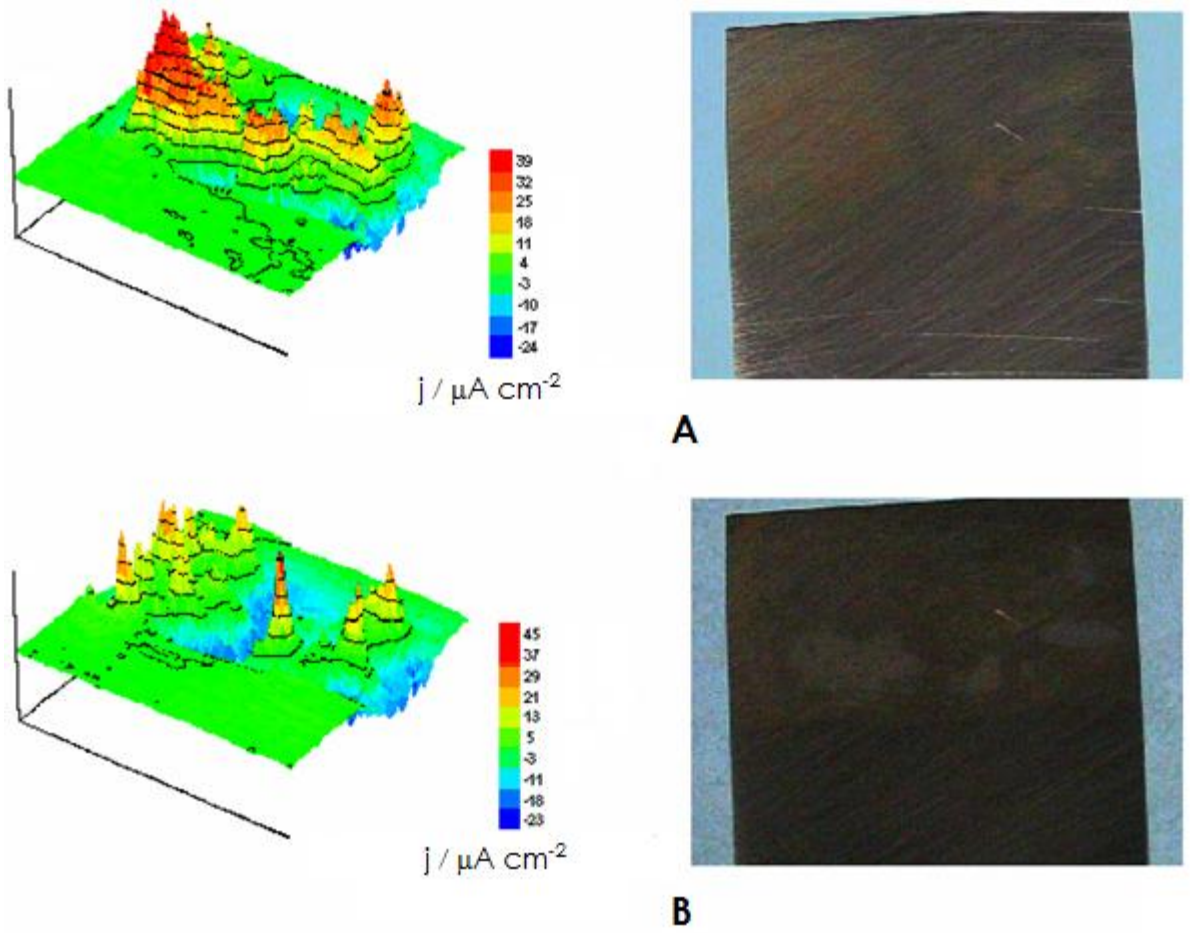

Figure 8.2.14. Images generated by SVET (left) and video microscope (right) of a Cu-BTAH (3 s pre-treatment) – Cu-BTAH (1 h pre-treatment) system immersed in 10 mM KCl for (A) 15 min, and (B) 195 min. The pre-treatment of the copper samples was conducted in 0.1 M Na_2SO_4 + 1 mM BTAH solution for the chosen immersion times. Tip-substrate distance: 100 µm. The *Z* scale is the ionic current in µA cm^{-2}. The figures represent an area of 8000 µm x 8000 µm in *X* and *Y* directions. The sample was left at its spontaneous open circuit potential in the electrolyte.

8.2.6. Conclusions

The operations and basic requirements for scanning electrochemical microscopy to be successfully employed for the characterization of thin inhibitor films formed on reactive metals such as copper are described. The reported data show promising results based in the measurement of *Z*-approach curves and spatially-resolved 3D images of the electrochemical activity of substrates when SECM is operated in the feedback mode.

Though *in situ* SECM experiments can be performed for this system, that is, when the inhibitor molecule is present in the test electrolyte, and the results seem to be consistent with previous observations concerning a thicker and more insulating

barrier film of Cu-BTAH as time elapses, and that such a film is formed at a faster rate in a chloride-containing environment, the observations must be considered with great caution. It has been demonstrated that surface active molecules such as benzotriazole not only interact with the metal surface to protect (copper in this case), but they exhibit chemical activity towards the SECM tip. In this way, the currents measured at the SECM tip during near-field operation do not exclusively arise from variations in the activity of the investigated surface, but from surface blockage of the tip as well.

The design of "*ex situ* tests" is thus recommended, as they can be used for SECM to be employed as a very valuable tool to gain information regarding the kinetics of inhibitor film formation and to image changes both in the surface activity of metal-inhibitor films arising from different pre-treatment conditions and in the extent of corrosion attack.

8.2.7.References

1. P. Marcus, F. Mansfeld (Editors). Analytical Methods in Corrosion Science and Engineering. CRC Press, Boca Raton, 2006.
2. R. Oltra, V. Maurice, R. Akid, P. Marcus (Editors). Local Probe Techniques for Corrosion Research. Woodhead Publishing, Cambridge, 2007.
3. S.B. Basame, H.S. White. Journal of Physical Chemistry 99 (1995) 16430.
4. J.W. Still, D.O. Wipf. Journal of the Electrochemical Society 144 (1997) 2657.
5. K. Fushimi, K. Azumi, M. Seo. Journal of the Electrochemical Society 147 (2000) 552.
6. C. Gabrielli, S. Joiret, M. Keddam, H. Perrot, P. Rousseau, V. Vivier. Journal of the Electrochemical Society 153 (2006) B68.
7. K. Eckhard, T. Erichsen, M. Stratmann, W. Schuhmann. Chemistry - A European Journal 14 (2008) 3968.
8. A.J. Bard, M.V. Mirkin (Editors). Scanning Electrochemical Microscopy. Marcel Dekker, New York, 2001.
9. A.C. Bastos, A.M. Simões, S. González, Y. González-García, R.M. Souto. Electrochemistry Communications 6 (2004) 1212.
10. A.M. Simões, A.C. Bastos, M.G. Ferreira, Y. González-García, S. González, R.M. Souto. Corrosion Science 49 (2007) 726.
11. K. Fushimi, M. Seo. Electrochimica Acta 47 (2001) 121
12. S. Hocevar, S. Daniele, C. Bragato, B. Ogorevic. Electrochimica Acta 53 (2007) 555.
13. D. Battistel, S. Daniele, R. Gerbasi, M.A. Baldo. Thin Solid Films 518 (2010) 2195.
14. R.M. Souto, Y. González-García, S. González, G.T. Burstein. Corrosion Science 46 (2004) 2621.
15. A.C. Bastos, A.M. Simões, S. González, Y. González-García, R.M. Souto. Progress in Organic Coatings 53 (2005) 177.

16. R.M. Souto, Y. González-García, S. González. Corrosion Science 47 (2005) 3312.
17. A.M. Simões, D. Battocchi, D.E. Tallman, G.P. Bierwagen. Corrosion Science 49 (2007) 3838.
18. R.M. Souto, Y. González-García, S. González. Corrosion Science 50 (2008) 1637.
19. R.M. Souto, Y. González-García, S. González. Progress in Organic Coatings 65 (2009) 435.
20. R.M. Souto, Y. González-García, S. González, G.T. Burstein. Electroanalysis 21 (2009) 2569.
21. R.M. Souto, L. Fernández-Mérida, S. González. Electroanalysis 21 (2009) 2640.
22. R.M. Souto, Y. González-García, J. Izquierdo, S. González. Corrosion Science 52 (2010) 748.
23. Y. González-García, G.T. Burstein, S. González, R.M. Souto. Electrochemistry Communications 6 (2004) 637.
24. N. Casillas, S. Charlebois, W.H. Smyrl, H.S. White. Journal of the Electrochemical Society 141 (1994) 636.
25. Y.Y. Zhu, D.E. Williams. Journal of the Electrochemical Society 144 (1997) L43.
26. F. Falkenberg, K. Fushimi, M. Seo. Corrosion Science 45 (2003) 2657.
27. C. Gabrielli, S. Joiret, M. Keddam, H. Perrot, N. Portail, P. Rousseau, V. Vivier. Electrochimica Acta 52 (2007) 7706.
28. C. Gabrielli, S. Joiret, M. Keddam, N. Portail, P. Rousseau, V. Vivier. Electrochimica Acta 53 (2008) 7539.
29. C.H. Paik, H.S. White, R.C. Alkire. Journal of the Electrochemical Society 147 (2000) 4120.
30. C.H. Paik, R.C. Alkire. Journal of the Electrochemical Society 148 (2001) B276.
31. S. Modiano, J.A.V. Carreno, C.S. Fugivara, R.M. Torresi, V. Vivier, A.V. Benedetti, O. R. Mattos. Electrochimica Acta 53 (2008) 3670.
32. J.B. Cotton, I.R. Scholes. British Corrosion Journal 2 (1967) 1.
33. G.W. Poling. Corrosion Science 10 (1970) 359.
34. M.M. Laz, R.M. Souto, S. González, R.C. Salvarezza, A.J. Arvia. Journal of Applied Electrochemistry 22 (1992) 1129.
35. S. González, M.M. Laz, R.M. Souto, R.C. Salvarezza, A.J. Arvia. Corrosion 49 (1993) 450.
36. F. Zucchi, M. Fonsati, G. Trabanelli. In: Giornate Nationali Sulla Corrosione e Protezione, 3rd edn. AIM, Milano, 1996, p. 115.
37. K. Rahmouni, N. Hajjaji, M. Keddam, A. Shriri, H. Takenouti. Electrochimica Acta 52 (2007) 7519.
38. M.M. Antonijević, S. Milić, M.B. Petrović. Corrosion Science 51 (2009) 1228.
39. J. Aljourani, K. Raeissi, M.A. Golozar. Corrosion Science 51 (2009) 1836.
40. Y. Yamamoto, H. Nishihara, K. Aramaki. Journal of the Electrochemical Society 140 (1993) 436.
41. N. Ohno, J. Uehara, K. Aramaki. Journal of the Electrochemical Society 140 (1993) 2512.
42. D. Jope, J. Sell, H.W. Pickering, K.G. Weil. Journal of the Electrochemical Society 142 (1995) 2170.

43. A. Shaban, E. Kálmán, J. Telegdi, Gy. Dóra. Journal of Applied Physics A 66 (1998) S545.
44. E. Szöcs, Gy. Vastag, A. Shaban, G. Konczos, E. Kálmán. Journal of Applied Electrochemistry 29 (1999) 1339.
45. Gy. Vastag, E. Szöcs, A. Shaban, I. Bertóti, K. Popov-Pergal, E. Kálmán. Solid State Ionics 141–142 (2001) 87.
46. R. Holm, D. Holtkamp, R. Kleinstück, H.-J. Rother, S. Storp. Fresenius' Journal of Analytical Chemistry 333 (1989) 546.
47. D.M. Briggs, M.P. Seah (Editors). Practical Surface Analysis. Vol. 1: AES and XPS. Wiley, New York, 1990.
48. R.V. Varma, J.R. Selman (Editors). Techniques for Characterization of Electrodes and Electrochemical Processes. Wiley, New York, 1991.
49. R.M. Souto, V. Fox, M. Pérez, M.M. Laz, S. González. Materials Science Forum 192-194 (1995) 385.
50. R.M. Souto, V. Fox, M.M. Laz, M. Pérez, S. González. Journal of Electroanalytical Chemistry 411 (1996) 161.
51. T. Kosec, D.K. Merl, I. Milošev. Corrosion Science 50 (2008) 1987.
52. B.J. Cruickshank, A.A. Gewirth, R.M. Rynders, R. Alkire. Journal of the Electrochemical Society 139 (1992) 2829.
53. M.R. Vogt, W. Polewska, O.M. Magnussen, R.J. Behm. Journal of the Electrochemical Society 144 (1997) L113.
54. M.R. Vogt, A. Lachenwitzer, O.M. Magnussen, R.J. Behm. Surface Science 399 (1998) 49.
55. W. Polewska, M.R. Vogt, O.M. Magnussen, R.J. Behm. Journal of Physical Chemistry B 103 (1999) 10440.
56. E. Szöcs, I. Bakó, T. Kosztolányi, I. Bertóti, E. Kálmán. Electrochimica Acta 49 (2004) 1371
57. A. Paszternák, S. Stichleutner, I. Felhösi, Z. Keresztes, F. Nagy, E. Kuzmann, A. Vértes, Z. Homonnay, G. Petö, E. Kálmán. Electrochimica Acta 53 (2007) 337.
58. K. Mansikkamäki, P. Ahonen, G. Fabricius, L. Murtomäki, K. Kontturi. Journal of the Electrochemical Society 152 (2005) B12.
59. K. Mansikkamäki, C. Johans, K. Kontturi. Journal of the Electrochemical Society 153 (2006) B311.
60. K. Mansikkamäki, C. Johans, K. Kontturi. Journal of the Electrochemical Society 153 (2006) B22.
61. M. Pourbaix, Atlas of Electrochemical Equilibria in Aqueous Solutions. NACE, Houston, 1974.
62. H.D. Speckmann, M.M. Lohrengel, J.W. Schultze, H.H. Strehblow. Berichte der Bunsengesellschaft für Physikalische Chemie 89 (1985) 392.
63. M. Pérez Sánchez, M. Barrera, S. González, R.M. Souto, R.C. Salvarezza, A.J. Arvia, Electrochimica Acta 35 (1990) 1337.
64. R.M. Souto, M. Pérez Sánchez, M. Barrera, S. González, R.C. Salvarezza, A.J. Arvia. Electrochimica Acta 37 (1992) 1437.
65. S. González, M. Pérez, M. Barrera, A.R. González Elipe, R.M. Souto. Journal of Physical Chemistry B 102 (1998) 5483.

66. Y.I. Kuznetzov. In: Organic Inhibitors of Corrosion of Metals (Edited by A.D. Mercer, J.G.N. Thomas). Plenum Press, New York, 1996, p. 101.
67. M.M. Antonijević, S.M. Milić, S.M. Ŝerbula, G.D. Bogdanović. Electrochimica Acta 50 (2005) 3693.
68. Y.N. Prasad, S. Ramanathan. Electrochimica Acta 52 (2007) 6353.
69. J.H. Chen, Z.C. Lin, S. Chen, L.H. Nie, S.Z. Yao. Electrochimica Acta 43 (1998) 265.
70. J.-O. Nilsson, C. Törnkvist, B. Liedberg. Applied Surface Science 37 (1989) 306.
71. K.L. Stewart, J. Zhang, S. Li, P.W. Carter, A.A. Gewirth. Journal of the Electrochemical Society 154 (2007) D57.
72. H.S. Isaacs. Journal of the Electrochemical Society 138 (1991) 723.
73. R.S. Lillard. In: Analytical Methods in Corrosion Science and Engineering (Edited by P. Marcus, F. Mansfeld). CRC Press, Boca Raton, 2006, Ch. 15.
74. A.J. Bard, M.V. Mirkin (Editors). Scanning Electrochemical Microscopy. Marcel Dekker, New York, 2001, p. 243.
75. A.C. Bastos, M.G.S. Ferreira, A.M. Simões. Progress in Organic Coatings 52 (2005) 339.
76. J. He, Applications of the Scanning Vibrating Electrode Technique to the Study of Corrosion Protection by Conductive Polymers. Ph.D. Dissertation, North Dakota State University, 2002.
77. G. Baril, C. Blanc, M. Keddam, N. Pébère. Journal of the Electrochemical Society 150 (2003) B488.
78. C. Sheffey. In: Ionic Currents in Development (Edited by A.R. Liss). A.R. Liss Inc., New York, 1986, p. xxv.
79. P. Sun, F.O. Laforge, M.V. Mirkin. Physical Chemistry Chemical Physics 9 (2007) 802.
80. K. Yliniemi. Different Approaches for Surface Modifications: Formation of Inhibitive Film on Copper Surfaces and Surfaces Functionalised with Ag Nanoparticles. TKK Dissertations 105, Espoo, 2008.
81. T. Hashemi, C.A. Hogarth. Electrochimica Acta 33 (1988) 1123.

8.3

Scanning microelectrochemical characterization of the anti-corrosion performance of inhibitor films formed by 2-mercaptobenzimidazole on copper

8.3.1. Abstract

The aim of this Section is to explore the applicability of the scanning electrochemical microscope (SECM) to characterize the inhibiting effect of 2-mercaptobenzimidazole against the corrosion of copper. SECM was operated in the feedback mode by using ferrocene-methanol as redox mediator, and the sample was left unbiased at all times. The kinetic changes in the corrosion processes were monitored over time from the Z-approach curves. Furthermore, inhibitor-modified copper samples presenting various surface finishes were imaged by SECM and the scanning vibrating electrode technique (SVET), allowing changes both in the surface activity of metal-inhibitor films and in the extent of corrosion attack to be spatially-resolved. Differences in the local electrochemical activity between inhibitor-free and inhibitor-covered areas of the sample were successfully monitored.

8.3.2. Resumen

En esta sección se ha evaluado la aplicabilidad de la microscopía electroquímica de barrido (SECM) en la caracterización de la capacidad inhibidora de la corrosión del 2-mercaptobenzimidazol aplicado sobre cobre. Se ha operado con el SECM en modo de retroalimentación utilizando el ferroceno-metanol como mediador redox, dejando en todo momento la muestra sin polarizar. Se han seguido los cambios cinéticos en los procesos de corrosión con el tiempo a través del análisis de las curvas de aproximación. Además se han visualizado, mediante SECM y mediante la técnica de barrido del electrodo vibrante (SVET), muestras de cobre modificadas con el inhibidor, produciendo en éstas varios acabados superficiales, facilitando de esta manera la resolución espacial tanto de los cambios en la actividad superficial de las películas de metal-inhibidor como en la extensión del ataque corrosivo. Se ha analizado con éxito las diferencias en actividad electroquímica entre las áreas libres y las cubiertas de inhibidor de tales muestras.

8.3.3. Introduction

Local electrochemical techniques are increasingly used in the corrosion laboratory to investigate the mechanisms of corrosion reactions in aqueous environments, as well as to develop new protection strategies due to their power to characterize surface reactivity *in situ* [1-2]. Among them, the scanning vibrating electrode technique (SVET) [3] has been the most successfully employed to characterize the efficiency of inhibitor systems for the protection of metals and alloys [4-11], and the inhibition of corrosion reactions at defects and cut edges in painted metals [12-19]. Additionally, experimental methodologies have been developed to perform the simultaneous screening of various inhibitors for a metal in a given environment [20], and to assist the development of self-healing coatings based on the controlled release of the inhibitors where needed [21-31]. Conversely, the scanning electrochemical microscope (SECM) [32,33] has been scarcely employed to investigate metal-inhibitor systems beyond the pioneering work of Kontturi *et al.* [34-36], focused in the copper–benzotriazole system exclusively. In their work, polarization of the modified metal substrate was performed, though inhibitor-protected metals usually function in unbiased conditions. The absence of further developments in the application of SECM to investigate metal-inhibitor systems is quite surprising because SECM has shown an unmatched power to investigate a variety of corrosion processes reactions and corrosion protection systems [37-39], such as the localized dissolution of metals [40,41], the detection of anodic and cathodic areas [42-44], the detection of precursor sites for pitting inclusion dissolution [45-48] and the formation of metastable pits [49], the degradation of organic films [50-55] and surface coatings [56-59], and hydrogen permeation [60]. Therefore, a series of studies to explore the use of this technique to characterize the formation and protection characteristics of other inhibitor films is proposed here. They were initiated by revisiting the copper-benzotriazole system in Section 8.2 of this Thesis. In that case, the metal substrate was left unbiased, and electrolyte-exchange procedures were employed to avoid the interference of specific interactions between the inhibiting organic molecules with the sensing SECM tip [61-63]. Further testing of the methodology is undertaken in this Section, where another well-established metal-inhibitor systems is considered, namely the inhibiting effect of 2-mercaptobenzimidazole against the corrosion of copper.

Benzotriazole (BTAH) and 2-mercaptobenzimidazole (MBI) are the most widely employed inhibitors for the anticorrosion protection of copper and its alloys [64]. They effectively protect these metals in various aggressive environments, and the most accepted mechanism to describe their operation involves the formation of a chemisorbed layer of these organic molecules on the metals. In particular, the adsorption of such layer on copper is considered to be favoured when copper oxides already exist on the surface of the metal [65-69], though the formation of a complex film of the inhibitor on the base metal has also been reported [70-72]. Though adsorption at the surface is regarded to be the first step in the process [66,73], the actual mechanism is not yet fully ascertained, neither the chemical

nature of the resulting inhibitor films is completely established, though the knowledge of both is necessary towards the development of new and more effective inhibitors.

2-Mercaptobenzimidazole (MBI) has been found to be more effective than BTAH for the corrosion protection of copper in aerated HCl aqueous environment [74], and its inhibitive action is exerted mainly on the anodic process. Conversely to BTAH, The MBI molecule ($C_7H_4N_2S$) contains two nitrogen atoms, and deprotonation of the imine group originates the anionic species MBI^- and MBI^{2-}, which are aromatic too. It is this negative charge distribution extended over several atoms (namely sulphur and nitrogen) that favours direct bonding to copper cations, and each metal ion is directly coordinated to two ligands. Furthermore, MBI contains a sulphur atom that is strongly adsorbed on the copper surface. This is the rationale behind the formation of a polymeric structure on the copper surface with the participation of MBI molecules. A variety of experimental techniques have been employed to characterize copper-MBI films, including cyclic voltammetry, electrochemical impedance spectroscopy, elemental surface analysis, infrared spectroscopy and mass spectrometry [75,76], thus making the copper-MBI system an attractive model for the investigation of the applicability of new experimental techniques and methods.

This Section reports on SECM and SVET studies of the surface films formed by MBI on copper, taking into account the anticorrosion protection characteristics and stability of the layers formed in either KCl or Na_2SO_4 aqueous solutions. The samples were left unpolarized in the test medium, which was maintained at room temperature and open to air. SECM was operated in the feedback mode by adding ferrocene-methanol as redox mediator, thus allowing for the surface conductivity properties of the copper-MBI films to be determined, and the surface chemical reactivity of samples displaying various regions with different inhibitor coverages to be imaged. On the other hand, SVET was used in order to measure the local distribution of the current density on the copper surfaces with and without MBI. In this technique, the ionic current flow due to metal corrosion results in a very minute electric field within an electrolyte medium, which can be imaged as the distribution of potentials and currents on the electrolytic phase in contact with the surface of the sample.

8.3.4. Experimental

SECM and SVET measurements were performed on 99.99% purity copper plates, supplied by Goodfellow (Cambridge, United Kingdom), which were cut to 2.4 cm x 2.4 cm and 1 mm thickness. The surface of the samples was ground mechanically using metallographic emery paper of increasing fineness of 800, 1200 and 4000 grit, degreased with acetone, rinsed with *Milli*Q grade water and dried to

air. For the preparation of the inhibitive films on the copper samples, the metal plates were immersed either in 0.1 M KCl + 1 mM MBI or in 0.1 M Na_2SO_4 + 1 mM MBI aqueous solutions for different immersion times ranging from a few seconds up to 7 days.

Samples presenting one or more regions of varying inhibitor-coverage were prepared as described next. Three different sample treatments were performed for the SECM investigations. Firstly, when homogeneously coated samples were endeavoured, all the metal sample was exposed flat at the bottom of the measuring cell, that the upper surface would face the electrolyte. In this case, the samples could be investigated using the scanning electrochemical techniques in the same cell after electrolyte exchange. On the other hand, when samples containing separate areas of different inhibitor efficiency were desired, they were subjected to a series of preparations steps. In this way, various areas with different immersion times in the inhibitor solution could be formed on the same side of the sample. The relevant sequence of steps is given schematically in Figure 8.3.1. In this procedure, half surface was immersed vertically in a beaker containing the inhibitor-containing solution for a chosen time t_1 (Figure 8.3.1B). Then, the sample was removed from the beaker, carefullly rinsed with low conductivity water, and dried by capillary action. The procedure could be repeated again for a different immersion after rotating the sample 90°, originating new areas of different treatment durations. The resulting sample contained 4 areas with different surface properties due to different pre-treatment durations (Figure 8.3.1D). A similar procedure was employed when the stability of inhibitor surface films was investigated, by performing the second step in an aggressive environment instead of using the inhibitor-containing solution. In that case, the *initial surface* mentioned in Figure 8.3.1 corresponds to the copper samples previously covered by MBI by exposure to the inhibitor during 7 days, and the *treatment solution* consisted on exposure to 3 wt.% NaCl solution.

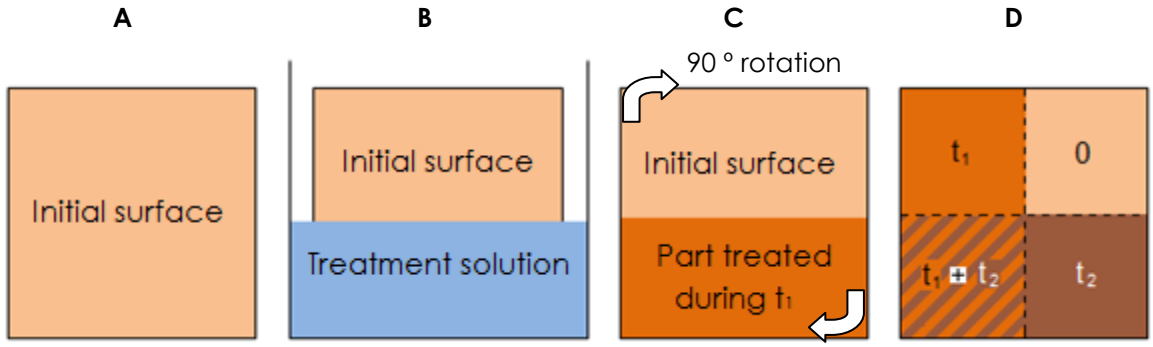

Figure 8.3.1. Sketch depicting sample preparation for SECM characterization. Portions of the sample were pre-treated in the corresponding inhibitor-containing solution for chosen times in order to produce 4 areas with different coverages. The untreated metal sample (A) is partially immersed in the solution (B) during a given time t_1. The resulting specimen (C) is then carefully rotated 90° and exposed again to the same solution, in this occasion during a given time t_2, resulting in the final distribution shown in (D).

For the SVET experiments, samples were prepared according to the procedure depicted in Figure 8.3.2. Firstly, the bare copper sample was immersed in 1 mM MBI + 0.1 M KCl 0.1 M for a short period of time (Figure 8.3.2B). After that, the sample was removed, rinsed in water and carefully dried by capillary action, and after 180º rotation, subsequently immersed in another beaker containing 1mM MBI + 0.1 M Na_2SO_4 0.1 M. The resulting sample had 3 regions with different surface properties (cf. Figure 8.3.2D), where the central stripe corresponded to a portion of the sample that was exposed to both inhibitor-containing solution.

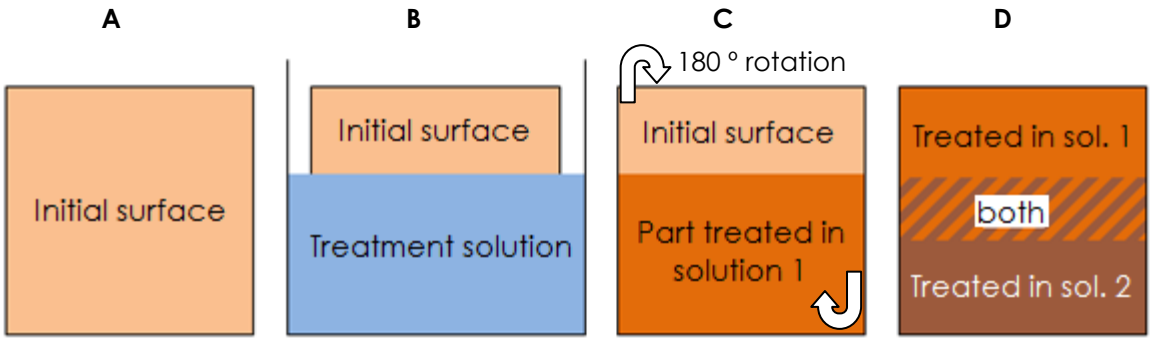

Figure 8.3.2. Sketch depicting sample preparation for SECM characterization. Portions of the sample were pre-treated in the corresponding inhibitor-containing solution for chosen times in order to produce 3 areas with different coverages. The untreated metal sample (A) is partially immersed in the solution 1 containing 1mM MBI and electrolyte KCl 0.1 M (B). Then, the obtained metal target (C) is carefully rotated 180º and exposed again, this time in a different beaker with solution containing 1mM MBI and electrolyte Na_2SO_4, resulting in the final distribution shown in (D). The central stripe corresponds to untreated copper.

SECM experiments were carried out using a scanning electrochemical microscope from Sensolytics (Bochum, Germany). Platinum microelectrodes of 10 µm diameter served as SECM tips. The tip-sample distance for SECM imaging was determined upon comparison of the approach curve recorded over a copper surface with the theoretical one assuming that the reduction of the mediator at the surface was under kinetic control [77]. Imaging was performed with the microelectrode at a height of 15 µm over the specimen surface. The SECM cell with the sample was mounted horizontally facing upwards at the bottom of a microflat cell [78]. An Ag/AgCl/KCl (3M) and a 316L stainless steel wire served as reference and counter electrodes, respectively. Ferrocene-methanol (Aldrich) was used as mediator.

SVET measurements were made using a system from Applicable Electronics (Forestdale, MA, USA). The vibrating probe consisted of a 20 µm platinum-black-coated tip that was placed above the surface of the substrate at a height of 60 µm. The vibrating amplitudes of the scanning probe were adjusted to 30 and 20 µm, parallel and normal to the surface, respectively. Two platinum wires served as signal and reference electrodes. When all adjustments had been made, about 5 mL of electrolyte solution was added to the cell and the three electrodes were

subsequently placed in the solution. A video–microscope was employed to establish the tip-sample distance and to record images of the most significant features on the substrate surface *in situ* at real time.

The test electrolytes employed in the microelectrochemical experiments were 1 mM Na_2SO_4 containing 1 mM ferrocene-methanol as redox mediator for SECM, and 10 and 50 mM KCl solutions for SVET. All aqueous solutions were prepared using *Milli*Q water. Measurements were performed in naturally aerated solutions at ambient conditions (22 °C).

8.3.5. Results and discussion

8.3.5.1. Monitoring of surface reactivity changes during early stages of Cu-MBI formation

SECM in the feedback mode probes surface reactivity towards the oxidation of ferrocene-methanol of the investigated area located under the SECM tip. Z-approach curves monitor the tip current as the ultramicroelectrode approaches the sample. In the case of a conducting surface such as that of a fresh copper sample, the corresponding increase of the faradaic current is related to the mediator's regeneration at the sample surface (i.e., positive feedback). In the case of the metallic material covered by an inhibitor film, the surface reactivity reflects mainly the ability to transport charge within the surface film and eventually may result in an insulating surface. In the latest case, the substrate sample does not regenerate the mediator, and effectively becomes a geometrical blockage towards the diffusion of the mediator from the bulk electrolyte. Smaller currents are then measured as the tip approaches the substrate (i.e., negative feedback). The copper substrates for SECM measurements were pre-treated by immersing them during different times in inhibitor-containing solutions, using either 0.1 M Na_2SO_4 or 0.1 M KCl as supporting electrolytes. The choice of supporting electrolytes would facilitate to observe the eventual influence of the smaller chloride ions towards the adsorption of the inhibitor on the metal surfaces. Next, the samples were placed in the SECM flat microcell, a controlled amount of the test electrolyte (namely, 1 mM Na_2SO_4 + 1 mM ferrocene-methanol) was added, and the corresponding Z-approach curves were measured starting from a fixed height. Figure 8.3.3 depicts the plots measured for copper samples pre-treated in either 0.1 M Na_2SO_4 or in 0.1 M KCl. Inspection of these graphs allows for the observation of a full transition from pure positive feedback behaviour characteristic of untreated copper to a negative feedback regime for the thickest inhibitor films produced after 7 days pre-treatment. Changes in the kinetics of inhibitor adsorption from the two supporting electrolytes can be deduced from the comparison of the approach curves measured for samples with the same duration of the pre-treatment step. Figure 8.3.4 shows the time dependence of the tip current measured at the distance of maximum approach to the substrate, and in all cases

significantly smaller currents are found for the samples pre-treated in the presence of chloride ions. This is strong evidence that chloride ions participate in the formation of the inhibitor film when present in the environment, and that the formed layers hinder charge transfer more efficiently. That is, a greater inhibiting effect is provided when chloride ions are present in the electrolyte, which may support previous reports on the incorporation of chloride to the protective layers formed on copper in the presence of MBI [15].

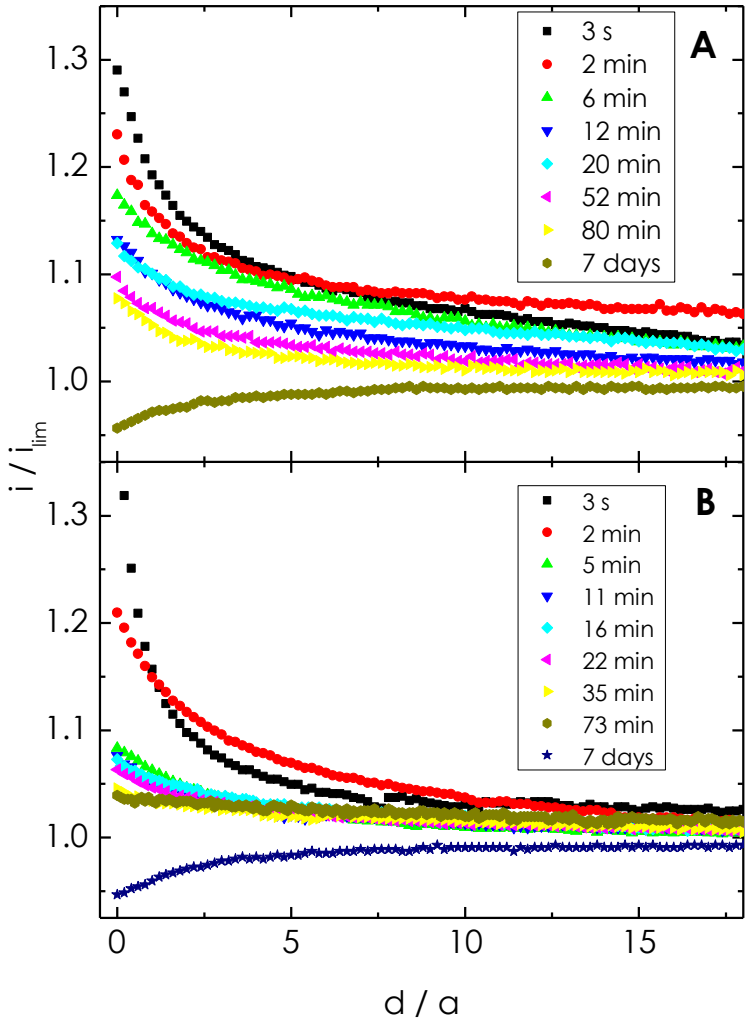

Figure 8.3.3. SECM normalized Z-approach curves towards inhibitor pre-treated copper surfaces measured in 1 mM Na_2SO_4 + 1 mM ferrocene-methanol solution with a 10 μm Pt electrode. Tip potential: +0.50 V vs. Ag/AgCl/KCl (3M). The copper samples were pre-treated by immersion in: (A) 0.1 M Na_2SO_4 + 1 mM MBI, and (B) 0.1 M KCl + 1 mM MBI for the times indicated in the legends. i / i_{lim} is the dimensionless tip current, and d / a is the dimensionless distance between the sample and the tip. The samples were left at their spontaneous open circuit potentials in the test electrolyte.

Similar conclusions could be derived by using the SECM in the imaging mode using ferrocene-methanol as redox mediator for feedback operation. In this case, copper samples were subjected to a sequence of immersion steps in the inhibitor-

containing electrolyte to prepare surfaces with four regions of different coverage by the inhibitor as shown in Figure 8.3.1.

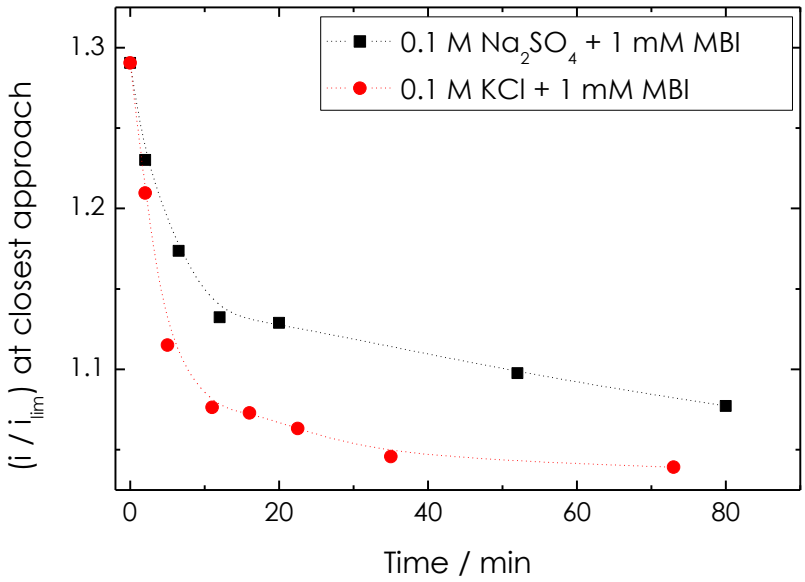

Figure 8.3.4. Time evolution of the normalized current values measured when the tip was placed at the closest distance attained during the measurement of the approach curves depicted in Figure 8.3.3 following treatment in the solutions given in the plot.

The four regions developed on the surface corresponded namely to exposures 0, t_1, t_2, and t_1+t_2, were t_1 = 5 min and t_2 = 10 min, what consequently resulted in four regions exposed 0, 5, 10 and 5+10 minutes to the inhibitor. The sample was then placed in the SECM flat microcell, and the test electrolyte 1 mM Na_2SO_4 + 1 mM ferrocene-methanol was carefully added. Then, the tip was rastered over the substrate at a constant height of 15 μm by using an *X-Y* grid centered in the sample, thus allowing pass above the four regions in a single scan. Figure 8.3.5 depicts the SECM images recorded for samples pre-treated in 0.1 M Na_2SO_4 and in 0.1 M KCl solutions containing 1 mM MBI, respectively. Though the samples are topographically flat for the vertical resolution of the technique employed, the regions of different inhibitor coverage are clearly displayed in the SECM images due to the variations in the faradaic current measured at the tip for ferrocene-methanol that are measured above each zone. The tip currents are always smaller over the areas covered by the inhibitor, and can be clearly observed in the images for the rather short pre-treatments of 5 min. Longer pre-treatments with MBI deliver surface portions with even smaller currents at the tip when passing above them. This is a clear indication that the insulating characteristics of the inhibitor layer increase when longer pre-treatments are given, and these surface layers hinder the charge conductivity, thus protecting the metal from oxidation.

The reported decrease observed in the conductivity of the surface for longer exposures to the inhibitor-containing solution may result from the organic molecules either blocking more active sites or forming a thicker surface film. At this stage it is

not possible to discriminate between the two mechanisms from the measurements given here. Again, the enhanced inhibiting effect of MBI films formed in chloride-containing environments can be derived from the comparison of the images in Figure 8.3.5. Indeed, the reduction in the faradaic currents measured at the tip after 15 min pre-treatment amounts to ca. 50% for the sample prepared in the chloride-containing solution, whereas it is only 35% for that fabricated in the chloride-free electrolyte.

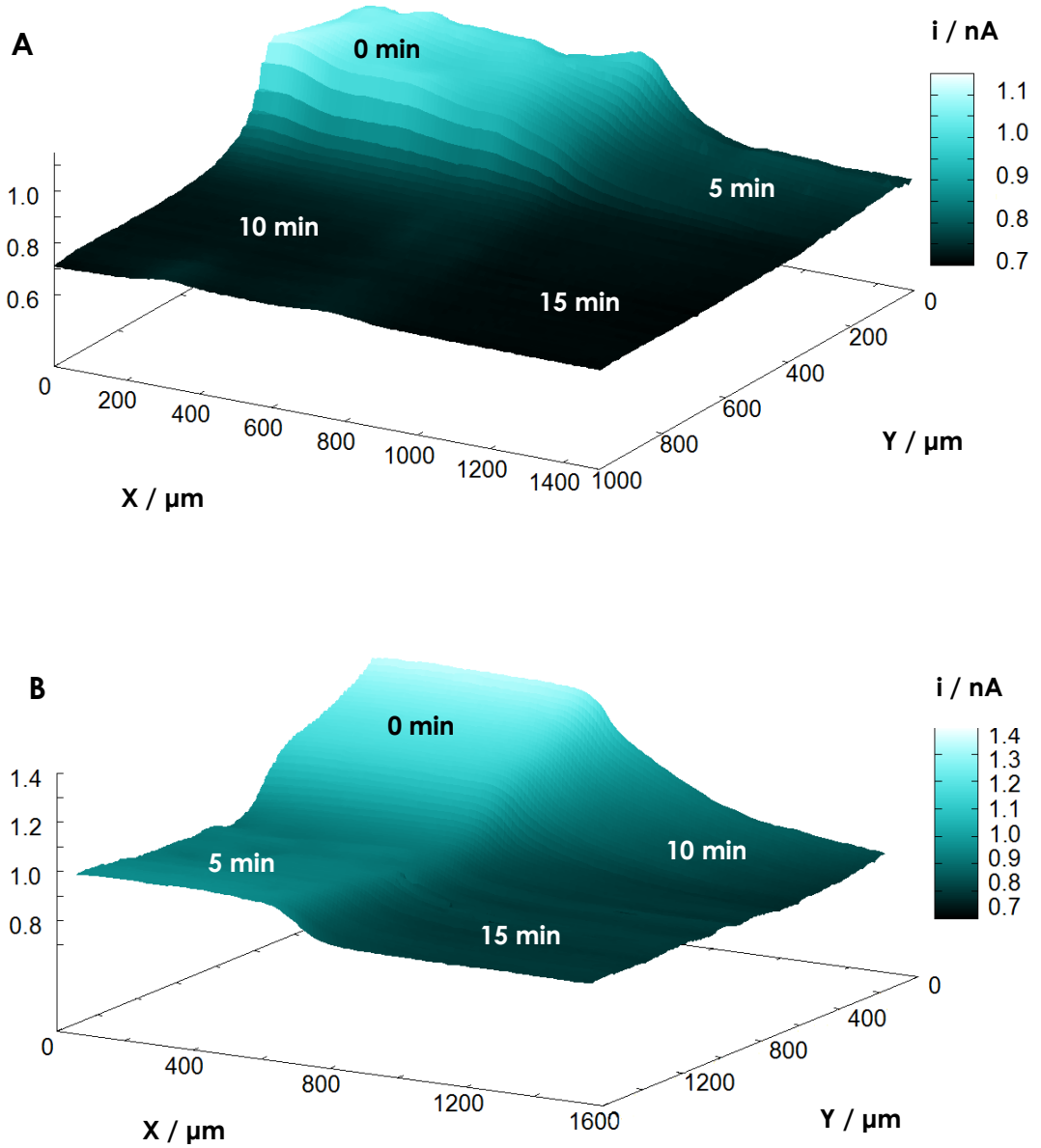

Figure 8.3.5. Images generated by SECM of copper samples treated with MBI for various times, as indicated in the figure. The solutions used for the pre-treatment of the copper samples were: (A) 0.1 M KCl + 1 mM MBI solution, and (B) 0.1 M Na_2SO_4 + 1 mM MBI solution. The images were registered with a 10 µm Pt electrode when the samples were exposed to 0.1 M Na_2SO_4 + 1 mM ferrocene-methanol solution. Tip-substrate distance: 15 µm. Tip potential: +0.50 V vs. Ag/AgCl/KCl (3M). i_{lim} = 0.99 nA. The samples were left at their spontaneous open circuit potentials in the electrolyte.

8.3.5.2. Probing degradation of Cu-MBI inhibitor layers by scanning microelectrochemical techniques

Considering the persistence of inhibitor films formed on a metal for anticorrosion protection, one can design experiments that would allow their susceptibility to attack by an aggressive environment to be investigated using scanning microelectrochemical techniques.

It was shown above that SECM could be employed to image copper samples prepared to present various regions of different surface finishes. A variation from the procedure employed in Section 8.3.5.1 was performed this time, such that the sequence and the nature of the pre-treatment steps would allow the stability of inhibitor films to be explored instead. In the new procedure, the first step involved the complete immersion of the copper sample in 0.1 M KCl + 1 mM MBI solution for 7 days. This electrolyte was chosen on the basis of the results described in Section 8.3.5.1 corresponding to thicker and less conductive surface layers. The duration of this step was also selected to be greatly in excess of what is required to form the thickest inhibitor film exclusively by immersion. After 7 days, the sample was removed from the inhibitor-containing electrolyte, rinsed with high-purity deionized water to secure the removal of inhibitor molecules in the thin electrolyte layer wetting the samples, and then dried under a flow of air. The corrosive attack was subsequently performed in 3 wt.% NaCl solution for various times, again following the procedure represented in Figure 8.3.1, though the immersion times in the different pre-treatment solutions were now, t_1 = 8 h and t_2 = 16 h to develop four regions on the surface corresponding to exposures 0, 8, 16 and 24 h. Upon immersion of this sample in 1 mM Na_2SO_4 + 1 mM ferrocene-methanol, the tip-substrate distance for SECM operation was established by measuring the Z-approach curve over the intact Cu-MBI surface, though the curve-modelling was done for the case of negative feedback this time [77].

Figure 8.3.6 shows the SECM image for this sample. The trend exhibited by the tip currents measured over the various regions is now the opposite that described above. Namely, faradaic currents at the tip are higher over the zones with longer exposures to the 3 wt.% NaCl solution, thus indicating partial removal of the protective layer or a loss in its insulating properties during the attack by chloride ions. Nevertheless, the great performance of the inhibitor film produced on copper is demonstrated in this case, because attacks in excess of 24 hours in this highly aggressive electrolyte were necessary for current measured at the tip to exhibit the same values as in the bulk of the electrolyte. This would correspond to the transition from negative to positive feedback regimes, though it must be realized that this is only an apparent observation. That is, the slow kinetics of charge transfer for the mediator regeneration at the surface (i.e., positive feedback) results in the measurement of values very close to i_{lim} when the tip is placed in the proximity of the surface portion attacked for 24 hours.

In this case, SVET could also be used in addition to SECM operated in the feedback mode, thus allowing for the visualization of ionic current flows occurring in

the electrolytic phase in contact with the sample as result of the corrosive process. That is, the onset of corrosive attack on the copper samples protected by MBI would result from the establishment of anodes and cathodes at the micrometer scale. The test environment was 10 mM KCl this time, since SVET resolution requires the use of poorly conductive electrolytes. Thus, the electrolyte responsible for the corrosive attack is less aggressive that the one employed in the SECM experiments, which hinders a quantitative comparison of the results obtained with the two scanning microelectrochemical techniques. Yet, qualitative trends could be found as described next.

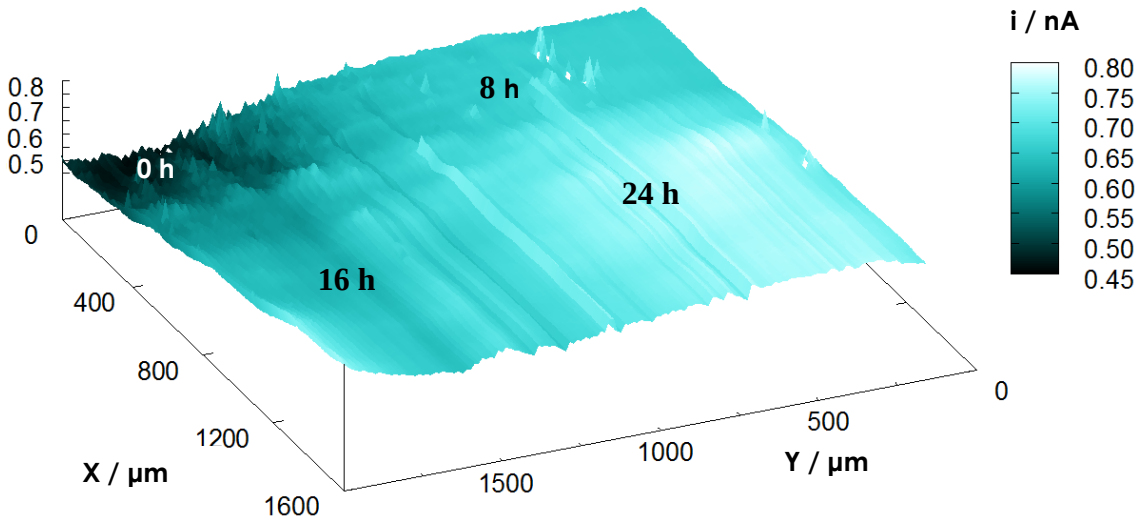

Figure 8.3.6. Image generated by SECM of a copper sample displaying 4 zones of different electrochemical activity during immersion in 0.1 M KCl + 1 mM ferrocene-methanol solution with a 25 µm Pt electrode. The copper sample was first treated during 7 days in 0.1 M KCl + 1 mM MBI solution to form a Cu-MBI inhibitive film. The corrosion resistance characteristics of the Cu-MBI inhibitive film was investigated by exposing the sample to 1 M NaCl solution for the various times indicated on the figure. Tip-substrate distance: 15 µm. Tip potential: +0.50 V vs. Ag/AgCl/KCl (3M). The *Z* scale is the tip current in nA. The sample was left at its spontaneous open circuit potential in the electrolyte.

Figure 8.3.7 shows the SVET images measured for a sample that was protected by a thin inhibitor film after immersion for 10 s in the MBI-containing electrolytes according to the sketch given in Figure 8.3.2. Though the optical micrograph in Figure 8.3.7A recorded after 21 hours immersion in the test electrolyte does not show any clear evidence of corrosive attack, the SVET maps consistently depict anodic activity occurring from the inhibitor film formed in Na_2SO_4 solution, even in the image started to record as early as 10 s after initiating the exposure of the sample to the measurement environment (see Figure 8.3.7A). This result is in agreement with the previous observations that inhibitor films formed by MBI on copper have superior corrosion protection characteristics when chloride ions are

also involved. The high resolution of SVET to resolve differences in chemical reactivity from one sample has also been demonstrated even from very early exposures.

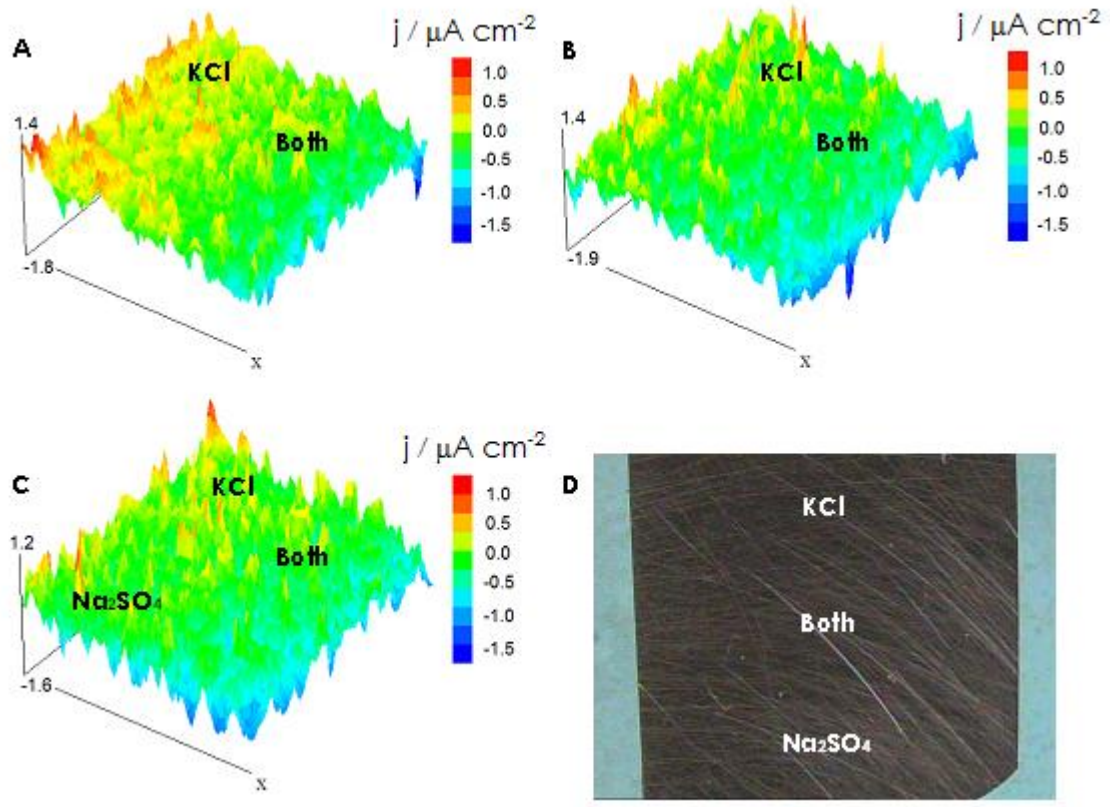

Figure 8.3.7. Images generated by SVET (A-C) and video microscope (D) of a Cu-MBI (10 s pre-treatment in 0.1 M KCl + 1 mM MBI solution) – Cu-MBI (10 s pre-treatment in 0.1 M Na_2SO_4 + 1 mM MBI solution) system immersed in 10 mM KCl for (A) 1, (B) 9, and (C) 21 h. The central part of the sample was immersed in both environments during the pre-treatment stage. Tip-substrate distance: 60 µm. The *Z* scale is the ionic current in µA cm^{-2}. The figures represent an area of 9000 µm x 9000 µm in *X* and *Y* directions. The sample was left at its spontaneous open circuit potential in the electrolyte.

The reported behaviour is more clearly observed when higher concentrations of KCl are employed, as it is the case for the SVET images shown in Figure 8.3.8. The onset of the corrosive attack is now clearly displayed, with the anodes occurring on the Cu-MBI zone formed in the chloride-free solution. The degradation of the inhibitor film results in higher corrosion rates as time elapses. Though initially very low corrosion rates are measured over the surface (Figure 8.3.8A), the cationic flow is greater by several orders of magnitude once the first pit is observed after 4 hours exposure to the corrosive medium (see Figure 8.3.8B). The corrosion reaction becomes even more violent for longer exposures with the nucleation of additional pits in the zone pre-treated in the sulphate environment (cf. Figures 8.3.8C and D). It is important to observe that the cathodes are not detected over the Cu-MBI film formed in the chloride environment at any time, including the image recorded after

24 hours exposure (Figure 8.3.8D) even when plotted under magnification (Figure 8.3.8E). The insulating characteristics of the inhibitor film are thus confirmed, whereas the cathodes were to be found in the region pre-treated in sulphate as well (cf. Figure 8.3.8E).

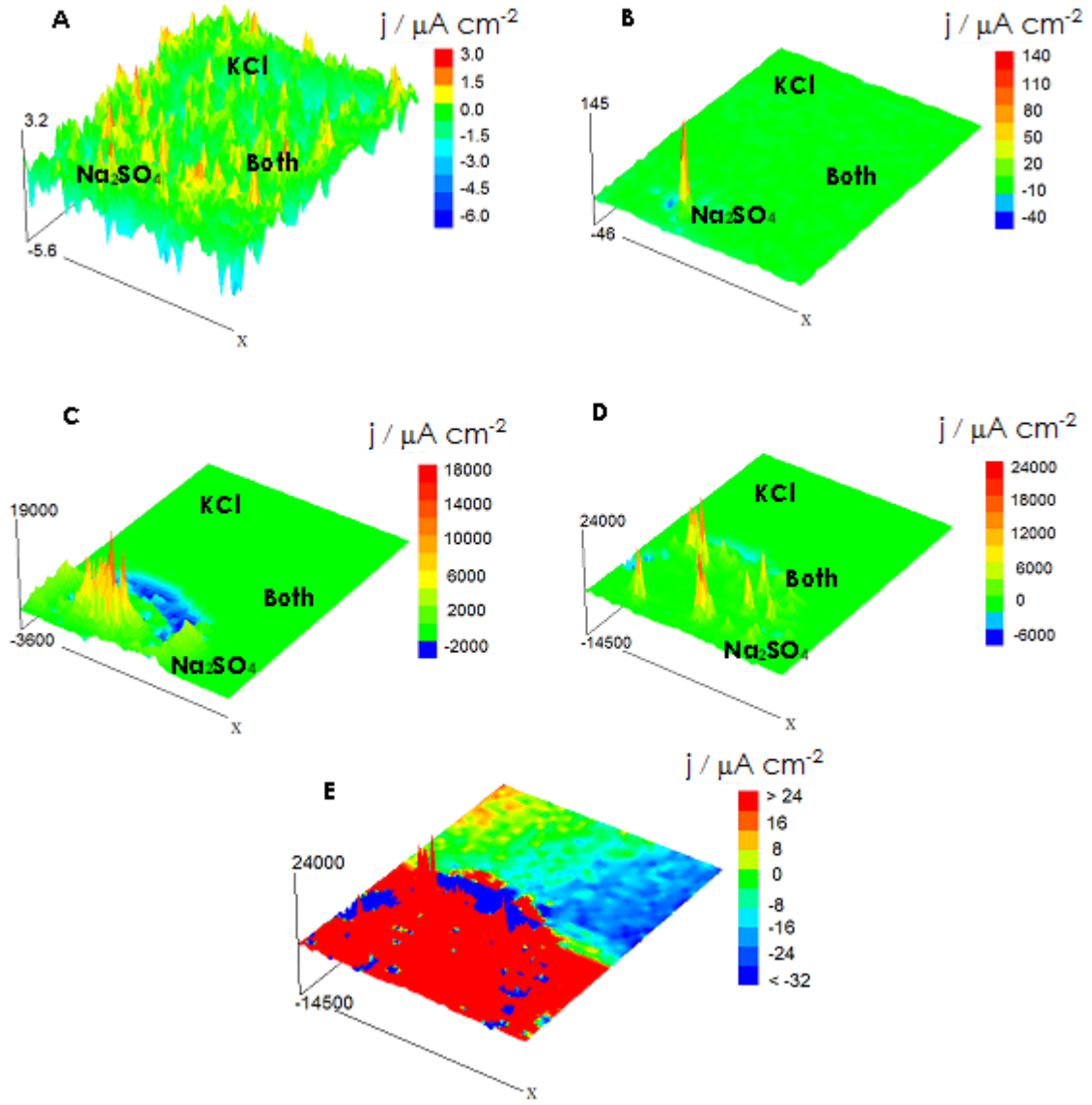

Figure 8.3.8. Images generated by SVET of a Cu-MBI (10 s pre-treatment in 0.1 M KCl + 1 mM MBI solution) – Cu-MBI (10 s pre-treatment in 0.1 M Na_2SO_4 + 1 mM MBI solution) system immersed in 50 mM KCl for (A) 1.5, (B) 4, (C) 10, and (D,E) 24 h. Tip-substrate distance: 60 µm. The *Z* scale is the ionic current in µA cm^{-2}. The figures represent an area of 9000 µm x 9000 µm in *X* and *Y* directions. The sample was left at its spontaneous open circuit potential in the electrolyte.

In summary, the use of scanning microelectrochemical techniques demonstrates that the inhibitor film formed on copper by MBI in the presence of chloride ions provides enhanced anticorrosion protection for the metal, possibly

through the formation of a thicker polymeric film [66,75]. In the case of very short pre-treatments (namely 10 s), though some protection is conferred to the base metal, charge conductivity through the film still occurs. This effect is more noticeable in the case of the inhibitor films formed in the absence of chloride, and SVET images show the distribution of microanodes and microcathodes under the film at the onset of the corrosion process.

8.3.6. Conclusions

Investigations performed in this Section showed that scanning microelectrochemical techniques can give valuable information regarding the protection characteristics and the kinetics of inhibitor films formed on metals, as illustrated by the inhibition of copper corrosion by 2-mercaptobenzimidazole. This study confirmed that even changes in the composition of the base electrolyte induce a significant effect on the inhibiting properties of the organic compound, thus chloride ions promoting the formation of thicker and more insulating layers than those formed in sodium sulphate solution.

SECM operated in the feedback mode and SVET techniques provides complementary information on corrosion and inhibition processes, with the great advantage that variations in the chemical reactivity at the surface of the samples can be spatially resolved.

8.3.7. References

1. P. Marcus, F. Mansfeld(Editors). Analytical Methods in Corrosion Science and Engineering. CRC Press, Boca Raton, 2006.
2. R. Oltra, V. Maurice, R. Akid, P. Marcus (Editors). Local Probe Techniques for Corrosion Research. Woodhead, Cambridge, 2007.
3. R.S. Lillard. In: Analytical Methods in Corrosion Science and Engineering (Edited by P. Marcus, F. Mansfeld). CRC Press, Boca Raton, 2006, p. 571.
4. M.J. Franklin, D.C. White, H.S. Isaacs. Corrosion Science 33 (1992) 251.
5. H.E. Jamil, A. Shriri, R. Boulif, C. Bastos, M.F. Montemor, M.G.S. Ferreira. Electrochimica Acta 49 (2004) 2753.
6. M. Zubielewicz, W. Gnot. Progress in Organic Coatings 49 (2004) 358.
7. A.C. Bastos, M.G.S. Ferreira, A.M. Simões. Progress in Organic Coatings 52 (2005) 339.
8. A. P. Nazarov, D. Thierry. Protection of Metals 42 (2006) 437.
9. A.C. Bastos, M.G.S. Ferreira, A.M. Simões. Corrosion Science 48 (2006) 1500.

10. G. Williams, A.J. Coleman, H.N. McMurray. Electrochimica Acta 55 (2010) 5947.
11. G. Williams, H.N. McMurray, R. Grace. Electrochimica Acta 55 (2010) 7824.
12. I.M. Zin, S.B. Lyon, A. Hussain. Progress in Organic Coatings 52 (2005) 126.
13. F. Thébault, B. Vuillemin, R. Oltra, K. Ogle, C. Allely. Electrochimica Acta 53 (2008) 5226.
14. A.M. Simões, J. Torres, R. Picciochi, J.C.S. Fernández. Electrochimica Acta 54 (2009) 3857.
15. O.V. Karavai, A.C. Bastos, M.L. Zheludkevich, M.G. Taryba, S.V. Lamaka, M.G.S. Ferreira. Electrochimica Acta 55 (2010) 5401.
16. R.M. Souto, B. Normand, H. Takenouti, M. Keddam. Electrochimica Acta 55 (2010) 4551.
17. A.M. Simões, J.C.S. Fernández. Progress in Organic Coatings 69 (2010) 219.
18. J.V. Custodio, S.M.L. Agostinho, A.M.P. Simões. Electrochimica Acta 55 (2010) 5523.
19. D. Fix, E.V. Skorb, D.G. Shchukin, H. Möhwald. Measurement Science and Technology 22 (2011) 0705704 1.
20. S. Kallip, A.C. Bastos, M.L. Zheludkevich, M.G.S. Ferreira. Corrosion Science 52 (2010) 3146.
21. A.N. Khramov, N.N. Voevodin, V.N. Balbyshev, M.S. Donley. Thin Solid Films 447–448 (2004) 549.
22. N.N. Voevodin, V.N. Balbyshev, M. Khobaib, M.S. Donley. Progress in Organic Coatings 47 (2003) 416.
23. S.V. Lamaka, M.L. Zheludkevich, K.A. Yasakau, M.F. Montemor, P. Cecílio, M.G.S. Ferreira. Electrochemistry Communications 8 (2006) 421.
24. S.V. Lamaka, M.L. Zheludkevich, K.A. Yasakau, R. Serra, S.K. Poznyak, M.G.S. Ferreira. Progress in Organic Coatings 58 (2007) 127.
25. E. Abdullayev, R. Price, D. Shchukin, Y. Lvov. ACS Applied Materials and Interfaces 1 (2009) 1437.
26. D. Fix, D.V. Andreeva, Y.M. Lvov, D.G. Shchukin, H. Möhwald. Advanced Functional Materials 19 (2009) 1720.
27. E.V. Skorb, D. Fix, D.V. Andreeva, H. Möhwald. Advanced Functional Materials 19 (2009) 2373.
28. A.F. Galio, S.V. Lamaka, M.L. Zheludkevich, L.F.P. Dick, I.L. Müller, M.G.S. Ferreira. Surface and Coatings Technology 204 (2010) 1479.
29. D. Snihirova, S.V. Lamaka, M. Taryba, A.N. Salak, S. Kallip, M.L. Zheludkevich, M.G.S. Ferreira, M.F. Montemor. Applied Materials and Interfaces 2 (2010) 3011.
30. D. Borisova, H. Möhwald, D.G. Shchukin. ACS Nano 5 (2011) 1939.
31. M.F. Montemor, D.V. Snihirova, M.G. Taryba, S.V. Lamaka, I.A. Kartsonakis, A.C. Balaskas, G.C. Kordas, J. Tedim, A. Kuznetsova, M.L. Zheludkevich, M.G.S. Ferreira, Electrochimica Acta 60 (2012) 31.
32. A.J. Bard, F.-R.F. Fan, J. Kwak, O. Lev. Analytical Chemistry 61 (1989) 132.
33. A.J. Bard, F.-R.F. Fan, M.V. Mirkin. In: Electroanalytical Chemistry, Vol. 18 (Edited by A.J. Bard). Marcel Dekker, New York, 1994, p. 243.
34. K. Mansikkamaki, P. Ahonen, G. Fabricius, L. Murtomaki, K. Kontturi. Journal of the Electrochemical Society 152 (2005) B12.

35. K. Mansikkamaki, C. Johans, K. Kontturi. Journal of the Electrochemical Society 153 (2006) B22.
36. K. Mansikkamaki, U.Haapanen, C. Johans, K. Kontturi, M. Valden. Journal of the Electrochemical Society 153 (2006) B22.
37. S.E. Pust, W. Maier, G. Wittstock. Zeitschrift für Physikalische Chemie 222 (2008) 1463.
38. L. Niu, Y. Yin, W. Guo, M. Lu, R. Qin, S. Chen. Journal of Materials Science 44 (2009) 4511.
39. R.M. Souto, S.V. Lamaka, S. González. In: Microscopy: Science, Technology, Applications and Education, Vol. 3 (Edited by A. Méndez-Vilas, J. Díaz). Formatex, Badajoz, 2010, p. 1769.
40. K. Fushimi, M. Seo. Electrochimica Acta 47 (2001) 121.
41. A.C. Bastos, A.M. Simões, S. González, Y. González-García, R.M. Souto. Electrochemistry Communications 6 (2004) 1212.
42. A.M. Simões, A.C. Bastos, M.G. Ferreira, Y. González-García, S. González, R.M. Souto. Corrosion Science 49 (2007) 726.
43. J. Izquierdo, L. Nagy, Á. Varga, J.J. Santana, G. Nagy, R.M. Souto. Electrochimica Acta 56 (2011) 8846.
44. J. Izquierdo, L. Nagy, Á. Varga, I. Bitter, G. Nagy, R.M. Souto. Electrochimica Acta 59 (2012) 398.
45. S.B. Basame, H.S. White. Journal of Physical Chemistry 99 (1995) 16430.
46. N. Casillas, S. Charlebois, W.H. Smyrl, H.S. White. Journal of the Electrochemical Society 141 (1994) 636.
47. Y.Y. Zhu, D.E. Williams. Journal of the Electrochemical Society 144 (1997) L43.
48. M.A. Malik, P.J. Kulesza, G. Pawlowska. Electrochimica Acta 54 (2009) 5537.
49. Y. González-García, G.T. Burstein, S. González, R.M. Souto. Electrochemistry Communications 6 (2004) 637.
50. R.M. Souto, Y. González-García, S. González, G.T. Burstein. Corrosion Science 46 (2004) 2621.
52. A. Simões, D. Battocchi, D. Tallman, G. Bierwagen. Progress in Organic Coatings 63 (2008) 260.
53. R.M. Souto, Y. González-García, S. González. Progress in Organic Coatings 65 (2009) 435.
54. Y. González-García, J.J. Santana, J. González-Guzmán, J. Izquierdo, S. González, R.M. Souto. Progress in Organic Coatings 69 (2010)110.
55. Y. Gonzalez-Garcia, J.M.C Mol, T. Muselle, I. De Graeve, G. Van Assche, G. Scheltjens, B. Van Mele, H. Terryn. Electrochemistry Communications 13 (2011) 169-173.
56. D.A. Walsh, L.E. Li, M.S. Bakare, K.T. Voisey. Electrochimica Acta 54 (2009) 4647.
57. D. Battistel, S. Daniele, G. Battaglin, M.A. Baldo. Electrochemistry Communications 11 (2009) 2195.
58. D. Battistel, S. Daniele, R. Gerbasi, M.A. Baldo. Thin Solid Films 518 (2010) 3625.
59. L. Johnson, A. Niaz, A. Boatwright, K.T. Voisey, D.A. Walsh. Journal of Electroanalytical Chemistry 657 (2011) 46.

60. S. Modiano, J.A.V. Carreno, C.S. Fugivara, R.M. Torresi, V. Vivier, A.V. Benedetti, O. R. Mattos. Electrochimica Acta 53 (2008) 3670.
61. J. Izquierdo, J.J. Santana, S. González, R.M. Souto. Electrochimica Acta 55 (2010) 8791.
62. M. Pähler, J.J. Santana, W. Schuhmann, R.M. Souto. Chemistry - A European Journal 17 (2011) 905.
63. J. Izquierdo, L. Nagy, J.J. Santana, G. Nagy, R.M. Souto. Electrochimica Acta 58 (2011) 707.
64. M.M. Antonijević, S.M. Milić, M.B. Petrović. Corrosion Science 51 (2009) 1228.
65. G. Xue, X.-Y. Huang, J. Dong, J. Zhang. Journal of Electroanalytical Chemistry 310 (1991) 139.
66. D. Chadwick, T. Hashemi. Surface Science 89 (1979) 649.
67. H.G. Tompkins, S.P. Sharma. Surface and Interface Analysis 4 (1982) 261.
68. S. Yoshida, H. Ishida. Journal of Materials Science 19 (1982) 2323.
69. S. Yoshida, H. Ishida. Applied Surface Science 20 (1985) 497.
70. G. Xue, Q. Dai, S. Jiang. Journal of the American Chemical Society 110 (1988) 2393.
71. G. Xue, J. Zhang, G. Shi, Y. Wu. Journal of the Chemical Society, Perkin Transactions II (1989) 33.
72. G. Xue, J. Ding, P. Wu, G. Ji. Journal of Electroanalytical Chemistry 270 (1989) 163.
73. G. Trabanelli, V. Carrassiti. In: Advances in Corrosion Science and Technology, Vol. 1 (Edited by M.G. Fontana, R.W. Staehle). Plenum Press, New York, 1970, p. 147.
74. D.-Q. Zhang, L.-X. Gao, G.-D. Zhou. Corrosion Science 46 (2004) 3031.
75. F.X. Perrin, J. Pagetti. Corrosion Science 40 (1998) 1647.
76. J. Aljourani, K. Raeissi, M.A. Golozar. Corrosion Science 51 (2009) 1836.
77. A.J. Bard, M.V. Mirkin (Editors). Scanning Electrochemical Microscopy. Marcel Dekker, New York, 2001, p. 243.
78. R.M. Souto, Y. González-García, J. Izquierdo, S. González. Corrosion Science 52 (2010) 748.

8.4

Study of the cathodic inhibition by benzotriazole of the galvanic corrosion of copper coupled to iron using SVET and dual potentiometric/amperometric operation in SECM

8.4.1. Abstract

A combined scanning microelectrochemical procedure is proposed to obtain information on the action of corrosion inhibitors on metals. The method uses the scanning vibrating electrode technique (SVET) and the scanning electrochemical microscopy (SECM). Antimony tips are employed as the sensing probe in SECM, allowing this technique to be operated in both potentiometric and amperometric modes. This novel approach allows the spatial distributions of pH, concentration of redox active species, and ionic currents associated to corrosion processes to be monitored. The potential of the proposed experimental strategy is tested on a model system, the inhibitor action of benzotriazole (BTAH) on the galvanic corrosion of an iron-copper couple immersed in sodium chloride solution. In this way, the effect of benzotriazole (BTAH) on the cathodic half-cell reaction occurring on the copper specimen was studied *in situ*. The results reveal that the inhibitor films formed on copper render this metal electrochemically inactive, though electrically connected to the iron specimen, and cathodic sites are developed on the less noble iron surface in addition to the anodic sites.

8.4.2. Resumen

En esta sección se propone un procedimiento que emplea técnicas microelectroquímicas de barrido para obtener información sobre la acción de inhibidores de corrosión en metales. El método utiliza la técnica de barrido del electrodo vibrante (SVET) y la microscopía electroquímica de barrido (SECM). Se han empleado puntas de antimonio como sensores de SECM, permitiendo a esta técnica operar en ambos modos, amperométrico y potenciométrico. Esta nueva aproximación permite analizar las distribuciones espaciales de pH, concentración de especies redox activas y corrientes iónicas asociadas a los procesos de corrosión. Se ha comprobado el potencial de la estrategia experimental propuesta en un sistema modelo, la acción inhibidora del benzotriazol (BTAH) en la corrosión galvánica de un par hierro-cobre inmerso en disolución de cloruro sódico. De esta manera, se ha podido estudiar *in situ* el efecto del benzotriazol (BTAH) sobre la semirreacción catódica que tiene lugar en la muestra de cobre. Los resultados revelan que las películas de inhibidor formadas en el cobre dejan a este metal electroquímicamente inactivo pese a su conexión con la muestra de hierro, permitiendo la aparición de sitios catódicos en la superficie del hierro, menos noble, junto a los sitios anódicos.

8.4.3. Introduction

Corrosion processes on metal electrodes can be inhibited by organic and inorganic molecules adsorbed to the metal surface. The formation of surface films containing these molecules may either retard metal dissolution or hinder the corresponding cathodic processes, rendering the protected metal more resistant against the attack of species present in the environment. Characterization of metal-inhibitor systems is frequently based on the use of conventional electrochemical techniques, though they average the response of relatively large specimen areas and they provide little information on the mechanism of the chemical interactions and processes which have their origin in micro- and nanometric scales. The recent development of scanning microelectrochemical techniques which are operated *in situ*, thus closely matching the natural conditions occurring during aqueous corrosion, are greatly contributing to a more detailed and efficient characterization of corrosion systems in general, and of corrosion inhibition more particularly. The introduction of scanning electrochemical microscopies to corrosion studies was due to Isaacs [1-3], when the scanning vibrating electrode technique (SVET) was employed to detect pathways for ionic currents above corroding metals. The vibrating probe actually measures potential differences in the electrolytic phase in contact with the corroding metal arising from the fluxes of ionic species that participate in the electrochemical reactions occurring at the metal/solution interface. Since then, this technique has found application to investigate a wide variety of corrosion processes and to characterize the protection properties of many surface films applied on metals [4], though a major limitation of the technique is the impossibility to identify the species that cause the ionic flux. A promising route to overcome this limitation has been offered by the use of ion-selective microelectrodes as a non-vibrating probe to potentiometrically monitor the concentration distributions of charged species in the solution adjacent to the surface under investigation [5,6]. This is the operation principle of the scanning ion-selective electrode technique (SIET) [7].

The electrochemical reactivity of a metal/electrolyte interface can be imaged with the scanning electrochemical microscope (SECM) [8]. This technique is based on the reaction that occurs at a mobile ultramicroelectrode tip (UME) immersed in an electrolyte solution in close vicinity of a surface [9], which is an amperometric electrochemical operation. Both the topography and/or redox activity of the solid/liquid interface can be characterized from the faradaic current measured at the tip [9]. Despite its more recent introduction in Corrosion Science, this technique has already found even wider application due to its higher spatial resolution and chemical selectivity [10-12]. Yet, some specific difficulties concerning the use of SECM have been reported when metal systems bearing redox potentials more negative than oxygen electroreduction [13-15] and/or hydrogen evolution were investigated. Another limitation is the observation of interferences to the detection of some redox systems due to the presence of other electrochemically-reactive species involved in the overall corrosion process which effectively affect

the chemical selectivity of the technique [16]. In the first case, non-aqueous environments had to be employed for the investigation of the electrochemical reactivity of the metallic systems [13,14], whereas higher chemical selectivity would be required to solve the later. This is the reason to investigate the applicability of the potentiometric operation in SECM [17,18] for the study of corrosion reactions [19], though from a practical point of view, it is very difficult to control the tip-sample distance in this case. A very promising way to combine the advantages of amperometric and potentiometric operation modes in SECM has arisen from the introduction as UME tips of materials that exhibit a dual-function in different potential ranges [20,21]. This is the case with antimony, a material that changes its open circuit potential in response to the pH of the environment [17].

The issue of corrosion inhibition of metallic surfaces is becoming increasingly addressed employing scanning microelectrochemical techniques. Most of the available studies make use of SVET, whereas SECM has been employed scarcely. In the latter case, only the copper-benzotriazole (BTAH) system has been investigated so far. Yet, those studies have shown the utility of SECM to monitor the kinetics of inhibitor film formation [22-25], which is derived from the progressive decrease in the conductive characteristics of the surface with the elapse of time. Furthermore, simple and fast operation procedures can be employed to inter-compare the inhibition efficiencies of Cu-BTAH films formed under different pre-treatments [25,26], as well as their resistance to the corrosive attack of aggressive environments [27]. Despite these outstanding advantages, it has not been possible to unambiguously identify the half-cell reaction affected by the presence of the benzotriazole-containing surface film exclusively on the basis of those experiments. Indeed, this effect remains to be controversial through the scientific literature [28-34], at least in relation to proton reduction in acidic and non-aerated media [29]. Thus, there is need to design new experiments to characterize localized electrochemical activity on corroding systems by monitoring the spatial distributions of pH, redox active species, and ionic currents associated to the corrosion reactions.

In the current Section, the SVET and SECM characterization of the pH distribution, oxygen consumption and ionic current flows related to the galvanic corrosion of an iron-copper pair exposed to aqueous chloride solution is described. The applicability of SVET to screen the efficiency of different inhibitors has been well established, when employed either alone [35-38], or in combination with SIET [39,40], and it has become an extremely powerful technique to analyze the self-healing capacity of a new generation of smart coatings containing nanocontainers of inhibitors [40-42]. Nevertheless, the combined used of SVET and dual potentiometric/amperometric SECM offers the major advantage of spatially separating the anodic and cathodic sites on a sample by recording the ionic fluxes in solution with the former, combined with the unique characteristics of SECM for the unambiguous identification of the species involved in the corresponding half-cell reactions, as well as to determine the concentration distribution of those species. In this way, additional information necessary to establish the interaction mechanism of corrosion inhibitors with metal surfaces will become available, whereas this

experimental approach can be employed to screen corrosion inhibitors for given applications as well. This combination of scanning microelectrochemical techniques has not been employed until now, and should greatly enhance the resources available for the investigation of corrosion processes. To check the validity of the proposed methodology, the ability of benzotriazole (BTAH) to inhibit the cathodic reaction during copper corrosion was chosen as model system. To accomplish this investigation, the copper surface has been pre-treated with benzotriazole for different times to form surface films of varying thickness, and consequently detect any variation in the distribution of anodic and cathodic sites between the two metals. Dual potentiometric and amperometric operation of the SECM has been achieved using antimony microelectrodes as tips [21].

8.4.4. Experimental

8.4.4.1. SVET instrumentation and experimental procedure

The scanning vibrating electrode instrumentation used was manufactured by Applicable Electronics Inc. (Forestdale, MA, USA) and controlled by dedicated software. The probe microelectrode consisted of Pt/Ir (80%/20%) wires insulated with paralene C® and arced at the tip to expose the metal, and they were platinized in order to produce a spherical platinum black deposit of 10-20 μm diameter. A video camera connected to an optical microscope was introduced in the system both to establish the probe-sample distance, and to follow the movement of the vibrating electrode over the sample during operation. The measurements were made with the electrode tip vibrating both normal (frequency, 195 Hz; amplitude, 37.5 μm) and parallel (frequency, 105 Hz; amplitude, 20 μm) to the sample mounted horizontally facing upwards. The mean distance between the microelectrode and the sample surface was 80 μm.

8.4.4.2. SECM instrumentation and experimental procedure

The scanning electrochemical microscope was a home-built system [43] that used a 3D positioning device driven by precision step motors with 75 nm minimal step size. A video camera was used to further assist positioning of the tip close to the surface. The distance between the tip and the substrate was established by allowing the probe to gently rest on the sample, and subsequently the probe was retracted to the chosen operation distance with the aid of the Z-positioning motor. In order to achieve dual potentiometric/amperometric operations with one single probe, an antimony microelectrode with a 25 μm diameter active disk surface at the tip was employed. The procedures employed both in the fabrication of the antimony microelectrode, and in the determination of its pH sensing performance are described in detail elsewhere [21]. In brief, the electrode was calibrated from the

measurement of the potential response transients toward pH change of the solution, using a sequence of seven buffer solutions covering the 3 < pH ≤ 11.5 range. Figure 8.4.1 is the calibration curve of the electrode's potential response to the pH value of the solution, which shows a good linear relationship. The slope of the line is -46.1 mV (pH unit)$^{-1}$.

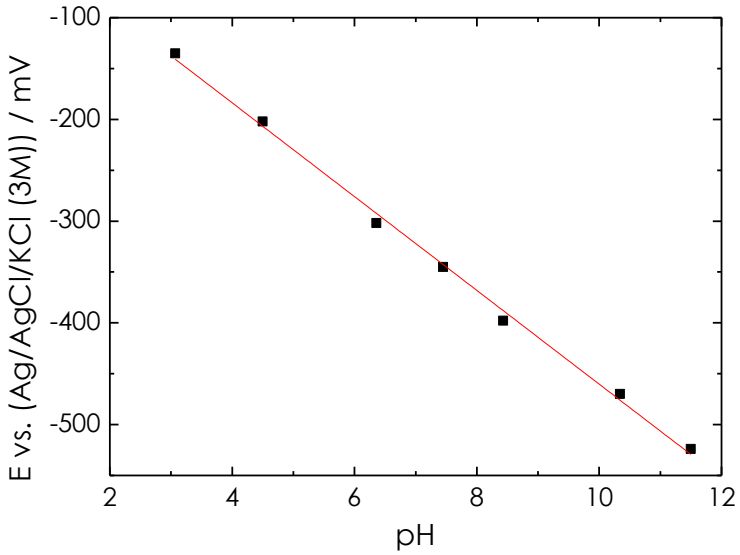

Figure 8.4.1. Calibration curve for the antimony microelectrode tip for pH measurement.

SECM experiments were carried out in a three-electrode cell. The electrolyte volume used in the microelectrochemical measurements amounted to 3.2 cm^3. The antimony tip was the working electrode, an Ag/AgCl/KCl (3M) reference electrode and a platinum counter electrode. Specimens were mounted horizontally facing upwards. The measurements were performed with the microelectrode at a height of 25 μm over the specimen surface.

8.4.4.3. Materials

The testing samples consisted of iron and copper wires (dia. 0.7 mm) mounted into an Epofix (Struers, Ballerup, Denmark) resin sleeve, so that only their cross sections area formed the testing metal substrate (see Figure 8.4.2). For the galvanic couple experiments the two electrodes embedded in the resin could be connected electrically at the back of the mount. The mounts with the samples were polished with silicon carbide paper down to 800 grit, and subsequently polished with alumina micropolish of 1 and of 0.3 μm particle size. The resulting surfaces were thoroughly rinsed with Millipore deionised water, dried with acetone and finally surrounded laterally by Sellotape, thus creating a container for the test electrolyte solution.

Reagents of analytical grade and twice-distilled water were employed to prepare all the solutions. Microelectrochemical measurements and surface preparation processes were performed at ambient temperature in the naturally

aerated solutions. Corrosion tests were carried out in aqueous 10 mM NaCl solution. Inhibitor solution was prepared at a 1 mM concentration by dissolving BTAH in a 0.1 M Na_2SO_4 solution. Inhibitor films were produced on the copper electrode *ex situ* by dipping the portion of the mount containing the copper wire in the inhibitor-containing solution for three different immersion times (5, 30, and 60 min, respectively) which were selected from the characteristic behaviours of the surface films formed on copper that were observed from the results discussed before in Section 8.2 of this Thesis.

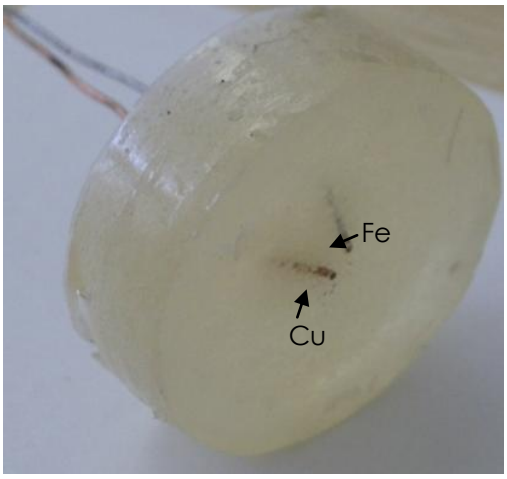

Figure 8.4.2. Photograph showing the lateral view of the iron-copper galvanic pair embedded in an insulating sleeve. The electrical connection was made at the rear of the mould.

8.4.5. Results and discussion

The inhibitory action of benzotriazole (BTAH) on copper has been investigated using scanning microelectrochemical techniques which provide spatially resolved information on the reactivity of surfaces, particularly in relation to the effect of this organic molecule on the cathodic half-cell reaction. Ionic current fluxes, pH changes and concentration variations of chemical species can be gathered using an experimental methodology based on the scanning vibrating electrode technique (SVET) and scanning electrochemical microscopy (SECM).

In order to check the validity of the proposed method, the inhibitor was put in contact with the copper specimen of the iron-copper galvanic couple exclusively. The two metals were chosen in order that copper would be the nobler metal, thus securing this metal to be free from the development of local anodes throughout the experiments. The behaviour of the two metals without electrical connection in the test environment was also investigated as a reference system. The rationale for this case was to gain further information on the inhibitory effect of BTAH on copper,

which ideally would result in the total blockage of the metal in case of a 100% inhibition efficiency, effectively leaving the iron sample as the only active metal surface in the system. Inhibitor films were formed on the copper specimen from their immersion in 1 mM BTAH + 0.1 M Na_2SO_4 solution for different treatment times. The duration of the treatments considered in this Section, namely 5, 30 and 60 min, were chosen on the basis of the trends observed in Section 8.2 on the kinetics of inhibitor film formation for the Cu-BTAH system using the same conditioning procedure as to match the main states revealed in that investigation. Another objective of this investigation was to explore the effect of pH on the corrosion of iron. Galvanic coupling of iron to copper leads to the removal of the cathodic reaction from the iron surface. This reaction is responsible for the alkalinisation of the electrolyte next to the reactive site. In this way, it will take longer for the iron specimen to be exposed to an alkaline environment, thus effectively preventing the precipitation of corrosion products on this metal, a situation usually found during the spontaneous corrosion of iron in otherwise neutral aqueous electrolytes.

8.4.5.1. Characterization of the galvanic coupling of iron and copper by SVET

The scanning vibrating electrode technique measures ionic fluxes in the electrolytic phase next to a corroding surface. In a neutral environment, the distribution of anodic sites can be revealed from the flux of cations departing from the surface as result of the dissolution reaction of the metal, whereas anions will be produced at the cathodic sites. The chemical reactions responsible for these ionic fluxes can be written as:

$$Fe \rightarrow Fe^{2+} + 2e^- \quad (8.4.1)$$

$$O_2 + 2H_2O + 4e^- \rightarrow 4OH^- \quad (8.4.2)$$

The sign of the ionic species departing from the surface in each half-cell reaction can be followed from the opposite sign of the potential gradients produced in the electrolyte as a result of their transport.

Figure 8.4.3 depicts the images generated by SVET of different experimental conditions of an iron-copper galvanic couple immersed in 10 mM NaCl. The images were always taken after a fixed period of immersion in the electrolyte, namely 120 minutes, in order to directly relate any changes in the activity of the samples to the differences in the experimental conditions applied to the metals. The case of the inhibitor-free metal surfaces is considered next, when the metals were either electrically disconnected (Figure 8.4.3A) or electrically connected to form the galvanic pair (Figure 8.4.3B). In the first case, ionic fluxes are only observed above the iron wire because of the greater tendency to corrode of this metal compared to copper in this environment.

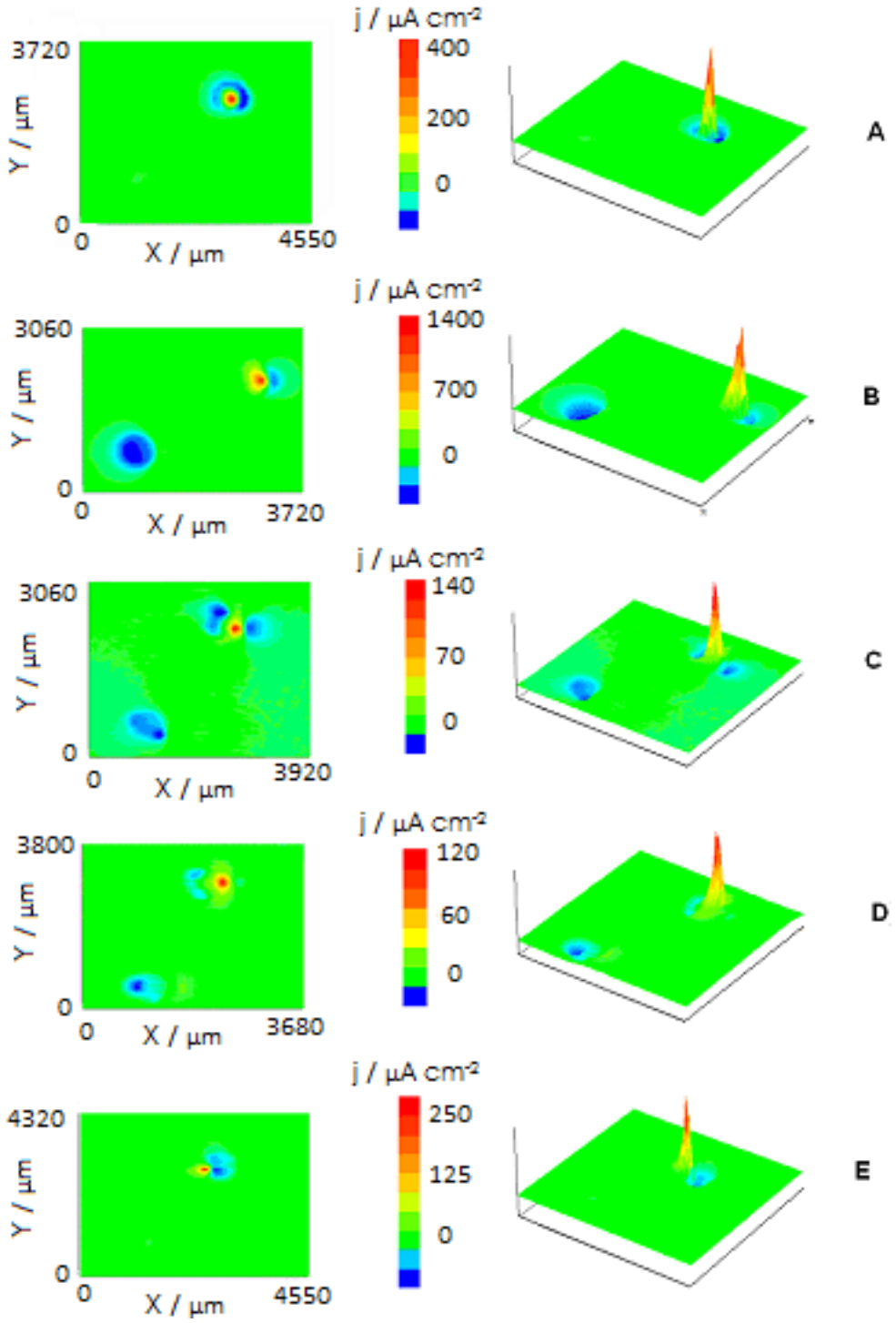

Figure 8.4.3. Images generated by SVET of different experimental conditions of an iron-copper sample. The samples were immersed in 10 mM NaCl. BTAH-containing surface films were prepared on the copper by dipping only the part of the mount with the wire in 1 mM BTAH + 0.1 M Na_2SO_4 solution for selected times as given below. Electric condition of the metal wires: (A) electrically insulated, i.e. there is no galvanic coupling; and (B-E) electrically connected to form a galvanic pair. Surface condition of the copper sample: (A-B) The metal has not been pretreated with BTAH; duration of pretreatment with BTAH: (C) 5 min, (D) 30 min, and (E) 60 min. The mounts with the metal wires were maintained in the test solution for 120 min before the SVET image was recorded. Tip-substrate distance: 80 µm.

The anodic reaction is found to be greatly localized over a small portion of the iron surface, whereas the corresponding cathodic process is distributed on the surrounding metal area almost concentrically. The magnitude of the fluxes measured for both processes is also an indication of the relative areas of anodic and cathodic sites distributed on the metal. The smaller size of the anodic site is responsible for the greater ionic flux associated to the dissolution of metal ions, whereas the release of hydroxyl ions is distributed over a wider area and smaller ion fluxes are measured at each point. The situation changes significantly in relation to the distribution of the anodic and cathodic reactions when the two metals are put in electric contact. In this case, the anodic process continues to occur on a small portion of the iron sample, whereas the cathodic process is mainly shifted to the copper sample, where it is found to distribute quite homogeneously over the totality of the metal surface. Yet some cathodic activity remains on the surrounding iron surface, as it could be expected because the two metals are at the same potential and the anodic activity occurs only in a portion of the iron surface. Another relevant feature is the observation of bigger electrochemical activity for the galvanic pair compared to the isolated metals. That is, the corrosive process on the iron specimen is facilitated by the displacement of the cathodic activity to the copper surface.

The electrochemical activity in the galvanic pair is reduced in a great extent when the copper surface is covered by a BTAH-containing film as shown in the sequence of images in Figure 8.4.3C-E. Not only the total activity decreases in the system, but it is also observed that the cathodic activity is shifted from the copper to the iron surface as the inhibitor film on copper is thicker. Eventually, for the thickest protective film, corresponding to the 60 min treatment of the copper specimen in the inhibitor-containing solution, it is found a situation closely matching that previously observed on iron when it was electrically disconnected from copper (cf. Figure 8.4.3A and 8.4.3E). Yet, a more detailed observation of Figure 8.4.3E in the region of the copper sample allows a very small cathodic activity to be detected. The inhibiting effect of BTAH on the cathodic reaction in copper has thus been revealed through this sequence of images taken by SVET.

The influence of the BTAH films deposited on copper towards the inhibition of the cathodic reaction is also deduced from the inspection of the SVET images given in Figure 8.4.4, which were recorded after 600 min immersion of the iron-copper galvanic pairs in the 10 mM NaCl test solution. Thicker BTAH films are formed on copper as immersion time elapses in the inhibitor-containing solution [33], and these layers help to greatly reduce the extent of galvanic corrosion on the coupled metals (cf. Figures 8.4.4A-B), until the copper wire becomes so effectively blocked that the cathodic reaction has to occur quantitatively on the iron specimen together with the anodic sites. These more aggressive conditions were chosen for the experiments using the SECM as described in the next Section 8.4.5.2.

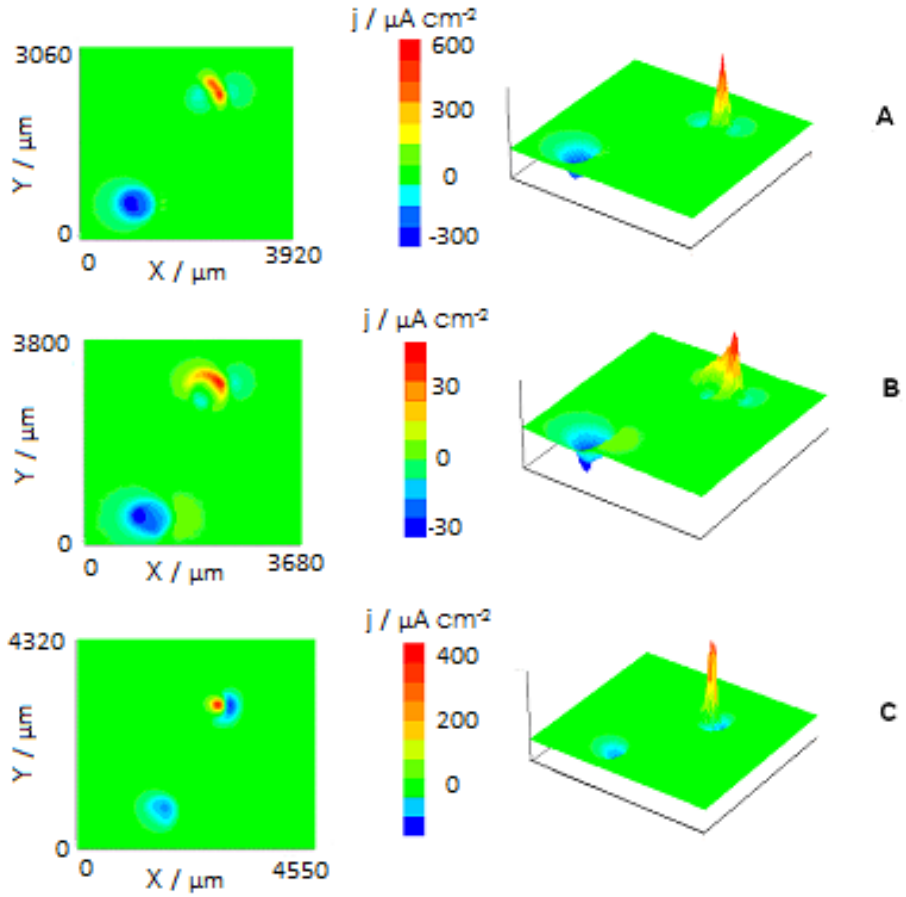

Figure 8.4.4. Images generated by SVET of iron-copper galvanic pairs immersed in 10 mM NaCl for 600 min before the SVET image was recorded. The copper specimen was pre-treated in 1 mM BTAH + 0.1 M Na_2SO_4 solution for: (A) 5 min, (B) 30 min, and (C) 60 min. Tip-substrate distance: 80 µm.

8.4.5.2. Characterization of the galvanic coupling of iron and copper by SECM

In order to better examine the corrosion reactions of the iron-copper galvanic pair and the origin of the inhibiting effect of BTAH on copper metal, SECM using an antimony tip was used. The antimony tip in potentiometric SECM allows pH distributions in the electrolyte next to the galvanic pair to be monitored, whereas the conventional amperometric operation could be used to follow the consumption of oxygen in the system in the course of the corrosion reaction. In the later case, the tip potential was set at -0.65 V vs. Ag/AgCl/KCl (3M).

The extent and location of the different active areas on the metals during their exposure to the 10 mM NaCl test solution could be imaged by acquiring bidimensional scans over the center of both iron and copper samples of the metal which give the local distribution of pH as shown in Figure 8.4.5. When the metal specimens were exposed to the test electrolyte without electric connection (i.e. no galvanic coupling exists in the system), pH changes can be observed only in the proximity of the iron sample (see Figure 8.4.5A). That is, the onset of corrosion occurs on this metal, whereas copper stays basically unreactive in this electrolyte, which is

consistent with the absence of ionic currents over this metal in the corresponding SVET measurements (cf. Figure 8.4.3A).

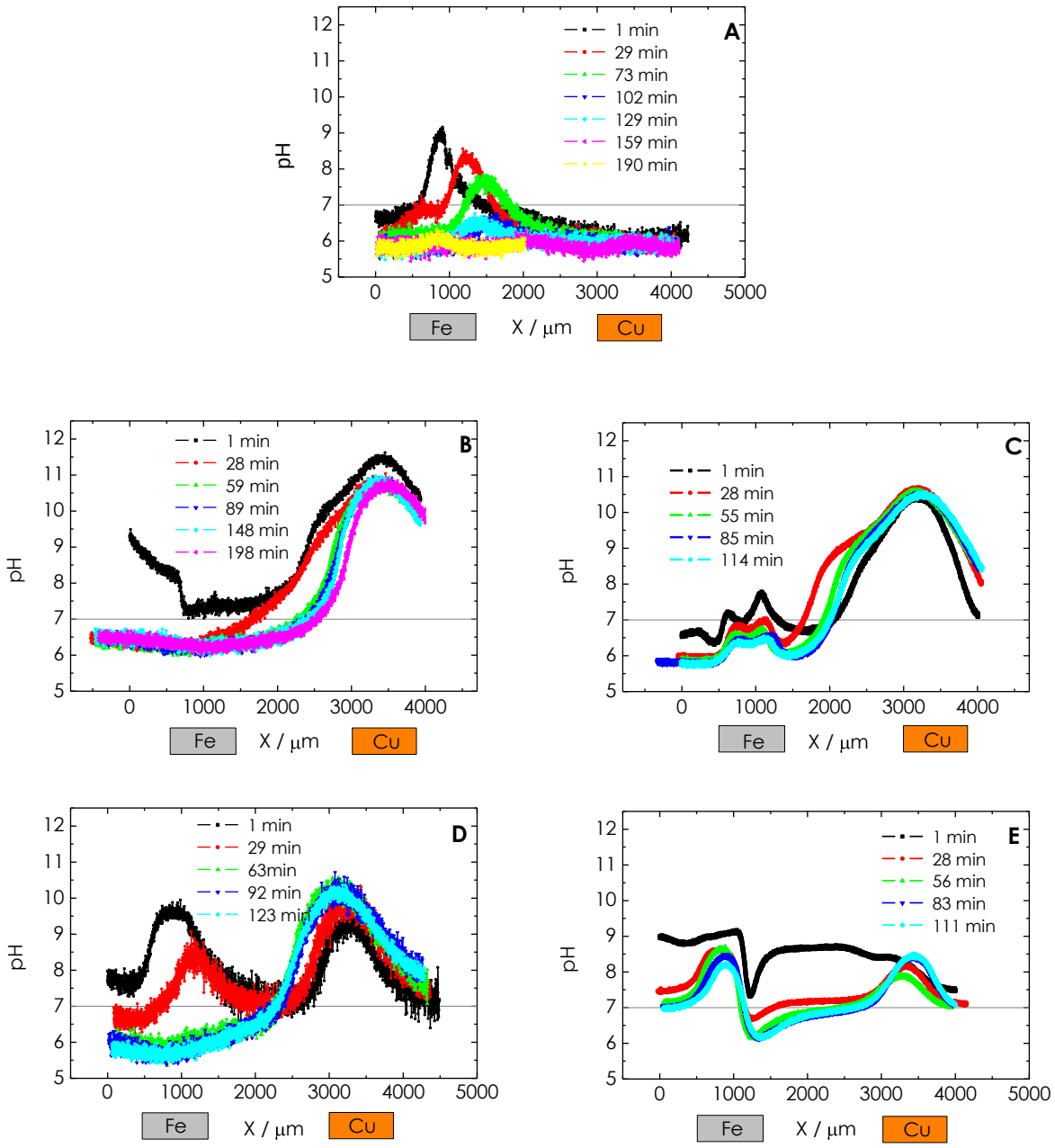

Figure 8.4.5. Local pH distribution lines generated by SECM with an antimony tip passing over the centres of iron-copper samples subjected to different pre-treatments with BTAH. The measurements were performed in 10 mM NaCl. Electric and surface conditions of the samples are the same described in the legend of Figure 8.4.3. Scan lines were initiated when the samples were immersed in the test solution for the times given in the plots. Tip-substrate distance: 25 µm.

The two half-cell reactions take place on the corroding iron, and significant alkalinisation of the electrolyte occurs in the proximity of the metal as it should be expected from equation (8.4.2). The highest pH values are observed shortly after immersion in the electrolyte, and less alkaline environments are found as time elapses. And after 190 min exposure, the pH of the solution volume next to the iron sample exhibits the typical values of the bulk electrolyte, which evidences that the corrosion process has been suppressed. It is also interesting to notice that the exact location on the iron surface at which the maximum pH values are observed in each pH distribution line moves progressively from left to right in the plots. The highest pH values are observed thus at the beginning of the experiment, with a maximum value of ca. 9 in the pH scale. All the observed results can be explained by considering that the surface becomes progressively blocked by the precipitation of iron-containing corrosion products, thus leading to the local anodes and cathodes to move when the precipitates blocked the surface. This feature was observable even with the naked eye, and it is shown in the optical micrographs given in Figure 8.4.6 which were taken for both wires just at the beginning of the experiment (image A) and after 3 hours exposure (image B). The shift of the pH distribution peaks from left to right in Figure 8.4.5A with the elapse of time is an indirect observation that the anodic dissolution reaction initially happened in a region close to the left border of the iron wire, and it progressed to the right as the anodic sites were getting blocked by the precipitation of corrosion products. This shift of the anodic activity towards the right side, produces a reduction in the area available for the cathodic reaction that becomes progressively more confined to the right side of the sample. On the other side, the pH of the volume of electrolyte directly in contact with the copper wire does not change during the duration of the experiment, and the local pH values coincide with those of the bulk electrolyte.

Figure 8.4.6. Optical micrographs of the Fe-Cu sample immersed in 10 mM NaCl: (A) Just after immersion in the electrolyte; (B) after 3 hours exposure. No electric contact existed between the two metals.

Conversely to the situation described in the previous paragraph, separation of the anodic and cathodic sites between the two metals occur when the two metals are galvanically coupled in the same test electrolyte as shown in Figure 8.4.5B. In this case, alkalinisation occurs exclusively above the copper wire. The dissolution of iron is enhanced as result of the galvanic coupling process, thus leading to significantly more alkaline environments in the electrolyte adjacent to the

cathode. In fact, the highest pH observed over isolated iron was ca. 9 just after immersion in the electrolyte (cf. Figure 8.4.5A), but values in the proximity of 11 are measured over copper in electrically connected with iron (cf. Figure 8.4.5B). Furthermore, the iron dissolution process is not blocked by corrosion products this time, and it seems to progress at rather constant rate. This feature is due to the spatial separation of the anodic and cathodic half-cell reactions on the two metals, which are placed at sufficient distance for the precipitation of corrosion product not to occur on the surface of the iron metal, which would eventually lead to blockage of the reactive surface, but on the resin between the two metals. In this way, the local pH above iron remains at the initial value of the bulk electrolyte during all the experiment.

The effect of benzotriazole on the iron-copper galvanic corrosion reaction was also investigated from the measurement of bidimensional local pH line scans for samples subjected to different pre-treatment durations in a solution containing the inhibitor. Figure 8.4.5C-E presents a selection of the lines measured at different exposures in the test solution of samples where the copper surfaces were pre-treated with BTAH for 5, 30 and 60 minutes, respectively. Major changes in both the shape and the evolution of the local pH distributions given by the line scans are evident from their comparison with the corresponding line scans measured for the untreated copper surface given in Figure 8.4.5B. Though the pH distribution values above the copper wire treated with BTAH for 5 minutes are still very similar to those measured for the untreated metal, some changes can already be observed in Figure 8.4.5C. Firstly, the electrolyte solution above iron is slightly more alkaline than in the previous case, which indicates the onset of some small cathodic activity on the iron wire. Though a defective inhibiting film on copper was formed in this case, yet it provides some blocking effect to the cathodic reaction on copper that leads to the observation of additional cathodic activity on the iron surface. Furthermore, the iron dissolution is restricted to a small area on the surface, allowing for a small peak at the left related to local acidification to be seen as result of the occurrence of the hydrolysis reaction of iron according to:

$$Fe^{2+} + n\ H_2O \rightarrow Fe(OH)_n^{2-n} + n\ H^+ \qquad (8.4.3)$$

The protective characteristics of the BTAH film formed on copper are very weak and the cathodic activity is increasingly concentrated on this metal with the elapse of time.

A more pronounced effect of BTAH on the galvanic corrosion process is observed as thicker films are produced on copper. Figure 8.4.5D shows the local pH distribution line scans measured for a sample pre-treated for 30 minutes with BTAH. In this case, the initial cathodic activity is observed to occur on the surface of both metals to almost the same extent thus resulting in two alkalinisation peaks with their maxima at ca. pH = 10. Therefore, the corrosion reaction is less vigorous than in the case of the untreated copper sample (Figure 8.4.5B), though the system is more active than for the isolated iron specimen in the same electrolyte (Figure 8.4.5A). Another interesting observation is that the inhibitor film is not compact enough to

withstand the aggressive electrolyte, and with the elapse of time the cathodic reaction becomes progressively concentrated on the copper wire. Increased alkalinisation of the electrolyte above the copper sample is thus observed, whereas the pH values above iron coincide with those of the bulk electrolyte for exposures in excess of 1 hour.

Analogously, the line scans measured when the copper sample was pre-treated with BTAH for 1 hour show the occurrence of both anodic and cathodic half-cell reaction on the surface of iron, and the copper surface is almost completely inactive at the beginning of the experiment. The localization of the dissolution reaction on the surface of iron leads to the observation of an acidification peak in the first line scan just above the site of the anodic reaction. The activation of the copper surface for the cathodic reaction can be observed at longer exposures, which is an indication of the little stability of the inhibitor films formed on copper simply by dipping the freshly polished metal in the solution containing the organic molecule. Indeed, the amperometric operation of the SECM for the electroreduction of oxygen shows the existence of two zones of depleted oxygen concentration in the electrolyte located above both metal wires after 3 hours exposure in the test electrolyte (cf. Figure 8.4.7). Though the pH line shows that the electrolyte is more acidic above the iron metal, the past cathodic activity of this metal has resulted in a volume of depleted oxygen concentration. On the other hand, the onset of the cathodic reaction on copper at a later time has resulted in the simultaneous depletion of oxygen and the alkalinisation of the electrolyte above this metal. Figure 8.4.7 is considered to provide a strong evidence of the great applicability of the combined potentiometric/amperometric operation of SECM for the in situ study of the evolution of corrosion reactions with high spatial resolution.

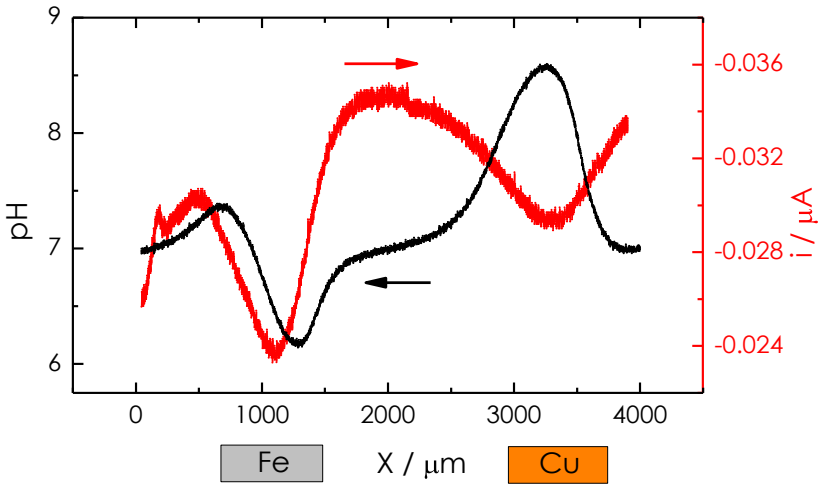

Figure 8.4.7. Line scans generated by SECM with an antimony tip passing over the centres of an iron-copper galvanic pair immersed in 10 mM NaCl for 3 hours. SECM operations: (black) potentiometric for pH monitoring, and (red) amperometric for the electroreduction of soluble oxygen (E_{tip} = -0.65 V vs. Ag/AgCl/KCl (3M)). Tip-substrate distance: 25 µm.

The distinctive activation process of the cathodic reaction on copper after immersion in the case of the metal protected by BTAH films can be observed with greater precision from the time evolution of the pH maximum values over the metal that are depicted in Figure 8.4.8. The cathodic reaction occurs exclusively on copper in the case of the untreated sample, and pH values around 11 are observed at all times. In the case of the 5 minutes pre-treatment with BTAH, the surface film is very thin and eventually does not cover the copper surface completely, and thus only a very weak inhibiting effect against galvanic corrosion being provided as revealed by pH values around 10.5 in the electrolyte next to the surface of this metal. The formation of a rather effective inhibiting film on copper is then observed for the sample pre-treated with BTAH for 30 minutes. Yet the film is not stable enough to withstand the aggressiveness of the test electrolyte for the duration of the experiment, and progressive activation of the cathodic activity on the metal is observed this time. After ca. 1 hour, the BTAH film on copper is no longer protective, and pH values similar to those measured in the previous cases are found. Finally, pH values below 9 are observed above the metal at all times in the case of the inhibitor films formed during 60 minutes. Furthermore, the progressive activation of the copper surface with the elapse of time can be followed from the plot obtained with this method, and this will be a measure of the persistence of the inhibitor film on the metal. Thus, the novel methodology presented in this Section may have a great applicability to the investigation of the stability inhibitor films for corrosion protection.

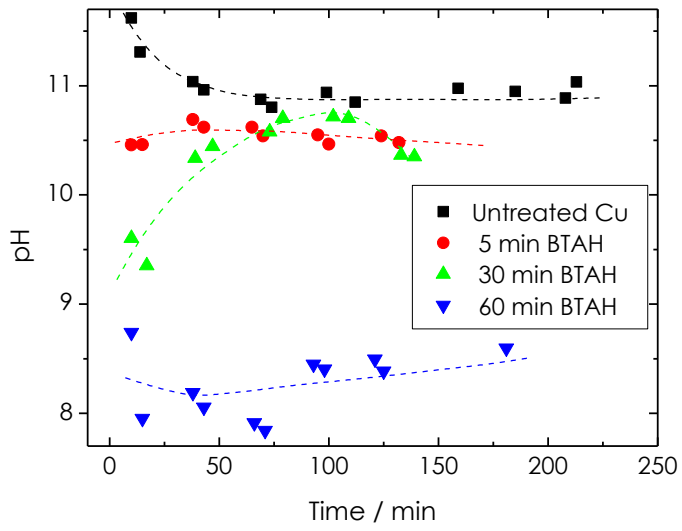

Figure 8.4.8. Time evolution of the maximum pH values measured over the copper sample taken from the curves displayed in Figure 8.4.5B-E. They are a measure of the cathodic activity occurring on copper galvanically-coupled to iron during immersion in 10 mM NaCl.

The anodic reaction occurring on iron can be investigated from the minimum pH values of the electrolyte directly above the metal in a similar manner. Figure 8.4.9A shows their time evolution for the different specimens considered in this

Section. Local acidification of the electrolyte is observed in all cases, though different trends can also be found in this figure among the different systems. Firstly, the dissolution of iron in a galvanic pair in which copper is not protected by an inhibiting film, leads to local acidification of the electrolyte for almost an hour, and then a constant pH value is observed for the remaining of the experiment. The dissolution reaction progresses at a constant velocity that helps to maintain the pH of the electrolyte despite the opposite effect of diffusion of the ionic species to the bulk of the electrolyte. No suppression of the corrosion reaction due to the precipitation of corrosion products occurs in the galvanic pair system. Acidification of the electrolyte above iron for about one hour prior to the attainment of a constant pH value also occurs when the copper sample has been pre-treated with BTAH for 5 minutes, and the pH plateau shows a slightly more acidic value than for the untreated sample. No efficient inhibition of the corrosion process is provided by the surface film formed by BTAH on copper by dipping during 5 minutes the metal in the inhibitor containing solution. A different situation is found when copper was treated for 30 minutes with BTAH. Both the anodic and cathodic reactions occur initially on the iron surface, and the high localization of the anodic site leads to the development of a more acidic environment. It is only after ca. 1 hour that the cathodic reaction is shifted to the copper surface (cf. Figures 8.4.7 and 8.4.8), and by then the electrolyte is more acidic and the system requires extra time before the rate of acidification starts to decrease. Indeed, the inflection point towards the development of a stationary pH value for this system may be found for times longer than 100 minutes.

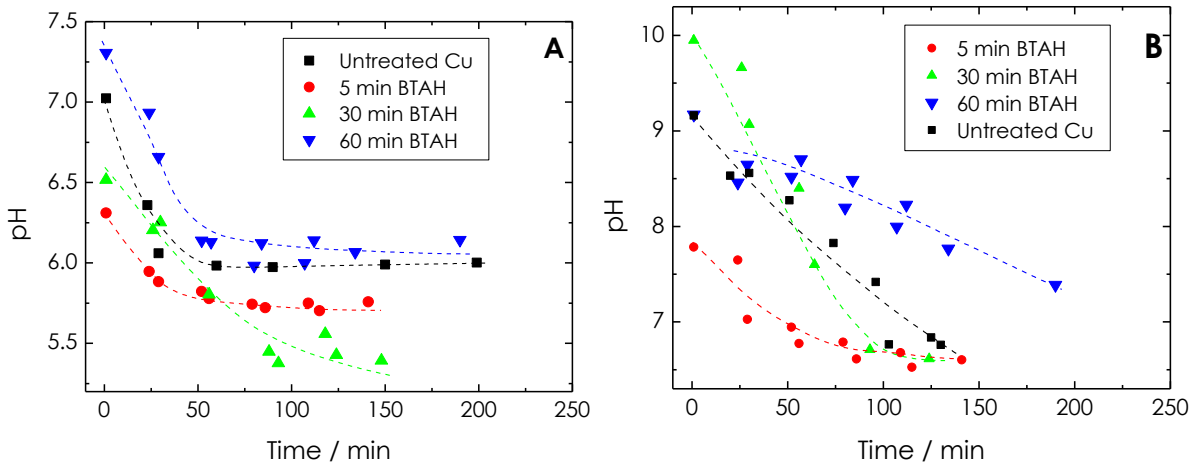

Figure 8.4.9. Time evolution of the (A) minimum and (B) maximum pH values measured over the iron sample taken from the curves displayed in Figure 8.4.5B-E. They are a measure of the (A) anodic and (B) cathodic activity occurring on iron galvanically-coupled to copper during immersion in 10 mM NaCl.

Finally, the curve given in Figure 8.4.9A for the system where copper was pre-treated for 60 minutes with BTAH closely resembles that of the untreated copper. This

is an indication of the physical separation of the anodic and cathodic sites in the system. In the case of the untreated system, this fact was evident as the anodic reaction occurs on one metal and the cathodic on the other. But, now both the anodic and the cathodic reactions must occur on iron as result of the effective inhibitor effect of BTAH on copper. Indeed, Figure 8.4.9B shows that the occurrence of the cathodic reaction on iron for all the duration of the experiment as described by the maximum pH values measured on this metal, and the special behaviour of this system is there observed. Both local acidification and alkalinisation occur simultaneously over different regions of the iron sample, and they remain in practically the same locations for the duration of the experiment, thus effectively resulting in a permanent separation of the anodic and cathodic sites. This is consistent with the observation of local acidification on iron at the same location above iron in Figure 8.4.5E at all times, and the cathodic reaction on this metal remains on another location as long as cathodic occurs on this metal, though the onset of the cathodic reaction on copper as well.

In summary, the combined potentiometric/amperometric operations of SECM allow local pH distributions and the concentration of different species to be (quasi) simultaneously imaged for corrosion reactions. But it has been demonstrated that this novel methodology allows for additional information on the kinetics of these processes to be gained because very precise measurements of local changes can be detected, certainly at much earlier times they can be evidenced by *ex situ* methods or by less sensitive *in situ* microelectrochemical techniques that operate at longer probe-substrate distances. A distinctive finding of this Section was the situation represented in Figure 8.4.7, when the cathodic reaction had already been removed from the iron to the copper surface as demonstrated by the local acidification above iron, and yet the past cathodic on the same metal could be detected from the depleted oxygen concentration in the same small volume of electrolyte. These findings may have a great potential for the investigation of real systems of greater complexity such of those occurring during the corrosion of alloys for aerospace applications in which diverse forms of localized and galvanic corrosion take place on the same portion of material.

Finally, some additional remarks should be made in relation to the dual potentiometric/amperometric operation of the antimony tips. Amperometric and potentiometric operations where commuted regularly, and no cross-effects were detected though amperometric reduction of dissolved oxygen might be expected to produce some local alkalinisation of solution around the amperometric tip through equation (8.4.2). The relevance of this effect was investigated by measuring the same scan line again, and no significant difference could be observed between two consecutive records. On the other hand, the potentiometric operation was performed before the amperometric operation, because the later implies the application of a rather negative potential value to the tip (namely E_{tip} = -0.65 V vs. Ag/AgCl/KCl (3M)) to monitor oxygen reduction. Subsequently, the Sb/Sb_2O_3 surface must be regenerated by setting the potential at 0 V vs. Ag/AgCl/KCl (3M) during a controlled time to regenerate the same surface.

8.3.6. Conclusions

Scanning electrochemical microscopy (SECM) operated with combined potentiometric/amperometric modes allows more information on the dynamics of corrosion processes to be gathered in the same experiment. The use of antimony microelectrodes as tips make possible to measure local distributions of pH above corroding systems, whereas amperometrically detecting the species participating in the corrosion reactions. In addition, the scanning vibrating electrode technique (SVET) was employed to assist the unambiguous localization of the cathodic and anodic half-cell reactions in the corroding system.

The corrosion protection efficiency of the films formed by the inhibitor benzotriazole on copper, and their stability in an aggressive electrolyte without reservoir of the inhibitor molecule could be determined in the same experiment by using the scanning microelectrochemical techniques SECM and SVET.

The galvanic coupling of copper with iron, if the metals are sufficiently separated, produces an increase in the dissolution rate of iron since the precipitation of corrosion products does not occur on this metal. Otherwise, the surface would have been blocked by the corrosion products and the corrosion reaction would have significantly been slowed.

Benzotriazole forms surface films on copper that inhibit the cathodic half-cell reaction on this metal, and may eventually lead to the both cathodes and anodes to be formed simultaneously on iron though the two metals are in electric contact during exposure to the same electrolyte.

8.3.7. References

1. H.S. Isaacs. Corrosion Science 28 (1988) 547.
2. H.S. Isaacs. Journal of the Electrochemical Society 138 (1991) 722.
3. M.J. Franklin, D.C. White, H.S. Isaacs. Corrosion Science 33 (1992) 251.
4. R.S. Lillard. In: Analytical Methods in Corrosion Science and Engineering (Edited by P. Marcus, F. Mansfeld). CRC Press, Boca Raton, 2006, p. 571.
5. S.V. Lamaka, O.V. Karavai, A.C. Bastos, M.L. Zheludkevich, M.G.S. Ferreira. Electrochemistry Communications 10 (2008) 259.
6. S.V. Lamaka, M.G. Taryba, M.L. Zheludkevich, M.G.S. Ferreira. Electroanalysis 21 (2009) 2447.
7. S.V. Lamaka, R.M. Souto, M.G.S. Ferreira. In: Microscopy: Science, technology, applications and education, Vol. 3 (Edited by A. Méndez-Vilas, J. Díaz). Formatex Research Center, Badajoz, 2010, p. 2162.
8. J. Kwak, A.J. Bard. Analytical Chemistry 61 (1989) 1221.

9. A.J. Bard, M.V. Mirkin (Editors). Scanning Electrochemical Microscopy. Marcel Dekker, New York, 2001.
10. S.E. Pust, W. Maier, G. Wittstock. Zeitschrift für Physikalische Chemie 222 (2008) 1463.
11. L. Niu, Y. Yin, W. Guo, M. Lu, R. Qin, S. Chen. Journal of Materials Science 44 (2009) 4511.
12. R.M. Souto, S.V. Lamaka, S. González. In: Microscopy: Science, Technology, Applications and Education, Vol. 3 (Edited by A. Méndez-Vilas, J. Díaz). Formatex Research Center, Badajoz, 2010, p. 1769.
13. I. Serebrennikova, H.S. White. Electrochemical Solid State Letters 4 (2001) B4.
14. I. Serebrennikova, S. Lee, H.S. White. Faraday Discussions 121 (2002) 199.
15. Y. González-García, R.M. Souto, S. Daniele. Chemistry - A European Journal, 18 (2011) 905.
16. R.M. Souto, J.J. Santana, L. Fernández-Mérida, S. González. Electrochimica Acta 56 (2011) 9596.
17. B. Horrocks, M.V. Mirkin, D.T. Pierce, A.J. Bard, G. Nagy, K. Toth. Analytical Chemistry 65 (1993) 1213.
18. G. Nagy, L. Nagy. Analytical Letters 40 (2007) 3.
19. Á. Varga, L. Nagy, J. Izquierdo, I. Bitter, R.M. Souto, G. Nagy. Analytical Letters 44 (2011) 2876.
20. B. Czoka, Z. Mekhalif. Electrochimica Acta 54 (2009) 3225.
21. J. Izquierdo, L. Nagy, J.J. Santana, R.M. Souto, G. Nagy. Electrochimica Acta 56 (2011) 8846.
22. K. Mansikkamäki, P. Ahonen, G. Fabricius, L. Murtomäki, K. Kontturi. Journal of the Electrochemical Society 152 (2005) B12.
23. K. Mansikkamäki, C. Johans, K. Kontturi. Journal of the Electrochemical Society 153 (2006) B311.
24. K. Mansikkamäki, C. Johans, K. Kontturi. Journal of the Electrochemical Society 153 (2006) B22.
25. J. Izquierdo, J.J. Santana, S. González, R.M. Souto. Electrochimica Acta 55 (2010) 8791.
26. M. Pähler, J.J. Santana, W. Schuhmann, R.M. Souto. Chemistry - A European Journal 17 (2011) 905.
27. J.J. Santana, M. Pähler, R.M. Souto, W. Schuhmann. Electrochimica Acta 77 (2012) 60.
28. M. Sugimasa, L.-J. Wan, J. Inukai, K. Itaya. Journal of the Electrochemical Society 149 (2002) E367.
29. D.-Q. Zhang, L.-X. Gao, G.-D. Zhou. Corrosion Science 46 (2004) 3031.
30. A.M. Abdullah, F.M. Al-Kharafi, B.G. Ateya. Scripta Materialia 54 (2006) 1673.
31. D.M. Bastidas. Surface and Interface Analysis 38 (2006) 1146.
32. K.L. Stewart, J. Zhang, S. Li, P.W. Carter, A.A. Gewirth. Journal of the Electrochemical Society 154 (2007) D57.
33. M.M. Antonijević, S.M. Milić, M.B. Petrović. Corrosion Science 51 (2009) 1228.
34. N.K. Allam, A.A. Nazeer, E.A. Ashour. Journal of Applied Electrochemistry 39 (2009) 961.

35. A.C. Bastos, M.L. Zheludkevich, M.G.S. Ferreira. Progress in Organic Coatings 63 (2008) 282.
36. M.F. Montemor, W. Trabelsi, S.V. Lamaka, K.A. Yasakau, M.L. Zheludkevich, A.C. Bastos, M.G.S. Ferreira. Electrochimica Acta 53 (2008) 5913.
37. J.V. Custódio, S.M.L. Agostinho, A.M.P. Simões. Electrochimica Acta 55 (2010) 5523.
38. S. Kallip, A.C. Bastos, M.L. Zheludkevich, M.G.S. Ferreira. Corrosion Science 52 (2010) 3146.
39. O.V. Karavai, A.C. Bastos, M.L. Zheludkevich, M.G. Taryba, S.V. Lamaka, M.G.S. Ferreira. Electrochimica Acta 55 (2010) 5401.
40. M. Taryba, S.V. Lamaka, D. Snihirova, M.G.S. Ferreira, M.F. Montemor, W.K. Wijting, S. Toews, C. Grundmeir. Electrochimica Acta 56 (2011) 4475.
41. D. Borisova, H. Möhwald, D.G. Shchukin. ACS Nano 5 (2011) 1939.
42. S.J. García, H.R. Fischer, P.A. White, J. Mardel, Y. González-García, J.M.C. Mol, A.E. Hughes. Progress in Organic Coatings 70 (2011) 142.
43. B. Kovács, B. Csóka, G. Nagy, I. Kapui, R.E. Gyurcsányi, K. Tóth. Electroanalysis 11 (1999) 349.

8.5

New opportunities for the study of organic films applied on metals for corrosion protection by means of alternating current scanning electrochemical microscopy

8.5.1. Abstract

A new method for the investigation of the inhibition efficiency against corrosion by organic films adsorbed on metals based on the measurement of Z-approach curves by AC-SECM is proposed. Preliminary measurements conducted on four copper-inhibitor systems exposed to aqueous solutions support that a characteristic frequency can be defined, which corresponds to the frequency of the AC potential signal applied to the SECM tip for which a transition between negative- and positive-feedback behaviours is observed in the approach curves. From the shift of this characteristic frequency towards higher values, the enhancement of the corrosion protection efficiency of the inhibitor system can be established. Furthermore, the effects of inhibitor nature, concentration, and pre-treatment duration for the formation of the surface films, can be readily investigated.

8.5.2. Resumen

Se propone un nuevo método para la investigación de la eficiencia inhibidora contra la corrosión por parte de películas orgánicas adsorbidas en metales, en base a la determinación de curvas de aproximación obtenidas mediante AC-SECM. Las medidas preliminares realizadas en cuatro sistemas cobre-inhibidor expuestos a disoluciones acuosas sostienen que puede definirse una frecuencia característica, la cual se corresponde con la frecuencia de la señal de potencial AC aplicado a la punta de SECM a la que se observa una transición desde el comportamiento de retroalimentación negativa a positiva en las curvas de aproximación. Se puede establecer la eficiencia del sistema inhibidor por el cambio de esta frecuencia característica a valores mayores. Además, se han podido investigar los efectos de la naturaleza del inhibidor, la concentración y la duración del tratamiento para la formación de las películas superficiales.

8.5.3. Introduction

The alternating current mode of AC-SECM was first employed to achieve a more sensitive determination of the tip-substrate distance in SECM aiming measurements to have greater resolution especially in the case of potentiometric operation [1,2]. In this way, application of a high frequency AC voltage signal to the tip, would facilitate more precise positioning since the resulting current signal flowing through the microelectrochemical cell greatly depends on the height of the electrolyte volume comprised between the tip and the substrate in electrolytes of sufficiently low conductivity [1,3]. Later studies demonstrated that the current response of the system is also affected by the conductive/insulating nature of the substrate, thus opening a wide range of applications for surface activity screening using more extended frequency ranges for the potential perturbation [4-6]. Applications of this technique to the study of corrosion processes have been demonstrated subsequently, namely for the detection of pinholes in coated metals [7], the monitoring of corrosion pits in otherwise passive metals [8], the visualization of selective dissolution reactions of alloys [9], and the characterization of thin inhibitor films on metals [10,11]. In the latter case, this technique has been successfully employed to follow the kinetics of film formation [10], to characterize the corrosion resistance of the resulting metal-inhibitor films [11], and to visualize the degradation of these films under the corrosive attack of the environment [11].

Because the effectiveness of organic inhibitors is related to the extent to which they adsorb and cover the metal oxide surface, and AC-SECM is highly sensitive to the conductive/insulating characteristics of the resulting inhibitor films formed on the metals, it has been considered that the following step of this kind of studies would be the establishment of a platform for inhibitor screening using this technique based on determinations of inhibitor efficiencies for different inhibitor-metal systems. Usually, the efficiency of inhibitor systems is determined from gravimetric and electrochemical methods, with the highest resolution being provided by electrochemical impedance spectroscopy (EIS) [12-18], and the electrochemical quartz crystal microbalance (EQMC) [19-24]. Nevertheless, these techniques average the behaviour of all the surface exposed to the environment and do not provide direct information on the structure and composition of the surface films. This is the rationale for the use of *ex situ* surface analytical techniques in these investigations too, namely X-ray photoelectron spectroscopy (XPS), Auger electron spectroscopy (AES), secondary ion mass spectrometry (SIMS), and laser micro mass analysis (LAMMA) [25-30]. Again these techniques exclusively provide global information as they lack enough spatial resolution, which is demanded to better understand the nature of the interactions and processes responsible for the inhibiting effect. Such knowledge is highly needed to elucidate the mechanisms involved, and it would facilitate inhibition to be optimized. This is the justification for the application of scanning probe microscopies (SPM) in this research area. Yet, their application has been exclusively directed to monitor how metal dissolution in acids is affected by the presence of inhibitor films previously formed on the metal

samples. Such effect is then evaluated by imaging the surface morphological changes occurring in micrometer and nanometer scales after various degrees of corrosive attack [31-35].

In this Section, four well-known corrosion inhibitor molecules against copper corrosion were considered as model systems for the investigation. The organic molecules are benzotriazole (BTAH), 5-methyl-benzotriazole (MBTAH), 2-mercaptobenzimidazole (MBI), and ethyl xanthate (KEX). This choice of inhibitors allows us to take advantage of the relative inhibition efficiencies of these compounds, as to check information rendered by the new methodology based in the use of AC-SECM.

8.5.4. Experimental

8.5.4.1. Materials

The metallic substrates were 99.99% purity copper plates, supplied by Goodfellow (Cambridge, United Kingdom), which were cut to 2.4 cm x 2.4 cm and 1 mm thickness. The surface of the samples was ground mechanically using metallographic emery paper to a 1500 grit finish, degreased with acetone, rinsed with *MilliQ* grade water and dried to air. For the preparation of the inhibitive films on the copper samples, the metal plates were immersed in 0.1 M KCl solutions containing 0.1 mM concentration of the chosen inhibitor for different immersion times. Benzotriazole (Avocado Research Chemicals Ltd., UK), 5-methyl-1H-benzotriazole (Aldrich, USA), 2-mercaptobenzimidazole (Aldrich, UK), and potassium ethyl xanthate (Fluka Chemica, Switzerland) were used as received. All aqueous solutions were prepared using ultra-pure water purified with a Milli-Q system from Millipore.

8.5.4.2. Experimental procedure

The SECM experiments were carried out using an AC-SECM built by Sensolitycs (Bochum, Germany), controlled with a personal computer. The electrochemical interface was an Autolab (Ecochemie, Utrecht, The Netherlands) electrochemical interface consisting of a bipotentiostat and a frequency response analyzer, though the system was operated in a three-electrode configuration since the coated sample was left unbiased for the duration of the experiments. Platinum microelectrodes (dia. 25 μm) were employed as AC-SECM tips. An Ag/AgCl/KCl (sat.) reference electrode and a platinum wire used as counter electrode were also introduced in the small electrochemical cell, which was placed inside a Faraday cage. AC voltage signals of 100 mV_{pp} amplitude were applied in the 351 to 55493 Hz frequency range. A total of 26 frequency values were used, and the values spaced logarithmically. For the sake of clarity, only selected frequencies have been

included in the plots. Testing was performed in naturally aerated 1 mM Na_2SO_4 aqueous solution at ambient temperature.

8.5.5. Results and discussion

AC-SECM probes surface reactivity by recording Z-approach curves as the ultramicroelectrode approaches the sample. They are plotted as the magnitude of the dimensionless tip current (i.e. the ratio between the current value at each location to the stationary value measured in the bulk of the electrolyte), and *d*/*a* is the dimensionless distance between the sample and the tip. The samples were left at their spontaneous open circuit potentials in the test electrolyte.

In the case of an insulating surface such as that of glass at the bottom of the electrochemical cell exposed to 1 mM KCl, the approach curves show smaller currents than in the bulk of the electrolyte when the microelectrode moves closer to the glass surface (see Figure 8.5.1). Though the extent of such decrease varies with the applied AC frequency for a given tip-substrate distance, such a "negative feedback" behaviour occurs at all frequencies. The term "negative feedback" has been taken from the conventional amperometric SECM operation that uses a reversible diffusing redox mediator [36] for imaging. In that situation, an insulating substrate hinders diffusion of this species to the reactive surface of the tip thus leading to the measurement of smaller faradaic currents.

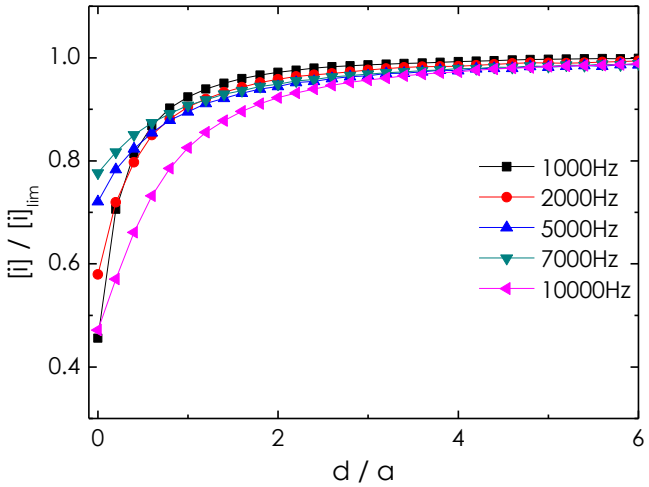

Figure 8.5.1. AC-SECM normalized Z-approach curves towards the glass bottom of the cell immersed in 1 mM Na_2SO_4 solution with a 25 μm electrode. $[i] / [i]_{lim}$ is the dimensionless AC tip current and *d* / *a* is the dimensionless tip-substrate distance. The excitation signal amplitude was 100 mV_{pp} and frequencies in Hz are indicated in the figure legend.

In the case of untreated copper, which is a conductive substrate, when it is immersed in 1 mM Na_2SO_4, two trends are observed for the variation of the current

magnitude with the tip-substrate distance within the frequency range as shown in Figure 8.5.2. First, negative-feedback type Z-approach curves are measured in the low AC frequency range applied, whereas the opposite occurs at higher frequencies. In the later, the current magnitude progressively increases from its value in the bulk electrolyte as the tip moves towards the sample, and thus it exhibits "positive-feedback" behaviour. The magnitude of this positive feedback type effect is observed to be dependent on the frequency of the AC signal, and it is highest at the high frequency limit. The Z-approach curve determined at the frequency of 8966 Hz only exhibits a weak positive feedback effect. Obviously, this frequency value is only slightly higher than the frequency at which the transition from negative to positive feedback type behaviour occurs.

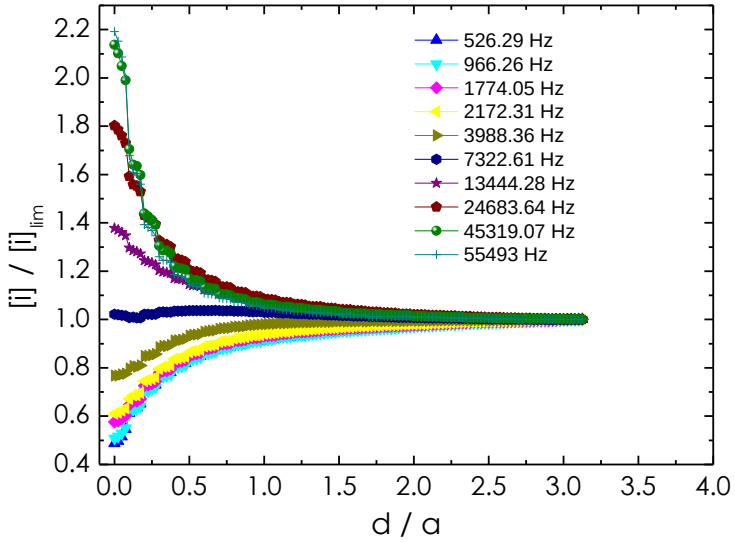

Figure 8.5.2. AC-SECM normalized Z-approach curves towards a freshly-polished Cu sample immersed in 1 mM Na_2SO_4 solution with a 25 μm electrode. $[i] / [i]_{lim}$ is the dimensionless AC tip current and d / a is the dimensionless tip-substrate distance. The excitation signal amplitude was 100 mV_{pp} and selected frequencies are indicated in the figure legend. The sample was left at its spontaneous open circuit potentials in the test electrolyte.

The protection characteristics conferred to copper surfaces by the organic molecules should result in a modification of the conductive properties of the surface, progressively adopting a more insulating behaviour as the adsorbed film becomes an effective barrier to electron transfer [37,38], was investigated by recording Z-approach curves as the ultramicroelectrode approaches the sample. The inhibitor molecules considered in this Section were benzotriazole (BTAH), 5-methyl-1H-benzotriazole (MBTAH), 2-mercaptobenzimidazole (MBI), and potassium ethyl xanthate (KEX). Inhibitor films were produced on the copper electrode *ex situ* by dipping the freshly polished metal samples in a 100 mM KCl + 0.1 mM inhibitor solution for controlled immersion times. Figure 8.5.3 shows some Z-approach curves measured for inhibitor-treated copper samples during immersion in 1 mM Na_2SO_4. They correspond to the four inhibitor molecules after two different pre-treatment durations (namely 5 and 45 min, respectively).

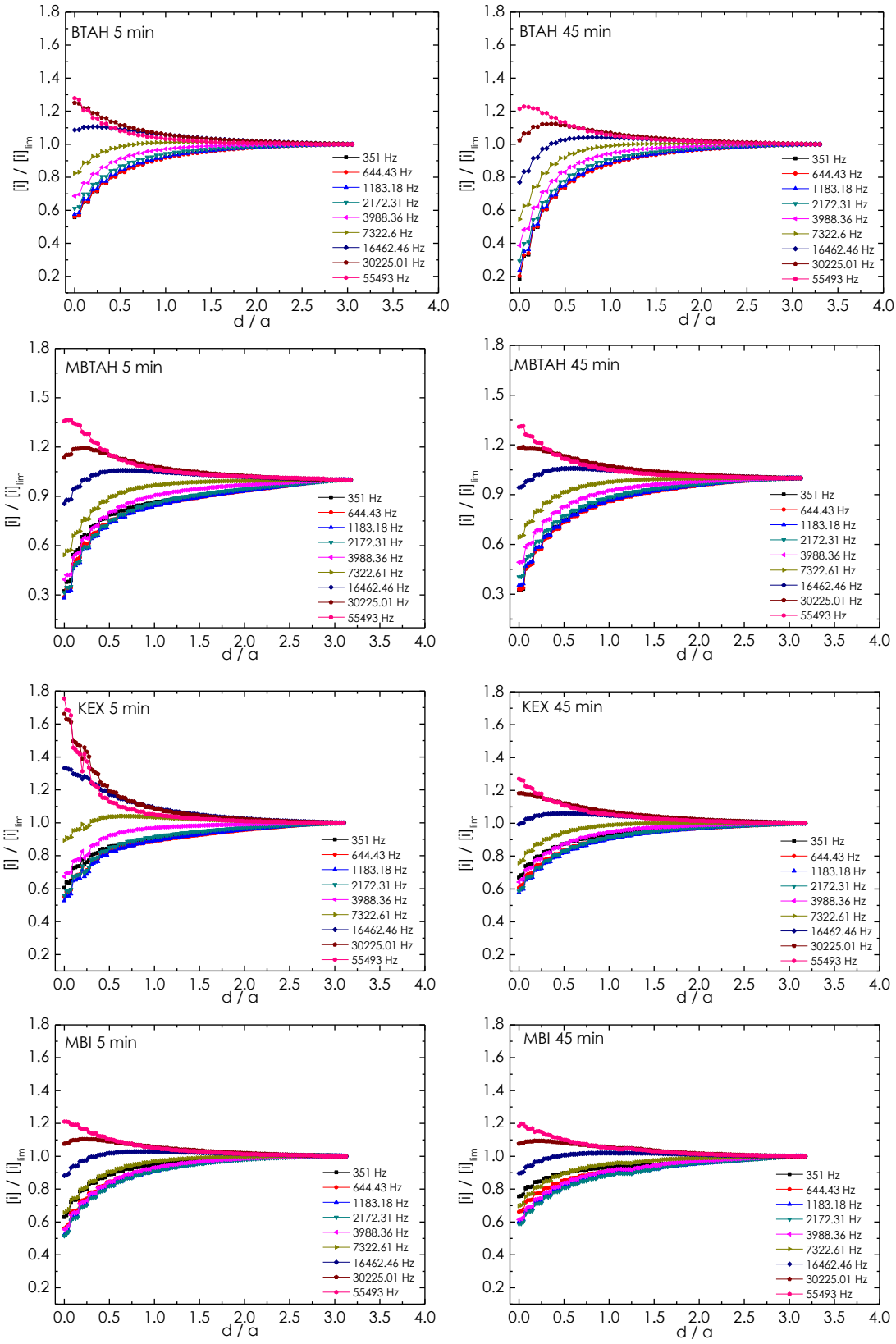

Figure 8.5.3. AC-SECM normalized Z-approach curves towards inhibitor-treated Cu samples immersed in 1 mM Na_2SO_4 solution with a 25 µm electrode. The inhibitors used and the duration of pre-treatments are indicated in the figure. $[i] / [i]_{lim}$ is the dimensionless AC tip current and d / a is the dimensionless tip-substrate distance. The excitation signal amplitude was 100 mV_{pp} and selected frequencies are indicated in the figure legend. The samples were left at their spontaneous open circuit potentials in the test electrolyte.

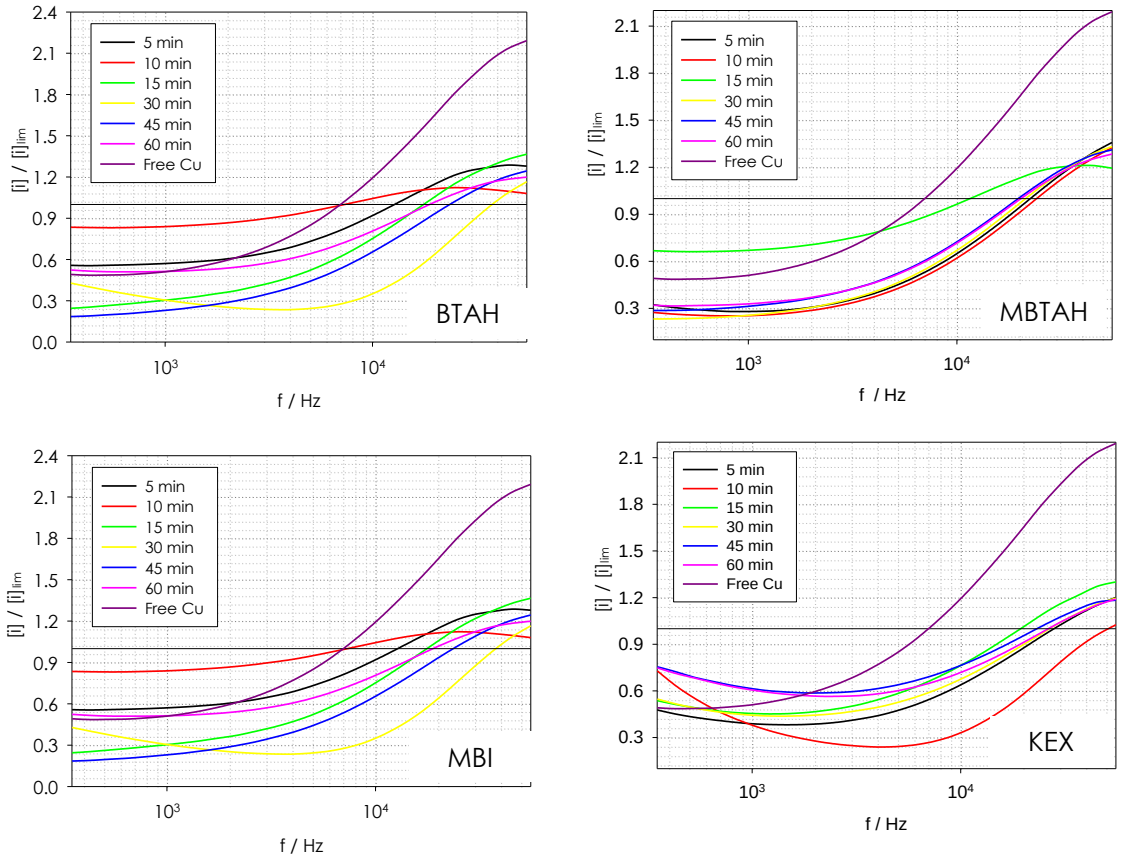

Figure 8.5.4. Frequency dependence of the normalized current magnitude values determined from Z-approach curves towards inhibitor-treated Cu samples immersed in 1 mM Na_2SO_4 solution with a 25 µm electrode. The inhibitors used and the duration of pre-treatments are indicated in the figure. *[i] / [i]lim* is the dimensionless AC tip current and *d / a* is the dimensionless tip-substrate distance. For the sake of comparison, the frequency dependence of the normalized currents for a freshly polished copper sample immersed in the test solution has also been included in the graphs.

Both positive- and negative-feedback trends are observed in all the cases, though the frequency range for either behaviour is observed to vary with both the nature of the inhibitor and the duration of the pre-treatment. In general, longer treatments lead to a narrower frequency range in which the positive-feedback is observed, a feature that is more pronounced in the case of the samples treated with KEX, and the smallest changes are presented by MBI and MBTAH. This observation indicates that the blocking characteristics towards electron transfer can be followed from the shift of the frequency ranges for positive- and negative-feedback behaviours as determined from AC-SECM approach curves. Therefore, the frequency distribution of the normalized current values at the distance of closest approach can be used to follow the formation of insulating films of inhibitors on active metals, and to characterize the inhibiting frequency of metal-inhibitor systems. **Figure 8.5.4** shows the resulting magnitude-frequency plots for the four model inhibitor systems, in which the behaviour for untreated copper has also been included. It can be readily observed that there is a shift in the characteristic

frequency for the transition between negative- and positive-feedback behaviours to higher values with thicker inhibitor films. These graphs also allow to observe that the inhibitor films formed with BTAH and MBTAH after 5 minutes immersion exhibit similar characteristics to those obtained at longer exposures, whereas longer exposures are necessary to form the thicker films with KEX. Additionally, aging of inhibitor films leading to a more compact layer is suggested to be responsible for the shift of the current magnitude values measured at the lowest AC frequencies with the elapse of time for the Cu-BTAH system, though this explanation is only tentative at this stage and requires further investigation.

8.5.6. Conclusions

Though the work is still in a rather preliminary stage, it can be regarded as a novel experimental methodology to investigate the protection skills and the kinetics of film formation for metal-inhibitor systems by AC-SECM has been developed. The inhibitor films can be described on the basis of the transition frequency values between negative- and positive-feedback behaviours determined from Z-approach curves. This method is highly sensitive, and may offer new insights in the study of corrosion inhibition by organic films applied on metals.

8.5.7. References

1. B.R. Horrocks, D. Schmidtke, A. Heller, A.J. Bard. Analytical Chemistry 65 (1993) 3605.
2. M.A. Alpuche-Aviles, D.O. Wipf. Analytical Chemistry 73 (2001) 4873.
3. R.T. Kurulugama, D.O. Wipf, S.A. Takacs, S. Pongmayteegul, P.A. Garris, J.E. Baur. Analytical Chemistry 77 (2005) 1111.
4. A.S. Baranski, P.M. Diakowski. Journal of Solid State Electrochemistry 8 (2004) 683.
5. M. Etienne, A. Schulte, W. Schuhmann. Electrochemistry Communications 6 (2004) 288.
6. P.M. Diakowski, A.S. Baranski. Electrochimica Acta 52 (2006) 854.
7. B.B. Katemann, C.G. Inchauspe, P.A. Castro, A. Schulte, E.J. Calvo, W. Schuhmann. Electrochimica Acta 48 (2003) 1115.
8. K. Eckhard, T. Erichsen, M. Stratmann, W. Schuhman. Chemistry - A European Journal 14 (2008) 3968.
9. D. Ruhlig, H. Gugel, A. Schulte, W. Theisen, W. Schuhmann. Analyst 133 (2008) 1700.
10. M. Pähler, J.J. Santana, W. Schuhmann, R.M. Souto. Chemistry - A European Journal 17 (2011) 905.

11. J.J. Santana, M. Pähler, W. Schuhmann, R.M. Souto. Electrochimica Acta 77 (2012) 60.
12. J.B. Cotton, I.R. Scholes. British Corrosion Journal 2 (1967) 1.
13. G.W. Poling. Corrosion Science 10 (1970) 359.
14. M.M. Laz, R.M. Souto, S. González, R.C. Salvarezza, A.J. Arvia. Journal of Applied Electrochemistry 22 (1992) 1129.
15. S. González, M.M. Laz, R.M. Souto, R.C. Salvarezza, A.J. Arvia. Corrosion 49 (1993) 450.
16. K. Rahmouni, N. Hajjaji, M. Keddam, A. Shriri, H. Takenouti, Electrochimica Acta 52 (2007) 7519.
17. M.M. Antonijević, S. Milić, M.B. Petrović. Corrosion Science 51 (2009) 1228.
18. J. Aljourani, K. Raeissi, M.A. Golozar. Corrosion Science 51 (2009) 1836.
19. Y. Yamamoto, H. Nishihara, K. Aramaki. Journal of the Electrochemical Society 140 (1993) 436.
20. N. Ohno, J. Uehara, K. Aramaki. Journal of the Electrochemical Society 140 (1993) 2512.
21. D. Jope, J. Sell, H.W. Pickering, K.G. Weil. Journal of the Electrochemical Society 142 (1995) 2170.
22. A. Shaban, E. Kálmán, J. Telegdi, Gy. Dóra. Journal of Applied Physics A 66 (1998) 545.
23. E. Szöcs, Gy. Vastag, A. Shaban, G. Konczos, E. Kálmán. Journal of Applied Electrochemistry 29 (1999) 1339.
24. Gy. Vastag, E. Szöcs, A. Shaban, I. Bertóti, K. Popov-Pergal, E. Kálmán. Solid State Ionics 141–142 (2001) 87.
25. R. Holm, D. Holtkamp, R. Kleinstück, H.-J. Rother, S. Storp. Fresenius' Journal of Analytical Chemistry 333 (1989) 546.
26. D.M. Briggs, M.P. Seah (Editors). Practical Surface Analysis, Vol. 1: AES and XPS. Wiley, New York, 1990.
27. R.V. Varma, J.R. Selman (Editors). Techniques for Characterization of Electrodes and Electrochemical Processes. Wiley, New York, 1991.
28. R.M. Souto, V. Fox, M. Pérez, M.M. Laz, S. González. Materials Science Forum 192-194 (1995) 385.
29. R.M. Souto, V. Fox, M.M. Laz, M. Pérez, S. González. Journal of Electroanalytical Chemistry 411 (1996) 161.
30. T. Kosec, D.K. Merl, I. Milošev. Corrosion Science 50 (2008) 1987.
31. B.J. Cruickshank, A.A. Gewirth, R.M. Rynders, R. Alkire. Journal of the Electrochemical Society 139 (1992) 2829.
32. M.R. Vogt, A. Lachenwitzer, O.M. Magnussen, R.J. Behm. Surface Science 399 (1998) 49.
33. W. Polewska, M.R. Vogt, O.M. Magnussen, R.J. Behm. Journal of Physical Chemistry B 103 (1999) 10440.
34. E. Szöcs, I. Bakó, T. Kosztolányi, I. Bertóti, E. Kálmán. Electrochimica Acta 49 (2004) 1371.
35. A. Paszternák, S. Stichleutner, I. Felhösi, Z. Keresztes, F. Nagy, E. Kuzmann, A. Vértes, Z. Homonnay, G. Petö, E. Kálmán. Electrochimica Acta 53 (2007) 337.

36. A.J. Bard, F.-R.F. Fan, M. Mirkin. In: Electroanalytical Chemistry, Vol. 18 (Edited by A.J. Bard). Marcel Dekker, New York, 1994, p. 243.
37. J. Izquierdo, J.J. Santana, S. González, R.M. Souto. Electrochimica Acta 55 (2010) 8791.
38. J. Izquierdo, J.J. Santana, S. González, R.M. Souto. Progress in Organic Coatings 74 (2012) 526.

8.6

Main conclusions

1. SECM and SVET techniques have been successfully employed for the characterization of spontaneously-formed organic inhibitor films on copper substrates, spatially resolving the eventual heterogeneities in chemical reactivity. Complementary information regarding the kinetics and the protection abilities of these layers could be imaged with the appropriate experimental procedures, thus avoiding the interference of the organic substance towards the sensing probe.

2. The kinetics of the benzotriazole and 2-mercaptobenzimidazole adsorption on copper was studied through the electrochemical activity of substrates by using the SECM in the conventional feedback mode. This operation, complemented by SVET employment for the visualization of the ionic fluxes, confirmed the positive influence of the presence of chloride ions in the base electrolyte for the faster formation of more durable protective layers.

3. A novel experimental procedure, based on the use of a galvanic Fe-Cu couple, was developed for the separate characterization of the cathodic inhibitor behaviour of the spontaneously formed inhibitor films on the metal. The combination of potentiometric and amperometric SECM operation allowed determination of the anodic and cathodic activities from the analysis of pH and oxygen consumption distributions. This unambiguous localization of the half-cell reactions occurring in the corroding system was supported by SVET measurements.

4. A novel experimental methodology to further investigate the protection skills and the kinetics of the films formation by AC-SECM has been developed. Preliminary results showing the transition frequency values between negative- and positive-feedback behaviours, determined from Z-approach curves, suggest that this method may offer new insights in the study of corrosion inhibition by organic films applied on metals with great sensitivity.

8.7

Conclusiones

1. Se han empleado con éxito las técnicas SECM y SVET para la caracterización de películas de inhibidores orgánicos formadas espontáneamente sobre substratos de cobre, resolviendo espacialmente las heterogeneidades en la reactividad química. Se ha podido visualizar información complementaria acerca de la cinética y las capacidades protectoras de dichas capas con los procedimientos experimentales apropiados, evitando además la interferencia de la substancia orgánica sobre la punta sensor.

2. Se ha estudiado la cinética de adsorción del benzotriazol y del 2-mercaptobenzimidazol en cobre a través de la visualización de la actividad electroquímica de los substratos mediante el uso del SECM en el modo convencional de retroalimentación. Esta operación, complementada por el empleo del SVET para la visualización de los flujos iónicos, confirma la influencia positiva de la presencia de iones cloruros en el electrolito de base en la formación más acelerada de capas protectoras, de mayor duración.

3. Se ha desarrollado un nuevo procedimiento experimental, basado en el uso de un acoplamiento galvánico Fe-Cu, para caracterizar separadamente el comportamiento de inhibición catódica de películas de inhibidores formadas espontáneamente sobre el metal. La combinación de la técnica amperométrica y potenciométrica en el SECM ha permitido la determinación de la actividad anódica y catódica a través del análisis de la distribución del pH y del consumo de oxígeno. Esta localización inequívoca de las reacciones de semi-celda que ocurren en los sistemas de corrosión se ha confirmado mediante medidas de SVET.

4. Se ha desarrollado una nueva metodología experimental para la investigación adicional de las habilidades protectoras y la cinética de formación de películas por AC-SECM. Los resultados preliminares muestran una transición de valores de frecuencia entre los comportamientos de retroalimentación negativa y positiva, determinados por curvas de aproximación. Ello sugiere que este método puede ofrecer nuevas revelaciones en el estudio de inhibición de la corrosión por moléculas orgánicas aplicadas sobre metales con gran sensibilidad.

CHAPTER 9

Conclusions

Index

9.1

Conclusions

Chemical imaging of reactive surfaces with high spatial resolution has become available with the use of scanning microelectrochemical methods. A power combination of SVET, SECM, AC-SECM and integrated AFM/SECM were employed to gather complementary information on the onset of corrosion reactions in a wide variety of technologically interesting materials, as well as to effectively characterize the protection efficiency of different protection methods. The main advantage of these methods is their ability to detect and quantify the electrochemical activity of materials related to the onset of degradation reactions with spatial resolution.

The application of scanning electrochemical microscopy in conventional amperometric mode has facilitated an advance in the understanding of corrosion reactions, by enabling the highly localized early stages of the process to be analyzed. But amperometric microdisks exhibit serious limitations for the quantification of some species of interest, mainly metal cations with sufficiently negative redox potentials for which the faradaic current associated with their reduction cannot be separated from the total current in the system. Next, local pH evolution can only be efficiently monitored by potentiometric operation with the use of ion selective microelectrodes. Since dual amperometric/potentiometric operation can be achieved in SECM, the quasi-simultaneous analysis of most of reactions involved in the corrosion phenomena is feasible.

Good agreement between the information provided by SVET and the new operation modes in SECM is the rule. Yet some apparent discrepancies originating from the localized nature of the dissolution process occurring on zinc, and the new evidences of an extension of the cathodic activity to this metal, were noticed. They originate from the different tip-substrate distances typically employed in both methods, but they were resolved by rastering the vibrating probe closer to the substrate.

Ion-selective microelectrodes (ISME) probes have been developed that can be employed as SECM tips as they exhibit sufficiently low resistances and response times. The applicability of this experimental approach was demonstrated by chemically imaging the behaviour of iron-zinc, iron-copper and iron-magnesium galvanic couples immersed in aqueous electrolyte. The dissolution of metal ions from anodic sites, the consumption of oxygen at the cathodic sites, and the local pH changes associated with both half-cell reactions are thus effectively monitored. In this way, novel contributions

towards elucidation of the mechanism responsible for the degradation of magnesium and its alloys in aqueous environments was provided from identification of the species participating in the local microcells distributed on the materials during their heterogeneous corrosion.

Heterogeneities in passivating oxide films related to microstructural differences in either the surface layers or the base material, localization of corrosion precursor sites and local defects in protective organic films, as well as monitoring of actively corroding pits, have been successfully visualised. Since the lateral electrochemical contrast differs among the techniques, and it can be further tuned by adequate selection of certain operation parameters, the proposed approach constitutes an indispensable tool for obtaining optimum electrochemical contrast.

9.2

Conclusiones

El uso de los métodos microelectroquímicos de barrido ha hecho posible el análisis químico local de superficies reactivas. Se han empleado poderosas combinaciones de SVET, SECM, AC-SECM e integración AFM/SECM para recoger información complementaria del comienzo de las reacciones de corrosión en una amplia variedad de materiales de interés tecnológico, así como caracterizar de forma efectiva la eficiencia de las diferentes estrategias de protección. La principal ventaja de estos métodos es su habilidad para detectar y cuantificar con resolución espacial la actividad electroquímica de los materiales relacionada con las etapas iniciales de las reacciones de degradación.

Con la aplicación de la microscopía electroquímica de barrido en el modo amperométrico convencional, se ha facilitado el entendimiento de las reacciones de corrosión, permitiendo el análisis altamente localizado de las etapas iniciales del proceso. Sin embargo, los microdiscos amperométricos exhiben serias limitaciones para la cuantificación de algunas especies de interés, particularmente cationes metálicos con potencial redox suficientemente negativo como para que la corriente faradáica asociada a su reducción no pueda ser distinguida de la corriente total del sistema. Además, las alteraciones locales de pH sólo pueden seguirse eficientemente a través de la operación potenciométrica, solo permitida por los microelectrodos de ion selectivo. Dado que se puede aplicar la operación dual amperométrica/potenciométrica con el SECM, el análisis quasi-simultáneo de la mayoría de las reacciones involucradas en los fenómenos de corrosión resulta factible.

La coherencia entre la información facilitada por el SVET y por los modos de operación del SECM es fundamental. Pese a ello, aparentemente se han observado discrepancias durante el análisis de la naturaleza localizada del proceso de disolución que tiene lugar en el cinc, con nuevas evidencias de cierta extensión de actividad catódica en este metal. Estas discrepancias se originaron por las diferentes distancias punta-substrato empleadas habitualmente en ambos métodos, pero se resuelven adecuadamente barriendo con la punta vibrante más cerca de la superficie.

Se han desarrollado sensores basados en electrodos de ion selectivo (ISME) utilizables como puntas de SECM, al mostrar resistencias y tiempos de respuesta suficientemente bajos. La aplicabilidad de esta aproximación experimental ha demostrado ser capaz de resolver químicamente el

comportamiento localizado de acoplamientos galvánicos de hierro-cinc, hierro-cobre y hierro-magnesio expuestos a electrolitos acuosos. Con ello, se ha seguido de forma efectiva la disolución de iones metálicos de sitios anódicos, el consumo de oxígeno en sitios catódicos, y los cambios locales de pH asociados con ambas semirreacciones. De esta forma, se han aportado nuevas contribuciones orientadas a la elucidación del mecanismo responsable de la corrosión del magnesio y sus aleaciones en ambientes acuosos, a través de la identificación de las especies que participan en las reacciones heterogéneas que tienen lugar en las microceldas locales distribuidas por la superficie el material.

Se han visualizado con éxito las heterogeneidades de la película pasiva de óxidos relacionadas con diferencias microestructurales, tanto en las capas superficiales como en el material de base; la localización de sitios precursores de la corrosión en defectos locales de películas orgánicas protectoras, así como el seguimiento de la corrosión activa en picaduras. Dado que el contraste electroquímico espacial difiere entre las distintas técnicas, y que puede ser selectivo a través de la adecuada elección de ciertos parámetros de operación, las aproximaciones propuestas constituyen herramientas indispensables para obtener un contraste electroquímico óptimo.